



University
of Glasgow

Zmuda, Filip (2016) *Development of radiotracers for nuclear imaging of poly(ADP-ribose) polymerase-1 and the translocator protein in glioblastoma*. PhD thesis.

<http://theses.gla.ac.uk/7498/>

Copyright and moral rights for this thesis are retained by the author

A copy can be downloaded for personal non-commercial research or study

This thesis cannot be reproduced or quoted extensively from without first obtaining permission in writing from the Author

The content must not be changed in any way or sold commercially in any format or medium without the formal permission of the Author

When referring to this work, full bibliographic details including the author, title, awarding institution and date of the thesis must be given

**DEVELOPMENT OF RADIOTRACERS FOR NUCLEAR
IMAGING OF POLY(ADP-RIBOSE) POLYMERASE-1
AND THE TRANSLOCATOR PROTEIN IN
GLIOBLASTOMA.**

Filip Zmuda

MPharm (Hons)

Submitted in the fulfilment of the requirements for the Degree of Doctor of
Philosophy at the College of Medical, Veterinary & Life Sciences, University of
Glasgow.

College of Medical, Veterinary & Life Sciences

University of Glasgow

April, 2016.



**University
of Glasgow** | College of Medical,
Veterinary & Life Sciences

ABSTRACT

Glioblastoma (GBM) is a highly aggressive and fatal brain cancer that is associated with a number of diagnostic, therapeutic, and treatment monitoring challenges. At the time of writing, inhibition of a protein called poly (ADP-ribose) polymerase-1 (PARP-1) in combination with chemotherapy was being investigated as a novel approach for the treatment of these tumours. However, human studies have encountered toxicity problems due to sub-optimal PARP-1 inhibitor and chemotherapeutic dosing regimens. Nuclear imaging of PARP-1 could help to address these issues and provide additional insight into potential PARP-1 inhibitor resistance mechanisms. Furthermore, nuclear imaging of the translocator protein (TSPO) could be used to improve GBM diagnosis, pre-surgical planning, and treatment monitoring as TSPO is overexpressed by GBM lesions in good contrast to surrounding brain tissue. To date, relatively few nuclear imaging radiotracers have been discovered for PARP-1. On the other hand, numerous tracers exist for TSPO many of which have been investigated in humans. However, these TSPO radiotracers suffer from either poor pharmacokinetic properties or high sensitivity to human TSPO polymorphism that can affect their binding to TSPO. Bearing in mind the above and the high attrition rates associated with advancement of radiotracers to the clinic, there is a need for novel radiotracers that can be used to image PARP-1 and TSPO. This thesis reports the pre-clinical discovery programme that led to the identification of two potent PARP-1 inhibitors, **4** and **17**, that were successfully radiolabelled to generate the potential SPECT and PET imaging agents [^{123}I]-**4** and [^{18}F]-**17** respectively. Evaluation of these radiotracers in mice bearing subcutaneous human GBM xenografts using *ex vivo* biodistribution techniques revealed that the agents were retained in tumour tissue due to specific PARP-1 binding. This thesis also describes the pre-clinical *in vivo* evaluation of [^{18}F]-AB5186, which is a novel radiotracer discovered previously within the research group with potential for PET imaging of TSPO. Using *ex vivo* autoradiography and PET imaging the agent was revealed to accumulate in intracranial human GBM tumour xenografts in good contrast to surrounding brain tissue, which was due to specific binding to TSPO. The *in vivo* data for all three radiolabelled compounds warrants further pre-clinical investigations with potential for clinical advancement in mind.

TABLE OF CONTENTS

Abstract	2
List of Figures	9
List of Schemes	14
List of Tables	17
Acknowledgements	18
Authors Declaration	20
Abbreviations	21
1 Introduction.	27
1.1 Glioblastoma.	27
1.1.1 Epidemiology, aetiology, and pathophysiology.....	27
1.1.2 Diagnosis.	29
1.1.3 Treatment and prognosis.	31
1.2 Nuclear imaging.	34
1.2.1 Technology (SPECT and PET).....	34
1.2.2 Strengths and weaknesses.	38
1.2.3 Nuclear imaging of glioblastoma	41
1.3 Poly(ADP-ribose) polymerase (PARP).	43
1.3.1 What is PARP and what does it do?	43
1.3.2 PARP-1 in glioblastoma and other cancers.	54
1.3.2.1 PARP-1 inhibitors.....	55
1.3.2.2 PARP-1 inhibition and synthetic lethality.....	60
1.3.2.3 PARP-1 inhibition and chemoradiosensitisation.	63
1.3.3 Nuclear imaging of PARP-1.	67
1.3.3.1 Applications in glioblastoma and other cancers.	67
1.3.3.2 Existing tracers for PARP-1.	69
1.4 The translocator protein (TSPO).	71
1.4.1 What is TSPO and what does it do?	71
1.4.2 TSPO in glioblastoma and other conditions.	74
1.4.3 Nuclear imaging of TSPO.	76
1.4.3.1 Applications in glioblastoma and other conditions.....	76
1.4.3.2 Existing tracers for TSPO.....	79
1.5 Radiotracer discovery and development.	82
1.5.1 Discovery and development pipeline.	82

1.5.2	From the laboratory to the clinic.	85
1.6	Aims and objectives.	86
2.	Thesis Outline.	87
3	Synthesising PARP-1 ligands with potential for nuclear imaging.	89
3.1	Introduction.	89
3.1.1	PARP inhibitor binding.	89
3.1.2	Olaparib core as a pharmacophore.	92
3.1.3	Aims and hypotheses.	94
3.2	Results and discussion.	94
3.3	Conclusion.	104
3.4	Experimental.	105
3.4.1	General experimental.	105
3.4.2	Experimental data for all synthesised compounds.	106
4	Identifying lead PARP-1 ligands with potential for nuclear imaging.	123
4.1	Introduction.	123
4.1.1	PARP-1 inhibitory potency.	123
4.1.2	Physicochemical properties and nuclear imaging.	126
4.1.2.1	Log P_{oct} and %PPB.	126
4.1.2.2	Physicochemical parameters and nuclear imaging of the brain. .	130
4.1.2.3	Ascertaining the log P_{oct} and %PPB parameters using HPLC.	134
4.1.3	Aims and hypotheses.	140
4.2	Results and discussion.	141
4.3	Conclusion.	151
4.4	Experimental.	152
4.4.1	General experimental.	152
4.4.2	Cell-free PARP-1 IC_{50}	152
4.4.3	Log P_{oct} using HPLC.	153
4.4.4	%PPB using HPLC.	154
4.4.5	Cellular PARP-1 IC_{50}	155
5	Developing radiosyntheses for PARP-1 nuclear imaging agents.	157
5.1	Introduction.	157
5.1.1	SPECT radioiodination chemistry.	161
5.1.1.1	Electrophilic techniques.	161
5.1.1.2	Nucleophilic techniques.	163

5.1.2	PET radiofluorination chemistry.	165
5.1.2.1	Electrophilic techniques.	165
5.1.2.2	Nucleophilic techniques.	165
5.1.2.3	Other techniques.	172
5.1.3	Radiotracer purification and formulation.	174
5.1.4	Aims and hypotheses.	178
5.2	Results and discussion.	179
5.2.1	Radioiodination, purification, and formulation of target SPECT tracer [¹²³ I]-4.	179
5.2.2	Radiofluorination of the target PET tracer [¹⁸ F]-11.	194
5.2.3	Radiofluorination, purification, and formulation of target PET tracer [¹⁸ F]-17.	203
5.3	Conclusion.	215
5.4	Experimental.	216
5.4.1	General experimental.	216
5.4.2	Chemistry experimental.	218
5.4.2.1	Experimental data for all synthesised compounds.	218
5.4.2.2	Non-radioactive dediazonisation chemistry.	225
5.4.2.2.1	Iodo-dediazonisation of isolated diazonium tosylate salt 65	225
5.4.2.2.2	Iodo-dediazonisation of <i>in situ</i> generated diazonium tosylate salt 65	225
5.4.2.2.3	Fluoro-dediazonisation of <i>in situ</i> generated diazonium tosylate salt 65	226
5.4.2.2.4	Fluoro-dediazonisation of isolated diazonium tosylate salt 65	226
5.4.2.3	General experimental for screening of reaction conditions for Boc-deprotection of 73	226
5.4.3	Radiochemistry experimental.	227
5.4.3.1	Manual radiosynthesis of [¹²⁵ I]-4 via radioiodo-dediazonisation of isolated diazonium tosylate salt 65	227
5.4.3.2	Manual radiosynthesis of [¹²⁵ I]-4 via radioiodo-dediazonisation of <i>in situ</i> generated diazonium tosylate salt 65	228
5.4.3.3	Manual radiosynthesis (via radioiodo-debromination of the brominated precursor 60), specific activity measurements, purification and formulation of [¹²³ I]-4.	228
5.4.3.4	Manual radiosynthesis of [¹⁸ F]-11 via aromatic nucleophilic substitution of the nitro precursor 63	230

5.4.3.5 Manual radiosynthesis of [¹⁸ F]-11 via radiofluoro-dediazonisation of isolated diazonium tosylate 65.	230
5.4.3.6 Manual radiosynthesis (via aliphatic nucleophilic substitution of the chlorinated precursor 72), specific activity measurements, purification, and formulation of [¹⁸ F]-17.	231
6 <i>In vitro</i> stability and <i>ex vivo</i> evaluation of the PARP-1 nuclear imaging agents [¹²³I]-4 and [¹⁸F]-17	233
6.1 Introduction.	233
6.1.1 Blood plasma stability.	233
6.1.2 Metabolic stability.	235
6.1.3 <i>Ex vivo</i> biodistribution.	243
6.1.4 Aims and hypotheses.	245
6.2 Results and discussion.	247
6.2.1 <i>In vitro</i> plasma and metabolic stability of 4 and 17.	247
6.2.2 <i>Ex vivo</i> biodistribution and specificity of [¹²³ I]-4 and [¹⁸ F]-17.	251
6.3 Conclusion.	264
6.4 Experimental.	265
6.4.1 General.	265
6.4.2 <i>In vitro</i> plasma stability of 4 and 17.	266
6.4.3 <i>In vitro</i> intrinsic clearance of diclofenac, olaparib, 4 and 17.	267
6.4.4 Gamma-counter calibration.	269
6.4.5 U87MG-Luc2 cell culture and subcutaneous tumour implantation.	269
6.4.6 Immunohistochemistry.	270
6.4.7 <i>Ex vivo</i> biodistribution.	271
6.4.7.1 [¹²³ I]-4 pilot biodistribution study.	271
6.4.7.2 [¹²³ I]-4 biodistribution study.	272
6.4.7.3 [¹⁸ F]-17 biodistribution study.	272
6.4.8 <i>Ex vivo</i> biodistribution with pre-blockade.	273
6.4.8.1 [¹²³ I]-4.	273
6.4.8.2 [¹⁸ F]-17.	274
7 <i>In vivo</i> evaluation of the potential TSPO nuclear imaging agent [¹⁸F]-AB5186	275
7.1 Introduction.	275
7.1.1 Discovery of [¹⁸ F]-AB5186.	275
7.1.2 <i>Ex vivo</i> autoradiography.	278
7.1.3 Small animal <i>in vivo</i> bioluminescence imaging of glioblastoma. ..	279

7.1.4	Aims and hypotheses.	281
7.2	Results and discussion.	282
7.2.1	Radiofluorination, purification, and formulation of [¹⁸ F]-AB5186.	282
7.2.2	Intracranial U87MG-Luc2 glioblastoma xenograft model.	284
7.2.3	<i>Ex vivo</i> autoradiography and PET imaging.	287
7.3	Conclusion.	294
7.4	Experimental.	295
7.4.1	General.	295
7.4.2	Manual radiosynthesis (via aliphatic nucleophilic substitution of chlorinated precursor 77), purification, and formulation of [¹⁸ F]-AB5186.	296
7.4.3	U87MG-Luc2 cell culture, intracranial tumour implantation, and bioluminescence imaging.	297
7.4.4	Immunohistochemistry.	297
7.4.4.1	Paraffin embedded tissue.	297
7.4.4.2	Frozen tissue.	298
7.4.5	<i>Ex vivo</i> autoradiography.	299
7.4.6	PET/CT imaging.	300
8	Conclusions and future work.	301
9	Appendices.	310
9.1	Cell-free IC ₅₀ curves for olaparib and compounds 4–21	310
9.2	Log P _{oct} HPLC calibration curve acquired on C ₁₈ column.	313
9.3	%PPB HPLC calibration curve acquired using human serum albumin column.	313
9.4	G7 and T98G cellular IC ₅₀ curves for olaparib and compounds 4, 11, 13, 17, and 18	314
9.5	UV-HPLC chromatogram of compound 4	316
9.6	UV-HPLC chromatogram of a mixture of compounds 4 and 60	317
9.7	Specific activity UV-HPLC calibration curve for compound 4	318
9.8	Specific activity UV-HPLC calibration curve for compound 17	319
9.9	TIC, MS, and LC-UV (254 nm) chromatograms of compound 73	320
9.10	MS chromatogram and graphs of compound 4 and internal standard 60	321
9.11	MS chromatogram and graphs of compound 17 and internal standard 60	322
9.12	MS and LC-UV (254 nm) chromatograms of diclofenac and internal standard 60	323

9.13	<i>In vitro</i> human liver microsome metabolism of olaparib, 4 and 17....	324
9.14	UV-HPLC chromatogram of AB5186.	325
10	Bibliography	326

LIST OF FIGURES

Figure 1.1. Cross-sectional diagram of a SPECT scanner.	35
Figure 1.2. Cross-sectional diagram of a PET scanner.	37
Figure 1.3. Structure of nicotinamide adenine dinucleotide.....	44
Figure 1.4. Diagram outlining the mechanisms of PARP catalysed poly(ADP-ribose)ylation.....	45
Figure 1.5. Schematic outline of the pathways of DNA damage.....	46
Figure 1.6. Schematic outline of the DNA repair pathways	47
Figure 1.7. Schematic outline of the proposed model of short-patch and long-patch nucleotide DNA repair involving PARP.	49
Figure 1.8. Schematic outline of the proposed model of PARP independent short-patch and long-patch nucleotide DNA repair.....	50
Figure 1.9. Schematic outline of the classical non-homologous end-joining model.....	51
Figure 1.10. Schematic outline of the back-up non-homologous end-joining model.....	52
Figure 1.11. Schematic outline of the homologous recombination model	53
Figure 1.12. Structures of first generation PARP-1 inhibitors.....	56
Figure 1.13. Discovery of the PARP-1 inhibitor rucaparib.	57
Figure 1.14. Discovery of the PARP-1 inhibitor olaparib.....	58
Figure 1.15. Discovery of the PARP-1 inhibitor veliparib.	59
Figure 1.16. Structures of other, less clinically advanced, PARP-1 inhibitors...	60
Figure 1.17. Initially proposed and refined mechanistic models of PARP-1 inhibitor mediated synthetic lethality of cells with BRCA gene mutations.	61
Figure 1.18. Mechanistic models of PARP-1 inhibitor mediated chemo- and radiosensitisation.....	65
Figure 1.19. Selected PARP-1 radiotracers that have been published to date. .	70
Figure 1.20. Structures of the benzodiazepine and isoquinoline carboxamide TSPO ligands Ro5-4864 and PK11195 respectively	71
Figure 1.21. First generation radiotracers for TSPO	80
Figure 1.22. Second and third generation radiotracers for TSPO	81
Figure 1.23. Typical discovery and development pathways taken for therapeutic drugs and diagnostic agents.....	84
Figure 3.1. The key binding interactions between the PARP inhibitor PD128763 and the PARP-CF.....	89
Figure 3.2. Key binding interactions between the PARP inhibitors 4ANI, 3MBA, and NU1025 and the PARP-CF.....	90
Figure 3.3. <i>In silico</i> predicted binding interactions between the PARP inhibitors 1 and 2, based around the phthalazinone scaffold, and the PARP-CF.....	91
Figure 3.4. Proposed binding interactions between the PARP inhibitor olaparib and the PARP-1 active site	92
Figure 3.5. Structures of olaparib and potential PARP-1 SPECT and PET nuclear imaging agents	93

Figure 3.6. The phtahalzinone scaffold of olaparib.	94
Figure 3.7. Structures of olaparib and the non-radioactive analogues that were chosen as potential PARP-1 nuclear imaging agents.	95
Figure 4.1. The four compartment model	123
Figure 4.2. Diagrammatic representation of the PARP-1 cell-free Trevigen™ colorimetric assay.	125
Figure 4.3. Diagrammatic representation of the intermolecular forces which affect the partitioning of solute molecules between an octanol and water phase..	127
Figure 4.4. Schematic representation of how the lipophilic and plasma protein binding properties of a radiotracer can influence its <i>in vivo</i> clearance.....	128
Figure 4.5. A modified version of the four compartment model, which includes the arterial plasma protein bound compartment.....	129
Figure 4.6. Cellular and molecular diagram of the blood brain barrier..	131
Figure 4.7. Diagram showing the relationship between the lipophilic character of organic compounds and their distance travelled on a RP-TLC plate	135
Figure 4.8. Diagram showing the relationship between the lipophilic character of organic compounds and their retention time on a RP-HPLC column	136
Figure 4.9. A graph showing the positive linear correlation between HPLC calculated %PPB and log P _{oct} values for olaparib and compounds 4-9 and 11-21	145
Figure 4.10. Structures of olaparib and selected non-radioactive lead candidate compounds.	148
Figure 4.11. Representative images obtained using the PARP cellular immunofluorescent IC ₅₀ assay.	149
Figure 4.12. Structures of non-radioactive lead candidate compounds selected for radiolabelling methodology development	151
Figure 5.1. Examples of oxidising agents used in radioiodination chemistry. .	162
Figure 5.2. Examples of commonly used electrophilic radiofluorination species.	165
Figure 5.3. Diagrammatic representation of a solvated ¹⁸ F ⁻ radionuclide with weak nucleophilic properties and a ¹⁸ F ⁻ radionuclide trapped by a phase transfer agent with improved nucleophilic properties	166
Figure 5.4. Structures of the phase transfer agents Kryptofix® and tetra- <i>n</i> -butylammonium hydrogen carbonate (52).....	167
Figure 5.5. Proposed mechanism by which <i>tert</i> -butyl alcohol facilitates aliphatic nucleophilic radiofluorination	169
Figure 5.6. Diagrammatic representation of radiotracer purification using solid phase extraction (SPE).....	175
Figure 5.7. Diagrammatic representation of radiotracer purification using HPLC	176
Figure 5.8. Diagrammatic representation of solubility enhancement using a cyclodextrin excipient.	177
Figure 5.9. Target radioligands with potential for PARP-1 SPECT ([¹²³ I]-4) and PET ([¹⁸ F]-11 and [¹⁸ F]-17) imaging.....	178

Figure 5.10. An analytical radio-HPLC chromatogram of the crude reaction mixture outlined in Scheme 5.18 showing multiple side and degradation products, as well as ¹²⁵ I-labelled 4	183
Figure 5.11. An analytical UV-HPLC (267 nm) chromatogram of the crude reaction mixture outlined in Scheme 5.19.....	184
Figure 5.12. An analytical radio-HPLC chromatogram of the reaction mixture outlined in Scheme 5.20.....	186
Figure 5.13. An analytical UV (254 nm)/radio-HPLC chromatogram of the crude reaction mixture outlined in table 5.3 entry 3 showing unreacted [¹²⁵ I]-NaI and precursor compound 60 , as well as ¹²⁵ I-labelled 4	189
Figure 5.14. Optimal mobile phase preparatory HPLC gradient conditions used for purification of [¹²³ I]- 4 synthesised using aromatic solid state interhalogen exchange methodology	191
Figure 5.15. An analytical quality control UV (254 nm)/radio-HPLC chromatogram of [¹²³ I]- 4 showing >99% radiochemical purity of the radiotracer formulated in 10.0% v/v ethanol in 0.9% w/v saline.. ..	192
Figure 5.16. The chromatographic gradient used to measure the retention times of compounds 11 and 63 on an analytical reverse-phase C ₁₈ column and the corresponding UV-HPLC (254 nm) chromatograms.....	195
Figure 5.17. Chromatographic gradients used to separate a mixture of compounds 11 and 63 on an analytical reverse-phase C ₁₈ column and the corresponding UV-HPLC (254 nm) chromatograms.....	196
Figure 5.18. An analytical UV (254 nm)/radio-HPLC chromatogram of the crude reaction mixture outlined in table 5.4, entry 5b showing unreacted ¹⁸ F ⁻ and precursor compound 63 , as well as ¹⁸ F-labelled 11	199
Figure 5.19. ¹ H NMR spectra of compound 38 and the crude reaction mixture outlined in Scheme 5.29.....	205
Figure 5.20. The chromatographic gradient used to measure the retention times of compounds 17 and 72 on an analytical reverse-phase C ₁₈ column and the corresponding UV-HPLC (254 nm) chromatograms.....	209
Figure 5.21. Analytical radio-HPLC chromatograms of the crude reaction mixtures as outlined in Scheme 5.31 following radiofluorination and hydrochloric acid and water catalysed Boc-deprotection.....	212
Figure 5.22. Optimal mobile phase preparatory HPLC gradient conditions used for purification of [¹⁸ F]- 17 synthesised using aliphatic nucleophilic substitution radiofluorination methodology.	214
Figure 5.23. An analytical quality control UV (254 nm)/radio-HPLC chromatogram of [¹⁸ F]- 17 showing >99% radiochemical purity of the radiotracer formulated in 5.0% v/v dimethyl sulfoxide in 0.9% w/v saline	214
Figure 6.1. Schematic outlining the processes of organic compound elimination from the body.....	236
Figure 6.2. Diagrammatic representation of phase I and II metabolism.....	237
Figure 6.3. Diagrammatic representation of a radiotracer <i>ex vivo</i> biodistribution study in a subcutaneous tumour bearing mouse utilising a gamma-counter....	243
Figure 6.4. Potential sites of phase I metabolism of compounds 4 and 17	246

Figure 6.5. Graphs showing the percentage amount of unchanged 4 and 17 remaining after 0 and 20 hour incubations in mouse plasma	248
Figure 6.6. Graphs showing the natural logarithm (ln) percentage amount of unchanged diclofenac remaining after 0, 5, 15, 30 and 45 minute incubations in human liver microsomes.....	249
Figure 6.7. Calibration graphs showing the liner relationship between the amount of radioactive ¹²³ I or ¹⁸ F and the counts per minute (CPM) obtained using the Cobra II Auto-Gamma® counter.....	252
Figure 6.8. A graph showing the biodistribution (expressed as the percentage of injected dose per gram of tissue [%ID/g]) of [¹²³ I]-4 in healthy female black-6 mice 5 minutes and 30 minutes post tracer injection.	253
Figure 6.9. Photographs of a subcutaneous U87MG-Luc2 GBM tumour xenograft grown in a female CD1 nude mouse for 28 days, pre- and post-excision	255
Figure 6.10. Representative immunohistochemistry images of four subcutaneous U87MG-Luc2 GBM tumour xenografts grown in female CD1 nude mice, fixed, sectioned and stained with haematoxylin and eosin, and antibodies against Ki67 and PARP-1.	256
Figure 6.11. A graph showing the biodistribution (expressed as the percentage of injected dose per gram of tissue [%ID/g]) of [¹²³ I]-4 in subcutaneous U87Mg-Luc2 GBM bearing female CD1 nude mice 30 minutes, 60 minutes, and 120 minutes post tracer injection.....	257
Figure 6.12. A graph showing the biodistribution (expressed as the percentage of injected dose per gram of tissue [%ID/g]) of [¹⁸ F]-17 in subcutaneous U87Mg-Luc2 GBM bearing female CD1 nude mice 30 minutes, 60 minutes, and 120 minutes post tracer injection.....	258
Figure 6.13. Representative immunohistochemistry images of muscle tissue originating from the left femur of a subcutaneous U87MG-Luc2 GBM bearing female CD1 nude mice.....	261
Figure 6.14. A graph showing the organ to muscle ratio of percentage injected dose per gram of tissue (%ID/g) of [¹²³ I]-4 60 minutes after intravenous injection in subcutaneous U87Mg-Luc2 GBM bearing female CD1 nude mice that were pre-treated with either intraperitoneal vehicle or 50 mg/kg olaparib.	262
Figure 6.15. A graph showing the organ to muscle ratio of percentage injected dose per gram of tissue (%ID/g) of [¹⁸ F]-17 60 minutes after intravenous injection in subcutaneous U87Mg-Luc2 GBM bearing female CD1 nude mice pre-treated with either intraperitoneal vehicle or 50 mg/kg olaparib.....	263
Figure 7.1. Structures of PK11195 and AB5186.....	275
Figure 7.2. ¹¹ C-labelled azaisosteres of PK11195 that are not affected by single nucleotide polymorphism of TSPO	277
Figure 7.3. Diagrammatic representation of a radiotracer <i>ex vivo</i> autoradiography study using an intracranial tumour bearing mouse	278
Figure 7.4. Diagrammatic representation of bioluminescence imaging of a mouse bearing an intracranial tumour expressing the luciferase enzyme.....	280

- Figure 7.5.** An analytical quality control UV (267 nm)/radio-HPLC chromatogram of [¹⁸F]-AB5186 showing >99% radiochemical purity of the radiotracer formulated in 10.0% v/v ethanol in 0.9% w/v saline **283**
- Figure 7.6.** Representative immunohistochemistry images of a single intracranial U87MG-Luc2 GBM tumour and contralateral brain regions from a female CD1 nude mouse stained with haematoxylin and eosin and antibodies against Ki67, TSPO, and Iba1..... **285**
- Figure 7.7.** Representative bioluminescence image of intracranial U87MG-Luc2 tumours 15 days after implantation acquired using the IVIS[®] Spectrum **288**
- Figure 7.8.** Representative coronal brain autoradiograms, and immunohistochemistry images showing staining with haematoxylin and eosin and the anti-TSPO antibody obtained from intracranial U87MG-Luc2 GBM bearing female CD1 nude mice that were injected with either vehicle or 1 mg/kg PK11195 followed by [¹⁸F]-AB5186 10 minutes later **289**
- Figure 7.9.** A graph showing the ratios of autoradiogram tumour to contralateral side optical densities from vehicle control and PK11195 treated intracranial U87MG-Luc2 GBM bearing mice **290**
- Figure 7.10.** Summed dynamic PET data fused with manually co-registered CT of an intracranial U87MG-Luc2 GBM xenograft bearing mouse acquired following [¹⁸F]-AB5186 administration **291**
- Figure 7.11.** Averaged summed dynamic PET images of a U87MG-Luc2 GBM xenograft bearing mouse brain acquired following [¹⁸F]-AB5186 administration, and a coronal histochemistry image showing staining of the brain tissue with haematoxylin and eosin **292**
- Figure 7.12.** Time-activity curves of [¹⁸F]-AB5186 in the U87MG-Luc2 GBM tumour xenograft and contralateral brain regions and tracer kinetics expressed as a ratio of tumour to contralateral brain tissue standardised uptake values **294**

LIST OF SCHEMES

Scheme 1.1. Nuclear reactions used to generate the ^{123}I radionuclide and its subsequent decay.	35
Scheme 1.2. Nuclear reactions used to generate the ^{18}F and ^{11}C radionuclides and their subsequent decay.....	36
Scheme 3.1. Synthesis of the Boc-protected phthalazinone intermediate 31 ...	97
Scheme 3.2. Proposed mechanism for HBTU (33) mediated amide coupling of compounds 27 and 30	98
Scheme 3.3. Boc-deprotection of 31 to give access to the phthalazinone scaffold 3	99
Scheme 3.4. Initial retrosynthetic analysis of the olaparib analogue 17 utilising a late-stage nucleophilic fluorination step.	101
Scheme 3.5. Alternative retrosynthetic analysis of the fluorinated olaparib analogue 17 utilising an early-stage nucleophilic fluorination step.	102
Scheme 3.6. The synthetic approach used to access compound 42	102
Scheme 3.7. The synthetic approach used to access compound 17 from the benzyl chloride 42	104
Scheme 5.1. Electrophilic aromatic substitution of aniline analogue 43	159
Scheme 5.2. Organometal mediated aromatic electrophilic exchange reaction.	160
Scheme 5.3. Isotopic halogen exchange radioiodination.	164
Scheme 5.4. Interhalogen exchange radioiodination.....	164
Scheme 5.5. Radioiodo-dediazonisation.....	164
Scheme 5.6. Drying of solvated $^{18}\text{F}^-$ using Kryptofix [®] as a phase transfer agent.	167
Scheme 5.7. Drying of solvated $^{18}\text{F}^-$ using TBAHCO ₃ as a phase transfer agent resulting in the <i>in situ</i> formation of [^{18}F]-TBAF (53).	168
Scheme 5.8. An example of an aliphatic nucleophilic radiofluorination reaction.	168
Scheme 5.9. Examples of aromatic nucleophilic substitution radiofluorination reactions.	170
Scheme 5.10. An example of radiofluorination of a non-activated (electron rich) arene ring using an unsymmetrical diaryliodonium salt.	170
Scheme 5.11. The proposed ‘turnstile’ mechanism for the reaction between a nucleophile ($^{18}\text{F}^-$) and an unsymmetrical diaryliodonium salt.	171
Scheme 5.12. Examples of diaryliodonium radiofluorination reactions where, in the absence of the <i>ortho</i> -effect, chemoselectivity is achieved through the use of an electron-donating substituent and an electron-rich heteroaromatic moiety	171
Scheme 5.13. Decomposition pathways of diaryliodonium salts.....	172
Scheme 5.14. Nickel-mediated aromatic radiofluorination using aqueous $^{18}\text{F}^-$ in the presence of the hypervalent iodine oxidant 54	172

Scheme 5.15. Synthesis of the nickel organometallic precursor 58	173
Scheme 5.16. Proposed electrophilic destannylation technique to access the potential SPECT PARP-1 radiotracer [¹²³ I]- 4	180
Scheme 5.17. Synthetic approach used to access the diazonium tosylate salt precursor 65	181
Scheme 5.18. Generation of [¹²⁵ I]- 4 using radioiodo-dediazonisation methodology..	183
Scheme 5.19. Non-radioactive iodination of an <i>in situ</i> generated diazonium salt 65 giving access to 4	184
Scheme 5.20. Radioiodination of an <i>in situ</i> generated diazonium salt 65 giving access to [¹²⁵ I]- 4	185
Scheme 5.21. Optimised solid state interhalogen exchange radioiodination methodology for the synthesis of the potential PARP-1 SPECT imaging agent [¹²³ I]- 4 using the brominated precursor 60	190
Scheme 5.22. Radioiodination approach used by Salinas <i>et al.</i> (2015) for the synthesis of [¹³¹ I]- 4	193
Scheme 5.23. Proposed aromatic nucleophilic substitution radiofluorination approach for the synthesis of [¹⁸ F]- 11 using the nitro bearing precursor 63 ...	194
Scheme 5.24. Proposed aromatic nucleophilic substitution radiofluorination approach for the synthesis of [¹⁸ F]- 11 using the aromatic diazonium salt precursor 65	200
Scheme 5.25. Attempted non-radioactive fluoro-dediazonisation of the <i>in situ</i> generated diazonium salt 65 for the synthesis of 11 ..	201
Scheme 5.26. Attempted non-radioactive and radioactive fluoro-dediazonisation of the diazonium salt 65 for the synthesis of 11 and [¹⁸ F]- 11	202
Scheme 5.27. Radiofluorination approach used by Carney <i>et al.</i> (2015) to access [¹⁸ F]- 11	203
Scheme 5.28. Proposed aliphatic nucleophilic substitution radiofluorination approach for the synthesis of [¹⁸ F]- 17 using the aliphatic chlorinated precursor 38	204
Scheme 5.29. Attempted aliphatic nucleophilic substitution fluorination for the synthesis of 17	205
Scheme 5.30. Proposed aliphatic nucleophilic substitution radiofluorination approach for the synthesis of [¹⁸ F]- 17 using the Boc-protected aliphatic chlorinated precursor 72	206
Scheme 5.31. Aliphatic nucleophilic substitution radiofluorination of precursor 72 followed by Boc-deprotection giving access to [¹⁸ F]- 17	211
Scheme 5.32. Optimised aliphatic nucleophilic substitution radiofluorination methodology for the synthesis of the potential PARP-1 PET imaging agent [¹⁸ F]- 17 using the Boc-protected chlorinated precursor 72	213
Scheme 6.1. The cytochrome P450 (CYP) catalytic cycle.	239
Scheme 7.1. Optimised aliphatic nucleophilic substitution radiofluorination methodology for the synthesis of the potential TSPO PET imaging agent [¹⁸ F]- AB5186 using the chlorinated precursor 77	282

Scheme 8.1. Proposed retrosynthetic analysis of [¹⁸ F]-17 accessed using the tosylated precursor 78.	304
Scheme 8.2. Proposed approach for access to [¹⁸ F]-11 using unsymmetrical diaryliodonium salts 87–89.	306
Scheme 8.3. Proposed approach for access to [¹⁸ F]-11 using the nickel organometallic precursor 91.....	307

LIST OF TABLES

Table 1.1. A table summarising the mode energies and the distance travelled in water of β^+ particles emitted from different radionuclides.....	38
Table 1.2. Spatial resolution limits of pre-clinical and clinical nuclear imaging scanners.....	39
Table 3.1. Synthesis of compounds 4–16 and 18–21 from the penultimate compound 3.	100
Table 3.2. Screen of reaction conditions for the non-radioactive nucleophilic substitution fluorination of 42.	103
Table 4.1. The cell-free IC_{50} , $\log P_{oct}$ and %PPB values for olaparib and compounds 4–21.....	142
Table 4.2. Cellular PARP inhibitory properties of olaparib and compounds 4, 11, 13, 17, and 18.....	150
Table 5.1. Screen of conditions for non-radioactive iodo-dediazonisation of 65 for the synthesis of 4.	182
Table 5.2. Summary of published halogen exchange radioiodination reactions for the labelling of TSPO ligand PK11195.	187
Table 5.3. Investigation and optimisation of solid state interhalogen exchange radioiodination methodology for the synthesis of [^{125}I]-4 using the brominated precursor 60.....	188
Table 5.4. Investigation and optimisation of aromatic nucleophilic substitution radiofluorination methodology for the synthesis of [^{18}F]-11 using the nitro bearing precursor 63.....	198
Table 5.5. Screen of reaction conditions for the non-radioactive nucleophilic substitution fluorination of precursor 72.	207
Table 5.6. Screen of reaction conditions for the Boc-deprotection of compound 73 to access compound 17.....	208
Table 5.7. Investigation and optimisation of aliphatic nucleophilic substitution radiofluorination methodology for the synthesis of [^{18}F]-73 using the Boc-protected chlorinated precursor 72.	210
Table 6.1. Calculated and literature <i>in vitro</i> intrinsic clearance values for diclofenac.	250
Table 6.2. Calculated <i>in vitro</i> intrinsic clearance values for olaparib, and compounds 4 and 17.....	250
Table 7.1. Inhibition constant (K_i), percentage plasma protein binding (%PPB), membrane permeability (P_m), and the membrane partition coefficient (K_m) parameter values for PK11195 and AB5186.....	276

ACKNOWLEDGEMENTS

I would like to start by thanking my supervisors, Dr. Sally Pimlott, Professor Anthony Chalmers, and Dr. Andrew Sutherland, for giving me the opportunity to undertake this PhD programme within their research groups and for their continual support and invaluable advice throughout the last three and a half years. I would also like to extend a special thanks to Dr. Deborah Dewer who has had valuable input at various stages of this project and Dr Marie Boyd at the Strathclyde Institute of Pharmacy and Biomedical Sciences, University of Strathclyde for allowing access to her laboratory facilities to conduct portions of the work described in this thesis.

A huge thanks to all my colleges and the technical staff, including: Dr. Adele Blair for synthesising a number of the compounds described throughout this thesis and for her support during my early days in the organic chemistry department; Harry Jackson who was responsible for running the School of Chemistry mass spectrometry service and for providing me with LC-MS training; Dr. David Adam from providing NMR spectroscopy training; Dr. Anthony McCluskey for his assistance with the cell free IC₅₀ assays; Dr. Shafiq Ahmed for his assistance in optimising the cellular IC₅₀ assays and for provision of tissue culture training; Linda Carberry for microtome training; Dr. Susan Champion for the supply of the radiofluoride isotope and for radiochemical advice; Colin Nixon who was responsible for managing the Cancer Research UK Beatson Institute histology service; Dr Katrina Stevenson for training me in immunohistochemistry techniques; Sandeep Chahal and Dr. Lesley Gilmour for setting up the small animal xenograft models, animal monitoring, and bioluminescence imaging; Dr. Gaurav Malviya for performing pre-clinical PET imaging and image reconstruction, and for his assistance with the biodistribution studies; Agata Mrowinska for her assistance with the biodistribution studies and for training me in the use of the PMOD software; and last, but by no means least, Dr. Adriana Tavares for providing valuable advice concerning PET data processing and for organising and supporting me with the *in vitro* TSPO human tissue binding assays.

I would like to acknowledge financial support from the University of Glasgow, the Engineering and Physical Sciences Research Council, and the Cancer Research UK Glasgow Centre Development Fund.

Outside of the laboratory environment, I would like to express my everlasting gratitude to my partner, Dr. Ourania Varsou, for putting up with me throughout this challenging time, keeping me motivated, and always being there for me, Σ'αγαπώ! Finally, I would like to say a huge heartfelt thank you to my parents, Andrzej and Beata, and my brother, Jakub, for believing in me and for everything that they have done for me, which allowed me to get to where I am.

AUTHORS DECLARATION

This thesis represents original work of Filip Zmuda unless explicitly stated otherwise in the text. This thesis has not been submitted in any other form to any other University. Portions of the work described herein have been published elsewhere as listed below.

Signature: _____

Filip Zmuda

April, 2016

List of papers:

Blair, A., Zmuda, F., Malviya, G., Tavares, A.S., Tamagan, G.D., Chalmers, A.J., *et al.*, 2015. A novel ^{18}F -labelled high affinity agent for PET imaging of the translocator protein. *Chemical Science*, 6(8), pp.4772–4777.

Zmuda, F., Malviya, G., Blair, A., Boyd, M., Chalmers, A.J., Sutherland, A., 2015. Synthesis and evaluation of a radioiodinated tracer with specificity for poly(ADP-ribose) polymerase-1 (PARP-1) in vivo. *Journal of Medicinal Chemistry*, 58(21), pp.8683–8693.

ABBREVIATIONS

95% CI	95% confidence interval
Ar	Arene
Ac	Acetyl
ADME	Absorption, distribution, metabolism and excretion
ADP	Adenosine diphosphate
AP	Apurinic/aprimidinic
APLF	Aprataxin and polynucleotide kinase-like factor
BBB	Blood brain barrier
BER	Base excision repair
B-NHEJ	Backup non-homologous end joining
Boc	<i>tert</i> -Butyloxycarbonyl
BP_{ND}	Binding potential
BRCA-2	Breast cancer 2 early onset protein
(Bu₃)Si	Tributyl silane
(Bu₃)Sn	Tributyl tin
BUI	Brain uptake index
C_a	Arterial compartment
CBR	Central benzodiazepine receptor
CHI	Chromatographic hydrophobicity index
CHIN	Chromatographic hydrophobicity index of non-ionised compound
Cl_{int,in vitro}	<i>In vitro</i> intrinsic clearance
Cl_{int,in vivo}	<i>In vivo</i> intrinsic clearance
C_N	Noise equivalent concentration
C_{nb}	Un-bound tissue compartment
C-NHEJ	Classical non-homologous end joining

C_{nsb}	Non-specifically bound tissue compartment
CSCs	Cancer stem cells
C_{tb}	Specifically bound tissue compartment
CT	Computed tomography
CYP450	Cytochrome P450
DAD	Diode array detector
dH₂O	distilled water
DMAP	4-dimethylaminopyridine
DME	Drug metabolising enzymes
DMEM	Dulbecco's Modified Eagle Medium
DMF	<i>N,N'</i> -Dimethylformamide
DMSO	Dimethyl sulfoxide
DNA-PKcs	Catalytic subunit of DNA-dependant protein kinase
DSBs	Double strand DNA breaks
E⁺	Electrophile
EAS	Electrophilic aromatic substitution
EGFR	Epidermal growth factor receptor
EMR	Electromagnetic radiation
EOS	End of synthesis
EWG	Electron withdrawing group
FEN1	Flap endonuclease 1
GBM	Glioblastoma
GCSF	Granulocyte-colony stimulating factor
HBC	Hydrogen bond count
HIV	Human immunodeficiency virus
HPLC	High performance liquid chromatography
HPR	Horseradish peroxidase

HR	Homologous recombination
HT_i	Total number of hydrogen-bonds exhibited by ionised compound
IC₅₀	Half maximal inhibitory concentration
IDH1	Isocitrate dehydrogenase 1
k	Retention factor
K	Apparent affinity constant
K₂₂₂	Kryptofix [®]
K_i	Inhibition constant
L	Leaving group
LC-MS	Liquid chromatography-mass spectrometry
Log P	Logarithm of partition coefficient
Log P₀	Ideal lipophilic character for central pharmacological effect
Log P_{cyl}	Logarithm of the cyclohexane/water partition coefficient
Log P_{oct}	Logarithm of the octanol/water partition coefficient
MBq	Megabequerel
MeCN	Acetonitrile
MEM	Minimum essential media
MGMT	O ⁶ -methylguanine-DNA-methyltransferase
MPT	Mitochondrial permeability transition
MPTP	Mitochondrial permeability transition pore
MRI	Magnetic resonance imaging
MRN	Mre11-Rad50-Nbs1
MS	Mass spectrometry
Mw	Molecular weight
m/z	Mass-to-charge ratio
NAD⁺	Nicotinamide adenine dinucleotide
NF1	Neurofibromin 1

NF2	Neurofibromin 2
NHEJ	Non-homologous end joining
Ni(COD)₂	bi(cyclooctadiene)nickel(0)
NMP	<i>N</i> -Methyl-2-pyrrolidone
NMR	Nuclear magnetic resonance
OMs	Mesylate
ONs	Nosylate
OTf	Triflate
OTs	Tosylate
PAR	Poly(ADP-ribose)
PARP	Poly(ADP-ribose) polymerase
PARP-CF	Catalytic domain of chicken PARP-1
PARG	Poly(ADP-ribose) glycohydrolase
PBR	Peripheral benzodiazepine receptor
PBS	Phosphate buffered saline
PCNA	Proliferating cell nuclear antigen
PCV	Procarbazine, lomustine and vincristine
PDGFA	Alpha type platelet derived growth factor
PEG	Polyethylene glycol
PET	Positron emission tomography
Ph	Phenol
PMT	Photomultiplier tube
Polβ	DNA polymerase-β
%PPB	Percentage plasma protein binding
RB1	Retinoblastoma 1
RCY	Radiochemical yield
ROS	Reactive oxygen species

RPA	Replication protein A
RP-HPLC	Reverse phase high performance liquid chromatography
RP-TLC	Reverse-phase thin layer chromatography
R_s	Resolution
rt	Room temperature
R_t	Retention time
S	Slope of graph
SAR	Structural activity relationship
SiBu₃	Tributyl silyl
SIM	Selected-ion monitoring
S_NAr	Aromatic nucleophilic substitution
SnBu₃	Tributyl tin
SPE	Solid phase extraction
SPECT	Single photon emission computed tomography
SSBs	Single strand DNA breaks
t_0	Column dead time
TBAF	Tetra- <i>n</i> -butylammonium fluoride
TBAHCO₃	Tetra- <i>n</i> -butylammonium hydrogen carbonate
<i>t</i>BuOH	<i>tert</i> -Butyl alcohol
TCGA	The Cancer Genome Atlas
TIC	Total ion current
TMEDA	Tetramethylethylenediamine
TMZ	Temozolomide
TP53	Tumour protein P53
t_R	Retention time
TSPO	Translocator protein
UDP	Uridine diphosphate

UV	Ultraviolet
VE-catherin	Vascular endothelial catherin
WHO	The World Health Organisation
XLF	XRCC-like factor
XRCC	X-ray cross complimenting protein
ZO	Zonula occludens

1 INTRODUCTION.

1.1 Glioblastoma.

1.1.1 Epidemiology, aetiology, and pathophysiology.

Gliomas are brain tumours that are thought to originate from glial cells. They can be classified into astrocytomas, oligodendromas, ependymomas, and mixed gliomas depending on the glial cell component of the tumour (Louis and Gusella, 1995). Glioblastoma (GBM) is a highly aggressive type of astrocytoma and it is the most common glioma in adults (Louis and Gusella, 1995; Ostrom *et al.*, 2014). Ostrom *et al.* (2014) reported the age-adjusted incidence of GBM to be between 0.59 and 3.59 per 100 000 people depending on the geographical location (data were acquired from Australia, England, Greece, Korea, and the United States between 1999 and 2010). To put this into perspective, the authors also reported the age-adjusted incidence rate of all gliomas to be between 4.67 and 5.73 per 100 000 people (data were acquired from Finland and Greece between 2000 and 2007). Since histological evaluation of tumour tissue is a core component of the diagnostic process, geographical variation in incidence can partly be explained by differences in histological data collection techniques used across different laboratories (Ostrom *et al.*, 2014). Schwartzbaum *et al.* (2006) identified a slight but a statistically significant average annual increase in glioma incidence of 0.9% between 1985 and 1994 (data were acquired from the Central Brain Tumour Registry of the United States). However, the authors attributed this increase to improvements in diagnostic imaging and access to medical care and suggested that glioma incidence has remained consistent during this time.

The aetiology of GBM is still poorly understood. There is evidence to suggest that exogenous environmental factors, such as exposure to high-dose radiation or high-dose chemotherapy for treatment of cancers, can contribute to the development of GBM. Genetics also play a part in the aetiology of GBM as links with certain rare inherited conditions, associated with specific genetic aberrations, have been established. Some examples include mutations of the

neurofibromin 1 (NF1) and 2 (NF2), retinoblastoma 1 (RB1), and Tumour Protein 53 (TP53) genes that have been found to be responsible for neurofibromatosis 1 and 2, retinoblastoma, and Li-Fraumeni syndrome respectively. A familial history of GBM has also been reported as a risk factor, where the likelihood of developing the condition can be two-fold higher (Schwartzbaum *et al.*, 2006). Based on data from animal studies, it has been recognised that certain exogenous and endogenous chemical entities such as *N*-nitroso compounds, reactive oxygen species, and polycyclic aromatic hydrocarbons possess neurocarcinogenic properties. However, human epidemiological studies investigating correlations between GBM and chemical occupational exposures have so far been inconclusive. Additionally, no significant relationship has been established between glioma incidence and the use of mobile phone devices. Interestingly, atopic conditions such as asthma, hay fever, eczema, and food allergies inversely correlate with glioma incidence (Schwartzbaum *et al.*, 2006; Omuro and DeAngelis, 2013; Ostrom *et al.*, 2014).

The World Health Organisation (WHO) Classification of Tumours of the Central Nervous System is an international histological standard for the definition, diagnosis, and grading of brain tumours. GBM falls under the WHO grade IV classification due to being highly malignant, mitotically active, rapidly evolving, and associated with histological features of micro-vascular proliferation, nuclear atypia, necrosis, and pseudo-palisading regions characterised by heaping up of tumour cells around necrotic lesions (Louis *et al.*, 2007). Clinically, the lesions are usually poorly defined due to the presence of highly invasive cells that can migrate up to several centimetres from the main tumour mass (Pilkington, 1994).

GBM can be further subcategorised into primary (*de novo*) and secondary tumours depending on the pathway that led to the origin of the corresponding lesion. Specifically, secondary glioblastomas originate from lower grade gliomas (e.g. astrocytoma WHO grade II or III) and affect individuals with a mean age of 40 years, while primary glioblastomas develop rapidly in individuals of a mean age of 55 years with no clinical, histological, or radiographic evidence of lower grade lesions (Louis and Gusella, 1995; Kleihues *et al.*, 1999). Historically, the

pathways leading to primary and secondary glioblastomas were believed to be associated with specific genetic traits, where epidermal growth factor receptor (EGFR) amplification and TP53 mutation were thought to be exclusive to primary and secondary glioblastomas respectively (Louis and Gusella, 1995; Deimling, Louis and Wiestler, 1995). However, more recent studies have disputed this genetic exclusivity. Okada *et al.* (2003) revealed that EGFR amplification occurred in 57% of GBM tumour samples with TP53 mutations ($n = 7$), and a comprehensive genomic GBM characterisation study conducted by The Cancer Genome Atlas (TCGA) Research Network (2008) showed that 42% of primary GBM samples ($n = 91$) had TP53 mutations. It is therefore evident that the genetic makeup of GBM is more complex than previously believed. By utilising TCGA (2008) GBM data, Verhaak *et al.* (2010) were able to subclassify GBM into four distinct subtypes (i.e. classical, mesenchymal, proneural, and neural) based on genetic abnormalities in numerous genes including the alpha type platelet derived growth factor (PDGFA), isocitrate dehydrogenase 1 (IDH1), EGFR, and NF1 genes. It was proposed that genetic subclassification of GBM could potentially be used to deliver patient tailored therapies leading to improved quality of life and prolonged survival (Taylor, 2010). However, such a tailored therapeutic approach may have limited clinical benefit as it has been revealed that a single GBM tumour can comprise of a mixture of genetic subtypes (Mayer *et al.*, 2015; Patel *et al.*, 2014).

1.1.2 Diagnosis.

The diagnosis of GBM is driven by the clinical presentation of patients, followed by neurological examination, structural imaging of the brain using either magnetic resonance imaging (MRI) or computed tomography (CT) (Omuro and DeAngelis, 2013; Taylor, 2010; National Institute for Health and Clinical Excellence, 2007), and finally histological assessment of lesion biopsy samples obtained at the time of surgical resection or by a single-event biopsy where surgery was not possible (National Institute for Health and Clinical Excellence, 2007). It is important to make a distinction between structural and functional imaging, where the former provides anatomical information and the latter can

reveal physiological activities of tissues. The use of functional nuclear imaging in GBM is discussed in greater detail in section 1.2.3.

Structural CT and MRI possess a number of advantages and disadvantages. CT is markedly cheaper than MRI, has shorter scan times, and provides good bone contrast (Keunen *et al.*, 2014). However, neuroimaging using CT is limited as the modality is less sensitive than MRI and exhibits poor soft tissue contrast, which makes it difficult to distinguish anatomical details of the brain (Landy *et al.*, 2000). Furthermore, CT requires exposure of the imaging subject to ionising radiation in the form of X-rays. Contrary to this, MRI allows for improved soft tissue contrast, it does not rely on the use of ionising radiation (Khalil *et al.*, 2011; Keunen *et al.*, 2014), and it is currently viewed as the 'gold standard' modality for GBM neuroimaging.

The signs and symptoms associated with gliomas are dependent on tumour size and location, and can include: i) new onset headache with a non-specific pain pattern, progressive severity and/or unilateral localisation; ii) cognitive difficulties; iii) behavioural changes; iv) sensory loss; v) visual field disturbances; vi) language difficulties; vii) seizures; viii) gait imbalance; and ix) incontinence. On presentation of one or more of these symptoms, a neurological examination may be conducted and, where indicated, structural MRI will be performed in the presence of a gadolinium contrast agent that enhances glioma lesions (Omuro and DeAngelis, 2013). Under normal circumstances, brain tissue is protected by a unique barrier called the blood brain barrier (BBB), which prevents brain uptake of the gadolinium contrast agent. However, gliomas are associated with BBB disruptions that allow the contrast agent to enter the tumour tissue, which subsequently enhances on the acquired MRI scans (see section 4.1.2.2 for details). Where the use of gadolinium is contraindicated (i.e. previous or pre-existing nephrogenic systemic fibrosis; renal impairment; hepatorenal syndrome; pregnancy; breast feeding; previous anaphylactic or anaphylactoid reaction), MRI may be performed in the absence of a contrast agent. On the MRI scans, glioma lesions often appear as diffuse, unifocal and more rarely multifocal, necrotic, and characteristically surrounded by white matter oedema (Omuro and DeAngelis, 2013). However, this imaging modality can fail to detect secondary

GBM lesions at early stages of the disease, which is likely a consequence of an intact BBB and poor contrast uptake. For example, Kracht *et al.* (2004) reported cases of histologically confirmed grade II and III astrocytomas that failed to enhance on gadolinium contrast MRI. Furthermore, Landy *et al.* (2000) described patients with radiographically visible high-grade gliomas that had normal or minimally abnormal structural MRI scans upon initial presentation with new onset seizures just a few months earlier. The specificity of structural MRI for glioma tissue has been reported as only 50% (Götz *et al.*, 2012), meaning that diagnostic ambiguity can be a common occurrence. Further problems arise for patients who are unable to undergo an MRI scan due to a contraindication (e.g. the presence of a pacemaker or implantable cardioverter defibrillator, claustrophobia, etc.). In such cases a structural CT scan may be performed (Omuro and DeAngelis., 2013), which can often fail to detect intracerebral lesions due to a lower sensitivity when compared to structural MRI (Landy *et al.*, 2000).

It is important to appreciate that structural CT and MRI are not definitive diagnostic methods. This is because metastatic brain cancers and a number of non-cancerous syndromes can mimic the appearance of gliomas upon imaging with these techniques. Non-cancerous glioma mimics include: i) stroke; ii) brain abscess; iii) demyelinating disease; and iv) sarcoidosis (Floeth *et al.*, 2006; Taylor, 2010; Omuro and DeAngelis, 2013). An accurate patient history is vital in aiding the differential diagnosis process of these radiographic glioma mimics (Taylor, 2010).

1.1.3 Treatment and prognosis.

Following neuroimaging, patients with suspected glioma will undergo either maximum safe surgical resection or partial resection aimed at relieving mass effect. The resected tissue will undergo histopathological evaluation for confirmatory diagnosis and tumour typing and grading. In some cases, surgical resection of the GBM lesion may be impossible or highly limited due to the localisation of the tumour. Where the lesion is deemed to be inoperable, stereotactic biopsy may be performed (National Institute for Health and Clinical

Excellence, 2007; Omuro and DeAngelis., 2013). In cases where the tumour is accessible, surgical resection can often be incomplete because of the diffuse nature of GBM and the inability to accurately delineate tumour from non-tumour tissue when performing MRI-guided volumetric resection (Pirotte *et al.*, 2009). In order to try and improve outcomes, excess brain tissue is usually removed as defined by 1–4 cm margin that is added to the MR contrast enhancing region. However, this approach is inaccurate and it can still lead to tumour volume underestimation as well as overestimation (Pirzkall *et al.*, 2001). As a consequence of incomplete surgical resection, the tumour is likely to reoccur (Kern and Shibata, 2007) as glioblastomas are known to contain a mixture of differentiated (Kelly *et al.*, 2007) and stem (Galli *et al.*, 2004; Singh *et al.*, 2004; Yuan *et al.*, 2004) tumour initiator cells that can drive the formation of new tumours. These cancer stem cells (CSCs) usually account for approximately 2–5% of GBM tumour mass, however they have been reported to constitute as much as 28% (Singh *et al.*, 2004).

GBM treatment is usually commenced following histopathological confirmation of the condition, and radiotherapy or a combination of radio- and chemotherapy are considered for all patients (National Institute for Health and Clinical Excellence, 2007). The current ‘gold standard’ chemotherapeutic agent for newly diagnosed GBM is temozolomide (TMZ) (National Institute for Health and Clinical Excellence, 2007; Omuro and DeAngelis., 2013). A study by Stupp *et al.* (2009) showed that combination treatment of TMZ and radiotherapy in newly diagnosed GBM patients, who underwent either biopsy or surgical resection (partial or complete), improved the overall survival five years after diagnosis by approximately five fold when compared to patients who received stand alone radiotherapy. However, it is important to bear in mind that GBM remains a fatal disease with a reported two and five year survival of 27.2% (95% confidence interval = 22.2–32.5) and 9.8% (95% confidence interval = 6.4–14.0) respectively following surgical intervention, and combination TMZ with radiotherapy (Stupp *et al.*, 2009).

The treatment of GBM is challenged by the fact that CSCs can exhibit resistance to both radio- and chemotherapy (Visvader and Lindeman, 2008). Radiotherapy

utilises ionising radiation to generate free radicals on DNA bases that then react with oxygen to form cytotoxic oxygen-DNA adducts (Leopold and Sebolt-Leopold, 1992). On the other hand, TMZ works by forming cytotoxic O⁶-alkylguanine DNA lesions. In all cases, cells need to be actively dividing for radio- and chemotherapeutic cytotoxic effects to take place (Rang *et al.*, 2007). The fact that CSCs have the ability to enter a quiescent state where cell division is halted may provide some explanation for their radiochemotherapeutic resistance (Dean, Fojo and Bates, 2005; Visvader and Lindeman, 2008). Moreover, the cytotoxic DNA-adducts formed by alkylating agents can be repaired by O⁶-methylguanine-DNA-methyltransferase (MGMT) that has been shown to be overexpressed or highly-active in a number of GBM CSC lines (Tentori *et al.*, 2014). Another contributory factor to CSC chemoresistance is the ability of these cells to overexpress drug transporter proteins that can actively pump out cytotoxic agents into extracellular spaces (Dean, Fojo and Bates, 2005; Visvader and Lindeman, 2008). Interestingly, it has been shown that glioma CSC populations can be enriched by ionising radiation in a dose dependant manner and can repair radiotherapy induced DNA damage much more effectively than tumour cells lacking the stem cell phenotype (Bao *et al.*, 2006).

CSCs are not the only driving force behind GBM treatment resistance. Brain tumours generally possess a degree of radioresistance due to the hypoxic nature of the brain (Leopold and Sebolt-Leopold, 1992) and local hypoxic regions caused by tumour mass induced vasoocclusion and vasocollapse (Brat *et al.*, 2004). This reduced oxygen concentration impedes the formation of oxygen-DNA adducts and reduces the effectiveness of radiotherapy (Leopold and Sebolt-Leopold, 1992).

It is also important to appreciate the challenges associated with monitoring the response to therapy, which is currently achieved using gadolinium contrast enhanced structural MRI. This technique may be misleading as surgery and radiotherapy can alter BBB permeability and subsequently contrast agent uptake, that can result in MRI enhancement irrespective of tumour recovery or progression (Hygino da Cruz *et al.*, 2011).

Based on the above information, it is clear that there is a need for further advances in the diagnostic capabilities of GBM, the subsequent surgical and radiochemotherapeutic approaches used to treat the disease, and techniques used to monitor treatment efficacy and disease progression.

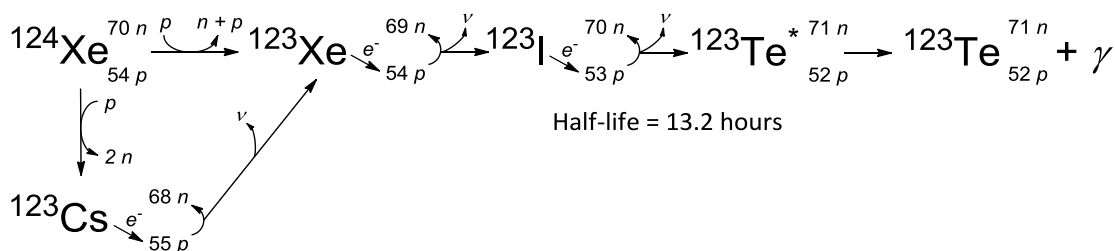
1.2 Nuclear imaging.

1.2.1 Technology (SPECT and PET).

SPECT and PET are functional nuclear imaging modalities that can detect trace amounts of radiolabelled probes *in vivo* in a non-invasive manner. These probes, or radiotracers, are administered to the subject being imaged (usually via an intravenous injection) and are designed to bind to specific biomarkers of interest or to accumulate in desired tissues, thereby allowing for imaging of pathological and biological processes on a molecular level.

SPECT imaging requires the use of radionuclides that emit gamma-rays following their decay. Some of the commonly used radionuclides for SPECT imaging include ^{99m}Tc (half-life = 6.0 hours), ^{67}Ga (half-life = 78.3 hours), and ^{123}I (half-life = 13.2 hours), where only the latter can be attached directly to small organic molecular probes (Pimlott and Sutherland, 2011). The ^{123}I radionuclide is synthesised in a cyclotron via the $^{124}\text{Xe}(p,pn)^{123}\text{I}$ nuclear reaction (Scheme 1.1). The process involves bombarding a ^{124}Xe atom with a proton, which can then have one of two outcomes. The first results in the loss of a neutron and a proton leading to the formation of ^{123}Xe , while the second results in the loss of two neutrons and the formation of unstable ^{123}Cs . In order to become more stable, an electron from the inner-shell of ^{123}Cs is drawn into the nucleus and combines with a proton to form a neutron and a neutrino; this process is called electron capture and leads to the formation of ^{123}Xe . In a similar manner, ^{123}Xe also undergoes electron capture generating ^{123}I , which again is unstable and decays with a half-life of 13.2 hours via the same electron capture pathway to form ^{123}Te . The ^{123}Te atom created via this route possesses a slight excess of energy

and is able to enter a stable ground state by releasing a gamma-ray photon (International Atomic Energy Agency, 2008) (Scheme 1.1).



Scheme 1.1. Nuclear reactions used to generate the ^{123}I radionuclide and its subsequent decay.

A SPECT scanner possesses between two to three gamma cameras attached to a rotatable gantry that detect the gamma-rays emitted directly by radionuclides. In order to obtain directional information, each gamma camera has in front of it a physical collimator, which comprises of either a pinhole or a set of parallel holes that only allow gamma-rays traveling in a single direction (i.e. at a single angle of incidence) to reach the detector (Figure 1.1). Using this directional information the scanner is able to generate a three dimensional tomographic image of the gamma-ray source. In practice, the gamma-ray source will correspond to the tracer compound labelled with the gamma-emitting radioisotope that has been injected into the subject being imaged (Pimlott and Sutherland, 2011; Ritt, Sanders, and Kuwert, 2014).

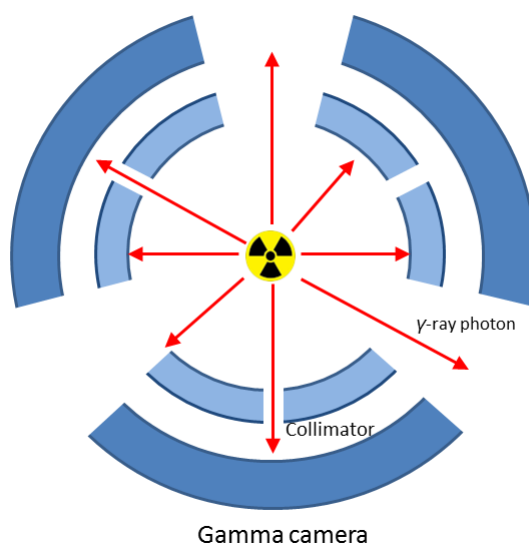
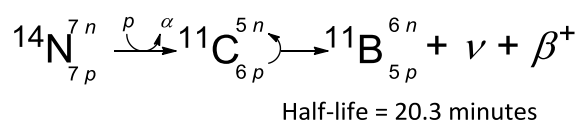
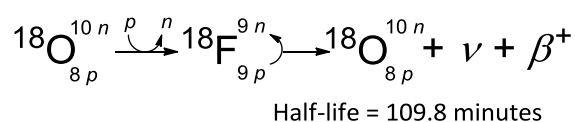


Figure 1.1. Cross-sectional diagram of a SPECT scanner.

In a similar manner to SPECT, PET scanners are able to detect tracers that have been radiolabelled with an appropriate radioisotope. In the case of PET, radioisotopes that can be used include ^{15}O , ^{13}N , ^{11}C and ^{18}F , which all decay via the β^+ pathway (Miller *et al.*, 2008). However, the use of the former three radioisotopes is associated with a number of challenges due to their short decay half-life's (i.e. $^{15}\text{O} = 2.04$ minutes; $^{13}\text{N} = 9.97$ minutes; $^{11}\text{C} = 20.3$ minutes) (Pimlott and Sutherland, 2011). Firstly, radiotracers labelled with these isotopes can only be utilised for short imaging times. Secondly, imaging multiple subjects in a single day may require multiple radiotracer production runs. Thirdly, radiolabelling and subsequent PET imaging is generally restricted to facilities that have an on-site cyclotron capable of producing ^{15}O , ^{13}N , and ^{11}C . The slightly longer half-life of ^{11}C radiopharmaceuticals allows their transport across different sites, although their transport will be restricted to short distances.

The ^{18}F radionuclide is generated using a cyclotron and the $^{18}\text{O}(p,n)^{18}\text{F}$ nuclear reaction, which involves proton bombardment of ^{18}O in gaseous form or water (i.e. H_2^{18}O). The oxygen atom accepts a proton and, in order to conserve mass, liberates a neutron resulting in the formation of ^{18}F . The unstable ^{18}F radionuclide then decays with a half-life of 109.8 minutes and emits a β^+ particle and a neutrino, and reforms the ^{18}O atom (Scheme 1.2). The ^{11}C radionuclide is made through a similar process, which involves introducing a proton into the ^{14}N atom, that then emits an α -particle (i.e. a ^4He atom) resulting in the formation of ^{11}C . The ^{11}C radionuclide decays to ^{11}B via the β^+ pathway with a half-life of 20.3 minutes (International Atomic Energy Agency, 2008) (Scheme 1.2).



Scheme 1.2. Nuclear reactions used to generate the ^{18}F and ^{11}C radionuclides and their subsequent decay.

Following radiotracer administration to the imaging subject and radioisotope decay, the emitted β^+ particles travel a short distance in tissue (approximately 0.5–2.5 cm) before colliding with an electron (i.e. a β^- particle) from surrounding matter. This collision results in an annihilation event that is associated with the release of energy in the form of two coincident gamma-ray photons of a specific energy (i.e. 511 KeV) travelling at approximately 180° to one another. The PET scanner contains a ring of sensors that detect these coincident photons and uses this information to generate a three dimensional tomographic image that provides an approximate location of the radioisotope source (Figure 1.2). Unlike SPECT, the PET scanner does not require physical collimators as the coincidence of the gamma-ray photons provides sufficient directional information for image generation; this is termed internal collimation (Miller *et al.*, 2008; Pimlott and Sutherland, 2011).

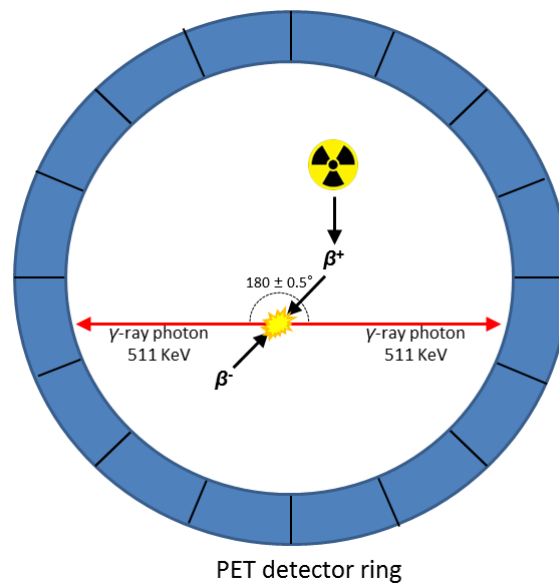


Figure 1.2. Cross-sectional diagram of a PET scanner.

It is important to note that annihilation of β^+ and β^- particles can only occur once the β^+ particle loses sufficient energy and is practically at rest. As the β^+ particle travels through tissue it will interact with matter via elastic and inelastic collisions losing energy each time. The energy of the β^+ particle emitted from the radioisotope will dictate how far the particle travels before losing sufficient energy to undergo annihilation, which will in turn influence the accuracy at which the location of the radioisotope source can be predicted. Consequently,

radioisotopes that generate high energy β^+ particles, which travel further before annihilation, will lead to reduced resolution of the PET image when compared to radioisotopes that emit lower energy β^+ particles (Bailey, Karp, and Surti, 2004). The below table summarises how the mode energies of emitted β^+ particles from different radionuclides affect their distance travelled in water (Table 1.1).

Table 1.1. A table summarising the mode energies and the distance travelled in water of β^+ particles emitted from different radionuclides (Bailey, Karp, and Surti, 2004).

Radionuclide	Mode energy of β^+ (Mev)	Mean distance travelled in water (mm)
^{18}F	0.202	0.6
^{11}C	0.326	1.1
^{13}N	0.432	1.5
^{15}O	0.696	2.5

1.2.2 Strengths and weaknesses.

SPECT and PET technologies possess a unique set of advantages and disadvantages. Pre-clinical SPECT scanners are capable of achieving superior spatial resolution when compared to pre-clinical PET, while in a clinical setting better spatial resolution is generally achieved with PET imaging (Khalil *et al.*, 2011) (Table 1.2). It is noteworthy that over the last few years new SPECT technologies have emerged that have exhibited substantial improvements in spatial resolution when compared to conventional SPECT. Specifically, these include xSPECT (Siemens) and G-SPECT (MILabs), which can achieve spatial resolutions in the region of 2–4 mm. However, at the time of writing, the former has so far only been utilised for bone scans while the latter was yet to be approved for clinical use (Ma and Vija, 2014; MILabs, 2015).

Table 1.2. Spatial resolution limits of pre-clinical and clinical nuclear imaging scanners (Khalil *et al.*, 2011).

Scanner	Spatial resolution (mm)
Pre-clinical SPECT	<1
Clinical SPECT	8–12
Pre-clinical PET	1–2
Clinical PET	4–6

In addition to better spatial resolution, clinical PET is also associated with greater accuracy and sensitivity when compared to SPECT. The reasons for this are two-fold. Firstly, directional information in PET is achieved through internal collimation, while SPECT requires physical collimation that restricts the number of gamma-ray photons that can reach the detector. Secondly, attenuation correction is more easily achieved in PET imaging than in SPECT (Rahmim *et al.*, 2008). Attenuation correction is necessary as gamma-ray photons, released either directly from the radionuclide or via a secondary annihilation event, can undergo photoelectric or scatter interactions. In the case of the former, the photon is completely absorbed by surrounding matter before reaching the detector, which in the absence of correction can reduce detector sensitivity. Similarly, if scatter interactions are not appropriately corrected for, the altered incident trajectories and energies of gamma-photons can have a negative effect on imaging accuracy (Zaidi and Hasegawa, 2006).

Despite a number of shortcomings over PET, SPECT imaging has a number of advantages. Firstly, the longer half-life of SPECT radionuclides allows for longer scan times, cheaper radiotracer production costs, and the ability to transport the radiopharmaceuticals across larger geographical distances (Keunen *et al.*, 2014). Secondly, SPECT can be utilised to perform simultaneous dual-tracer imaging, which is made possible as different radionuclides can emit gamma-ray photons of different energies (for example $^{99m}\text{Tc} = 140 \text{ KeV}$ and $^{123}\text{I} = 159 \text{ KeV}$) that can be detected simultaneously using the SPECT scanner. In contrast to this, a conventional PET scanner is designed to detect gamma-ray photons of a single energy (i.e. 511 KeV). Performing dual-tracer imaging could be utilised to

visualise two different biomarkers simultaneously, which could in turn reduce acquisition times and patient discomfort. Furthermore, interpretation of data is simplified as simultaneous acquisition removes potential image registration artefacts that could be introduced when performing two separate imaging sessions (Rahmim *et al.*, 2008). Thirdly, SPECT could be utilised to ascertain *in vivo* pharmacokinetic properties of novel ^{131}I -labelled radionuclide therapy agents, which decay to release a β^- particles and gamma-ray photons. The β^- particle is highly ionising and induces DNA damage, which can be exploited therapeutically for the treatment of cancer, while the gamma-ray photons can be detected using a SPECT scanner. Non-invasive pharmacokinetic information ascertained in this manner could provide valuable data for calculating tissue dosimetry, and predicting therapeutic effectiveness and radiation toxicity to off target organs.

A key advantage shared by both SPECT and PET is that they can be combined with structural imaging, which brings together the strengths of the individual modalities into a single imaging system. Specifically, PET and SPECT scanners are capable of detecting pathological processes on a molecular and functional level with a greater degree of specificity than structural imaging, while structural imaging techniques generally allow for better spatial resolution than nuclear imaging (Khalil *et al.*, 2011; Keunen *et al.*, 2014). Spatial resolution can be defined as the limiting distance in distinguishing between two point sources close to one another (Bailey, 2004).

Multimodality SPECT/CT and PET/CT scanners are now common place and they allow for precise registration of functional information to anatomical regions visible in the CT image. However, such systems are disadvantaged by the poor soft tissue contrast of CT and increased exposure to ionising radiation when compared to SPECT or PET alone. In order to address these shortcomings, recent scientific endeavours have focused on the refinement of hybrid PET/MRI and SPECT/MRI systems. Importantly, certain hybrid nuclear/MRI imaging systems are capable of acquiring functional and structural data simultaneously, unlike hybrid nuclear imaging/CT scanners that acquire the two data sets sequentially. Sequential acquisition not only increases scan times but also image processing

times as the two sequential data sets require post-imaging software driven integration (Cherry, 2009). In the context of clinical imaging, reducing scan and processing times are important in maximising patient comfort and the number of patients that can be imaged on a single day, which can in turn reduce costs associated with radiopharmaceutical production.

1.2.3 Nuclear imaging of glioblastoma

Due to the complementary strengths of nuclear and structural imaging, the combined use of the two modalities has the potential to address the previously described issues associated with GBM structural neuroimaging (see sections 1.1.2 and 1.1.3 for details).

The most clinically researched tracers for nuclear imaging of brain tumours include the PET agents [^{18}F]-fluorodexoyglucose ([^{18}F]-FDG), methyl-[^{11}C]-methionine ([^{11}C]-MET), and [^{18}F]-fluoroethyl-L-tyrosine ([^{18}F]-FET), and the SPECT agent [^{123}I]-iodo-*alpha*-methyl-L-tyrosine ([^{123}I]-IMT). The former is a glucose analogue and shows proportional tissue uptake to its parent molecule. Tumour cells express higher amounts of glucose transporters when compared to non-tumorous cells and are subsequently associated with higher glucose uptake (Juhász *et al.*, 2014). The other listed probes are amino acid analogues that are actively taken up into tumour tissue by amino acid transporters, which are overexpressed by glioma cells (Waerzeggers *et al.*, 2011; Götz *et al.*, 2012). The disadvantage of [^{18}F]-FDG is that healthy grey matter is also associated with high uptake of glucose (Juhász *et al.*, 2014), which results in a low tumour to background signal ratio. This low contrast between tumour and non-tumour tissue can make tumour detection and delineation difficult, particularly during early stages of the disease where the lesions are small (Cook, Maisey, and Fogelman, 1999; Götz *et al.*, 2012; Juhász *et al.*, 2014). Poor imaging contrast with [^{18}F]-FDG PET has also been reported in a number of high grade gliomas (including GBM), where uptake of the tracer in glioma lesions was similar to the cortex tissue (Schifter *et al.*, 1993).

Amino acid based radiotracers have shown more promise as GBM nuclear imaging agents, due to their low uptake in normal brain tissue. Götz *et al.* (2012) reviewed past literature and reported the specificity of [^{11}C]-MET PET and [^{123}I]-IMT SPECT for glioma tumours to be between 80–100%, compared to only 50% for structural MRI. Similarly, a study by Pauleit *et al.* (2005) revealed that the combined use of [^{18}F]-FET PET and MRI improved the glioma specificity from 53% (using MRI alone) to 94%. Moreover, amino acid based radiotracers have been shown to be effective at identifying low grade astrocytomas, which can be difficult to detect using structural MRI (Kracht *et al.*, 2004). These data support the potential for improved diagnostic accuracy offered by nuclear and multimodality imaging using amino acid based radiotracers. However, it is important to appreciate that conditions that can mimic gliomas on structural neuroimaging (see section 1.1.2 for details) may also be difficult to distinguish using nuclear imaging and amino acid based radiotracers due to non-neoplastic uptake of the probes (Floeth *et al.*, 2006; Salber *et al.*, 2007).

Kracht *et al.* (2004) were able to show that [^{11}C]-MET PET was capable of detecting not only solid tumours but also invasive tumour cells in patients with grade 2 to 4 astrocytomas with high sensitivity and specificity, which was not achievable using structural MRI. The authors highlighted that the approach could improve diagnosis and surgical management of patients with glioma compared to structural neuroimaging (Kracht *et al.*, 2004). In line with these proposals, Pirotte *et al.* (2005) reported that combining [^{11}C]-MET PET and MR imaging improved total resection of low grade gliomas in children when compared to MRI guided resection alone. Similarly, the combined use of these modalities was found to improve low grade glioma and glioblastoma tumour volume definition for resective surgery in 52 out of 59 (88%) and 18 out of 23 (78%) cases respectively when compared to MRI (Pirotte *et al.*, 2006).

As highlighted previously, measuring GBM therapeutic response using MRI can be misleading due to therapeutically induced alterations in BBB permeability (see section 1.1.3 for details). Nuclear imaging using amino acid based radiotracers could provide an alternative means of therapeutic monitoring of these tumours. This is justified by the good correlations that were observed between GBM [^{18}F]-

FET uptake and therapeutic responses to convection-enhanced delivery of paclitaxel and locally administered radioimmunotherapy, which can both affect BBB permeability (Pöpperl *et al.*, 2005; Pöpperl *et al.*, 2006). However, it is important to note that BBB disruptions secondary to glioma or acute radiation injury have been reported to increase unspecific uptake of [^{11}C]-MET (Roelcke *et al.*, 1995) and [^{18}F]-FET (Spaeth *et al.*, 2004) respectively. Therefore, further studies are required in order to evaluate the utility of amino acid based radiotracers as a means of GBM treatment monitoring.

The above described findings outline that amino acid based radiotracers have the potential for improving diagnosis and management of patients with gliomas, including nuclear imaging guided resective surgery and possibly treatment monitoring. However, it is important to bear in mind that the use of the aforementioned radiotracers for neurooncological applications is still under on-going investigation, and their exact place in the clinic is yet to be determined.

1.3 Poly(ADP-ribose) polymerase (PARP).

1.3.1 What is PARP and what does it do?

The mammalian poly(ADP-ribose) polymerase (PARP) family comprises of 17 different proteins. Six of these family members, namely PARP-1 to 4, and tankyrases 1 and 2, have the ability to perform a type of protein post-translational modification called poly(ADP-ribosyl)ation. This process involves the transfer of adenosine diphosphate (ADP) ribose molecules from nicotinamide adenine dinucleotide (NAD^+) (Figure 1.3) onto target proteins to form linear or branched ADP-ribose chains (Hottiger *et al.*, 2010; Bürke, 2005).

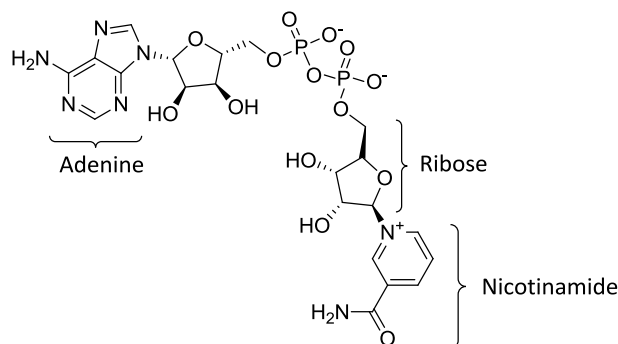


Figure 1.3. Structure of nicotinamide adenine dinucleotide (NAD^+).

The mechanism of PARP mediated poly(ADP-ribose)ation is outlined in figure 1.4. The process begins with the binding of the ribose functionality of an NAD^+ molecule to an acceptor site in the PARP enzyme or in histones, while the nicotinamide moiety binds to the PARP catalytic fragment. Binding to the catalytic fragment is driven by hydrogen bonding between the amide functionality of nicotinamide and Gly₈₆₃ and Ser₉₀₄ amino acid residues. Planar π -stacking interactions between the aromatic rings of nicotinamide and the Tyr₉₀₇ amino acid residues also contribute to the binding. Together, these interactions facilitate the dissociation of nicotinamide leading to the formation of an ADP-ribose oxonium ion intermediate. A Glu₉₈₈ amino acid residue forms a hydrogen bond with the 2'-hydroxyl of the adenine ribose moiety of a second NAD^+ molecule, which then facilitates the formation of a glycosidic bond between the PARP-acceptor bound ADP-ribose oxonium ion and the secondary NAD^+ molecule. Repetitions of this process at the positions highlighted in figure 1.4 lead to PAR chain elongation and PAR chain branching (Ferraris, 2010).

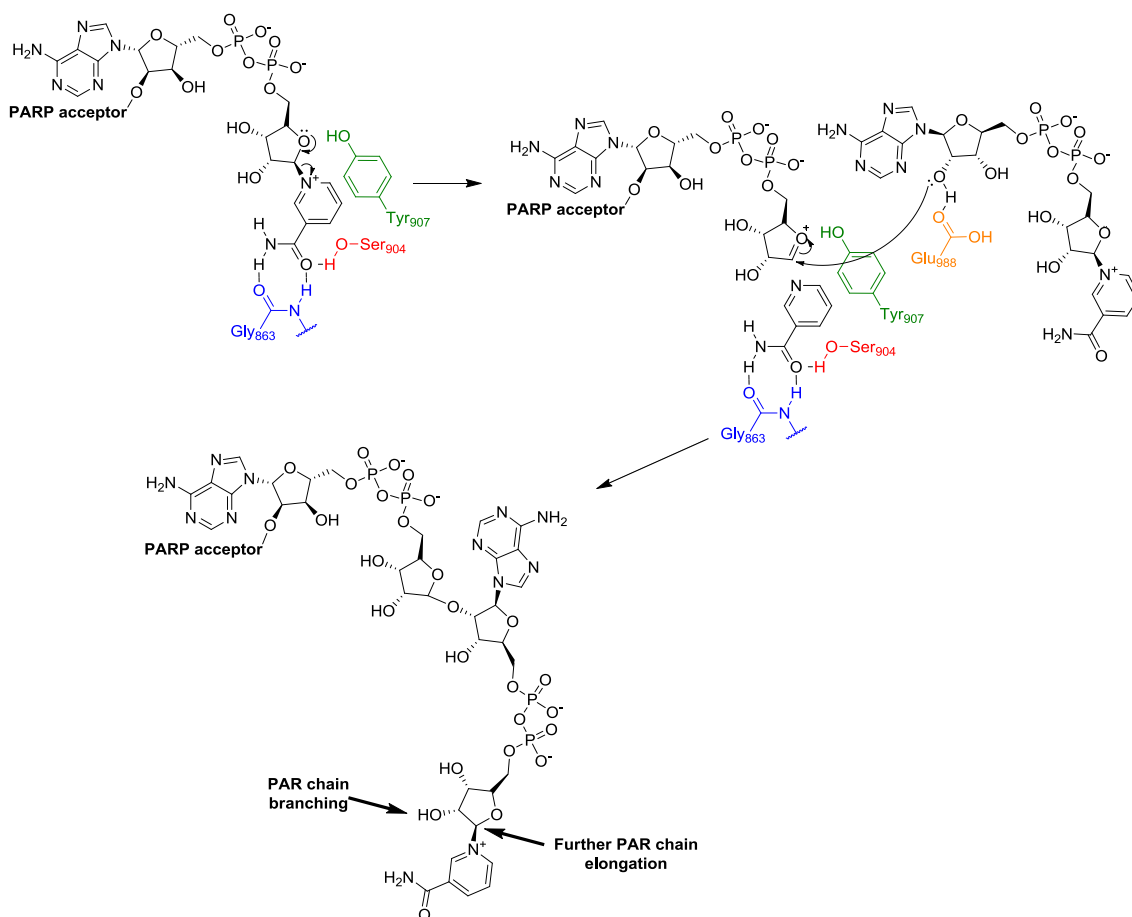


Figure 1.4. Diagram outlining the mechanisms of PARP catalysed poly(ADP-ribosylation).

PARP mediated poly(ADP-ribosylation) has been implicated in numerous cellular processes including transcription, mitosis, apoptosis and DNA damage repair (reviewed by Amé, Spenlehauer, and de Murcia (2004), and Bürke, (2005)). However, the majority of these fall outside of the scope of this thesis and only the role of PARP in DNA damage response mechanisms will be described. The precise enzymatic roles of the other 11 members of the mammalian PARP family are still being elucidated. However, all 17 PARP proteins share gene sequence homology to the catalytic region of the bacterial diphtheria toxin which possesses mono(ADP-ribosylation) activity (Hottiger *et al.*, 2010).

The cellular DNA damage response system is complex and comprises of multiple different pathways that are responsible for the repair of different types of DNA damage. The integrity of DNA can become compromised in a number of different ways (Figure 1.5.). Firstly, DNA can undergo spontaneous hydrolysis resulting in the formation of a gap, or apurinic/apyrimidinic (AP) site, in the DNA chain.

Secondly, endogenous reactive oxygen species (ROS), alkylating agents and various metabolites produced by the body can lead to the formation of foreign adducts on DNA bases. Finally, there are exogenous sources of DNA damage such as chemical agents and ionising radiation that can also result in the formation of DNA adducts (Hoeijmakers, 2009). Certain DNA adduct lesions can disintegrate spontaneously resulting in the direct formation of single strand DNA breaks (SSBs). In other cases, cleavage of the adduct-bearing base by a DNA glycosylase protein leaves an AP site that is then cleaved by an AP endonuclease, AP lyase or a dual function glycosylase, resulting in the indirect formation of a SSB (Caldecott, 2008; Hoeijmakers, 2001) (Figure 1.5).

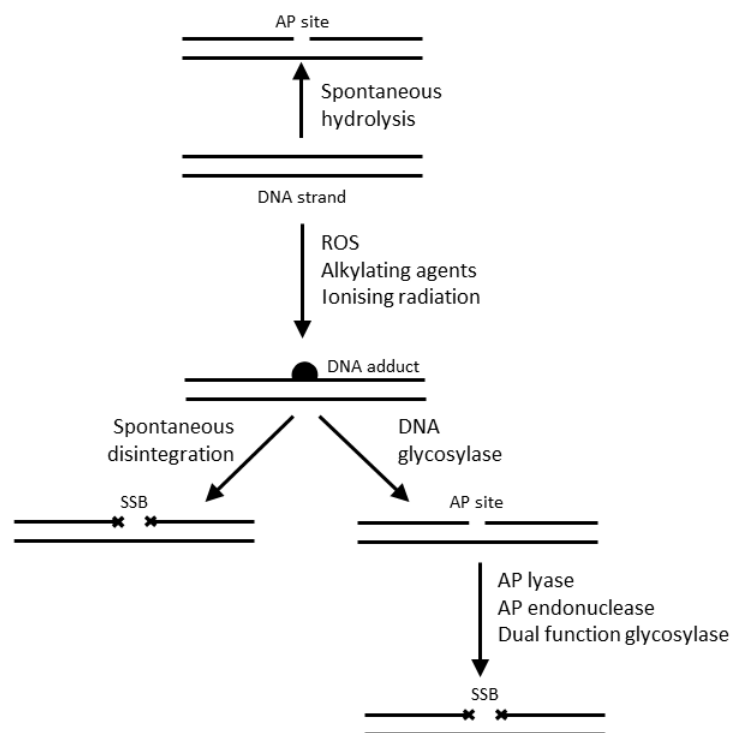


Figure 1.5. Schematic outline of the pathways of DNA damage. AP = apurinic/aprimidic; ROS = reactive oxygen species; SSB = single strand break.

SSBs are repaired via the base excision repair (BER) pathway and the efficiency of this repair mechanism allows for a degree of cellular SSB tolerance. However, SSBs that are not repaired prior to DNA replication can lead to the blockage or collapse of DNA replication forks and subsequently double strand DNA breaks (DSBs) (Caldecott, 2001; Caldecott, 2008). DSBs can also be induced directly by ionising radiation at a ratio of 1 : 25 of DSBs to SSBs (Lieber, *et al.*, 2010; Chalmers *et al.*, 2010). Non-homologous end-joining (NHEJ) and homologous

recombination (HR) are processes that are responsible for the repair of these DSBs. The former of these two processes is inaccurate and prone to mutagenesis (Hoeijmakers, 2001), while error-free HR can become saturated by large amounts of DSBs leading to cytotoxicity (Caldecott, 2008) (Figure 1.6).

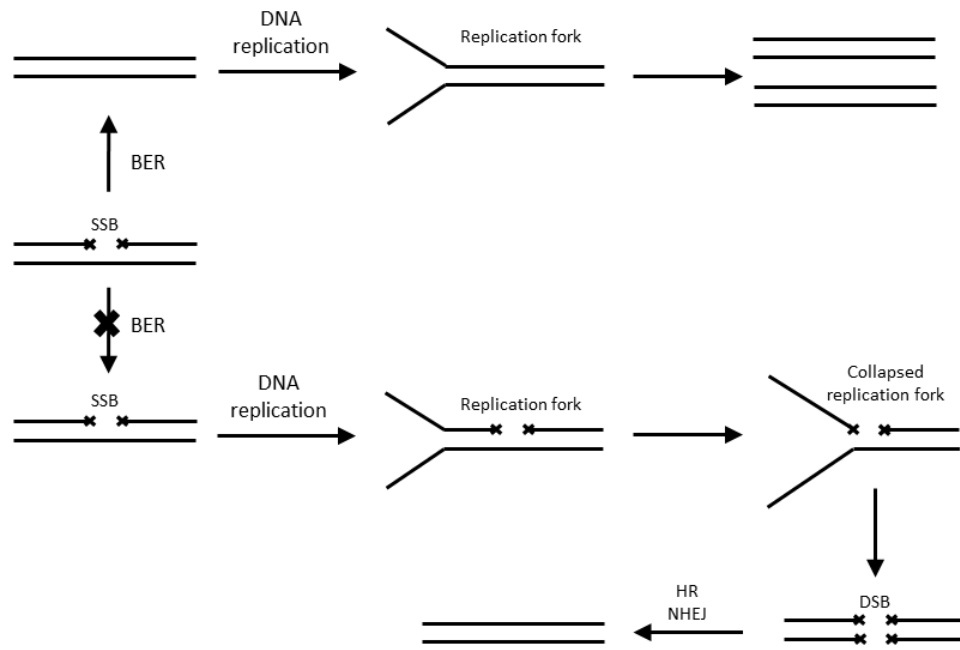


Figure 1.6. Schematic outline of the DNA repair pathways. SSB = single strand break; BER = base excision repair; DSB = double strand break; HR = homologous recombination; NHEJ = non-homologous end joining.

It has been shown that in the presence of DNA damage poly(ADP-ribosyl)ation increases dramatically (Juarez-Salinas, Sims and Jakobson, 1979), while under basal conditions this activity is low (Bürke, 2005). PARP-1 was the first member of the PARP family to be discovered (Chambon, Weill, and Mandel, 1963) and it accounts for approximately 90% of poly(ADP-ribose) (PAR) formation under genotoxic stress (Shieh *et al.*, 1998). PARP-2, which was discovered much more recently, is the only other member of the PARP family that is activated by DNA damage and it accounts for approximately 5–10% of PAR formation under genotoxic stress (Amé *et al.*, 1999). These proteins can exist as heterodimers (Schreiber *et al.*, 2002), although the exact function of PARP-2 in DNA damage repair remains elusive.

The BER pathway is subdivided into short-patch and long-patch nucleotide DNA repair. The first of these is the predominant processes and it is initiated by the indirect formation of a SSB by AP endonucleases, AP lyases or glycosylases in the presence of a single damaged DNA base as described earlier. On the other hand, the long-patch nucleotide DNA repair process is responsible for the repair of SSBs where approximately 2–10 DNA bases have been damaged (Amé, Spenlehauer and de Murcia, 2004; Hoeijmakers, 2001). It was originally proposed that specific zinc motifs on PARP-1 recognise and bind to SSBs, resulting in the activation of PARP-1 and subsequent synthesis of negatively charged PAR chains that are transferred either to itself or other key proteins including histones H1 and H2B. Accumulation of these negatively charged chains leads to dissociation of PARP-1 from DNA and to the relaxation of chromosomes through repulsive forces. It was thought that this facilitates the access and recruitment of DNA repair proteins to the site of DNA damage. In the case of short-patch nucleotide DNA repair, DNA polymerase- β (pol β) and the X-ray cross-complementing protein (XRCC) 1 ligase III complex are recruited, where the former performs a one-nucleotide gap filling reaction and the remaining nick in the DNA is sealed by the ligase. The less common long-patch nucleotide DNA repair pathway makes use of DNA pol β , polymerase- δ , polymerase- ϵ and proliferating cell nuclear antigen (PCNA), which displace the damaged DNA sequence of bases and replaces them with complementary bases. Then flap endonuclease 1 (FEN1) then removes this displaced flap of bases, and finally DNA ligase I seals the DNA strands (Amé, Spenlehauer and de Murcia, 2004; Caldecott, 2008; Hoeijmakers, 2001). Dissociated poly(ADP-ribosyl)ated PARP-1 remains inactive until the PAR chains are degraded by poly(ADP-ribose) glycohydrolase (PARG), thereby restoring its activity (Caldecott, 2008) (Figure 1.7).

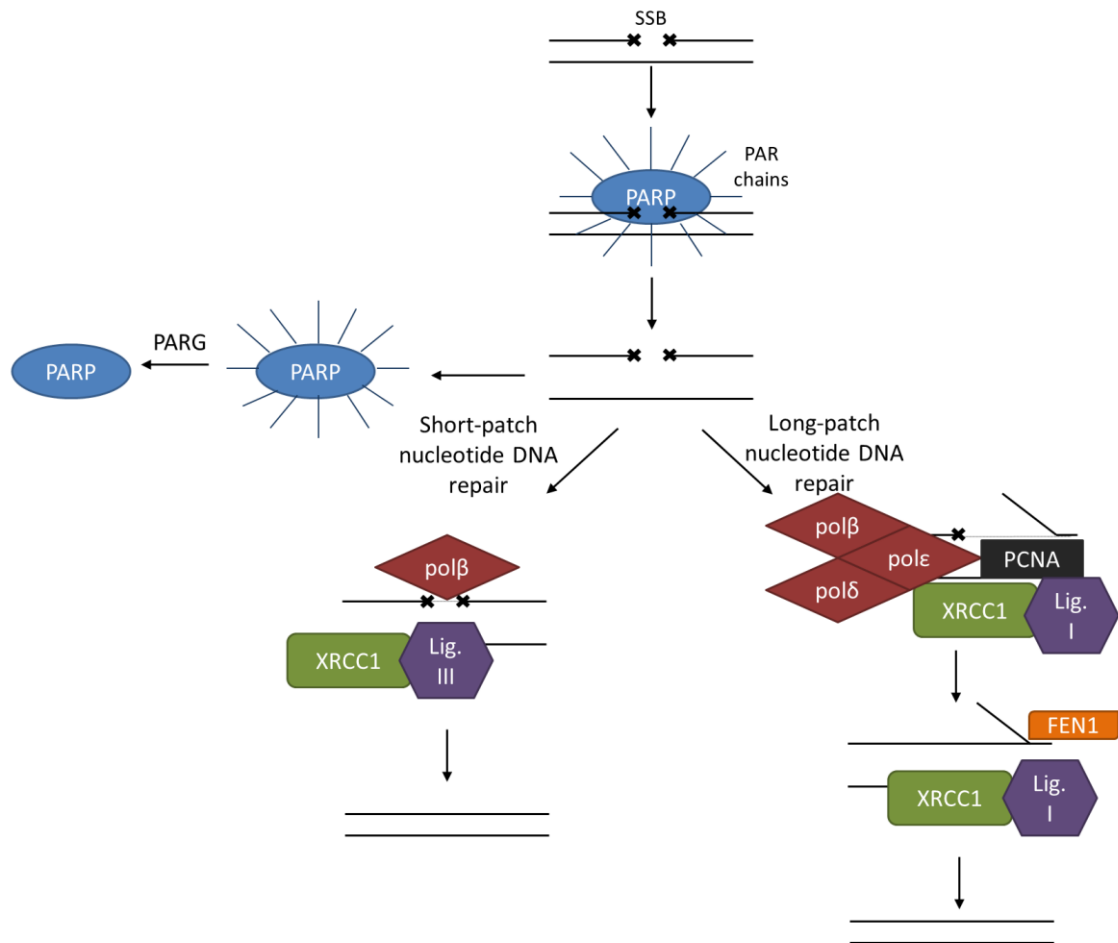


Figure 1.7. Schematic outline of the proposed model of short-patch and long-patch nucleotide DNA repair involving PARP. SSB = single strand break; PAR = poly(ADP-ribose); PARG = poly(ADP-ribose) glycohydrolase; pol = polymerase; lig. = ligase; XRCC1 = X-ray cross-complimenting protein; PCNA = proliferating cell nuclear antigen; FEN1 = flap endonuclease 1.

However, recent findings revealed that BER was able to occur efficiently in PARP-1 negative cells, and the presence of PARP-1 actually reduced the rate of BER (Storm *et al.*, 2011). These observations suggested that PARP-1 was not directly involved in BER. The authors were also able to show that inhibition of PARP-1 prevented SSB ligation due to trapping of the protein on DNA (Storm *et al.*, 2011). Based on these results, Helleday (2011) proposed an alternative mechanism for BER, which shares many similarities with the previously postulated mechanism. In this newly proposed model, DNA repair proteins are recruited to the SSB independently of PARP-1, where short-patch nucleotide DNA repair is initially attempted. If short-patch repair fails due to ligation difficulties then long-patch nucleotide DNA repair will take place (Figure 1.8). Despite

PARP-1 not being involved in the process, Helleday (2011) proposed that the protein can transiently bind to the SSB and become trapped when inhibited pharmacologically.

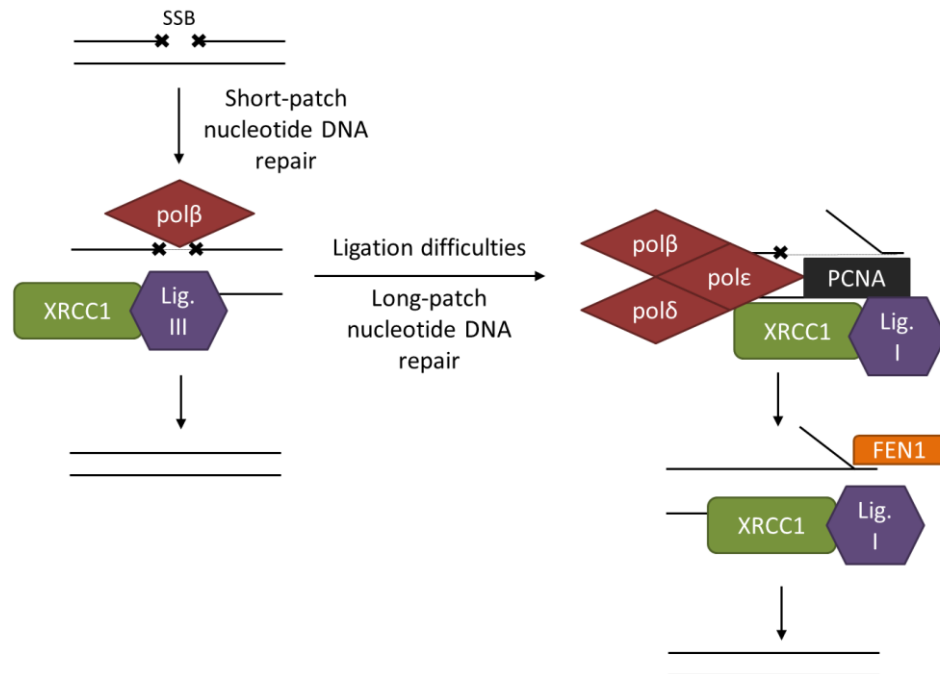


Figure 1.8. Schematic outline of the proposed model of PARP independent short-patch and long-patch nucleotide DNA repair. SSB = single strand break; pol = polymerase; lig. = ligase; XRCC1 = X-ray cross-complementing protein 1; PCNA = proliferating cell nuclear antigen; FEN1 = flap endonuclease 1.

As mentioned earlier, NHEJ is one of the DNA damage response mechanisms responsible for the repair of DSBs. It is a complex process as variable sub-pathways can exist depending on the extent of DNA damage that is being repaired (Davis and Chen, 2013). The two pathways of NHEJ include the classical NHEJ (C-NHEJ or D-NHEJ) and backup NHEJ (B-NHEJ) (Wang *et al.*, 2012). Both of these can take place at any stage of the cell cycle, but they predominate in cells that lack identical copies of DNA (sister chromatids) at the time of repair (Takada *et al.*, 1998).

C-NHEJ begins with the recruitment of a Ku protein heterodimer comprising of Ku70 and Ku80 to the DSB (Figure 1.9). This complex is thought to stabilise the DSB termini and protect them from non-specific processing that otherwise could lead to chromosomal aberrations. The Ku complex is also thought to facilitate

the recruitment of the remaining proteins involved in C-NHEJ, which include the catalytic subunit of DNA-dependant protein kinase (DNA-PKcs), XRCC4, DNA-ligase IV, XRCC4-like factor (XLF) and, where necessary, various DNA end processing enzymes. It is believed that the function of DNA-PKcs is to tether the two broken ends of the DNA molecule together. Moreover, XRCC4 and XLF form a filament complex that may also be involved in bridging the DSB gap. If the nature of the DNA break is such that the terminal ends cannot be ligated, then the next step involves DNA end processing where the bases at the end of DNA termini are cleaved. This is performed by either artemis or aprataxin- and polynucleotide kinase-like factor (APLF) that both exhibit exo- and endonuclease activity. However, in the case of artemis, endonuclease activity has to first be activated by DNA-PKcs mediated phosphorylation. Following cleavage of bases any newly formed gaps are filled in by DNA polymerase- μ or polymerase- λ . The final step involves ligation of the two ends of the broken DNA molecule by the XRCC4-ligase IV complex (Davis and Chen, 2013) (Figure 1.9).

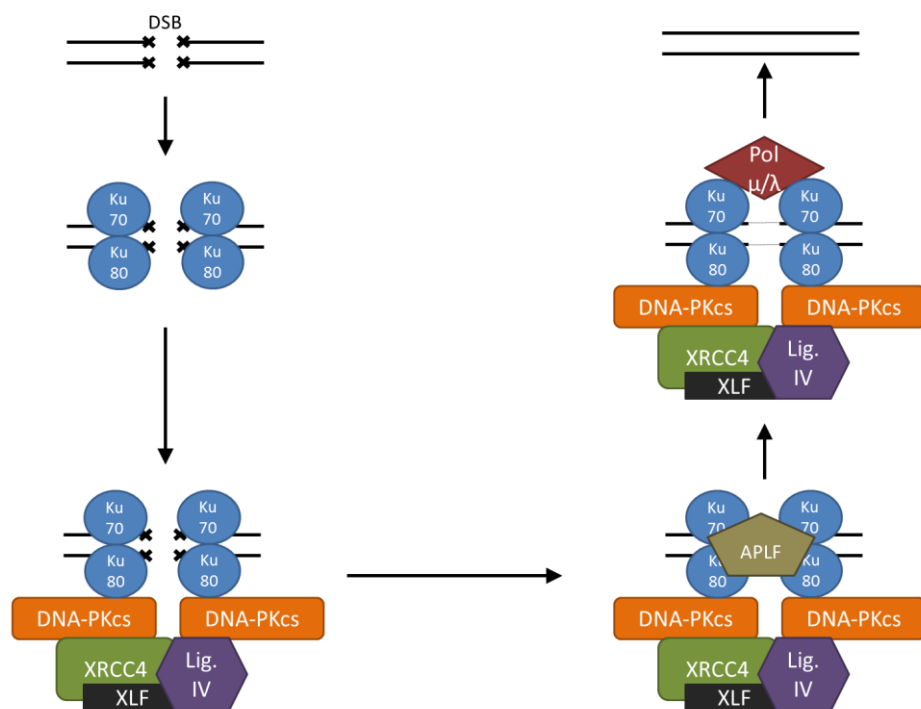


Figure 1.9. Schematic outline of the classical non-homologous end-joining (C-NHEJ) model. DSB = double strand break; DNA-PKcs = DNA-dependant protein kinase; XRCC4 = X-ray cross-complimenting protein 4; XLF = XRCC4-like factor; lig. = ligase; APLF = artemis or aprataxin-and polynucleotide kinase-like factor; pol = polymerase.

B-NHEJ is less understood, but PARP-1 has been implicated in its mechanism (Figure 1.10). It is thought that PARP-1 is recruited to DSB where it becomes activated and performs poly(ADP-ribose)ation on itself as well as histones. This then facilitates the recruitment of the Mre11-Rad50-Nbs1 (MRN) and the XRCC1-ligase III complexes to the DSB. MRN exhibits exonuclease activity and it processes the termini of the broken DNA strands, which then allows for ligase III to perform the final ligation step (Wang *et al.*, 2012) (Figure 1.10).

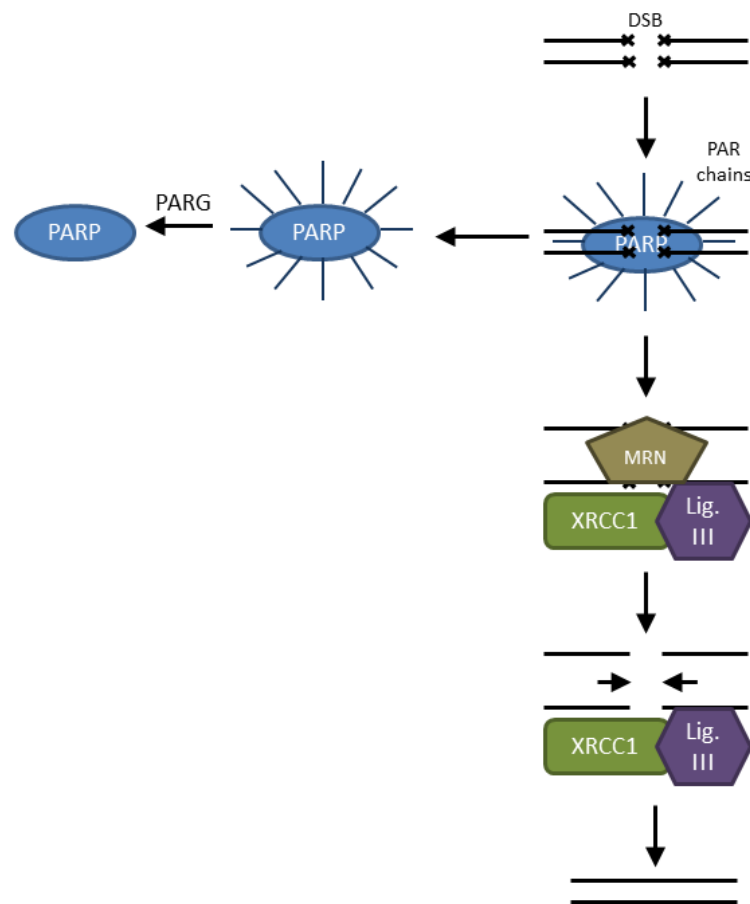


Figure 1.10. Schematic outline of the back-up non-homologous end-joining (B-NHEJ) model. DSB = double strand break; PAR = poly(ADP-ribose); PARG = poly(ADP-ribose) glycohydrolase; MRN = Mre11-Rad50-Nbs1; lig. = ligase; XRCC1 = X-ray cross-complimenting protein 1.

In contrast to NHEJ, HR requires a sister chromatid (Takada *et al.*, 1998) and is an error-free repair mechanism. The repair process begins with the recruitment of the MRN complex and replication protein A (RPA) to the DSB (Figure 1.11). RPA protect the 5' ends of the broken DNA strands while the MRN complex

performs limited resection at the 3' ends. RPA also facilitates the assembly of Rad51 (Hoeijmakers, 2001) that is recruited to the 5'-ends of the DSB by the breast cancer 2 early onset (BRCA-2) protein (Yuan *et al.*, 1999; Davies *et al.*, 2001), which in turn results in the displacement of RPA. BRCA-2 is recruited to DSBs by the Fanconi anaemia pathway (reviewed by Wang and D'Andrea (2004)). At the same time, Rad54 identifies the sister chromatid (Hoeijmakers, 2001) and, once the DNA sequences are aligned, Rad51 exchanges a single strand of the damaged DNA with the same sequence from a non-damaged double-stranded DNA molecule in a process called strand invasion (Baumann, Benson, and West, 1996). Finally, DNA polymerases use the homologous DNA sequences for DNA synthesis and the process is complete by ligation of the DNA strands (Hoeijmakers, 2001) (Figure 1.11).

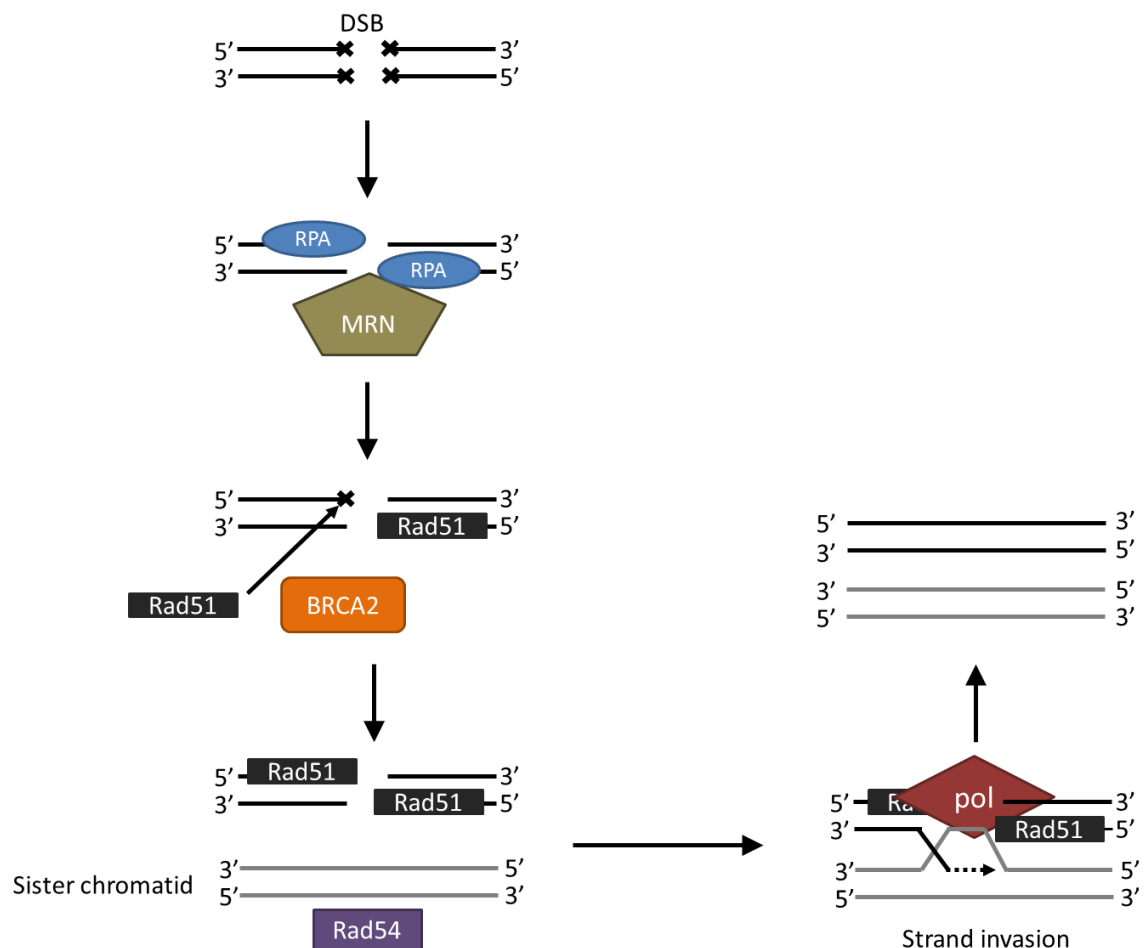


Figure 1.11. Schematic outline of the homologous recombination (HR) model. DSB = double strand break; MRN = Mre11-Rad50-Nbs1; RPA = replication protein A; BRCA2 = breast cancer 2 early onset; pol = polymerase.

1.3.2 PARP-1 in glioblastoma and other cancers.

Expression levels of PARP-1 in healthy brain are generally low and fairly homogenous relative to other body tissues (Galia *et al.*, 2012; The Human Protein Atlas, 2015). However, high levels of PARP-1 have been revealed to be present in human glioma lesions when compared to surrounding grey matter using immunohistochemical staining techniques (The Human Protein Atlas, 2015; Wharton *et al.*, 2000; Galia *et al.*, 2012). Prominent PARP-1 immunohistochemical staining was also observed in tumour spheroids prepared from four different human malignant astrocytoma cell lines (Wharton *et al.*, 2000). The latter findings would suggest that glioma PARP-1 overexpression *in vivo* was localised to neoplastic cells. However, glioma lesions are known to exhibit prominent infiltration by microglia, which are resident immune cells of the CNS (Olah *et al.*, 2011; Wu *et al.*, 2013) and can also express high levels of PARP-1 (Kim *et al.*, 2014). Therefore, it is possible that these immune cells could contribute to the high PARP-1 expression levels found in glioma tumours *in vivo*. To the best of the author's knowledge, there are no published studies that attempted to delineate between neoplastic and immune PARP-1 expression within glioma lesions.

In addition to gliomas, PARP-1 overexpression was also found to be present in a number of primary tumours. Specifically, microarray analysis of PARP-1 gene expression in surgical samples from more than 8000 primary malignant and human tissues revealed elevated PARP-1 mRNA expression in cancers of the breast, endometrium, ovary, lung, skin, and non-Hodgkin's lymphoma. This trait was not characteristic of all types of cancers as samples from adrenal, bone, colon, and prostate tumours did not exhibit PARP-1 overexpression relative to corresponding non-cancerous tissues. Interestingly, analysis of PARP-2 expression in cancerous and healthy tissues did not reveal any significant differences (Ossovskaya *et al.*, 2010).

1.3.2.1 PARP-1 inhibitors.

The role of PARP-1 in DNA damage repair and the fact that the protein has been shown to be overexpressed in a number of cancers have made it an attractive target for anti-cancer therapy. Interest from the pharmaceutical industry in this target led to the development of number clinical PARP-1 inhibitor candidates that, at the time of writing, were being investigated as synthetically lethal (see section 1.3.2.2) and chemoradiosensitising (see section 1.3.2.3) agents. In the context of GBM, pursuing alternative therapeutic approaches is of value as current chemo- and radiotherapeutic regimens are associated with poor patient outcomes (see section 1.1.3 for details).

PARP-1 inhibitors work by blocking the binding of NAD^+ to the PARP-1 active site in a competitive manner (reviewed by Ferraris (2010)). The discovery of these inhibitors can be traced back to Clark, Ferris, and Pinder (1977) who showed that nicotinamide, a by-product of PAR chain formation (see section 1.3.1 for details), had weak PARP-1 inhibitory properties and an inhibition constant (K_i) value, which denotes the affinity of a ligand for its receptor, of 20 μM . Soon after it was established that the structurally related compounds benzamide and pyrazinamide (Figure 1.12) were also capable of inhibiting PARP-1 (Shall, 1975). However, the presence of ring nitrogens made the pyrazinamide liable to metabolism, while benzamide exhibited poor solubility properties (Purnell and Wish, 1980). Therefore, Purnell and Wish (1980) investigated a number of benzamide analogues with improved solubility properties as potential inhibitor candidates. The authors found 3-aminobenzamide and 3-methoxybenzamide (Figure 1.12) to be the most potent inhibitors with K_i values of 1.8 and 1.5 μM respectively. These analogues became known as first generation PARP inhibitors.

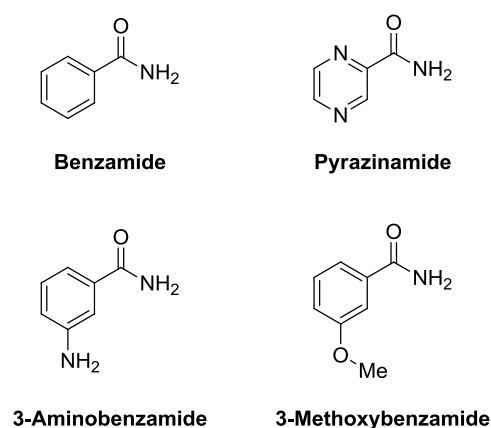


Figure 1.12. Structures of first generation PARP-1 inhibitors.

Substantial effort was made by a number of pharmaceutical companies to discover and develop second generation PARP-1 inhibitors that exhibited improved potency, cellular residence time, and *in vivo* activity. The first of these clinical candidates was rucaparib (Figure 1.13), which was discovered by Newcastle University and Pfizer. The drug discovery programme for this compound involved screening 42 agents based around a number of core scaffolds including quinazolinones, benzimidazoles, and tricyclic indoles. As a result of this process, AG14447 was identified as the most potent with a K_i value of 1.4 nM and with favourable *in vivo* chemosensitisation activity against colorectal tumour xenografts. In this case, chemosensitisation refers to the increase in cancer cell sensitivity to chemotherapeutic agents as a consequence of PARP-1 inhibition. The phosphate salt of this compound (rucaparib) exhibited improved solubility properties and was advanced to clinical studies (Thomas *et al.*, 2007). At the time of writing this thesis, rucaparib was undergoing a number of phase II studies investigating its use as monotherapy for BRCA deficient pancreatic, ovarian, and breast cancers (ClinicalTrials.gov).

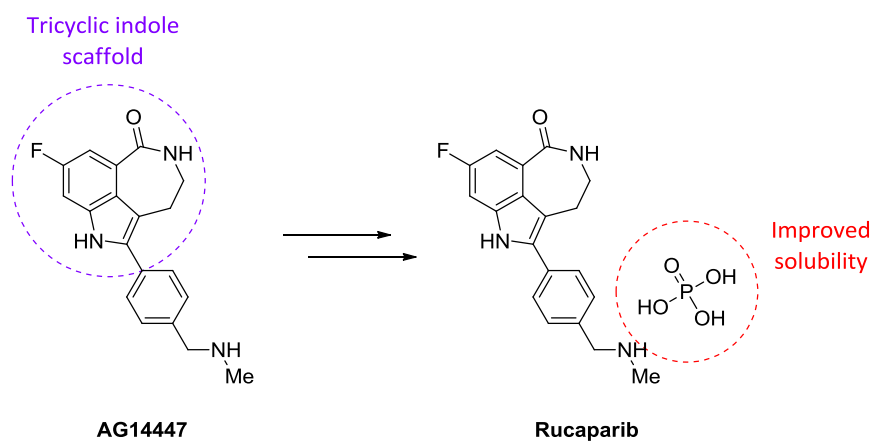


Figure 1.13. Discovery of the PARP-1 inhibitor rucaparib.

Rucaparib was shortly followed by the discovery of the potent PARP-1 inhibitor olaparib (Figure 1.14) by KuDOS Pharmaceuticals Ltd., Maybridge, and Astra Zeneca. The former two companies filed a number of patents for 2-substituted quinazolinones, 3- and 4-substituted isoquinolines, and 4-substituted phthalazinones in the early 2000s, and identified the phthalazinone scaffold as suitable for further optimisation (reviewed by Ferraris (2010)). The discovery of the phthalazinone KU0051529 (Figure 1.14) was a key milestone as the compound exhibited good activity against PARP-1 *in vitro* with a half maximal inhibitory concentration (IC_{50}) of 770 nM (see section 4.1.1 for details concerning the IC_{50} parameter). Moreover, structural activity relationship studies utilising chicken PARP-1 crystallography data revealed that the *meta* position on the benzyl ring was a beneficial site for structural elaboration. Initial efforts found that *meta* benzyl aniline analogues of KU0051529 exhibited good activity against PARP-1 but suffered from poor metabolic stability. Constraining the aniline into a 5-membered lactam resulted in a slight drop off in potency but markedly improved metabolic stability. PARP-1 inhibitory activity was rescued by addition of a fluorine atom *ortho* to the imine ring, thereby resulting in the metabolically stable and potent PARP-1 inhibitor ($IC_{50} = 5$ nM) KU0058684 (Loh *et al.*, 2005) (Figure 1.14). Despite the compound showing a reasonable level of oral bioavailability (Loh *et al.*, 2005), KuDOS Pharmaceuticals Ltd. re-directed their medicinal chemistry efforts to further improve on the bioavailability parameter for clinical use. The result of these efforts was olaparib, which maintained excellent PARP-1 inhibitory potency ($IC_{50} = 5$ nM), and exhibited approximately two-fold greater chemosensitisation activity and improved oral bioavailability when compared to KU0058684. Key structural alterations included the addition

of a piperazine moiety that was found to improve aqueous solubility, and functionalisation of the distal nitrogen atom of the piperazine with a cyclopropane that reduced the pKa and subsequently improved oral bioavailability. Importantly, it was also found that PARP-1 inhibitory potency of this compound class was tolerant to structural modifications in the cyclopropane bearing region (Menaar *et al.*, 2008). The synthetic development of olaparib was shortly followed by the acquisition of KuDOS Pharmaceuticals Ltd. by Astra Zeneca (reviewed by Ferraris (2010)), who implemented an aggressive clinical development programme that resulted in the accelerated marketing authorisation of olaparib in the EU and US as a monotherapeutic anticancer agent (see section 1.3.2.2 for details). At the time of writing, olaparib was also undergoing multiple phase I, II, and III studies looking at its use as either monotherapy or adjuvant therapy for the treatment of pancreatic, ovarian, breast, prostate, soft tissue, oesophageal, head and neck, gastric, colorectal, skin, small cell and non-small cell lung cancers, and glioblastoma (ClinicalTrials.gov).

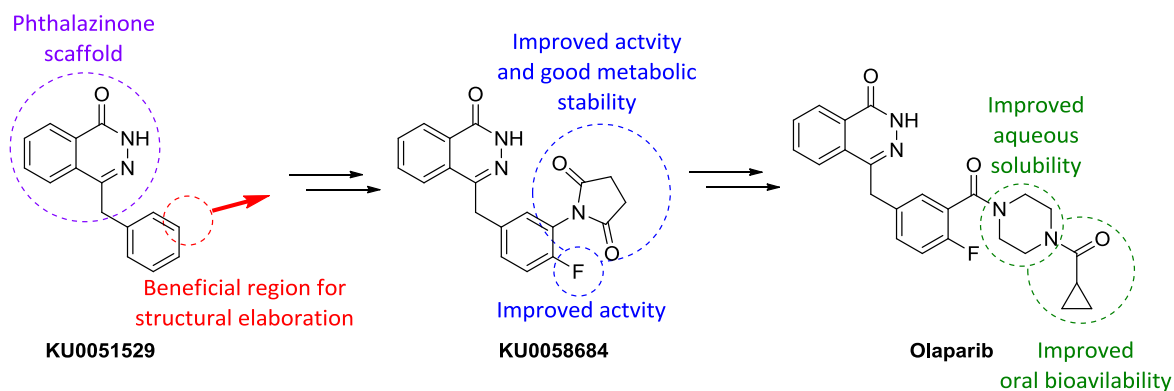


Figure 1.14. Discovery of the PARP-1 inhibitor olaparib.

Another important contender in the PARP-1 inhibitor arena is Abbot with their clinical candidate veliparib (Figure 1.15). Discovery of this compound can be traced back to the BASF group who accumulated PARP-1 inhibitor intellectual property based around a number of core structures including indole carboxamides, phthalazinones and benzimidazole carboxamides. In 2001, Abbot acquired the BASF pharmaceutical division and initiated a medicinal chemistry programme focusing on the benzimidazole carboxamide scaffold (reviewed by Ferraris (2010)). This led to the development of the lead candidate A-620223

(Figure 1.15), which was a potent PARP-1 inhibitor ($K_i = 8 \text{ nM}$, and $EC_{50} = 3 \text{ nM}$) with good aqueous solubility, oral bioavailability, and *in vivo* tumour chemosensitisation activity. The tertiary amine moiety was key in improving solubility and activity against PARP-1 (Penning *et al.*, 2008). Further optimisation of this compound focused on the introduction of a tertiary centre adjacent to the benzimidazole ring, which was previously found to be beneficial in improving PARP-1 inhibitory potency of the benzimidazole carboxamide scaffold. These efforts led to the synthesis of the clinical candidate veliparib, which exhibited improved PARP-1 and cellular activity ($K_i = 5 \text{ nM}$, and $EC_{50} = 2 \text{ nM}$). Interestingly, it was found that the stereochemistry of this tertiary centre did not affect cellular activity, but was crucial in maximising oral bioavailability (Penning *et al.*, 2009). The clinical development programme for veliparib has resulted in numerous phase I, II and III trials where, at the time of writing, the PARP inhibitor was being assessed as monotherapy or adjuvant therapy for ovarian, cervical, breast, pancreatic, rectal, gastric, bladder, liver, oesophageal, skin, head and neck, lung, and brain cancer as well as lymphomas, and leukaemias (ClinicalTrials.gov).

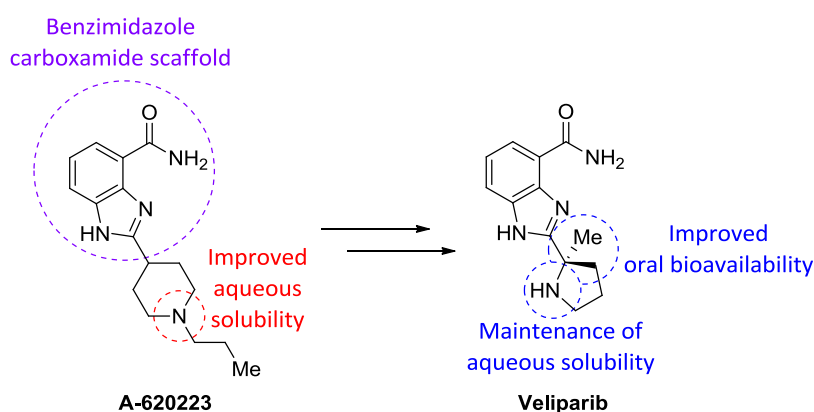


Figure 1.15. Discovery of the PARP-1 inhibitor veliparib.

Other PARP-1 inhibitors that, at the time of writing, were at less advanced stages of clinical development include the indazole carboxamide niraparib, the pyrrolocarbazole lactam pro-drug CEP9722, and E7016 developed by Merck, Cephalon, and MGI Pharma respectively. It is noteworthy that the exact structure of E7016 has not been disclosed, but it is thought to be structurally related to GPI15427 (Figure 1.16). For further information regarding the

discovery and development of these agents please refer to the reviews by Ferraris (2010) and Anwar M, Aslam, and Anwar S (2015).

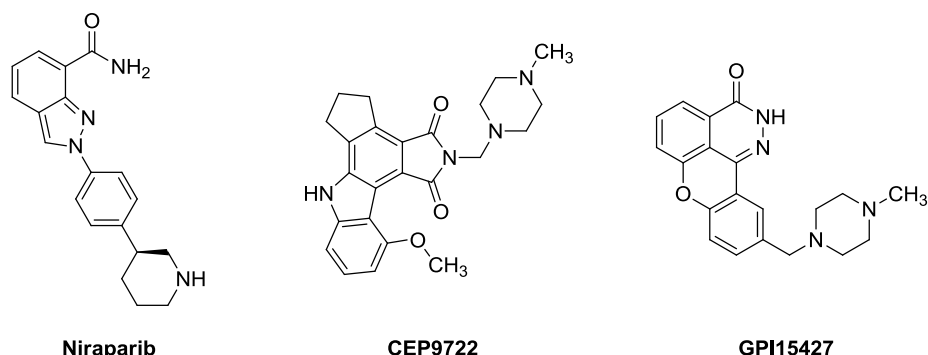


Figure 1.16. Structures of other, less clinically advanced, PARP-1 inhibitors.

1.3.2.2 PARP-1 inhibition and synthetic lethality.

Synthetic lethality may be defined as the situation where disruption of two related parallel cellular pathways leads to cell death, where disruption of either one of the pathways individually has no effect on cell viability (Guarente, 1993; Kaelin, 2005). This concept of synthetic lethality has been shown to be an effective way of targeting cancers *in vitro* and *in vivo*. Specifically, cancer cells with an impaired ability to repair DNA DSBs via the HR pathway, due to a mutation of the BRCA gene, were found to be highly sensitive to PARP inhibitors (Bryant *et al.*, 2005; Farmer *et al.*, 2005). Moreover, PARP inhibition was revealed to completely inhibit BRCA-2 negative tumour xenograft formation following transplantation into nude mice, while BRCA-2 positive wild-type tumour formation was not affected (Farmer *et al.*, 2005). PARP inhibitor treatment was also shown to reduce BRCA-1 or BRCA-2 negative tumour xenograft size when compared to corresponding wild-type tumours that showed no response (Bryant *et al.*, 2005; Rottenberg *et al.*, 2008).

Mechanistically, it was originally proposed that PARP inhibition leads to impairment of the BER pathway and subsequently an accumulation of DNA SSBs. This was then thought to cause a collapse of replication forks into toxic DSBs that are normally repaired by HR, and finally cell death (Bryant *et al.*, 2005; Farmer *et al.*, 2005) (Figure 1.17 A). However, recent findings by Gottipati *et al.*

(2010) and Storm *et al.* (2011) suggested that this is not the case. It was shown that the addition of hydrogen peroxide (a DNA damaging agent) and a PARP inhibitor to BRCA-2 defective and wild-type cells did not affect the steady state levels of DNA SSBs (Gottipati *et al.*, 2010). Furthermore, PARP inhibition and siRNA knockdown in undamaged cells did not result in the accumulation of SSBs (Storm *et al.*, 2011). In light of these findings, Helleday (2011) proposed that PARP inhibition leads to the trapping of PARP-1 on the DNA SSB. This then acts as an obstacle to BER proteins and DNA replication, which subsequently requires bypassing by HR (Figure 1.17 B). The mechanism of PARP-BRCA synthetic lethality was further refined by Patel, Sarkaria, and Kaufmann (2011) who showed that in HR deficient cells, PARP acts to suppress DNA-PK activity, which is a key player in the error prone NHEJ pathway (see section 1.3.1 for details). Counterintuitively, the authors also observed that disabling NHEJ diminished genomic instability and lethality of PARP inhibition. Therefore, it was proposed that in the presence of impaired HR, PARP inhibition leads to activation of NHEJ and subsequent genomic instability followed by cell death (Figure 1.17 B).

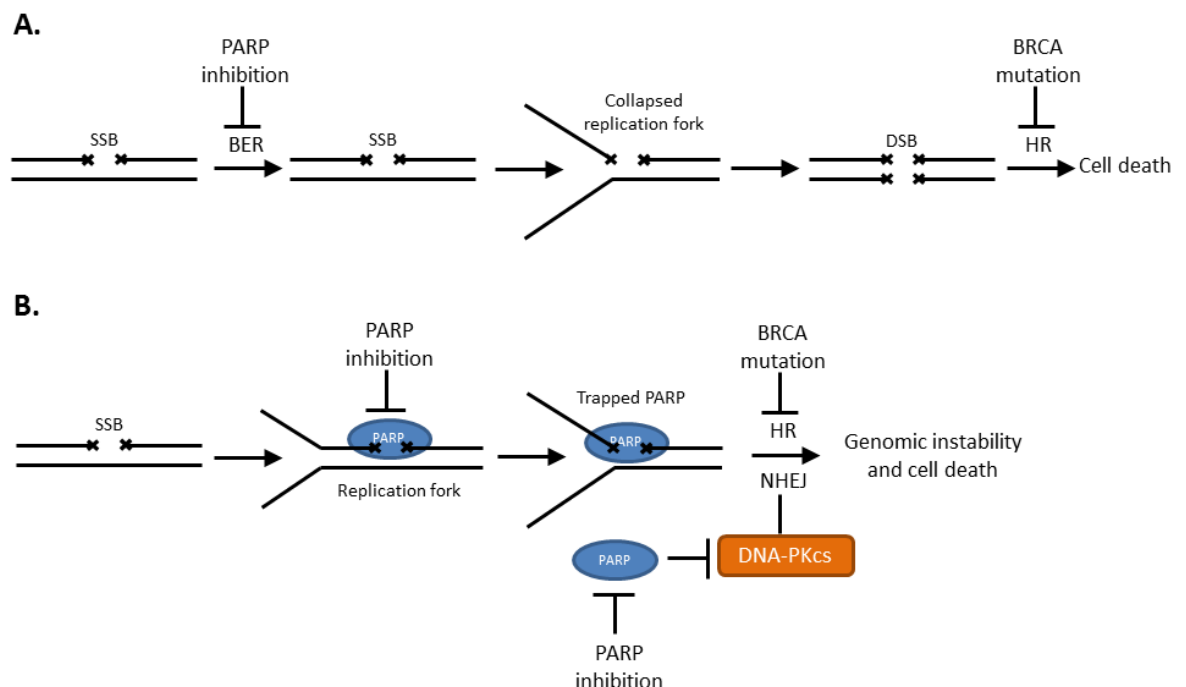


Figure 1.17. Initially proposed (A) and refined (B) mechanistic models of PARP-1 inhibitor mediated synthetic lethality of cells with BRCA gene mutations.

These early mechanistic discrepancies concerning PARP-BRCA synthetic lethality did not impede the clinical application of this approach. The major advantage of

PARP-BRCA synthetic lethality is that it is selective for neoplastic cells with the BRCA mutation, while cells with functional HR are not affected. This was confirmed in early clinical trials that showed good tolerability and few side effects following monotherapy with PARP inhibitors such as olaparib (Fong *et al.*, 2009; Yamamoto *et al.*, 2012; Bundred *et al.*, 2013), veliparib (Kummar *et al.*, 2009), niraparib (Sandhu *et al.*, 2013), and CEP9722 (Plummer *et al.*, 2014).

Epithelial ovarian cancer is the second most common and most deadly gynaecological malignancy in the Western World. Approximately 10–15% of cases of the disease are associated with a mutation of the BRCA gene, while up to 60% could be associated with other deficiencies of the HR pathway (Marchetti *et al.*, 2012). It is therefore not surprising that epithelial ovarian cancer has received interest from the pharmaceutical industry as a target for PARP inhibitor mediated synthetic lethality.

A phase II study investigating the maintenance treatment of women with relapsed ovarian cancer with olaparib (n = 136) showed a significant improvement in the progression-free survival relative to a placebo control group (n = 129) (median progression-free survival = 8.4 months in olaparib treated group versus 4.8 months in placebo treated group; hazard ratio = 0.35, 95% confidence interval = 0.25–0.49). However, interim analysis of data revealed that the improvement in progression-free survival did not appear to translate into an improvement in overall survival (median overall survival = 29.7 months in olaparib treated group versus 29.9 months in placebo treated group). The authors advised cautious interpretation of these data as at the time of writing the manuscript 21% and 3% of patients were still receiving olaparib and placebo respectively. Moreover, the BRCA mutation status of patients enrolled onto the study was not confirmed (Lederman *et al.*, 2012). Retrospective genotyping of patients allowed for analysis of data according to BRCA mutation status. From the patients with confirmed BRCA status, 56% (74 out of 131) of individuals in the olaparib treated group and 50% (62 out of 123) of individuals from the placebo treated group had mutations in the BRCA genes. The median progression free survival was found to be 11.2 months in the olaparib treated BRCA mutated group versus 4.3 months in the placebo treated BRCA mutated group (hazard

ratio = 0.18, 95% confidence interval = 0.10–0.31). As before, the authors failed to show a statistically significant improvement in the overall survival rate (Lenderman *et al.*, 2014).

Despite ongoing phase III trials (Deeks, 2015), the marked improvement in the aforementioned progression-free survival led to the accelerated approval of olaparib as a monotherapy for advanced recurrent ovarian cancer in the EU and the US in late 2014 (AstraZeneca, 2014; Food and Drug Administration, 2014). Phase I and II studies have also shown that olaparib monotherapy is beneficial for the treatment of triple negative breast cancer (reviewed by Deeks (2015)), where the incidence of BRCA mutations is approximately 30% (Greenup *et al.*, 2013). Olaparib is currently undergoing phase III studies comparing its effectiveness as monotherapy for BRCA mutated breast cancer versus chemotherapy (Deeks, 2015). For further information concerning the use of less clinically advanced PARP inhibitors as synthetically lethal agents please see the reviews by Buege and Mahajan (2015), and Anwar M, Aslam, and Anwar S, (2015).

1.3.2.3 PARP-1 inhibition and chemoradiosensitisation.

Numerous *in vitro* and *in vivo* studies have shown that the effect of chemotherapeutic agents can be enhanced by pharmacological PARP-1 inhibition; this phenomenon has been termed chemosensitisation. PARP-1 inhibition was found to potentiate antitumour effects, such as cytotoxicity and tumour cell growth inhibition, of TMZ *in vitro* using glioma (Wedge *et al.*, 1996; Tentori *et al.*, 2002; Miknyoczki *et al.*, 2003), leukaemia (Boulton *et al.*, 1995), neuroblastoma (Miknyoczki *et al.*, 2007), melanoma (Wedge *et al.*, 1996; Tentori *et al.*, 2003), lymphoma (Tentori *et al.*, 2003), lung carcinoma (Skalitzky *et al.*, 2003), colon carcinoma (Wedge *et al.*, 1996; Skalitzky *et al.*, 2003; Curtin *et al.*, 2004; Calabrese *et al.*, 2004; Thomas *et al.*, 2007), ovarian carcinoma (White *et al.*, 2000; Curtin *et al.*, 2004), and breast carcinoma (Wedge *et al.*, 1996) cell lines. Similar chemosensitisation effects were also seen when PARP-1 inhibition was combined with other cytotoxic agents such as irinotecan for the treatment of colon carcinoma cells (Miknyoczki *et al.*, 2003), topotecan for the treatment

of ovarian (White *et al.*, 2000), lung (Skalitzky *et al.*, 2003) and colorectal (Calabrese *et al.*, 2004; Thomas *et al.*, 2007) cancer cells, and finally cyclophosphamide (Donawho *et al.*, 2007) and doxorubicin (Mason *et al.*, 2008) for the treatment of breast carcinoma cells.

Crucially, the above mentioned *in vitro* findings were also translatable to small animal pre-clinical studies where combination treatment with TMZ and a PARP-1 inhibitor resulted in improved outcomes in glioma (Miknyoczki *et al.*, 2003; Tentori *et al.*, 2003; Miknyoczki *et al.*, 2007), lymphoma (Tentori, Leonetti *et al.*, 2002), colon carcinoma (Calabrese *et al.*, 2004; Thomas *et al.*, 2007), and malignant melanoma (Zhu *et al.*, 2008) models of cancer when compared to TMZ alone. The outcomes that were monitored included tumour xenograft growth inhibition, growth delay, reduction in volume, and increased animal survival.

PARP-1 inhibition was also found to potentiate ionising radiation induced killing of glioma (Chalmers *et al.*, 2004; Barazzuol *et al.*, 2013), leukaemia (Griffin *et al.*, 1998), non-small cell lung carcinoma (Senra *et al.*, 2011), breast carcinoma (Efimova *et al.*, 2010), colon carcinoma (Calabrese *et al.*, 2004; Donawho *et al.*, 2007), and pancreatic carcinoma (Hirai *et al.*, 2012) cells, and improved outcomes in pre-clinical studies of radiotherapy treated small animals bearing breast (Rojas *et al.*, 1996; Efimova *et al.*, 2010) and colon (Calabrese *et al.*, 2004; Donawho *et al.*, 2007) cancers. These findings support the premise that PARP-1 inhibition can also have a radiosensitising effect.

The proposed mechanisms of PARP-1 inhibitor mediated chemo- and radiosensitisation are outlined in Figure 1.18. Briefly, alkylating agents and cross linking agents result in the formation of DNA SSBs and DSBs respectively, while ionising radiation generates SSBs and DSBs in an approximate ratio of 25 : 1 (Lieber, *et al.*, 2010; Chalmers *et al.*, 2010). PARP-1 inhibition leads to the trapping of the protein on SSBs lesions, which subsequently prevents BER ligation from taking place. This results in an accumulation of unrepaired DNA SSBs, which upon DNA replication cause the collapse of replication forks and subsequent generation of DNA DSBs (Chalmers *et al.*, 2010; Storm *et al.*, 2011; Helleday *et al.*, 2011). The large amount of DNA DSBs eventually cause the HR repair

pathway to become overwhelmed, while NHEJ drives genomic instabilities. The end result of these events is cell death (Caldecott, 2008).

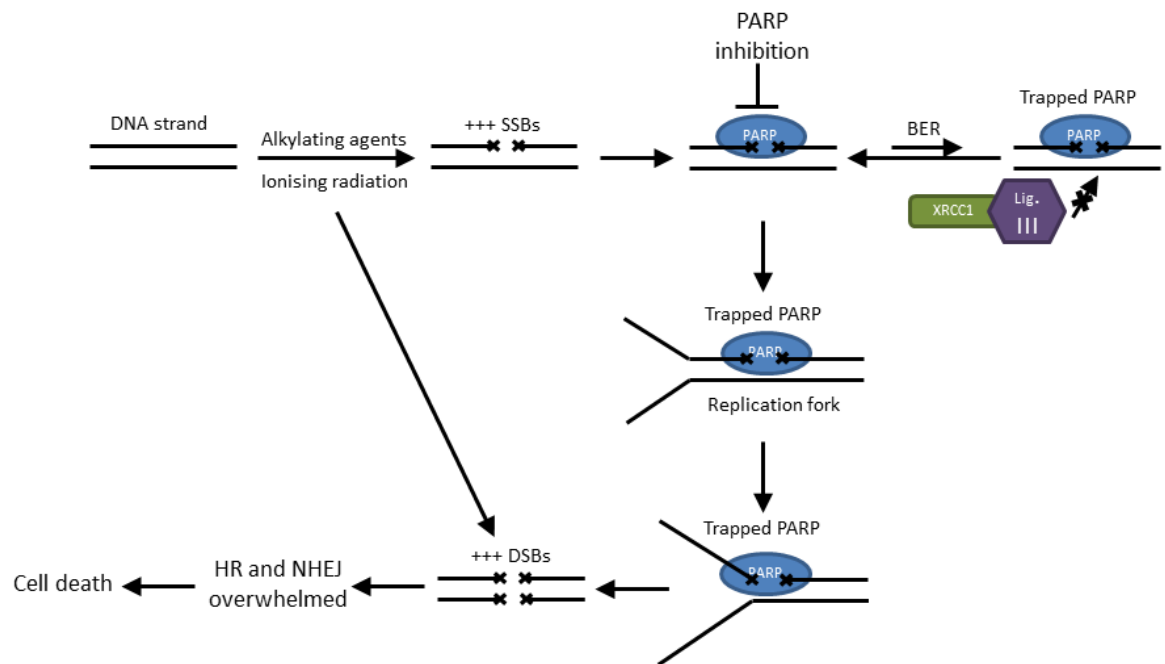


Figure 1.18. Mechanistic models of PARP-1 inhibitor mediated chemo- and radiosensitisation.

The use of PARP-1 as chemo- and radiosensitisers has also been investigated in multiple human trials. However, early human studies identified that PARP-1 inhibitor mediated chemosensitisation lacked tumour selectivity and affected other body tissues, in particular the bone marrow. The addition of either rucaparib (Plummer *et al.*, 2008) or veliparib (Isakoff *et al.*, 2010) to TMZ, or olaparib to chemotherapeutic agents such as dacarbazine (Khan *et al.*, 2011), cisplatin, and gemcitabine (Rajan *et al.*, 2012), topotecan (Samol *et al.*, 2012) or paclitaxel (Dent *et al.*, 2013) resulted in increased incidence and severity of myelosuppression than expected for patients treated with these chemotherapeutic agents in the absence of PARP-1 inhibition. In one case, the high incidence of haematological adverse events resulted in the discontinuation of the trial (Samol *et al.*, 2012). In an effort to combat this myelosuppressive effect, Dent *et al.* (2013) recruited additional patients to their trial that were then treated prophylactically with granulocyte-colony stimulating factor (GCSF). However, this approach was not successful as two out of three patients developed high grade recurrent neutropenia, despite GCSF prophylaxis.

Rajan *et al.* (2012) highlighted the importance of further studies to assess novel schedules of administration with the aim of enhancing tolerance to PARP-1 inhibitor and chemotherapeutic agent combinations. This could be achieved by identifying timepoints for chemotherapy dosing in relation to PARP-1 inhibitor dosing, such that the concentration of the PARP-1 inhibitor is minimal in peripheral tissues at the time of chemotherapy administration. This approach can be justified by the fact that the PARP-1 inhibitor olaparib has been shown to be retained in mouse tumour xenografts for up to 96 hours while clearance from peripheral tissues appeared to be more rapid (Chalmers *et al.*, 2014).

At the time of writing, the number of published human trials investigating the radiosensitising effect of PARP-1 inhibition was limited, although multiple studies are currently underway looking at exploiting this effect for the treatment of GBM and lymphoma, and head and neck, breast, ovarian, oesophageal, non-small cell lung, and pancreatic cancers (ClinicalTrials.gov). Studies that have been published utilised nicotinamide (Kaanders, Bussink, and van der Kogel, 2002; Janssens *et al.*, 2012), which has weak PARP-1 inhibitory properties. However, early pre-clinical investigations suggested that PARP-1 inhibition is not the only mechanism through which nicotinamide achieved radiosensitisation. It was thought that nicotinamide reduced tumour hypoxia by enhancing perfusion, which in turn facilitated generation of cytotoxic oxygen adducts on DNA base radicals formed by ionising radiation (Kaanders, Bussink, and van der Kogel, 2002).

The potential advantage of PARP-1 mediated radiosensitisation over chemosensitisation is that the therapeutic beam of ionising radiation can be focused on tumours, such that exposure of healthy tissues is minimised. In practice, this approach has the potential to circumvent the issues of enhanced myelosuppression seen with PARP-1 inhibitor and chemotherapeutic agent combinations. However, in the case of GBM, accurate anatomical localisation and delineation of the tumour lesion is required in order to maximise therapeutic benefit and minimise adverse events to surrounding non-tumorous tissue.

1.3.3 Nuclear imaging of PARP-1.

1.3.3.1 Applications in glioblastoma and other cancers.

Nuclear imaging of PARP-1 has the potential to identify GBM lesions in good contrast compared to surrounding brain tissue, unlike [¹⁸F]-FDG PET, provided that the radiotracer is capable of crossing the BBB. This is justified by the high levels of PARP-1 expression in glioma lesions relative to non-cancerous brain tissue (see section 1.3.2 for details), which is a key criterion for a biological imaging biomarker (Prescott, 2013). However, this is already achievable with amino acid based radiotracers, which have been shown to provide a benefit over structural neuroimaging in the context of GBM diagnosis and surgical planning (see section 1.2.3 for details). Importantly, such applications are reliant on the ability of the radiolabelled probe to cross the BBB, and conclusive data regarding existing PARP-1 radiotracers and their BBB permeability is currently lacking. For these reasons, this section will focus on the clinical applications of PARP-1 nuclear imaging that are outside of the realm of amino acid based radiotracer imaging.

At the time of writing, olaparib was being investigated as a TMZ sensitising agent for the treatment of relapsed GBM in a phase I trial (Trial identifier: NCT01390571) (ClinicalTrials.gov). Despite not being able to cross the BBB, therapeutic levels of olaparib in recurrent GBM tissue samples obtained from patients treated with the drug were detected. It was proposed that BBB disruptions associated with the tumour allowed for occupancy of the tumour by the PARP-1 inhibitor (Chalmers *et al.*, 2014). It is important to bear in mind that these data were based on a small population (n = 8) and tissue samples that corresponded to only a portion of the entire tumour mass. Gliomas can exhibit different degrees of BBB disruption (Roelcke *et al.*, 1995; Kracht *et al.*, 2004; Wolburg *et al.*, 2012) and variable levels of perfusion (Vajkoczy and Menger, 2000) that could affect the amount and extent of olaparib tumour penetration, and subsequently the clinical effectiveness of this therapeutic approach. Nuclear imaging of an appropriately radiolabelled version of olaparib could be used to directly establish the occupancy of the radioligand within the tumour tissue, and

using blockade protocols indirectly establish olaparib tumour occupancy. Clinically, this information could be used to identify patients that are unlikely to respond to therapy as a consequence of poor PARP-1 inhibitor tumour drug uptake and occupancy prior to commencing treatment.

In the broader context of cancer therapy, such an imaging platform could also be used to confirm the presence of tumour resistance to PARP-1 inhibitor mediated synthetic lethality and chemo/radiosensitisation in a clinical setting, which to date has only been shown in *in vitro* and pre-clinical *in vivo* studies. Specifically, *in vitro* resistance to olaparib has been observed in PARP-1 deficient mouse embryonic stem cell mutants and PARP-1 siRNA knockout human breast and colorectal cancer cell lines (Pettitt *et al.*, 2013). Furthermore, long-term treatment of mice bearing BRCA-1 deficient tumours with olaparib was found to increase efflux transporter (i.e. P-glycoprotein) expression and consequently reduce sensitivity to olaparib (Rottenberg *et al.*, 2008). It is possible that human tumours could develop resistance through similar mechanisms following prolonged treatment. Nuclear imaging using a radiolabelled PARP-1 inhibitor could be used to confirm such resistance mechanisms in humans, and subsequently identify patients that are unlikely to benefit from continued PARP-1 inhibitor therapy, thereby allowing for pursuit of alternative therapeutic approaches (Edmonds *et al.*, 2016).

As highlighted previously (see section 1.3.2.3 for details), PARP-1 mediated chemosensitisation has been associated with severe haematological complications due to the lack of tumour selectivity. Nuclear imaging of a radiolabelled PARP-1 probe could be used to non-invasively and indirectly study the biodistribution of the PARP-1 inhibitor *in vivo*, and subsequently establish the duration of PARP-1 inhibition in different tissues. In turn, this information could guide dosing decisions for PARP-1 inhibitors when used as chemosensitising adjuvants, such that tumour cytotoxicity is maximised and bone marrow toxicity is minimised.

1.3.3.2 Existing tracers for PARP-1.

The first reported nuclear imaging agent for PARP-1 was the ^{11}C -labelled version of the phenanthridinone PJ34 (Figure 1.19). The compound exhibited good PARP-1 inhibitory properties ($\text{IC}_{50} = 20 \text{ nM}$) and was shown to accumulate in tissue expressing high levels of PARP-1 (Tu *et al.*, 2005). However, the radiotracer was disadvantaged by the short half-life of the ^{11}C radioisotope (see section 1.2.1 for details). In order to address this limitation, a number of academic groups focused their efforts on utilising the longer lived ^{18}F radionuclide (half-life = 109.8 minutes) in their PARP-1 radiotracer development programmes. The first of these radiofluoride-bearing ligands was [^{18}F]-FE-LS-75 (Figure 1.19), which was an analogue of the M_1 muscarinic antagonist pirenzepine and exhibited only moderate affinity for PARP-1 ($K_i = 200 \text{ nM}$) (Riss *et al.*, 2009). This was then followed by the discovery of the olaparib analogue [^{18}F]-BO by Reiner *et al.* (2012). Despite the addition of a bulky molecular entity to the piperazine functionality, the compound exhibited good PARP-1 inhibitory properties ($\text{IC}_{50} = 17.9 \text{ nM}$) and specificity for PARP-1 *in vivo* (Reiner *et al.*, 2012). The same research group have also utilised the olaparib scaffold to develop the dual modality optical/PET imaging tracer [^{18}F]-PARPi-FL ($\text{IC}_{50} = 12.2 \text{ nM}$). The radiolabelling methodology for this radioligand relied on the $^{18}\text{F}/^{19}\text{F}$ transfluorination of a BODIPY fluorescent component (Carlucci *et al.*, 2015). However, the inherent disadvantage of this kind of approach was the low specific activity of the final product, which could necessitate the use of higher radiotracer doses for nuclear imaging (see section 5.1 for details concerning radiotracer specific activity). Furthermore, it was found that the compound exhibited marked *in vivo* metabolic defluorination and subsequent bone accumulation of the free $^{18}\text{F}^-$ radionuclide, which resulted in high PET background signal (Carlucci *et al.*, 2015) (see chapters 4 and 6 for details concerning ^{18}F -defluorination).

The olaparib scaffold was also utilised by Carney *et al.* (2015) and Salinas *et al.* (2015) for the discovery of ^{18}F - and ^{131}I -labelled PET and SPECT PARP-1 nuclear imaging agents respectively. The synthesis of these agents by the

mentioned authors is described in more detail in sections 5.2.2 and 5.2.1 respectively, and their reported *in vivo* behaviour is discussed in section 6.2.2.

[¹⁸F]-FluorThanatrace ([¹⁸F]-FTT) (Figure 1.19) was one of the most potent (IC₅₀ = 6.3 nM) and advanced PARP-1 PET imaging agent. It was developed by Zhou *et al.* (2014) and is based on the clinical PARP-1 inhibitor candidate rucaparib (see section 1.3.2.1). The radiotracer was shown to exhibit good metabolic stability and *in vivo* specificity for PARP-1 (Zhou *et al.*, 2014; Edmonds *et al.*, 2016). Interestingly, the binding of [¹⁸F]-FTT to PARP-1 in pre-clinical breast cancer models was also shown to correlate with PARP-1 activity (Edmonds *et al.*, 2016). The utility of this tracer as a probe of PARP-1 activity in breast cancer is currently being investigated in a humans as part the phase 0 “PET Imaging of PARP Activity in Cancer (NCT02469129)” trial (ClinicalTrials.gov).

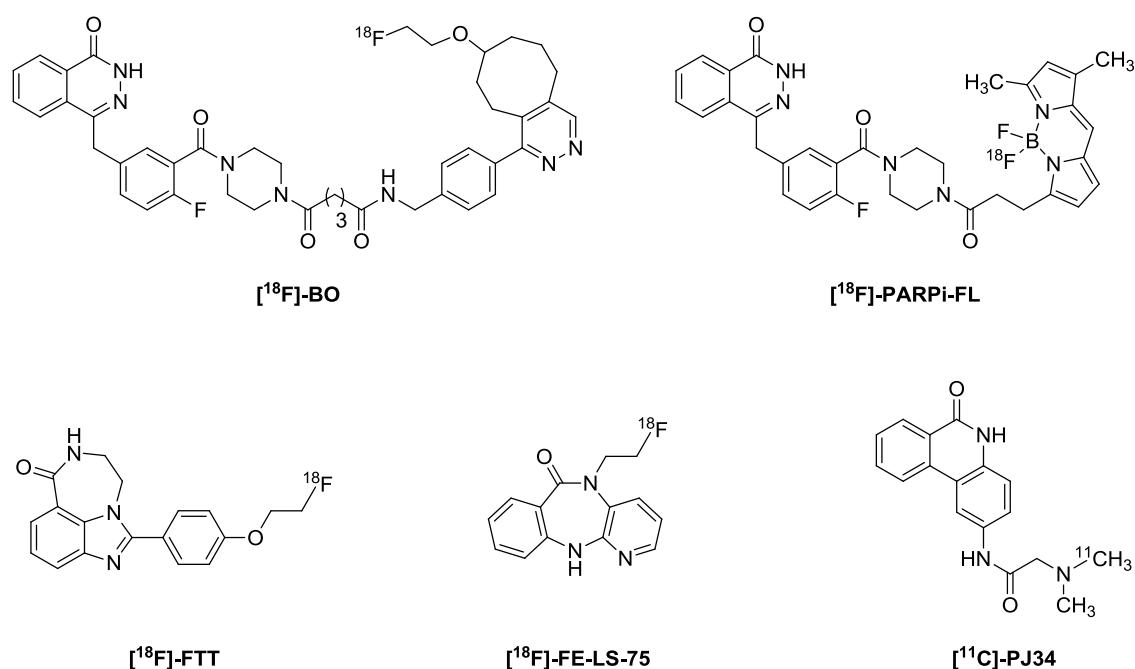


Figure 1.19. Selected PARP-1 radiotracers that have been published to date.

With the exception of one agent, the above mentioned PARP-1 radiotracers have all been developed with PET imaging in mind. As described earlier, the PET imaging modality possesses a number of advantages over SPECT. However, SPECT imaging is likely to remain a key tool in the nuclear medicine arsenal due to new technological developments and unique capabilities such as dual tracer imaging (see section 1.2.2 for more details). Furthermore, the challenges associated with

bridging the gap between pre-clinical development and clinical application are substantial and associated with high attrition rates (see section 1.5.2 for details). Therefore, there is a need for novel PARP-1 nuclear imaging tracers in order to address the limited number of probes for the SPECT imaging modality, and to maximise the prospect of clinical progression of PARP-1 PET imaging probes.

1.4 The translocator protein (TSPO).

1.4.1 What is TSPO and what does it do?

The discovery of TSPO can be traced back to as early as 1977. Braestrup and Squires (1977) were the first to identify two different subclasses of benzodiazepine receptors, namely peripheral benzodiazepine receptors (PBRs) and central benzodiazepine receptors (CBRs), by examining the biodistribution and binding profiles of tritium (i.e. ^3H) labelled diazepam (a centrally acting benzodiazepine). The authors showed that the binding of [^3H]-diazepam to receptors in the brain differed significantly from the binding to receptors located in peripheral organs such as the kidney, liver, and lungs. Specifically, receptor binding in peripheral organs was shown to occur with 15-fold less affinity than to central receptors. Moreover, the pharmacologically inactive benzodiazepine Ro5-4864 (Figure 1.20) was shown to displace [^3H]-diazepam from kidney receptors, while exhibiting only negligible displacement from brain tissue receptors.

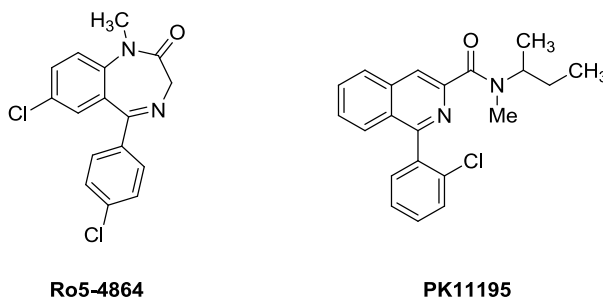


Figure 1.20. Structures of the benzodiazepine and isoquinoline carboxamide TSPO ligands Ro5-4864 and PK11195 respectively.

Over the following decades these newly discovered PBRs have received much scientific attention. On a subcellular level, they have been found to be mainly localised in the outer mitochondrial membrane, although the receptors have been reported to be present in liver nuclei and other organelle membranes (Papadopoulos *et al.*, 2006). Functionally, they have been thought to possess two main biological roles, namely cholesterol transport for steroid synthesis and mitochondrial permeability transition (MPT). The latter refers to a sudden increase in inner mitochondrial membrane permeability, through the mitochondrial permeability transition pore (MPTP), which subsequently leads to rupture of the outer mitochondrial membrane and cellular apoptosis (Selvaraj and Stocco, 2015). Thus, in order to represent more accurately the localisation and putative functions of PBRs, Papadopoulos *et al.* (2006) proposed that name “PBR” is replaced with the term “translocator protein” (TSPO). This new nomenclature became widely accepted amongst the scientific community.

A number of key observations justified the role of TSPO in steroid synthesis. Firstly, in the periphery TSPO is known to be primarily localised in steroid hormone producing tissues such as the adrenal glands, testes, and ovaries (Selvaraj and Stocco, 2015). Secondly, Mukhin *et al.* (1989) showed a strong positive correlation ($R = 0.99$) between the binding potency of nine TSPO ligands and the degree of steroid synthesis by Y-1 mouse adrenal tumour cells. The authors proposed that binding of exogenous ligand to TSPO resulted in facilitation of cholesterol transport from extramitochondrial stores to the inner mitochondrial membrane, where metabolism of cholesterol to pregnenolone (the common intermediate for steroid biosynthesis) takes place. Thirdly, Papadopoulos *et al.* (1997) showed that knockout of TSPO gene in steroid producing R2C rat Leydig tumour cells resulted in a 95% reduction in pregnenolone synthesis when compared to the wild-type cell line. Moreover, steroid synthesising capabilities of TSPO negative cells were not rescued in the presence of exogenous cholesterol. However, addition of a hydrosoluble derivative of cholesterol that can freely pass the mitochondrial membrane resulted in recovery of steroidogenesis. Finally, experimental homology modelling of the protein revealed a channel like structure with an interior core lined with a cholesterol-recognition amino acid consensus motif (Selvaraj and Stocco, 2015).

Taken together, the above observations provide good evidence for the hypotheses that TSPO is involved in cholesterol transport and steroid synthesis. However, more recent findings refuted this premise. It has been shown that PK11195 (Figure 1.20), a compound with nanomolar affinity for TSPO, resulted in an equal increase in progesterone production in both TSPO knockout and wild-type steroidogenic Leydig cells (Tu *et al.*, 2015), suggesting that steroid synthesis was independent of TSPO. Moreover, Morohaku *et al.* (2014) revealed that targeted genetic knockout of TSPO in steroidogenic Leydig cells in male mice did not affect testosterone synthesis. Similarly, Tu *et al.* (2014) and Banati *et al.* (2014) showed that global knockout of TSPO in mice did not affect steroid hormone production and mouse fertility. Furthermore, data acquired using high-resolution nuclear magnetic resonance (NMR) spectroscopy disputed the initial TSPO structural findings, as it has been shown that the cholesterol-recognition amino acid consensus motif was located on the outside of the structure as opposed to lining the internal channel (reviewed by Selvaraj and Stocco (2015)).

The role of TSPO in MPT was first suspected following gel chromatography co-purification of TSPO with other known key components of the MPTP (McEnery *et al.*, 1992). Further evidence for this association was provided by Chelli *et al.* (2001) who showed that exposure of rat cardiac mitochondria to TSPO ligands Ro5-4864 and PK11195 resulted in dose-dependent MPT and mitochondrial swelling. The authors proposed that this was a potential consequence of MPTP opening. Similar observations were made by Azarashvili *et al.* (2014) who utilised rat brain mitochondria transmembrane potential measurements to show that TSPO ligand protoporphyrin IX stimulated MPTP opening. Additionally, this effect was shown to be potentiated by carbenoxolone, which is a substance known to induce MPTP opening. The authors followed on to show that protoporphyrin IX and carbenoxolone driven MPTP opening could be prevented by using an anti-TSPO antibody. However, as in the case of TSPO and steroidogenesis, recent findings do not support the involvement of TSPO in MPT. Using a tissue specific TSPO knockout animal model, Šileikytė *et al.* (2014) revealed that the reduction in calcium retention capacity of rat liver mitochondrial (indicative of MPT) caused by TSPO ligands Ro5-4864 and PK11195 was identical in TSPO knockout wild type control rat liver mitochondria. These findings suggested that TSPO ligand induced MPTP opening was likely an off-target effect, which brought into

question the validity of the earlier mentioned studies that investigated the pharmacological link between TSPO and MPT. This off-target effect of TSPO ligands is further strengthened by the fact that PK11195 has been shown to interact with F₀F₁ ATP synthase (Cleary *et al.*, 2007), which has recently been revealed to form part of the MPTP (Giorgio *et al.*, 2013).

Evidence also exists to suggest that TSPO may play a role in the activation of endoplasmic reticulum-associated protein degradation, inhibition of autophagy and increased pro-inflammatory cytokine production (reviewed by Selvaraj and Stocco (2015)). However, despite approximately three decades of research, the precise functions of TSPO remain elusive and require further investigation.

1.4.2 TSPO in glioblastoma and other conditions.

Relative to other body tissues, expression levels of TSPO (Doble *et al.*, 1987) in healthy brain are generally low and homogenous within the cerebral cortex, the hippocampus, and the cerebellum (The Human Protein Atlas, 2015). However, higher levels of TSPO have been reported in the thalamic and hypothalamic nuclei, the substantia nigra, the caudate, the putamen, the dorsal raphe nucleus, and the hippocampal dentate gyrus (Doble *et al.*, 1987). In the case of human glioma, high levels of TSPO have been observed in the tumour tissue relative to surrounding brain tissue using immunohistochemical staining techniques (The Human Protein Atlas, 2015; Miettinen *et al.*, 1995). Overexpression of TSPO in glioma has also been observed in humans (Cornu *et al.*, 1992) and rodents (Starosta-Rubenstein *et al.*, 1987; Black *et al.*, 1990) using a tritium-labelled version of TSPO ligand PK11195 (i.e. [³H]-PK11195) and *ex vivo* autoradiography, which allows for visualisation of the distribution of a radiolabelled compound bound to solid sections of biological tissue (see section 7.1.2 for details concerning autoradiography). Interestingly, Miettinen *et al.* (1995) were able to correlate the levels of TSPO expression in gliomas to the tumour grade and patient survival. However, as with PARP-1, the overexpression of TSPO in glioma lesions was found to originate from a mixture of neoplastic and microglial cells (Banati *et al.*, 2000; Brown *et al.*, 2000; Winkeler *et al.*, 2012).

Over the past three decades, TSPO has received much interest as a biomarker of neurodegenerative and neuroinflammatory pathology (reviewed by Chen and Guilarte (2008)). The link between TSPO and such conditions can be traced back to the work performed by Schoemaker *et al.* (1982), who showed that chemical lesioning of rat striatum resulted in a ten-fold increase in binding of the tritium labelled TSPO ligand Ro5-4864 when compared to the striatum of healthy control animals. Importantly, the authors concluded that this increase was due to an increase in binding sites as opposed to an increase in binding affinity of the ligand. Benavides *et al.* (1987) performed a similar study looking at the relationships between chemical striatum lesion models and animal TSPO striatal density. It was revealed that administration of chemical neurotoxins resulted in a dose-dependent increase in levels of neuronal damage and TSPO expression (Benavides *et al.*, 1987). These early findings paved the way for numerous animal studies, which showed similar relationships between neurodegeneration and neuroinflammation and TSPO expression (reviewed by Weissman and Raveh (2003), and Chen and Guilarte (2008)). Importantly, Banati *et al.* (2000) were able to show that a type of glial cells called microglia were the main cells expressing TSPO during active CNS pathology. They did this by examining post-mortem brain tissue sections from rats and humans with neurodegenerative pathology using [³H]-PK11195 and immunohistochemistry. Microglial cells account for approximately 10–20% of the total glial population of the CNS and are the principal immune cells of the brain. During resting state conditions, the cells exhibit long ramified (i.e. branching) processes that are highly mobile and act as sensors that allow the microglia to express their housekeeping function, which involves removal of accumulated metabolic products and deteriorated tissue components (Raivich *et al.*, 1999; Nimmerjahn, Kirchhoff and Helmchen, 2005). In the presence of brain injury or an inflammatory response, microglial morphology changes and their processes become deramified; this allows the microglia to home onto and adhere to damaged neuros. Where neuronal damage is such that cellular death occurs, then the adhered microglia transform into phagocytes that remove cellular debris (Raivich *et al.*, 1999; Nimmerjahn, Kirchhoff and Helmchen, 2005; Davaloes *et al.*, 2005). However, in the absence of cellular death the microglia return to a non-activated phenotype (Raivich *et al.*, 1999). Interestingly, using a mouse model of neuronal demyelination and remyelination, Chen and Guilarte (2006) showed that overexpression of TSPO

following brain injury also took place in another type of glial cells called astrocytes. In addition to this, the authors revealed that overexpression of TSPO was not only a direct response to brain injury, but also took place during the recovery stage (i.e. remyelination) of the model. This recovery response was more pronounced and sustained in astrocytic cells when compared to microglial cells. The precise functions of TSPO overexpression by glial cells in response to brain injury and recovery are unknown. It has been proposed that TSPO may be involved in microglial proliferation, migration and phagocytic capacity during the neuronal damage response, and in astrocytic neurosteroid synthesis during the recovery response (Chen and Guilarte, 2006). However, the latter is unlikely as recent findings regarding the function of TSPO disputed its role in steroid synthesis (see section 1.4.1 for details).

1.4.3 Nuclear imaging of TSPO.

1.4.3.1 Applications in glioblastoma and other conditions.

Nuclear imaging of TSPO in the brain can have multiple clinical applications. In the context of GBM, such imaging could be used to complement structural neuroimaging and improve GBM delineation and diagnostic accuracy. This can be rationalised by the high contrast in TSPO expression between GBM lesions and surrounding grey matter (see section 1.4.2 for details), and the fact that the majority of existing TSPO radiotracers are able to freely permeate the BBB. Pre-clinical PET imaging of intracranial 9L glioma bearing rats revealed that TSPO radioligand [¹⁸F]-DPA-714 (see section 1.4.3.2 for details) was taken up by GBM lesions in good contrast to surrounding brain tissues. The size and anatomical locations of the hotspots were found to correlate with the PET signal obtained using the amino acid based radiotracer [¹¹C]-MET and with histological data acquired post-mortem, thereby confirming the diagnostic potential of this imaging agent (Winkeler *et al.*, 2012). Importantly, a clinical study evaluating the use of the first generation TSPO radiotracer [¹¹C]-PK11195 showed high levels of uptake of the radioligand in high grade gliomas, which were not visible on contrast enhanced structural MRI (Su *et al.*, 2015). Furthermore, Buck *et al.* (2015) reported that TSPO radiotracer [¹⁸F]-PBR06 was capable of detecting

infiltrative glioma cells in rat brains that were once again undetectable on MRI. These findings were suggestive of improved sensitivity of TSPO nuclear imaging for glioma when compared to conventional structural imaging techniques. In addition to this, Buck *et al.* (2015) proposed that improved delineation of glioma lesions from surrounding grey matter could allow for more accurate resective removal of tumour tissue (Buck *et al.*, 2015), which could translate into improved patient outcomes.

However, as with structural and nuclear imaging using amino acid based radiotracers, utilisation of TSPO as a glioma biomarker is disadvantaged by the potential for misdiagnosis as a consequence of TSPO overexpression associated with other neuropathological conditions such as stroke, brain abscess, and demyelinating diseases (Chen and Guilarte, 2008). Despite this, radiotracers targeting TSPO may have some advantages over the amino acid based probes for GBM imaging. Non-specific uptake of the amino acid based radiotracer [^{11}C]-MET in gliomas has been found to be increased by the presence of BBB disruptions (Roelcke *et al.*, 1995). In contrast to this, the uptake of TSPO SPECT radiotracer [^{123}I]-CLINDE (see section 1.4.3.2 for details) was not influenced by surgically induced BBB alterations in humans (Feng *et al.*, 2014). Therefore, imaging of TSPO has potential as an alternative means of GBM treatment monitoring, particularly following surgical interventions. Although, it is important to bear in mind that this approach may not be suitable for monitoring the effectiveness of radiotherapy, which can cause neuroinflammation (Moravan *et al.*, 2011). Furthermore, a direct comparison of [^{123}I]-CLINDE SPECT and [^{18}F]-FET PET imaging in patients with GBM revealed that the former was able to detect regions of tumour progression, which was confirmed by baseline and follow-up gadolinium enhanced MRI. Based on these findings, the authors proposed that TSPO may be a useful marker of tumour progression (Jensen *et al.*, 2015).

In addition to glioma imaging, nuclear imaging of TSPO has been heavily investigated in neuroinflammatory conditions such as: ischaemic stroke; multiple sclerosis; cerebral vasculitis; human immunodeficiency virus (HIV) encephalitis; Alzheimer's disease; Parkinson's disease; Huntington's disease; and amyotrophic lateral sclerosis (reviewed by Chen and Guilarte (2008)). Such functional imaging

can have multiple applications depending on the pathology in question. For the purpose of this thesis, the potential applications of nuclear imaging of TSPO will be discussed in the context of three common and highly debilitating neurodegenerative conditions, namely Parkinson's disease, Alzheimer's disease, and multiple sclerosis.

Parkinson's disease is a condition that is characterised by a loss of dopaminergic neurons in a brain structure called the substantia nigra (Hirsch, Vyas, and Hunot, 2012). Diagnosis of the condition can be aided with structural neuroimaging using three-dimensional volumetric structural MRI acquisitions that can detect substantia nigra pathology. However, such imaging is limited to active disease. Since PET and SPECT are functional imaging modalities, they can be utilised to visualise a biological biomarker that can identify subclinical disease and individuals at risk of neurodegenerative disorders such as Parkinson's (Brooks, 2004). Neuroinflammation, associated with TSPO overexpression, has the potential to act as such a biological biomarker as it has been linked to Parkinson's disease aetiology (Hirsch, Vyas, and Hunot, 2012). Neuroinflammation can also drive progression of the disease (Esposito *et al.*, 2007; Hirsch, Vyas, and Hunot, 2012), and a number of pre-clinical studies have investigated the use of anti-inflammatory agents as adjuvants to conventional therapies (Esposito *et al.*, 2007). Nuclear imaging of TSPO could be utilised to monitor the effects of such adjuvants by directly measuring the anti-inflammatory response. Similarly, this type of functional imaging could be used to objectively monitor disease progression *in vivo*, which can often be biased when using subjective clinical disability rating scales (Brooks, 2004).

Alzheimer's disease is another example of a neurodegenerative condition where structural MRI is used to facilitate diagnosis. This is achieved through the detection of brain atrophy characterised by onset and progression originating from the medial temporal lobe. However, despite characteristic patterns for most cases of Alzheimer's disease, brain atrophy presentation is variable in atypical cases of the condition. Therefore, a definite diagnosis requires histopathological confirmation (Johnson *et al.*, 2012). The ability to visualise neuroinflammation through *in vivo* nuclear imaging of TSPO could potentially aid

Alzheimer's disease diagnosis and monitoring, as inflammation has been linked to the pathogenesis of the condition (Heneka *et al.*, 2015).

Multiple sclerosis is an autoimmune disease associated with neurodegeneration and neuroinflammation at all stages of the condition. As with Parkinson's and Alzheimer's disease, MRI is an invaluable tool for the diagnosis and monitoring of progression of multiple sclerosis. However, the technique lacks the ability to detect diffuse pathology, which is particularly prominent in progressive multiple sclerosis, and is known to be associated with microglial activation and neurodegeneration. Since TSPO is overexpressed by activated microglia, nuclear imaging of this protein could be used to identify patients at risk of entering the progressive stage of the disease. In turn, this could be used to tailor pharmacological treatment to the individual with the aim of slowing down disease progression. Moreover, pharmacological management involves using disease-modifying drugs that suppress inflammation. Therefore, nuclear imaging of TSPO could also be utilised as a means of monitoring treatment efficacy (Airas, Rissanen, and Rinne, 2015).

1.4.3.2 Existing tracers for TSPO.

The earliest example of a nuclear imaging radiotracer for TSPO is the [^{11}C]-labelled version of the benzodiazepine Ro5-4864 (Figure 1.21). However, the good specificity of the compound for TSPO in rats was not translatable to human subjects in which little binding to TSPO *in vivo* was observed on PET scans (Junck *et al.*, 1989). The contrary was true for the isoquinoline carboxamide PK11195, which was first radiolabelled with ^{11}C in 1984 (Camsonne *et al.*, 1984) and ^{123}I in 1996 (Gildersleeve *et al.*, 1996) (Figure 1.21). [^{11}C]-PK11195 in particular has been used extensively to study TSPO *in vivo* using PET imaging (reviewed by Chen and Guilarte (2008) and Luus *et al.* (2010)). However, as a consequence of its physicochemical properties, PK11195 suffers from poor brain uptake and high non-specific binding (Petit-Taboulé *et al.*, 1991; Shah *et al.*, 1994), which can lead to a low nuclear imaging signal to noise ratio in the brain. It is also important to note that the ^{11}C -labelled version of PK11195 has the inherent

disadvantage of a short half-life making its use for nuclear imaging more challenging (see section 1.2.1 for details).

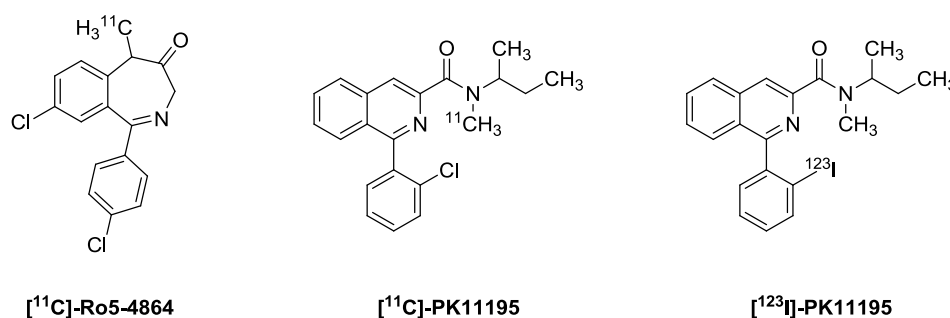


Figure 1.21. First generation radiotracers for TSPO.

In order to improve the quality of TSPO nuclear neuroimaging, numerous second and third generation radioligands have been developed (Figure 1.22). [¹²³I]-CLINDE was second generation SPECT candidate with improved affinity for TSPO and better brain tissue penetration properties when compared to the first generation agents (Mattner, Mardon, and Katsifis *et al.*, 2008). The ¹¹C-labelled pyrazolopyrimidine DPA-713 and the phenoxyphenyl acetamides DAA1106 and PBR28 appeared to be promising imaging candidates as the agents exhibited good brain uptake and specific binding properties in a number of pre-clinical pathology models. However, as with [¹¹C]-PK11195, these radiotracers were disadvantaged by the short half-life of the radioisotope. Therefore, a number of tracers bearing the longer lived ¹⁸F radioisotope (half-life = 109.8 minutes) were developed based on the pyrazolopyrimidine and phenoxyphenyl acetamide classes (reviewed by Luus *et al.* (2010) and Vivash and O'Brien (2015)). Interestingly, it was found that the deuterated methyl-radiofluoride functionality (CD₂¹⁸F) of [¹⁸F]-d₂FMDAA1106 reduced the rate of *in vivo* defluorination when compared to the corresponding methyl-radiofluoride (CH₂¹⁸F). Despite this improvement in metabolic stability, the generation of free ¹⁸F⁻ metabolite was still prominent upon pre-clinical nuclear imaging with [¹⁸F]-d₂FMDAA1106, which interfered with the signal observed for TSPO in the brain (Zhang *et al.*, 2005) (see chapters 4 and 6 for details concerning ¹⁸F-defluorination). These issues of *in vivo* defluorination were subsequently addressed with the development of the metabolically stable [¹⁸F]-FEDAA1106. Similarly to the ¹¹C-labelled agents, the ¹⁸F-bearing radiotracers exhibited

improved brain uptake and specific binding properties when compared to PK11195 (reviewed by Luus *et al.* (2010) and Vivash and O'Brien (2015)).

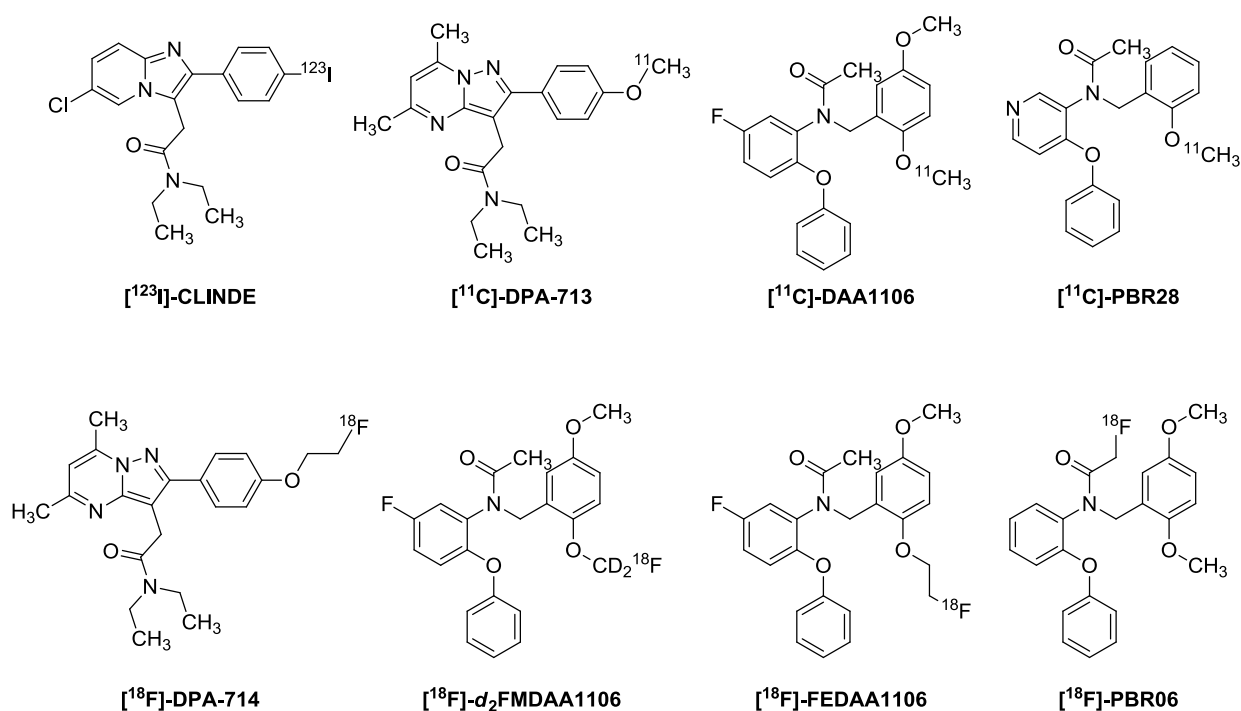


Figure 1.22. Second and third generation radiotracers for TSPO.

However, clinical advancement of these second and third generation radiotracers has been significantly hindered by the existence of human TSPO single-nucleotide polymorphism that is associated with the substitution of an alanine to a threonine amino acid in the protein. This small change has been shown to have a significant effect on the binding affinities of these TSPO ligands, resulting in populations of patients that can be classed as high-affinity, low-affinity or mixed-affinity binders (Owen *et al.*, 2011; Owen *et al.*, 2012; Mizrahi *et al.*, 2012; Kreisl *et al.*, 2013). Importantly, the binding of the first generation TSPO ligand PK11195 is not influenced by this genetic polymorphism (Owen *et al.*, 2011). This could be explained by the fact that TSPO possesses a number of different binding sites, including separate binding sites for benzodiazepine and isoquinoline compounds (Luus *et al.*, 2010).

It has been reported that, amongst persons of European ancestry, the prevalence of people who fall into the high-affinity and low-affinity binder categories are approximately 49% and 9% respectively, while the remaining 42% are classified as mixed-affinity binders (Kreisl *et al.*, 2013). From the perspective of nuclear

imaging, radiotracers that are affected by this type of polymorphism have limited clinical application as different binding affinities amongst patients can mislead diagnoses and prevent quantitative comparison of data (Mizrahi *et al.*, 2012; Kreisl *et al.*, 2013). This issue could be addressed by genotyping patients before nuclear imaging in order to establish their TSPO polymorph (Mizrahi *et al.*, 2012). Obtaining such information from patients before scanning would allow for exclusion of individuals that would likely exhibit poor specific signal (i.e. 'low-affinity binders') (Owen *et al.*, 2011), and subsequent correction of data to account for 'high-' and 'mixed-affinity binders' (Mizrahi *et al.*, 2012). However, such an approach would not only introduce scanning delays and an increased financial strain on the healthcare system, but also prevent a significant proportion of the population from accessing this nuclear imaging technology. Therefore, there is a need for novel TSPO radiotracers that exhibit low sensitivity to human TSPO polymorphism and improved *in vivo* characteristics when compared to the first generation agents.

1.5 Radiotracer discovery and development.

1.5.1 Discovery and development pipeline.

Discovery and development of novel pharmaceuticals is a complex, multistage, and multidisciplinary process. It is important to make the distinction between discovery and development of therapeutic and imaging agents as the pipelines differ for the two types of agents. The involvement of academic and industrial sectors in the discovery and development of therapeutic and imaging agents is a key difference. Pharmaceutical companies are the main drivers behind therapeutic agent development, while only a small number of companies exist that commercialise imaging agents. Consequently, the main players involved in imaging agent development are academics, who can be credited for the majority of PET and SPECT radiotracers that are currently in existence (Agdeppa and Spilker, 2009).

Figure 1.23 outlines the typical discovery and development pathways taken for therapeutic drugs and imaging agents. In the case of the former, the overall process is usually linear and can be subdivided into pre-clinical discovery and clinical development stages. Similarly, the imaging agent discovery and development pipeline also consists of pre-clinical and clinical stages (Hoffman, Gambhir, and Kelloff, 2007; Agdeppa and Spilker, 2009). However, the pre-clinical stage often follows a non-linear path, where the discovery of the imaging agent is an iterative process. The reasoning is that companies or academic institutions involved in generating imaging agents do not have access to large libraries of chemical compounds that can be screened. Moreover, it can frequently be the case that positive *in vitro* data for an imaging agent do not translate into adequate *in vivo* performance, for example due to poor *in vivo* stability of a radionuclide label. As a consequence, chemical synthesis, *in vitro* screening, and *in vivo* testing fall into an iterative discovery cycle, where *in vitro* and *in vivo* information is fed back to medicinal chemists who refine their approaches before repeating the screening process. *In vitro* screening usually involves assessment of the agent's physicochemical properties, the target binding affinity, and the stability. In the case of radiotracers, part of this process also involves the development of labelling methodology that can efficiently introduce the desired radionuclide necessary for nuclear imaging (Agdeppa and Spilker, 2009). The *in vivo* testing component of this cycle exhibits marked differences to what is usually performed for investigational therapeutic agents. Therapeutic drugs are designed to be administered via a specific route, for example orally as a tablet or capsule. In such cases, pre-clinical testing will involve assessment of oral bioavailability. However, the route of administration of radiotracers is usually parenteral and evaluation of oral bioavailability is not necessary. Furthermore, due to the technical capabilities of nuclear imaging equipment, pre-clinical radiotracer imaging studies are able to ascertain biodistribution and pharmacokinetic information for the investigational diagnostic agent before advancing to human trials. These imaging studies can also be planned to allow blood sampling for metabolic analysis. The imaging data will often be validated by correlating radiotracer uptake to autoradiographic or gamma-counting biodistribution and histologic data acquired from parallel studies. Another important component of pre-clinical radiotracer assessment is the establishment of the degree of specific binding of the agent for its target, which is usually

achieved by performing radioligand blockade or displacement studies using a non-radioactive compound with known specificity for the target. These data can then be used to establish organ dosimetry, and the dose-limiting organ for radiation exposure and toxicity (Agdeppa and Spilker, 2009; Sharma and Aboagye, 2011). Despite the fact that radiotracers are usually administered at doses that are below the level required to elicit a pharmacological response, toxicological evaluation forms a key part of the pre-clinical assessment stage (Sharma and Aboagye, 2011). The aim of this iterative discovery cycle is to identify a lead imaging agent candidate that then enters the clinical stage of development, which follows a similar general pathway to that outlined earlier for therapeutic agents (Agdeppa and Spilker, 2009).

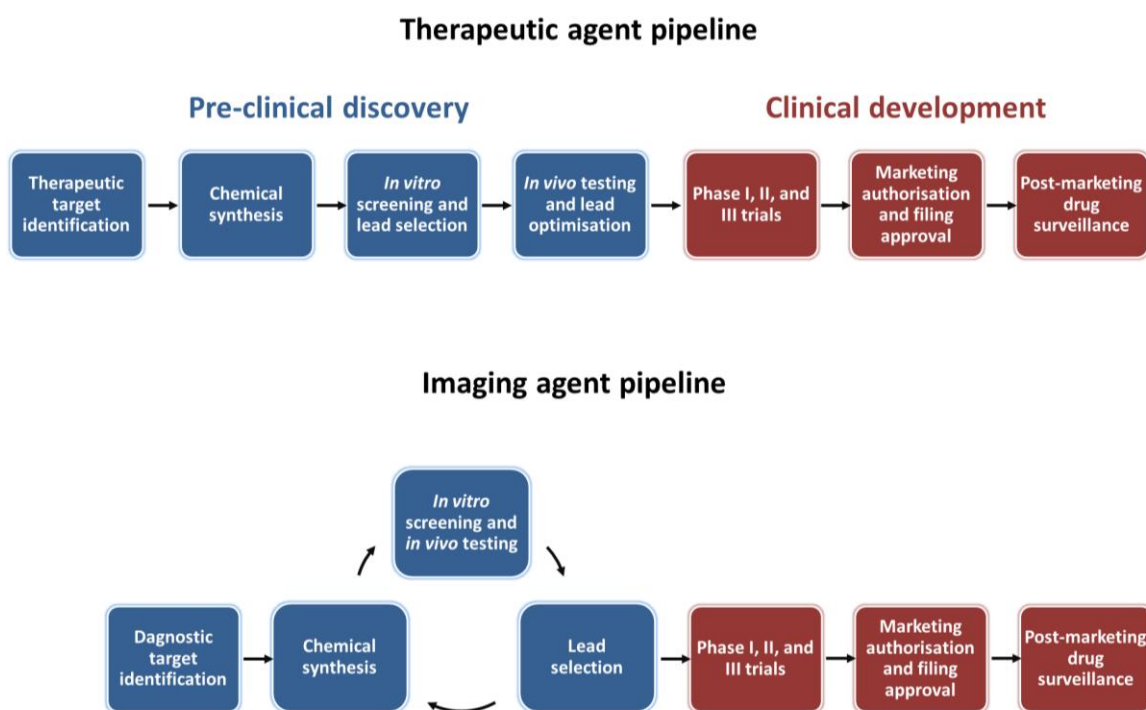


Figure 1.23. Typical discovery and development pathways taken for therapeutic drugs and imaging agents.

It is important to note that the specific requirements for clinical development of both therapeutic and imaging agents will be dictated by the regulatory body responsible for its commercial approval. In the USA, the body responsible for this is the Food and Drug Administration (FDA), which has clearly defined requirements for phase I, II, and III and post-marketing studies; these requirements are very similar for therapeutic and imaging agents (reviewed by

Hoffman, Gambhir, and Kelloff (2007). The situation is more complex in Europe, where overarching legislation outlines the specific requirements for human studies using investigational medicinal products and radiopharmaceuticals, which can be subjected to change and variable timelines depending on the member state (reviewed by Salvadori, 2008).

1.5.2 From the laboratory to the clinic.

Commercialisation of imaging agents requires substantial monetary investment, with an estimated cost in the region of \$100–\$200 million. Based on figures from 2003, the global sales of the top three nuclear imaging agents (i.e. Cardiolite[®], Myoview[®], and [¹⁸F]-FDG) were between \$190 and \$405 million. To put these figures into perspective, the development costs of therapeutic drugs have been estimated to be \$800–\$1700 million, where the top blockbuster drugs have been reported to have earned as much as \$3400 million. Poor return on investment combined with long development time (between 8–10 years) led to reduced industrial interest in the area of imaging agent development (Nunn, 2006). It is therefore not surprising that between the period of 1995 and 2010 [¹³N]-ammonia was the only PET radiopharmaceutical to receive FDA approval for human use (VanBroklyn, 2010).

It has been proposed that decreasing pre-clinical development cost could help to bridge the gap between discovery of new nuclear imaging agents and their subsequent clinical commercialisation. This could be achieved by reducing the toxicological assessment of novel radiotracers (Nunn, 2006), as the likelihood of a pharmacological response following radiotracer administration is minimal. Another solution could involve the formation of partnerships between nuclear imaging instrument companies and companies or academic institutions responsible for radiotracer development (Nunn, 2006). However, as it stands commercialisation of radiotracers remains an expensive process that is associated with high attrition rates.

1.6 Aims and objectives.

This thesis aimed to discover novel SPECT and PET nuclear imaging tracers for PARP-1 and assess them pre-clinically, and to continue the pre-clinical discovery of a potential TSPO PET imaging agent synthesised and investigated previously by Dr Adele Blair as part of her PhD project within the research group. The pre-clinical discovery of these radiotracer compounds was focused on potential GBM neuroimaging applications.

With respect to the PARP-1 nuclear imaging agents the objectives were to: i) utilise the structure of the clinical PARP-1 inhibitor olaparib as a pharmacophore for the synthesis of novel compounds designed to represent potential PARP-1 SPECT and PET imaging agents, from which lead candidates could be selected based on outcomes of *in vitro* screening procedures; ii) develop methodologies to allow access to the radiolabelled versions of the lead candidates with potential for PARP-1 SPECT and PET nuclear imaging; and iii) test the lead radiolabelled candidates as potential PARP-1 nuclear imaging agents in mice bearing human GBM xenograft models using *ex vivo* biodistribution methodology.

With respect to the previously discovered potential TSPO PET imaging agent the objectives were to: i) utilise previously established methodology to access the radiolabelled compound; and ii) investigate the utility of this compound as a TSPO imaging agent in mice bearing intracranial human GBM tumours using *ex vivo* autoradiography and pre-clinical PET imaging.

2. THESIS OUTLINE.

This thesis describes the pre-clinical discovery of radiotracers for PARP-1 and TSPO. With regard to the former, the thesis is structured according to the typical imaging agent pre-clinical discovery pipeline (as outlined in section 1.5.1), with each experimental chapter addressing a key set of steps in this process. Since a large proportion of the pre-clinical discovery process of the candidate radiotracer for TSPO has already been achieved (i.e. chemical and radiochemical syntheses, as well as *in vitro* assessment), the final chapter of this thesis focuses on the latter stages of pre-clinical discovery pipeline for this tracer (i.e. pre-clinical *in vivo* assessment).

The thesis comprises of five experimental sections and a concluding chapter, and a brief outline of each chapter is provided below.

Chapter 3 is entitled “Synthesising PARP-1 ligands with potential for nuclear imaging” and it describes the identification and organic synthesis of non-radioactive compounds, based on the clinical PARP-1 inhibitor olaparib, designed to represent potential SPECT and PET nuclear imaging agents. A total of eighteen olaparib analogues were made. Seven of these contained a stable iodine atom and were representative of [¹²³I]-labelled SPECT agents, seven were fluorine bearing and representative of [¹⁸F]-labelled PET imaging agents, and four compounds comprised a methoxy functionality and were representative of [¹¹C]-OMe labelled PET agents.

Chapter 4, entitled “Identifying lead PARP-1 ligands with potential for nuclear imaging”, outlines key *in vitro* testing that was conducted on the earlier synthesised PARP-1 ligands (Chapter 3) with the aim of identifying lead candidates for advancement to the next stage of radiotracer discovery. Assessment of *in vitro* cell-free PARP-1 inhibitory potency and physicochemical parameters allowed for the ranking of these compounds, followed by subsequent elimination of candidates showing undesirable properties. These data, combined with further *in vitro* assessment of cellular PARP-1 inhibitory potency, allowed

for the identification of one lead SPECT and two lead PET PARP-1 imaging candidates.

Chapter 5 is entitled “Developing radiosyntheses for PARP-1 nuclear imaging agents”. This section describes the steps that were taken towards establishing and optimising methodology for generating, purifying and formulating the [^{123}I]-iodide and [^{18}F]-fluoride labelled versions of the lead candidates identified in Chapter 4. Suitable radiosynthetic methodology was developed for two of the three desired PARP-1 radiotracers, thereby leading to their advancement to the pre-clinical discovery process (Chapter 6). One of the potential PET candidates could only be radiolabelled in low yield, which was not sufficient for *in vivo* pre-clinical evaluation.

Chapter 6, entitled “*In vitro* stability and *ex vivo* evaluation of the PARP-1 molecular imaging agents”, discusses the *in vitro* assessment of plasma and metabolic stability of the non-radioactive counterparts of the two PARP-1 tracers that were successfully radiolabelled in Chapter 5. This chapter also describes the evaluation of the radiolabelled tracers in mice bearing human GBM xenograft tumours using *ex vivo* biodistribution techniques.

Chapter 7, entitled “*In vivo* evaluation of TSPO molecular imaging agent [^{18}F]-AB5186”, describes the radiosynthesis and *ex vivo* autoradiographic evaluation of the potential TSPO nuclear imaging agent [^{18}F]-AB5186, which was synthesised and investigated previously by Dr Adele Blair as part of her PhD thesis, in mice bearing intracranial human GBM tumours. The chapter also discusses the *in vivo* evaluation of this tracer in the same tumour model using pre-clinical PET imaging.

Chapter 8, entitled “Conclusions and future work”, summarises the progress that was made in the pre-clinical discovery of nuclear imaging radiotracers for PARP-1 and TSPO and outlines the future work that can be conducted in this area.

3 SYNTHESISING PARP-1 LIGANDS WITH POTENTIAL FOR NUCLEAR IMAGING.

3.1 Introduction.

3.1.1 PARP inhibitor binding.

The binding interactions between PARP inhibitors and the PARP-1 active site differ depending on the structure of the inhibitor in question. However, a number of similar interactions across a range of PARP inhibitors have been identified. In 1996, Ruf *et al.* reported the crystal structure of the catalytic fragment of chicken PARP-1 (PARP-CF), which is a close homologue to the human enzyme. The authors were able to elucidate key binding interactions between PARP-CF and the nitocinamide PARP inhibitor PD128763 by co-crystallising the two structures. These interactions included: i) nonpolar π -stacking between a Tyr-907 amino acid residue and the aromatic region of PD128763; ii) hydrogen bonding between a Ser-904 residue and the carbonyl of PD128763; and iii) hydrogen bonding between a Gly-863 residue and the lactam functionality of PD128763 (Ruf *et al.*, 1996) (Figure 3.1).

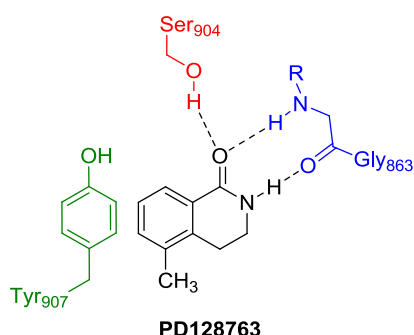


Figure 3.1. The key binding interactions between the PARP inhibitor PD128763 and the PARP-CF.

The binding of organic compounds to the PARP-CF was further evaluated by Ruf *et al.* (1998) who were able to co-crystallise the enzyme fragment with three other PARP inhibitors, namely the benzamide analogue 3-MBA, the

dihydroisoquinolinone analogue 4-ANI, and the quinazolinone derivative NU1025. All three inhibitors exhibited identical interactions with Gly-863, Ser-904 and Tyr-907 as those identified for PD128763 (Figure 3.2).

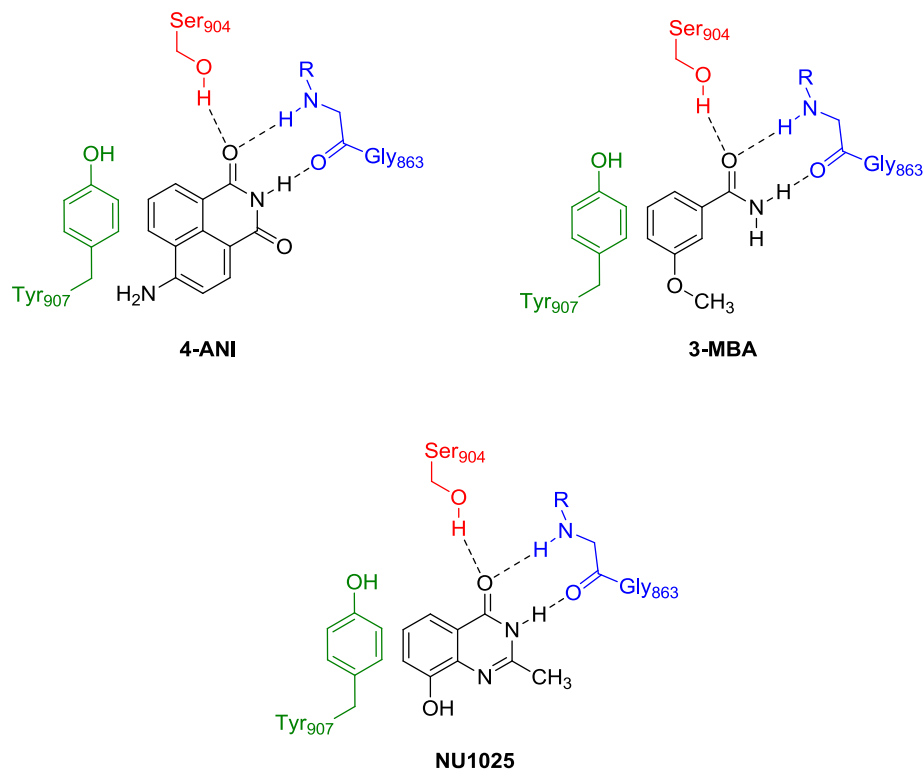


Figure 3.2. Key binding interactions between the PARP inhibitors 4ANI, 3MBA, and NU1025 and the PARP-CF.

Cockroft *et al.* (2006) utilised crystal data acquired for the PARP-CF to perform computerised (*in silico*) modelling of the binding interactions between the PARP-CF and two PARP inhibitors (1 and 2) based on the phthalazinone scaffold (Figure 3.3). As expected, the phthalazinone aromatic region of compounds 1 and 2 was shown to associate with a Tyr-907 residue, and the amido NH and carbonyl functionalities characteristic of phthalazinones exhibited hydrogen bonding with Gly-863 and Ser-904 residues. In addition to the above, the *in silico* approach revealed a further key interaction between the NH residue of Met-890 and the *meta*-benzyl positioned anilide and amide functionalities of compounds 1 and 2, respectively (Figure 3.3).

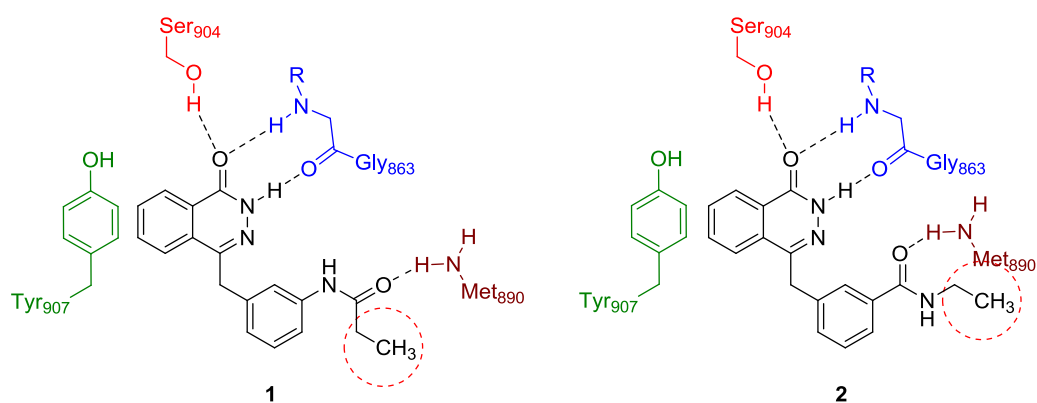


Figure 3.3. *In silico* predicted binding interactions between the PARP inhibitors **1** and **2**, based around the phthalazinone scaffold, and the PARP-CF. The circled regions highlight areas that are tolerant to structural modification with respect to PARP-1 inhibitory activity.

The above described binding model of compounds **1** and **2** to the PARP-1 active site, predicted using *in silico* methodology, correlates with physical structural activity relationship (SAR) data obtained by Cockroft *et al.* (2006) and Menear *et al.* (2008). In both cases the authors reported that structural modification in regions distal to the *meta*-benzyl anilide and amide of compounds **1** and **2** (Figure 3.3 circled regions) had little influence on PARP-1 inhibition. This phenomenon was instrumental in the development of the clinical PARP inhibitor olaparib as it allowed for the synthesis of a broad range of phthalazinone based compounds, which exhibited potent PARP-1 inhibitory properties. Taking all of the above findings under consideration, it is proposed that olaparib binds to the PARP-1 active site via the interactions depicted in figure 3.4.

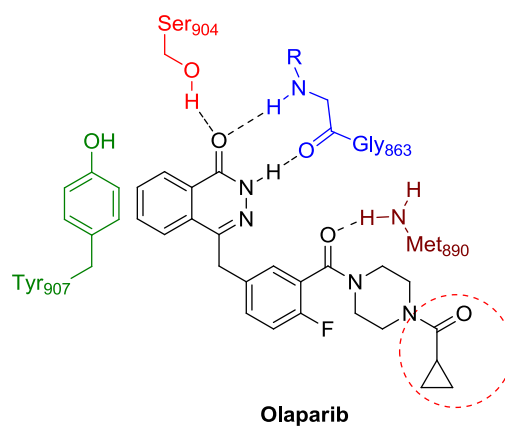


Figure 3.4. Proposed binding interactions between the PARP inhibitor olaparib and the PARP-1 active site. The circled region highlights the area that is tolerant to structural modification with respect to PARP-1 inhibitory activity.

It should be appreciated that existing inhibitors of PARP-1 also exhibit PARP-2 inhibitory properties through interactions similar to those described above (Karlberg *et al.*, 2010; Oliver *et al.*, 2004). This can be attributed to the high degree of homology that exists between the catalytic domains of the two enzymes. For the purpose of the following section the term ‘PARP inhibitors’ was utilised as an umbrella term describing inhibitors of both PARP-1 and 2.

From the perspective of developing a PARP-1 radiotracer, knowledge concerning binding to different PARP isoforms is less crucial when compared to PARP inhibitors utilised for therapeutic applications. This is because, as their name entails, radiotracers are administered in trace amounts that, in the case of PARP-1 and PARP-2, are below the levels required to elicit a clinically significant pharmacological response. Therefore, the clinical consequences associated with off-target radiotracer binding are regarded as negligible.

3.1.2 Olaparib core as a pharmacophore.

Olaparib is a potent inhibitor of PARP-1 (Menear *et al.*, 2008) and it is the most clinically advanced compound in its class (see section 1.3.2.1 for details). These properties, coupled with the fact that it is open to structural modification in the cyclopropane bearing region (Figure 3.4), make the core of the compound an ideal pharmacophore for novel PARP-1 radiotracer discovery.

Direct radiolabelling of olaparib for PET or SPECT imaging, without performing structural modifications to the parent compound, would represent the ideal scenario. Reiner *et al.* (2012) attempted to exploit the aromatic fluorine already present in the structure of olaparib for direct ^{18}F labelling, but were unable to do so due to steric hindrance imposed by the amide functionality positioned *ortho* to the labelling site. Moreover, radiolabelling of olaparib with the ^{11}C radioisotope using established methylation methodology would not be feasible as attachment of a [^{11}C]-methyl functionality to the amido NH group of the phthalazinone would likely impede binding of the compound to the PARP-1 active site. In order to circumvent these issues, it was proposed that structural modifications can be performed in the cyclopropane bearing region of olaparib, without impeding PARP-1 binding properties, to include moieties that can easily be labelled with the desired radioisotope for SPECT or PET imaging (Figure 3.5). It is noteworthy that a similar approach was effectively utilised by Reiner *et al.* (2012) and Carlucci *et al.* (2015) for the development of the PARP-1 tracers [^{18}F]-BO and [^{18}F]-PARPi-FL respectively (see section 1.3.3.2 for details).

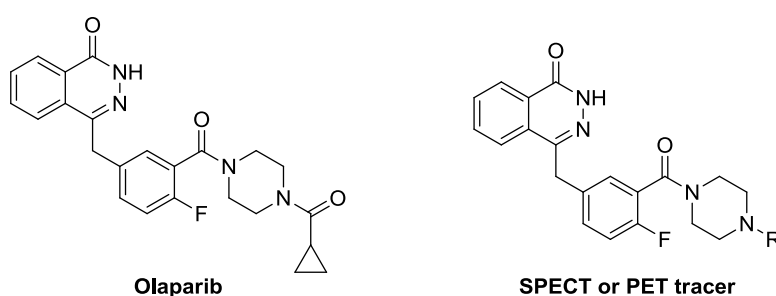


Figure 3.5. Structures of olaparib and potential PARP-1 SPECT and PET nuclear imaging agents, where the 'R' group represents appropriately radiolabelled moieties.

3.1.3 Aims and hypotheses.

The work described in this chapter aimed to identify and synthesise non-radioactive iodinated, fluorinated, and methoxy containing analogues of olaparib that were designed to represent potential PARP-1 ^{123}I labelled SPECT, and ^{18}F and ^{11}C -methoxy labelled PET imaging agents. It was hypothesised that previously published methodology for the synthesis of olaparib (Menear *et al.*, 2008) could be exploited as a means of rapidly accessing these novel iodinated, fluorinated, and methoxy containing compounds.

3.2 Results and discussion.

Due to the wealth of pre-clinical and clinical data available for the PARP inhibitor olaparib, and the unique opportunity for structural expansion in the terminal cyclopropane bearing region, the phthalazinone scaffold **3** of olaparib was chosen as the pharmacophore for PARP-1 radiotracer development (Figure 3.6).

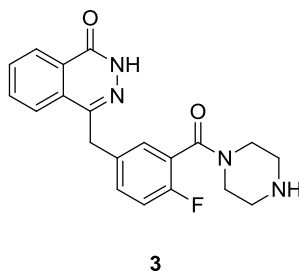


Figure 3.6. The phthalazinone scaffold of olaparib.

A total of eighteen non-radioactive compounds, based around the phthalazinone scaffold **3** of olaparib, were identified as potential PARP-1 SPECT and PET nuclear imaging agents (Figure 3.7).

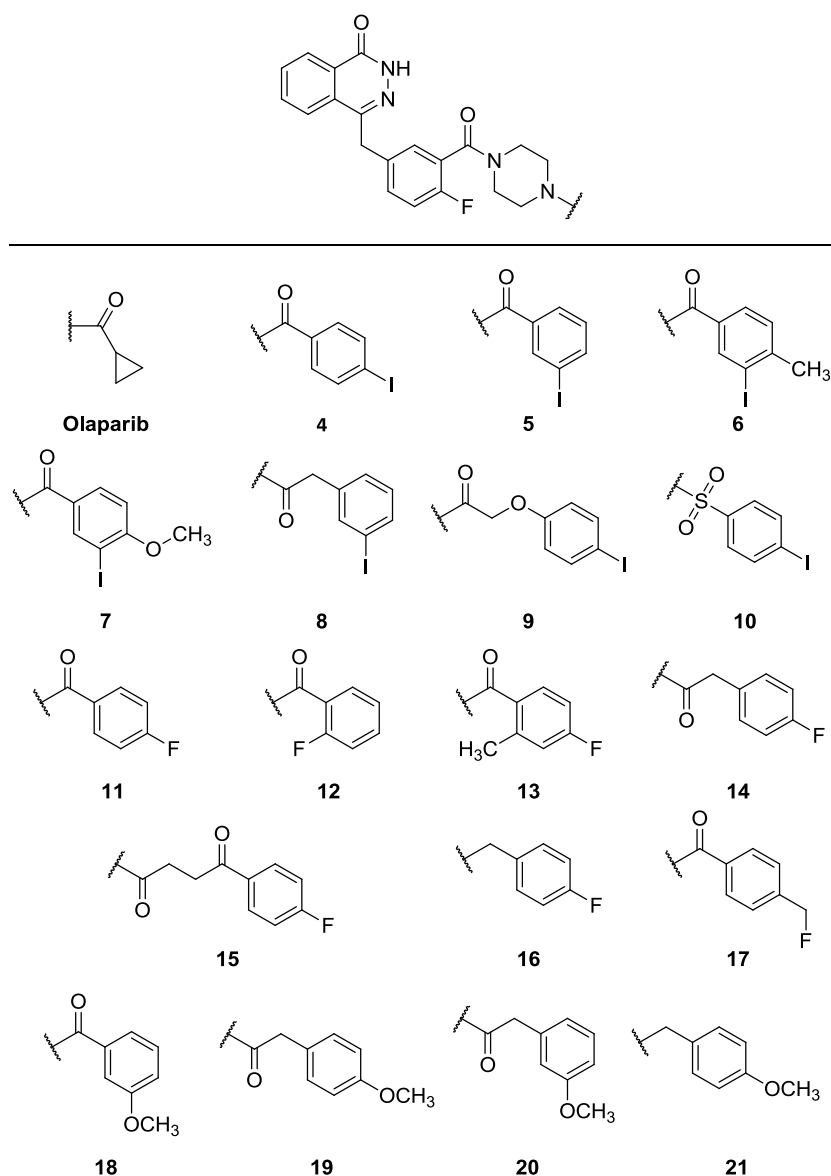


Figure 3.7. Structures of olaparib and the non-radioactive analogues that were chosen as potential PARP-1 nuclear imaging agents. Compounds 4–10 represented potential ^{123}I -labelled SPECT tracers, while 11–17 and 18–21 represented potential ^{18}F and $[^{11}\text{C}]$ -OMe-labelled PET imaging agents, respectively.

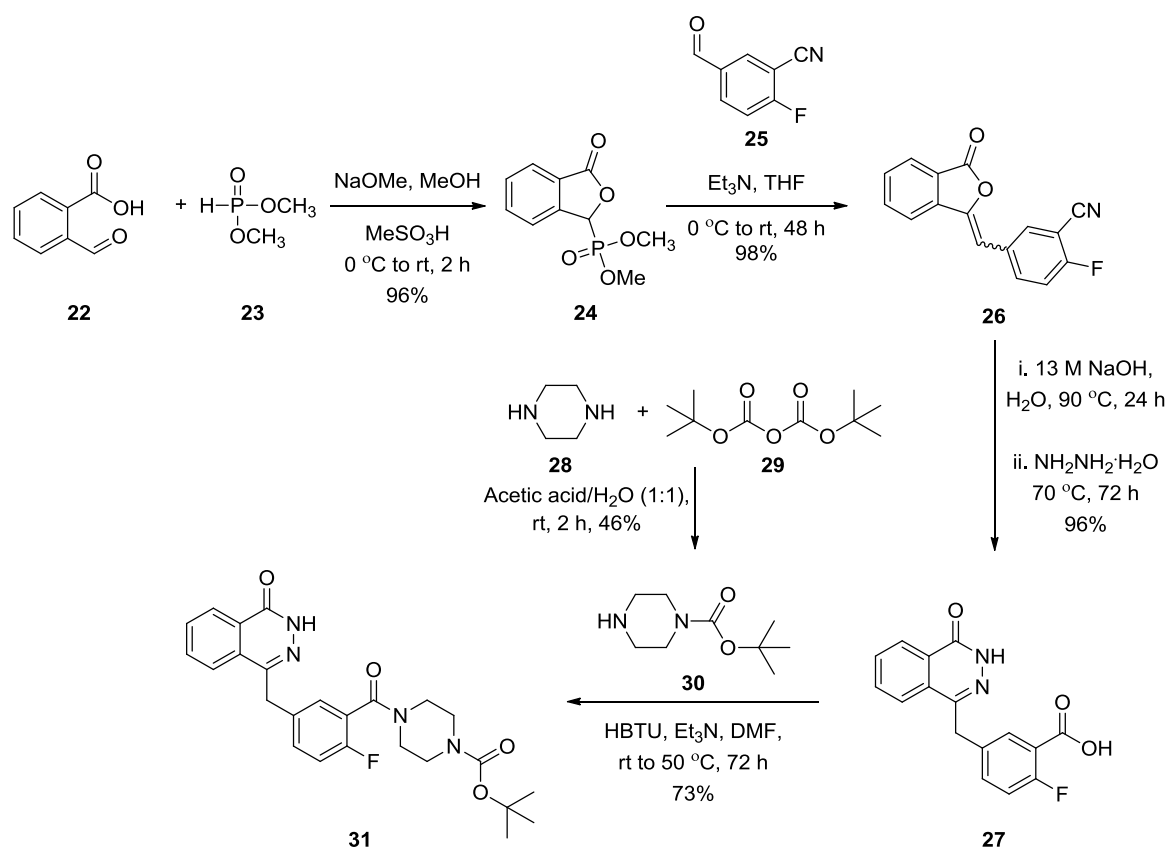
Specifically, compounds 4–10 were identified as representatives of aromatic ^{123}I -labelled tracers, 11–16 and compound 17 represented aromatic and aliphatic, respectively, ^{18}F -labelled tracers, and 18–21 represented $[^{11}\text{C}]$ -OMe labelled radioligands. It was envisaged that previously established chemistry (Menear *et al.*, 2008) could be utilised to access the penultimate compound 3 (Figure 3.6) that could in turn be exploited in coupling reactions with commercially available

iodinated, fluorinated, and methoxy bearing aromatic carboxylic acids, alkyl halides or sulfonyl halides.

The advantage of such an approach would be the potential to access olaparib analogues in a rapid manner. Therefore, with the exception of compound **17**, one of the key drivers behind selection of **4–16** and **18–21** as target compounds was the commercial availability of the desired aromatic carboxylic acids, and alkyl and sulfonyl halides. This approach could not be applied to compound **17** as 4-(fluoromethyl)benzoic acid was not obtainable commercially. However, this compound was pursued as a viable nuclear imaging candidate due to the potential for greater radiochemical accessibility of the aliphatic fluorine when compared to compounds **4–10** that all contain fluorine atoms attached directly to aromatic rings (see section 5.1.2.2 for further information concerning aliphatic and aromatic radiofluorination chemistry).

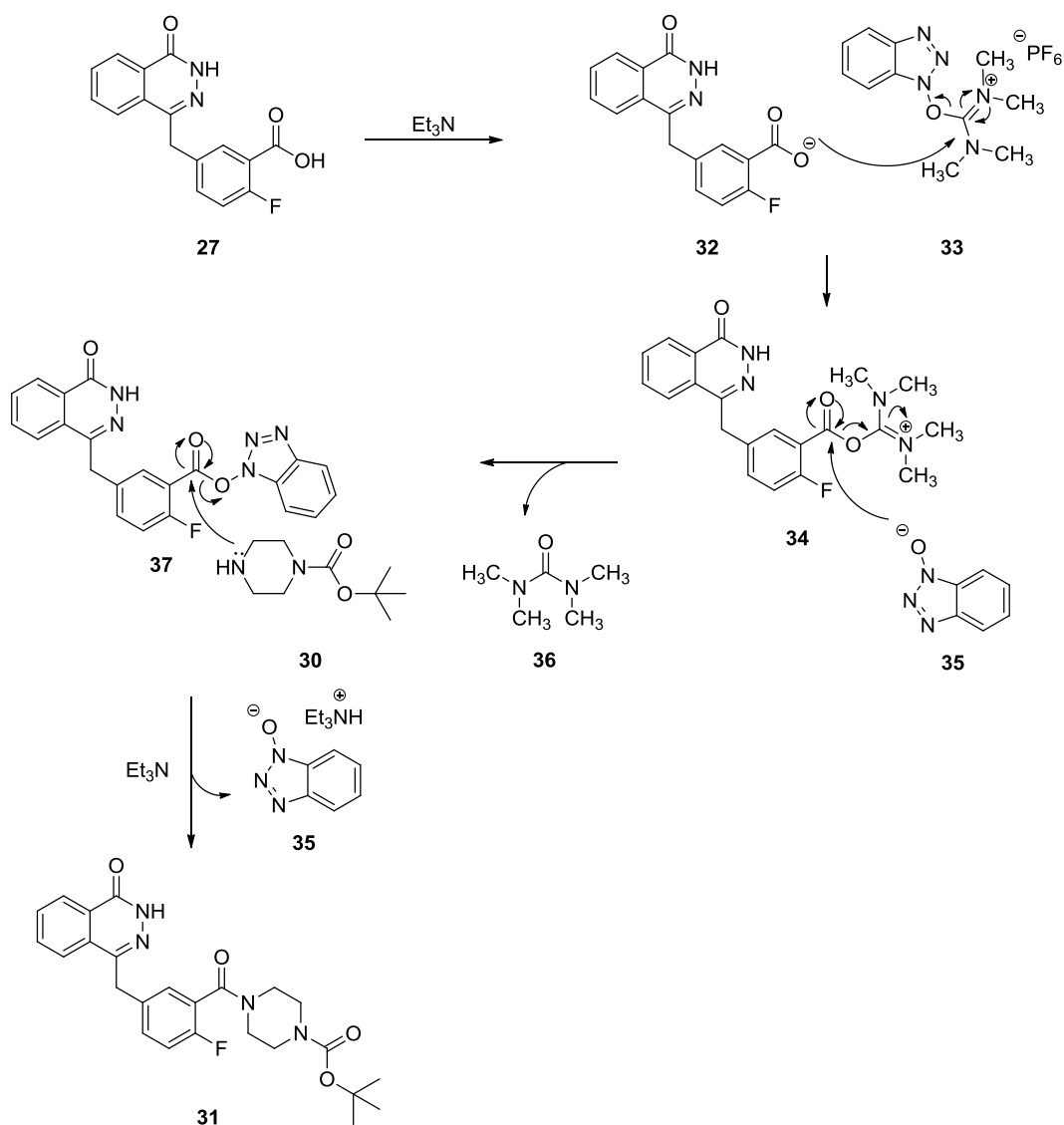
The phthalazinone scaffold **3** was accessed using synthetic methodology described by Menear *et al.* (2008) with slight modifications. Optimisation of the synthetic route was performed by Dr Adele Blair and further details concerning these endeavours can be found in the author's thesis (Blair, 2014). To briefly describe the synthesis, commercially available dimethylphosphite **23** and 2-carboxybenzaldehyde **22** underwent a coupling reaction under basic conditions to give the phosphonate intermediate **24** in 96% yield (Scheme 3.1). Next, compound **24** was subjected to Horner-Wadsworth-Emmons coupling, a technique originally reported by Horner, Hoffmann and Wippel (1958) and further developed by Wadsworth and Emmons (1961), with 2-fluoro-5-formylbenzotrile **25**, resulting in the formation of alkene **26** in a *E*- and *Z*-isomer mixture and 98% yield (Scheme 3.1). The Horner-Wadsworth-Emmons reaction mechanism is well established and further information can be found in the review by Maryanoff and Reitz (1989). The ratio of *E*- and *Z*-isomers was not determined as the non-separated mixture was subjected to a one-pot process that allowed for formation of a carboxylic acid via base hydrolysis of the nitrile, followed by formation of the characteristic phthalazinone core of **27** with concurrent removal of the alkene using hydrazine monohydrate. Compound **30**, accessed by mono-Boc protection of piperazine **28** using di-*tert*-butyl

dicarbonate **29** as reported by Kovács and Szegezdi (2003), underwent an amide coupling reaction with intermediate **27** to afford **31** in 73% yield (Scheme 3.1).



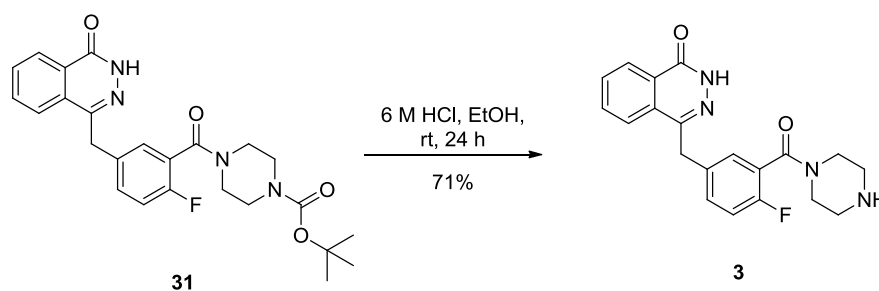
Scheme 3.1. Synthesis of the Boc-protected phthalazinone intermediate **31**.

The proposed mechanism for HBTU (**33**) mediated amide coupling of compounds **27** and **28** is depicted in Scheme 3.2 (Valeur and Bradley, 2009). Addition of a base to compound **27** resulted in deprotonation of the terminal carboxylic acid and the formation of the corresponding carboxylate anion **32**. This intermediate then underwent nucleophilic substitution with the uranium moiety of **33** to afford **34**, which then reacted with the anionic oxygen of the benzotriazole **35** via another nucleophilic substitution, resulting in the formation of the activated ester **37** and the water soluble urea by-product **36**. Finally, the nitrogen lone pair of mono-Boc protected piperazine **30** performed nucleophilic attack at the carbonyl position of ester **37** resulting in the generation of amide **31** and the 1-hydroxybenzotriazole **35** by-product. A key advantage of the HBTU coupling agent is the water solubility of the urea and hydroxybenzotriazole by-products, which can be removed via a straight forward aqueous phase extraction.



Scheme 3.2. Proposed mechanism for HBTU (**33**) mediated amide coupling of compounds **27** and **30**.

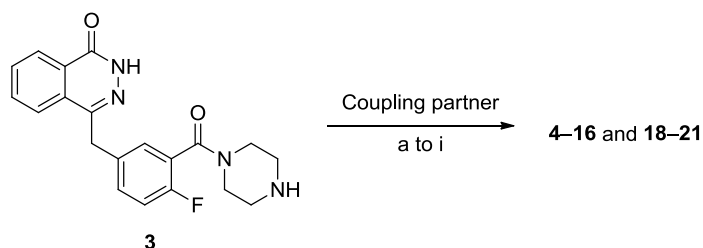
The final step in the synthesis of the penultimate compound **3** involved acid-mediated Boc-deprotection of **31** resulting in the generation of the desired product in 71% yield (Scheme 3.3), and an overall 46% yield over the six steps. It is noteworthy that the above described synthesis did not necessitate the use of column chromatography for compound purification, thereby enabling rapid synthetic progression.



Scheme 3.3. Boc-deprotection of **31** to give access to the phthalazinone scaffold **3**.

As envisaged, the generation of compound **3** allowed for the synthesis of olaparib, and **4–16** and **18–21** in a straight-forward manner by utilising the terminal secondary amine of the piperazine as a coupling point for the corresponding iodinated, fluorinated, and methoxy-bearing coupling partners (Table 3.1). The syntheses of compounds **11–16** and **18–21** were performed by Dr Adele Blair and further information, beyond what is included in Table 3.1, can be found in the author's thesis (Blair, 2014). The choice of HBTU as an amide coupling agent for the synthesis of compounds **4–10** was driven by previous success with this agent in the synthesis of compound **31** (Scheme 3.1), and the difficulties reported by Blair (2014) in utilising an alternative carbodiimide coupling agent EDCI. It should be noted that the reported yields in Table 3.1 for compounds **4–5** and **7–10** were based on single un-optimised reactions. The exception was compound **6**, where an initial attempt at its synthesis via amide coupling between **3** and 3-iodo-4-methylbenzoic acid at room temperature afforded the product in only 8% yield. However, an increase in temperature to 40 °C allowed for a markedly improved yield of 48%. Higher temperatures were not investigated due to the potential explosive risks associated with the 1-hydroxybenzotriazole by-product of HBTU (Wehrstedt, Wandrey, and Heitkamp, 2005).

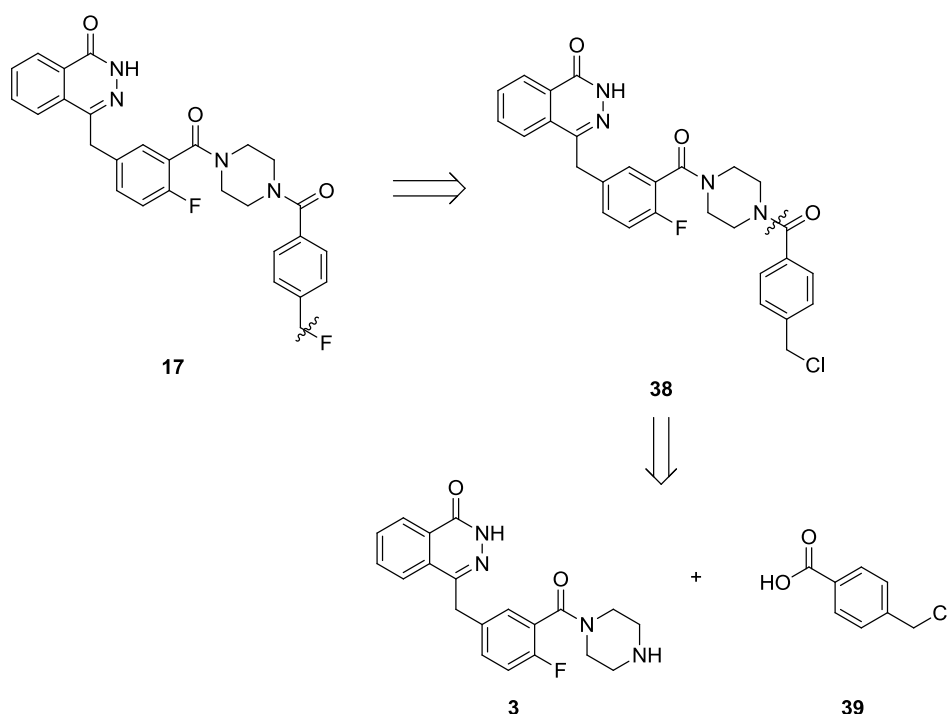
Table 3.1. Synthesis of compounds **4–16** and **18–21** from the penultimate compound **3**.



Coupling partner	Reaction conditions	Compound	Yield (%)
Cyclopropanecarboxylic acid	a	Olaparib	51
4-Iodobenzoic acid	b	4	34
3-Iodobenzoic acid	b	5	44
3-Iodo-4-methylbenzoic acid	c	6	48
3-Iodo-4-methoxybenzoic acid	b	7	26
2-(3-Iodophenyl)acetic acid	b	8	40
2-(4-Iodophenoxy)acetic acid	b	9	32
4-Iodobenzene-1-sulfonyl chloride	d	10	52
4-Fluorobenzoic acid	e	11	75
2-Fluorobenzoic acid	e	12	53
4-Fluoro-2-methylbenzoic acid	f	13	31
2-(4-Fluorophenyl)acetic acid	g	14	46
4-(4-Fluorophenyl)-4-oxobutanoic acid	f	15	34
4-Fluorobenzyl bromide	h	16	34
3-Methoxybenzoic acid	g	18	40
2-(4-Methoxyphenyl)acetic acid	g	19	64
2-(3-Methoxyphenyl)acetic acid	g	20	53
4-Methoxybenzyl bromide	i	21	42

Reagents and conditions: (a) HBTU, Et₃N, DMF, rt, 72 h; (b) HBTU, Et₃N, DMF, rt, 48 h; (c) HBTU, Et₃N, DMF, 40 °C, 22 h; (d) Et₃N, CH₂Cl₂, rt, 6 h; (e) HBTU, DIPEA, DCM, rt, 24 h; (f) EDCI, DMAP, DCM, rt then reflux, 24 h; (g) HBTU, DIPEA, DMF, 50 °C, 24 h; (h) DIPEA, DCM, rt, 12 h; (i) DIPEA, DCM, rt, 24 h.

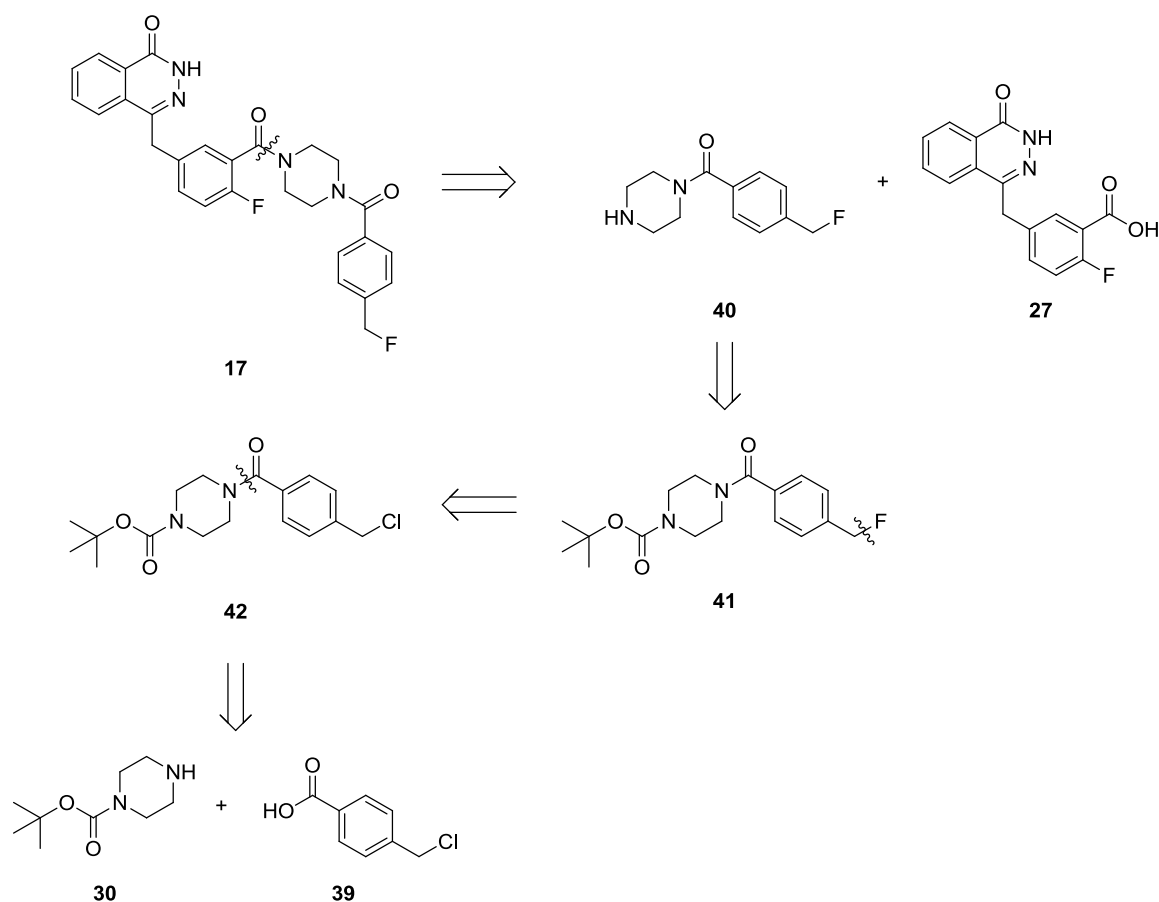
As mentioned earlier, access to compound **17** was complicated by the lack of commercial availability of the 4-(fluoromethyl)benzoic acid coupling partner. As a consequence, retrosynthetic analyses were performed in order to establish an optimal synthetic route for **17** utilising commercially available 4-(chloromethyl)benzoic acid (**39**). The initial proposed retrosynthetic route (Scheme 3.4) consisted of a disconnection of the terminal fluoride of **17**, affording the chlorinated compound **38** that could be accessed by amide coupling of **39** and **3**. However, it was thought that late-stage nucleophilic fluorination of **38** could prove challenging due to potential reactivity of the phthalazinone core.



Scheme 3.4. Initial retrosynthetic analysis of the olaparib analogue **17** utilising a late-stage nucleophilic fluorination step.

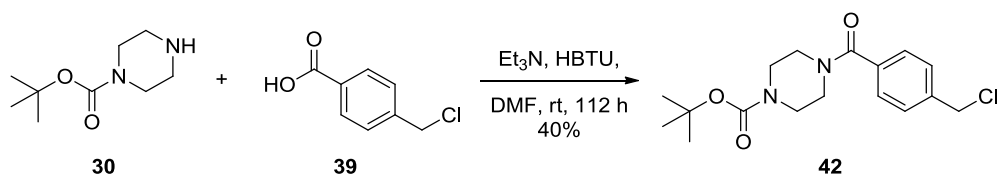
Consequently, an alternative retrosynthetic route utilising early-stage fluorination was established (Scheme 3.5). An initial disconnection of the amide linkage of **17** afforded the previously synthesised phthalazinone **27** and the functionalised piperazine **40**, which could in turn be synthesised by Boc-deprotection of the fluorinated intermediate **41**. The fluorine atom could be introduced via a nucleophilic substitution reaction of the corresponding benzyl chloride **42**. A final disconnection of the amide bond of **42** led to the mono-Boc

protected piperazine **30** and commercially available 4-(chloromethyl)benzoic acid **39**.



Scheme 3.5. Alternative retrosynthetic analysis of the fluorinated olaparib analogue **17** utilising an early-stage nucleophilic fluorination step.

As per the above described retrosynthetic analysis, mono-Boc protected piperazine **30** was subjected to an amide coupling reaction with 4-(chloromethyl)benzoic acid **39** generating intermediate **42** in 40% yield (Scheme 3.6).

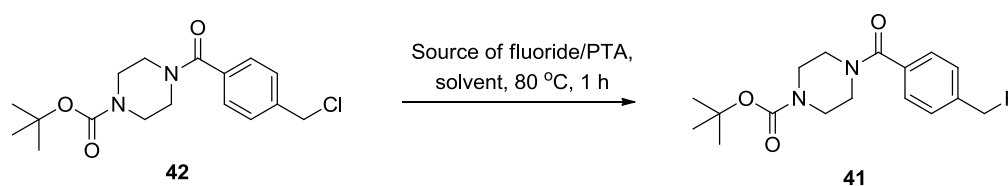


Scheme 3.6. The synthetic approach used to access compound **42**.

Compound **42** was then subjected to a number of small scale reactions with the aim of establishing optimal conditions for the nucleophilic substitution of the

benzyl chloride functionality with a fluorine atom (Table 3.2). An initial attempt at nucleophilic fluorination involved using an excess of KF (2 eq.) in the presence of the phase transfer agent (PTA) 18-crown-6 (18-Cr-6) (see section 5.1.2.2 for further information concerning the use of PTAs). However, these conditions afforded poor conversion with a 1.0 : 25.0 ratio of desired product **41** to starting material **42** (Table 3.2, Entry 1). By using an excess of tetra-*n*-butylammonium fluoride (TBAF) (2 eq.) complete conversion was achieved within one hour (Entry 2). This was also the case in the presence of 1 eq. of TBAF when using both acetonitrile and *N,N'*-dimethylformamide as reaction solvents (Entries 3 and 4). However, for practical reasons concerning compound purification acetonitrile was chosen as the preferred solvent.

Table 3.2. Screen of reaction conditions for the non-radioactive nucleophilic substitution fluorination of **42**.

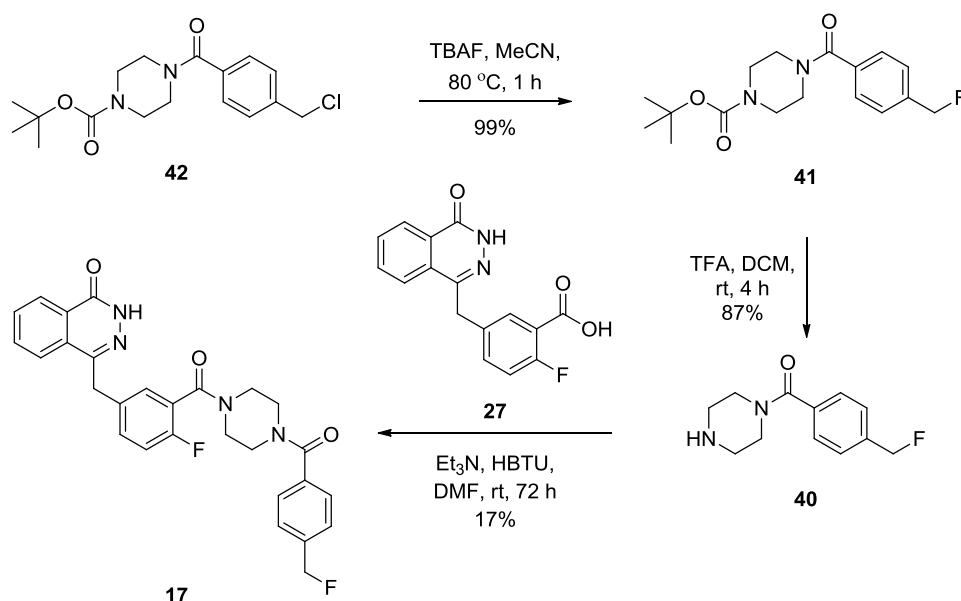


Entry	Source of fluoride/PTA	Number of equivalents	Solvent	Ratio 41 : 42 ^a
1	KF/18-Cr-6	2	MeCN	1.0 : 25.0
2	TBAF	1	MeCN	1.0 : 0.0
3	TBAF	1	MeCN	1.0 : 0.0
4	TBAF	1	DMF	1.0 : 0.0

^aThe ratio was calculated from the ¹H NMR spectrum of the crude mixture following *in vacuo* acetonitrile removal or dichloromethane/aqueous extraction in order to remove *N,N'*-dimethylformamide. PTA = phase transfer agent; TBAF = tetra-*n*-butylammonium fluoride; MeCN = acetonitrile; DMF = *N,N'*-dimethylformamide.

The reaction conditions described in entry 3 (Table 3.2) were replicated on a larger scale affording compound **41** in 99% yield (Scheme 3.7). Following successful fluorination, the Boc protecting group of compound **41** was cleaved

using trifluoroacetic acid (TFA), and the corresponding deprotected amine (**40**) was then used in a HBTU mediated amide coupling with compound **27**, resulting in the generation of the fluorinated phthalazinone **17**. The final step afforded the desired compound in only 17%. However, this result was based on a single reaction and it is possible that with appropriate optimisation the product yield could be improved.



Scheme 3.7. The synthetic approach used to access compound **17** from the benzyl chloride **42**.

3.3 Conclusion.

Eighteen non-radioactive compounds, based around the olaparib phthalazinone scaffold **3**, were identified as potential PARP-1 SPECT and PET nuclear imaging agents and were subsequently synthesised. Synthesis of scaffold **3** was achieved in six linear steps using slightly modified methodology to that described by Menear *et al.* (2008). This compound was then utilised as a penultimate precursor for coupling with commercially available carboxylic acids, alkyl halides and sulfonyl halides giving access to seven iodinated (**4–10**), six fluorinated (**11–16**) and four methoxy-bearing (**18–21**) analogues of olaparib. The benzyl-fluoride **17** could not be synthesised using the same approach due to lack of commercial availability of the 4-(fluoromethyl)benzoic acid coupling partner. Instead, an alternative method was used, which relied on early-stage

nucleophilic fluorination of a functionalised 4-(chloromethyl)benzoic acid (**42**) that was coupled with **27** to afford the desired product **17**.

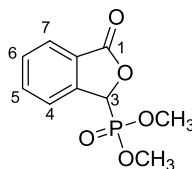
3.4 Experimental.

3.4.1 General experimental.

The general experimental and the synthesis of compounds **3–10**, **24**, **26–27**, and **30–31** has been reported previously by Zmuda *et al.* (2015). All reagents and starting materials were obtained from commercially reputable suppliers and were used as received. Compound purification via flash column chromatography was carried out using Fisher matrix silica 60, and thin layer chromatography was performed using Macherey-Nagel aluminium-backed plates pre-coated with silica gel 60 (UV254). Visualisation of compounds on thin layer chromatography plates was achieved by staining with KMnO_4 . ^1H NMR and ^{13}C NMR spectra were recorded on a Bruker DPX 400 spectrometer with chemical shift values reported in ppm relative to TMS (δ_{H} 0.00 and δ_{C} 0.0), residual chloroform (δ_{H} 7.26 and δ_{C} 77.2), residual methanol (δ_{H} 3.31 and δ_{C} 49.0) or residual dimethyl sulfoxide (δ_{H} 2.50 and δ_{C} 39.5) as standard. Analyses of NMR data were performed using the iNMR 2.0.7 software. Where necessary, two-dimensional COSY, HSQC, and DEPT experiments were performed on a Bruker DPX 400 spectrometer in order to aid NMR assignments. Mass spectra were obtained using a JEOL JMS-700 spectrometer. Infrared spectra were obtained neat using a Shimadzu IRPrestige-21 spectrometer. All reactions were performed under an atmosphere of argon and using anhydrous solvent unless stated otherwise.

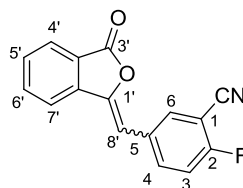
3.4.2 Experimental data for all synthesised compounds.

3-Dimethoxyphosphoryl-3H-2-benzofuran-1-one (**24**) (Menear *et al.*, 2008).



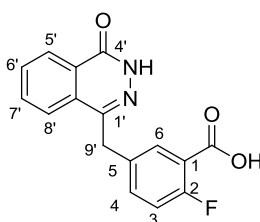
Dimethylphosphite (**23**) (0.92 mL, 10.0 mmol) was added dropwise to a solution of sodium methoxide (0.583 g, 10.8 mmol) in methanol (15 mL) at 0 °C. To the solution, 2-carboxybenzaldehyde (**22**) (1.00 g, 6.66 mmol) was added portionwise while stirring. The mixture was gradually warmed to room temperature and stirred for 2 hours. Methanesulfonic acid (0.77 mL, 11.9 mmol) was added dropwise and the mixture was allowed to stir for a further 0.5 hours. The solution was concentrated *in vacuo* to produce a white solid, to which water was added (30 mL) and the crude product was extracted into dichloromethane (3 × 30 mL). The organic layer was washed with water (2 × 30 mL), dried with magnesium sulfate and filtered. The filtrate was concentrated *in vacuo* and washed with diethyl ether (3 × 20 mL) to give 3-dimethoxyphosphoryl-3H-2-benzofuran-1-one (**24**) (1.54 g, 96%) as a white solid. Mp 90–91 °C; δ_{H} (400 MHz, CD₃OD) 3.72 (3H, d, *J* 10.8 Hz, OCH₃), 3.91 (3H, d, *J* 10.8 Hz, OCH₃), 6.10 (1H, d, *J* 10.8 Hz, 3-H), 7.68 (1H, t, *J* 7.5 Hz, 5-H), 7.75 (1H, d, *J* 7.5 Hz, 4-H), 7.83 (1H, t, *J* 7.5 Hz, 6-H), 7.94 (1H, d, *J* 7.5 Hz, 7-H); δ_{C} (101 MHz, CD₃OD) 54.9 (CH₃, d, *J*_{C-O-P} 6.8 Hz), 55.3 (CH₃, d, *J*_{C-O-P} 7.4 Hz), 76.4 (CH, d, *J*_{C-P} 167.0 Hz), 124.7 (CH, d, *J*_{C-C-C-P} 3.0 Hz), 126.2 (C, d, *J*_{C-C-P} 4.1 Hz), 126.8 (CH, d, *J*_{C-C-C-C-P} 1.9 Hz), 131.2 (CH, d, *J*_{C-C-C-C-P} 2.9 Hz), 135.9 (CH, d, *J*_{C-C-C-C-P} 2.8 Hz), 145.2 (C, d, *J*_{C-C-C-P} 4.0 Hz), 171.3 (C, d, *J*_{C-O-C-P} 2.7 Hz); *m/z* (EI) 242 (M⁺, 37%), 213 (10), 199 (9), 133 (100), 105 (13), 77 (17), 51 (5).

2-Fluoro-5-[(3'-oxo-2'-benzofuran-1'-ylidene)methyl]benzonitrile (26)
(Menear *et al.*, 2008).



A solution of 3-dimethoxyphosphoryl-3*H*-2-benzofuran-1-one (**24**) (3.87 g, 16.0 mmol) and 2-fluoro-5-formylbenzonitrile (**25**) (2.26 g, 15.2 mmol) in tetrahydrofuran (50 mL) was prepared at room temperature. The solution was then cooled to 0 °C followed by the addition of triethylamine (2.15 mL, 16.0 mmol). The reaction mixture was allowed to warm up to room temperature and was stirred for 48 hours, followed by concentration *in vacuo* to produce a white solid. The solid was suspended in water, collected by vacuum filtration and washed with hexane (2 × 20 mL), diethyl ether (2 × 20 mL), and methanol (2 × 20 mL) to give 2-fluoro-5-[(3'-oxo-2'-benzofuran-1'-ylidene)methyl]benzonitrile (**26**) (3.77 g, 98%) as a white solid. NMR spectra showed a mixture of *E* and *Z* isomers. Only data for the major isomer were recorded. Mp 164–167 °C; δ_{H} (400 MHz, DMSO-*d*₆) 6.98 (1H, s, 8'-H), 7.65 (1H, t, *J* 9.0 Hz, ArH), 7.67–7.75 (1H, m, ArH), 7.92 (1H, td, *J* 7.6, 1.0 Hz, ArH), 7.97–8.00 (1H, m, ArH), 8.08 (1H, dt, *J* 8.0, 1.0 Hz, ArH), 8.12–8.21 (2H, m, ArH); δ_{C} (101 MHz, DMSO-*d*₆) 100.8 (C, d, *J*_{C-C-F} 15.8 Hz), 103.4 (CH), 113.8 (C), 117.4 (CH, d, *J*_{C-C-F} 20.0 Hz), 121.0 (CH), 122.6 (C), 125.4 (CH), 130.9 (CH), 131.0 (C, d, *J*_{C-C-C-F} 3.7 Hz), 134.2 (CH), 135.4 (CH), 136.7 (CH, d, *J*_{C-C-C-F} 9.0 Hz), 139.5 (C), 145.4 (C), 161.5 (C, d, *J*_{C-F} 258.1 Hz), 165.9 (C); *m/z* (EI) 265 (*M*⁺, 100%), 237 (12), 208 (64), 182 (10), 133 (13), 104 (14), 63 (29), 45 (8).

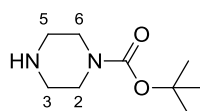
2-Fluoro-5-[(4'-oxo-3'*H*-phthalazin-1'-yl)methyl]benzoic acid (27) (Menear *et al.*, 2008).



2-Fluoro-5-[(3'-oxo-2'-benzofuran-1'-ylidene)methyl]benzonitrile (**26**) (1.77 g, 7.00 mmol) was suspended in water (30 mL) and 13 M sodium hydroxide was

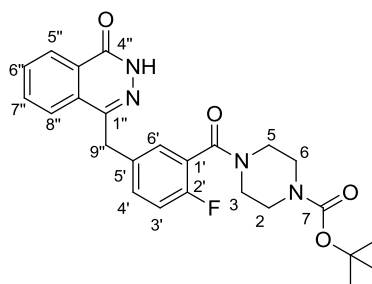
added (30 mL). The mixture was heated to 90 °C and stirred for 24 hours, after which it was cooled to 70 °C followed by the addition of hydrazine monohydrate (4.76 mL, 98.0 mmol) and a further 72 hours of stirring. The mixture was then cooled to room temperature and acidified with 8 M hydrochloric acid to an approximate pH of 4. The solid precipitate was collected by vacuum filtration and washed with water (3 × 25 mL) and diethyl ether (4 × 25 mL) to give 2-fluoro-5-[(4'-oxo-3'-H-phthalazin-1'-yl)methyl]benzoic acid (**27**) (2.00 g, 96%) as a red solid. Mp >300 °C; δ_{H} (400 MHz, DMSO- d_6) 4.36 (2H, s, 9'-H₂), 7.24 (1H, dd, J 10.8, 8.5 Hz, 3-H), 7.54–7.62 (1H, m, 4-H), 7.79–7.87 (2H, m, 6-H and 6'-H), 7.90 (1H, td, J 7.5, 1.3 Hz, 7'-H), 7.98 (1H, d, J 7.5 Hz, 8'-H), 8.26 (1H, dd, J 7.8, 1.3 Hz, 5'-H), 12.60 (1H, s, NH), 13.24 (1H, br s, COOH); δ_{C} (101 MHz, DMSO- d_6) 36.3 (CH₂), 117.0 (CH, d, $J_{\text{C-C-F}}$ 22.8 Hz), 119.1 (C, d, $J_{\text{C-C-F}}$ 10.7 Hz), 125.5 (CH), 126.1 (CH), 127.9 (C), 129.1 (C), 131.6 (CH), 131.9 (CH), 133.6 (CH), 134.3 (C, d, $J_{\text{C-C-C-C-F}}$ 3.4 Hz), 134.9 (CH, d, $J_{\text{C-C-C-F}}$ 8.7 Hz), 144.9 (C), 159.4 (C), 160.3 (C, d, $J_{\text{C-F}}$ 255.5 Hz), 165.0 (C, d, $J_{\text{C-C-C-F}}$ 2.8 Hz); m/z (ESI) 297.0671 ([M-H]⁻. C₁₆H₁₀¹⁹FN₂O₃ requires 297.0681).

tert-Butyl piperazine-1-carboxylate (30).



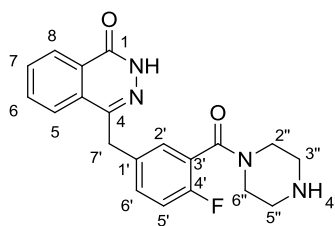
Di-*tert*-butyl dicarbonate (**29**) (4.04 g, 18.5 mmol) was dissolved in glacial acetic acid (20 mL) and this was added dropwise to a solution of piperazine (**28**) (1.60 g, 18.5 mmol) in 50% v/v acetic acid (40 mL) at room temperature. The mixture was stirred for 2 hours, followed by addition of water (50 mL), and removal of the precipitate by filtration. The filtrate was basified to approximately pH 10 using 6 M potassium hydroxide, and the product was extracted into dichloromethane (3 × 25 mL). The organic layer was dried with sodium sulfate and concentrated *in vacuo* to give *tert*-butyl piperazine-1-carboxylate (**30**) (1.58 g, 46%) as a white solid. Mp 46–48 °C (lit. (Moussa *et al.*, 2010) 46–47 °C); δ_{H} (400 MHz, CD₃OD) 1.46 (9H, s, O^tBu), 2.75 (4H, t, J 5.0 Hz, 3-H₂ and 5-H₂), 3.38 (4H, t, J 5.0 Hz, 2-H₂ and 6-H₂); δ_{C} (101 MHz, CD₃OD) 28.7 (3 × CH₃), 44.8 (2 × CH₂), 46.3 (2 × CH₂), 81.1 (C), 156.4 (C); m/z (CI) 187 (MH⁺, 78%), 175 (5), 131 (100), 87 (20), 73 (10).

***tert*-Butyl 4-[2'-fluoro-5'-[(4''-oxo-3''*H*-phthalazin-1''-yl)methyl]benzoyl]piperazine-1-carboxylate (31)** (Menear *et al.*, 2008).



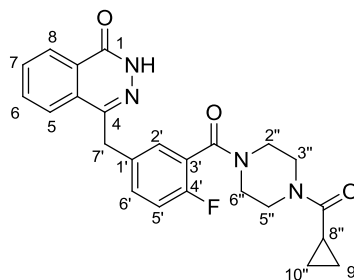
To a solution of 2-fluoro-5-[(4'-oxo-3'*H*-phthalazin-1'-yl)methyl]benzoic acid (**27**) (2.75 g, 9.23 mmol) in *N,N'*-dimethylformamide (70 mL) was added triethylamine (2.00 mL, 14.8 mmol), followed by *O*-benzotriazole-*N,N,N',N'*-tetramethyluroniumhexafluorophosphate (**33**) (3.85 g, 10.2 mmol). The mixture was stirred at room temperature for 1 hour, after which it was warmed to 50 °C and *tert*-butyl piperazine-1-carboxylate (**30**) (1.72 g, 9.23 mmol) was added with continued stirring for 72 h. Water (70 mL) was then added and the mixture was stirred at 50 °C for a further 2 hours, followed by cooling to 0 °C. The resulting precipitate was collected by vacuum filtration and washed with water (5 × 25 mL), diethyl ether (2 × 25 mL), and isopropan-2-ol (50 mL) to give *tert*-butyl 4-[2'-fluoro-5'-[(4''-oxo-3''*H*-phthalazin-1''-yl)methyl]benzoyl]piperazine-1-carboxylate (**31**) (3.04 g, 71%) as an orange solid. Mp 214–216 °C; δ_{H} (400 MHz, CDCl₃) 1.46 (9H, s, O^tBu), 3.27 (2H, br s, NCH₂), 3.38 (2H, t, *J* 5.1 Hz, NCH₂), 3.51 (2H, br s, NCH₂), 3.75 (2H, br s, NCH₂), 4.28 (2H, s, 9''-H₂), 7.03 (1H, t, *J* 8.8 Hz, 3'-H), 7.27–7.36 (2H, m, 4'-H and 6'-H), 7.68–7.73 (1H, m, ArH), 7.74–7.80 (2H, m, ArH), 8.44–8.50 (1H, m, 5''-H), 10.52 (1H, s, NH); δ_{C} (101 MHz, CDCl₃) 28.5 (3 × CH₃), 37.9 (CH₂), 42.1 (2 × CH₂), 47.0 (2 × CH₂), 80.5 (C), 116.3 (CH, d, *J*_{C-C-F} 22.2 Hz), 124.1 (C, d, *J*_{C-C-F} 17.9 Hz), 125.2 (CH), 127.3 (CH), 128.5 (C), 129.3 (CH, d, *J*_{C-C-C-F} 3.7 Hz), 129.7 (C), 131.7 (CH, d, *J*_{C-C-C-F} 8.1 Hz), 131.8 (CH), 133.8 (CH), 134.5 (C, d, *J*_{C-C-C-C-F} 3.0 Hz), 145.7 (C), 154.6 (C), 157.1 (C, d, *J*_{C-F} 246.1 Hz), 160.6 (C), 165.2 (C); *m/z* (EI) 466.

4-[4'-Fluoro-3'-(piperazine-1''-carbonyl)benzyl]-2H-phthalazin-1-one (3) (Menear *et al.*, 2008).



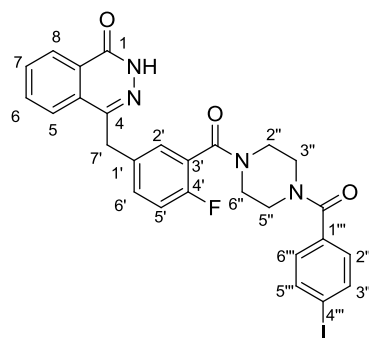
To a suspension of *tert*-butyl 4-[2'-fluoro-5'-[(4''-oxo-''H-phthalazin-1''-yl)methyl]benzoyl]piperazine-1-carboxylate (**31**) (1.40 g, 3.00 mmol) in ethanol (30 mL) was added 6 M hydrochloric acid (60 mL) and the mixture was stirred overnight at room temperature. Ethanol was removed under reduced pressure and the aqueous layer was basified to approximately pH 10 using 4 M sodium hydroxide. The product was extracted into dichloromethane (3 × 30 mL) and the organic layer was washed with water (3 × 50 mL), dried with magnesium sulfate, and concentrated *in vacuo*. Purification by recrystallisation with dichloromethane (5 mL) and petroleum ether (25 mL) gave 4-[4'-fluoro-3'-(piperazine-1''-carbonyl)benzyl]-2H-phthalazin-1-one (**3**) (0.776 g, 71%) as a yellow foam. δ_{H} (400 MHz, CDCl_3) 2.25–3.15 (4H, m, 2 × NCH_2), 3.16–3.96 (4H, m, 2 × NCH_2), 4.25 (2H, s, 7'- H_2), 5.99 (1H, br s, 4''-H), 6.97 (1H, t, J 8.8 Hz, 5'-H), 7.24–7.35 (2H, m, 2'-H and 6'-H), 7.64–7.76 (3H, m, 5-H, 6-H and 7-H), 8.38–8.46 (1H, m, 8-H), 12.01 (1H, br s, 2-H); δ_{C} (101 MHz, CDCl_3) 37.9 (CH_2), 43.3 (CH_2), 45.9 (CH_2), 46.4 (CH_2), 48.4 (CH_2), 116.1 (CH, d, $J_{\text{C-C-F}}$ 22.1 Hz), 124.4 (C, d, $J_{\text{C-C-F}}$ 18.4 Hz), 125.2 (CH), 127.3 (CH), 128.4 (C), 129.2 (CH, d, $J_{\text{C-C-C-F}}$ 3.8 Hz), 129.7 (C), 131.3 (CH, d, $J_{\text{C-C-C-F}}$ 8.0 Hz), 131.7 (CH), 133.8 (CH), 134.3 (C, d, $J_{\text{C-C-C-F}}$ 3.0 Hz), 145.7 (C), 157.2 (C, d, $J_{\text{C-F}}$ 247.7 Hz), 160.8 (C), 165.0 (C); m/z (ESI) 367.1553 (MH^+ . $\text{C}_{20}\text{H}_{20}\text{FN}_4\text{O}_2$ requires 367.1565).

4-[3'-(4''-Cyclopropanecarbonylpiperazine-1''-carbonyl)-4'-fluorobenzyl]-2*H*-phthalazin-1-one (olaparib) (Menear *et al.*, 2008).



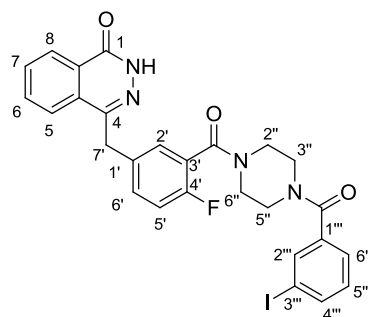
To a solution of cyclopropanoic acid (11.0 μL , 0.137 mmol) in *N,N'*-dimethylformamide (2 mL) was added triethylamine (29.0 μL , 0.218 mmol), followed by *O*-benzotriazole-*N,N,N',N'*-tetramethyluroniumhexafluorophosphate (**33**) (57.0 mg, 0.150 mmol), and the mixture was stirred at room temperature for 1 hour. 4-[4'-Fluoro-3'-(piperazine-1''-carbonyl)benzyl]-2*H*-phthalazin-1-one (**3**) (50.0 mg, 0.137 mmol) was then added and the mixture was stirred for a further 71 hours. The crude product was extracted into chloroform (3 \times 10 mL) and the organic layer was washed with water (6 \times 20 mL), dried with magnesium sulfate, filtered, and concentrated *in vacuo* to give a yellow solid. Purification by flash column chromatography (methanol/dichloromethane, 4:96) and then recrystallisation with dichloromethane and petroleum ether gave 4-[3'-(4''-cyclopropanecarbonylpiperazine-1''-carbonyl)-4'-fluorobenzyl]-2*H*-phthalazin-1-one (olaparib) (30 mg, 51%) as a white foam. ^1H NMR spectra showed a 3:2 mixture of rotamers. Only data for the major rotamer were recorded. δ_{H} (400 MHz, CDCl_3) 0.67–0.86 (2H, m, CH_2), 0.97–1.03 (2H, m, CH_2), 1.75 (1H, br s, 8''-H), 3.20–3.43 (2H, m, NCH_2), 3.51–3.93 (6H, m, 3 \times NCH_2), 4.29 (2H, s, 7'- H_2), 7.04 (1H, t, J 8.9 Hz, 5'-H), 7.29–7.41 (2H, m, 2'-H and 6'-H), 7.67–7.82 (3H, m, 5-H, 6-H and 7-H), 8.43–8.51 (1H, m, 8-H), 11.12 (1H, br s, NH); δ_{C} (101 MHz, CDCl_3) 7.8 (2 \times CH_2), 11.2 (CH), 37.8 (CH_2), 41.8 (CH_2), 42.4 (CH_2), 45.3 (CH_2), 47.0 (CH_2), 116.3 (CH, d, $J_{\text{C-C-F}}$ 22.3 Hz), 123.9 (C, d, $J_{\text{C-C-F}}$ 18.3 Hz), 125.1 (CH), 127.3 (CH), 128.5 (C), 129.4 (CH), 129.7 (C), 131.7 (CH), 131.8 (CH, d, $J_{\text{C-C-C-F}}$ 8.1 Hz), 133.8 (CH), 134.5 (C, d, $J_{\text{C-C-C-C-F}}$ 3.4 Hz), 145.6 (C), 157.2 (C, d, $J_{\text{C-F}}$ 247.4 Hz), 160.7 (C), 165.3 (C), 172.4 (C); m/z (ESI) 457.1636 (MNa^+ . $\text{C}_{24}\text{H}_{23}\text{FN}_4\text{NaO}_3$ requires 457.1646).

4-[3'-[4''-(4'''-iodobenzoyl)piperazine-1''-carbonyl]-4'-fluorobenzyl]-2*H*-phthalazin-1-one (4).



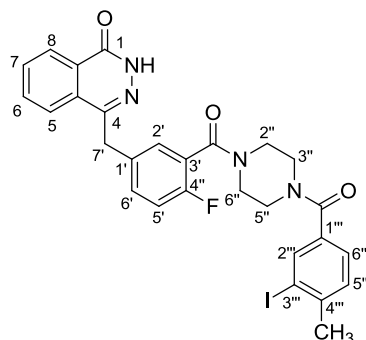
To a solution of 4-iodobenzoic acid (42.0 mg, 0.170 mmol) in *N,N'*-dimethylformamide (7 mL) was added triethylamine (37.0 μL , 0.272 mmol), followed by *O*-benzotriazole-*N,N,N',N'*-tetramethyluroniumhexafluorophosphate (**33**) (71.0 mg, 0.187 mmol) and the mixture was stirred at room temperature for 2 hours. 4-[4'-Fluoro-3'-(piperazine-1''-carbonyl)benzyl]-2*H*-phthalazin-1-one (**3**) (60.0 mg, 0.170 mmol) was added and the mixture was stirred for a further 48 hours. Water (14 mL) was then added, followed by 1 hour of stirring after which the mixture was cooled to 0 $^{\circ}\text{C}$. The resulting precipitate was collected by vacuum filtration and washed with diethyl ether (4 \times 10 mL) and hexane (4 \times 10 mL). Purification by flash column chromatography (methanol/dichloromethane, 4:96) gave 4-[3'-[4''-(4'''-iodobenzoyl)piperazine-1''-carbonyl]-4'-fluorobenzyl]-2*H*-phthalazin-1-one (**4**) (34.8 mg, 34%) as a white foam. R_f (4% v/v methanol/dichloromethane) 0.34; $\nu_{\text{max}}/\text{cm}^{-1}$ (neat) 3198 (NH), 3003 (ArH), 2899 (CH), 1628 (CO), 1587 (C=C), 1427, 1001, 747; δ_{H} (400 MHz, CDCl_3) 3.14–4.02 (8H, m, 4 \times NCH_2), 4.29 (2H, s, 7'- H_2), 7.03 (1H, t, J 7.8 Hz, 5'-H), 7.14 (2H, d, J 8.0 Hz, 3'''-H and 5'''-H), 7.29–7.37 (2H, m, 2'-H and 6'-H), 7.67–7.84 (5H, m, ArH), 8.42–8.51 (1H, m, 8-H), 10.96 (1H, s, NH); δ_{C} (101 MHz, CDCl_3) 37.8 (CH_2), 42.2 (2 \times CH_2), 47.3 (2 \times CH_2), 96.6 (C), 116.3 (CH, d, $J_{\text{C-C-F}}$ 21.7 Hz), 123.6 (C, d, $J_{\text{C-C-F}}$ 17.7 Hz), 125.1 (CH), 127.3 (CH), 128.4 (C), 128.9 (2 \times CH), 129.4 (CH, d, $J_{\text{C-C-C-F}}$ 3.6 Hz), 129.6 (C), 131.8 (CH), 131.9 (CH, d, $J_{\text{C-C-F}}$ 8.0 Hz), 133.8 (CH), 134.5 (C), 134.6 (C, d, $J_{\text{C-C-C-C-F}}$ 3.7 Hz), 138.0 (2 \times CH), 145.6 (C), 157.1 (C, d, $J_{\text{C-F}}$ 247.1 Hz), 160.7 (C), 165.3 (C), 169.8 (C); m/z (ESI) 619.0597 (MNa^+ . $\text{C}_{27}\text{H}_{22}\text{FIN}_4\text{NaO}_3$ requires 619.0613).

4-[3'-[4''-(3''''-iodobenzoyl)piperazine-1''-carbonyl]-4'-fluorobenzyl]-2*H*-phthalazin-1-one (5).



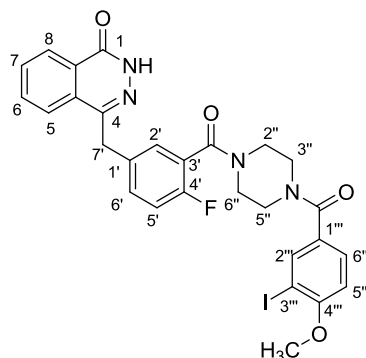
The reaction was carried out as described for 4-[3'-[4''-(4''''-iodobenzoyl)piperazine-1''-carbonyl]-4'-fluorobenzyl]-2*H*-phthalazin-1-one (4) using a solution of 3-iodobenzoic acid (34.0 mg, 0.137 mmol) in *N,N*-dimethylformamide (3 mL), triethylamine (29.0 μ L, 0.218 mmol), *O*-benzotriazole-*N,N,N',N'*-tetramethyluroniumhexafluorophosphate (33) (57.0 mg, 0.151 mmol) and 4-[4'-fluoro-3'-(piperazine-1''-carbonyl)benzyl]-2*H*-phthalazin-1-one (3) (50.0 mg, 0.137 mmol). Purification by flash column chromatography (methanol/dichloromethane, 4:96) gave 4-[3'-[4''-(3''''-iodobenzoyl)piperazine-1''-carbonyl]-4'-fluorobenzyl]-2*H*-phthalazin-1-one (5) (36.4 mg, 45%) as a white foam. R_f (4% v/v methanol/dichloromethane) 0.28; $\nu_{\max}/\text{cm}^{-1}$ (neat) 3190 (NH), 3053 (ArH), 2862 (CH), 1628 (CO), 1559 (C=C), 1427, 1252, 1005, 791, 729; δ_{H} (400 MHz, CDCl_3) 3.16–4.01 (8H, m, 4 \times NCH₂), 4.29 (2H, s, 7'-H₂), 7.03 (1H, br s, 5'-H), 7.15 (1H, br s, 4''''-H), 7.27–7.39 (3H, m, ArH), 7.67–7.82 (5H, m, ArH), 8.42–8.49 (1H, m, 8-H), 10.70 (1H, s, NH); δ_{C} (101 MHz, CDCl_3) 37.8 (CH₂), 42.2 (2 \times CH₂), 47.4 (2 \times CH₂), 94.5 (C), 116.3 (CH, d, $J_{\text{C-C-F}}$ 21.7 Hz), 123.6 (C, d, $J_{\text{C-C-F}}$ 17.7 Hz), 125.1 (CH), 126.2 (CH), 127.3 (CH), 128.4 (C), 129.4 (CH, d, $J_{\text{C-C-C-F}}$ 3.6 Hz), 129.6 (C), 130.4 (CH), 131.8 (CH), 131.9 (CH, d, $J_{\text{C-C-C-F}}$ 8.0 Hz), 133.8 (CH), 134.6 (C, d, $J_{\text{C-C-C-C-F}}$ 3.9 Hz), 136.0 (CH), 137.1 (C), 139.2 (CH), 145.6 (C), 157.1 (C, d, $J_{\text{C-F}}$ 247.1 Hz), 160.8 (C), 165.3 (C), 168.8 (C); m/z (ESI) 619.0605 (MNa^+ . $\text{C}_{27}\text{H}_{22}\text{FIN}_4\text{NaO}_3$ requires 619.0613).

4-[3'-[4''-(3'''-iodo-4'''-methylbenzoyl)piperazine-1''-carbonyl]-4'-fluorobenzyl]-2*H*-phthalazin-1-one (6).



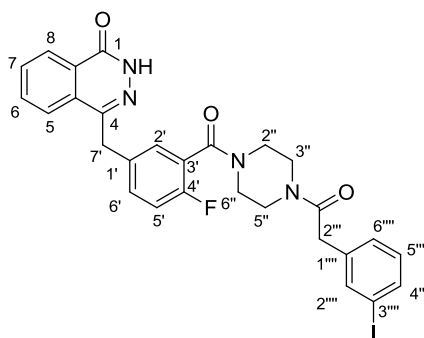
To a solution of 3-iodo-4-methylbenzoic acid (36.0 mg, 0.137 mmol) in *N,N'*-dimethylformamide (3 mL) was added triethylamine (29.0 μL , 0.218 mmol), followed by *O*-benzotriazole-*N,N,N',N'*-tetramethyluroniumhexafluorophosphate (**33**) (57.0 mg, 0.151 mmol), and the mixture was stirred at room temperature for 1 hour. 4-[4'-Fluoro-3'-(piperazine-1''-carbonyl)benzyl]-2*H*-phthalazin-1-one (**3**) (50.0 mg, 0.137 mmol) was then added and the mixture was stirred for a further 22 hours at 40 °C. The mixture was cooled to room temperature and water (6 mL) was added, followed by 1 hour of stirring after which the mixture was cooled to 0 °C. The resulting precipitate was collected by vacuum filtration and dissolved in chloroform (10 mL). The organic layer was washed with water (3 \times 20 mL) and concentrated *in vacuo*. Purification by flash column chromatography (methanol/dichloromethane, 3:97) gave 4-[3'-[4''-(3'''-iodo-4'''-methylbenzoyl)piperazine-1''-carbonyl]-4'-fluorobenzyl]-2*H*-phthalazin-1-one (**6**) (40.0 mg, 48%) as a white foam. R_f (3% v/v methanol/dichloromethane) 0.26; $\nu_{\text{max}}/\text{cm}^{-1}$ (neat) 3203 (NH), 3011 (ArH), 2893 (CH), 1629 (CO), 1425, 1252, 1006, 746; δ_{H} (400 MHz, CDCl_3) 2.44 (3H, s, 4'''-CH₃), 3.13–4.05 (8H, m, 4 \times NCH₂), 4.27 (2H, s, 7'-H₂), 7.03 (1H, t, *J* 8.4 Hz, 5'-H), 7.23–7.37 (4H, m, ArH), 7.67–7.80 (3H, m, ArH), 7.85 (1H, s, ArH), 8.43–8.49 (1H, m, 8-H), 10.85 (1H, s, NH); δ_{C} (101 MHz, CDCl_3) 28.2 (CH₃), 37.8 (CH₂), 42.3 (2 \times CH₂), 47.1 (2 \times CH₂), 101.1 (C), 116.3 (CH, d, $J_{\text{C-C-F}}$ 22.0 Hz), 123.7 (C, d, $J_{\text{C-C-F}}$ 17.6 Hz), 125.1 (CH), 127.0 (CH), 127.3 (CH), 128.4 (C), 129.4 (CH, d, $J_{\text{C-C-C-F}}$ 3.2 Hz), 129.6 (C), 129.8 (CH), 131.8 (CH), 131.9 (CH, d, $J_{\text{C-C-C-F}}$ 7.8 Hz), 133.8 (CH), 134.2 (C), 134.6 (C, d, $J_{\text{C-C-C-C-F}}$ 3.8 Hz), 137.6 (CH), 143.9 (C), 145.6 (C), 157.1 (C, d, $J_{\text{C-F}}$ 249.9 Hz), 160.8 (C), 165.3 (C), 168.9 (C); *m/z* (ESI) 633.0759 (MNa⁺. C₂₈H₂₄FIN₄NaO₃ requires 633.0769).

4-[3'-[4''-(3'''-iodo-4'''-methoxybenzoyl)piperazine-1''-carbonyl]-4'-fluorobenzyl]-2*H*-phthalazin-1-one (7).



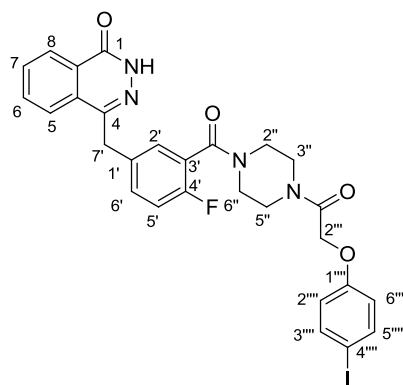
The reaction was carried out as described for 4-[3'-[4''-(4'''-iodobenzoyl)piperazine-1''-carbonyl]-4'-fluorobenzyl]-2*H*-phthalazin-1-one (4) using a solution of 3-iodo-4-methoxybenzoic acid (76.0 mg, 0.273 mmol) in *N,N'*-dimethylformamide (5 mL), triethylamine (59.0 μ L, 0.437 mmol), *O*-benzotriazole-*N,N,N',N'*-tetramethyluroniumhexafluorophosphate (33) (114 mg, 0.300 mmol), and 4-[4'-fluoro-3'-(piperazine-1''-carbonyl)benzyl]-2*H*-phthalazin-1-one (3) (100 mg, 0.273 mmol). Purification by flash column chromatography (methanol/dichloromethane, 3:97) gave 4-[3'-[4''-(3'''-iodo-4'''-methoxybenzoyl)piperazine-1''-carbonyl]-4'-fluorobenzyl]-2*H*-phthalazin-1-one (7) (44.5 mg, 26%) as a white foam. R_f (3% v/v methanol/dichloromethane) 0.29; $\nu_{\max}/\text{cm}^{-1}$ (neat) 3192 (NH), 3009 (ArH), 2897 (CH), 1628 (CO), 1593 (C=C), 1425, 1256, 1005, 747; δ_H (400 MHz, CDCl_3) 3.34 (2H, br s, NCH_2), 3.45–3.85 (6H, m, $3 \times \text{NCH}_2$), 3.90 (3H, s, 4'''- OCH_3), 4.29 (2H, s, 7'- H_2), 6.82 (1H, d, J 8.3 Hz, 5'''-H), 7.03 (1H, t, J 8.7 Hz, 5'-H), 7.29–7.36 (2H, m, 2'-H and 6'-H), 7.40 (1H, dd, J 8.3, 2.0 Hz, 6'''-H), 7.68–7.81 (3H, m, 5-H, 6-H and 7-H), 7.85 (1H, d, J 2.0 Hz, 2'''-H), 8.43–8.50 (1H, m, 8-H), 10.82 (1H, s, NH); δ_C (101 MHz, CDCl_3) 37.8 (CH_2), 42.3 ($2 \times \text{CH}_2$), 47.2 ($2 \times \text{CH}_2$), 56.7 (CH_3), 86.0 (C), 110.6 (CH), 116.3 (CH, d, $J_{\text{C-C-F}}$ 21.7 Hz), 123.6 (C, d, $J_{\text{C-C-F}}$ 17.7 Hz), 125.1 (CH), 127.4 (CH), 128.5 (C), 129.1 (C), 129.3 (CH), 129.4 (CH, d, $J_{\text{C-C-C-F}}$ 3.6 Hz), 129.7 (C), 131.8 (CH), 131.9 (CH, d, $J_{\text{C-C-C-F}}$ 8.0 Hz), 133.8 (CH), 134.6 (C, d, $J_{\text{C-C-C-C-F}}$ 3.9 Hz), 138.8 (CH), 145.6 (C), 157.1 (C, d, $J_{\text{C-F}}$ 247.1 Hz), 159.7 (C), 160.6 (C), 165.3 (C), 169.0 (C); m/z (ESI) 649.0713 (MNa^+ . $\text{C}_{28}\text{H}_{24}\text{FIN}_4\text{NaO}_4$ requires 649.0718).

4-[3'-[4''-[2'''-(3''''-iodophenyl)acetyl]piperazine-1''-carbonyl]-4'-fluorobenzyl]-2*H*-phthalazin-1-one (8).



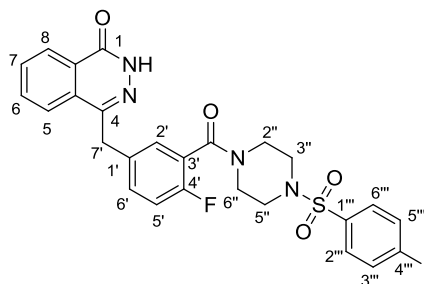
The reaction was carried out as described for 4-[3'-[4''-(4''''-iodobenzoyl)piperazine-1''-carbonyl]-4'-fluorobenzyl]-2*H*-phthalazin-1-one (4) using a solution of 3-iodophenylacetic acid (72.0 mg, 0.273 mmol) in *N,N*-dimethylformamide (5 mL), triethylamine (59.0 μ L, 0.437 mmol), *O*-benzotriazole-*N,N,N',N'*-tetramethyluroniumhexafluorophosphate (33) (114 mg, 0.300 mmol), and 4-[4'-fluoro-3'-(piperazine-1''-carbonyl)benzyl]-2*H*-phthalazin-1-one (3) (100 mg, 0.273 mmol). Purification by flash column chromatography (methanol/dichloromethane, 3:97) gave 4-[3'-[4''-[2'''-(3''''-iodophenyl)acetyl]piperazine-1''-carbonyl]-4'-fluorobenzyl]-2*H*-phthalazin-1-one (8) (67.0 mg, 40%) as a white foam. NMR spectra showed a 55:45 mixture of rotamers. Only data for the major rotamer were recorded. R_f (3% v/v methanol/dichloromethane) 0.23; $\nu_{\max}/\text{cm}^{-1}$ (neat) 3190 (NH), 3005 (ArH), 2899 (CH), 1632 (CO), 1589 (C=C), 1433, 1223, 1013, 748; δ_{H} (400 MHz, CDCl_3) 3.27 (2H, br s, NCH_2), 3.39 (2H, t, J 4.6 Hz, NCH_2), 3.50–3.90 (6H, m, $2 \times \text{NCH}_2$ and $2'''$ -H₂), 4.28 (2H, s, $7'$ -H₂), 6.97–7.10 (2H, m, $5'$ -H and $5''''$ -H), 7.14–7.24 (1H, m, $4''''$ -H), 7.29–7.37 (2H, m, $2'$ -H and $6'$ -H), 7.53–7.63 (2H, m, $2''''$ -H and $6''''$ -H), 7.67–7.73 (1H, m, 5-H), 7.74–7.81 (2H, m, 6-H, and 7-H), 8.43–8.50 (1H, m, 8-H), 10.90 (1H, br s, NH); δ_{C} (101 MHz, CDCl_3) 37.8 (CH_2), 40.3 (CH_2), 41.6 (CH_2), 42.1 (CH_2), 45.8 (CH_2), 46.8 (CH_2), 94.8 (C), 116.3 (CH, d, $J_{\text{C-C-F}}$ 21.7 Hz), 123.5 (C, d, $J_{\text{C-C-F}}$ 17.7 Hz), 125.0 (CH), 127.2 (CH), 128.1 (CH), 128.3 (C), 129.3 (CH, d, $J_{\text{C-C-C-F}}$ 3.3 Hz), 129.6 (C), 130.6 (CH), 131.7 (CH), 131.9 (CH, d, $J_{\text{C-C-F}}$ 7.9 Hz), 133.8 (CH), 134.6 (C, d, $J_{\text{C-C-C-C-F}}$ 3.2 Hz), 136.3 (CH), 136.9 (C), 137.7 (CH), 145.6 (C), 157.0 (C, d, $J_{\text{C-F}}$ 247.8 Hz), 161.0 (C), 165.3 (C), 169.1 (C); m/z (ESI) 633.0750 (MNa^+ . $\text{C}_{28}\text{H}_{24}\text{FIN}_4\text{NaO}_3$ requires 633.0769).

4-[3'-[4''-[2'''-(4''''-iodophenoxy)acetyl]piperazine-1''-carbonyl]-4'-fluorobenzyl]-2*H*-phthalazin-1-one (9).



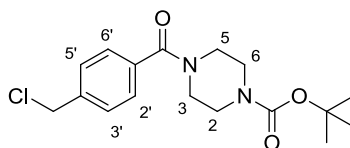
The reaction was carried out as described for 4-[3'-[4''-(4''''-iodobenzoyl)piperazine-1''-carbonyl]-4'-fluorobenzyl]-2*H*-phthalazin-1-one (4) using a solution of 4-iodophenoxyacetic acid (76.0 mg, 0.273 mmol) in *N,N'*-dimethylformamide (5 mL), triethylamine (59.0 μ L, 0.437 mmol), *O*-benzotriazole-*N,N,N',N'*-tetramethyluroniumhexafluorophosphate (33) (114 mg, 0.300 mmol), and 4-[4'-fluoro-3'-(piperazine-1''-carbonyl)benzyl]-2*H*-phthalazin-1-one (3) (100 mg, 0.273 mmol). Purification by flash column chromatography (methanol/dichloromethane, 4:96) gave 4-[3'-[4''-[2'''-(4''''-iodophenoxy)acetyl]piperazine-1''-carbonyl]-4'-fluorobenzyl]-2*H*-phthalazin-1-one (9) (55.0 mg, 32%) as a white foam. NMR spectra showed a 55:45 mixture of rotamers. Only data for the major rotamer were recorded. R_f (4% v/v methanol/dichloromethane) 0.28; $\nu_{\max}/\text{cm}^{-1}$ (neat) 3167 (NH), 3007 (ArH), 2901 (CH), 1634 (CO), 1585 (C=C), 1485, 1431, 1217, 1009, 745; δ_{H} (400 MHz, CDCl_3) 3.22 (2H, br s, NCH_2), 3.40–3.83 (6H, m, $3 \times \text{NCH}_2$), 4.22 (2H, s, 7'- H_2), 4.64 (2H, s, 2'''- H_2), 6.67 (2H, d, J 6.7 Hz, 2''''-H and 6''''-H), 6.96 (1H, t, J 8.6 Hz, 5'-H), 7.23–7.31 (2H, m, 2'-H and 6'-H), 7.48 (2H, t, J 9.2 Hz, 3''''-H and 5''''-H), 7.60–7.75 (3H, m, 5-H, 6-H and 7-H), 8.37–8.44 (1H, m, 8-H), 11.23 (1H, s, NH); δ_{C} (101 MHz, CDCl_3) 37.7 (CH_2), 42.4 ($2 \times \text{CH}_2$), 45.2 (CH_2), 46.8 (CH_2), 67.7 (CH_2), 84.4 (C), 116.3 (CH, d, $J_{\text{C-C-F}}$ 22.1 Hz), 117.0 ($2 \times \text{CH}$), 123.5 (C, d, $J_{\text{C-C-F}}$ 17.6 Hz), 125.1 (CH), 127.3 (CH), 128.4 (C), 129.3 (CH, d, $J_{\text{C-C-C-F}}$ 3.4 Hz), 129.6 (C), 131.7 (CH), 131.9 (CH, d, $J_{\text{C-C-C-F}}$ 7.9 Hz), 133.8 (CH), 134.6 (C, d, $J_{\text{C-C-C-C-F}}$ 3.6 Hz), 138.6 ($2 \times \text{CH}$), 145.6 (C), 157.0 (C, d, $J_{\text{C-F}}$ 247.4 Hz), 157.6 (C), 160.9 (C), 165.3 (C), 166.5 (C); m/z (ESI) 649.0714 (MNa^+). $\text{C}_{28}\text{H}_{24}\text{FIN}_4\text{NaO}_4$ requires 649.0718).

4-[3'-[4''-[4'''-iodobenzenesulfonyl]piperazine-1''-carbonyl]-4'-fluorobenzyl]-2*H*-phthalazin-1-one (10).



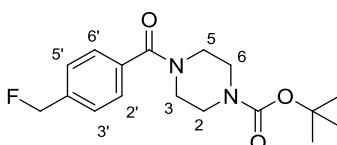
Triethylamine (28.0 μL , 0.205 mmol) and 4-iodobenzenesulfonyl chloride (50.0 mg, 0.164 mmol) were added to a solution of 4-[4'-fluoro-3'-(piperazine-1''-carbonyl)benzyl]-2*H*-phthalazin-1-one (**3**) (50.0 mg, 0.137 mmol) in dichloromethane (3 mL). The mixture was stirred at room temperature for 6 h after which, water (3 mL) was added. The crude product was extracted into dichloromethane (3 \times 10 mL), dried with sodium sulfate, filtered, and concentrated *in vacuo*. Purification by flash column chromatography (methanol/dichloromethane, 3:97) gave 4-[3'-[4''-[4'''-iodobenzenesulfonyl]piperazine-1''-carbonyl]-4'-fluorobenzyl]-2*H*-phthalazin-1-one (**10**) (45.0 mg, 52%) as a white foam. R_f (3% v/v methanol/dichloromethane) 0.30; $\nu_{\text{max}}/\text{cm}^{-1}$ (neat) 3185 (NH), 3006 (ArH), 2895 (CH), 1637 (CO), 1568 (C=C), 1438, 1349, 1164, 1005, 742; δ_{H} (400 MHz, CDCl_3) 2.97 (2H, t, J 4.8 Hz, NCH_2), 3.09 (2H, br s, NCH_2), 3.39 (2H, br s, NCH_2), 3.85 (2H, br s, NCH_2), 4.27 (2H, s, 7'- H_2), 7.00 (1H, t, J 8.8 Hz, 5'-H), 7.24–7.34 (2H, m, 2'-H and 6'-H), 7.40–7.46 (2H, m, 3'''-H and 5'''-H), 7.66–7.72 (1H, m, 5-H), 7.73–7.80 (2H, m, 6-H and 7-H), 7.88–7.93 (2H, m, 2'''-H and 6'''-H), 8.44–8.51 (1H, m, 8-H), 11.31 (1H, s, NH); δ_{C} (101 MHz, CDCl_3) 37.8 (CH_2), 41.5 (CH_2), 45.8 (CH_2), 46.2 (CH_2), 46.6 (CH_2), 101.0 (C), 116.3 (CH, d, $J_{\text{C-C-F}}$ 21.8), 123.4 (C, d, $J_{\text{C-C-F}}$ 17.9 Hz), 125.1 (CH), 127.3 (CH), 128.4 (C), 129.1 (2 \times CH), 129.5 (CH, d, $J_{\text{C-C-C-F}}$ 3.5 Hz), 129.7 (C), 131.8 (CH), 132.0 (CH, d, $J_{\text{C-C-C-F}}$ 8.1 Hz), 133.8 (CH), 134.6 (C, d, $J_{\text{C-C-C-C-F}}$ 3.2 Hz), 135.4 (C), 138.7 (2 \times CH), 145.6 (C), 156.9 (C, d, $J_{\text{C-F}}$ 247.7 Hz), 160.8 (C), 165.0 (C); m/z (ESI) 655.0274 (MNa^+ . $\text{C}_{26}\text{H}_{22}\text{FIN}_4\text{NaO}_4\text{S}$ requires 655.0283).

***tert*-Butyl piperazine-4-(((4'-chloromethyl)benzoyl)-1'-carbonyl)-1-carboxylate (42).**



The reaction was carried out as described for 4-[3'-[4''-(4'''-iodobenzoyl)piperazine-1''-carbonyl]-4'-fluorobenzyl]-2*H*-phthalazin-1-one (4) using a solution of 4-(chloromethyl)benzoic acid (39) (183 mg, 1.07 mmol) in *N,N'*-dimethylformamide (5 mL), triethylamine (23.1 μ L, 1.71 mmol), *O*-benzotriazole-*N,N,N',N'*-tetramethyluroniumhexafluorophosphate (33) (446 mg, 1.18 mmol). *tert*-Butyl piperazine-1-carboxylate (30) (200 mg, 1.07 mmol) was added and the mixture was stirred for a further 112 hours. After this water (10 mL) was added and the crude product was extracted into dichloromethane (3 \times 10 mL). The organic layers were combined and washed with water (6 \times 20 mL), dried with magnesium sulfate, filtered, and concentrated *in vacuo* to give a white solid. Purification by flash column chromatography (hexane/ethyl acetate, 50:50) gave *tert*-butyl piperazine-4-(((4'-chloromethyl)benzoyl)-1'-carbonyl)-1-carboxylate (42) as a white solid (144 mg, 40%). R_f (50% v/v hexane/ethyl acetate) 0.40; Mp 140–142 $^{\circ}$ C (lit. (An *et al.*, 1998) 147–148 $^{\circ}$ C); $\nu_{\max}/\text{cm}^{-1}$ (neat) 3003 (ArH), 2881 (CH), 1681 and 1622 (CO), 1568, 1426, 1349, 1263, 1012, 724, 668; δ_{H} (400 MHz, CDCl_3) 1.47 (9H, s, O^tBu), 3.28–3.84 (8H, m, 4 \times N- CH_2), 4.60 (2H, s, 4'- CH_2Cl), 7.43 (4H, q, J 11.9 Hz, 2'-H, 3'-H, 5'-H and 6'-H); δ_{C} (101 MHz, CDCl_3) 28.5 (3 \times CH_3), 43.8 (2 \times CH_2), 45.6 (CH_2), 47.7 (2 \times CH_2), 80.5 (C), 127.6 (2 \times CH), 128.8 (2 \times CH), 135.6 (C), 139.4 (C), 154.6 (C), 170.1 (C); m/z (ESI) 361.1273 (MNa^+ . $\text{C}_{17}\text{H}_{23}^{35}\text{Cl}_2\text{N}_2\text{NaO}_3$ requires 361.1289).

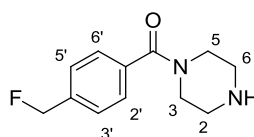
***tert*-Butyl piperazine-4-(((4'-fluoromethyl)benzoyl)-1'-carbonyl)-1-carboxylate (41).**



To a solution of *tert*-butyl piperazine-4-(((4'-chloromethyl)benzoyl)-1'-carbonyl)-1-carboxylate (42) (55.0 mg, 0.162 mmol) in acetonitrile (1.5 mL) was added 1 M

solution of tatra-*n*-butylammonium fluoride (325 μL , 0.325 mmol) in tetrahydrofuran. The mixture was heated to 80 $^{\circ}\text{C}$ and stirred for 1 hour followed by evaporation of solvent *in vacuo*. The crude product was extracted into dichloromethane (5 mL) and the organic layer was washed with water (10 mL \times 3), dried with magnesium sulfate, filtered, and concentrated *in vacuo* to give *tert*-butyl piperazine-4-(((4'-fluoromethyl)benzoyl)-1'-carbonyl)-1-carboxylate (**41**) (52.0 mg, 100%) as a white solid. Mp 96–98 $^{\circ}\text{C}$; $\nu_{\text{max}}/\text{cm}^{-1}$ (neat) 3013 (ArH), 2928 (CH), 1690 and 1630 (CO), 1420, 1250, 1009, 909, 756, 731; δ_{H} (400 MHz, CDCl_3) 1.45 (9H, s, O^tBu), 3.25–3.84 (8H, m, 4 \times N- CH_2), 5.40 (2H, d, J 47.4 Hz, 4'- CH_2F), 7.37–7.43 (4H, m, 2'-CH, 3'-CH, 5'-CH and 6'-CH); δ_{C} (101 MHz, CDCl_3) 28.5 (3 \times CH_3), 42.2 (CH_2), 43.7 (2 \times CH_2), 47.6 (CH_2), 80.5 (C), 83.9 (CH_2 , d, $J_{\text{C-F}}$ 167.6 Hz), 127.4 (2 \times CH, d, $J_{\text{C-C-F}}$ 6.2 Hz), 127.5 (2 \times CH), 135.9 (C, d, $J_{\text{C-C-C-C-F}}$ 2.6 Hz), 138.1 (C, d, $J_{\text{C-C-F}}$ 17.4 Hz), 154.6 (C), 170.2 (C); m/z (ESI) 345.1569 (MNa^+ . $\text{C}_{17}\text{H}_{23}\text{FN}_2\text{NaO}_3$ requires 345.1585).

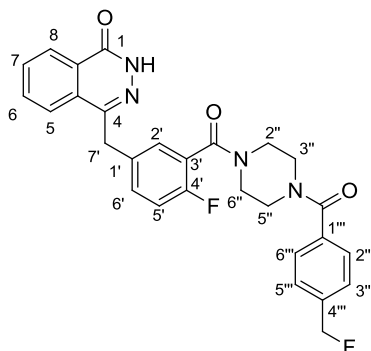
Piperazine-4-((4'-fluoromethyl)benzoyl)-1'-carbonyl (**40**).



To a solution of *tert*-butyl piperazine-4-(((4'-fluoromethyl)benzoyl)-1'-carbonyl)-1-carboxylate (**42**) (52.0 mg, 0.161 mmol) in dichloromethane (1 mL) was added trifluoroacetic acid (124 μL , 1.61 mmol) and the mixture was stirred at room temperature for 4 hours. The crude product was extracted into ethyl acetate (5 mL) and the organic layer was washed using water saturated with potassium carbonate (10 mL \times 3), dried with magnesium sulfate, filtered, and concentrated *in vacuo* to give piperazine-4-((4'-fluoromethyl)benzoyl)-1'-carbonyl (**40**) (31.0 mg, 87%) as an orange oil. $\nu_{\text{max}}/\text{cm}^{-1}$ (neat) 3411 (NH), 3001 (ArH), 2957 (CH), 1613 (CO), 1437, 1276, 1263, 1016, 748; δ_{H} (400 MHz, CDCl_3) 2.80 (2H, br s, N- CH_2), 2.94 (2H, br s, N- CH_2), 3.38 (2H, br s, N- CH_2), 3.75 (2H, br s, N- CH_2), 5.40 (2H, d, J 47.5 Hz, 4'- CH_2F), 7.38–7.45 (4H, m, 2'-CH, 3'-CH, 5'-CH and 6'-CH); δ_{C} (101 MHz, CDCl_3) 43.3 (CH_2), 46.0 (CH_2), 46.5 (CH_2), 49.0 (CH_2), 84.0 (CH_2 , d, $J_{\text{C-F}}$ 167.4 Hz), 127.3 (2 \times CH, d, $J_{\text{C-C-F}}$ 6.4 Hz), 127.4 (2 \times CH), 136.3 (C, d, $J_{\text{C-C-C-C-F}}$

2.8 Hz), 137.7 (C, d, J_{C-C-F} 17.4 Hz), 170.0 (C); m/z (ESI) 245.1064 (MNa^+ . $C_{12}H_{15}FN_2NaO$ requires 245.1061).

4-[3'-[4''-(4'''-Fluoromethyl)benzoyl]piperazine-1''-carbonyl]-4'-fluorobenzyl]-2*H*-phthalazin-1-one (17).



To a solution of 2-fluoro-5-[(4'-oxo-3*H'*-phthalazin-1'-yl)methyl]benzoic acid (**27**) (38.0 mg, 0.126 mmol) in *N,N'*-dimethylformamide (1 mL) was added triethylamine (26.0 μ L, 0.189 mmol), followed by *O*-benzotriazole-*N,N,N',N'*-tetramethyluroniumhexafluorophosphate (**33**) (52.6 mg, 0.139 mmol) and the mixture was stirred at room temperature for 1 hour. Piperazine-4-((4'-fluoromethyl)benzoyl)-1'-carbonyl (**40**) (28.0 mg, 0.126 mmol) was added and the mixture was stirred for a further 72 hours. Water (4 mL) was then added, followed by 1 hour of stirring after which the mixture was cooled to 0 °C. The resulting precipitate was collected by vacuum filtration and the crude orange solid was purified by flash column chromatography (methanol/ethyl acetate, 5:95) gave 4-[3'-[4''-(4'''-fluoromethyl)benzoyl]piperazine-1''-carbonyl]-4'-fluorobenzyl]-2*H*-phthalazin-1-one (**17**) (10.7 mg, 17%) as a yellow foam. R_f (5% v/v methanol/ethyl acetate) 0.50; ν_{max}/cm^{-1} (neat) 3213 (NH), 3005 (ArH), 2926 (CH), 1613 (CO), 1572 (C=C), 1429, 1256, 1225, 1003, 750; δ_H (400 MHz, $CDCl_3$) 3.13–4.02 (8H, m, 4 \times N- CH_2), 4.29 (2H, s, 7'- H_2), 5.41 (2H, d, J 47.3 Hz, 4'''- CH_2F), 7.04 (1H, br s, 5'-H), 7.34 (2H, d, J 6.15 Hz, 2'-H and 6'-H), 7.43 (4H, br s, 2'''-H, 3'''-H, 5'''-H and 6'''-H), 7.67–7.72 (1H, m, 5-H), 7.73–7.80 (2H, m, 6-H and 7-H), 8.44–8.49 (1H, m, 8-H), 10.70 (1H, br s, NH); δ_C (101 MHz, $CDCl_3$) 37.8 (CH_2), 42.3 (2 \times CH_2), 47.2 (2 \times CH_2), 84.0 (CH_2 , d, J_{C-F} 167.8 Hz), 116.3 (CH, d, J_{C-C-F} 19.9 Hz), 123.8 (C, d, J_{C-C-F} 18.2 Hz), 125.1 (CH), 127.4 (CH), 127.5 (2 \times CH, d, $J_{C-C-C-F}$ 6.0 Hz), 127.6 (2 \times CH), 128.5 (C), 129.4 (CH, d, $J_{C-C-C-F}$ 3.7 Hz),

129.7 (C), 131.8 (CH), 132.0 (CH, d, J_{C-C-F} 8.2 Hz), 133.8 (CH), 134.6 (C, d, $J_{C-C-C-F}$ 3.5 Hz), 135.5 (C, d, $J_{C-C-C-C-F}$ 2.8 Hz), 138.5 (C, d, J_{C-C-F} 17.5 Hz), 145.6 (C), 157.1 (C, d, J_{C-F} 247.1 Hz), 160.5 (C), 165.3 (C), 170.3 (C); m/z (ESI) 525.1738 (MNa^+ . $C_{28}H_{24}F_2N_4NaO_3$ requires 525.1714).

4 IDENTIFYING LEAD PARP-1 LIGANDS WITH POTENTIAL FOR NUCLEAR IMAGING.

4.1 Introduction.

4.1.1 PARP-1 inhibitory potency.

The affinity of a radiotracer for its target is a crucial property to consider when designing a novel nuclear imaging tracer. The higher the affinity for the target, the greater the contrast to noise ratio that can be achieved in the final PET or SPECT image (Jacobson and Chen, 2013). This becomes apparent when the *in vivo* behaviour of the tracer is represented using a typical pharmacokinetic model, as shown in figure 4.1. In this model, the radiotracer can exist in four different body compartments: i) the arterial tissue compartment (C_a); ii) the un-bound tissue compartment (C_{nb}); iii) the non-specifically bound tissue compartment (C_{nsb}); and iv) the specifically bound tissue compartment (C_{tb}). When a radiotracer is injected it immediately enters the C_a and eventually distributes to body tissues (C_{nb}). The tracer can then bind to its target specifically (C_{tb}) or it can exhibit off-target binding, resulting in accumulation in C_{nsb} (Watabe *et al.*, 2006). The lower the affinity of the radiotracer for its target, the greater the preference for C_{nb} and C_{nsb} over C_{tb} . The consequence of this, as mentioned before, is a low contrast to noise ratio and ultimately a poor quality PET or SPECT image.

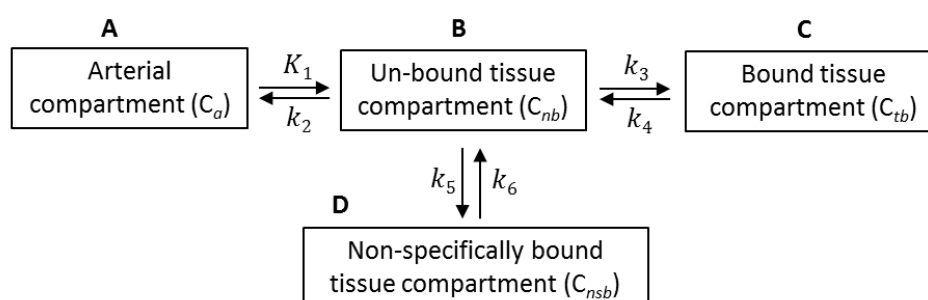


Figure 4.1. The four tissue compartment model where the flux of substance between compartments is described by the rate constants K_1 and k_2 - k_6 .

In the case of an inhibitor, the affinity of the compound for its target can be measured indirectly by establishing its inhibitory potency. The half maximal inhibitory concentration (IC_{50}) is an *in vitro* parameter that describes the concentration of a compound that is required to inhibit half of the activity of a target enzyme. Therefore, the lower the IC_{50} , the more potent the inhibitor. The IC_{50} can be determined under cell-free conditions or in a cellular system. Since PARP-1 is a nuclear protein expressed intracellularly, compounds tested under cell-free conditions do not face the challenges associated with cellular penetration and retention. Consequently, the cell-free assay does not provide an accurate representation of *in vivo* PARP inhibitor behaviour. However, this is a high-throughput method that can allow multiple compounds to be screened and ranked relative to one another in a short period of time. On the other hand, cellular IC_{50} assays are low-throughput and labour intensive, but they provide a more accurate representation of PARP-1 inhibition *in vivo*.

The cell-free PARP-1 IC_{50} can be ascertained using a commercially available TrevigenTM colorimetric kit (Figure 4.2), which is a modified version of the assay developed by Cheung and Zhang (2000). By introducing varying concentrations of a test PARP inhibitor into the assay, a dose response can be measured and used to calculate the IC_{50} of the compound.

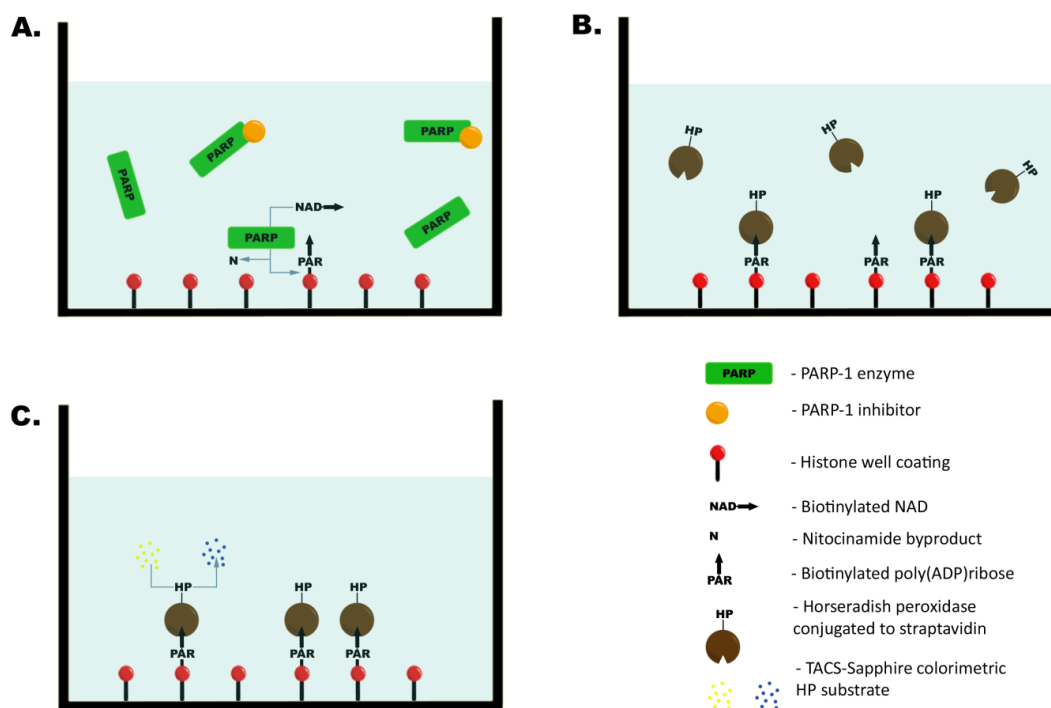


Figure 4.2. Diagrammatic representation of the PARP-1 cell-free Trevigen™ colorimetric assay. Biotinylated-NAD⁺ is used by the PARP-1 enzyme to synthesise biotinylated-PAR chains onto histone proteins that are conjugated to the assay plate. In order to initiate PAR synthesis, damaged DNA is introduced into the assay, which activates the PARP-1 enzyme (A). The high binding affinity of Streptavidin for biotin is exploited to label the newly synthesised biotinylated-PAR chains with a streptavidin-horseradish peroxidase (HPR) conjugate (B). The final part of the assay relies on a colorimetric reaction where a substrate that reacts with HPR is used to generate a colour (C). The amount of PAR chains synthesised by PARP-1 can then be indirectly quantified through colour intensity measurements.

A similar approach to the one described in Figure 4.2 can be used to establish the cellular response to PARP inhibitors, except in this case living cells are incubated in different concentrations of inhibitor and PAR chains are visualised using a fluorescently labelled anti-PAR antibody. A key limitation of this assay is the ability of the anti-PAR antibody to detect the PAR chains. It has been reported that different antibodies exhibit variable affinity for PAR depending on whether the chains are linear or branched (Kawamitsu *et al.*, 1984). These differences in affinity can result in the under estimation of the cellular IC₅₀ as a proportion of the PAR chains may not be detected. In addition, prior to immunolabelling and immunofluorescence imaging, the cells must undergo a

process of fixation and permeabilisation using a mixture of chemicals and solvents. Fixation allows for the preservation of the cell and its internal components, while permeabilisation makes the cell membrane porous allowing for the antibody to reach its intracellular target. Both of these processes can lead to immunofluorescent imaging artefacts (Schnell *et al.*, 2012) that may bias the overall IC₅₀ calculation.

4.1.2 Physiochemical properties and nuclear imaging.

The physiochemical properties of a compound can have a significant influence on its *in vivo* pharmacokinetic behaviour, such as absorption, distribution, metabolism, and excretion (ADME). This section will focus on how two key physiochemical parameters, namely lipophilicity ($\log P_{\text{oct}}$) and percentage plasma protein binding (%PPB), can affect the pharmacokinetic behaviour of radiotracers and influence nuclear imaging. As described in the following section, the use of a single physiochemical parameter (e.g. $\log P_{\text{oct}}$) as a predictor of absolute *in vivo* compound behaviour is limited. However, combining datasets of multiple physiochemical parameters (e.g. $\log P_{\text{oct}}$ and %PPB) for a series of related compounds can provide relative predictive information. This can in turn be used to either rank compounds according to optimal physiochemical parameters, or eliminate compounds that may not exhibit optimal *in vivo* behaviour.

4.1.2.1 $\log P_{\text{oct}}$ and %PPB.

$\log P_{\text{oct}}$ is the log value of the partition coefficient (P), which describes the net result of all interactions of a solute molecule (i.e. a chemical compound) and two immiscible phases between which it partitions, where one phase is hydrophilic (aqueous) and the other lipophilic (octanol) (Figure 4.3). In simpler words, $\log P_{\text{oct}}$ acts as a descriptor of a compounds lipophilic character as it expresses the affinity of the compound for a lipophilic octanol phase relative to an aqueous water phase (Testa *et al.*, 2000).

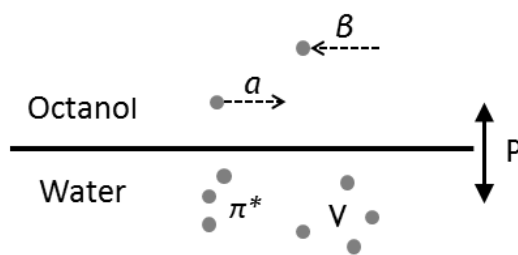


Figure 4.3. Diagrammatic representation of the intermolecular forces which affect the partitioning (i.e. partition coefficient, P) of solute molecules (grey spheres) between an octanol and water phase, where a and B represent hydrogen bond donor acidity and acceptor basicity respectively, π^* represents a measure of the solutes polarisability and V represents the molecular volume of the solute.

The effects of $\log P_{\text{oct}}$ on *in vivo* pharmacokinetics of an organic compound are complex. Lipophilicity is a key determinant of the route of elimination of a compound, which can be renal or metabolic (see section 6.1.2 for details). The aqueous component of the blood, including solubilised compounds, undergoes filtration by the kidney glomerulus (Figure 4.4). Following filtration, compounds with a $\log P_{\text{oct}} > 0$ are mostly reabsorbed by the kidney tubule and re-enter circulation, while compounds that are too hydrophilic for this reabsorption ($\log P_{\text{oct}} < 0$) are excreted in the urine (van de Waterbeemd *et al.*, 2001). From the perspective of nuclear imaging, radiotracers that undergo renal reabsorption have an extended blood circulation time allowing for greater opportunity to reach the imaging target. Compounds that are in circulation, including those that have been reabsorbed from the renal tubule, can also undergo metabolic clearance that is mainly driven by cytochrome P450 enzymes (CYP450) (see section 6.1.2 for details). A positive correlation exists between $\log P_{\text{oct}}$ and liver metabolism due to the fact that the interaction between compounds and the CYP450 enzymes is lipophilic in nature (van de Waterbeemd *et al.*, 2001). Therefore, radiotracers exhibiting a high $\log P_{\text{oct}}$ are likely to undergo more rapid metabolic clearance than those with less lipophilic properties. The consequences of this are twofold; firstly this can reduce the amount of tracer available *in vivo* for nuclear imaging resulting in reduced signal intensity and secondly radiolabelled metabolites may be generated that could reduce the nuclear imaging signal to noise contrast (Jacobson and Chen, 2013). An example of the latter is metabolic defluorination of [^{18}F]-labelled tracers, where the high

bone uptake of the free radiofluoride metabolite can lead to signal noise originating from the skull when performing a PET scan of the brain (Pike, 2009).

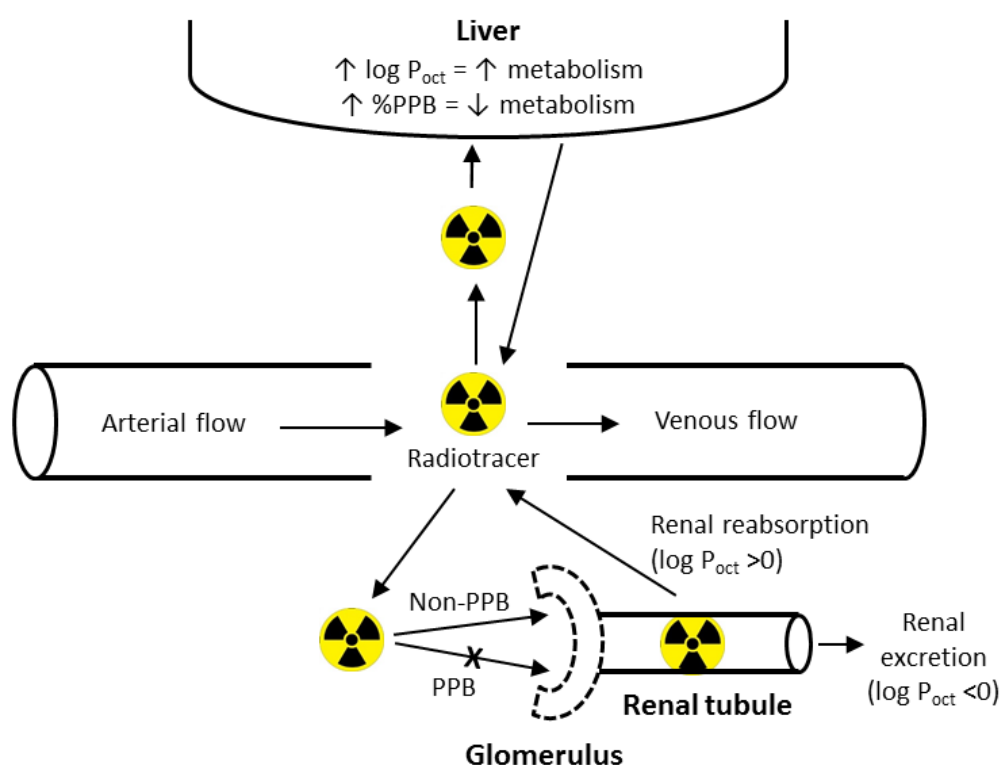


Figure 4.4. Schematic representation of how the lipophilic ($\log P_{oct}$) and plasma protein binding (PPB) properties of a radiotracer can influence its *in vivo* clearance. An increase in the $\log P_{oct}$ of a radiotracer is associated with its increased liver metabolism. Highly plasma protein bound radiotracers exhibit greater *in vivo* retention as they are unable to cross the glomerulus and are refractory to liver metabolism. Non-bound radiotracers are able to enter the renal tubules where they can be either reabsorbed ($\log P_{oct} > 0$) or excreted in urine ($\log P_{oct} < 0$).

In addition to the influence of $\log P_{oct}$ on clearance, the parameter can also dictate the ability of a compound to penetrate biological membranes. If the $\log P_{oct}$ is not sufficiently high ($\log P_{oct} < 1.5$) then compounds could suffer from poor diffusive membrane permeability (Jacobson and Chen, 2013). This is because the phospholipid bilayer structure of biological membranes comprises of a lipophilic centre through which hydrophilic molecules are unable to diffuse (van de Waterbeemd *et al.*, 2001). In turn, poor membrane permeability can lead to the accumulation of tracer in the blood and un-bound tissue compartments (section

4.1.1, Figure 4.1), thereby reducing the nuclear imaging signal to noise ratio. Increasing the $\log P_{\text{oct}}$ parameter of a given compound can also increase its %PPB. This positive correlation can be attributed to the fact that the binding of a compound to plasma proteins is driven by lipophilic interactions (Helmer, Kiehs and Hansch, 1968). In order to understand how %PPB can influence the *in vivo* behaviour of a radiotracer, the earlier depicted pharmacokinetic model requires refinement to include an additional arterial plasma protein bound tissue compartment (C_{apb}) (Figure 4.5). Under normal circumstances compounds bound to plasma proteins are trapped in the blood vasculature as they are unable to diffuse out of the blood and are protected from clearance organs. Consequently, a high degree of plasma protein binding of a radiotracer can lead to nuclear imaging noise originating from the blood vasculature (C_{apb}).

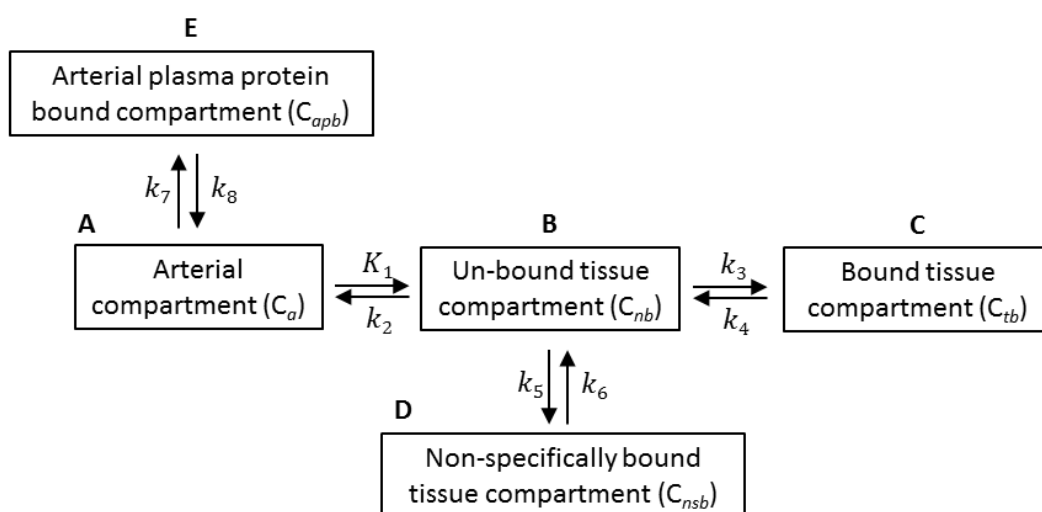


Figure 4.5. A modified version of the four tissue compartment model, which includes the arterial plasma protein bound tissue compartment (C_{apb}). The flux of substance between compartments is described by the rate constants K_1 and k_2 - k_8 .

It is important to note that the %PPB parameter does not influence the overall concentration of a compound at its target (e.g. PARP inhibitor concentration at PARP-1). Reducing the plasma protein binding properties of a compound will increase the non-bound fraction available for distribution to the target. However, any increase in the amount of a compound reaching its target will be counteracted by a simultaneous increase in delivery to elimination organs (Smith and Kerns, 2010; van de Waterbeemd *et al.*, 2001). Consequently, the overall

concentration of the compound reaching its target will remain constant despite a drop in %PPB.

In addition to the above, the $\log P_{\text{oct}}$ parameter can also influence the degree of specific binding exhibited by a compound (depicted by the C_{tb} , Figure 4.5). As in the case of plasma proteins, interactions between an organic compound and other non-specific proteins/macromolecules are driven by non-polar lipophilic interactions. Therefore, from the perspective of a PARP-1 radiotracer, a $\log P_{\text{oct}}$ above certain value, generally regarded as >3.0 , can result in reduced specificity for the target (i.e. PARP-1) and increased off-target binding (Jacobson and Chen, 2013).

To summarise, physiochemical parameters such as $\log P_{\text{oct}}$ and %PPB can have profound influences on the *in vivo* behaviour of radiotracers. Therefore, care has to be taken during the radiotracer design process to ensure that the compound exhibits an optimal $\log P_{\text{oct}}$ value ($>1.5 - <3.0$), without excessively high %PPB ($<95\%$). This should allow the radiotracer to effectively diffuse out of the vascular compartment and across biological membranes, reaching its imaging target with minimum off-target binding.

4.1.2.2 Physiochemical parameters and nuclear imaging of the brain.

Due to the additional pharmacokinetic complexity associated with the brain, this section will focus on the effects of physiochemical parameters on nuclear imaging of this organ. Unlike other body tissues, the brain is protected by the BBB that is composed of a number of cellular components. At the core of the BBB are endothelial cells that line cerebral microvessels and are connected with one another through adherens and tight junctions (Figure 4.6). Tight junctions impede molecular traffic via the paracellular route (i.e. between endothelial cells) and only small ions (e.g. Na^+ or Cl^-) are able to utilise this pathway. Therefore, in order to reach the brain, larger chemical entities such as radiotracers must exit the microvascular compartment by the transcellular route (Sage and Wilson, 1994; Abbott, Rönnbäck, and Hansson, 2006).

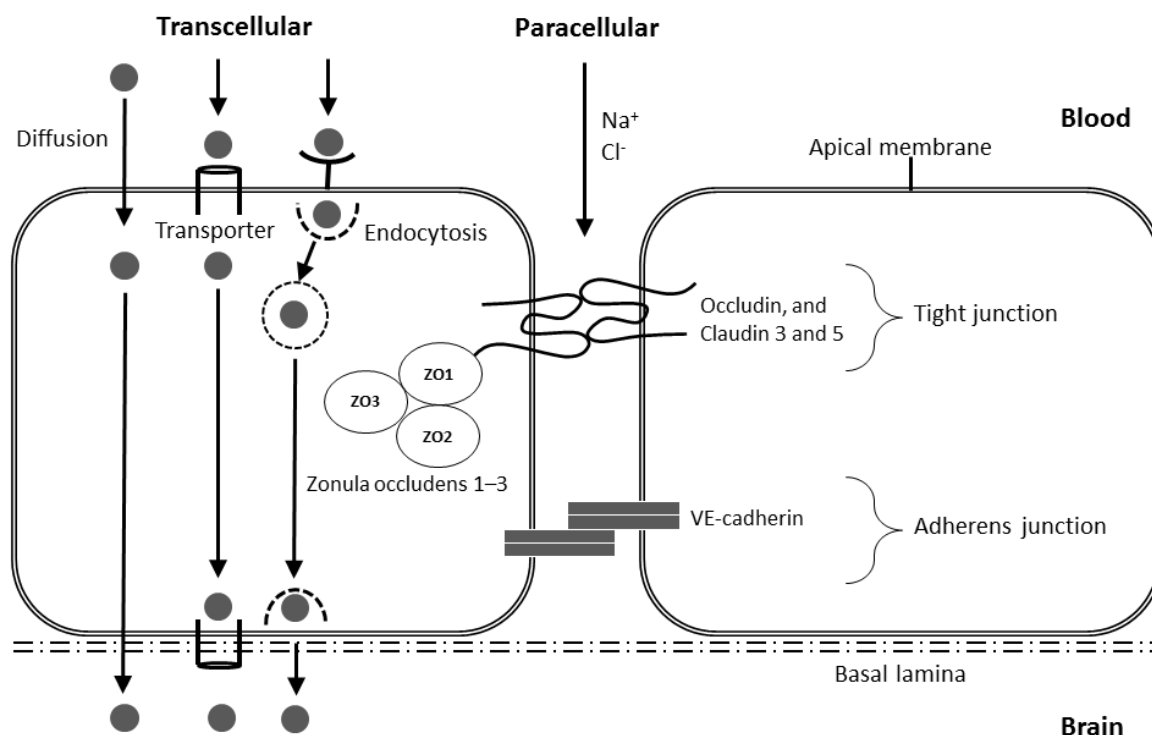


Figure 4.6. Cellular and molecular diagram of the blood brain barrier (BBB). The two endothelial cells are structurally held together by vascular endothelial catherin (VE-cadherin) proteins that make up the adherens junctions. Tight junctions comprise of occludin and claudin proteins, which possess extracellular loops and transmembrane domains linked to the scaffolding proteins zonula occludens (ZO) 1–3. Chemical entities are unable to cross the BBB via the paracellular route and are restricted to transcellular pathways that include passive diffusion, transporter mediated movement and endocytosis.

Log P_{oct} and %PPB are important parameters in dictating whether a compound is able to penetrate the BBB via passive diffusion. As discussed earlier, in order to passively penetrate biological membranes, compounds must possess sufficient lipophilic character. On the other hand, excessive lipophilicity may have a negative impact on BBB penetration due to the increase in macromolecular binding (e.g. %PPB). However, in cases where protein binding is rapidly reversible, this negative effect is minimised (Pike, 2009). The relationship between %PPB and BBB penetration has been shown to be gaussian ($r^2 = 0.66$) with an optimal %PPB range of 45–85%; although it is generally regarded that a %PPB value of <95% is sufficient for nuclear imaging of the brain (Tavares *et al.*,

2012). The upper %PPB value in this optimal range can be explained by the inability of plasma protein bound compounds to penetrate the BBB, while the lower value is likely a consequence of the function that plasma proteins play in the aqueous solubilisation of compounds and their transport around the vasculature.

Various lipophilicity parameter values have been reported in the literature as 'optimal' for BBB penetration. Hansch *et al.* (1967) developed a mathematical model using a set of barbiturate (n = 102) and non-barbiturate (n = 74) based hypnotics that allowed them to calculate the ideal lipophilic character ($\log P_0$) required for the hypnotic effect. Since hypnosis by these compounds is induced in the central nervous system (CNS), the $\log P_0$ parameter describes in part the ability of the investigated compounds to penetrate the BBB. The authors reported the $\log P_0$ to be approximately 1.9 and 1.8 for the barbiturate and non-barbiturate analogues respectively. However, it should be noted that in addition to biological membrane penetration, $\log P_0$ also defines the optimal lipophilic properties for receptor binding (Hansch *et al.*, 1967). The work by Dischino *et al.* (1983) showed that the optimal $\log P_{\text{oct}}$ range for BBB penetration was between 0.9 and 2.5. The authors came to this conclusion by investigating the relationship between the lipophilicity of a small library of [^{11}C]-radiolabelled compounds (n = 15) and their uptake in the brain of healthy baboons following parenteral administration of the radiopharmaceuticals (Dischino *et al.*, 1983).

It is important to note that other molecular parameters, such as size and hydrogen donor capacity, can also influence the ability of compounds to permeate the BBB. By analysing the molecular weight (Mw) and the total number of potential hydrogen-bonds exhibited by ionised compounds (HT_i) with and without CNS activity (n = 37), van de Waterbeemd *et al.* (1998) showed that the upper Mw and HT_i limits for brain penetration were 450 and 7 respectively. Therefore, the isolated use of $\log P_{\text{oct}}$ as a predictor of BBB penetration is limited. This was highlighted by Tavares *et al.* (2012) who showed only a weak correlation ($r^2 = 0.47$) between $\log P_{\text{oct}}$ of known nuclear imaging agents of the brain (n = 9) and the amount of these agents reaching brain tissue. Similarly, Young *et al.* (1988) reported little correlation between $\log P_{\text{oct}}$ and rat brain

uptake ($r^2 = 0.16$) of a small library of [^{14}C]-labelled H_2 (central) receptor antagonists. This correlation was substantially improved ($r^2 = 0.98$) when the $\log P_{\text{oct}}$ parameter was substituted for $\Delta\log P$, which is a descriptor of hydrogen-bond donor capacity. Specifically, $\Delta\log P$ is the difference between $\log P_{\text{oct}}$ and the \log cyclohexane/water partition coefficient ($\log P_{\text{cyl}}$) (Young *et al.*, 1988). Since the $\log P$ values in octanol/water and in cyclohexane/water do not express the same balance of polar forces, their difference (i.e. $\Delta\log P$) expresses mainly the hydrogen-bond donor capacity of solutes (Testa *et al.*, 2000). Similarly, Cornford *et al.* (1982) showed a linear correlation ($r = 0.72$) between the hydrogen-bond donor capacity of a range of [^{14}C]-labelled compounds ($n = 41$) and rat brain uptake. Taken collectively, the above findings suggest that, as a single parameter, hydrogen-bond donor capacity is a more accurate predictor of BBB permeability than $\log P_{\text{oct}}$. One explanation for this is that binding of compounds to biomembranes is the rate limiting step in passive membrane permeability. This binding occurs through donation of hydrogen-bonds to the hydrophilic outer-layer of the membrane that is rich in hydrogen-bonding acceptors (Testa *et al.*, 2000). Interestingly, Cornford *et al.* (1982) were able to attain a good linear relationship ($r = 0.86$) between the $\log P_{\text{oct}}$ of a broad range of [^{14}C]-labelled compounds ($n = 48$) and their brain uptake in healthy adult rats by correcting for the molecular weights of these compounds. They achieved this by multiplying the \log Brain Uptake Index (BUI) by the square root of molecular weight ($\sqrt{\text{Mw}}$), where the latter parameter is a good approximation of diffusion coefficient variability (Cornford *et al.*, 1982).

It is clear that nuclear imaging of the brain is a challenging task that requires careful radiotracer design to ensure that physiochemical parameters such as $\log P_{\text{oct}}$, %PPB, Mw, and HT_i are within an optimal range for BBB penetration. However, the situation is simplified in cases where the BBB is compromised and its permeability is increased. GBM is one example of a pathological state where this may occur. Morphological changes of the BBB in brain tumours include fragmentation of the blood capillary basement membranes, defects of tight junctions, and blood vessel fenestration (Sage and Wilson, 1994; Vajkoczy and Menger *et al.*, 2000; Wolburg *et al.*, 2012). The overall consequence of these changes is increased 'leakiness' of the BBB that can be visualised using MRI and the contrast enhancement medium gadolinium. This technique can also give an

indication of the degree of BBB disruption with lower grade brain tumours (e.g. WHO grade I) producing less MRI enhancement than higher grade tumours (e.g. WHO grade IV; GBM) (Wolburg *et al.*, 2012). Furthermore, Lepällä *et al.* (1995) exploited disruptions in the BBB to image glioma lesions in human patients using ^{99m}Tc -labelled human plasma proteins (human serum albumin, HSA), which are normally too large to cross the BBB. Similarly, Kremer *et al.* (2009) used HSA labelled with a fluorophore to perform fluorescent imaging of glioma lesions as a means of guiding surgical tumour resection. However, it is important to bear in mind that imaging GBM using radiotracers that are unable to freely penetrate the BBB is associated with a number of limitations such as the inability to detect low grade lesions and invasive cells and effectively monitor treatment (see section 1.2.3 for details).

4.1.2.3 Ascertaining the $\log P_{\text{oct}}$ and %PPB parameters using HPLC.

The 'shake-flask' method remains the gold standard for the measurement of $\log P_{\text{oct}}$. This technique involves introducing a compound (or solute) into two immiscible phases (i.e. water and octanol), followed by vigorous shaking, which allows the solute to partition between the two phases (Eadsforth and Moser, 1983). Measurement of the concentration of the solute in each phase allows for the calculation of $\log P_{\text{oct}}$. Despite high accuracy, this methodology is limited to compounds that exhibit good solubility properties in either the octanol or aqueous phases. Furthermore, the results acquired using this technique can often be affected by the presence of impurities (Eadsforth and Moser, 1983). The 'shake-flask' method also suffers from a lack of automation, making it labour intensive and low throughput (Arnott and Planey, 2012). An alternative technique that addresses some of these issues relies on the principle of reverse-phase thin layer chromatography (RP-TLC) (Figure 4.7). RP-TLC involves the application of a small amount of solution of the compound under investigation to a plate supporting a reverse-phase stationary material, such as lipophilic long chain hydrocarbons (e.g. C_{18}). The compound bearing plate is then exposed to a polar solvent or solvent mixture (i.e. a mobile phase) that travels in a single direction along the surface of the C_{18} material (the stationary phase). As this happens, the compound moves over the surface of the plate in the direction of

the solvent front. The distance moved by the compound, in a set time period, will be dependent on its affinity for the stationary phase and proportional to its lipophilic properties. Therefore, the $\log P_{\text{oct}}$ of a compound can be calculated by fitting the travel distance parameter to a regression model derived from a set of calibration compounds of known $\log P_{\text{oct}}$ values. The advantages of this technique include its low cost, speed, and greater tolerance to impurities that are often separated on the RP-TLC plate. However, the method still lacks automation, requires calibration, and is generally less accurate than the 'shake-flask' method (Eadsforth and Moser, 1983).

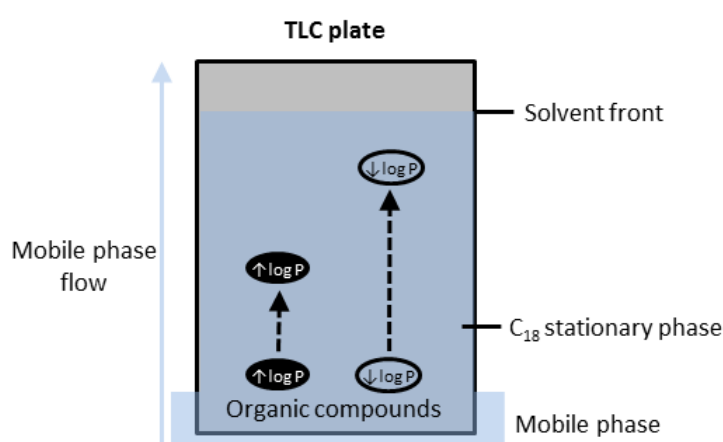


Figure 4.7. Diagram showing the relationship between the lipophilic character of organic compounds and their distance travelled on a RP-TLC plate. In a given time period, compounds with low lipophilicity ($\downarrow \log P$) will have lower affinity for the C₁₈ stationary phase and will travel further than compounds with high lipophilic character ($\uparrow \log P$).

Greater accuracy in $\log P_{\text{oct}}$ prediction and automation can be achieved with the analogous technique called reverse-phase high performance liquid chromatography (RP-HPLC) (Eadsforth and Moser, 1983; Valkó, 2004) (Figure 4.8). In this case, the mobile phase (usually a mixture of organic and aqueous liquids) passes through a column that is packed with stationary C₁₈-material. The compound under investigation is injected as a solution onto one end of the column and elutes on the other side. The elution time, or retention time, will be influenced by the compounds affinity for the stationary and mobile phases, and can be used to calculate the $\log P_{\text{oct}}$ parameter.

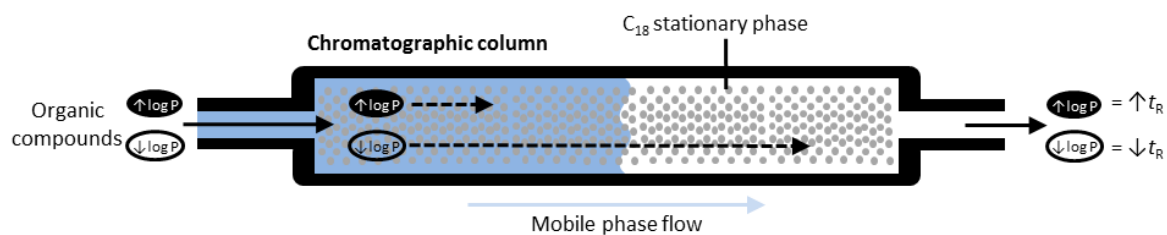


Figure 4.8. Diagram showing the relationship between the lipophilic character of organic compounds and their retention time on a RP-HPLC column. Compounds with low lipophilicity ($\downarrow \log P$) will elute more rapidly and have a lower retention time ($\downarrow t_R$) than compounds with high lipophilic character ($\uparrow \log P$).

Two different types of HPLC methodology exist for predicting $\log P_{\text{oct}}$, these are the isocratic HPLC method and the gradient HPLC method. The former uses a mobile phase that remains constant; i.e. the concentration of the organic solvent in the mobile phase does not change during the elution process. By performing multiple retention time measurements using mobile phases containing different concentrations of organic solvent, a relationship between organic solvent concentration (φ) and the logarithm of the retention factor k (calculated from the retention time; see equation 4.1) can be established (Equation 4.2) (Valkó, Bevan and Reynolds, 1997; Valkó, 2004).

$$k = (t_R - t_0) / t_0 \quad (\text{Equation 4.1})$$

where k is the retention factor, t_R is the retention time and t_0 is the column dead time that is equal to the packed column volume divided by the mobile phase flow rate.

$$\text{Log } k = S\varphi + \log k_w \quad (\text{Equation 4.2})$$

where S is the slope of the graph, φ is the organic solvent concentration and k_w is the intercept.

The quotient of the slope and intercept of Equation 4.2 ($-\log k_w / S$) is equal to the isocratic chromatographic hydrophobicity index (φ_0) which can be used to

estimate the $\log P_{\text{oct}}$ parameter using Equation 4.3 (Valkó, Bevan and Reynolds, 1997; Valkó, 2004)

$$\text{Log } P_{\text{oct}} = A\varphi_0 + B \quad (\text{Equation 4.3})$$

where φ_0 is the isocratic chromatographic hydrophobicity index, and *A* and *B* are regression coefficients obtained from a set of calibration compounds of known φ_0 and $\log P_{\text{oct}}$ values.

Good correlation has been shown to exist between $\log P_{\text{oct}}$ and φ_0 using a large set of known structurally diverse compounds (Valkó, Bevan and Reynolds, 1997). Therefore, the isocratic HPLC methodology can be used to provide an accurate prediction of the $\log P_{\text{oct}}$ parameter. This technique shares the advantages of RP-TLC with the added benefit of automation. However, this methodology remains relatively low throughput because of the need to establish retention times using multiple mobile phase compositions (Eadsforth and Moser, 1983; Valkó, Bevan and Reynolds, 1997).

The gradient HPLC method for predicting $\log P_{\text{oct}}$ is a fully automated and high-throughput variant of the isocratic technique. This method utilises a linear gradient increase in the concentration of mobile phase organic solvent during the elution process; this eliminates the need to perform separate chromatographic runs using fixed mobile phase compositions. Valkó, Bevan and Reynolds (1997) have shown that the retention time values obtained using a mobile phase gradient exhibit a linear correlation with the φ_0 values for a set of 76 compounds ($r = 0.992$). The authors also showed that a high degree of correlation ($r = 0.992$) is retained when just 10 of these compounds, with a range of lipophilic properties, were selected (Equation 4.4).

$$\varphi_0 = 14.00 (\pm 0.64)t_{\text{R}} - 55.88 (\pm 5.3) \quad (\text{Equation 4.4})$$

The above coefficients were used by Valkó, Bevan and Reynolds (1997) to calculate the gradient chromatographic hydrophobicity index (CHI) parameter for each of the 10 compounds that were used to establish this regression model.

To eliminate inter-laboratory variability in predicting $\log P_{\text{oct}}$, these 10 compounds of known CHI values are used as calibration compounds. Specifically, the retention time values of these molecules are established using a mobile phase gradient and are then plotted against their literature CHI values. Fitting a regression model to this calibration plot allows for the calculation of CHI values for unknown compounds by simply establishing their retention times under the same gradient conditions (Valkó, Bevan and Reynolds, 1997). The CHI values can then be converted to $\log P_{\text{oct}}$ values using the below regression model (Equation 4.5), which describes the linear correlation between these parameters for diverse set of 86 compounds ($r = 0.943$) (Valkó, 2004).

$$\text{Log } P_{\text{oct}} = 0.047\text{CHIN} + 0.36\text{HBC} - 1.10 \quad (\text{Equation 4.5})$$

where CHIN is the gradient chromatographic hydrophobicity index of the non-ionised compound and HBC is the hydrogen bond count of that compound.

The gradient HPLC method of ascertaining $\log P_{\text{oct}}$ is reliant on multiple regression models. Therefore, despite good literature correlation values, emphasis should be placed on the fact that this technique only provides a prediction of $\log P_{\text{oct}}$ as opposed to an absolute value; this is also true for the RP-TLC and isocratic HPLC methods.

HPLC technology is highly versatile as numerous columns packed with different stationary phases are commercially available. One such stationary phase comprises plasma proteins (e.g. HSA) that have been immobilised on a silica support material. This system can be exploited for the determination of organic compound %PPB using isocratic and gradient methods, which are similar to those described above for $\log P_{\text{oct}}$ evaluation. Both techniques are based on the assumption that the silica bonded proteins retain binding specificity and conformational mobility of native proteins (Valkó *et al.*, 2003). Furthermore, the HPLC assays are limited by the fact that the stationary phase comprises of only one type of protein. Even though HSA is the most abundant plasma protein, over 60 different proteins exist in human serum with a range of binding affinities and capacities. Therefore, *in vitro* HPLC assessment of the %PPB of an organic

compound provides only an estimate of its potential *in vivo* protein binding behaviour (Banker and Clark, 2008). Despite these shortcomings, HPLC methodology possesses a number of advantages over the traditional gold standard methods of %PPB determination, such as equilibrium dialysis and ultrafiltration. These are: i) low cost; ii) good reproducibility and accuracy at high %PPB values; iii) automation; and iv) high-throughput capability (Valkó *et al.*, 2003). Equilibrium dialysis is precise and utilises whole serum plasma samples, but is expensive, low throughout, and requires large volumes of serum plasma. Ultrafiltration is a slightly more rapid technique, but is prone to variability due to non-specific binding of the compounds to apparatus components (Banker and Clark, 2008).

The isocratic HPLC method for estimating %PPB is based on establishing the retention factor (k), which describes the ratio of the number of moles of organic compound in the stationary and mobile phases. Therefore, the $\log k$ can be related to %PPB using Equation 4.6 shown below (Valkó *et al.*, 2003).

$$\%PPB = 100 (k/k+1) \quad \text{(Equation 4.6)}$$

where k is the retention factor.

It should be noted that in this case the isocratic HPLC method provides an absolute value of percentage protein binding. In practice, this can be disadvantageous as the absolute retention times of compounds can decrease as the HPLC column containing the protein stationary phase ages. Therefore, the potential for %PPB underestimation increases with column age. The isocratic method is also limited by the fact that the choice of mobile phase composition may be difficult as the retention properties of a compound on the immobilised protein column will be unknown. Both issues can be overcome with the gradient HPLC method where a set of calibration compounds of known %PPB are utilised, and where the concentration of organic solvent increases steadily during the chromatographic run. The use of calibration compounds means that the calculated %PPB will be relative and not influenced by column age, while the linear gradient of organic solvent concentration dismisses the need to predict

the retention properties of the compound under investigation (Valkó *et al.*, 2003).

When predicting %PPB using the gradient HPLC method, the literature %PPB values of the calibration compounds must first be converted to the logarithm of the apparent affinity constants ($\log K$), which are linearised values of %PPB, using Equation 4.7 (Valkó *et al.*, 2003).

$$\log K = \log (\%PPB / (101 - \%PPB)) \quad (\text{Equation 4.7})$$

where K is the apparent affinity constant.

A linear plot of the retention times against the literature $\log K$ values of the calibration compounds is then used to generate a regression model. This model is used to convert retention time values of unknown compounds into the corresponding $\log K$ values, and ultimately into the %PPB parameter using Equation 4.8 (Valkó *et al.*, 2003).

$$\%PPB = (101 \times 10^{\log K}) / (1 + 10^{\log K}) \quad \text{oi(Equation 4.8)}$$

To summarise, HPLC methodology can be utilised to perform *in vitro* estimation of $\log P_{\text{oct}}$ and %PPB parameters in a rapid and reproducible manner, which is ideally suited for lead compound selection during early stages of radiotracer discovery. Gold standard techniques, such as the ‘shake-flask’ method for absolute $\log P_{\text{oct}}$ determination and equilibrium dialysis for establishing absolute %PPB, have a place in lead advancement further down the discovery and developmental pathways.

4.1.3 Aims and hypotheses.

The aims of the research presented in this chapter were to acquire and use cell-free and cellular IC_{50} , $\log P_{\text{oct}}$, and %PPB *in vitro* data for olaparib and

compounds 4–21, together with knowledge of radiochemical accessibility, to identify lead candidate compounds suitable for radiolabelling chemistry development.

The following hypotheses were set for this work:

i) Olaparib analogues 4–21 will exhibit potent PARP-1 inhibitory properties (i.e. cell-free and cellular $IC_{50} < 100$ nM). The reasoning for this hypothesis is based on previous literature that showed potent PARP-1 inhibitory activity of numerous analogues based around the phthalazinone scaffold 3 (see section 3.1 for details).

ii) Olaparib analogues 4–21 will exhibit an increase in both $\log P_{oct}$ and %PPB values when compared to the parent compound. This hypothesis is justified by the fact that compounds 4–21 comprise additional structural moieties with added lipophilic character. Additionally, as per literature, the increase in lipophilicity is predicted to facilitate plasma protein binding (see section 4.1.2.1 for details).

iii) Iodinated compounds (4–10) will exhibit greater average $\log P_{oct}$ and %PPB values than the fluorinated (11–17) and methoxy bearing (18–21) compounds. This is justified by the fact the iodine atom is known to possess greater lipophilic character than the fluorine atom and the methoxy functionality.

4.2 Results and discussion.

Olaparib and the non-radioactive analogues synthesised in chapter 3, that were representatives of potential PARP-1 SPECT (4–10) and PET (11–21) imaging agents (section 3.2, Figure 3.7), were evaluated for their cell-free PARP-1 inhibitory (IC_{50}), $\log P_{oct}$ and %PPB properties; the results of this *in vitro* screen are summarised in Table 4.1.

Table 4.1. The cell-free IC₅₀, log P_{oct} and %PPB values for olaparib and compounds 4–21.

Compound	Cell-free IC ₅₀ (95% CI), nM ^a	Log P _{oct} ^b	%PPB ^c
Olaparib	11.9 (10.5–13.6)	1.95	75.9
4	3.3 (2.6–4.2)	3.00	96.2
5	3.9 (3.4–4.4)	2.97	96.1
6	16.9 (12.5–22.9)	3.23	97.6
7	17.6 (14.3–21.7)	2.95	96.5
8	5.8 (4.9–6.8)	3.13	97.5
9	3.0 (2.5–3.6)	3.25	98.1
10	22.6 (18.5–27.6)	>3.25 ^d	98.4
11	5.9 (4.9–7.0)	2.51	85.9
12	3.6 (3.4–3.9)	2.46	86.4
13	2.9 (2.3–3.7)	2.66	86.1
14	1.3 (0.9–1.7)	2.67	89.9
15	4.1 (3.6–4.6)	2.81	90.6
16	11.2 (7.3–17.3)	3.14	94.7
17	2.0 (1.9–2.2)	2.51	86.3
18	1.1 (0.9–1.4)	2.51	89.3
19	4.5 (4.0–5.0)	2.55	90.3
20	5.1 (4.7–5.6)	2.56	93.9
21	9.6 (8.0–11.4)	2.94	87.7

^aCell-free IC₅₀ values were obtained using the commercially available Trevigen™ assay and were based on three experiments; corresponding dose-response curves can be found in Appendix 9.1. Each cell-free IC₅₀ value was reported with its 95% confidence interval (95% CI). ^bLipophilicity (log P_{oct}) was determined using a C₁₈ HPLC column; representative assay calibration data for the column can be found in Appendix 9.2. ^cPercentage plasma protein binding (%PPB) was determined using a human serum albumin coated HPLC column; representative assay calibration data for the column can be found in Appendix 9.3. ^dThe exact log P_{oct} could not be calculated as the value exceeded the assay limit.

Overall, all eighteen analogues of olaparib appeared to be potent inhibitors of PARP-1 with cell-free IC_{50} values <100 nM. Compound **10** was the weakest PARP inhibitor in the series with a cell-free IC_{50} 1.9 fold greater than that obtained for olaparib (i.e. cell-free IC_{50} = 22.6 vs. 11.9 nM), while compound **18** was the most potent inhibitor with a cell-free IC_{50} 10.8 fold lower when compared to olaparib (i.e. cell-free IC_{50} = 1.1 vs. 11.9 nM). Despite the variability in cell-free PARP-1 inhibitory potency of a select few compounds, the majority of olaparib analogues exhibited low nanomolar IC_{50} values, suggesting high potency against PARP-1. These observations agree with previous literature findings which showed that structural modifications in the cyclopropane bearing region of olaparib were tolerated by the PARP-1 binding site (Cockroft *et al.*, 2006; Meaner *et al.*, 2008) (see section 3.1.1 for details).

Due to the widespread interest in developing PARP-1 nuclear imaging agents, it is not surprising that other research groups have pursued compounds that exhibit similarities, or are identical, to those described in this chapter. As part of their PARP-1 radiotracer discovery programme, Carney *et al.* (2015) synthesised compound **11** and Salinas *et al.* (2015) synthesised compounds **4**, **5**, and **8**. In both cases the authors performed *in vitro* cell-free IC_{50} evaluation of these compounds using the TrevigenTM colorimetric assay, and reported cell-free IC_{50} values of 2.83 (Carney *et al.*, 2015), 9.0, 11.0 and 34.0 nM (Salinas *et al.*, 2015) for **11**, **4**, **5**, and **8** respectively. Comparison of these literature values to those listed in Table 4.1 is difficult due to the influence of inter-laboratory and inter-personal variability. Despite this, the cell-free IC_{50} data reported by Carney *et al.* (2015) and Salinas *et al.* (2015), with the exception of compound **8**, correlate with data shown in table 4.1 in the sense that the compounds exhibited low nanomolar IC_{50} values. This trait is important from a nuclear imaging standpoint, as high potency of a radioligand for its target allows for greater specific binding (depicted by the C_{tb} compartment, section 4.1.1, Figure 4.1) and higher target to noise contrast (Jacobson and Chen, 2013).

The SAR information that can be extracted from compounds **4–21** is limited due to the small size of the compound library. However, it appears likely that a carbonyl functionality positioned adjacent to the piperazine and reduced steric

bulk at the aromatic *meta* and *para* positions are favourable for PARP-1 inhibition. The evidence for the former observation can be drawn from the sulfonamide (**10**) and *N*-alkyl linked (**16** and **21**) analogues which exhibited markedly higher cell-free IC₅₀ values than analogues possessing a carbonyl-bearing linker. Furthermore, Meaner *et al.* (2008) reported a 2.2 fold improvement in PARP-1 inhibitory potency between a piperazine *N*-methyl and a piperazine *N*-methanamide analogue of olaparib (cell-free IC₅₀ = 13.0 vs. 6.0 nM). With regard to the statement concerning the negative effect of steric bulk, it can be seen that compounds **6** and **7**, bearing *para* methyl and methoxy functionalities respectively, were approximately 4.3 and 4.5 fold less potent PARP-1 inhibitors than compound **5**.

HPLC methodology was chosen as a means of establishing the physicochemical parameters of olaparib and analogues **4–21** due to the accuracy, reproducibility, and high-throughput capabilities of the technique. For the purpose of this chapter, HPLC predicted log P_{oct} and %PPB values were compared against absolute physicochemical parameter values. This is justified by the strong correlations that exist between HPLC derived and absolute log P_{oct} and %PPB values (Valkó *et al.*, 2003; Valkó, 2004).

As hypothesised, analogues **4–21** exhibited higher log P_{oct} and %PPB values than olaparib (Table 4.1). The increase in both parameters can be attributed to the addition of the aromatic, iodine, and methyl moieties which all have the potential to increase lipophilic character. The increase in lipophilicity can in turn result in an increase in %PPB due to fact that plasma protein binding is driven by hydrophobic interactions (Helmer, Kiehs and Hansch, 1968) (see section 4.1.2.1 for details). The positive correlation between log P_{oct} and %PPB for this compound series can be clearly seen in figure 4.9.

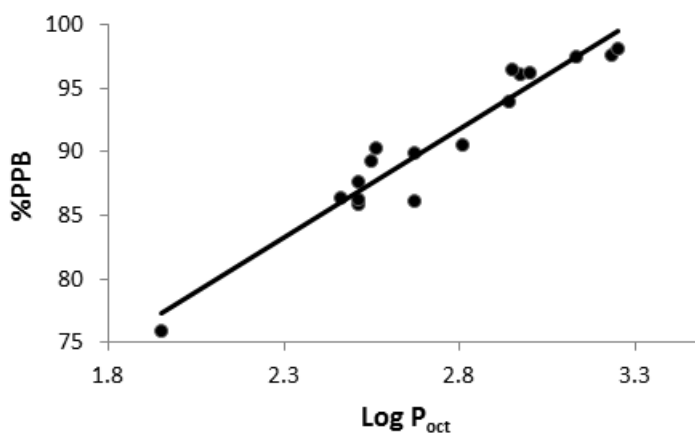


Figure 4.9. A graph showing the positive linear correlation between HPLC calculated %PPB and $\log P_{\text{oct}}$ values for olaparib and compounds 4–9 and 11–21. Compound 10 was omitted from the analysis due to the $\log P_{\text{oct}}$ value exceeding the assay limit. The plot was generated using the GraphPad Prism 6.0 software.

The average $\log P_{\text{oct}}$ of the iodinated (4–9), fluorinated (11–17), and methoxy bearing (18–21) compounds was 1.13, 0.73 and 0.69 units greater than that of olaparib, respectively. Compound 10 was excluded from this comparison as the $\log P_{\text{oct}}$ value exceeded the assay limit. A similar increase in lipophilic character between the fluorinated compound 11 (Carney *et al.*, 2015) and the iodinated compounds 4, 5 and 8 (Salinas *et al.*, 2015) has been reported in the literature.

Taken in isolation, the increase in lipophilicity of analogues 4–21 compared to olaparib could correspond to an increase *in vivo* metabolism (van de Waterbeemd *et al.*, 2001). However, it is likely that the potential increase in metabolism driven by an increase in lipophilicity will be rendered negligible *in vivo* by the corresponding increase in %PPB (Smith and Kerns, 2010; van de Waterbeemd *et al.*, 2001) (see section 4.1.2.1 for details). The markedly greater lipophilicity of compounds 4–10, when compared to the other analogues in the series, can be explained by the presence of the large lipophilic iodine atoms. Due to the positive relationship that exists between $\log P_{\text{oct}}$ and non-specific macromolecular (off-target) binding (Jacobson and Chen, 2013), it may be predicted that compounds 4–10 will exhibit greater *in vivo* non-specific binding characteristics than compounds 11–21. Furthermore, 6, 8, 10, and 16 exhibited $\log P_{\text{oct}}$ values that fall outside of the optimal range for passive diffusion across biological membranes (i.e. $\log P_{\text{oct}}$ 1.5–3.0) (Jacobson and Chen, 2013). As a

consequence, these four analogues may potentially exhibit greater *in vivo* retention in the vascular compartment (C_a , section 4.1.1, Figure 4.1), and may be less likely to reach the intracellular imaging target PARP-1. It should also be noted that **4–10** exhibited %PPB values that are in excess of 95%, which is an additional contributing factor to potential vascular retention. Based on the above observations, it can be predicted that the agents representing potential SPECT tracers (**4–10**) will exhibit less favourable *in vivo* pharmacokinetic behaviour, resulting in lower target to noise imaging contrast, when compared to the potential PET imaging agents (**11–21**).

An important potential application of radiotracers targeting PARP-1 is nuclear imaging of the protein in GBM. With that in mind, it is important to consider how the $\log P_{\text{oct}}$ and %PPB parameters obtained for compounds **11–21** can influence their usefulness as brain imaging agents. A distinction should be made between imaging healthy brain tissue, or brain pathology where the BBB is intact, and GBM tissue where the BBB is known to exhibit increased permeability (Wolburg *et al.*, 2012). In the case of the former, it is unlikely that analogues **11–21** would be able to passively cross the BBB *in vivo* as they exhibit high %PPB values (particularly compounds **4–10**, %PPB = >95%) and exceed the upper Mw limits for crossing this biological barrier (Mw = 450) (van de Waterbeemd *et al.*, 1998). This prediction is further strengthened by the observations made by Chalmers *et al.* (2014) who reported that after a single dose of ^{14}C -labelled olaparib, there was no detectable radioactivity in the central nervous system of subcutaneous colorectal xenograft bearing rats. As highlighted earlier (section 4.1.2.2), the isolated use of the $\log P_{\text{oct}}$ parameter as a predictor of BBB penetration is controversial (Young *et al.*, 1988; Tavares *et al.*, 2012), although a $\log P_{\text{oct}}$ range of 0.9–2.5 has been reported as optimal (Dischino *et al.*, 1983). All of the analogues under investigation, with the exception of compound **12**, fall outside of this ‘optimal’ range, providing further evidence that compounds **4–21** are likely to exhibit poor BBB permeability properties. However, it is envisaged that the BBB disruptions associated with GBM will allow for the *in vivo* uptake of these agents into the tumour lesions. There are a number of studies that provide evidence for this. Firstly, Chalmers *et al.* (2014) showed therapeutic levels of olaparib in resected GBM specimens from patients who received oral doses of

the drug. Secondly, Carney *et al.* (2015) were able to successfully generate a radiofluorinated version of compound **11** (see section 5.2.2 for details), which was shown by the authors to accumulate in intracranial tumour tissue following intravenous administration. Finally, work done by Kremer *et al.* (2009) and Leppäla *et al.* (1995) showed that it is possible to passively target gliomas with fluorescent- and radiolabelled human plasma protein conjugates, which under normal circumstances are unable to enter brain tissue, for fluorescent and SPECT imaging of these lesions respectively.

Based on all of the above findings, one potential SPECT (**4**) and four potential PET (**11**, **13**, **17**, and **18**) PARP-1 imaging candidates were chosen for further *in vitro* assessment (Figure 4.10). The selected PET compounds exhibited only a moderate increase in $\log P_{\text{oct}}$ and %PPB when compared to olaparib, with a range of 0.56–0.61 and 10.2–14.4% respectively, while the SPECT candidate **4** appeared to possess less favourable physicochemical properties. However, compound **4** ranked as having the second lowest %PPB value and third lowest $\log P_{\text{oct}}$ value relative to the remaining iodinated analogues (**5–10**) (Table 4.1).

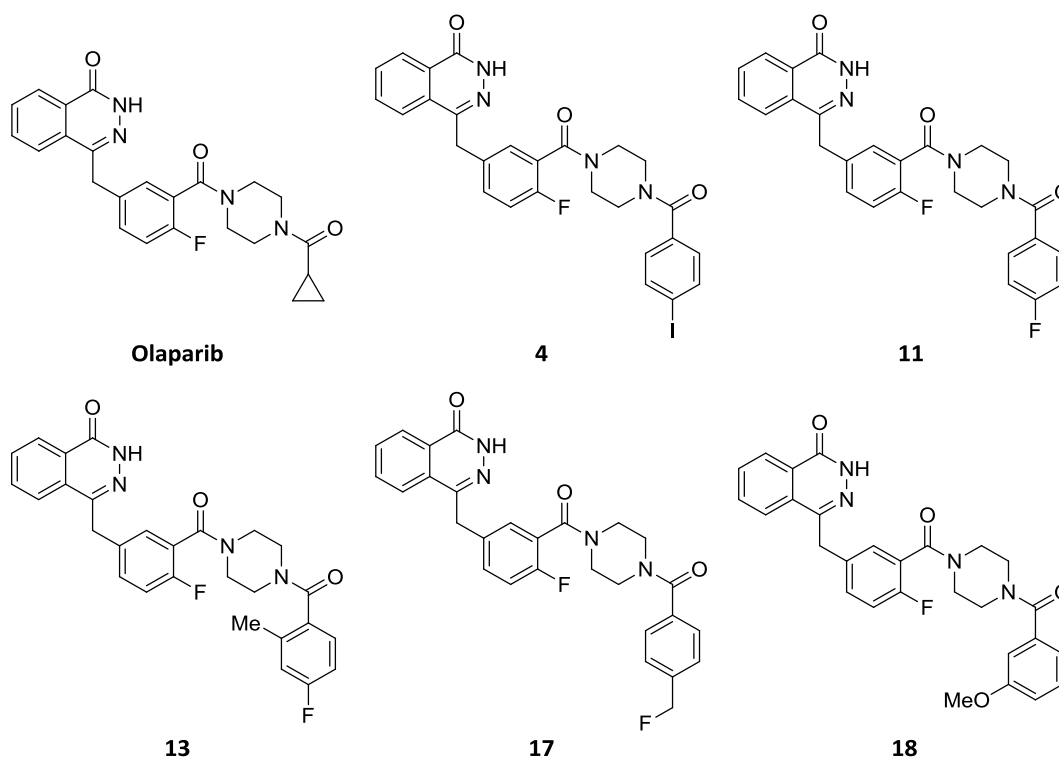


Figure 4.10. Structures of olaparib and selected non-radioactive lead candidate compounds. Compound 4 represented a potential ^{123}I -labelled SPECT PARP-1 imaging agent, compounds 11, 13, and 17 represented potential ^{18}F -labelled PET PARP-1 imaging agents, and compound 18 represented a potential $[^{11}\text{C}]$ -OMe-labelled PET PARP-1 imaging agent.

Importantly, all five selected compounds were potent inhibitors of PARP-1, with cell-free IC_{50} values ranging from 1.1–5.9 nM. However, the cell-free parameter provides limited information as it does not account for the ability of these compounds to enter living cells and reach PARP-1 within the cell nucleus. To address these unknowns, immunofluorescence imaging of PAR chains was employed as a means of assessing *in vitro* PARP activity of the test inhibitors in primary G7 and established T98G human GBM cell lines. Figure 4.11 shows a representative set of immunofluorescent images generated as part of the assay. The calculated cellular IC_{50} values for olaparib and compounds 4, 11, 13, 17 and 18 can be found in table 4.2.

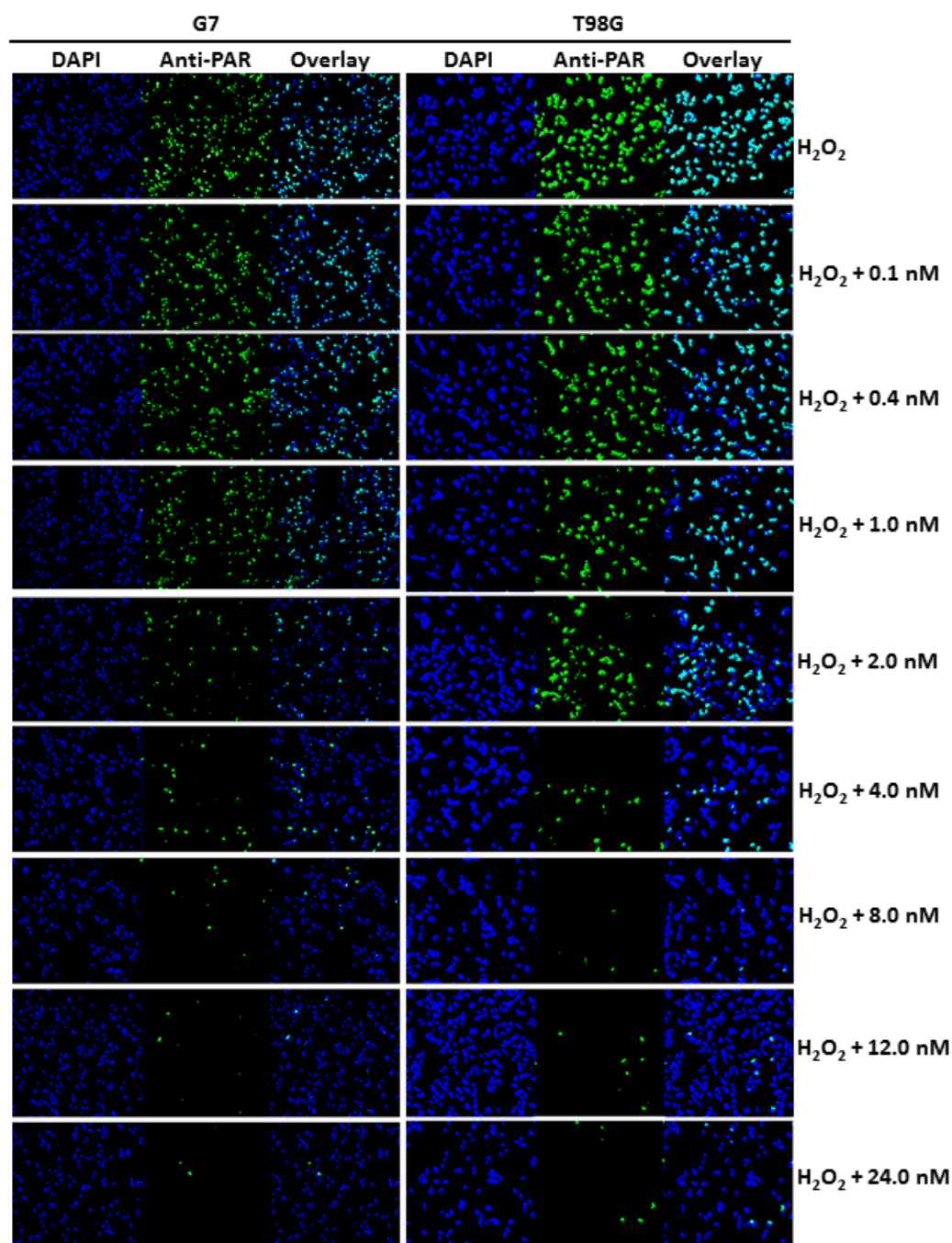


Figure 4.11. Representative images obtained using the PARP cellular immunofluorescent IC₅₀ assay. Primary G7 and established T98G human GBM cell lines were incubated in increasing concentrations of PARP inhibitor under investigation (in this case olaparib) for 1 h followed by induction of DNA damage using hydrogen peroxide (H₂O₂). Cellular nuclei were stained using an anti-poly(ADP-ribose) (anti-PAR) (10H) antibody and counterstained using DAPI. Green staining represents PAR, the product of PARP, and blue staining represents cellular nuclei. Cellular nuclei were counted and PARP activity was expressed as a ratio of PAR producing to total number of nuclei per image.

Table 4.2. Cellular PARP inhibitory properties of olaparib and compounds **4**, **11**, **13**, **17**, and **18**.

Compound	Cellular IC ₅₀ (95% CI), nM ^a	
	G7	T98G
Olaparib	1.6 (1.4–1.8)	1.6 (1.4–1.8)
4	7.0 (6.3–7.9)	7.4 (6.4–8.5)
11	1.0 (0.9–1.2)	0.8 (0.7–0.9)
13	2.2 (2.1–2.4)	1.5 (1.3–1.8)
17	1.3 (0.7–2.3)	2.0 (1.3–3.1)
18	3.5 (2.9–4.1)	1.8 (1.6–2.2)

^aCellular IC₅₀ values were obtained using primary G7 and established T98G human GBM cell lines and were based on two experiments; corresponding dose-response curves can be found in Appendix 9.4. Each cellular IC₅₀ value was reported with its 95% confidence interval (95% CI).

From these data it is clear that all five lead candidates were potent PARP inhibitors in living cells, exhibiting little variability in IC₅₀ values between the two cell lines. Olaparib exhibited lower cellular IC₅₀ values when compared to the cell-free parameter (G7 and T98G cellular IC₅₀ = 1.6 nM vs. cell-free IC₅₀ = 11.9 nM), which could be explained by the potential for the cellular assay to underestimate PARP-1 IC₅₀ values (see section 4.1.1 for details). In contrast to this, a slight reduction in cellular compared with cell-free PARP-1 inhibitory potency was observed for compound **4** (G7 and T98G cellular IC₅₀ = 7.0 and 7.4 nM respectively vs. cell-free IC₅₀ = 3.3 nM). It is possible that the higher lipophilic character of this compound (log P_{oct} = 3.0), when compared to the other analogues, resulted in a slight reduction in cellular permeability, and subsequently in the ability of **4** to reach the nuclear target PARP-1.

Prior to developing radiolabelling methodology, the selected lead candidates (**4**, **11**, **13**, **17**, and **18**) were further scrutinised for their potential radiochemical accessibility. Compound **13** was not shortlisted for further radiotracer development as it was envisaged that the additional steric bulk imposed by the methyl functionality *meta* to the radiolabelling position would have a negative inference on potential radiochemical yields. Similarly, compound **18** which

represents a potential [^{11}C]-OMe-labelled tracer was not advanced due to the logistical difficulties of working with the short-lived ^{11}C isotope (^{11}C half-life = 20.3 minutes) and the current lack of ^{11}C radiolabelling facilities.

4.3 Conclusion.

Lead PARP-1 ligands, with potential for SPECT and PET nuclear imaging, have been identified by acquiring and analysing *in vitro* cell-free IC_{50} , cellular IC_{50} , and physicochemical ($\log P_{\text{oct}}$ and %PPB) data from a library of non-radioactive olaparib analogues. Considerations were also made for the potential radiochemical accessibility of the chosen compounds. The acquired *in vitro* data were in line with the earlier proposed hypotheses (section 4.1.3).

The identified lead candidates are depicted in figure 4.12 and include one potential SPECT (**4**) and two potential PET (**11** and **17**) imaging agents. All three compounds exhibited low nanomolar cell-free and cellular IC_{50} values. The PET candidates exhibited favourable physicochemical properties ($\log P_{\text{oct}} >1.5$ and <3.0 ; %PPB $<95\%$) when compared to the SPECT analogue. Consequently, compounds **11** and **17** are likely to exhibit less off-target binding (i.e. greater specific binding), better membrane permeability properties, less vascular retention, and ultimately a better imaging target to noise ratio.

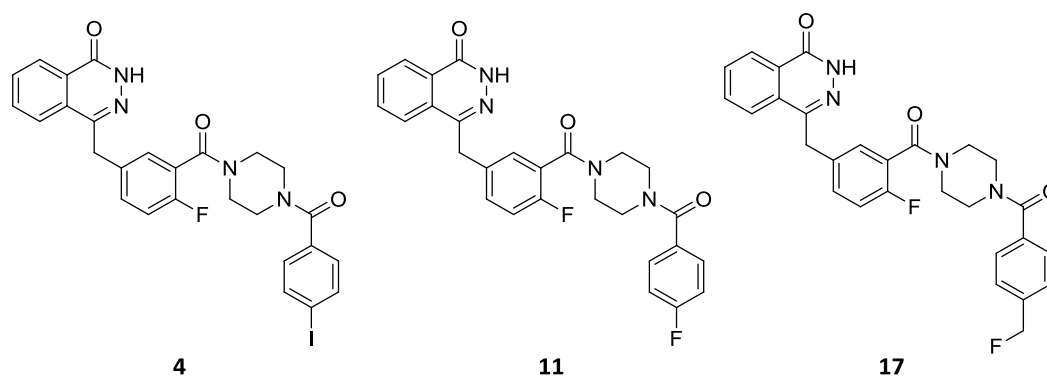


Figure 4.12. Structures of non-radioactive lead candidate compounds selected for radiolabelling methodology development. Compound **4** represents a potential ^{123}I -labelled SPECT PARP-1 imaging agent, while compounds **11** and **17** represent potential ^{18}F -labelled PET PARP-1 imaging agents.

4.4 Experimental.

4.4.1 General experimental.

With the exception of the compounds under investigation (4–21) that were synthesised in-house (see chapter 3 for details), all chemicals, reagents, and cells were obtained from commercially reputable suppliers and were used as received. G7 and T98G human GBM cell lines were cultured in Dulbecco's Modified Eagle Medium (DMEM) supplemented with 10% w/v fetal calf serum, 2 mM L-glutamine, and 1 mM sodium pyruvate and Minimum Essential Media (MEM) supplemented with 10% w/v fetal calf serum and 2 mM L-glutamine respectively. All cellular incubations were performed at 37 °C and 5% v/v CO₂ unless stated otherwise. Physicochemical HPLC analyses were performed using a Dionex Ultimate 3000 series, and data acquisition and processing performed using the Chromeleon 6.8 Chromatography software. The HPLC system was set to 25 °C, and UV detection was achieved using a UltiMate diode array detector (190–800 nm).

4.4.2 Cell-free PARP-1 IC₅₀.

The below described work was conducted at the Strathclyde Institute of Pharmacy and Biomedical Sciences, University of Strathclyde. A commercially available TrevigenTM colorimetric assay comprising of 96-histone coated well plates was used to determine the PARP-1 cell-free IC₅₀ values of olaparib and compounds 4–21. The assay was performed as per the manufacturer protocol and as reported by Zmuda *et al.* (2015). Briefly, the compounds were dissolved in ethanol followed by serial dilution with the supplied PARP buffer in order to attain the desired assay concentrations. The final concentration of ethanol in each case was <1% v/v. To the histone-coated wells containing 10 µL of inhibitor was added 15 µL (0.5 units) of the supplied PARP enzyme diluted with PARP buffer. A positive control, containing PARP enzyme in the absence of test compound, and a negative control, lacking PARP enzyme, were also prepared. Following a 10 minute incubation at room temperature, 25 µL of a 1.0 : 1.0 : 8.0

solution of PARP cocktail (containing biotinylated NAD⁺), activated (damaged) DNA, and PARP buffer was introduced into each well using a multichannel pipette. Note that the final volume in each well was 50 μ L. The mixtures were incubated for 60 minutes at room temperature followed by four washes using 0.1% v/v Triton X-100 in PBS. Next, the Strep-HRP conjugate was diluted 500-fold using the supplied diluent and 50 μ L of this solution was added to each well. Following a further 60 minute incubation at room temperature the wells were once again washed four times with 0.1% v/v Triton X-100 in PBS. Finally, TACS-SapphireTM was introduced into each well and the colorimetric reaction was allowed to develop over 15 minutes at room temperature in the dark; the reaction was terminated by adding 50 μ L of 0.2 M hydrochloric acid. Absorbance measurements were performed at 450 nm using a Tecan Infinite M200 Pro microplate reader and were normalised to the positive and negative control values. The mean absorbance measurements were plotted against the corresponding log concentrations of each compound under investigation, and a four-parameter logistic model was fitted to the resulting curves using the GraphPad Prism 6.0 software allowing for calculation of the IC₅₀. The reported IC₅₀ values for each compound were based on three experiments.

4.4.3 Log P_{oct} using HPLC.

The experiments were conducted as reported by Zmuda *et al.* (2015) using slightly modified methodology from that described by Valkó, Bevan, and Reynolds (1997) and Valkó (2004). Solutions of olaparib and compounds 4–21 were prepared in a 1.0 : 1.0 mixture of acetonitrile and 0.01 mM PBS; the resulting concentrations ranged from 0.5–1.5 mg/mL. The mean retention time of each compound was measured three times using a reverse phase Phenomenex Luna 5 μ m C₁₈ 100Å (50 \times 30 mm) column under the following mobile phase conditions: 0.0–10.5 min = 100:0 A:B to 10:90 A:B; 10.5–11.5 minutes = 10:90 A:B; 11.5–12.5 minutes = 10:90 A:B to 100:0 A:B; 12.5–15.0 minutes = 100:0 A:B where A = PBS and B = acetonitrile. The mobile phase flow rate was 1.0 mL/min. Three separate experiments were performed using PBS pH 4.0, pH 7.4, and pH 10.0; the necessary pH was achieved by addition of either hydrochloric acid 0.1% v/v or 0.05 M ammonium hydroxide. The mean retention times (n = 3) were

plotted against the known gradient chromatographic hydrophobicity indices (CHIs) of the following standard compounds to generate a calibration regression model: theophylline (CHI = 15.76), phenyltetrazole (CHI = 20.18), benzimidazole (CHI = 30.71), colchicine (CHI = 41.37), acetophenone (CHI = 64.90), indole (CHI = 69.15), and butyrophenone (CHI = 88.49) (Valkó, Bevan and Reynolds, 1997). The CHI values of unknown compounds in their non-ionised state (CHIN) were obtained by fitting their mean retention times obtained using the above described chromatographic conditions to the calibration regression model. The CHIN values were then converted to log P_{oct} values using the below equation (Valkó, 2004):

$$\text{Log } P_{\text{oct}} = 0.047\text{CHIN} + 0.36\text{HBC} - 1.10$$

where CHIN is the gradient chromatographic hydrophobicity index of the non-ionized compound and HBC is hydrogen-bond donor count. The Microsoft Excel 2010 software was utilised for calculations and plot generation.

4.4.4 %PPB using HPLC.

The experiments were conducted as reported by Zmuda *et al.* (2015) using slightly modified methodology from that described by Valkó *et al.* (2003). Solutions of olaparib and compounds 4–21 were prepared in a 1.0 : 3.0 : 3.0 mixture of acetonitrile, 0.01 mM PBS and isopropyl alcohol; the resulting concentrations ranged from 0.5–1.5 mg/mL. The mean retention time of each compound was measured three times using a ChromTech HSA 5 μm (50 \times 30 mm) column under the following mobile phase conditions: 0.0–3.0 minutes = 100:0 A:B to 70:30 A:B; 3.0–10.5 minutes = 70:30 A:B; 10.5–11.0 minutes = 70:30 A:B to 100:00 A:B; 11.0–15.0 minutes = 100:0 A:B where A = PBS (pH 7.4) and B = isopropyl alcohol. The mobile phase flow rate was 1.8 mL/min. The chromatographic system was calibrated using the following standard compounds of known %PPB: nizatidine (%PPB = 35.0), bromazepam (%PPB = 60.0), carbamazepine (%PPB = 75.0), budesonide (%PPB = 88.0), nicardipine (%PPB = 95.0), warfarin (%PPB = 98.0), ketoprofen (%PPB = 98.7%), indometacin (%PPB =

99.0), and diclofenac (%PPB = 99.8%) (Valkó, 2004). The %PPB values of the standard compounds were converted to the linear log K values using the below equation (Valkó *et al.*, 2003):

$$\text{Log } K = \log (\% \text{PPB} / (101 - \% \text{PPB}))$$

where K is the apparent affinity constant.

The mean retention times ($n = 3$) of the standard compounds were plotted against their corresponding log K values to generate a calibration regression model. The log K values of unknown compounds were then obtained by fitting their mean retention times, obtained using the above described chromatographic conditions, to the calibration regression model. The log K values were then converted to the %PPB using the below equation (Valkó *et al.*, 2003):

$$\% \text{PPB} = (101 \times 10^{\log K}) / (1 + 10^{\log K})$$

The Microsoft Excel 2010 software was utilised for calculations and plot generation.

4.4.5 Cellular PARP-1 IC₅₀.

The experiments were conducted as reported by Zmuda *et al.* (2015) using slightly modified methodology from that described by Ye *et al.* (2013). Cells were seeded onto 19 mm diameter glass coverslips in 12-well plates, at concentrations of 8×10^4 (G7) or 5×10^4 (T98G) cells per well, and were incubated for 48 hours. The cells were then incubated for 60 minutes in 1 mL of cell media containing increasing concentrations of compound under investigation (olaparib or compounds **4**, **11**, **13**, **17**, and **18**). The desired compounds were dissolved in dimethyl sulfoxide, followed by serial dilution using PBS to obtain the necessary stock solutions. These stock solutions were further diluted using cell media to attain the desired assay concentrations, such that the final concentration of dimethyl sulfoxide was $\leq 1.0\%$ v/v. Following aspiration of media

solutions, DNA damage was induced by incubating the coverslips under in 20 mM hydrogen peroxide in PBS (prepared immediately prior to use) in the dark, at room temperature for 10 minutes. A negative control, containing media alone minus hydrogen peroxide treatment, and a positive control, containing media alone plus hydrogen peroxide treatment, were also used. The cells were washed with PBS and fixed with ice cold 4.0% v/v formaldehyd PBS and incubated at 4–8 °C for 15 minutes. Following fixation the cells were washed with PBS, permeabilised with 0.3% v/v Triton X-100 in PBS for 10 minutes at room temperature, and then washed three more times with PBS. The fixed cells were then incubated in 2% w/v bovine serum albumin in PBS for 30 minutes at room temperature. Primary antibody staining was performed using 1:200 anti-PADPR antibody (mouse antibody; ab14459; 10H; Abcam) in KB buffer (10 mM Tris pH 7.5, 150 mM sodium chloride, 0.1% w/v bovine serum albumin) by incubating the coverslips on parafilm at room temperature for 60 minutes. The coverslips were washed once with PBS and twice with KB buffer and secondary staining was performed using 1:500 anti-mouse antibody (goat anti-mouse antibody; Alexa Fluor 488; A11029; Life Technologies) in KB buffer; the cells were incubated with the secondary antibodies at room temperature in the dark for 60 minutes. Next, the coverslips were washed three times with KB buffer and mounted onto glass slides using VectaShield[®] mounting medium. Immunofluorescence imaging was performed within 48 hours of staining using a Zeiss LSM 710 confocal microscope. The following imaging parameters were used: i) 40 × magnification (oil); ii) resolution = 512 × 512; iii) tiling = 3 × 3; iv) Z-stacking = 3–4 sections; and v) image depth = 12 bit. PARP activity was expressed as a ratio of PAR positive nuclei to the total number of nuclei; nuclei counted per well ≥ 120 . Mean PARP activity was normalised to the positive and negative control values, and plotted against the corresponding log concentrations of each compound under investigation. A four-parameter logistic model was fitted to the resulting curves using the GraphPad Prism 6.0 software allowing for calculation of the IC₅₀ parameter. Where necessary (i.e. an incomplete sigmoidal curve) constraints defining 0% and 100% PARP activity were introduced into the curve fitting model. The reported IC₅₀ values for each compound were based on two experiments.

5 DEVELOPING RADIOSYNTHESSES FOR PARP-1 NUCLEAR IMAGING AGENTS.

5.1 Introduction.

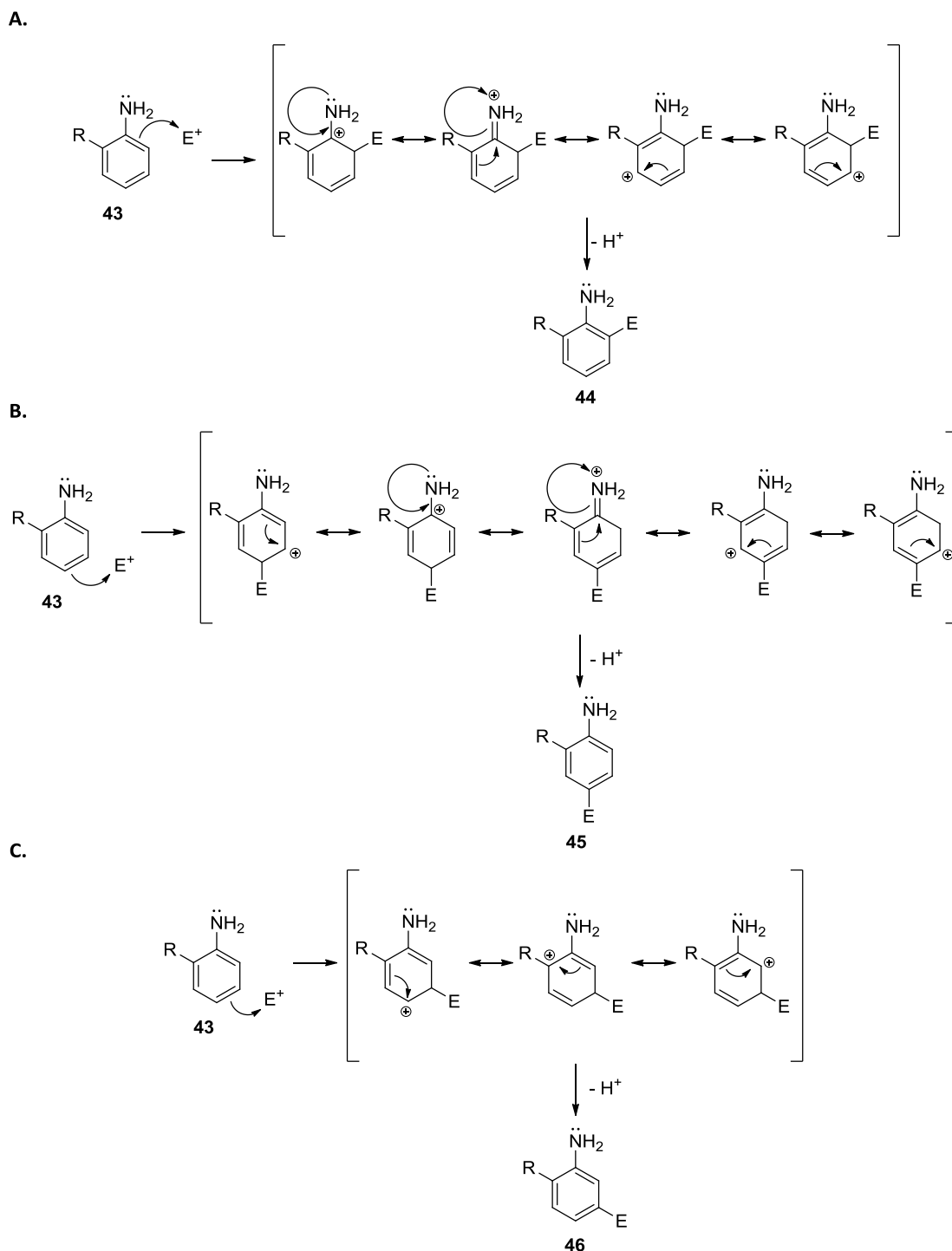
Radiosynthesis is a process that is used to generate a radionuclide labelled agent that can then be used for nuclear imaging or therapeutic purposes. This process can be broken down into three key steps: i) radiolabelling; ii) purification; and iii) formulation. The first of these steps is generally regarded as the most challenging and it is the main focus of this chapter.

Many different types of radiolabelling techniques exist. The choice of methodology can be influenced by the radioisotope that is being utilised for nuclear imaging (e.g. ^{123}I or $^{99\text{m}}\text{Tc}$ for SPECT), the type of compound that is being labelled (e.g. small molecule or biologic), and the chemical functionality that is being labelled (e.g. aromatic or aliphatic). In this chapter, radiolabelling methodology will be described in the context of small molecules, and iodine (^{123}I and ^{125}I) and fluorine (^{18}F) radionuclides only. Labelling with ^{11}C for PET imaging was not pursued as part of this project due to the current lack of facilities and infrastructure required for such radiochemistry. An outline of ^{11}C radiolabelling methodology can be found in the reviews by Miller *et al.* (2008) and Antoni (2015).

The methods that are used to incorporate radioactive isotopes of iodine or fluorine into target molecules can be subdivided into electrophilic and nucleophilic techniques.

Electrophilic radiolabelling is restricted to electron rich systems such as aryls and alkenes, and it requires the use of electrophilic radioisotope species. Since the radioisotopes of iodine and fluorine are available in their nucleophilic form (e.g. $^{18}\text{F}^-$ and $^{123}\text{I}^-$), the necessary electrophiles must first be generated to allow for successful radiolabelling. In the case of iodine this is usually achieved *in situ*

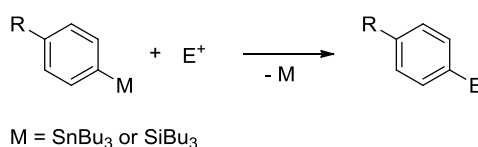
using an appropriate oxidising agent, while electrophilic radiofluorination relies on the use of electrophilic ^{18}F -species such as $[\text{}^{18}\text{F}]\text{-F}_2$. This is discussed in more detail in the following sections. Electrophilic radiolabelling can be further subdivided into either direct electrophilic or electrophilic exchange approaches. In the case of the former, the electrophilic radioisotope is attacked by an electron rich target and this leads to the subsequent loss of a hydrogen atom. The actual labelling position is often directed by the presence of appropriate activating functionalities on the aromatic ring (Scheme 5.1). Electron-donating groups (e.g. hydroxyls, ethers, amines, alkyls, and aryls) act to facilitate electrophilic aromatic substitution (EAS) (i.e. they are activating functionalities) and are *ortho* and *para* directing. In contrast to this, electron-withdrawing groups (e.g. carbonyls, nitros, nitriles, trialkylammonium salts, sulfonates, and esters) are *meta* directing and deactivating functionalities. Halides are an exception as they possess *ortho* and *para* directing properties but are deactivating.



Scheme 5.1. Electrophilic aromatic substitution of aniline analogue **43** where the electrophile is represented as 'E⁺'. The amino functionality acts as an activating, and *ortho* and *para* directing, group (**A** and **B**) as it is able to donate electron density into the *pi* system, thereby enhancing the stability of the cationic intermediate. Electrophilic substitution at the *meta* position (**C**) is not favoured as the amino group can no longer contribute to stabilising the cationic intermediate.

Despite this, direct electrophilic radiolabelling often leads to the formation of multiple radiolabelled products due to lack of regioselectivity. Furthermore, direct electrophilic radiolabelling using the [^{18}F]- F_2 or [$^*\text{I}$]- I_2 species is often associated with low specific activity as both the radioactive and non-radioactive halogen atoms can act as attacking electrophiles (Miller *et al.*, 2008; Wager, and Jones, 2010; Pimlott and Sutherland, 2011). Specific activity is defined as the activity of a radioactive isotope of an atom (i.e. a radionuclide) divided by the molar amount of the sum of all isotopes (radioactive and stable) of that atom (de Goeij and Bonardi, 2005). As an example, an ^{18}F -labelled radiotracer with a low specific activity will have a lower amount of radiofluoride per mole than an equivalent tracer of high specific activity. Therefore, in order to obtain an equivalent nuclear imaging signal, a higher molar amount of the low specific activity tracer will need to be injected when compared to the high specific activity tracer. Consequently, tracers of low specific activity are more likely to elicit an *in vivo* pharmacological response and potentially result in toxicity issues.

In contrast to the above, electrophilic exchange allows for regioselectivity and higher specific activity. This technique relies on the use of an appropriate organometal leaving group on the target molecule that can be replaced by the radioisotope (Scheme 5.2) (Miller *et al.*, 2008; Wager and Jones, 2010; Pimlott and Sutherland, 2011). However, organometal radiotracer precursors are often unstable and may require frequent re-syntheses, which are complicated by the high toxicity of organometal starting materials (see section 5.1.1.1 for details).



Scheme 5.2. Organometal mediated aromatic electrophilic exchange reaction. E^+ = electrophile; SnBu_3 = tributyl tin; SiBu_3 = tributyl silyl.

Nucleophilic radiolabelling can be performed on aryls and, unlike electrophilic methods, alkanes. However, radioiodination at aliphatic positions is usually avoided due to the instability of the alkyl-iodine bond. In a similar manner to electrophilic exchange, the nucleophilic approach relies on the presence of a

leaving group that can be substituted by the radioisotope. The advantages of this technique are good regioselectivity, generally high specific activity, and greater stability of radiolabelling precursors that can be synthesised without the need for highly toxic organometals (Miller *et al.*, 2008; Wager and Jones, 2010; Pimlott and Sutherland, 2011).

It is often the case that the choice of the above mentioned radiolabelling technique will be guided by the compound that is to be labelled and by the labelling position on that molecule. Purification and formulation are also key steps in the radiosynthetic process. The ultimate goal is to develop a radiosynthetic protocol that allows for high radionuclide incorporation and end of synthesis yield, as well as high specific activity and purity of the formulated radiotracer. This is important as it allows maximising the amount of radiotracer that is produced from the radioisotope, which is associated with high production costs. It is also desirable that the radiosynthetic protocol is rapid and allows for radionuclide incorporation at the latest possible stage of the entire synthesis to minimise the influence of radionuclide decay on the end of synthesis yield (Pimlott and Sutherland, 2011). This is particularly important for short lived radioisotopes such as ^{11}C and ^{18}F .

5.1.1 SPECT radioiodination chemistry.

5.1.1.1 Electrophilic techniques.

As mentioned above, this technique relies on the presence of an electrophilic iodine radionuclide. For the purpose of this explanation ^{123}I , ^{124}I , ^{125}I and ^{131}I radionuclides will be depicted collectively as ‘*I’. The simplest approach of electrophilic radioiodination involves using a commercially available electrophilic species such as $[*\text{I}]-\text{I}_2$ which can form the electrophilic radioiodide cation ($*\text{I}^+$) during the labelling reaction. However, the stable iodine atom can also act as the electrophile, which can lead to the generation of a non-radioactive iodinated (^{127}I) compound. Therefore, the use of $[*\text{I}]-\text{I}_2$ is usually associated with the formation of an inseparable mixture of *I and ^{127}I labelled compounds that can ultimately reduce the overall specific activity of the

radiolabelled product. This issue can be overcome by using the radioiodine monochloride ($[^*I]-ICl$) species, which can be generated by treating non-radioactive ICl with commercially available sodium radioiodide ($[^*I]-NaI$) (Seevers and Counsell, 1982). It is thought that $[^*I]-ICl$ forms $[^*I]-HOI$ *in situ*, which acts as the electrophilic species during labelling (Helmkamp, Contreras, and Bale, 1967). This species was a step in the right direction, but its utility relies on the complete conversion of ICl to $[^*I]-ICl$, which may not always be the case. Alternatively, the radioiodine atom can be oxidised using an oxidising agent such as peracetic acid **47**, chloramine T and Iodogen (Figure 5.1) (Seevers and Counsell, 1982).

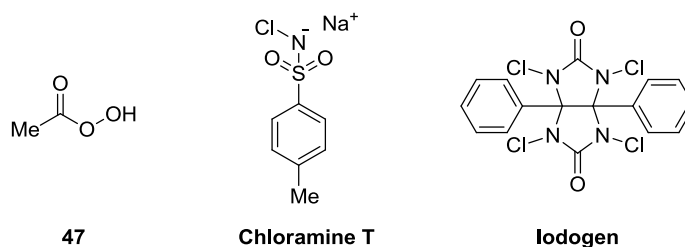


Figure 5.1. Examples of oxidising agents used in radioiodination chemistry.

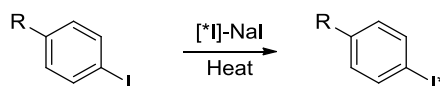
Peracids are generated *in situ* by reacting hydrogen peroxide with an organic acid (e.g. acetic acid). This class of oxidising agent allows for radiolabelling under mild conditions but it has been associated with lower radiochemical yields when compared to other oxidants (Wager and Jones, 2010). Chloramine T is an oxidising agent that decomposes under aqueous conditions to form $HOCl$, which in the presence of $[^*I]-NaI$ is thought to generate the electrophile H_2O^+I . The disadvantage of chloramine T is its high oxidising potential that can result in various undesirable side reactions including oxidation of thiol and thioether groups, cleavage of certain peptide bonds, and chlorinations. These harsh oxidising conditions can be circumvented by using an analogue of chloramine T called iodogen that operates via the same mechanism. Since iodogen is water insoluble, it must be coated onto the radiochemical reaction vessel wall as a thin film. This minimises the contact of the labelling precursor with the oxidant, thus reducing the risk of side reactivity (Seevers and Counsell, 1982; Pimlott and Sutherland, 2011).

As mentioned previously, electrophilic radiolabelling can either be direct or it can rely on the exchange of an organometal functionality. The former approach generally allows for high radiochemical yields but requires the labelling precursor to be sufficiently activated. The type and the position of the activating moiety will to an extent determine the regioselectivity of the radioiodination, but a single reaction will often lead to the formation of multiple radiolabelled products. An organometal leaving group can be utilised in order to gain control over the radioiodination regioselectivity whilst maintaining good radiolabelling yields (Wager and Jones, 2010) (Scheme 5.2). The two most commonly used organometals are tributyl tin and tributyl silyl. The advantage of organosilyl precursors are their greater stability when compared to organotin compounds, but they suffer from lower reactivity. Furthermore, the high toxicity of both organometals imposes complications with regard to precursor synthesis, precursor handling and radiopharmaceutical purification (Pimlott and Sutherland, 2011). For example, tributyl tin precursors are synthesised using hexabutylditin starting material, which is a highly lipophilic and potent neurotoxin. The lipophilicity of this material allows it to rapidly permeate the skin and enter brain tissue where it accumulates and destroys astrocytes. This damage is irreversible and progressive, eventually leading to death (Chang, 1990). Therefore, great care must be taken during the synthesis of the precursor and during the radiochemical synthesis. Moreover, utmost diligence is necessary to ensure that the final radiopharmaceutical is completely free of any organometal residues.

5.1.1.2 Nucleophilic techniques.

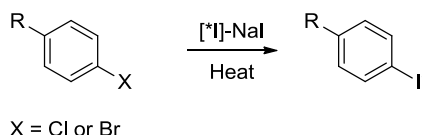
Nucleophilic radioiodination involves the substitution of a leaving group for an iodo radionuclide ($^*I^-$); iodine radioisotopes are generally available commercially in their nucleophilic form as sodium iodide ($[^*I^-]NaI$) in 0.05-0.10 M sodium hydroxide. The three types of nucleophilic radioiodination techniques that exist are: i) isotopic halogen exchange; ii) interhalogen exchange; and iii) radioiodo-dediazonisation. The first and simplest of these approaches relies on the exchange of an iodine radionuclide for a stable iodine atom already present in the precursor molecule (Scheme 5.3). In addition to the precursor and the

radioactive iodine, a copper catalyst may be added to improve the overall radionuclide incorporation. The simplicity of this technique is often overshadowed by the necessity for high reaction temperatures (>100 °C) and the low specific activities of the labelled product (Seevers and Counsell, 1982).



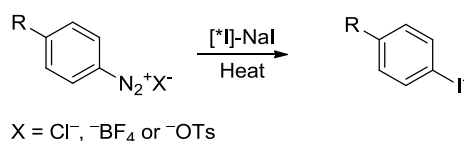
Scheme 5.3. Isotopic halogen exchange radioiodination.

Interhalogen exchange utilises bromine or chlorine leaving groups that can allow for much greater specific activities following radioiodination (Scheme 5.4). However, purification of the radiopharmaceutical can be time consuming as the separation of the radioiodinated compound from its brominated or chlorinated precursor may require slower chromatographic runs. Another advantage of both halogen exchange techniques is that they can be performed in the absence of solvent under solid state conditions, which is beneficial when a precursor exhibits unfavourable organic solubility (Seevers and Counsell, 1982).



Scheme 5.4. Interhalogen exchange radioiodination.

Classical iodo-dediazonisation relies on the use of diazonium salt leaving groups (Scheme 5.5) that are known to be highly unstable and explosive. Despite this, the use of these salts for radiodination reactions is well established (reviewed by Seevers and Counsell (1982)). Furthermore, the discovery of stable and non-explosive diazonium tosylate salts ($-N_2^+OTs$) by Filimonov *et al.* (2008) has the potential to further enhance the utility of this radioiodination chemistry.



Scheme 5.5. Radioiodo-dediazonisation.

5.1.2 PET radiofluorination chemistry.

5.1.2.1 Electrophilic techniques.

Electrophilic radiofluorination can be subdivided into direct and exchange labelling techniques that share the same disadvantages as those described earlier for electrophilic radioiodinations. Additionally, these types of reactions rely on the use of an electrophilic radiofluoride (i.e. $^{18}\text{F}^+$) species. The simplest of these is $[^{18}\text{F}]\text{-F}_2$, which is a gas that is highly reactive and often leads to poor electrophilic regioselectivity and low specific activity of the final radiolabelled product (Miller *et al.*, 2008). Furthermore, the gaseous form of $[^{18}\text{F}]\text{-F}_2$ introduces radiosynthetic and waste management challenges. In order to address this issue of ‘high reactivity’, the softer (less reactive) acetyl hyporadiofluorite (CH_3COOF) electrophilic species has been developed (Rozen and Lerman, 1981), which has been shown to be superior in the synthesis of the PET tracer $[^{18}\text{F}]\text{-FDG}$ when compared to the $[^{18}\text{F}]\text{-F}_2$ species (Ehrenkaufer, Potocki, and Jewett, 1984). Some of the other commonly used electrophilic radiofluorination reagents are depicted in figure 5.2.

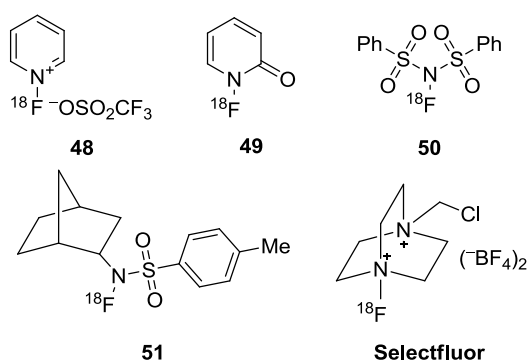


Figure 5.2. Examples of commonly used electrophilic radiofluorination species.

5.1.2.2 Nucleophilic techniques.

Nucleophilic substitution is the preferred approach for radiofluorination as it provides control over regioselectivity, allows for greater specific activities of labelled product compared to electrophilic radiofluorination, and eliminates the need for toxic organometal precursors. As described previously (see section

1.2.1), ^{18}F is produced from heavy-oxygen water ($[^{18}\text{O}]\text{H}_2\text{O}$) in a cyclotron via proton bombardment. The resulting radioisotope is usually collected as a mixture of $^{18}\text{F}^-$ in $[^{18}\text{O}]\text{H}_2\text{O}$ and due to the high degree of solvation the nucleophilicity of $^{18}\text{F}^-$ is extinguished (Figure 5.3 A) (Miller *et al.*, 2008). Therefore, removal of the aqueous component is an important step in the nucleophilic radiofluorination process. This is usually achieved by heating the solvated radioisotope in the presence of acetonitrile that facilitates azeotropic drying. However, such drying can lead to large losses of $^{18}\text{F}^-$ due to the formation of the highly volatile and weakly nucleophilic $[^{18}\text{F}]$ -hydrogen fluoride (Cai, Lu and Pike, 2008). Therefore, prior to the drying process, a mildly basic phase transfer agent is added which has two functions; firstly it traps the radiofluoride and prevents the formation of acidic $[^{18}\text{F}]$ -hydrogen fluoride, and secondly it allows for solubilisation of the hydrophilic radiofluoride in organic solvent (Figure 5.3 B). The overall benefits are increased nucleophilicity of the radiofluoride and improved radiochemical yields (Miller *et al.*, 2008).

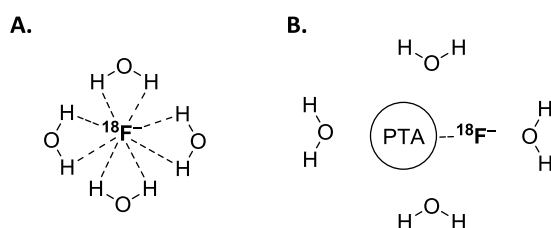


Figure 5.3. Diagrammatic representation of a solvated $^{18}\text{F}^-$ radionuclide with weak nucleophilic properties (A) and a $^{18}\text{F}^-$ radionuclide trapped by a phase transfer agent with improved nucleophilic properties (B).

It is important to note that the degree of dryness that is required for successful radiofluorination is dependent on the compound that is being radiolabelled. For example, forming the challenging aromatic-radiofluoride bond requires a high degree of dryness while less challenging aliphatic radiofluorinations are more tolerant to water (Cai, Lu, and Pike, 2008).

The two most commonly used phase transfer agents in nucleophilic radiofluorination chemistry are Kryptofix[®] (K_{222}) in combination with potassium carbonate and tetra-*n*-butylammonium hydrogen carbonate (TBAHCO_3) (**52**) (Figure 5.4).

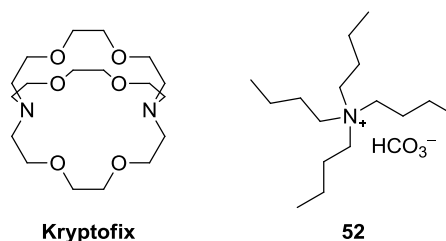
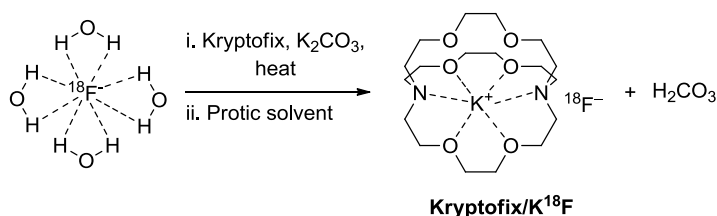


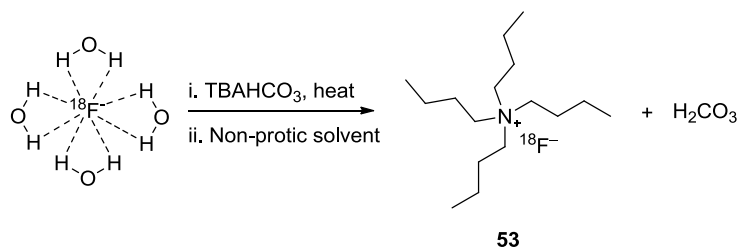
Figure 5.4. Structures of the phase transfer agents Kryptofix[®] and tetra-*n*-butylammonium hydrogen carbonate (**52**).

In the case of the former, the potassium cation (K^+) made available from potassium carbonate is trapped in the core of the K_{222} structure. This in turn attracts the radiofluoride anion ($^{18}F^-$) leaving it exposed and highly nucleophilic. The entire complex is then solubilised in a non-protic organic solvent (e.g. acetonitrile, *N,N'*-dimethylformamide, dimethyl sulfoxide, tetrahydrofuran or dichloromethane), which prevents further radiofluoride solvation from taking place. Additionally, the basic potassium carbonate prevents formation of the acidic, volatile and weakly nucleophilic [^{18}F]-hydrogen fluoride by forming carbonic acid instead (Scheme 5.6) (Cai, Lu, and Pike, 2008; Miller *et al.*, 2008).



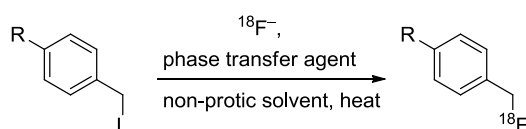
Scheme 5.6. Drying of solvated $^{18}F^-$ using Kryptofix[®] as a phase transfer agent.

TBAHCO₃ has the same function of enhancing radiofluoride nucleophilicity and organic solubility as K_{222} , which it achieves by forming [^{18}F]-tetra-*n*-butylammonium fluoride ([^{18}F]-TBAF) (**53**) *in situ* (Scheme 5.7) (Cai, Lu, and Pike, 2008; Miller *et al.*, 2008). The large cesium cation (Cs^+) can also be used to enhance nucleophilicity of the radiofluoride anion, but it is used less commonly due to poor organic solubility.



Scheme 5.7. Drying of solvated $^{18}\text{F}^-$ using TBAHCO_3 as a phase transfer agent resulting in the *in situ* formation of $[\text{}^{18}\text{F}]\text{-TBAF}$ (**53**).

Nucleophilic radiofluorinations can be subdivided into direct aliphatic and aromatic labelling reactions. For aliphatic radiofluorination to proceed efficiently, the precursor must possess a good leaving group on the aliphatic chain (Scheme 5.8). Such leaving groups usually include sulfonate analogues such as triflate (OTf), tosylate (OTs), mesylate (OMs) and nosylate (ONs) moieties, or halogens such as bromine, chlorine and iodine. The weaker the basicity of the leaving group the better its leaving ability and the greater the radiofluorination yield. Consequently, the sulfonate analogues exhibit similar leaving ability properties, followed by iodine, bromine, and finally chlorine (Mason and Mathis, 2004). Furthermore, radiofluorination proceeds more readily and higher yields are generally achievable when the leaving group is attached to a primary carbon when compared to a secondary carbon (Cai, Lu, and Pike, 2008).



L = OTf, OTs, OMs, ONs, Br, Cl, or I

Scheme 5.8. An example of an aliphatic nucleophilic radiofluorination reaction.

Interestingly, the addition of a sterically-hindered protic alcohol such as *tert*-butyl alcohol to an aliphatic radiofluorination reaction can have a beneficial effect on the radiofluoride incorporation (Lee *et al.*, 2007; Kim *et al.*, 2008). It has been proposed that these protic alcohols facilitate aliphatic nucleophilic substitution by enhancing the leaving group ability through hydrogen bonding and by solvating the radiofluoride while maintaining its nucleophilicity (Figure 5.5) (Kim *et al.*, 2008). Moisture contamination due to the hygroscopic

properties of these bulky protic alcohols has been reported to have no effect on the consistency of radiofluorination yields (Lee *et al.*, 2007).

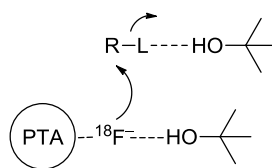
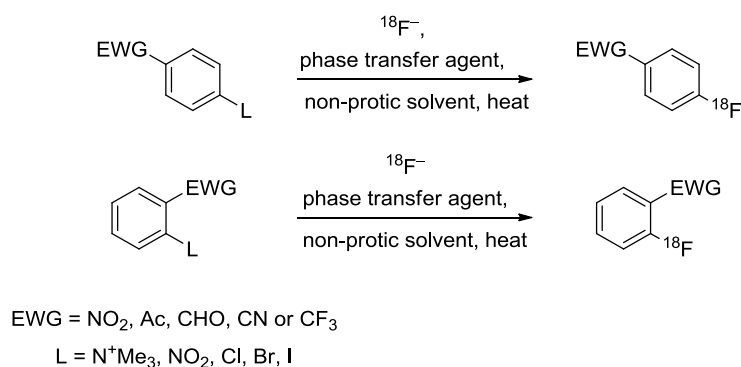


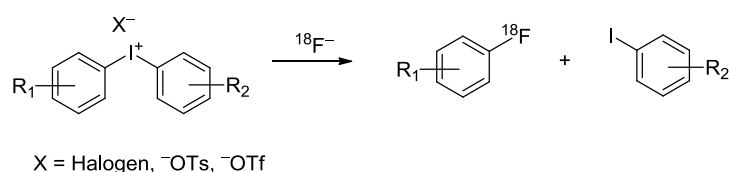
Figure 5.5. Proposed mechanism by which *tert*-butyl alcohol facilitates aliphatic nucleophilic radiofluorination. Hydrogen bonding between the bulky protic alcohol and the leaving group (L) enhances its leaving ability. Solvation of the $^{18}\text{F}^-$ anion weakens its interaction with the phase transfer agent (PTA) and enhances its nucleophilicity.

Aromatic nucleophilic radiofluorination is more complex as in addition to a leaving group, the aromatic ring undergoing labelling must be sufficiently activated. Such activation is usually achieved by the presence of an electron withdrawing group next to (*ortho*) or directly opposite (*para*) the leaving group (Cai, Lu, and Pike, 2008). The first and rate determining step of an aromatic nucleophilic substitution ($\text{S}_{\text{N}}\text{Ar}$) is the attack of the nucleophile, in this case $^{18}\text{F}^-$, on the carbon *ipso* to the leaving group (Scheme 5.9). The stronger the electron-withdrawing ability of the activating moiety the lower the electron density of the carbon undergoing attack, and the greater the ease of nucleophilic substitution (Hashizume *et al.*, 1997). Therefore, it is not surprising that a positive correlation exists between radiochemical yield and the electron-withdrawing potential of the activating functionality. Commonly used electron-withdrawing moieties in approximate order of increasing ability are: *meta*-nitrite (*meta*- NO_2) < *para*-acetyl (*para*-Ac) < *para*-aldehyde (*para*-CHO) < *para*-nitrile (*para*-CN) = *para*-trifluoromethane (*para*- CF_3) < *para*- NO_2 . Established leaving groups utilised for $\text{S}_{\text{N}}\text{Ar}$ radiofluorination reactions, in order of leaving ability, are: $\text{I} < \text{Br} < \text{Cl} < \text{F} < \text{NO}_2 = \text{trimethyl ammonium} (\text{N}^+\text{Me}_3)$ (Cai, Lu and Pike, 2008).



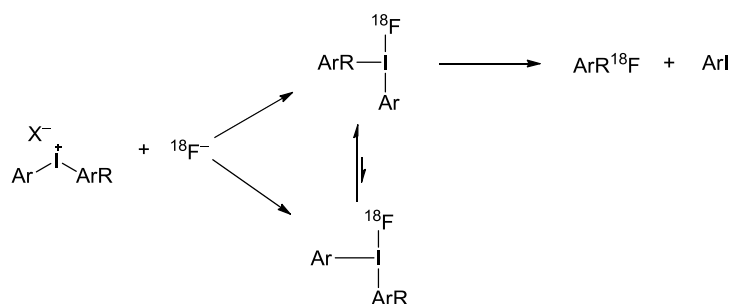
Scheme 5.9. Examples of aromatic nucleophilic substitution radiofluorination reactions.

The main disadvantage of the $\text{S}_{\text{N}}\text{Ar}$ approach is that it is limited to aromatic systems that are sufficiently activated for nucleophilic substitution. Where such activation is lacking (i.e. aryl rings with electron rich substituents) an unsymmetrical diaryliodonium salt may be utilised instead. The use of such salts to facilitate aromatic substitutions is well established (Beringer *et al.*, 1952) and their usefulness in radiofluorination chemistry has been proven (Pike and Aigbirhio, 1995; Gail, Hocke and Coenen 1997; Ross *et al.* 2007; Moon *et al.*, 2011; Xu *et al.*, 2013). A general outline of radiofluorination of an unsymmetrical diaryliodonium salt is presented in scheme 5.10 (Cai, Lu and Pike, 2008).



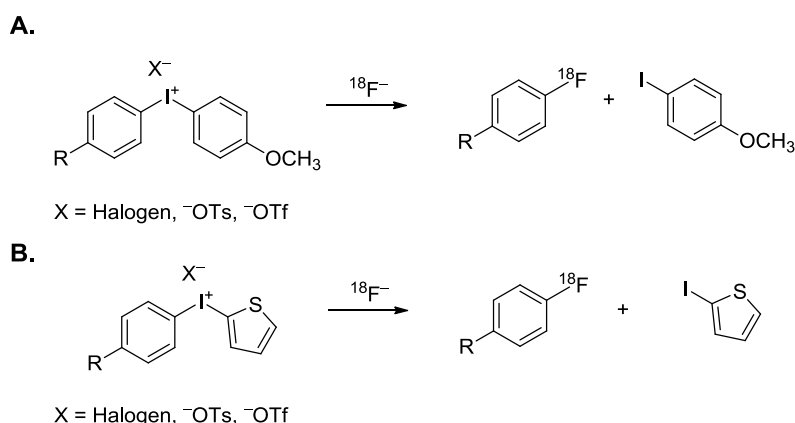
Scheme 5.10. An example of radiofluorination of a non-activated (electron rich) arene ring using an unsymmetrical diaryliodonium salt.

Such salts can be utilised in a chemoselective manner where the radiofluorination is directed to the desired arene ring. This directing effect can occur as a consequence of two mechanisms. The first of these is the “*ortho*-effect” where an *ortho* substituent on one of the aromatic rings will direct the substitution to that ring; this can be explained by the proposed “turnstile” mechanism (Scheme 5.11) (Cai, Lu and Pike, 2008; Malmgren *et al.*, 2013).



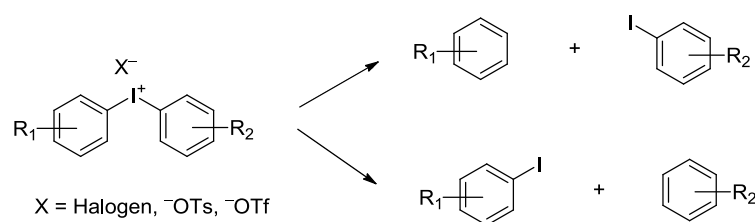
Scheme 5.11. The proposed ‘turnstile’ mechanism for the reaction between a nucleophile ($^{18}\text{F}^-$) and an unsymmetrical diaryliodonium salt. Nucleophilic attack upon the positive iodine atom forms a tricovalent intermediate where the bulky *ortho*-substituted arene (ArR) prefers to occupy the equatorial position in order to reduce steric strain. The reaction proceeds by ligand coupling between the nucleophile and the equatorial aryl functionality through the process of reductive elimination.

In the absence of the *ortho*-effect, the substitution is directed by the electronics of the diaryliodonium salt where nucleophilic attack will occur preferentially at the more electron-deficient ring. Therefore, diaryliodonium salts are often designed to either possess a heteroaromatic moiety or an aromatic moiety bearing electron-donating substituents, which are more electron rich than the other arene system. These electron-rich arenes will direct radiofluoride incorporation to the desired less-electron rich arene (Scheme 5.12) (Ross *et al.*, 2007).



Scheme 5.12. Examples of diaryliodonium radiofluorination reactions where, in the absence of the *ortho*-effect, chemoselectivity is achieved through the use of an electron-donating substituent (OCH_3) (A) and an electron-rich heteroaromatic moiety (B).

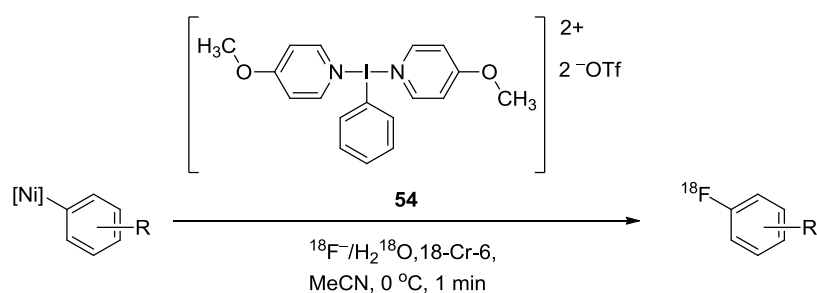
The main problem with the use of diaryliodonium salts is their lack of stability, particularly at high temperatures and under basic conditions (Moon *et al.*, 2011); although they are generally regarded as air- and moisture-stable (Merritt and Olfson, 2009). Scheme 5.13 outlines the two major decomposition pathways of these salts (Moon *et al.*, 2011). The synthesis of diaryliodonium salts falls outside of the scope of this thesis and further information concerning the subject can be found in the review by Merritt and Olfson (2009).



Scheme 5.13. Decomposition pathways of diaryliodonium salts.

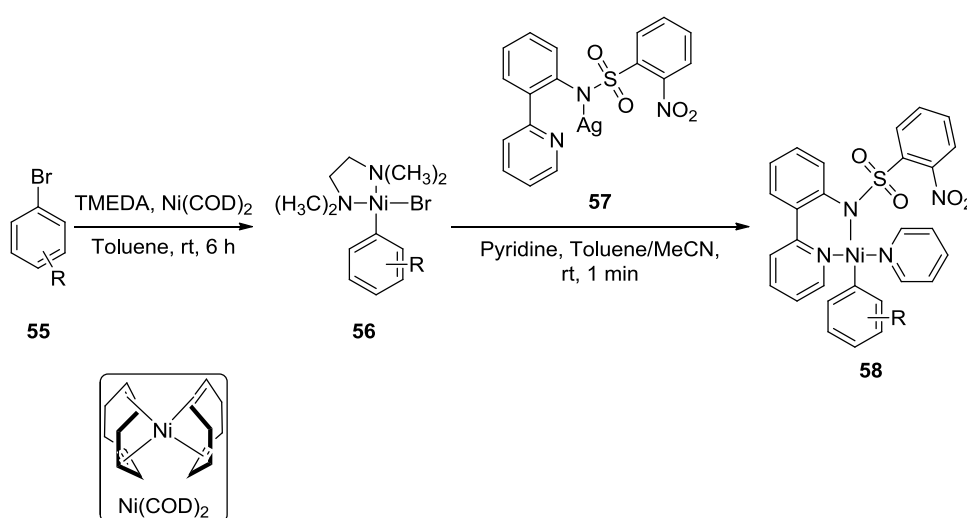
5.1.2.3 Other techniques.

More recently, Lee, Hooker, and Ritter (2012) developed nickel-mediated methodology that allowed for rapid (<1 minute) oxidative radiofluorination of arenes in the presence of aqueous ¹⁸F⁻ under mild conditions (Scheme 5.14). The ability to use the radioisotope in its solvated form eliminates the necessity for radiofluoride drying which allows for a shorter overall reaction time. Furthermore, this technique has a broad substrate scope and it can be utilised to perform [¹⁸F]-labelling of compounds that lack the necessary activation required for S_NAr.



Scheme 5.14. Nickel-mediated aromatic radiofluorination using aqueous ¹⁸F⁻ in the presence of the hypervalent iodine oxidant **54**.

The above described methodology relies on the use of the nickel organometallic precursor **58**, which can be accessed in two synthetic steps as shown in scheme 5.15. This synthesis involves the oxidative addition of an aryl bromide **55** and tetramethylethylenediamine (TMEDA) to commercially available bis(cyclooctadiene)nickel(0) ($\text{Ni}(\text{COD})_2$) resulting in the generation of intermediate **56**, followed by the introduction of silver salt **57** affording precursor **58**. Importantly, these organometallic complexes have been shown to be stable and can be stored under ambient conditions (Lee, Hooker, and Ritter, 2012).



Scheme 5.15. Synthesis of the nickel organometallic precursor **58** (Lee, Hooker, and Ritter, 2012).

However, the group identified two significant limitations of this technique. Firstly, the aqueous radiofluoride that is incorporated into the reaction must be highly concentrated as amounts of water greater than 1% of the reaction volume resulted in complete degradation of both the nickel complex and the oxidant species. Secondly, concentration of the aqueous radiofluoride using conventional drying techniques resulted in solutions that were too basic for efficient radiofluorination. As a consequence, these limitations severely restricted the amount of radiotracer that could be isolated (Ren *et al.*, 2014). In a follow-up study, Hooker and co-workers were able to improve the scale-up potential of this methodology by utilising a pH buffering system that sufficiently counteracted the increase in basicity during the drying process (Ren *et al.*,

2014). However, this radiofluorination methodology still suffered from the need to concentrate the aqueous $^{18}\text{F}^-$ to <1% of the reaction volume through drying.

5.1.3 Radiotracer purification and formulation.

During radiotracer discovery, great effort, time and resources are dedicated to ensure that the nuclear imaging agent exhibits high selectivity and/or specificity for its target. This is imperative in maximising the signal to noise ratio of the nuclear images that are acquired using the radiotracer (see chapter 4 for more information). Another factor that is important in maintaining a high signal to noise ratio is the radiochemical purity of the formulated tracer. Radiolabelling reactions can often lead to the formation of multiple labelled compounds due to the lack of regioselectivity of the chosen technique, the presence of multiple reactive functionalities on the precursor molecule, or degradation of the precursor/target molecule as a consequence of harsh reaction conditions. Contamination of the final radiotracer formulation by these side products can increase the background signal of the output image. Moreover, radiolabelling is rarely a quantitative process, meaning that at the end of the reaction free radionuclide atoms often remain. Removal of these prior to radiotracer formulation is important as they can also enhance background signal. For example, free $^{18}\text{F}^-$ is known to accumulate in bone tissue (Chitneni *et al.*, 2007) and free $^{131}\text{I}^-$ radioisotopes accumulate in the thyroid (Kaul and Roedler, 1980).

The main methods of radiotracer purification include solid phase extraction (SPE), preparative HPLC separation, or a mixture of the two. SPE involves the partitioning of solutes between a liquid phase (i.e. a solvent or mixture of solvents) and a solid (sorbent) phase, of which there are many different types (Żwir-Ferenc and Biziuk, 2006). The principle of purification using SPE relies on choosing the appropriate sorbent phase that will bind the desired radiolabelled product such that the impurities (i.e. the side product(s) and/or the free unbound radioisotope) can be washed away. The radiolabelled product can then be eluted from the sorbent by using an appropriate liquid phase (Figure 5.6).

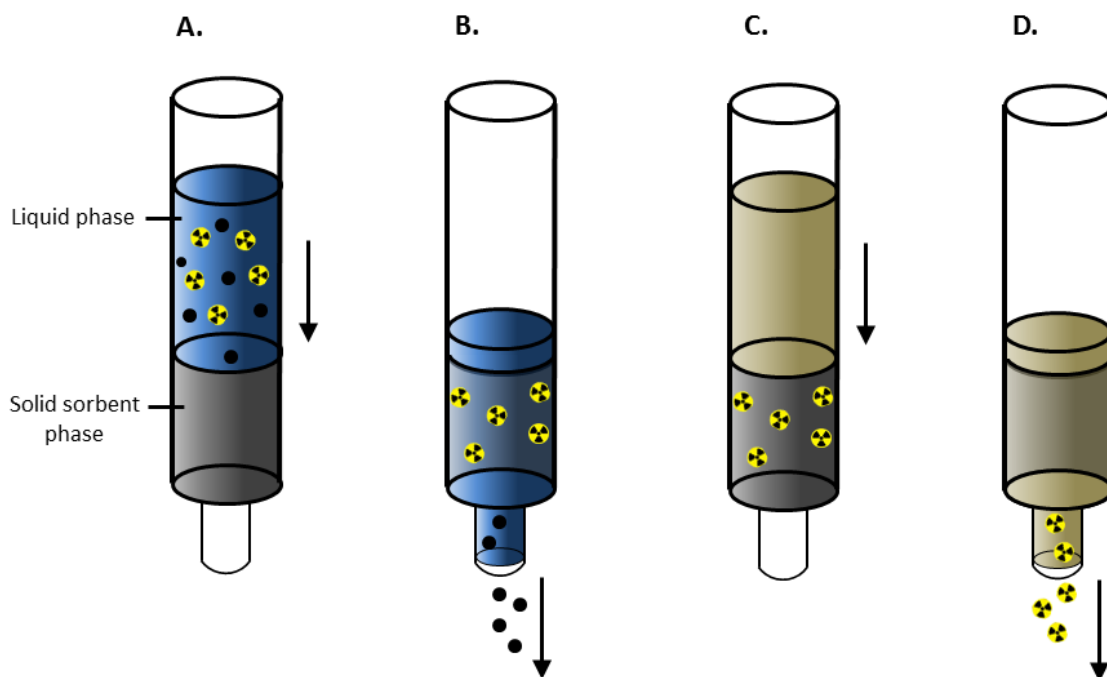


Figure 5.6. Diagrammatic representation of radiotracer purification using solid phase extraction (SPE). Crude radiotracer product is loaded onto a SPE cartridge in a suitable solvent mobile phase (A). The mixture is passed through a solid sorbent phase where the radiolabelled product is retained and impurities are removed (B). The mobile phase is changed and the pure radiotracer is eluted from the sorbent phase (C and D).

SPE is generally a rapid purification technique that is easy to automate making it a popular choice for tracers labelled with short-lived radioisotopes (Zheng and Mock, 2005). However, SPE is significantly limited by the fact that it can only separate compounds exhibiting large physiochemical differences (e.g. polarity). This issue can be overcome by utilising the slower HPLC technique, which has the ability to separate multiple radiolabelled products from the unlabelled precursor compound with only slight differences in physiochemical properties (Zheng and Mock, 2005) (Figure 5.7). The main disadvantages of this technique include the complexity associated with automation and increased purification times when compared to SPE (Pimlott and Sutherland, 2011).

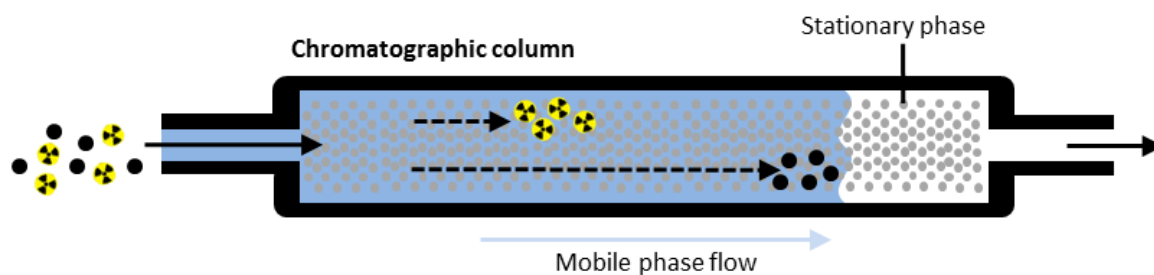


Figure 5.7. Diagrammatic representation of radiotracer purification using HPLC. Crude radiotracer product solubilised in a suitable solvent mobile phase is injected into a column packed with a solid stationary phase. Separation of the radiolabelled product from impurities is made possible by differences in affinity for the solid stationary phase.

It is also possible to perform a pre-purification using SPE to remove the free radionuclide, followed by HPLC purification to remove other undesirable components of the reaction mixture. However, this approach is not only time-consuming, but it also requires sample dilution prior to SPE and analyte elution. As a consequence, large volumes of the sample mixture may need to be injected onto the HPLC column which can result in poor separation (Chitneni *et al.*, 2007).

Following successful purification of the radiotracer, the final step of the radiosynthetic process is the formulation. For the purpose of this thesis formulation of radiotracers will be described in a pre-clinical context only with a focus on dosing mice. When developing a radiotracer formulation, a compromise must be reached between maximising the amount of radiolabelled compound that enters the solution and minimising the amount of additives (e.g. co-solvents or complexing agents) that are required to achieve this. Other considerations that can influence the final formulation include the stability of the radioligand, the maximum dose volume that can be administered to the animal, the viscosity of the solution, and the route of administration.

Intravenous injection is the most commonly used route for the administration of nuclear imaging agents (Kim *et al.* 2011). For that reason physiological saline (0.9% w/v sodium chloride) is the vehicle of choice for radiotracer compounds that exhibit high aqueous solubility. In a radiotracer suffers from poor aqueous

solubility, some form of solubility enhancement may be necessary. The most commonly used technique is co-solvency, which is both simple and inexpensive. It involves the addition of a water-miscible solvent (i.e. a co-solvent) in which the radiotracer is known to be soluble, such as ethanol, polyethylene glycol, propylene glycol, or dimethyl sulfoxide, (Vemula, Lagishetty and Lingala, 2010). The co-solvent reduces the interfacial tension between the aqueous solution and the solute molecule, thereby enhancing its aqueous solubility.

Another technique of solubility enhancement involves the addition of cyclodextrin excipients, which are cyclic oligosaccharide ring systems that contain a hydrophobic core and a hydrophilic exterior (Figure 5.8). Compounds exhibiting poor aqueous solubility complex with the lipophilic core of the cyclodextrin via hydrophobic interactions, and are subsequently taken into solution through hydrophilic interactions between the aqueous phase and the exterior surface of the cyclodextrin. Dissociation of compounds from cyclodextrins is generally a rapid, quantitative and predictable process (Vemula, Lagishetty and Lingala, 2010).

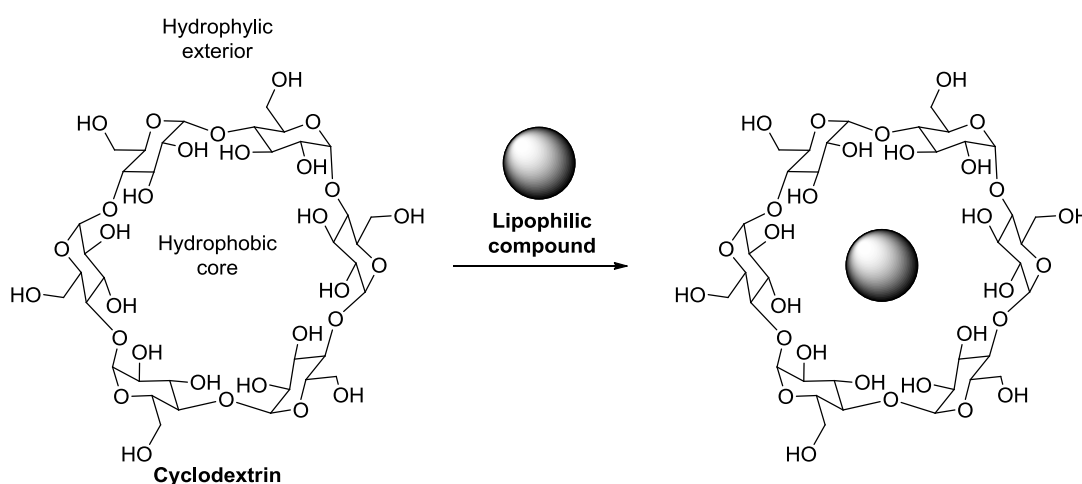


Figure 5.8. Diagrammatic representation of solubility enhancement using a cyclodextrin excipient.

There are two main disadvantages of using additives such as co-solvents and cyclodextrins as solubility enhancing agents. Firstly, a risk exists that the solubilised compound may precipitate upon dilution in the bloodstream following intravenous injection. Secondly, co-solvents and cyclodextrins are associated with toxicity issues. When administered orally, cyclodextrins are generally not

toxic as they do not enter systemic circulation due to lack of gastrointestinal absorption. However, it has been reported that most cyclodextrins are not suitable for intravenous administration due to toxicity, and only the γ -cyclodextrin variant together with some derivatives of β -cyclodextrins are appropriate for parenteral use (del Valle, 2004). Similarly, co-solvents also exhibit systemic toxicity and care has to be taken not to exceed established limits of tolerance (Thackaberry *et al.*, 2014). Moreover, the addition of solvents can have an effect on compound pharmacokinetics, meaning that the distribution and elimination properties of the formulated radiotracer may be altered (reviewed by Buggins, Dickinson and Taylor (2007)). Despite these issues, co-solvency remains the most widely accepted form of radiotracer solubility enhancement.

5.1.4 Aims and hypotheses.

The aim of the research presented in this chapter was to develop radioiodination and radiofluorination protocols that allow access to target radioligands with potential for SPECT and PET imaging of PARP-1 (Figure 5.9) in sufficient quantities, specific activities, purities, and formulations for pre-clinical *in vivo* studies in mice.

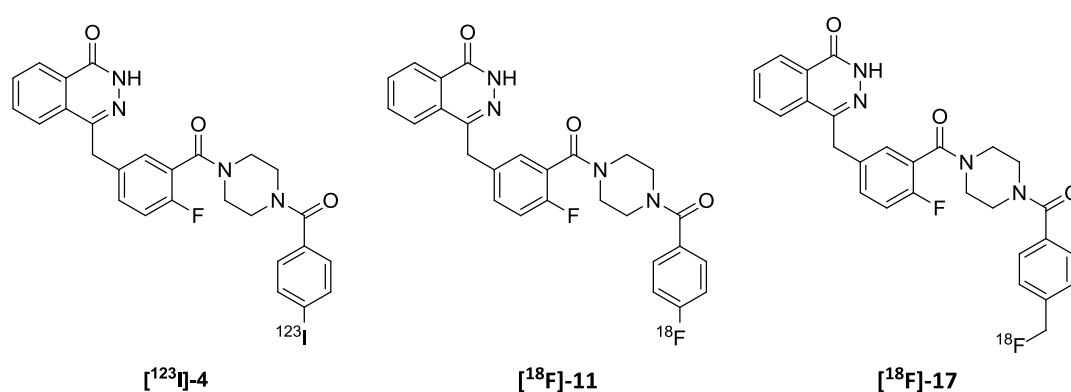


Figure 5.9. Target radioligands with potential for PARP-1 SPECT ([¹²³I]-4) and PET ([¹⁸F]-11 and [¹⁸F]-17) imaging.

The following hypotheses were set for this work:

i) Radiolabelling methodology will be developed that will allow for generation of target radioligands in sufficient quantities for *in vivo* pre-clinical studies; i.e. a radiochemical end of synthesis yield $\geq 5\%$. Practical aspects of pre-clinical work together with the designated limits of radioisotope quantities that can be handled manually (i.e. ≤ 500 MBq) were used to establish the required minimum end of synthesis yield.

ii) Purification methodologies will be developed that will allow for isolation of radiolabelled products with radiochemical purities of $>95\%$. This level of purity is generally regarded as sufficient for pre-clinical radiotracer use.

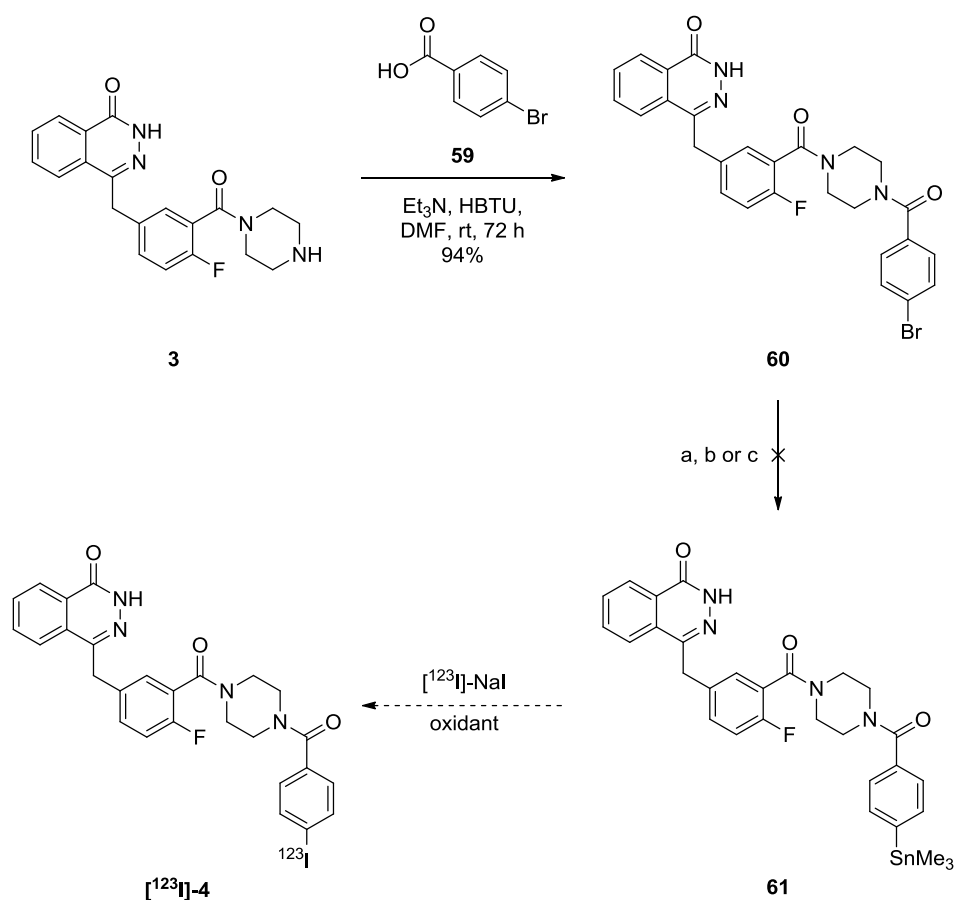
iii) Co-solvency techniques will allow for the formulation of the radiotracers into doses that can be injected intravenously into mice and the amount of solvent in each dose will not exceed established limits of tolerance (see publication by Thackaberry *et al.* (2014) for further information).

5.2 Results and discussion.

5.2.1 Radioiodination, purification, and formulation of target SPECT tracer [^{123}I]-4.

Electrophilic radioiodination using an organotin leaving group was initially investigated as a means of generating the target SPECT compound [^{123}I]-4. Despite high toxicity of the organotin materials, this methodology was chosen as it is generally associated with high radiochemical yields and good regioselectivity (see section 5.1.1.1 for details). Based on past experience within the research group and published literature methodologies (Tavares *et al.*, 2011; Rudebusch, Zakharov, and Liu, 2013), it was proposed that the organotin precursor (**61**) could be accessed from the corresponding aryl-bromide **60** using hexamethylditin (SnMe_3)₂ and a tetrakis(triphenylphosphine)palladium(0) ($\text{Pd}(\text{PPh}_3)_4$) catalyst (scheme 5.16). However, following a number of attempts,

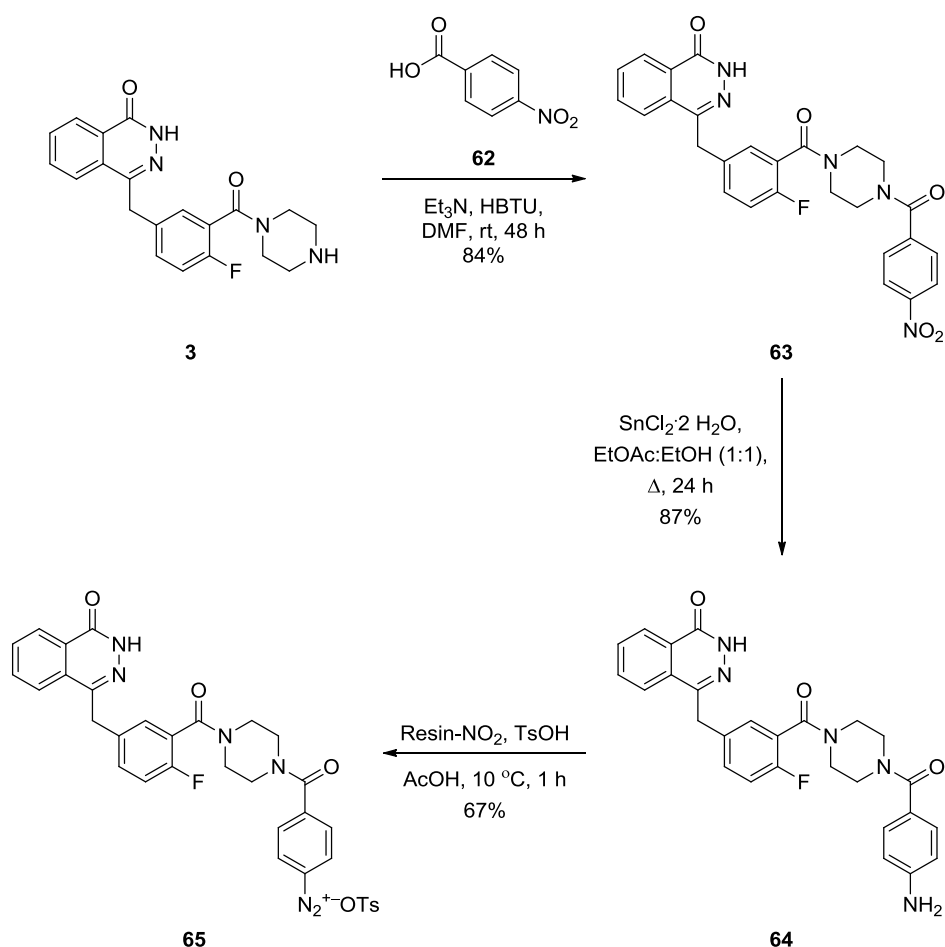
no stannylated precursor was observed, which was thought to be due to competing dehalogenation of the bromine-bearing aromatic ring.



Scheme 5.16. Proposed electrophilic destannylation technique to access the potential SPECT PARP-1 radiotracer $[^{123}\text{I}]\text{-4}$. Reagents and conditions: (a) $(\text{SnMe}_3)_2$, $\text{Pd}(\text{PPh}_3)_4$, 1,4-dioxane, 85 °C, 24 h; (b) $(\text{SnMe}_3)_2$, $\text{Pd}(\text{PPh}_3)_4$, 1,4-dioxane, 85 °C, 48 h; (c) $(\text{SnMe}_3)_2$, $\text{Pd}(\text{PPh}_3)_4$, 1,4-dioxane, 100 °C for 24 h.

Therefore, focus was shifted to nucleophilic techniques of radioiodination. Iodo-dediazonisation was investigated as a potential means of accessing $[^{123}\text{I}]\text{-4}$ due to the established nature of this chemistry (reviewed by SeEVERS and Counsell (1982) and the reported stability of diazonium tosylate salts ($-\text{N}_2^+\text{OTs}$) (Filimonov *et al.*, 2008). The diazonium tosylate salt precursor **65** was accessed in 49% yield over three linear steps from compound **3** (Scheme 5.17). HBTU amide coupling of **3** and commercially available 4-nitrobenzoic acid (**62**) afforded **63**, followed by tin(II) chloride reduction of the *para*-nitro group to generate the corresponding amine **64**. Aryldiazonium salt formation was then performed in the presence of resin-bound nitrite and tosic acid to generate precursor **65**. The

use of resin bound-nitrite was advantageous as it allowed for rapid purification of the aryldiazonium salt **65** via filtration.

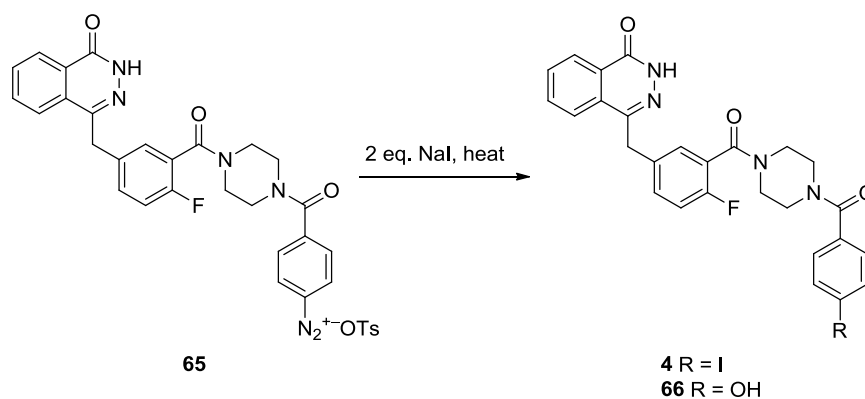


Scheme 5.17. Synthetic approach used to access the diazonium tosylate salt precursor **65**.

Despite previous literature reports confirming stability of diazonium tosylate salts (Filimonov *et al.*, 2008), salt **65** underwent complete degradation within 24 hours under ambient storage conditions. It was proposed that the degradation of salt **65** occurred through the hydroxylation of the diazonium moiety resulting in the corresponding phenol by-product. In order to establish the utility of salt **65** as a precursor of **4**, iodo-dediazonisation reaction conditions were screened using non-radioactive sodium iodide and **65** immediately post-isolation (Table 5.1). In an attempt to minimise the risk of hydroxylation, anhydrous N,N' -dimethylformamide was investigated as a potential solvent for this reaction (Entries 1 and 2). In both cases the major reaction product was thought to be phenol **66**; although it should be noted that increasing temperature to 75°C

resulted in a moderate improvement in the ratio of iodinated (**4**) to hydroxylated (**66**) products (Entries 1 and 2). Changing the solvent to acetic acid and further increasing the reaction temperature resulted in a marked improvement in the ratio of desired to undesired products (Entry 3).

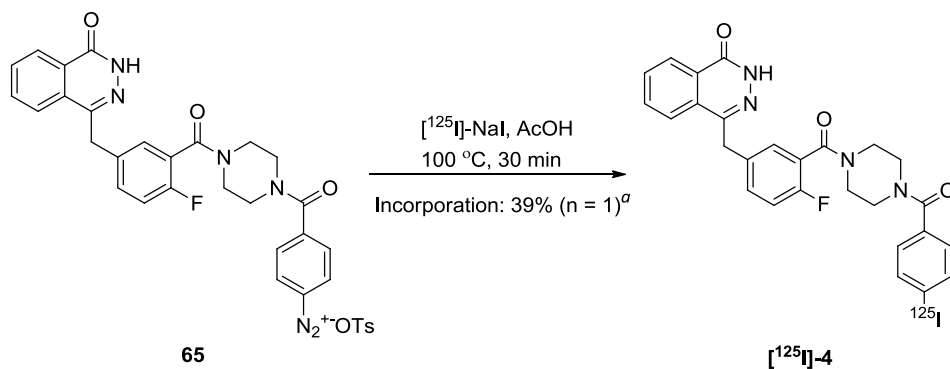
Table 5.1. Screen of conditions for non-radioactive iodo-dediazonisation of **65** for the synthesis of **4**.



Entry	Solvent	Temperature (°C)	Reaction time (h)	Ratio 4 : 66 ^a
1	DMF	rt	2.0	1.0 : 10.0
2	DMF	75	2.0	1.0 : 7.0
3	AcOH	100	1.0	1.0 : 1.4

^aThe ratio was calculated from the ¹H NMR spectrum (acquired using deuterated chloroform as the solvent) of the solid precipitate formed after trituration with diethyl ether using the iNMR 2.0.7 software. DMF = *N,N'*-dimethylformamide; AcOH = acetic acid.

A radioiodination trial was attempted using the long-lived ¹²⁵I isotope (half-life = 60.1 days), the isolated diazonium tosylate salt **65**, and reaction conditions similar to those described in table 5.1 entry 3 (Scheme 5.18). This approach allowed for a radioiodine incorporation yield of 39% (n = 1). It is clear from the radio-HPLC chromatogram that the reaction resulted in the generation of multiple radiolabelled products (Figure 5.10), possibly due to side reactivity and/or degradation of [¹²⁵I]-**4**.



Scheme 5.18. Generation of [¹²⁵I]-4 using radioiodo-dediazonisation methodology. ^aCalculated from the radio-HPLC chromatogram of the crude reaction mixture (Figure 5.10).

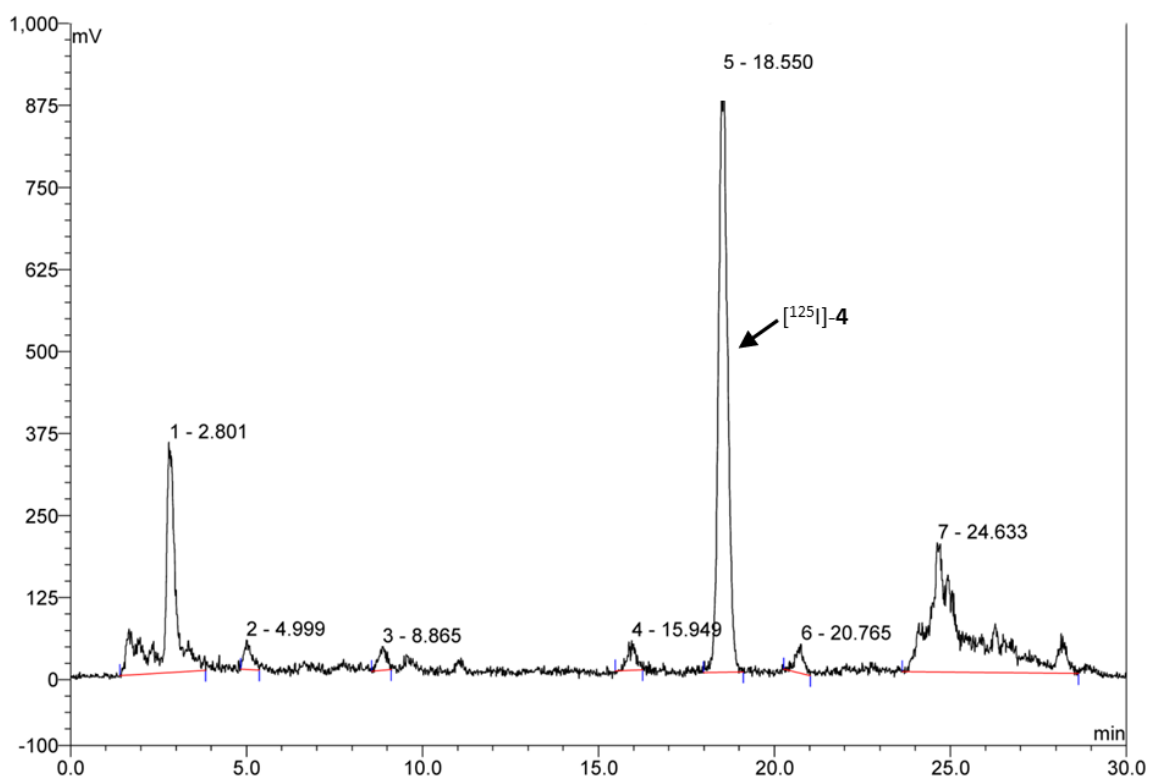
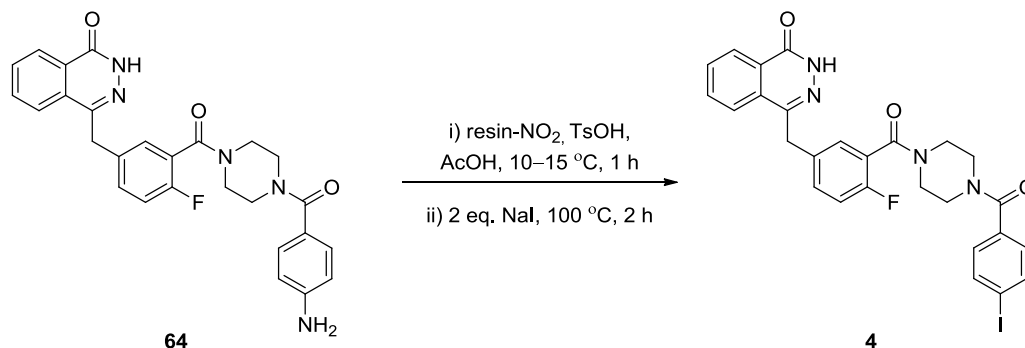


Figure 5.10. An analytical radio-HPLC chromatogram of the crude reaction mixture outlined in scheme 5.18 showing multiple side and degradation products, as well as ¹²⁵I-labelled **4**. The identity of [¹²⁵I]-**4** was confirmed by comparing the retention time of the radiolabelled (i.e. ¹²⁵I-bearing) product against the retention time of unlabelled (i.e. ¹²⁷I-bearing) **4** (Appendix 9.5).

Due to the lack of stability of precursor **65**, it was proposed that *in situ* diazonium salt formation would improve radioiodine incorporation yields. This

approach was initially investigated for non-radioactive iodination as outlined in Scheme 5.19. Analysing the crude reaction mixture by UV-HPLC (267 nm) (Figure 5.11) revealed that the desired iodinated product (**4**) was formed.



Scheme 5.19. Non-radioactive iodination of an *in situ* generated diazonium salt **65** giving access to **4**.

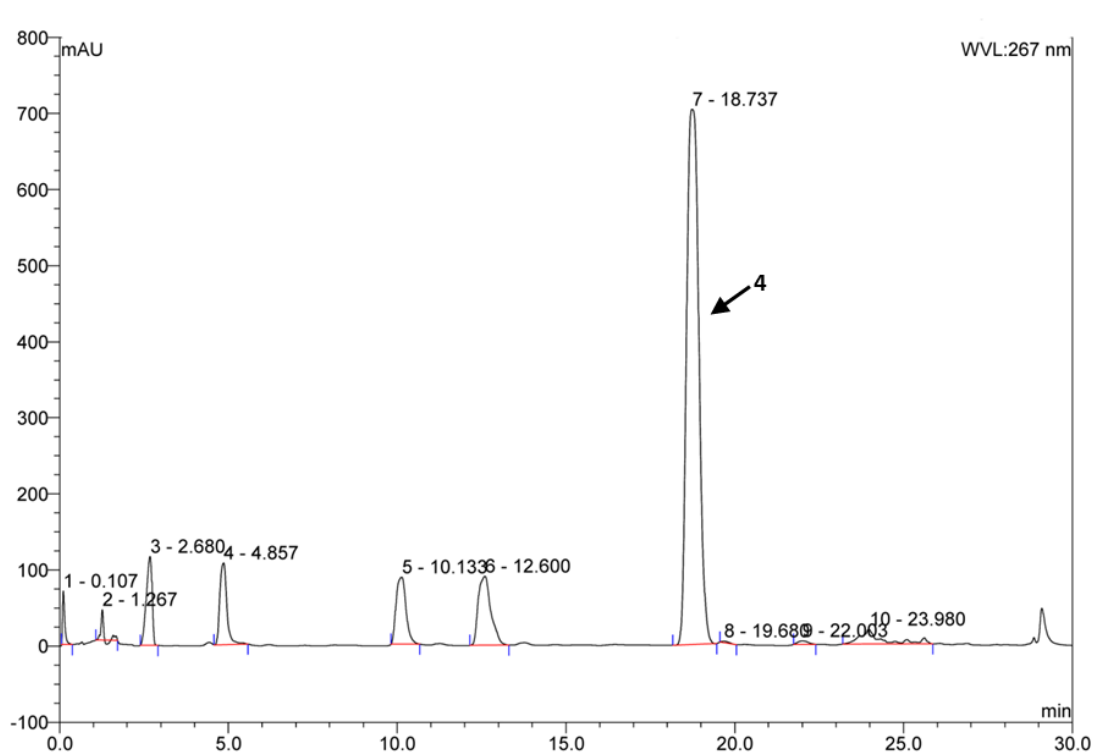
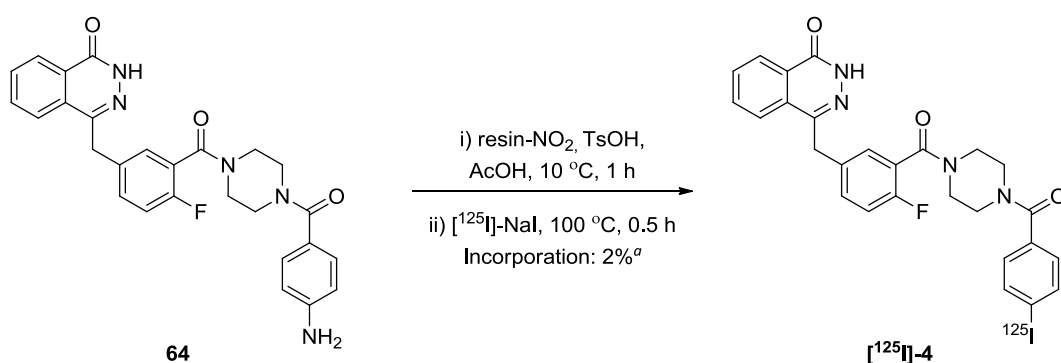


Figure 5.11. An analytical UV-HPLC (267 nm) chromatogram of the crude reaction mixture outlined in scheme 5.19. The identity of **4** in the reaction mixture was confirmed by comparing the retention time to that of **4** in a previously established UV-HPLC chromatogram using the same mobile phase conditions (Appendix 9.5).

However, under radiochemical conditions only 2% ^{125}I incorporation yield was observed (Scheme 5.20 and Figure 5.12). Stoichiometric differences between the radioactive and non-radioactive reactions could account for the low radioiodination yield. In the non-radioactive reaction (Scheme 5.19) the source of stable iodine was available in excess (i.e. two equivalents of NaI relative to **64**), while the ^{125}I -NaI in the radioactive reaction (Scheme 5.20) was available in amounts 10^5 fold less than the starting material **64** (i.e. 9.45×10^{-5} equivalents; calculated from the amount of ^{125}I -NaI used [3.62 MBq] and its specific activity [629 GBq/mg]).



Scheme 5.20. Radioiodination of an *in situ* generated diazonium salt **65** giving access to [^{125}I]-**4**. ^aCalculated from the radio-HPLC chromatogram of the crude reaction mixture (Figure 5.12).

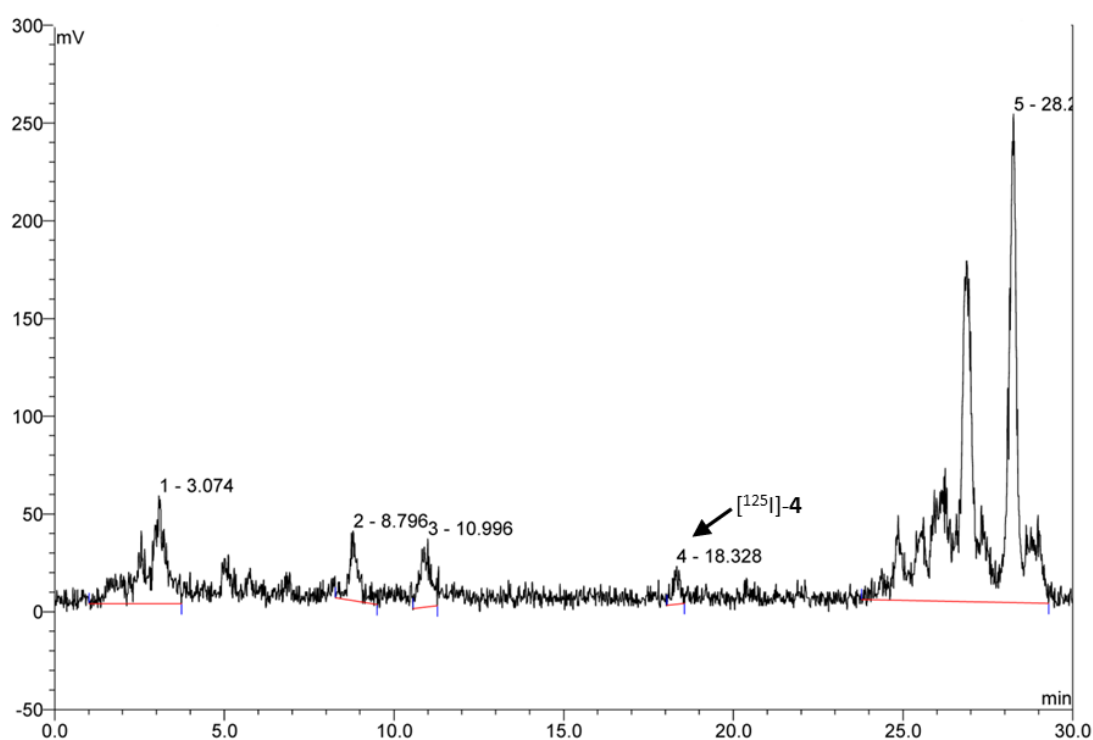


Figure 5.12. An analytical radio-HPLC chromatogram of the reaction mixture outlined in Scheme 5.20 following removal of resin-bound nitrite via filtration. The identity of $[^{125}\text{I}]\text{-4}$ was confirmed by comparing the retention time of the radiolabelled (i.e. ^{125}I -bearing) product against the retention time of unlabelled (i.e. ^{127}I -bearing) **4** (Appendix 9.5).

The radioiodo-dediazonisation methodology was not pursued further due to the instability of salt **65** and the underwhelming radioiodine incorporation yield obtained using the *in situ* synthesised salt. Overcoming the poor stability of salt **65** by its synthesis and purification immediately prior to radiolabelling would extend the duration of the overall radiosynthetic protocol, thereby introducing delays for *in vivo* applications.

Therefore, efforts were focused on investigating the interhalogen exchange approach (see section 5.1.1.2 for details) as a means of accessing the target SPECT tracer $[^{123}\text{I}]\text{-4}$. Halogen exchange of aromatic chlorine, bromine, and iodine functionalities have been reported in the literature as ways of generating radioiodinated versions of TSPO ligand PK11195 (Table 5.2) (Gildersleeve *et al.*, 1989; Gildersleeve *et al.*, 1996; Pimlott *et al.*, 2008).

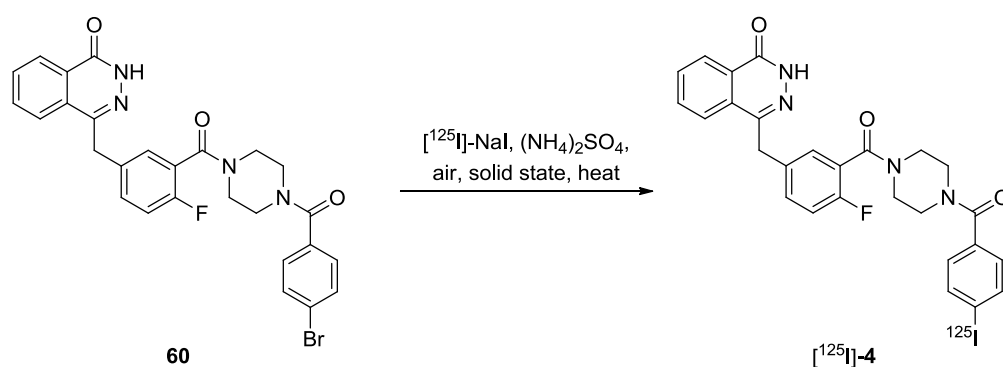
Table 5.2. Summary of published halogen exchange radioiodination reactions for the labelling of TSPO ligand PK11195.

Entry	Precursor	Radioisotope	Isolated radiochemical yield (%)	Specific activity (Ci/ μ mol)
1 ^a	(Cl)-PK11195	¹²⁵ I	10–20	0.015–0.017
2 ^b	I-PK11195	¹²³ I	>60	0.233–0.348
3 ^c	Br-PK11195	¹²³ I	41 \pm 11 (n = 2)	1.9 \pm 0.7 (n = 2)

^aGildersleeve *et al.*, 1989; ^bGildersleeve *et al.*, 1996; ^cPimlott *et al.*, 2008.

It is clear from table 5.2 that the brominated precursor allowed access to the radioiodinated compound in the highest specific activity and in good end of synthesis radiochemical yield (Entry 3). Based on these data, the previously synthesised brominated analogue of olaparib **60** (Scheme 5.16) was chosen as a candidate for solid state interhalogen exchange with the long lived ¹²⁵I radioisotope (Table 5.3). The initial set of reaction conditions that were investigated were based on those described by Gildersleeve *et al.* (1996) and allowed for an ¹²⁵I incorporation yield of 38% (n = 1) (Table 5.3, Entry 1). Incremental increases in reaction temperature and time resulted in improved yields of 78% (n = 1) (Entry 2) and 90% (n = 1) (Entry 3) respectively, while removal of air from the reaction led to a marked reduction in percentage radionuclide incorporation (Entry 4). The latter observation can be explained by the fact that a mildly oxidising environment is necessary for efficient solid state aromatic halogen exchange to take place (Mangner, Wu, and Wieland, 1982). In addition to an excellent radioiodide incorporation yield, the interhalogen exchange methodology proceeded efficiently without the formation of side or degradation products (Figure 5.13).

Table 5.3. Investigation and optimisation of solid state interhalogen exchange radioiodination methodology for the synthesis of [^{125}I]-4 using the brominated precursor **60**.



Entry	Air injection	Temperature (°C)	Reaction time (min)	Radioisotope incorporation (%) ^a
1	Yes	150	20	37
2	Yes	180	30	78
3	Yes	210	30	90
4	No	210	30	67

^aCalculated from analytical radio-HPLC chromatograms obtained from crude reaction mixtures.

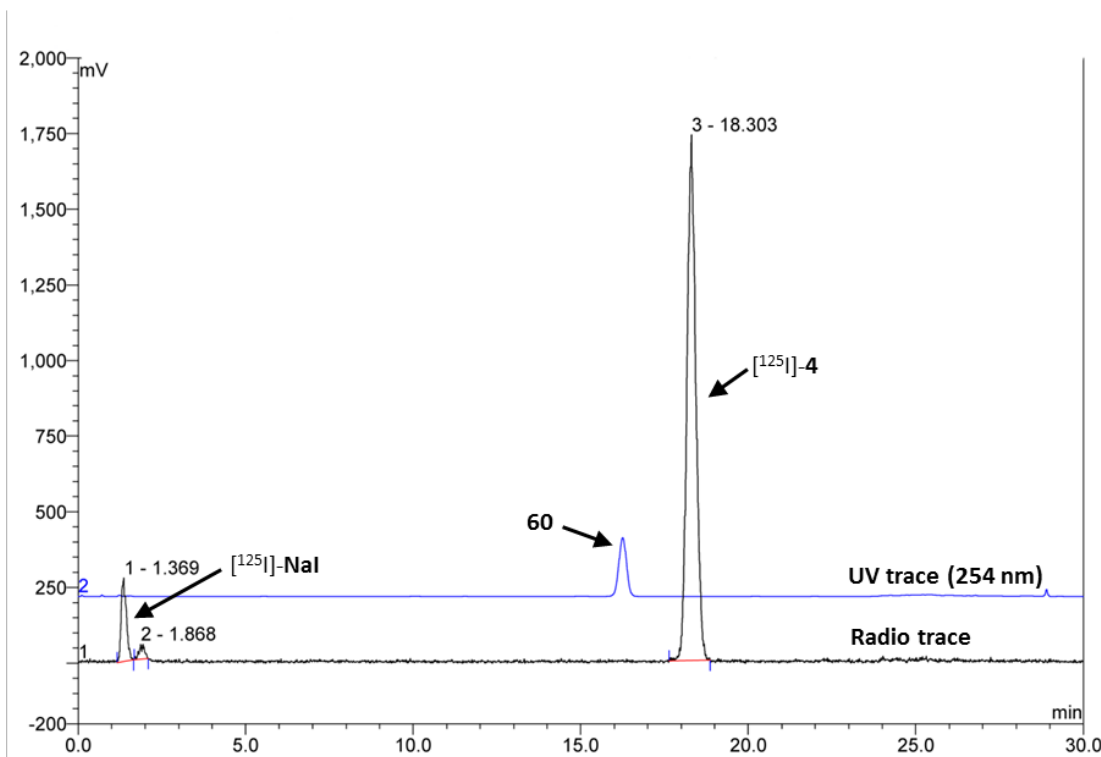
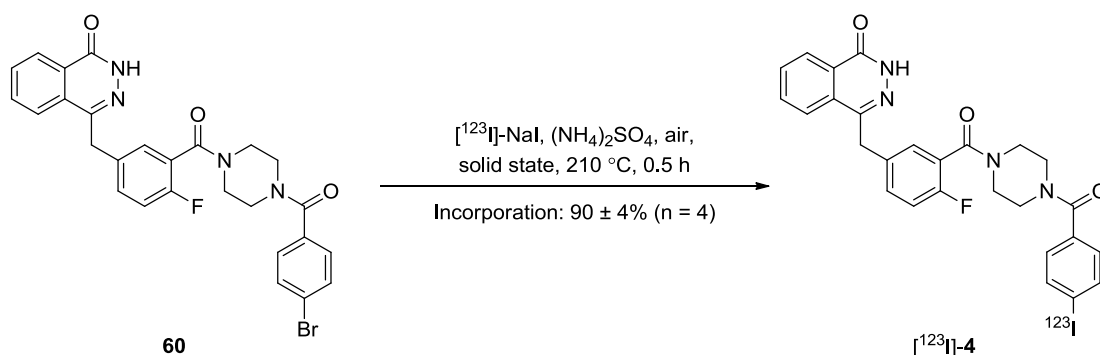


Figure 5.13. An analytical UV (254 nm)/radio-HPLC chromatogram of the crude reaction mixture outlined in table 5.3 entry 3 showing unreacted $[^{125}\text{I}]\text{-NaI}$ and precursor compound **60**, as well as ^{125}I -labelled **4**. The identity of $[^{125}\text{I}]\text{-4}$ was confirmed by comparing the retention time of the radiolabelled (i.e. ^{125}I -bearing) product against the retention time of unlabelled (i.e. ^{127}I -bearing) **4** (Appendix 9.5).

The conditions described in entry 3 (Table 5.3) were identified as optimal and were used for ^{123}I -radiolabelling to generate the potential PARP-1 SPECT imaging agent $[^{123}\text{I}]\text{-4}$ (Scheme 5.21). The methodology exhibited good reproducibility with a radioiodide incorporation yield of $90 \pm 4\%$ ($n = 4$) (measured using a preparatory-HPLC system).



Scheme 5.21. Optimised solid state interhalogen exchange radioiodination methodology for the synthesis of the potential PARP-1 SPECT imaging agent [^{123}I]-4 using the brominated precursor **60**.

As mentioned earlier (section 5.1.1.2), one of the disadvantages of interhalogen exchange radiolabelling is the potential difficulty associated with separating the radiolabelled product from the precursor compound. With this in mind, HPLC equipment was chosen for the purpose of radiotracer purification as the technique has the ability to separate compounds with small differences in polarities (see section 5.1.3 for details). Initial HPLC purification methodology development involved utilising a preparatory reverse-phase C_{18} column and screening a number of HPLC mobile phase gradient conditions (comprising of acetonitrile and distilled water) for their ability to separate a mixture of unlabelled (^{127}I -bearing) **4** and **60**. Mobile phase gradient conditions outlined in Figure 5.14 were identified as optimal as they allowed for adequate separation between the two compounds with a resolution of 2.14 (calculated from the corresponding UV-HPLC chromatogram), where a resolution of >1.5 is indicative of complete baseline peak separation (Appendix 9.6).

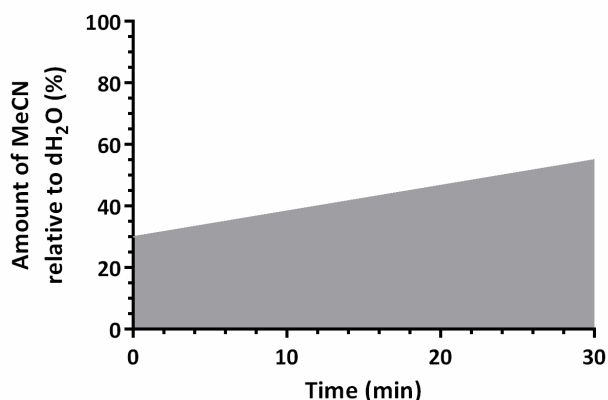


Figure 5.14. Optimal mobile phase preparatory HPLC gradient conditions used for purification of [^{123}I]-4 synthesised using aromatic solid state interhalogen exchange methodology. MeCN = acetonitrile; dH₂O = distilled water.

Application of the above described HPLC purification methodology to the ^{123}I interhalogen exchange radiolabelling protocol allowed for the isolation of [^{123}I]-4 in excellent radiochemical purity (>99%; n = 6) (Figure 5.15), which is in accordance with the earlier set hypothesis. It is generally accepted that radiochemical purity of >95% is sufficient for pre-clinical nuclear imaging purposes. This stems from the fact that a high degree of radiochemical purity is important in minimising off-target binding and maximising the target signal to noise ratio (see section 5.1.3 for details).

As hypothesised, [^{123}I]-4 was generated in high specific activity ($>19.0 \pm 10.3$ Ci/ μmol ; n = 4), which is important in minimising the molar amount of compound that needs to be administered for *in vivo* applications (see section 5.1 for details). The specific activity was calculated from the UV-HPLC chromatogram obtained during the radiotracer purification step and with the aid of a UV calibration plot acquired using non-labelled (^{127}I -bearing) 4 (Appendix 9.7). Since the amount of [^{123}I]-4 that was produced fell below the sensitivity threshold of the UV detector for this particular compound ($<1.68 \times 10^{-4}$ μmol), an absolute value for the specific activity could not be calculated.

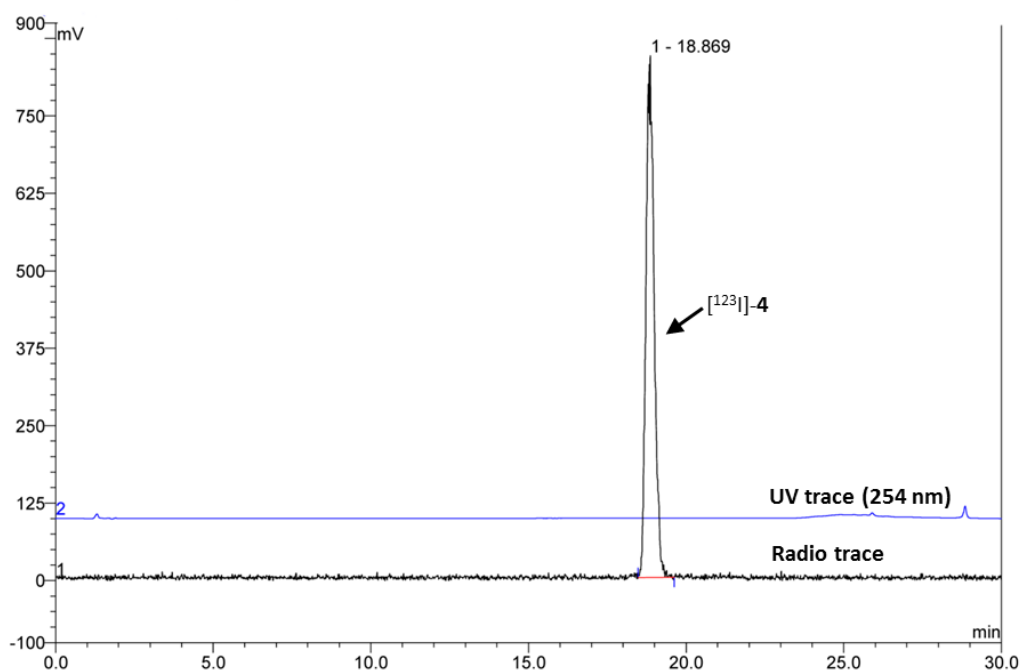
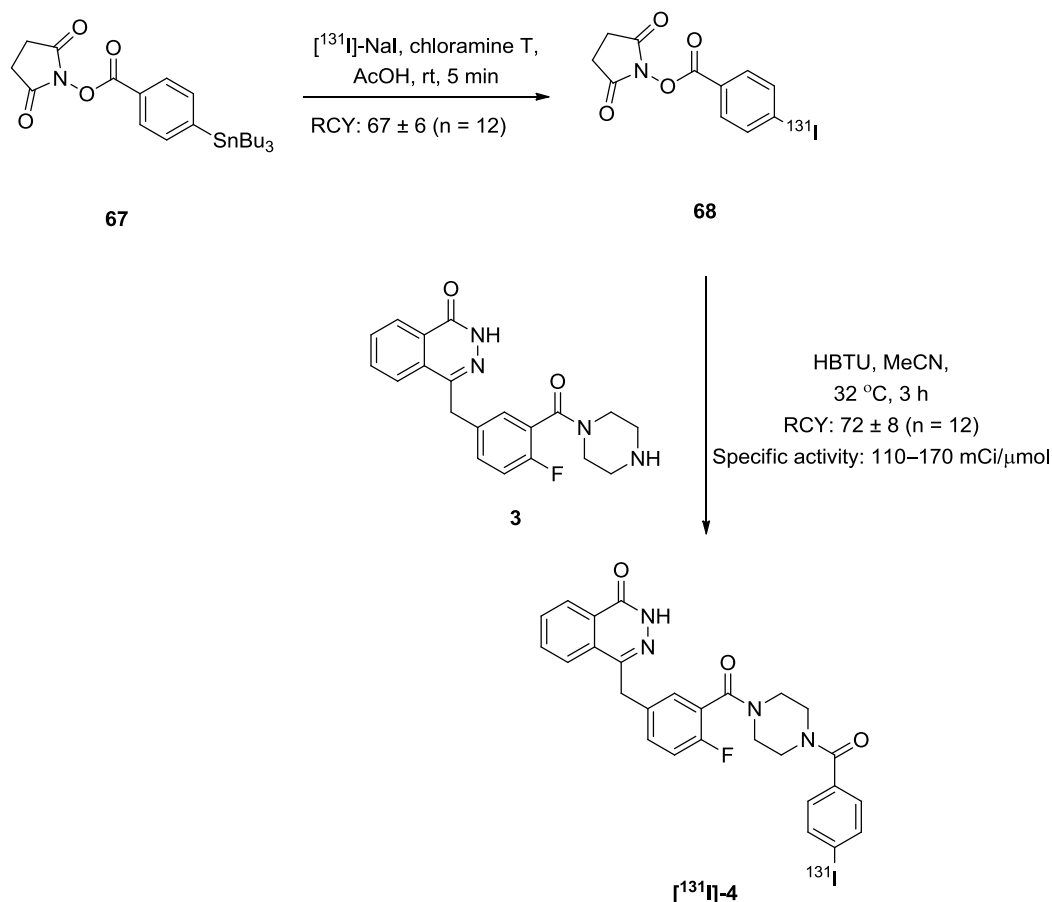


Figure 5.15. An analytical quality control UV (254 nm)/radio-HPLC chromatogram of $[^{123}\text{I}]\text{-4}$ showing >99% radiochemical purity of the radiotracer formulated in 10.0% v/v ethanol in 0.9% w/v saline. The identity of $[^{123}\text{I}]\text{-4}$ was confirmed by comparing the retention time of the radiolabelled (i.e. ^{123}I -bearing) product against the retention time of unlabelled (i.e. ^{127}I -bearing) **4** (Appendix 9.5).

The final step of the radiosynthesis process was radioligand formulation. As described earlier, the aim of this research was to develop radioligands for pre-clinical *in vivo* evaluation in mice. With this in mind, physiological saline (0.9% sodium chloride) was chosen as the formulation vehicle for $[^{123}\text{I}]\text{-4}$. However, due to poor aqueous solubility of **4**, ethanol co-solvency was utilised as a solubility enhancement technique. Based on the recommended dose limits of solvents administered intravenously to CD1 nude mice (Thackaberry *et al.*, 2014), it was decided that the final concentration of ethanol in the formulation would equate 10%. This concentration has been reported to cause only minor hyperactivity in mice compared to mild ataxia observed with higher amounts of ethanol (Thackaberry *et al.*, 2014). Formulation of $[^{123}\text{I}]\text{-4}$ in a solution of 10.0% ethanol in 0.9% saline allowed for an end of synthesis yield of $37 \pm 7\%$ ($n = 6$).

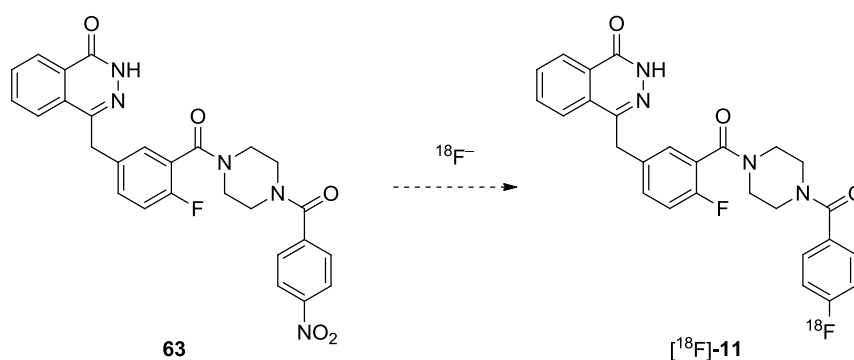
It is important to note that, since commencing this work, Salinas *et al.* (2015) developed a [^{131}I]-labelled version of compound **4** via the methodology depicted in Scheme 5.22. The authors utilised an early-stage labelling synthesis where an *N*-succinimidyl-4-(tributylstannyl) benzoate (**67**) precursor was initially radioiodinated in the presence of the oxidant chloramine T, followed by amide coupling of the labelled intermediate **68** with the phthalazinone **3** to afford [^{131}I]-**4**. The radiochemical yield of this synthesis was approximately 48% over the two reaction steps; the authors did not report an end of synthesis yield. The two key disadvantages of this radiosynthesis were the use of the highly toxic stannylated precursor **67** and the early-stage radioiodination, which increases the overall radiosynthesis time.



Scheme 5.22. Radioiodination approach used by Salinas *et al.* (2015) for the synthesis of [^{131}I]-**4**.

5.2.2 Radiofluorination of the target PET tracer [¹⁸F]-11.

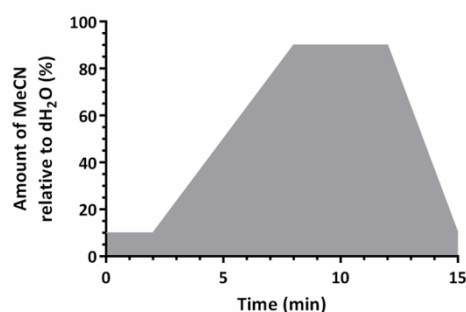
As described previously (section 5.1.2.1), direct electrophilic radiofluorination can be associated with poor regioselectivity and low specific activity of the labelled tracer. These issues can be overcome with electrophilic exchange methodology, which requires the use of organometal precursors that are synthesised using highly toxic organometal starting materials (see section 5.1.1.1 for details). However, since the stannylated compound **61** (Scheme 5.16) was not accessible, efforts were focused on S_NAr methodology as a means of synthesising [¹⁸F]-**11**. Nucleophilic substitution offers the same advantages of high regioselectivity and good specific activity as electrophilic exchange radiofluorination, with the addition of reduced toxicity issues. It was envisaged that the *para* positioned nitro group of compound **63** would act as a sufficient leaving group to allow for radiofluoride nucleophilic attack at the *ipso* position (Scheme 5.23). Despite only weak electron withdrawing properties of the amide functionality positioned *para* to the leaving group in compound **63**, the approach was justified by the fact that Yamasaki *et al.* (2011) were able to utilise an aryl-nitro leaving group with a *para*-positioned amide for ¹⁸F-labelling of the metabotropic glutamate receptor 1 ligand FITM. The authors did not report an end of synthesis yield but state that they were able to produce and formulate between 429–936 MBq of the tracer from 6.7–13.0 GBq of ¹⁸F⁻ (n = 8) (Yamasaki *et al.*, 2011).



Scheme 5.23. Proposed aromatic nucleophilic substitution radiofluorination approach for the synthesis of [¹⁸F]-**11** using the nitro bearing precursor **63**.

The small difference in hydrophobicity constants between the nitrite functionality and the fluorine atom (Hashizume *et al.*, 1997) could make separation of precursor **63** from the radiolabelled product ($[^{18}\text{F}]\text{-11}$) difficult during the tracer purification process. To investigate this, the retention times of the nitro compound **63** and non-radioactive **11** were measured on an analytical reverse-phase C_{18} HPLC column using a six minute gradient of increasing acetonitrile concentration relative to water (Figure 5.16). The difference between the retention times of these two compounds was just 0.05 minutes, suggesting poor separation under these chromatographic conditions.

A.



B.

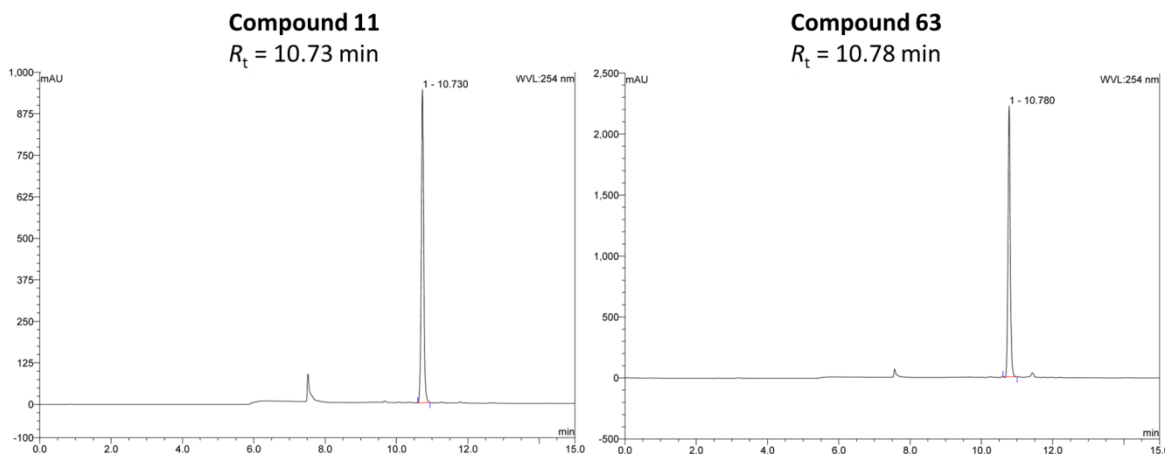


Figure 5.16. The chromatographic gradient used to measure the retention times (R_t) of compounds **11** and **63** on an analytical reverse-phase C_{18} column (A) and the corresponding UV-HPLC (254 nm) chromatograms (B). MeCN = acetonitrile; dH₂O = distilled water.

In an effort to improve the chromatographic resolution between **11** and **63**, mobile phase conditions were screened using the same analytical HPLC system and a mixture of **11** and **63** as the analyte (Figure 5.17). It is clear from figure 5.17 that slowing down the mobile phase gradient of acetonitrile concentration

was associated with an increase in resolution. By implementing a slow twenty minute mobile phase gradient a resolution of 1.54 was achieved between the UV peaks of the two compounds (Figure 5.17 C), where a resolution of >1.50 is indicative of complete baseline peak resolution.

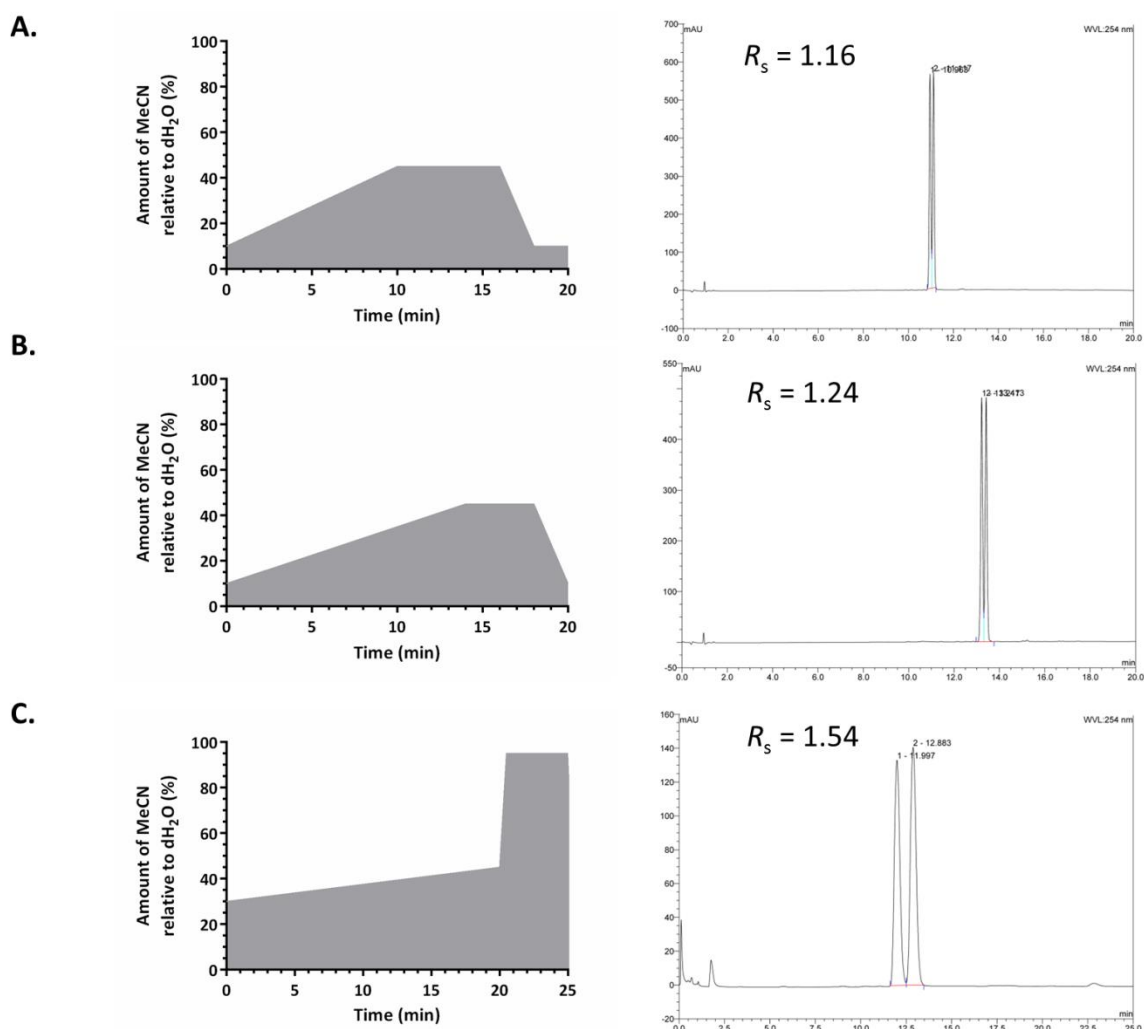
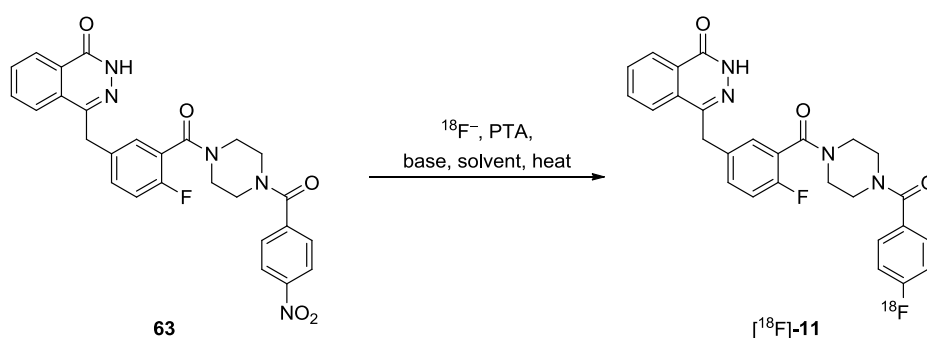


Figure 5.17. Chromatographic gradients used to separate a mixture of compounds **11** and **63** on an analytical reverse-phase C₁₈ column and the corresponding UV-HPLC (254 nm) chromatograms. MeCN = acetonitrile; dH₂O = distilled water; R_s = resolution.

With the principle of chromatographic separation between **11** and **63** confirmed, focus was directed at developing S_NAr radiofluorination methodology for the synthesis of [¹⁸F]-**11**. Screening of radiofluorination conditions is a complex process due the large amount of variables that require investigation (i.e. type of solvent or solvent mixtures; type and amount of phase transfer agent; type and

amount of base; reaction temperature; and reaction time). Initial attempts involved using *N,N'*-dimethylformamide, K_{222} , and potassium carbonate as the solvent, phase transfer agent, and base respectively (Table 5.4, Entries 1 and 2). An increase in temperature from 150 °C to 180 °C improved the radionuclide incorporation yields from 4% to 6% and 5% to 10% at 15 and 30 minute reaction timepoints, respectively. Replacing the solvent with dimethyl sulfoxide resulted in accelerated precursor degradation (data not shown) and only 1% radiofluoride incorporation into the desired product (Entry 3). However, utilising *N*-methyl-2-pyrrolidone allowed for a radiofluoride incorporation of 7% after just 15 minutes at 150 °C (Entry 4a). Increasing the reaction temperature to 180 °C and time to 30 minutes resulted in a marked improvement in radiolabelling with 19% $^{18}\text{F}^-$ incorporation (Table 5.4, Entry 5b; Figure 5.18). A further 20 °C rise in temperature improved the radioincorporation yield at 10 minutes from 14% (Entry 5a) to 17% (Entry 6a). However, this temperature increase was also associated with accelerated thermal degradation of both the precursor and radiolabelled compound (data not shown) resulting in a slight reduction in radionuclide incorporation into the desired product after 30 minutes (Entry 6b), when compared to the reaction performed at 180 °C (Entry 5b). Interestingly, utilising a 1.0 : 1.0 mixture of *N*-methyl-2-pyrrolidone and acetonitrile resulted in a 12.2% radiofluoride incorporation yield after a 15 minute reaction at 150 °C (Entry 7a), compared to only 7% when *N*-methyl-2-pyrrolidone was used alone (Entry 4a). Since the boiling point of acetonitrile is approximately 82 °C, it was thought that the build-up of back-pressure in the sealed reaction vial due to gaseous acetonitrile had a facilitatory effect on the radiofluorination yield. Replacing K_{222} with either TBAHCO_3 or caesium carbonate resulted in low ^{18}F incorporation yields of 3% and 5% after 15 minute reactions at 150 °C (Entries 8 and 9). The poor yield achieved with TBAHCO_3 was due to accelerated degradation of precursor and radiolabelled compounds.

Table 5.4. Investigation and optimisation of aromatic nucleophilic substitution radiofluorination methodology for the synthesis of [^{18}F]-11 using the nitro bearing precursor **63**.



Entry	Solvent	PTA	Base	Temperature (°C)	Reaction time (min.)	Radioisotope incorporation (%) ^a
1a	DMF	K ₂₂₂	K ₂ CO ₃	150	15	4
1b					30	5
2a	DMF	K ₂₂₂	K ₂ CO ₃	180	10	6
2b					30	10
3	DMSO	K ₂₂₂	K ₂ CO ₃	180	10	1
4a	NMP	K ₂₂₂	K ₂ CO ₃	150	15	7
4b					30	7
5a	NMP	K ₂₂₂	K ₂ CO ₃	180	10	14
5b					30	19
6a	NMP	K ₂₂₂	K ₂ CO ₃	200	10	17
6b					30	18
7a	NMP:MeCN (1.0 : 1.0)	K ₂₂₂	K ₂ CO ₃	150	15	12
7b					30	13
8	NMP:MeCN (1.0 : 1.0)	TBAHCO ₃	–	150	15	3
9	NMP	–	Cs ₂ CO ₃		15	5

^aCalculated from analytical radio-HPLC chromatograms obtained from crude reaction mixtures. DMF = *N,N'*-dimethylformamide; DMSO = dimethyl sulfoxide; NMP = *N*-methyl-2-pyrrolidone; MeCN = acetonitrile; PTA = phase transfer agent; K₂₂₂ = Kryptofix[®]; TBAHCO₃ = tetra-*n*-butylammonium hydrogen carbonate.

It was thought that this degradation was driven by the increased amount of base (hydrogen carbonate) in the reaction where the phase transfer agent (TBA⁺) to

base ratio was 1.0 : 1.0, versus a phase transfer agent (K_{222}) to base ratio (potassium carbonate) of 1.0 : 0.1 in previous entries. Further justification for this is provided by the fact that increasing the K_{222} to potassium carbonate ratio from 1.0 : 0.1 to 1.0 : 0.4 was also associated with increased precursor and product degradation, and subsequently reduced ^{18}F incorporation yields (data not shown). Moreover, a similar observation was made by Yamasaki *et al.* (2011) who reported that lowering the concentration of potassium carbonate reduced precursor degradation in their radiosynthesis. Low radionuclide incorporation observed with caesium carbonate can be explained by the weak phase transfer properties of caesium due to poor solubility in the reaction solvent.

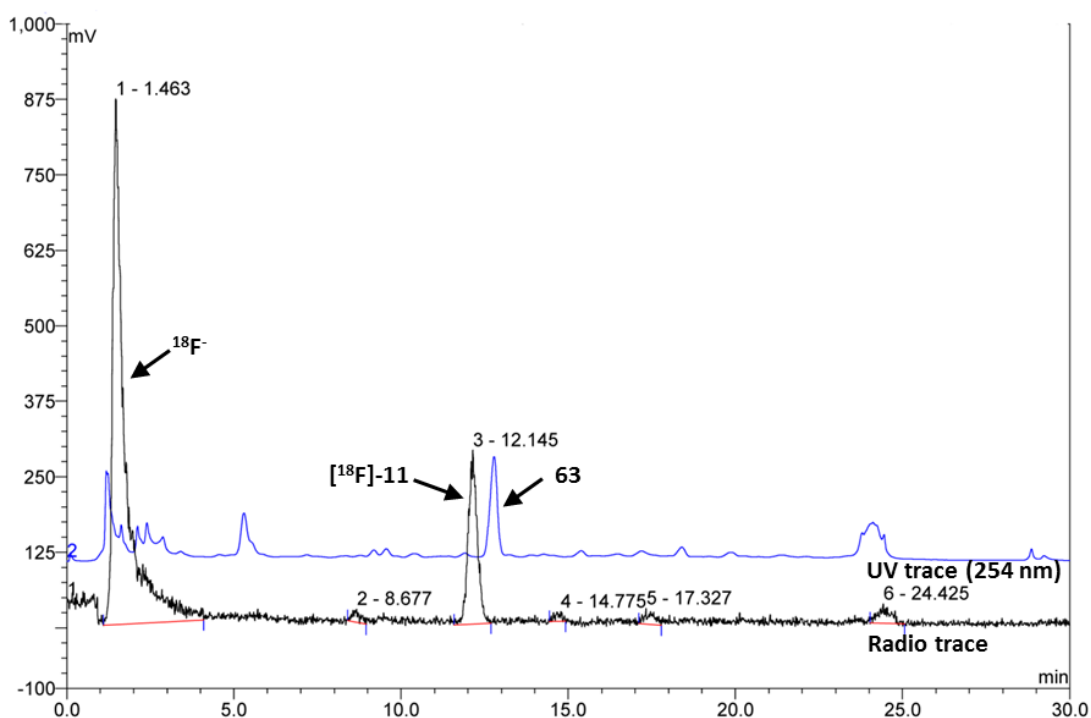
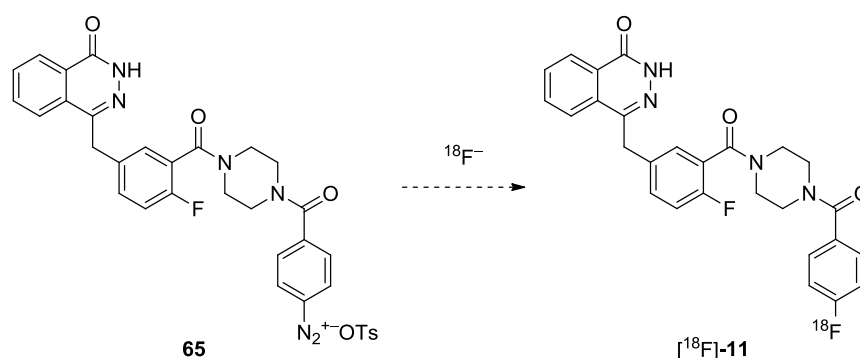


Figure 5.18. An analytical UV (254 nm)/radio-HPLC chromatogram of the crude reaction mixture outlined in table 5.4, entry 5b showing unreacted $^{18}\text{F}^-$ and precursor compound **63**, as well as ^{18}F -labelled **11**. The identity of ^{18}F -**11** was confirmed by comparing the retention time of the radiolabelled (i.e. ^{18}F -bearing) product against the retention time of unlabelled (i.e. ^{19}F -bearing) **11** (Figure 5.17 C).

Despite a thorough screen of reaction conditions, the $\text{S}_{\text{N}}\text{Ar}$ approach utilising the nitro precursor **63** afforded the radiolabelled compound (^{18}F -**11**) in low yields

with a maximum 19% radiofluoride incorporation (Table 5.4, Entry 5b), which was not sufficient for pre-clinical imaging applications. This is because manual synthesis of [^{18}F]-11 was restricted to 500 MBq of starting radioactivity ($^{18}\text{F}^-$) in order to minimise operator dosimetry. Consequently, sufficient amounts of [^{18}F]-11 for *in vivo* investigations would not be attainable. Furthermore, when considering potential future clinical applications, the radiosynthetic protocol should be optimised such that it will allow the maximum output of radiotracer from a single production batch of $^{18}\text{F}^-$ radionuclide. This is important in minimising cost and maximising the number of patients that could be scanned using the radiotracer in a single day. It is likely the poor radiofluoride incorporation yields were a consequence of the lack of activation of the system for $\text{S}_{\text{N}}\text{Ar}$ due to weak electron withdrawing properties of the amide functionality *para* to the nitro leaving group. In light of the above limitations, an alternative approach to produce sufficient quantities of [^{18}F]-11 was sought.

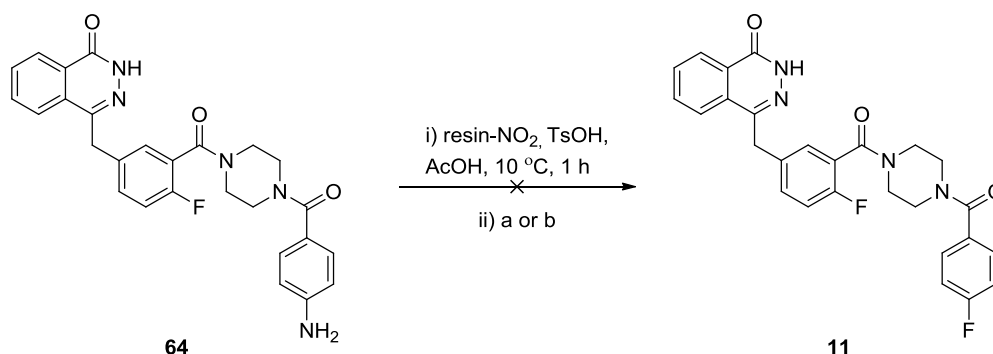
The diazonium functionality is known to be an excellent leaving group, exhibiting better leaving potential than nitro and trialkyl ammonium groups. Therefore, it was proposed that a diazonium bearing precursor (**65**) (Scheme 5.24) would allow for better ^{18}F $\text{S}_{\text{N}}\text{Ar}$ incorporation yields when compared to the above described methodology using precursor **63**.



Scheme 5.24. Proposed aromatic nucleophilic substitution radiofluorination approach for the synthesis of [^{18}F]-11 using the aromatic diazonium salt precursor **65**.

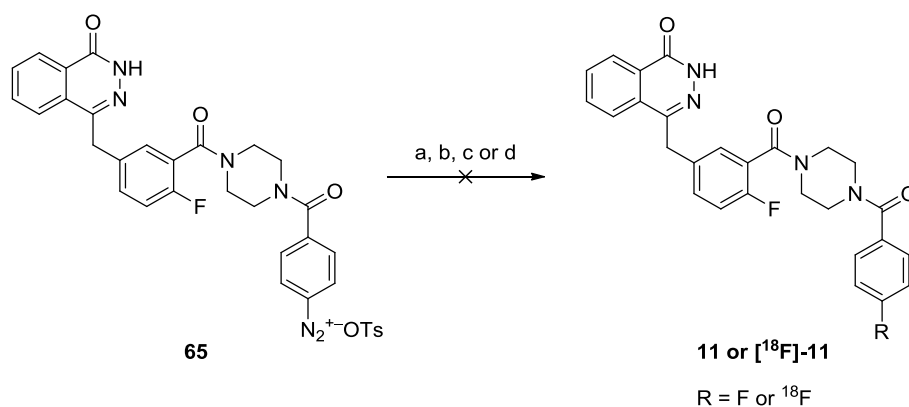
Initial efforts utilising this approach as a means of fluorination involved generating the diazonium salt **65** *in situ*, followed by non-radioactive fluorination in the presence or absence of a phase transfer agent (Scheme 5.25).

In the previous section, this approach was successfully utilised for non-radioactive aromatic iodination (Scheme 5.19). However, the desired product **11** was not detectable on UV-HPLC (254 nm) analysis of the crude reaction mixtures (data not shown). HPLC based analysis was chosen as interpretation of ^1H NMR spectra proved challenging due to difficulties associated with isolation of products using conventional methods of purification.



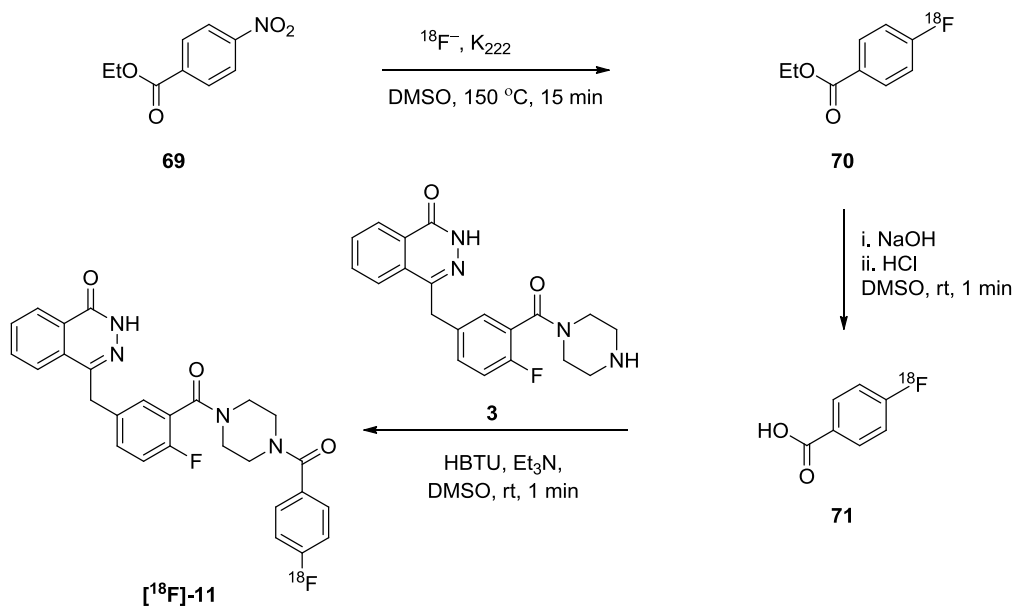
Scheme 5.25. Attempted non-radioactive fluoro-dediazonisation of the *in situ* generated diazonium salt **65** for the synthesis of **11**. Reagents and conditions: (a) 2 eq. KF, 100 °C, AcOH, 2.5 h; (b) 2 eq. KF, 100 °C, 18-Cr-6, AcOH, 2.0 h.

In an attempt to probe this reaction further, the diazonium salt **65** was isolated and exposed to a range of non-radioactive and radioactive fluorination conditions (Scheme 5.26). The non-radioactive reaction was performed using conditions that were established earlier to be effective for the aromatic iodination of salt **65** (Table 5.1, Entry 3). However, the desired products (**11** or [^{18}F]-**11**) were not detectable on UV (254 nm)/radio-HPLC chromatograms obtained for the crude reaction mixtures (data not shown). In the case of both non-radioactive and radioactive fluoro-dediazonisation reactions the formation of other products could be visualised on the UV-HPLC chromatograms (254 nm). It is possible that side reactivity and the poor stability of salt **65** impeded the fluorination chemistry.



Scheme 5.26. Attempted non-radioactive and radioactive fluoro-dediazonisation of the diazonium salt **65** for the synthesis of **11** and [^{18}F]-**11**. Reagents and conditions: (a) 2 eq. KF, 18-Cr-6, 100 °C, NMP, 1 h; (b) $^{18}\text{F}^-$, K_{222} , K_2CO_3 , DMF, 80 °C, 0.5 h; (c) $^{18}\text{F}^-$, K_{222} , K_2CO_3 , DMF, 155 °C, 0.5 h; (d) $^{18}\text{F}^-$, TBAHCO₃, DMF, 120 °C, 0.5 h.

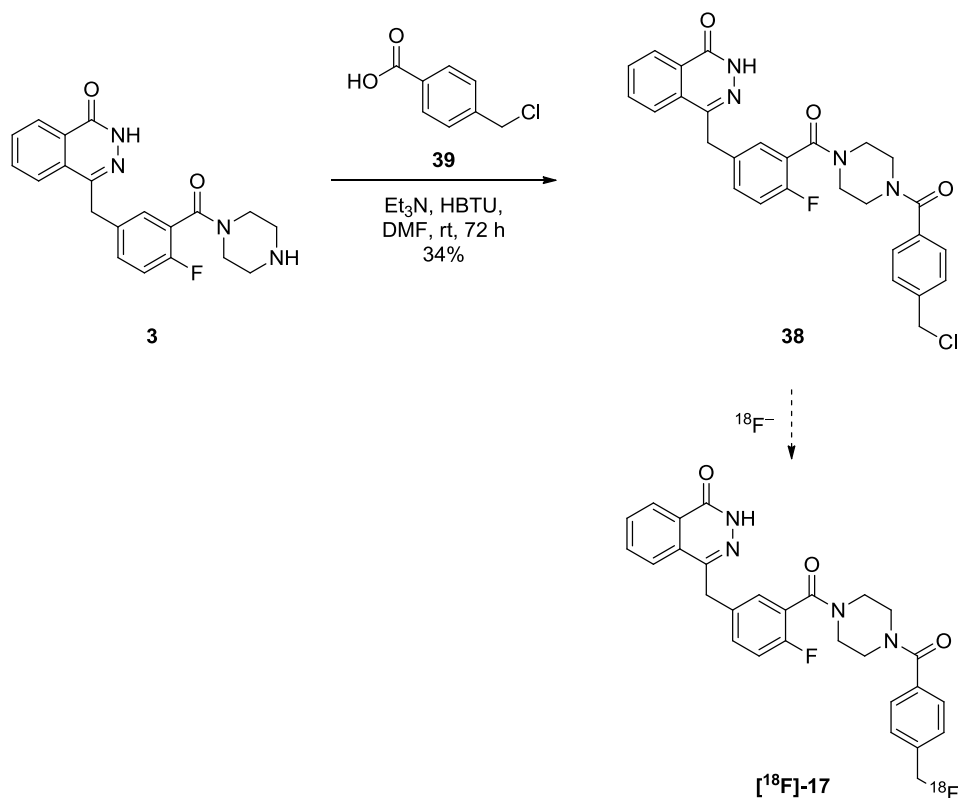
Alternative methods for accessing [^{18}F]-**11** could include using unsymmetrical diaryliodonium salt or a nickel organometallic precursors (see chapter 8 for details), as these methodologies have been designed for radiofluorinations of systems that are weakly activated for $\text{S}_{\text{N}}\text{Ar}$. Since commencing this work, Carney *et al.* (2015) were successful in developing a radiochemical protocol that allowed access to [^{18}F]-**11** with an end of synthesis yield of 10.0% (Scheme 5.27). The authors opted for an early stage fluorination approach as a way of circumventing the issue of weak $\text{S}_{\text{N}}\text{Ar}$ activation of precursor **60**. Radiofluorination of ethyl 4-nitrobenzoate was achieved in 15 minutes at 150 °C in the presence of K_{222} with a decay corrected $^{18}\text{F}^-$ incorporation of 35%. Subsequent base mediated hydrolysis afforded the terminal carboxylic acid moiety that was then used in a rapid (1 minute) amide coupling reaction with compound **3** to give [^{18}F]-**11**. The rapid kinetics of this amide coupling were surprising as experience from this project (Section 3.2), albeit from non-radioactive (stoichiometric) reactions, was that a reaction time exceeding 24 hours was generally required. Moreover, Menear *et al.* (2008) reported similar non-radioactive amide coupling reactions with compound **3** conducted over a 16 hour period.



Scheme 5.27. Radiofluorination approach used by Carney *et al.* (2015) to access [^{18}F]-11.

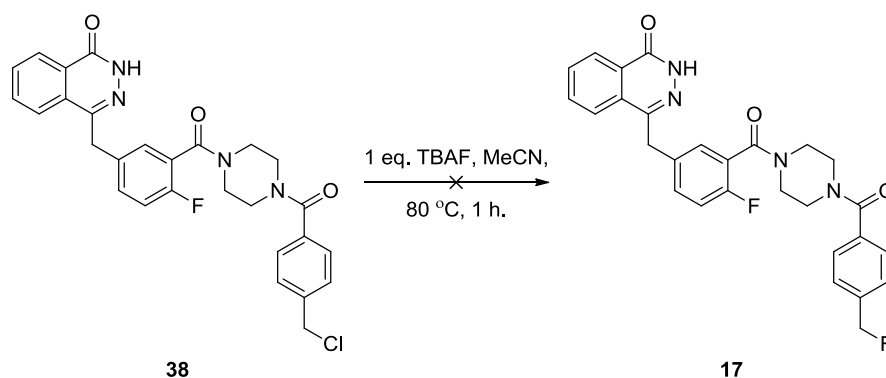
5.2.3 Radiofluorination, purification, and formulation of target PET tracer [^{18}F]-17.

Since the formation of an alkyl-F bond is generally regarded as less challenging than an aromatic-F bond, it was proposed that nucleophilic substitution of the benzyl chloride precursor **38** with radiofluoride would allow for efficient synthesis of [^{18}F]-17 (Scheme 5.28). The chlorinated precursor was generated by performing an amide coupling reaction between compound **3** and commercially available 4-(chloromethyl)benzoic acid (**39**) in the presence of HBTU (Scheme 5.28). The key driving force behind the choice of an alkyl-chlorine bearing precursor was the simplicity in its synthetic accessibility. However, future work could investigate the use of a sulfonate based leaving group (e.g. OTs), which would likely exhibit better leaving ability and potentially result in improved radiofluoride incorporation yields (see chapter 8 for details).



Scheme 5.28. Proposed aliphatic nucleophilic substitution radiofluorination approach for the synthesis of [^{18}F]-17 using the aliphatic chlorinated precursor 38.

It was shown previously (Section 3.2, Scheme 3.7) that TBAF can be used to effectively fluorinate compound 42 via nucleophilic substitution of a methyl-chloride functionality. However, utilising the same reaction conditions for the non-radioactive fluorination of compound 38 did not afford any of the desired product 17 (Scheme 5.29). It was observed that a solid white precipitate formed during the reaction. ^1H NMR spectroscopic analysis of the crude reaction mixture revealed a disappearance of the phthalazinone-NH peak and a shift in the $-\text{CH}_2\text{Cl}$ signal from 4.58 ppm to 5.40 ppm (Figure 5.19). Even though the change in ^1H NMR chemical shift corresponded to that expected for $-\text{CH}_2\text{F}$, the lack of signal splitting associated with fluorine was indicative of the formation of a different product. Based on these observations, it was believed that compound 38 underwent self-oligomerisation through nucleophilic substitution between the phthalazinone core of one molecule and the chlorine-bearing carbon of a secondary molecule, thereby preventing fluorination from taking place.



Scheme 5.29. Attempted aliphatic nucleophilic substitution fluorination for the synthesis of **17**.

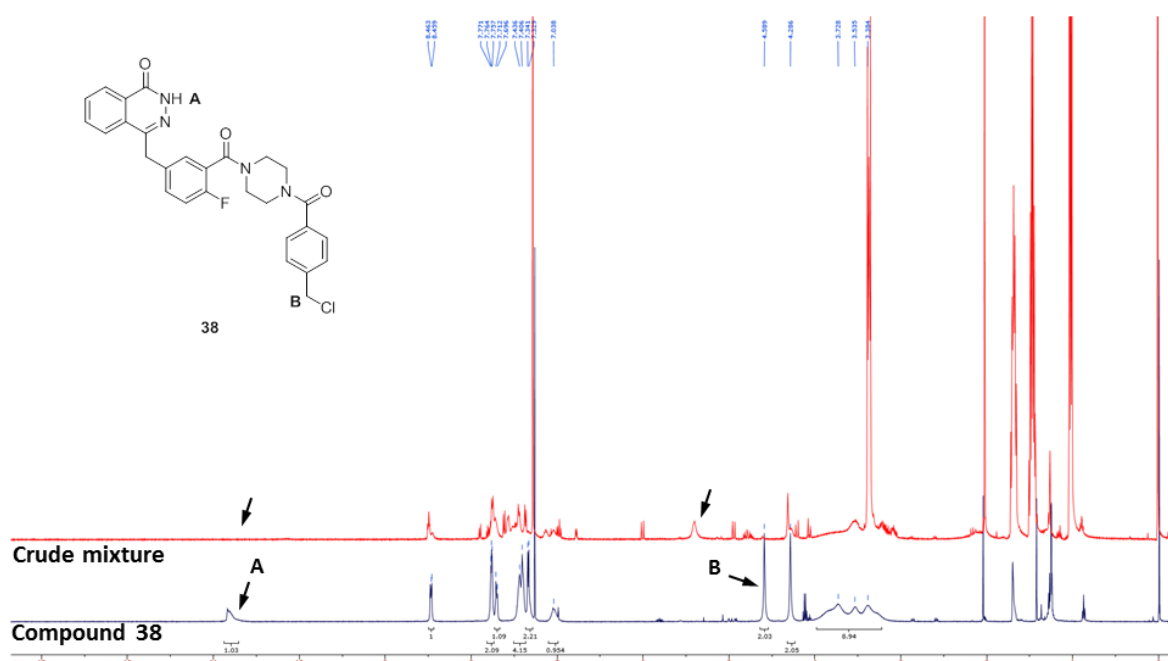
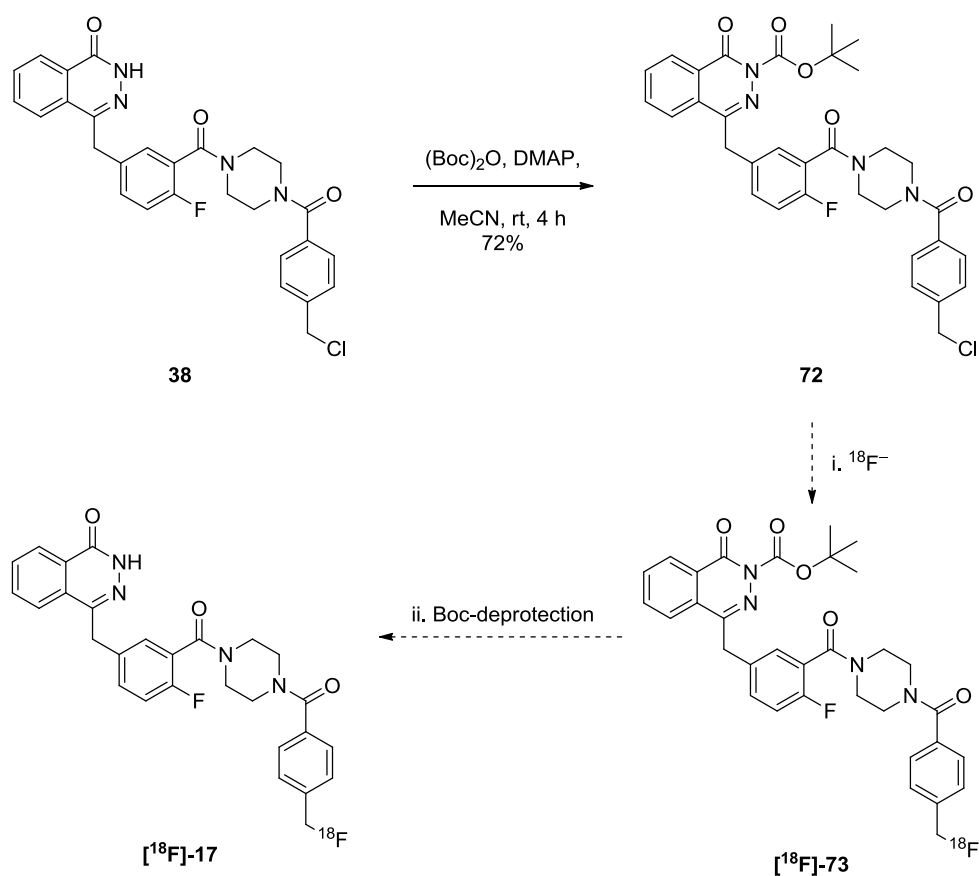


Figure 5.19. ^1H NMR spectra of compound **38** and the crude reaction mixture outlined in Scheme 5.29. NMR data were acquired using deuterated chloroform as the solvent and analysed using the iNMR 2.0.7 software.

In order to overcome the issue of self-oligomerisation, the phthalazinone-NH functionality of compound **38** was Boc protected using di-*tert*-butyl dicarbonate (**29**) and a catalytic amount of DMAP to generate **72** (Scheme 5.30). Utilising precursor **72** as a way of accessing compound $[^{18}\text{F}]\text{-17}$ has the disadvantage of necessitating a multi-step radiochemical approach comprising of a radiofluorination step followed by a successive Boc-deprotection step. Such prolongation of radiosynthesis can have a negative effect on the radiotracer end

of synthesis yield due to decay of the short lived fluoride radioisotope (^{18}F half-life = 109.8 minutes).

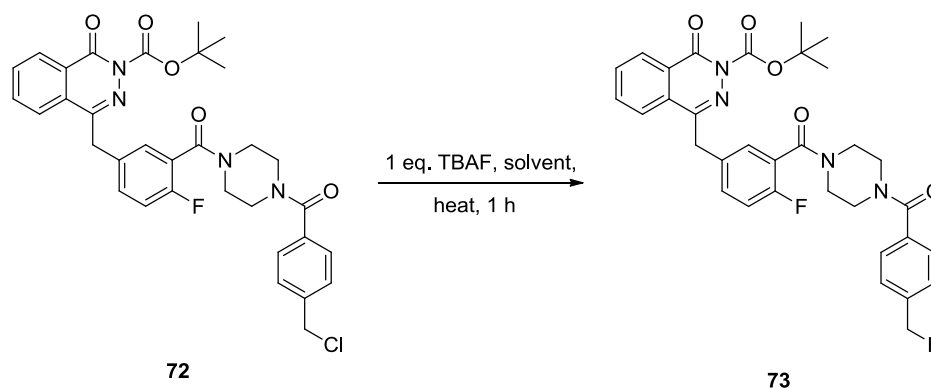


Scheme 5.30. Proposed aliphatic nucleophilic substitution radiofluorination approach for the synthesis of ^{18}F -17 using the Boc-protected aliphatic chlorinated precursor 72.

Prior to developing the radiochemistry for accessing ^{18}F -17, non-radioactive fluorination conditions were investigated using precursor 72 (Table 5.5). Earlier described fluorination conditions, utilising TBAF as a nucleophilic source of fluorine and acetonitrile as a non-protic solvent, resulted in a poor conversion with a 10.0 : 1.0 ratio of starting material (72) to desired product (73) (Entry 1). In an attempt to enhance the degree of conversion, a higher boiling point solvent was used and the temperature was increased from 80 °C to 120 °C (Entry 2). However, the 5.0 : 1.0 ratio of 72 : 73 was only a marginal improvement. As described earlier (Section 5.1.2.2), bulky protic alcohols can facilitate aliphatic nucleophilic substitution reactions by enhancing the leaving group ability and by solvating the fluoride while maintaining its nucleophilicity (Kim *et al.*, 2008). Therefore, a 1.0 : 2.0 mixture of acetonitrile and *tert*-butyl alcohol was used as

a reaction solvent, resulting in a marked improvement in the ratio of **72** : **73** (i.e. 1.0 : 4.0) (Entry 3).

Table 5.5. Screen of reaction conditions for the non-radioactive nucleophilic substitution fluorination of precursor **72**.



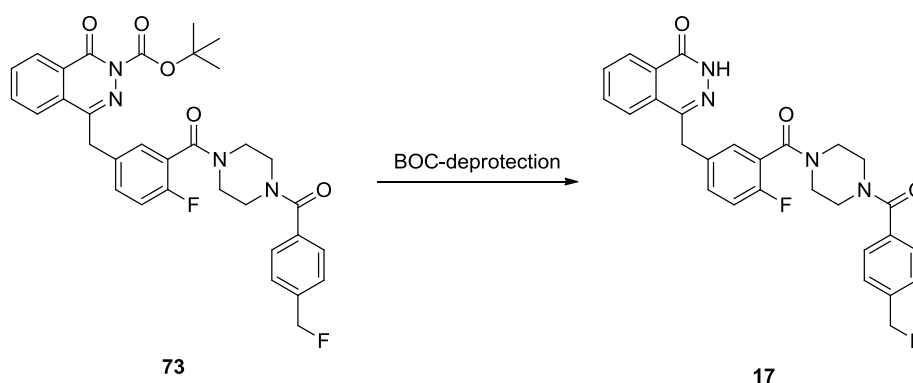
Entry	Solvent	Temperature (°C)	Ratio 72 : 73 ^a
1	MeCN	80	10.0 : 1.0
2	DMF	120	5.0 : 1.0
3	MeCN : <i>t</i> -BuOH (1.0 : 2.0)	80	1.0 : 4.0

^aThe ratio was calculated from the ¹H NMR spectrum (acquired using deuterated chloroform as the solvent) of the crude mixture following *in vacuo* reaction solvent removal (Entries 1 and 3) or dichloromethane/aqueous extraction (Entry 2) using the iNMR 2.0.7 software. MeCN = acetonitrile; DMF = *N,N'*-dimethylformamide; *t*-BuOH = *tert*-butanol.

With non-radioactive fluorination conditions established, focus was directed at optimising the Boc-deprotection chemistry to allow for rapid and efficient synthesis of **17** from **73**; the results of this reaction screen can be found in table 5.6. Utilising acid as a means of Boc-cleavage at room temperature resulted in a low degree of Boc-deprotection over a 10 minute reaction period (Entry 1). By increasing the temperature to 110 °C complete cleavage of the protecting group was achieved in just 5 minutes (Entry 2). However, the generation of multiple side products was observed with a 2.9 : 1.0 ratio of desired product **17** to side products. It is possible that side product generation was a consequence of compound degradation, as well as acid hydrolysis of the alkyl-Cl and alkyl-F functionalities of **17** and **73** respectively. Reducing the temperature to 80 °C

resulted in a decrease in side product formation, while maintaining Boc-deprotection efficacy (Entry 3). Thermal conditions in the presence of *N,N'*-dimethylformamide were less successful at cleaving the Boc protecting group, resulting in a 1.1 : 1.0 and 4.2 : 1.0 ratio of **73** : **17** for reactions conducted at 120 °C and 140 °C, respectively, over a period of 10 minutes (Entries 4 and 5). In an attempt to minimise the possibility of degradation and hydrolysis, mild reactions conditions developed by Wang, Liang, and Qu (2009) utilising water as an acid-base catalyst were applied (Entry 6). Despite poor aqueous solubility of **73**, complete cleavage of the Boc protecting group was achieved in 5 minutes without the formation of any side products. Therefore, the deprotection conditions described in entry 6 (Table 5.6) were identified as optimal.

Table 5.6. Screen of reaction conditions for the Boc-deprotection of compound **73** to access compound **17**.

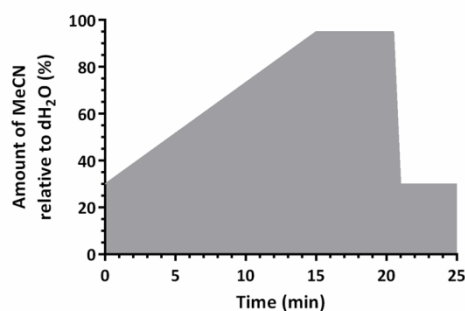


Entry	Deprotection agent	Temperature (°C)	Reaction time (min)	Ratio 73 : 17 ^a	Ratio 17 : side products ^{a,b}
1	1 M HCl	rt	10	11.5 : 1.0	1.0 : 0.0
2	1 M HCl	110	5	0.0 : 1.0	2.9 : 1.0
3	1 M HCl	80	5	0.0 : 1.0	9.1 : 1.0
4	DMF	120	10	1.1 : 1.0	3.3 : 1.0
5	DMF	140	10	4.2 : 1.0	3.0 : 1.0
6	H ₂ O	120	5	0.0 : 1.0	1.0 : 0.0

^aThe ratio was calculated from the total ion current (TIC) chromatogram of the LC-MS spectrum of the crude reaction mixture. ^bThe term 'side products' entails all other reaction products excluding compound **17**. rt = room temperature; DMF = *N,N'*-dimethylformamide.

The final step before translation of non-radioactive chemistry to radiofluorination chemistry involved establishing chromatographic conditions for the purposes of radiotracer purification and quality control. Measurement of the retention times of compounds **17** and **72** on an analytical reverse-phase C₁₈ HPLC column, using the mobile phase gradient conditions depicted in Figure 5.20 A, revealed good separation between the fluorinated target compound **17** and the Boc-protected chlorinated precursor **72** (Figure 5.20).

A.



B.

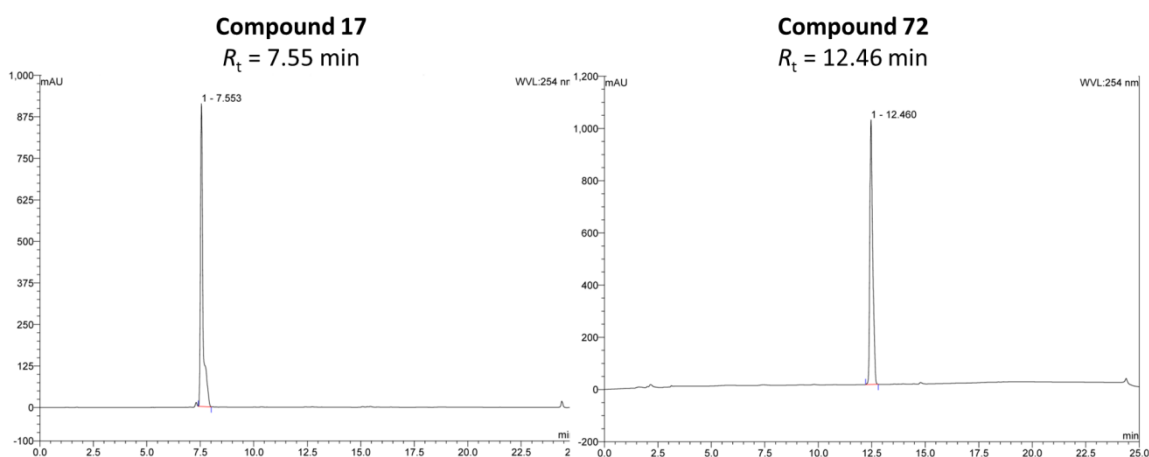
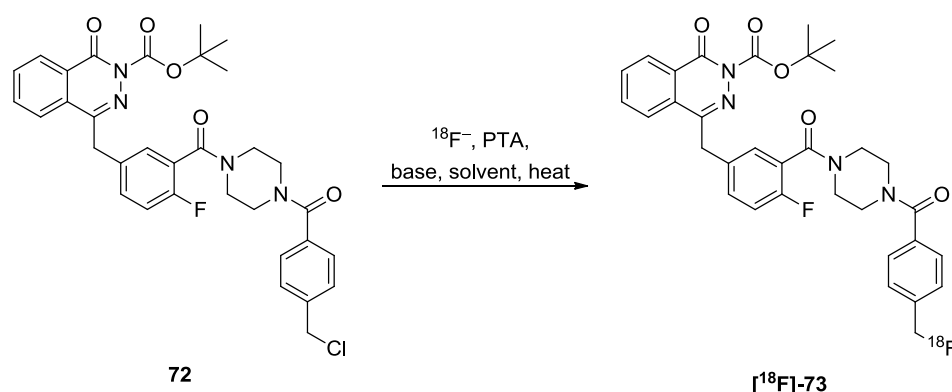


Figure 5.20. The chromatographic gradient used to measure the retention times (R_t) of compounds **17** and **72** on an analytical reverse-phase C₁₈ column (A) and the corresponding UV-HPLC (254 nm) chromatograms (B). MeCN = acetonitrile; dH₂O = distilled water; R_s = resolution.

With non-radioactive fluorination, Boc-deprotection, and chromatographic methodology in place, focus was shifted toward the development of radiofluorination chemistry. An initial attempt at ¹⁸F radiolabelling of precursor **72**, utilising TBAHCO₃ as a phase transfer agent and acetonitrile as a solvent, allowed for a radioisotope incorporation of 30% following a 30 minute reaction (Table 5.7, Entry 1).

Table 5.7. Investigation and optimisation of aliphatic nucleophilic substitution radiofluorination methodology for the synthesis of [^{18}F]-73 using the Boc-protected chlorinated precursor 72.



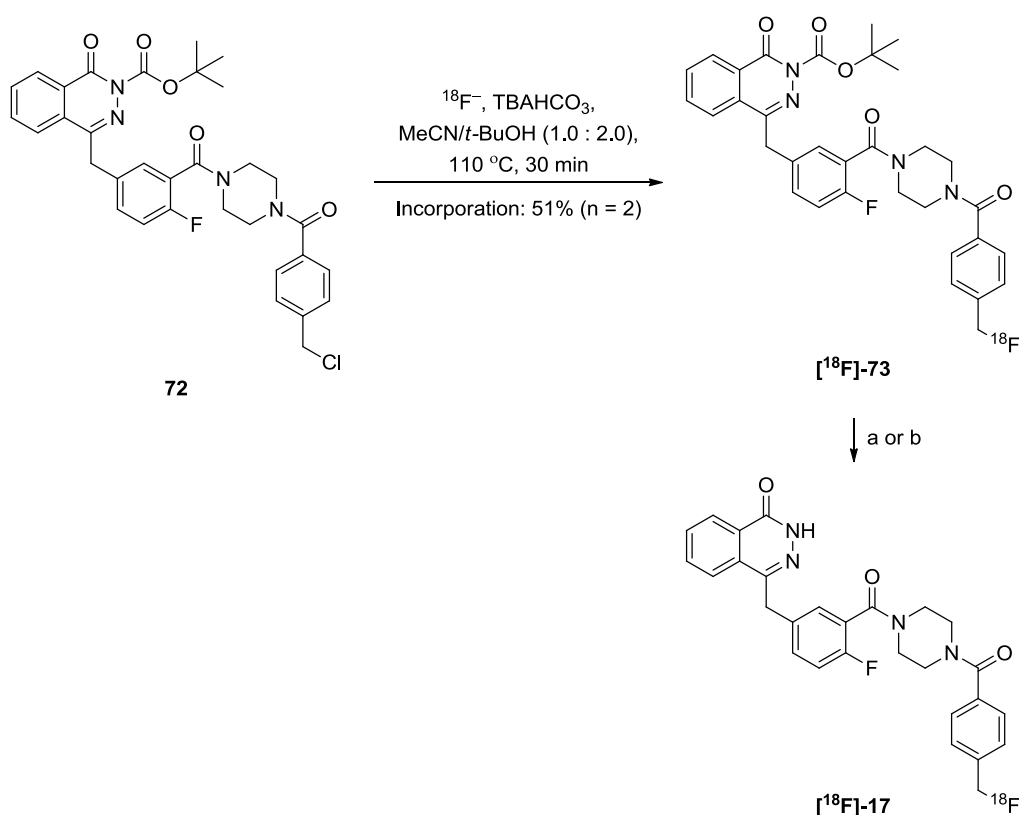
Entry	Solvent (volume, mL)	PTA	Base	Temperature (°C)	Reaction time (min.)	Radioisotope incorporation (%) ^a
1	MeCN	TB	—	100	30	30
2	MeCN	K ₂₂₂	K	100	30	4
3	MeCN (0.1)/ <i>t</i> -BuOH (0.2)	TB AH	—	100	10	22
4	MeCN (0.1)/ <i>t</i> -BuOH (0.2)	TB AH	—	100	30	48
5	MeCN (0.1)/ <i>t</i> -BuOH (0.2)	TB AH	—	110	30	51
6	MeCN (0.2)/ <i>t</i> -BuOH (0.4)	TB AH	—	110	30	37

^aCalculated from analytical radio-HPLC chromatograms obtained from crude reaction mixtures. MeCN = acetonitrile; *t*-BuOH = *tert*-butyl alcohol; PTA = phase transfer agent; K₂₂₂ = Kryptofix; TBAHCO₃ = tetra-*n*-butylammonium hydrogen carbonate.

Replacing the phase transfer agent with K₂₂₂ in the presence of basic potassium carbonate (in a phase transfer agent to base ratio of 1.0 : 0.4) resulted in a marked drop in the radioincorporation yield to only 4% (Entry 2). Introduction of *tert*-butyl alcohol resulted in 22% and 48% radiofluoride incorporation yields following a 10 and 30 minute reactions respectively (Table 5.5, Entry 3). Radiolabelling yield was further improved by increasing the reaction temperature from 100 °C to 110 °C (Entry 5). Interestingly, doubling the reaction volume was associated with a 14% drop in ^{18}F incorporation (Entry 6), suggesting

that the concentration of reagents in the reaction is an important variable. Solvent volumes below 0.3 mL were not investigated due to the potential lack of surface contact between precursor **72** and the ^{18}F -phase transfer agent complex adhered to reaction vessel walls. Based on the above data, radiofluorination conditions outlined in entry 5 were identified as optimal.

Next, hydrochloric acid and water mediated Boc-deprotection conditions, as investigated previously on non-radioactive **73** (Table 5.6), were applied to $[^{18}\text{F}]$ -**73** (Scheme 5.31).



Scheme 5.31. Aliphatic nucleophilic substitution radiofluorination of precursor **72** followed by Boc-deprotection giving access to $[^{18}\text{F}]$ -**17**. Reagents and conditions: (a) 1 M HCl, 100 °C, 5 min; (b) H₂O, 120 °C, 5 min.

By scrutinising the radio-HPLC chromatograms of the crude reaction mixtures before and after Boc-deprotection (Figure 5.21), it could be seen that ratio of free (unbound) $^{18}\text{F}^-$ to labelled product increased by 0.80 in the presence of hydrochloric acid, compared to a ratio increase of just 0.20 when water was used as the deprotecting agent. These data are indicative of hydrolytic benzyl-

^{18}F cleavage from $[^{18}\text{F}]\text{-17}$, thus leading to an increase in free $^{18}\text{F}^-$. It is noteworthy that the hydrolytic loss of labelled radiofluoride was markedly lower in the presence of water than hydrochloric acid. With this in mind, Boc-cleavage utilising water and a temperature of 120 °C was identified as optimal for accessing $[^{18}\text{F}]\text{-17}$ from $[^{18}\text{F}]\text{-73}$.

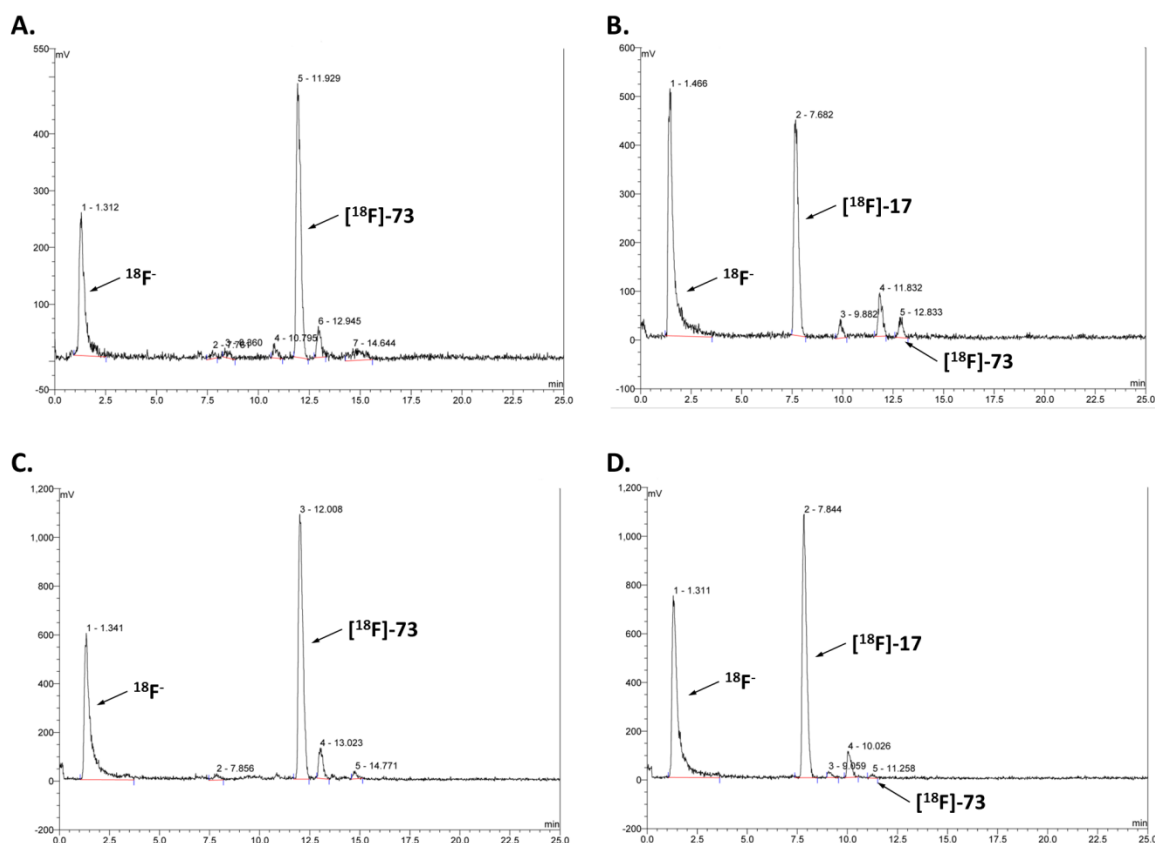
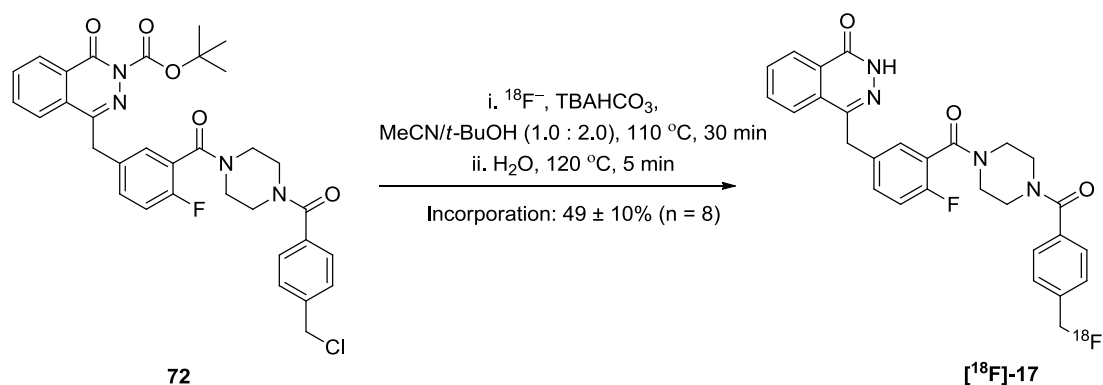


Figure 5.21. Analytical radio-HPLC chromatograms of the crude reaction mixtures as outlined in Scheme 5.31 following radiofluorination (A and C), and hydrochloric acid (B) and water (D) catalysed Boc-deprotection. The identity of $[^{18}\text{F}]\text{-17}$ was confirmed by comparing the retention time of the radiolabelled product (i.e. ^{18}F -bearing) against the retention time of unlabelled 17 (i.e. ^{19}F -bearing) (Figure 5.20).

The optimised two-stage radiofluorination protocol, consisting of a radiofluorination and a subsequent Boc-deprotection step, was used for the synthesis of $[^{18}\text{F}]\text{-17}$ (Scheme 5.32), allowing for a radiofluoride incorporation of $49 \pm 10\%$ ($n = 8$) (measured using a preparatory HPLC system after the deprotection step). It was envisaged that this level of incorporation will be

sufficient to achieve an overall radiochemical end of synthesis yield that will be in line with the earlier stipulated hypothesis (see section 5.1.4 for details).



Scheme 5.32. Optimised aliphatic nucleophilic substitution radiofluorination methodology for the synthesis of the potential PARP-1 PET imaging agent [^{18}F]-**17** using the Boc-protected chlorinated precursor **72**.

Since **72** was used in a large excess relative to $^{18}\text{F}^-$, the unreacted precursor was expected to form the chlorinated analogue **38** when subjected to the Boc-deprotection step. To ensure adequate separation of **38** from [^{18}F]-**17** during radiotracer purification, the analytical chromatographic conditions as described earlier in figure 5.20 were slightly modified for the preparatory HPLC system. The modification consisted of slowing down the mobile phase gradient of acetonitrile as shown in figure 5.22. HPLC methodology was chosen for purification due to the chemical similarities between the chlorine and fluorine bearing compounds, which could be difficult to separate using SPE. Future work could involve utilisation of an alternative precursor, such as a compound bearing an OTs leaving group, which could potentially simplify the purification process and allow for radiosynthetic automation using SPE (see chapter 8 for details). However, it should be noted an OTs bearing precursor may exhibit reduced stability properties when compared to compound **72**, potentially resulting in the need for frequent re-synthesis.

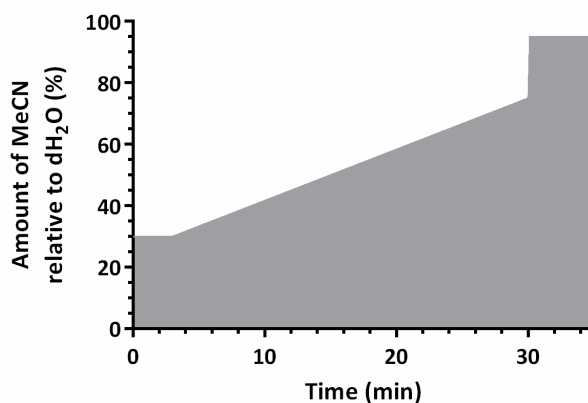


Figure 5.22. Optimal mobile phase preparatory HPLC gradient conditions used for purification of [^{18}F]-17 synthesised using aliphatic nucleophilic substitution radiofluorination methodology.

It was found that these preparatory chromatographic conditions allowed for adequate separation between [^{18}F]-17 and the various UV active chemical entities generated as part of the reaction. This allowed for effective purification of the radiotracer and >99% radiochemical purity ($n = 4$) (Figure 5.23).

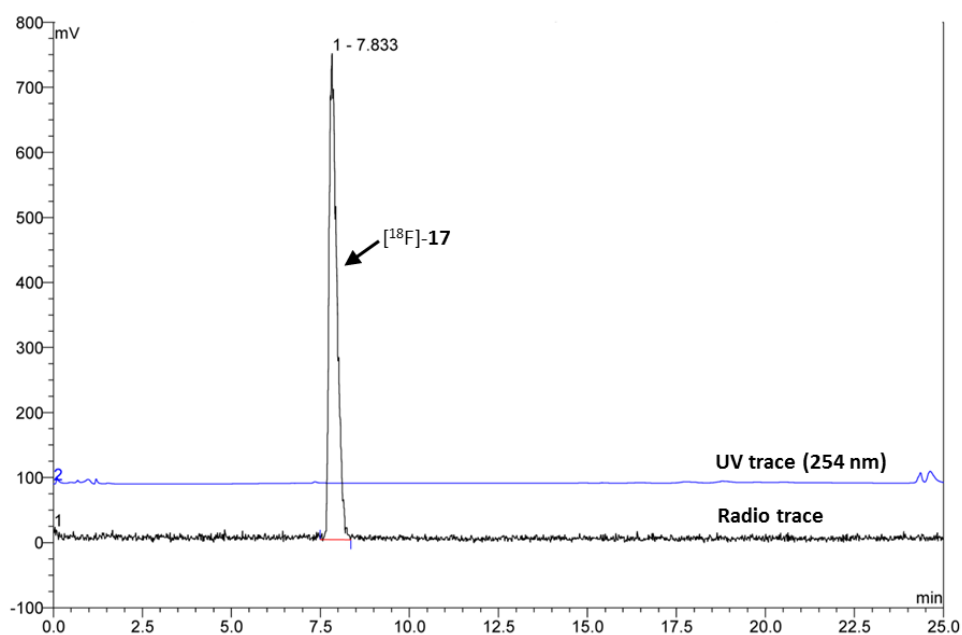


Figure 5.23. An analytical quality control UV (254 nm)/radio-HPLC chromatogram of [^{18}F]-17 showing >99% radiochemical purity of the radiotracer formulated in 5.0% v/v dimethyl sulfoxide in 0.9% w/v saline. The identity of [^{18}F]-17 was confirmed by comparing the retention time of the radiolabelled product (i.e. ^{18}F -bearing) against the retention time of unlabelled 17 (i.e. ^{19}F -bearing) (Figure 5.20).

As described earlier for [^{123}I]-4 (section 5.2.1), the specific activity for [^{18}F]-17 was calculated from the UV-HPLC chromatogram obtained during the radiotracer purification step and with the aid of a UV calibration plot acquired using non-labelled (^{19}F -bearing) 17 (Appendix 9.8). The specific activity of [^{18}F]-17 was calculated to be $>4.32 \pm 1.46 \text{ Ci}/\mu\text{mol}$ ($n = 3$). Since the amount of [^{18}F]-17 that was produced fell below the sensitivity threshold of the UV detector for this particular compound ($<1.68 \times 10^{-4} \mu\text{mol}$), an absolute value for the specific activity could not be calculated.

As for [^{123}I]-4 (Section 5.2.1), physiological saline (0.9% w/v sodium chloride) combined with a co-solvent was chosen as the formulation vehicle for [^{18}F]-17. Due to poor solubility of 17 in ethanol, dimethyl sulfoxide was utilised for co-solvency. Dimethyl sulfoxide is generally associated with low systemic toxicity and it has been shown that as much as 30.0% of the solvent by volume can be administered parenterally to CD1 nude mice without any observable adverse reactions (Thackaberry *et al.*, 2014). However, due to the effects of dimethyl sulfoxide on compound pharmacokinetics (reviewed by Buggins, Dickinson, and Taylor (2007)), a low concentration of 5.0% by volume was utilised in the final radiotracer formulation. Formulation of [^{18}F]-17 in a solution of 5.0% v/v dimethyl sulfoxide in 0.9% w/v saline allowed for an end of synthesis yield of $9 \pm 2\%$ ($n = 7$).

5.3 Conclusion.

The research presented in this chapter was successful in developing radiosynthetic methodologies for the generation of the potential PARP-1 SPECT tracer [^{123}I]-4. The radiotracer was accessed in a manner that is in line with the earlier stipulated hypotheses (section 5.1.4), and in quantities sufficient for pre-clinical evaluation. [^{123}I]-4 was generated in a high specific activity of $>19.0 \pm 10.3 \text{ Ci}/\mu\text{mol}$ ($n = 4$), a radiochemical end of synthesis yield of $37 \pm 7\%$ ($n = 6$), and a radiochemical purity of $>99\%$ ($n = 6$). However, adequate radiolabelling methodology for the manual synthesis of the potential PET imaging agent [^{18}F]-11 was not established. Work involving the optimisation of aromatic nucleophilic

substitution radiofluorination chemistry, utilising the *para* nitro precursor **63**, afforded a maximum radiofluoride incorporation yield of just 19%, which was not sufficient for further radiochemical protocol development. Efforts to improve the amount of radioisotope incorporation via the use of a diazonium tosylate salt leaving group were not successful due to unprecedented side reactivity taking place. These issues were circumvented by pursuing [¹⁸F]-**17** as alternative target radiotracer with potential for PARP-1 PET imaging. The synthesis of [¹⁸F]-**17** was achieved in a specific activity of $>4.32 \pm 1.46$ Ci/ μ mol ($n = 3$), an end of synthesis yield of $9 \pm 2\%$ ($n = 7$) and a radiochemical purity of $>99\%$ ($n = 4$). The markedly lower end of synthesis yield of the radiofluorinated tracer [¹⁸F]-**17** when compared to [¹²³I]-**4** can be explained by the lower radioincorporation yields associated with the former ($49 \pm 10\%$; $n = 8$ versus $90 \pm 4\%$; $n = 4$) and the shorter half-life of the radioisotope (¹⁸F half-life = 109.8 minutes versus ¹²³I half-life = 13.2 hours). It is noteworthy that since commencing this work, Carney *et al.* (2015) were able to generate [¹⁸F]-**11** in quantities sufficient for pre-clinical evaluation by utilising early-stage radiofluorination chemistry.

5.4 Experimental.

5.4.1 General experimental.

Please see chapter 3 for details concerning the general chemistry experimental and experimental information for compounds **3**, **4**, **11** and **17**. The synthesis of compound **60** has been reported previously by Zmuda *et al.* (2015). Resin-bound nitrite was prepared by making a solution of sodium nitrite (2.07 g, 30.0 mmol) in water (30 mL), to which Amberlyst™ A26 resin (3.50 g) was added. This was allowed to stir at room temperature for 10 minutes. The resin beads were then collected by filtration and washed with water to yield resin-bound nitrite at a literature predicted nitrite loading of 3.5 mmol per gram (Filimonov *et al.*, 2008).

For radiofluorination chemistry, [¹⁸F]-fluoride was produced by staff employed at the PET Radiopharmaceutical Production Unit at NHS Greater Glasgow Clyde in a

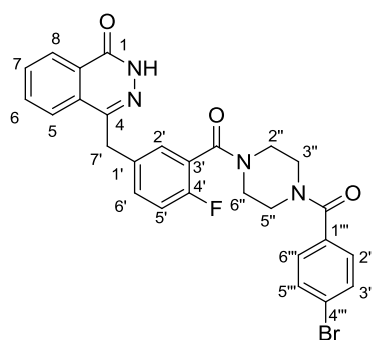
cyclotron (GE PETtrace 6 cyclotron) via the [$^{18}\text{O}(p, n)^{18}\text{F}$] nuclear reaction by irradiation of [^{18}O]-water. Irradiation of the target water was performed with a 16.5 MeV proton beam (40 μA). HPLC analysis and purification was performed using analytical and preparatory systems, respectively, that belonged to the Dionex UltiMate 3000 series. Phenomenex Synergi 4 μm Hydro-RP 80Å 150 \times 4.60 mm and 150 \times 10 mm columns were used in the analytical and preparatory systems respectively, with column temperatures set to 25 $^{\circ}\text{C}$. Mobile phase flow rates were 1 mL/min and 3 mL/min for the analytical and preparatory systems respectively. Analytical UV detection was performed using a UltiMate diode array detector (190–800 nm) and radiodetection was achieved using a Berthold Technologies Flow Star LB513 detector. Preparatory UV detection was performed using a Knauer Advanced Scientific Instruments Smartline UV Detector 2500 and radiodetection was achieved with either a pin-diode (for ^{18}F) or a photomultiplier tube (for ^{123}I) connected to a Lab Logic Flow-Count radiodetector. HPLC data acquisition and analyses were carried out using the Chromeleon 6.8 Chromatography software.

A stock solution of K_{222} /potassium carbonate was prepared by dissolving 100.0 mg of K_{222} (0.266 mmol) in 2 mL of acetonitrile and adding 12.0 mg of K_2CO_3 (0.087 mmol) in 0.5 mL of distilled water. A stock solution of 0.750 M TBAHCO_3 was prepared by diluting 2.5 mL of 1.5 M TBAOH with 2.5 mL of distilled water. Carbon dioxide was bubbled through the solution for 2 hours until a pH 7.7 was reached, and then excess carbon dioxide was removed by bubbling argon through the mixture until pH 9.0 was reached. A stock solution of caesium carbonate was prepared by dissolving 6.8 mg of caesium carbonate (0.021 mmol) in 1 mL of distilled water.

5.4.2 Chemistry experimental.

5.4.2.1 Experimental data for all synthesised compounds.

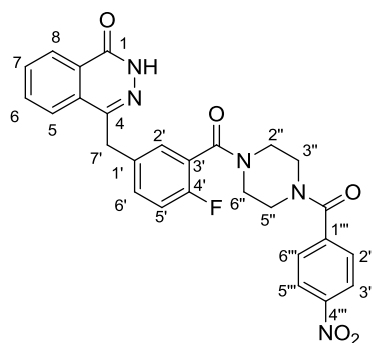
4-[3'-[4''-(4'''-Bromobenzoyl)piperazine-1''-carbonyl]-4'-fluorobenzyl]-2H-phthalazin-1-one (60)



To a solution of 4-bromobenzoic acid (**59**) (165.0 mg, 0.820 mmol) in *N,N'*-dimethylformamide (10 mL) was added triethylamine (177.0 μL , 1.31 mmol), followed by *O*-benzotriazole-*N,N,N',N'*-tetramethyluroniumhexafluorophosphate (**33**) (341.0 mg, 0.900 mmol) and the mixture was stirred at room temperature for 2 hours. 4-[4'-Fluoro-3'-(piperazine-1''-carbonyl)benzyl]-2H-phthalazin-1-one (**3**) (300 mg, 0.820 mmol) was added and the mixture was stirred for a further 72 hours. Water (14 mL) was then added, followed by 1 hour of stirring after which the mixture was cooled to 0 °C. The resulting precipitate was collected by vacuum filtration, washed with water (4 \times 30 mL) and dried *in vacuo* to yield 4-[3'-[4''-(4'''-bromobenzoyl)piperazine-1''-carbonyl]-4'-fluorobenzyl]-2H-phthalazin-1-one (**60**) (424 mg, 94%) as a yellow foam. $\nu_{\text{max}}/\text{cm}^{-1}$ (neat) 3233 (NH), 2934 (CH), 1668 (CO), 1593 (C=C), 1460, 1433, 1269, 1221, 1003, 772; δ_{H} (500 MHz, CDCl_3) 3.20-4.00 (8H, m, 4 \times NCH_2), 4.31 (2H, s, 7'- H_2), 7.06 (1H, br s, 5'-H), 7.27-7.39 (4H, m, 2'-H, 6'-H, 3'''-H and 5'''-H), 7.52-7.63 (2H, m, 2'''-H and 6'''-H), 7.70-7.75 (1H, m, 5-H), 7.75-7.78 (2H, m, 6-H and 7-H), 8.46-8.53 (1H, m, 8-H), 10.99 (1H, s, NH); δ_{C} (126 MHz, CDCl_3) 37.7 (CH_2), 42.2 (2 \times CH_2), 47.0 (2 \times CH_2), 116.2 (CH, d, $J_{\text{C-C-F}}$ 23.1 Hz), 123.5 (C, d, $J_{\text{C-C-F}}$ 17.6 Hz), 124.6 (C), 125.0 (CH), 127.2 (CH), 128.3 (C), 128.8 (2 \times CH), 129.3 (CH, d, $J_{\text{C-C-C-F}}$ 3.5 Hz), 129.5 (C), 131.6 (CH), 131.8 (CH, d, $J_{\text{C-C-C-F}}$ 8.0 Hz), 132.0 (2 \times CH), 133.7 (CH), 133.8 (C), 134.5 (C, d, $J_{\text{C-C-C-C-F}}$ 3.5 Hz), 145.5 (C), 156.9 (C, d, $J_{\text{C-F}}$ 248.3

Hz), 160.5 (C), 165.2 (C), 169.6 (C); m/z (ESI) 571.0732 (MNa^+ . $C_{27}H_{22}^{79}BrFN_4NaO_3$ requires 571.0752).

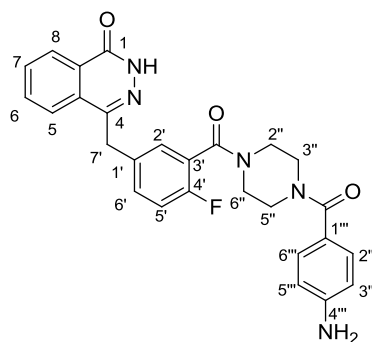
4-[3'-[4''-(4'''-Nitrobenzoyl)piperazine-1''-carbonyl]-4'-fluorobenzyl]-2H-phthalazin-1-one (63)



The reaction was carried out as described for 4-[3'-[4''-(4'''-bromobenzoyl)piperazine-1''-carbonyl]-4'-fluorobenzyl]-2H-phthalazin-1-one (**60**) using a solution of 4-nitrobenzoic acid (**62**) (92.0 mg, 0.550 mmol) in *N,N'*-dimethylformamide (6 mL), triethylamine (119 μ L, 0.880 mmol), *O*-benzotriazole-*N,N,N',N'*-tetramethyluroniumhexafluorophosphate (**33**) (231 mg, 0.610 mmol). Following the addition of 4-[4'-fluoro-3'-(piperazine-1''-carbonyl)benzyl]-2H-phthalazin-1-one (**3**) (200 mg, 0.550 mmol) the mixture was stirred at room temperature for a further 48 hours. Water (12 mL) was then added, followed by 1 hour of stirring, after which the mixture was cooled to 0 $^{\circ}$ C. The resulting precipitate was collected by vacuum filtration, washed with water (4 \times 20 mL) and dried *in vacuo* to yield 4-[3'-[4''-(4'''-nitrobenzoyl)piperazine-1''-carbonyl]-4'-fluorobenzyl]-2H-phthalazin-1-one (**63**) (239.0 mg, 84%) as an orange foam. NMR spectra showed a 60:40 mixture of rotamers. Only data for the major rotamer were recorded. ν_{max}/cm^{-1} (neat) 3167 (NH), 3012 (ArH), 2904 (CH), 1638 (CO), 1616 (C=C), 1599 (NO₂), 1346 (NO₂), 1433, 1265, 1004, 735; δ_H (400 MHz, d_6 -DMSO) 3.23 (2H, s, N-CH₂), 3.38 (2H, s, N-CH₂), 3.57–3.86 (4H, m, NCH₂), 4.39 (2H, d, J 18.6 Hz, 7'-HH and 7''-HH), 7.21–7.34 (1H, m, 5'-H), 7.35–7.53 (2H, m, 2'-H and 6'-H), 7.69–7.79 (2H, m, 2'''-H and 6'''-H), 7.79–8.05 (3H, m, 5-H, 6-H, and 7-H), 8.25–8.38 (3H, m, 8-H, 3'''-H, and 5'''-H), 12.65 (1H, s, NH); δ_C (101 MHz, d_6 -DMSO) 37.0 (CH₂), 41.9 (2 \times CH₂), 46.9 (2 \times CH₂), 116.3 (CH, d, J_{C-C-F} 18.2 Hz), 123.8 (C, d, J_{C-C-F} 18.0 Hz), 124.0 (2 \times CH), 125.9 (CH), 126.5 (CH), 128.3 (C), 128.8 (2 \times CH), 129.4 (CH), 129.5 (C), 132.0 (CH), 132.2 (CH, d, $J_{C-C-C-F}$ 8.8 Hz), 133.9 (CH), 135.3 (C, d, $J_{C-C-C-C-F}$ 3.4

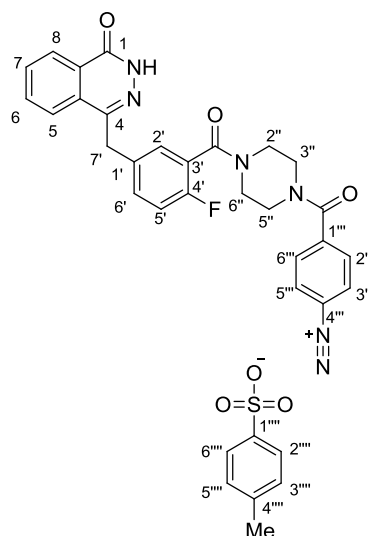
Hz), 142.3 (C), 145.2 (C), 148.4 (C), 156.8 (C d, J_{C-F} 245.7 Hz), 159.8 (C), 164.5 (C), 167.8 (C); m/z (ESI) 538.1488 (MNa^+ . $C_{27}H_{22}FN_5NaO_5$ requires 538.1497).

4-[3'-[4''-(4'''-Aminobenzoyl)piperazine-1''-carbonyl]-4'-fluorobenzyl]-2H-phthalazin-1-one (64)



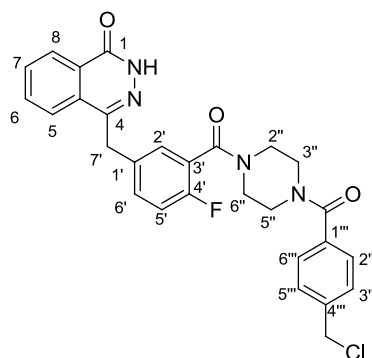
4-[3'-[4''-(4'''-Nitrobenzoyl)piperazine-1''-carbonyl]-4'-fluorobenzyl]-2H-phthalazin-1-one (**63**) (55.0 mg, 0.107 mmol) was suspended in a 1:1 mixture of ethanol and ethyl acetate (6 mL), and tin(II) chloride dihydrate was added (120 mg, 0.533 mmol). The suspension was stirred under reflux for 24 hours after which the mixture was cooled to ambient temperature and a saturated solution of sodium hydrogen carbonate (12 mL) was added. The product was extracted into ethyl acetate (3 × 10 mL), dried with magnesium sulfate, filtered and concentrated *in vacuo* to give 4-[3'-[4''-(4'''-aminobenzoyl)piperazine-1''-carbonyl]-4'-fluorobenzyl]-2H-phthalazin-1-one (**64**) (45.0 mg, 87%) as an orange foam. ν_{max}/cm^{-1} (neat) 3347 and 3221 (NH), 3007 (ArH), 2924 and 2863 (CH), 1605 (CO), 1424, 1256, 1177, 1003, 748, 729; δ_H (400 MHz, $CDCl_3$) 3.30 (2H, br s, N- CH_2), 3.49–4.16 (8H, m, 3 × N- CH_2 , and 4'''- NH_2), 4.27 (2H, s, 7'- H_2), 6.61 (2H, d, J 8.37 Hz, 3'''-H and 5'''-H), 7.01 (1H, t, J 8.7 Hz, 5'-H), 7.22 (2H, d, J 8.4 Hz, 2'''-H and 6'''-H), 7.28–7.36 (2H, m, 2'-H and 6'-H), 7.66–7.77 (3H, m, 5-H, 6-H and 7-H), 8.42–8.48 (1H, m, 8-H), 11.61 (1H, s, NH); δ_C (101 MHz, $CDCl_3$) 37.6 (CH_2), 42.1 (2 × CH_2), 47.0 (2 × CH_2), 114.1 (2 × CH), 116.0 (CH, d, J_{C-C-F} 22.0 Hz), 123.6 (C, d, J_{C-C-F} 17.9 Hz), 123.9 (C), 124.9 (CH), 127.0 (CH), 128.2 (C), 129.1 (CH, d, $J_{C-C-C-F}$ 3.6 Hz), 129.3 (2 × CH), 129.4 (C), 131.5 (CH), 131.6 (CH, d, $J_{C-C-C-F}$ 8.1 Hz), 133.5 (CH), 134.3 (C, d, $J_{C-C-C-C-F}$ 3.5 Hz), 145.4 (C), 148.6 (C), 156.8 (C, d, J_{C-F} 247.6 Hz), 160.7 (C), 165.1 (C), 171.1 (C); m/z (ESI) 508.1912 (MNa^+ . $C_{27}H_{24}FN_5NaO_3$ requires 508.1902).

4-[3'-[4''-[4'''-Diazonium-(4''''-methylbenzenesulfonate)benzoyl]piperazine-1''-carbonyl]-4'-fluorobenzyl]-2H-phthalazin-1-one (65)



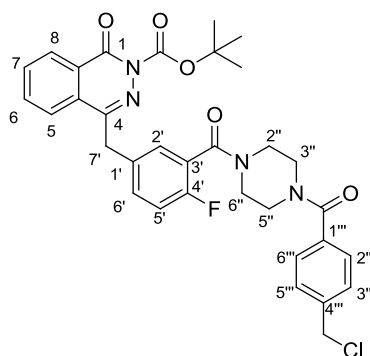
4-[3'-[4''-(4'''-aminobenzoyl)piperazine-1''-carbonyl]-4'-fluorobenzyl]-2H-phthalazin-1-one (**64**) (30.0 mg, 0.035 mmol) was added to a solution of *p*-toluenesulfonic acid (20.0 mg, 0.12 mmol) in glacial acetic acid (1 mL). The mixture was cooled to 10 °C using a water bath and resin-bound nitrite was added (30.0 mg, equivalent to 0.11 mmol of nitrite; see general experimental section), and stirred for 1 hour. Diethyl ether (5 mL) was added and the resulting yellow precipitate was collected by filtration, washed with diethyl ether (3 × 10 mL) and dried *in vacuo* to yield 4-[3'-[4''-[4'''-diazonium-(4''''-methylbenzenesulfonate)benzoyl]piperazine-1''-carbonyl]-4'-fluorobenzyl]-2H-phthalazin-1-one (**65**) (15.0 mg, 62%) as a yellow foam. Due to the instability of the salt complete characterisation was not attainable. δ_{H} (400 MHz, CD₃OD) 2.35 (3H, s, 4''''-CH₃), 3.22–3.33 (2H, m, NCH₂), 3.40–3.48 (2H, m, N-CH₂), 3.67–3.77 (2H, m, NCH₂), 3.86 (2H, br s, NCH₂), 4.37 (2H, d, *J* 19.7 Hz, 7'-HH and 7'-HH), 7.10–7.19 (1H, m, 5'-H), 7.20 (2H, d, *J* 7.9 Hz, 3''''-H and 5''''-H), 7.33–7.40 (1H, m, 2'-H), 7.45–7.54 (1H, m, 6'-H), 7.67 (2H, d, *J* 8.2 Hz, 2''''-H and 6''''-H), 7.76–8.05 (5H, m, 5-H, 6-H, 7-H, 2'''-H, and 6'''-H), 8.35 (1H, m, 8-H), 8.70 (2H, t, *J* 9.9 Hz, 3'''-H and 5'''-H).

4-[3'-[4''-(4'''-Chloromethyl)benzoyl]piperazine-1''-carbonyl]-4'-fluorobenzyl]-2H-phthalazin-1-one (38)



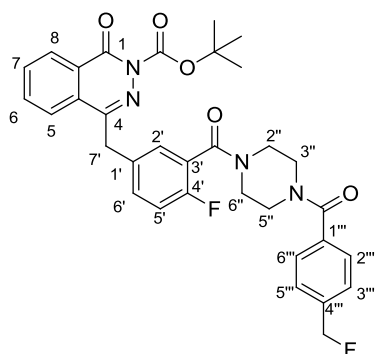
The reaction was carried out as described for 4-[3'-[4''-(4'''-bromobenzoyl)piperazine-1''-carbonyl]-4'-fluorobenzyl]-2H-phthalazin-1-one (60) using a solution of 4-(chloromethyl)benzoic acid (39) (18.7 mg, 0.110 mmol) in *N,N'*-dimethylformamide (1 mL), triethylamine (24.0 μ L, 0.180 mmol), *O*-benzotriazole-*N,N,N',N'*-tetramethyluroniumhexafluorophosphate (33) (45.6 mg, 0.120 mmol). Following the addition of 4-[4'-fluoro-3'-(piperazine-1''-carbonyl)benzyl]-2H-phthalazin-1-one (3) (40.0 mg, 0.110 mmol) the mixture was stirred at room temperature for a further 72 hours. Water (6 mL) was then added, followed by 0.5 hours of stirring, after which the mixture was cooled to 0 $^{\circ}$ C. The resulting precipitate was collected by vacuum filtration and washed with water (4 \times 20 mL). Purification by flash column chromatography (methanol/ethyl acetate, 5:95) gave 4-[3'-[4''-(4'''-chloromethyl)benzoyl]piperazine-1''-carbonyl]-4'-fluorobenzyl]-2H-phthalazin-1-one (38) (19.0 mg, 34%) as a white foam. R_f (methanol/ethyl acetate, 5:95) 0.40; $\nu_{\max}/\text{cm}^{-1}$ (neat) 3200 (NH), 2924 (CH), 1630 (CO), 1429, 1256, 1005, 750, 731; δ_{H} (400 MHz, CDCl_3) 3.21–3.99 (8H, m, 4 \times N- CH_2), 4.27 (2H, s, 7'- H_2), 4.59 (2H, s, 4'''- CH_2Cl), 7.03 (1H, br s, 5'-H), 7.30–7.36 (2H, m, 3'''-H and 5'''-H), 7.37–7.49 (4H, m, 2'-H, 6'-H, 2'''-H, and 6'''-H), 7.67–7.72 (1H, m, 5-H), 7.73–7.80 (2H, m, 6-H and 7-H), 8.44–8.49 (1H, m, 8-H), 10.84 (1H, br s, NH); δ_{C} (101 MHz, CDCl_3) 37.8 (CH_2), 42.3 (2 \times CH_2), 45.6 (CH_2), 47.1 (2 \times CH_2), 116.3 (CH, d, $J_{\text{C-C-F}}$ 19.9 Hz), 123.8 (C, d, $J_{\text{C-C-F}}$ 17.7 Hz), 125.1 (CH), 127.4 (CH), 127.7 (2 \times CH), 128.5 (C), 129.0 (2 \times CH), 129.4 (CH, d, $J_{\text{C-C-C-F}}$ 3.6 Hz), 129.7 (C), 131.8 (CH), 132.0 (CH, d, $J_{\text{C-C-C-F}}$ 8.2 Hz), 132.1 (2 \times CH), 133.8 (CH), 134.6 (C, d, $J_{\text{C-C-C-C-F}}$ 3.5 Hz), 135.2 (C), 139.7 (C), 145.6 (C), 157.2 (C, d, $J_{\text{C-F}}$ 248.1 Hz), 160.5 (C), 165.3 (C), 170.2 (C); m/z (ESI) 541.1413 (MNa^+ . $\text{C}_{28}\text{H}_{24}^{35}\text{ClFN}_4\text{NaO}_3$ requires 541.1413).

4-[3'-[4''-(4'''-Chloromethyl)benzoyl]piperazine-1''-carbonyl]-4'-fluorobenzyl]-2-*tert*-butyloxycarbonylphthalazin-1-one (72)



To a solution of 4-[3'-[4''-(4'''-chloromethyl)benzoyl]piperazine-1''-carbonyl]-4'-fluorobenzyl]-2H-phthalazin-1-one (**38**) (170 mg, 0.328 mmol) in acetonitrile (1.5 mL) was added di-*tert*-butyl dicarbonate (**29**) (86.0 mg, 0.393 mmol) and 4-dimethylaminopyridine (4.00 mg, 0.0328 mmol). The mixture was stirred at room temperature for 4 hours followed by evaporation of solvent *in vacuo*. The crude product was extracted into ethyl acetate (5 mL) and the organic layer was washed with water (3 × 10 mL), dried with magnesium sulfate, filtered and concentrated *in vacuo* to give 4-[3'-[4''-(4'''-chloromethyl)benzoyl]piperazine-1''-carbonyl]-4'-fluorobenzyl]-2-*tert*-butyloxycarbonylphthalazin-1-one (**72**) as a white foam (148 mg, 72%). $\nu_{\max}/\text{cm}^{-1}$ (neat) 2982 (CH), 1634 (CO), 1427, 1248, 1003, 750; δ_{H} (400 MHz, CDCl_3) 1.66 (9H, s, O^tBu), 3.15–3.99 (8H, m, 4 × N- CH_2), 4.30 (2H, s, 7'- H_2), 4.59 (2H, s, 4'''- CH_2Cl), 7.03 (1H, br s, 5'-H), 7.30–7.36 (2H, m, 3'''-H and 5'''-H), 7.37–7.49 (4H, m, 2'''-H, 6'''-H, 2'-H and 6'-H), 7.59–7.67 (1H, m, 5-H), 7.69–7.78 (2H, m, 6-H and 7-H), 8.42–8.49 (1H, m, 8-H); δ_{C} (101 MHz, CDCl_3) 27.8 (3 × CH_3), 38.1 (CH_2), 42.2 (2 × CH_2), 45.4 (CH_2), 47.1 (2 × CH_2), 85.9 (C), 116.2 (CH, d, $J_{\text{C-C-F}}$ 20.4 Hz), 123.7 (C, d, $J_{\text{C-C-F}}$ 18.2 Hz), 125.1 (CH), 127.6 (2 × CH), 128.1 (CH), 128.7 (C), 128.8 (2 × CH), 129.1 (C), 129.2 (CH, d, $J_{\text{C-C-F}}$ 3.4 Hz), 131.8 (CH, d, $J_{\text{C-C-C-F}}$ 7.6 Hz), 132.0 (CH), 134.0 (CH), 134.1 (C, d, $J_{\text{C-C-C-C-F}}$ 3.7 Hz), 135.1 (C), 139.5 (C), 145.3 (C), 151.1 (C), 157.0 (C, d, $J_{\text{C-F}}$ 247.7 Hz), 158.2 (C), 165.1 (C), 170.0 (C); m/z (ESI) 641.1915 (MNa^+ . $\text{C}_{33}\text{H}_{32}^{35}\text{ClFN}_4\text{NaO}_5$ requires 641.1937).

4-[3'-[4''-(4'''-Fluoromethyl)benzoyl]piperazine-1''-carbonyl]-4'-fluorobenzyl]-2-*tert*-butyloxycarbonylphthalazin-1-one (73)



The reaction was carried out as described for 4-[3'-[4''-(4'''-chloromethyl)benzoyl]piperazine-1''-carbonyl]-4'-fluorobenzyl]-2-*tert*-butyloxycarbonylphthalazin-1-one (**72**) using a solution of 4-[3'-[4''-(4'''-fluoromethyl)benzoyl]piperazine-1''-carbonyl]-4'-fluorobenzyl]-2*H*-phthalazin-1-one (**17**) (3.30 mg, 0.00656 mmol), di-*tert*-butyl dicarbonate (**29**) (1.70 mg, 0.00790 mmol) and 4-dimethylaminopyridine (0.08 mg, 0.000656 mmol) in acetonitrile (0.4 mL). The mixture was stirred at room temperature for 1.25 hours followed by evaporation of solvent *in vacuo*. The crude product was extracted into ethyl acetate (2 mL) and the organic layer was washed with water (3 × 4 mL), dried with magnesium sulfate, filtered and concentrated *in vacuo* to give

4-[3'-[4''-(4'''-fluoromethyl)benzoyl]piperazine-1''-carbonyl]-4'-fluorobenzyl]-2-*tert*-butyloxycarbonylphthalazin-1-one (**73**) (3.50 mg, 81%) as a yellow-white foam. $\nu_{\max}/\text{cm}^{-1}$ (neat) 2930 (CH), 1635 (CO), 1216, 1005, 754; δ_{H} (400 MHz, CDCl_3) 1.67 (9H, s, O^tBu), 3.14–4.00 (8H, m, 4 × N- CH_2), 4.31 (2H, s, 7'- H_2), 5.41 (2H, d, J 47.4 Hz, 4'''- CH_2F), 7.05 (1H, br s, 5'-H), 7.34 (2H, d, J 6.3 Hz, 2'-H and 6'-H), 7.44 (4H, br s, 2'''-H, 3'''-H, 5'''-H and 6'''-H), 7.61–7.66 (1H, m, 5-H), 7.71–7.77 (2H, m, 6-H and 7-H), 8.44–8.49 (1H, m, 8-H); δ_{C} (101 MHz, CDCl_3) 28.0 (3 × CH_3), 38.2 (CH_2), 42.1 (2 × CH_2), 47.7 (2 × CH_2), 84.0 (CH_2 , d, $J_{\text{C-F}}$ 167.8 Hz), 86.0 (C), 116.3 (CH, d, $J_{\text{C-C-F}}$ 21.7 Hz), 123.8 (C, d, $J_{\text{C-C-F}}$ 17.6 Hz), 125.4 (CH), 127.5 (2 × CH, d, $J_{\text{C-C-C-F}}$ 6.1 Hz), 127.6 (2 × CH), 128.3 (CH), 128.9 (C), 129.2 (C), 129.3 (CH, d, $J_{\text{C-C-C-F}}$ 3.4 Hz), 131.9 (CH, d, $J_{\text{C-C-C-F}}$ 8.6 Hz), 132.1 (CH), 134.2 (CH), 134.5 (C, d, $J_{\text{C-C-C-C-F}}$ 3.6 Hz), 135.5 (C), 138.4 (C, d, $J_{\text{C-C-F}}$ 17.6 Hz), 145.5 (C), 151.2 (C), 157.1 (C, d, $J_{\text{C-F}}$ 245.4 Hz), 158.4 (C), 165.3 (C), 170.2 (C); m/z (ESI) 625.2221 (MNa^+ . $\text{C}_{33}\text{H}_{32}\text{F}_2\text{N}_4\text{NaO}_5$ requires 625.2233).

5.4.2.2 Non-radioactive dediazonisation chemistry.

5.4.2.2.1 Iodo-dediazonisation of isolated diazonium tosylate salt **65**.

A general procedure involved addition of sodium iodide (1.6 mg, 0.0108 mmol) to a solution of 4-[3'-[4''-[4'''-diazonium-(4''''-methylbenzenesulfonate)benzoyl]piperazine-1''-carbonyl]-4'-fluorobenzyl]-2*H*-phthalazin-1-one (**65**) (3.7 mg, 0.0054 mmol) in either *N,N'*-dimethylformamide or glacial acetic acid (0.3 mL). The reaction was stirred for 1 or 2 hours either at room temperature, 75 °C or 100 °C. Following this, and once cooled to room temperature, the crude mixture was extracted into dichloromethane (2 mL) and the organic layer was washed with water (3 × 4 mL), dried with magnesium sulfate, filtered and concentrated *in vacuo*. The resulting solid material was then dissolved in dichloromethane and filtered through a pad of silica using 6% v/v methanol/dichloromethane. The filtrate was concentrated *in vacuo*, dissolved in deuterated chloroform and analysed using ¹H NMR spectroscopy.

5.4.2.2.2 Iodo-dediazonisation of *in situ* generated diazonium tosylate salt **65**.

To solution of tosic acid (8.2 mg, 0.043 mmol) and 4-[3'-[4''-(4'''-aminobenzoyl)piperazine-1''-carbonyl]-4'-fluorobenzyl]-2*H*-phthalazin-1-one (**64**) (7.0 mg, 0.014 mmol) in glacial acetic acid (1.0 mL) was added resin-bound nitrite (12.3 mg, equivalent to 0.043 mmol nitrite). The mixture was cooled to 10 °C using a water bath and stirred for 1 hour, after which sodium iodide (4.3 mg, 0.029 mmol) was added. The reaction was heated to 100 °C and stirred for a further 2 hours. The crude reaction mixture was then cooled to room temperature and the resin-bound nitrite was removed by filtration. A sample of the filtrate was removed and ran on the analytical HPLC system using the following mobile phase conditions: 0.0–20.0 minutes = 30:70 A:B to 55:45 A:B, 20.0–20.5 minutes = 55:45 A:B to 5:95 A:B, 20.5–25.0 minutes = 5:95 A:B where A = acetonitrile and B = distilled water.

5.4.2.2.3 Fluoro-dediazonisation of *in situ* generated diazonium tosylate salt **65**.

A general procedure involved addition of resin-bound nitrite (8.6 mg, 0.030 mmol) to a solution of tosic acid (6.0 mg, 0.030 mmol) and 4-[3'-[4''-(4'''-aminobenzoyl)piperazine-1''-carbonyl]-4'-fluorobenzyl]-2*H*-phthalazin-1-one (**64**) (5.0 mg, 0.010 mmol) in glacial acetic acid (5.0 mL). The mixture was cooled to 10 °C using a water bath and stirred for one hour, after which potassium fluoride (1.2 mg, 0.020 mol) was added with or without 18-crown-6 (5.3 mg, 0.020 mmol). The reaction was heated to 100 °C and stirred for a further 2 or 2.5 hours. The crude reaction mixture was then cooled to room temperature, and the resin-bound nitrite was removed by filtration. A sample of the filtrate was removed and run on the analytical HPLC system using mobile phase conditions as described for the non-radioactive iodo-dediazonisation of *in situ* generated diazonium tosylate salt **65** (section 5.4.2.2.2).

5.4.2.2.4. Fluoro-dediazonisation of isolated diazonium tosylate salt **65**.

To a solution of 4-[3'-[4''-[4'''-diazonium-(4''''-methylbenzenesulfonate)benzoyl]piperazine-1''-carbonyl]-4'-fluorobenzyl]-2*H*-phthalazin-1-one (**65**) (6.0 mg, 0.0088 mmol) in *N*-methyl-2-pyrrolidone (0.30 mL) was added potassium fluoride (1.0 mg, 0.0176 mmol) and 18-crown-6 (7.0 mg, 0.0176 mmol). The reaction was stirred at 100 °C for 1.0 hour. Following this, the reaction was cooled to room temperature, and a sample was run on the analytical HPLC system using mobile phase conditions as described for the non-radioactive iodo-dediazonization of *in situ* generated diazonium tosylate salt **65** (section 5.4.2.2.2).

5.4.2.3 General experimental for screening of reaction conditions for Boc-deprotection of **73**.

To 1 M hydrochloric acid or *N,N'*-dimethylformamide (0.30 mL), or distilled water (0.50 mL), was added a 0.0166 M solution of **73** in acetonitrile (20 µL). The reaction vial was sealed and the mixture was stirred for 5 to 10 minutes at either room temperature, 80 °C, 110 °C, 120 °C or 140 °C. Following this, the

reaction was cooled to room temperature, where necessary, and diluted with either 0.20 mL of acetonitrile (for reactions conducted in *N,N'*-dimethylformamide or water) or 0.30 mL of 1 M sodium hydroxide (for reactions conducted in 1 M hydrochloric acid). The diluted crude mixtures were passed through a 0.22 μm filter and analysed using LC-MS.

LC-MS analysis was performed using Shimadzu LC-2010AHT and LCMS-2010EV systems. Liquid chromatography was performed on 10 μL sample injections using a Kinetex 5 μm XB-C18 100 \AA (50 \times 4.60 mm) column and the following mobile phase conditions: 0.0–10.0 minutes = 30:70 to 60:40 A:B; 10.0–12.0 minutes = 60:40 to 30:70 A:B; 12.0–14.0 minutes = 30:70 A:B where A = acetonitrile and B = 0.1% v/v formic acid in distilled water; flow rate 1.2 mL/min. Compound detection was performed using MS and the following detector settings: positive ionisation; 1.50 kV; total ion current. Data were recorded and analysed using the LabSolutions LCMS software. The identity of compound **73** in the reaction mixture was confirmed by establishing the chromatographic retention time of **73** (Appendix 9.9) and through detection of the MH^+ ($m/z = 603$) or MNa^+ ($m/z = 625$) ions from the MS chromatogram. The identity of compound **17** in the reaction mixture was established by detection of the MH^+ ($m/z = 503$) or MNa^+ ($m/z = 525$) ions from the MS chromatogram.

5.4.3 Radiochemistry experimental.

5.4.3.1 Manual radiosynthesis of [^{125}I]-**4** via radioiodo-dediazonisation of isolated diazonium tosylate salt **65**.

To a 2 mL v-vial was added 1.80 MBq of [^{125}I]-NaI in 50.0 mM of sodium hydroxide (30 μL). Water was removed by passing a constant stream of argon over the solution at 100 $^\circ\text{C}$ for approximately 15 minutes; aliquots of anhydrous acetonitrile (3 \times 0.5 mL) were added to facilitate azeotropic drying. A solution of 4-[3'-[4''-[4'''-diazonium-(4''''-methylbenzenesulfonate)benzoyl]piperazine-1''-carbonyl]-4'-fluorobenzyl]-2*H*-phthalazin-1-one (**65**) (1.5 mg, 0.0022 mmol) in glacial acetic acid (0.20 mL) was then added to the v-vial and the reaction

was allowed to proceed at 100 °C for 30 minutes. The mixture was then cooled to room temperature and a sample was removed and run on the analytical HPLC system using the mobile phase conditions as described for the non-radioactive iodo-dediazonization of *in situ* generated diazonium tosylate salt **65** (section 5.4.2.2.2). To confirm the identity of the radiolabelled product, the retention time of [¹²⁵I]-**4** was compared to the retention time obtained for non-radioactive **4** using the same chromatographic conditions.

5.4.3.2 Manual radiosynthesis of [¹²⁵I]-**4** via radioiodo-dediazonisation of *in situ* generated diazonium tosylate salt **65**.

To a 2 mL v-vial was added a solution of tosic acid (2.4 mg, 0.012 mmol) and 4-[3'-[4''-(4'''-aminobenzoyl)piperazine-1''-carbonyl]-4'-fluorobenzyl]-2H-phthalazin-1-one (**64**) (2.0 mg, 0.004 mmol) in glacial acetic acid (0.40 mL), followed by resin-bound nitrite (3.5 mg, equivalent to 0.012 mmol nitrite). The mixture was cooled to 10 °C using a water bath and stirred for 60 minutes, after which 3.62 MBq of [¹²⁵I]-NaI in 50.0 mM of sodium hydroxide (30 µL) was added. The reaction vessel was heated to 100 °C and stirred for a further 30 minutes. The crude reaction was then cooled to room temperature and a sample was removed and ran on the analytical HPLC system using the mobile phase conditions as described for the non-radioactive iodo-dediazonisation of *in situ* generated diazonium tosylate salt **65** (section 5.4.2.2.2).

5.4.3.3 Manual radiosynthesis (via radioiodo-debromination of the brominated precursor **60**), specific activity measurements, purification and formulation of [¹²³I]-**4**.

The synthesis was performed as reported by Zmuda *et al.* (2015). To a 2 mL v-vial, half-filled with 3 mm borsilicate glass beads, was added a 0.492 M solution of (NH₄)₂SO₄ in distilled water (0.1 mL), followed by a solution of 4-[3'-[4''-(4'''-bromobenzoyl)piperazine-1''-carbonyl]-4'-fluorobenzyl]-2H-phthalazin-1-one (**60**) (5.0 mg, 0.0091 mmol) in glacial acetic acid (0.1 mL). The mixture was

vortexed and then 35.5–175.0 MBq of [^{123}I]-NaI in 50.0 mM sodium hydroxide was added; the edges of the v-vial were rinsed with a 1.0 : 2.0 solution of ethanol and distilled water (0.15 mL). Solvents and water were removed by passing a constant stream of argon over the solution at 150 °C for approximately 30 minutes; aliquots of anhydrous acetonitrile (3×0.5 mL) were added to facilitate azeotropic drying. The argon supply was removed and the sealed v-vial was heated to 210 °C. Once at the correct temperature, air was injected (8 mL) and the reaction was heated for a further 30 minutes. The contents of the v-vial were allowed to cool to room temperature and the organic components were dissolved in acetonitrile (0.3 mL), followed by the addition of a 3.0 : 7.0 solution of acetonitrile and distilled water (0.15 mL). The crude reaction mixture was purified using the preparatory HPLC system using the following mobile phase conditions: 0.0–30.0 minutes = 30:70 A:B to 55:45 A:B where A = acetonitrile and B = distilled water. The radiolabelled product was collected at approximately 27.0 minutes and concentrated *in vacuo* in an evaporator flask. The flask was rinsed with acetonitrile (3×0.3 mL) to extract the radiolabelled compound and the solution was transferred to a 2.0 mL v-vial; the solvent was removed by passing a constant stream of argon over the solution at 100 °C for approximately 15 minutes. The radiotracer was then dissolved in ethanol followed by dilution using 0.9% w/v saline solution such that the final volume was up to 0.9 mL and the final concentration of ethanol was 10.0% v/v; the mixture was vortexed for up to 0.5 minutes to maximise solubilisation of [^{123}I]-4. The total radiosynthesis time was 160 ± 32 minutes ($n = 6$).

A sample of the formulated radiotracer was run on the analytical HPLC system using the same mobile phase conditions as described above for the purification step. To confirm the identity of the radiolabelled product, the retention time of [^{123}I]-4 was compared to the retention time obtained for non-radioactive 4 using the same chromatographic conditions.

To measure the specific activity of the synthesised radiotracer, a calibration graph of UV peak area (254 nm) against molar quantity of non-radioactive 4 was produced (Appendix 9.7). The calibration graph was then used to establish the amount in micromoles of radiolabelled product that was produced. However,

since the amount of [^{123}I]-4 that was produced fell below the sensitivity threshold of the UV detector ($<1.68 \times 10^{-4} \mu\text{mol}$), specific activity ($\text{Ci}/\mu\text{mol}$) was calculated using the lowest detectable amount of non-labelled 4 established from the calibration plot.

5.4.3.4 Manual radiosynthesis of [^{18}F]-11 via aromatic nucleophilic substitution of the nitro precursor **63**.

To a 2 mL v-vial containing between 20–100 MBq of $^{18}\text{F}^-/\text{H}_2^{18}\text{O}$ was added either K_{222} /potassium carbonate (0.25 mL), TBACO_3 (10 μL), or caesium carbonate (0.1 mL) stock solution (see general experimental section). The mixture was vortexed and the [^{18}F]-fluoride was dried by passing a constant stream of argon over the solution at 100 °C for approximately 20 minutes; aliquots of anhydrous acetonitrile ($3 \times 0.50 \text{ mL}$) were added to facilitate azeotropic drying. A solution of 4-[3'-[4''-(4'''-nitrobenzoyl)piperazine-1''-carbonyl]-4'-fluorobenzyl]-2H-phthalazin-1-one (**63**) (1.0–5.0 mg, 0.0019–0.0095 mmol) in anhydrous solvent (0.3–0.6 mL) was then added to the v-vial and the reaction was allowed to proceed for between 10–30 minutes at either 150 °C, 180 °C or 200 °C. Next, the crude reaction mixture was cooled to room temperature and a sample was ran on the analytical HPLC system using the mobile phase conditions as described for the non-radioactive iodo-dediazonisation of *in situ* generated diazonium tosylate salt **65** (section 5.4.2.2.2). To confirm the identity of the radiolabelled product, the retention time of [^{18}F]-11 was compared to the retention time obtained for non-radioactive 11 using the same chromatographic conditions.

5.4.3.5 Manual radiosynthesis of [^{18}F]-11 via radiofluoro-dediazonisation of isolated diazonium tosylate **65**.

To a 2 mL v-vial containing between 41.0–66.1 MBq of $^{18}\text{F}^-/\text{H}_2^{18}\text{O}$ was added either K_{222} /potassium carbonate (0.25 mL) or TBACO_3 (10 μL) stock solution (see general experimental section). The mixture was vortexed and the [^{18}F]-fluoride was dried by passing a constant stream of argon over the solution at 100 °C for approximately 20 minutes; aliquots of anhydrous acetonitrile ($3 \times 0.5 \text{ mL}$) were

added to facilitate azeotropic drying. A solution of isolated 4-[3'-[4''-[4'''-diazonium-(4''''-methylbenzenesulfonate)benzoyl]piperazine-1''-carbonyl]-4'-fluorobenzyl]-2*H*-phthalazin-1-one (**65**) (2.0–2.67 mg, 0.0030–0.0040 mmol) in *N*-methyl-2-pyrrolidone (0.3 mL) was then added to the v-vial and the reaction was allowed to proceed 30 minutes at either 80, 120 or 155 °C. Next, the crude reaction mixture was cooled to room temperature and a sample was run on the analytical HPLC system using the mobile phase conditions as described for the non-radioactive iodo-dediazonisation of *in situ* generated diazonium tosylate salt **65** (section 5.4.2.2.2). To confirm the identity of the radiolabelled product, the retention time of [¹⁸F]-**11** was compared to the retention time obtained for non-radioactive **11** using the same chromatographic conditions.

5.4.3.6 Manual radiosynthesis (via aliphatic nucleophilic substitution of the chlorinated precursor **72**), specific activity measurements, purification, and formulation of [¹⁸F]-**17**.

To a 2 mL v-vial containing 469–572 MBq of ¹⁸F⁻/H₂¹⁸O (0.16 mL) was added 0.750 M TBAHCO₃ (10 μL) (see general experimental section). The mixture was vortexed and the [¹⁸F]-fluoride was dried by passing a constant stream of argon over the solution at 100 °C for approximately 20 minutes; aliquots of anhydrous acetonitrile (3 × 0.5 mL) were added to facilitate azeotropic drying. A solution of the chloride precursor **72** (4.9 mg, 0.0079 mmol) in acetonitrile (0.1 mL) and *tert*-butanol (0.2 mL) was then added to the v-vial and the reaction was allowed to proceed for 30 minutes at 110 °C. After this, distilled water was added (0.45 mL) and the reaction was heated at 120 °C for a further 5 minutes. Next, the crude reaction mixture was cooled to room temperature and was purified using the preparatory HPLC system using the following mobile phase conditions: 0.0–3.0 minutes = 30:70 A:B; 3.0–30.0 minutes 30:70 to 75:25 A:B; 30.0–30.1 minutes = 75:25 to 95:5 A:B; 30.1–35.0 minutes = 95:5 A:B where A = acetonitrile and B = distilled water. The radiolabelled product was collected at approximately 13.5 minutes and concentrated *in vacuo* in an evaporator flask. The flask was rinsed with acetonitrile (3 × 0.3 mL) to extract the radiolabelled compound and the solution was transferred to a 2 mL v-vial; the solvent was removed by passing a

constant stream of argon over the solution at 100 °C for approximately 15 minutes. The radiotracer was then dissolved in dimethyl sulfoxide followed by dilution using 0.9% w/v saline solution such that the final volume was up to 0.65 mL and the final concentration of dimethyl sulfoxide was 5.0% v/v; the mixture was vortexed for up to 0.5 minutes to maximise solubilisation of [¹⁸F]-**17**. The total radiosynthetic time was 138 ± 16 minutes (n = 6).

A sample of the formulated radiotracer was run on the analytical HPLC system using the following mobile phase conditions: 0.0–15.0 minutes = 30:70 A:B to 90:10; 15.0–20.0 minutes = 90:10 A:B; 20.0–20.5 minutes = 90:10 to 30:70 A:B; 20.5–25.0 minutes = 30:70 A:B where A = acetonitrile and B = distilled water. To confirm the identity of the radiolabelled product, the retention time of [¹⁸F]-**17** was compared to the retention time obtained for non-radioactive **17** using the same chromatographic conditions.

To measure the specific activity of the synthesised radiotracer, a calibration graph of UV peak area (254 nm) against molar quantity of non-radioactive **17** was produced (Appendix 9.8). The calibration graph was then used to establish the amount in micromoles of radiolabelled product that was produced. However, since the amount of [¹⁸F]-**17** that was produced fell below the sensitivity threshold of the UV detector ($<1.68 \times 10^{-4}$ μmol), specific activity (Ci/μmol) was calculated using the lowest detectable amount of non-labelled **17** established from the calibration plot.

6 *IN VITRO* STABILITY AND *EX VIVO* EVALUATION OF THE PARP-1 NUCLEAR IMAGING AGENTS [¹²³I]-4 AND [¹⁸F]-17.

6.1 Introduction.

6.1.1 Blood plasma stability.

In addition to the effects of plasma proteins on the pharmacokinetics of radiotracers (see section 4.1.2.1), further considerations have to be made during the tracer discovery process for the stability of these agents in blood plasma.

Blood plasma is a complex medium that comprises not only plasma proteins (albumin) but also coagulation factors, immunoglobulins, carbohydrates, amino acids, vitamins, hormones, inorganic constituents, and enzymes (Krebs, 1950). The majority of plasma enzymes exhibit hydrolytic functions (Krebs, 1950), which means that certain organic compounds may be labile to blood plasma hydrolysis (Hartman, 2003). Interestingly, albumin itself also possesses hydrolytic properties due to its esterase-like catalytic site which has been shown to be involved in the cleavage of various esterified drugs (Salvi *et al.*, 1997). It is important to note that the hydrolytic properties of albumin and plasma enzymes, as well as the expression of these enzymes, can vary depending on the species. As a consequence, the substrates that can undergo plasma hydrolysis and the rate of these biotransformations can also vary between species. For example, rodents have been shown to express higher levels of plasma carboxylesterases than humans, resulting in substantially more rapid hydrolysis of propranolol analogues (Bahar *et al.*, 2012).

Ascertaining the plasma stability of a compound is usually performed *in vitro* by incubating the article in question in an isolated sample of blood plasma from a chosen species, followed by determination of the amount of unchanged parent compound remaining (Nomeir *et al.*, 1998; Di *et al.*, 2005; Uchôa *et al.*, 2008; Liu *et al.*, 2014). The latter step is usually achieved with the aid of HPLC

coupled with an appropriate detection method that allows for the visualisation of the parent compound and potential metabolites. When assessing the plasma stability of a radiotracer, either the radionuclide labelled tracer or the equivalent non-radioactive analogue can be used; the choice of compound will ultimately determine the type of detection technique that is utilised.

In the case of a radiolabelled compound, detection is performed using a radiodetector, which is a highly sensitive piece of equipment that can detect trace amount of radiolabelled compound. However, the use of radiolabelled compounds for plasma stability analysis is an expensive and labour intensive process, particularly when the compound under investigation is labelled with a short lived radioisotope (e.g. ^{11}C or ^{18}F) as multiple radiosyntheses will be necessary. The two most commonly used methods for non-radioactive compound and metabolite analysis rely on ultraviolet (UV) absorbance and mass detection (Siddiqui, AlOthman and Rahman, 2013). Simple detectors allow for the measurement of UV absorbance of a pre-set wavelength; these are called fixed-wavelength UV-detectors. Despite their cheap cost they are disadvantaged by the fact that the absorbance properties of the compound under analysis must be known. This issue can be circumvented with a diode array detector (DAD), which works on the same principle except it possesses an array of photodiodes located at the detector plane that can sense a range of wavelengths simultaneously (Siddiqui, AlOthman and Rahman, 2013). The main advantage of UV detection is the simplicity of the technique and the low level of chemical and electrical background of the output signal (Barbarin, Henion, and Wu, 2002). UV detectors exhibit good sensitivity with a noise equivalent concentration, C_N (the solute concentration that produces a signal equal to the detector noise level) of approximately 1 ng/mL (Hani, 1999).

Mass detection is achieved using a mass spectrometer that works by ionising and fragmenting the organic compound under investigation. The ion fragments are separated according to their mass-to-charge ratio (m/z) and, upon detection, are recorded as the abundance of each ion fragment relative to the overall amount of detected ions. Mass spectrometry (MS) is a more sensitive detection technique when compared to UV-absorbance measurement with an approximate

C_N of 10 pg/mL (Hani, 1999). Furthermore, MS provides useful structural information such as molecular masses and fragmentation patterns that can be used in the identification of unknown compounds and/or metabolites. In a similar way to the DAD, a mass spectrometer can simultaneously detect multiple different unknown chemical entities if in full-scan mode. However, such a scan is often associated with a high background signal due to chemical noise that can interfere with the detection of small concentrations of analyte (Barbarin, Henion and Wu, 2002). This issue can be overcome by performing a selected ion monitoring (SIM) scan where only ions of a pre-selected mass are detected. Consequently, the SIM approach is limited to the analysis of compounds and/or metabolites of known mass.

To summarise, the *in vitro* assessment of compound stability in blood plasma is an important step in the radiotracer development process, where considerations have to be made with regard to the choice of species from which the blood plasma originates and the detection method used for data acquisition.

6.1.2 Metabolic stability.

Organic compounds, including radiotracers, which enter the body are ultimately eliminated through the two key pharmacokinetic processes of metabolism and excretion. Metabolism involves enzymatic conversion of one chemical entity into another, while excretion refers to the process of removal of an unchanged chemical entity or an enzymatically-modified chemical entity (i.e. a metabolite) from the body. The three body systems involved in excretion include the kidneys, the hepatobiliary system, and the lungs. The elimination properties of a radiotracer can have a significant influence on its utility as a nuclear imaging agent. For example, tracers excreted predominately by the kidneys will exhibit little usefulness as renal imaging agents, while tracers that are rapidly eliminated may result in low intensity imaging signal in the desired tissue. Furthermore, as mentioned previously, metabolism of radiotracers may lead to the generation of radiolabelled metabolites that can ultimately reduce the molecular imaging signal to noise contrast due to altered distribution of

metabolites (Jacobson and Chen, 2013). The processes underpinning compound elimination have been depicted in Figure 6.1.

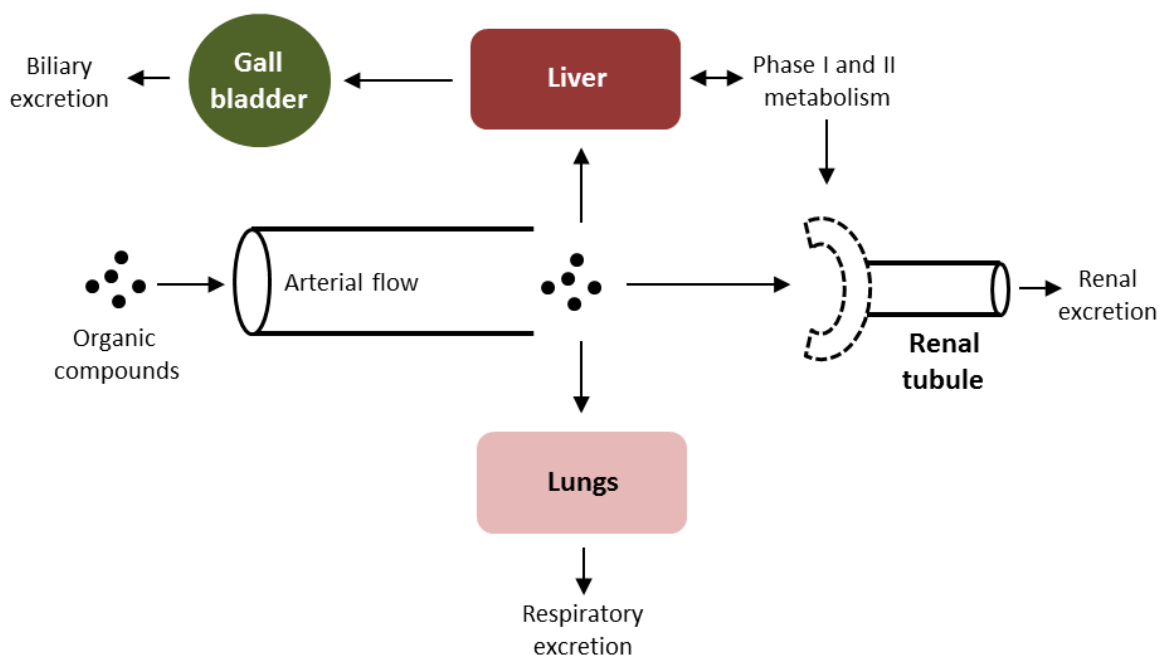


Figure 6.1. Schematic outlining the processes of organic compound elimination from the body.

Compounds that are excreted by the lungs include volatile substances such as anaesthetic gases; this excretory pathway falls outside of the scope of this thesis and will not be discussed further (Rang *et al.*, 2007). The kidneys play a crucial role in the excretion of hydrophilic compounds or metabolites that are dissolved in blood plasma. Approximately 20% of plasma that reaches the kidneys is filtered by the glomerular capillaries that prevent large macromolecules ($M_w > 20000$) from diffusing into the glomerular filtrate; this includes plasma protein bound compounds. Smaller non-bound chemical entities enter renal tubules and are either excreted in the urine or reabsorbed into circulation (see section 4.1.2.1 for details). The remaining 80% of renal plasma is delivered to the peritubular capillaries of the kidney proximal tubules where two active transport systems, or phase III transporters, secrete acidic and basic chemical entities into the kidney tubules resulting in their subsequent urinary excretion (Rang *et al.*, 2007).

The hepatobiliary system is more complex as it possesses both metabolic and excretory potential (Rang *et al.*, 2007). In addition to the elimination of chemical entities, metabolism can also result in the bioactivation of previously non-active compounds (Xu, Li, and Kong, 2005). For the purpose of this chapter emphasis will be placed on the elimination pathway; further information concerning compound bioactivation can be found in the review paper by Tang and Lu (2010). Key players involved in the metabolism of chemical entities are drug metabolising enzymes (DME), which can be described according to the ‘Williams Classification’ introduced in 1959. This system classifies DME according to two main types of biotransformation termed ‘phase I’ and ‘phase II’. Broadly speaking, phase I reactions can be regarded as functionalisations where a new functional group is introduced into the organic compound that then allows for conjugation with a highly-polar moiety introduced by a phase II conjugative-reaction. The purpose of the conjugation step is to make the organic compound more hydrophilic and allow for its excretion (Figure 6.2) (Josephy, Guengerich, and Miners, 2008).

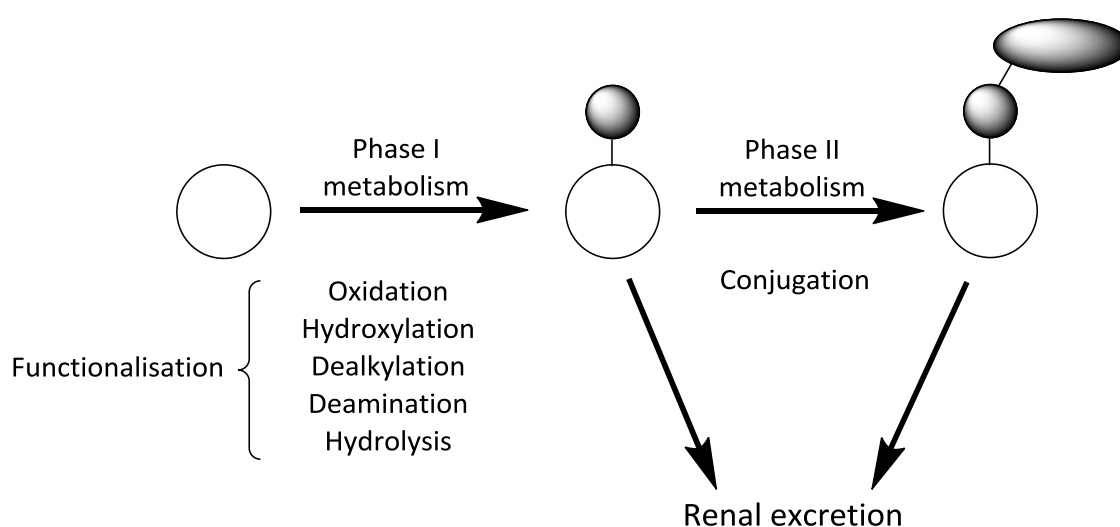
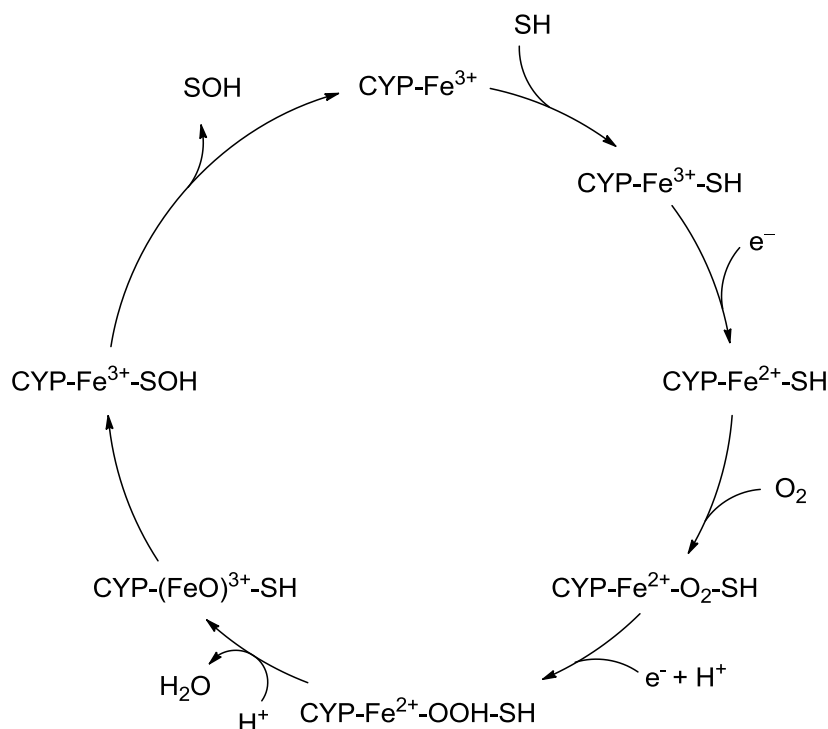


Figure 6.2. Diagrammatic representation of phase I and II metabolism.

Phase I DME consist primarily of the cytochrome P450 (CYP450) superfamily of microsomal enzymes located in large quantities in the liver, gastrointestinal tract, lungs, and kidneys (Xu, Li and Kong, 2005). It should be noted that the numbers of CYP450 enzymes present in different species can vary dramatically; for example in humans 57 distinct CYP450 genes have been identified compared to the 102 genes found in mice. Mice not only possess four subfamilies of CYP450

genes that have been lost in humans, but they also exhibit expansions in a number of other CYP450 subfamily clusters including the CYP2D cluster, which is known to be a key player in phase I metabolism (Nelson *et al.*, 2004). In humans, approximately 15 out of the 57 CYP450 enzymes are responsible for metabolism of exogenous organic compounds that are not normally present in the body, where 90% of these biotransformations are performed by only 5 enzymes (i.e. CYP1A2, CYP2C9, CYP2C19, CYP2D6, and CYP3A4) (Guengerich, 2006). These CYP450 enzymes act as potent oxidants and are responsible for the hydroxylation of saturated-hydrogen bonds, the epoxidation of double bonds, the oxidation of heteroatoms and aromatics, as well as dealkylation and deamination reactions. The mechanism of these oxidation reactions involves the transfer of a single oxygen atom from molecular oxygen to the substrate organic molecule; the remaining oxygen atom is reduced to water by a reductase enzyme using two electrons provided by NADPH (Scheme 6.1) (Meunier, Visser, and Shaik, 2004; Rang *et al.*, 2007). The role of this type of functionalisation can be twofold. Firstly structural changes can reduce or abolish biological activity of a compound, and secondly the introduction of a hydroxyl moiety provides a conjugative site for phase II metabolism (Josephy, Guengerich, and Miners, 2008).



Scheme 6.1. The cytochrome P450 (CYP) catalytic cycle. Fe³⁺ at the core of the CYP enzyme combines with a substrate molecule (SH) to generate a CYP-Fe³⁺-SH complex. The Fe³⁺ is reduced to Fe²⁺ by an electron (e⁻) made available from NADPH, and subsequently the CYP-Fe²⁺-SH combines with molecular oxygen to form the corresponding CYP-Fe²⁺-O₂-SH complex. Addition of a further e⁻, made available from another molecule of NADPH, and a proton (H⁺) forms the peroxide complex CYP-Fe²⁺-OOH-SH, which in the presence of another proton yields water and the ferric oxene CYP-(FeO)³⁺-SH complex. Finally, the (FeO)³⁺ extracts a hydrogen atom from the substrate resulting in radical formation and subsequent hydroxylation of the substrate (SOH).

Phase II DME utilise suitable 'handles' found on organic compounds (e.g. hydroxyl, thiol or amino moieties), which are already present or have been introduced as a consequence of phase I metabolism, to introduce large water-soluble moieties through conjugation (Rang *et al.*, 2007). The main phase II DME include aryl sulfotransferase, uridine diphosphate (UDP)-glucuronyl transferase, and glutathione S-transferase (Meunier, Visser, and Shaik, 2004) that are responsible for introducing sulfate, glucuronic acid, and glutathione conjugates respectively. The purpose of such conjugation is to inactivate biologically active compounds and to enhance their water-solubility thereby facilitating clearance in urine or bile (Xu, Li, and Kong, 2005; Rang *et al.*, 2007; Josephy, Guengerich,

and Miners, 2008). It should be noted that in some cases phase II metabolism can result in the bioactivation of compounds thereby enhancing their toxicity (Xu, Li, and Kong, 2005).

Since its conception, the 'Williams Classification' has been expanded to include phase III transporter enzymes. These include membrane transporters such as P-glycoprotein (P-gp), multidrug resistance-associated protein (MRP), and organic anion transporting polypeptide (OATP) that can be found in the liver, kidney, intestines, and brain. These proteins are responsible for the active transport of a wide variety of substrate molecules across cell membranes, and they play an important role in both the metabolism and excretion of organic molecules (Xu, Li, and Kong, 2005). The presence of these phase III transporters in liver cells (hepatocytes) accounts for the excretory component of the hepatobiliary system. Some chemical entities, either unchanged compounds or more commonly phase II metabolites (e.g. glucuronides), can be actively secreted by hepatocyte MRPs into bile, which subsequently works its way down the gastrointestinal tract and is excreted in faecal matter (Shitara, Horie, and Sugiyama, 2005; Rang *et al.*, 2007). It is noteworthy that some chemical entities must first be actively taken up into hepatocytes by transporter proteins (e.g. MRP and OATP) before they can undergo phase I metabolism. This active hepatocyte uptake can be the rate limiting step in organic compound elimination (Shitara, Horie, and Sugiyama, 2005).

The 'Williams Classification' of drug metabolism has recently come under scrutiny and a number of key issues have been highlighted. Firstly, the classification system does not account for the mechanisms behind phase I and II biotransformations. For example, the mechanism driving hydrolysis and glutathione conjugation is identical as both biotransformations involve nucleophilic attack onto an electrophilic organic compound. However, the 'Williams Classification' separates these into distinct phase I (hydrolysis) and phase II (conjugation) reactions. Secondly, phase I and II reactions do not always occur sequentially, as suggested in this classification system, but are often competing pathways. Finally, the concept that phase I functionalisation allows for phase II conjugation is misleading as there are cases where oxidation of some

organic compounds can impede phase II conjugation (Guengerich, 2006; Josephy, Guengerich, and Miners, 2008). Attention should also be drawn to the misleading nature of the term ‘phase III transporters’ due to the fact that certain compounds rely on utilising these transporters to enter hepatocytes prior to phase I metabolism. Despite these limitations, the ‘Williams Classification’ will be utilised for discussion of data presented in this chapter as it is a well-established system that remains in common use.

The above information highlights the complexity of organic compound elimination and the various interconnected pathways that are involved in this process. From a radiotracer discovery perspective, the ultimate aim would be to ascertain information regarding a novel tracer when exposed to all of these pathways simultaneously; i.e. radiotracer elimination. This can be achieved *in vivo* through the process of blood sampling and radio-HPLC analysis at different time-points post tracer injection. Such an approach allows monitoring of how the amount of unchanged (parent) radiotracer decreases in blood plasma with time relative to radionuclide-containing metabolites. However, this technique is limited to larger animal species (e.g. rats, dogs, primates, etc.) where multiple blood samples can be withdrawn manually from a single subject in a single session. In the case of mice, which have an approximate total blood volume of only 1.0–2.0 mL (Sluiter *et al.*, 1984), such sampling requires the use of specialist equipment that can accommodate automatic blood sampling in low microliter volumes (Convert *et al.*, 2007). Where access to such equipment or larger animal species is not available, then the *in vitro* approach can be utilised as an alternative means of radiotracer elimination assessment. However, a complete picture of radiotracer elimination would necessitate multiple *in vitro* assays, as elimination involves multiple different process. Fortunately, it is often the case that hepatocyte driven metabolism precedes urinary or biliary excretion. For this reason, it is not uncommon for *in vitro* studies to focus on the metabolic component of the elimination pathway.

Methodologically, *in vitro* metabolic assays are analogous to those described previously for assessment of compound plasma stability (section 6.1.1). Briefly, the radiolabelled tracer, or its stable non-labelled analogue, is incubated in

phase I or II DME from a chosen species, and either the amount of parent compound remaining or the appearance of specific metabolites are assessed over time (Iyer and Sinz, 1999; Diaz and Squires, 2003; Soars *et al.*, 2003; Walsky, and Obach, 2004; Tipre *et al.*, 2006) with the use of an appropriate detector. The obvious limitation of investigating the appearance of specific metabolites is that the metabolic pathway(s) of the compound under investigation must be known. Assessing the disappearance of parent compound over time is regarded as a simpler approach as no prior metabolic knowledge is necessary. A plot depicting the reduction of parent compound remaining versus DME incubation time allows for the calculation of the *in vitro* intrinsic clearance ($Cl_{int,in vitro}$) parameter, which is a predictor of the metabolic clearance component of the elimination pathway. The majority of the literature in this area has shown bias towards phase I (CYP450) DME, with phase II *in vitro* studies lagging behind (Rodrigues, 1994; Iyer and Sinz, 1999). This can be explained by the fact that commercial availability of phase I DME preceded phase II enzymes by a number of years (Rodrigues, 1994). Furthermore, there is a current lack of knowledge concerning specific substrates for phase II isoenzymes. This can lead to the selection of a probe that is metabolised by multiple phase II isoenzymes, thereby preventing establishment of individual isoenzyme contribution to the overall phase II metabolic process (Iyer and Sinz, 1999).

The key advantage of utilising the *in vitro* approach to assess metabolic properties of a new chemical entity is that data can easily be acquired using human DME early on in the drug or tracer developmental process. Comparable *in vivo* human data are usually acquired at a late stage, where significant investment into the lead compound has already been made (Rodrigues, 1994). However, it must be emphasised that the simplicity and predictive power of this *in vitro* approach is limited to the metabolic pathway only. Where a chemical entity has the ability to be excreted in its unchanged form, either in the urine or bile, then $Cl_{int,in vitro}$ data will only account for a single component of the overall elimination process.

6.1.3 *Ex vivo* biodistribution.

Ascertaining the biodistribution profile of a radiotracer in small animals is a key step in the pre-clinical radiotracer discovery process. Such data can be acquired *ex vivo* using a study design similar to that depicted in figure 6.3. This type of study involves administration of the radioligand under investigation to a small animal (e.g. a mouse), usually via intravenous injection. Once *in vivo*, the tracer will be subjected to pharmacokinetic processes such as distribution, metabolism, and excretion. The animal is then killed after a pre-determined time period, which leads to cessation of blood circulation and biological functions, meaning that any radioactivity (radiotracer and/or metabolites) deposited to various tissue and bodily materials (i.e. stomach, small bowel, and large bowel matter) will remain unchanged. Organs and bodily materials of interest are then removed and the amount of radioactivity in each biological sample is ascertained via gamma-counting, which is a highly accurate and sensitive detection method.

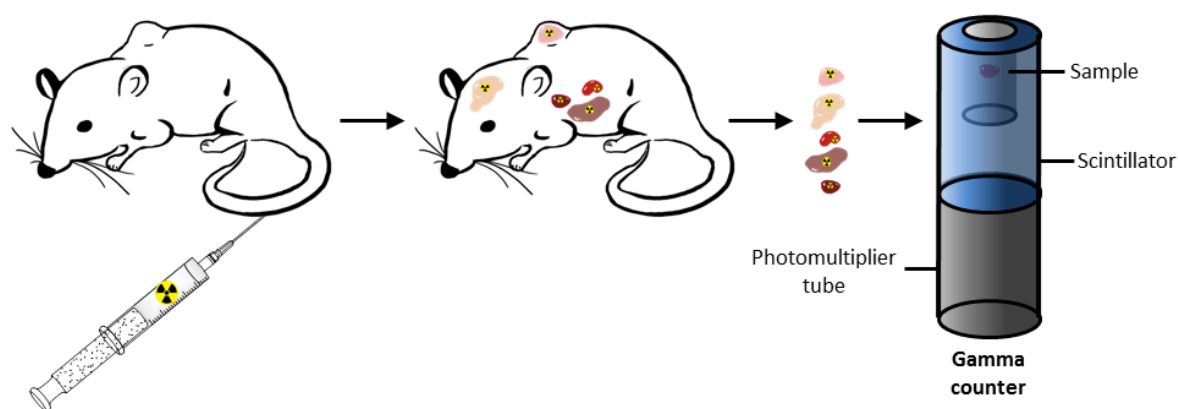


Figure 6.3. Diagrammatic representation of a radiotracer *ex vivo* biodistribution study of in a subcutaneous tumour bearing mouse utilising a gamma-counter.

Histological analysis of the tissue samples is often performed to support the *ex vivo* biodistribution findings. Haematoxylin and eosin (H&E) is a commonly used histochemical stain and, as the name suggests, it is a combination of two dyes where the haematoxylin component is present as the oxidation product (haematein) complexed with a metal ion. The haematein-metal complex is cationic and subsequently binds to basic (basophilic) cellular components, such

as nucleic acids in the nucleus, and stains blue. In contrast to this, eosin is an anionic dye that binds to acidic (eosinophilic) cellular components, which include amino groups in cytoplasm and proteins, and stains red-pink (Avwioro, 2011). Such staining can provide valuable information, particularly when utilising small animal models of human pathology. For example, H&E staining can be used to visualise the degree of vasculature and necrosis in a tumour xenograft model, which can affect radiotracer uptake and occupancy. More specific histological information can be obtained by utilising antibodies, which could be used to ascertain the expression levels of the radioligand target in different tissue. Histological staining using antibodies is a two-step process, where the tissue sample is first incubated in the presence of a primary antibody that binds to the protein of interest. This is then followed by exposure of the tissue to a secondary antibody that is conjugated to a 'reporter' (i.e. a colorimetric enzyme or fluorescent moiety) and binds to the primary antibody. Detection of the 'reporter' confirms the presence of the protein of interest.

It is important to bear in mind that *ex vivo* biodistribution data are often associated with a large degree of variability and multiple animals are required for each investigated biodistribution timepoint. Animal experimentation in the United Kingdom is regulated by the Home Office and falls under the Animals (Scientific Procedures) Act (1986) and the Council Directive 2010/63/EU. The latter piece of legislation enforces the use of the principles of replacement, reduction and refinement (first described by Russell and Burch (1959)) by scientists as a means of minimising experimental animal use and improving animal welfare. Specifically, the term 'replacement' refers to the use of alternative methods that avoid the use of animals (e.g. *in vitro* assays), 'reduction' denotes to use of methods that allow for acquisition of comparable levels of information using fewer animals, and finally 'refinement' refers to use of methods that minimise pain and distress caused to animals (Olsson *et al.*, 2012).

With the above principle of 'reduction' in mind, alternative methods for ascertaining tracer biodistribution data would be dynamic PET and SPECT imaging. Such imaging techniques are capable of acquiring qualitative and

quantitative biodistribution data at multiple timepoints (e.g. every minute) after radiotracer injection from a single animal and a single scan. This is in contrast to the above described *ex vivo* technique that is restricted to quantitative data only, and the necessity for the use of different animals for each timepoint under investigation. An important limitation of pre-clinical nuclear imaging is the necessity to maintain the animal being imaged under anaesthesia, unlike *ex vivo* biodistribution techniques that can be performed in the absence of anaesthesia. Prolonged anaesthesia of animals is associated with a risk of mortality during the scanning procedure, which is greater when using animal models of human pathology. Furthermore, anaesthetic agents can alter radiotracer pharmacokinetics and uptake into desired tissues. Consequently, SPECT or PET findings acquired in anaesthetised animals may fail to correlate to human data that were acquired in awake patients (reviewed by Kristian, Alstrup, and Smith, (2013)). Bearing the above in mind, the *ex vivo* biodistribution technique is often used to validate PET or SPECT data and remains an important tool in pre-clinical radiotracer discovery (Zhang *et al.*, 2005; Carney *et al.*, 2015; Carlucci *et al.*, 2015; Salinas *et al.*, 2015).

6.1.4 Aims and hypotheses.

The work described in this chapter aimed to establish the *in vitro* stability properties of the potential PARP-1 SPECT and PET compounds **4** and **17** respectively, in the presence of mouse plasma and human liver microsomal enzymes, and evaluate the biodistribution and PARP-1 specific binding profiles of the corresponding radiolabelled compounds ($[^{123}\text{I}]\text{-4}$) and $[^{18}\text{F}]\text{-17}$) in subcutaneous GBM bearing mice.

The following hypotheses were set for this work:

- i) Compounds **4** and **17** will exhibit mouse plasma stability. The reasoning behind this hypothesis is based on the reported stability of olaparib in human plasma (Sparidans *et al.*, 2011) and whole blood (Roth *et al.*, 2014).

ii) Compounds **4** and **17** will exhibit more rapid *in vitro* liver enzyme metabolism when compared to olaparib. This hypothesis is justified by the fact that the metabolically stable cyclopropane functionality (Gagnon *et al.*, 2007; Coleridge, Bello, and Leitner, 2009) of olaparib has been replaced with aromatic moieties liable to phase I hydroxylation reactions. Moreover, the terminal halogen atoms of **4** and **17** have potential for liver microsomal cleavage (Scott and Sinsheimer, 1983; Kharasch and Thummel, 1993) (Figure 6.4). Another important factor to consider is the increased lipophilic character of **4** and **17** when compared to olaparib (see section 4.2 for details). As discussed previously, the interactions between organic compounds and CYP450 enzymes are lipophilic in nature meaning that an increase in lipophilicity is often associated with an increase in the rate of metabolism (Waterbeemd *et al.*, 2001).

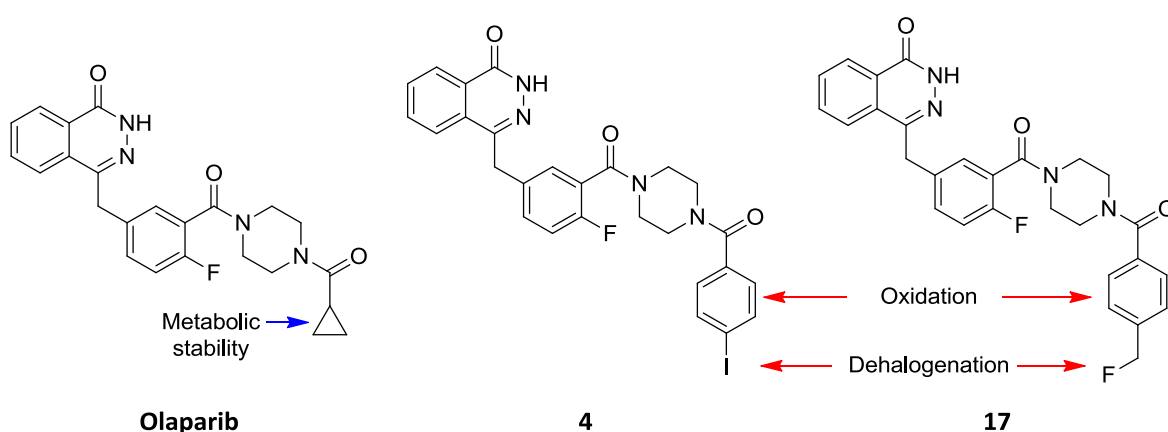


Figure 6.4. Potential sites of phase I metabolism of compounds **4** and **17**.

iii) [^{123}I]-**4** and [^{18}F]-**17** will undergo hepatobiliary clearance *in vivo*. The reasoning behind this statement is supported by the fact that olaparib (European Medicines Agency, 2014) and the structurally related tracer [^{18}F]-BO (Reiner *et al.*, 2012) has been shown to be cleared via hepatobiliary means.

iv) [^{123}I]-**4** and [^{18}F]-**17** will bind to PARP-1 with specificity *in vivo*. This hypothesis was drawn based on the earlier established low nanomolar *in vitro* potency of **4** and **17** for PARP-1 (see section 4.2 for details), and the *in vivo* PARP-1 specific binding reported by Reiner *et al.* (2012) and Carlucci *et al.* (2015) for the structurally related tracers [^{18}F]-BO and [^{18}F]-PARPi-FL respectively.

6.2 Results and discussion.

6.2.1 *In vitro* plasma and metabolic stability of **4** and **17**.

As described earlier (section 6.1.1), blood plasma possesses hydrolytic properties that can result in the degradation of certain organic compounds, including radiotracers. It was therefore imperative to ascertain the stability properties of the lead PARP-1 SPECT and PET imaging candidates **4** and **17**, respectively, prior to pre-clinical *in vivo* evaluation. Due to the expense and labour associated with ^{123}I and ^{18}F radiolabelling, non-radioactive **4** and **17** were incubated in mouse plasma for 0 and 20 hours, after which the amount of unchanged (parent) compounds remaining was quantified using LC-MS (Figure 6.5). Example MS graphs for compound **4** and **17** can be found in Appendix 9.10 and 9.11 respectively. The amount of parent compounds remaining was expressed as a percentage that was normalised to negative controls lacking plasma. It is clear from figure 6.5 that both **4** and **17** did not exhibit significant change in the amount of parent compound remaining between the two timepoints, suggesting mouse plasma stability over the 20 hour incubation period. These observations are in line with the earlier stipulated hypothesis (section 6.1.4) and literature reports, which showed olaparib to be stable in human plasma at 4 °C (Sparidans *et al.*, 2011) and whole human blood at room temperature (Roth *et al.*, 2014) for 24 hours. However, it is important to bear in mind that these data were acquired using mouse plasma, which can exhibit different hydrolytic properties from human plasma (see section 6.1.1 for details).

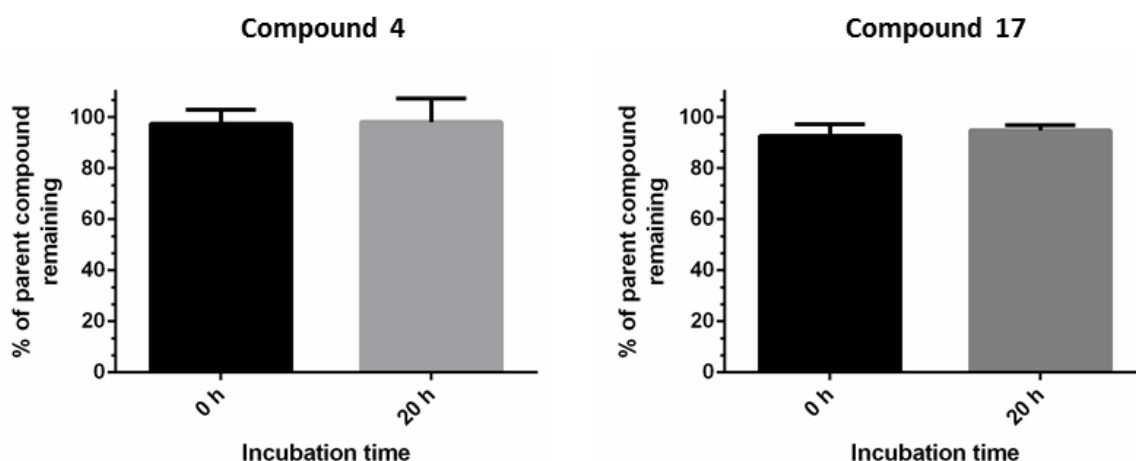


Figure 6.5. Graphs showing the percentage amount of unchanged **4** and **17** remaining after 0 and 20 hour incubations in mouse plasma. Error bars represent the mean + standard deviation ($n = 3$). Unpaired t test P values = >0.05 . The plots were generated and statistical analyses were performed using the GraphPad Prism 6.0 software.

Pharmacokinetic studies of [^{14}C]-labelled olaparib in female human patients, as described in the Committee for Medicinal Products for Human Use assessment report (European Medicines Agency, 2014), revealed that approximately 44% of the administered dose was eliminated in urine, where the most abundant component was unchanged [^{14}C]-olaparib (10–19% of the dose). In addition to this, 37 different drug related components were identified in the urine, of which 18 were quantifiable. A monooxygenated analogue of [^{14}C]-olaparib (i.e. a product of phase I metabolism) was found to be the most abundant metabolite in urine (4–8% of dose). In addition to the monooxygenated compound, other phase I metabolites of [^{14}C]-olaparib were identified in blood plasma samples, such as dehydrogenated piperazine and ring opened hydroxyl-cyclopropyl analogues. It should also be noted that faecal samples contained approximately 42% of the administered dose of [^{14}C]-labelled olaparib, confirming a hepatobiliary clearance pathway for the compound. Importantly, the main metabolite identified in faecal matter was the monooxygenated analogue (European Medicines Agency, 2014). Therefore, it is clear from the above described findings that phase I metabolism is a major contributor to the elimination of olaparib. Due to the possibility for increased phase I metabolism of **4** and **17** when compared to olaparib (see section 6.1.4 for details), attention was directed at

ascertaining the *in vitro* stability of these compounds in the presence of pooled human liver microsomes (phase I DME).

An initial pilot study was conducted to calculate the $Cl_{int,in vitro}$ parameter for the positive control compound diclofenac. The amount of parent compound (unchanged diclofenac) remaining after incubation in commercially available human liver DME was established at a number of different timepoints using LC-MS. Example LC-MS chromatograms and graphs can be found in Appendix 9.12. These data were represented as the natural logarithm of the percentage of parent compound remaining over time plots (Figure 6.6), which were then used to calculate the $Cl_{int,in vitro}$ parameter.

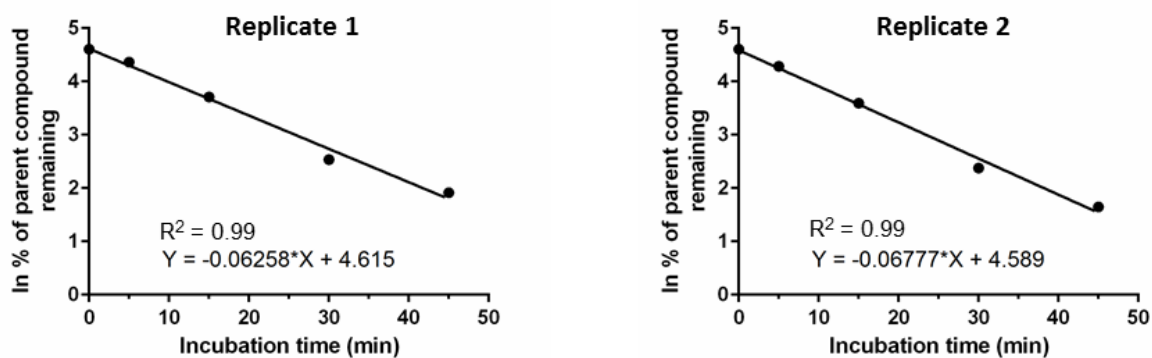


Figure 6.6. Graphs showing the natural logarithm (ln) percentage amount of unchanged diclofenac remaining after 0, 5, 15, 30 and 45 minute incubations in human liver microsomes. The plots were generated using the GraphPad Prism 6.0 software.

The $Cl_{int,in vitro}$ parameter calculated for diclofenac from the pilot study was similar to previously published values (Table 6.1). However, variability existed between the reported values, which can be explained by the fact that each of the authors used different sources of liver microsomes originating from different population samples.

Table 6.1. Calculated and literature *in vitro* intrinsic clearance values for diclofenac.

Entry	$Cl_{int, in vitro}$ ($\mu\text{L}/\text{mL}/\text{mg}$)
1 ^a	136 and 125
2 ^b	189 \pm 39
3 ^c	80 \pm 18

^aCalculated *in vitro* intrinsic clearance ($Cl_{int, in vitro}$) values (replicates 1 and 2);

^bObach (1999), \pm standard deviation (n = 3); ^cSoars *et al.* (2003), \pm standard deviation (n = 3).

To address the issue of inter-source liver enzyme variability, the $Cl_{int, in vitro}$ parameter was used to compare the rate of phase I metabolism of compounds **4** and **17** relative to olaparib using a single batch of pooled human liver microsomes. The $Cl_{int, in vitro}$ values were calculated from the corresponding natural logarithm of the percentage of parent compound remaining over time plots, which can be found in Appendix 9.13. Compounds **4** and **17** exhibited more rapid intrinsic clearance when compared to olaparib (Table 6.2), with approximately three fold greater $Cl_{int, in vitro}$ values. This outcome correlated with the earlier mentioned hypothesis (section 6.1.4), and the fact that both compounds exhibited higher log P_{oct} values when compared to olaparib (see section 4.2 for details).

Table 6.2. Calculated *in vitro* intrinsic clearance values for olaparib, and compounds **4** and **17**.

Compound	$Cl_{int, in vitro}$ ($\mu\text{L}/\text{mL}/\text{mg}$) ^a	
	Replicate 1	Replicate 2
Olaparib	23	34
4	82	87
17	74	90

^aThe *in vitro* intrinsic clearance ($Cl_{int, in vitro}$).

Despite accelerated *in vitro* phase I metabolism relative to olaparib, it was proposed that retention of these agents in PARP-1 overexpressing tumour tissue will be sufficient to allow for nuclear imaging. This can be justified by the fact that [^{14}C]-olaparib has been found to be present in subcutaneous human colon carcinoma xenografts excised from rats up to 96 hours after administration of the ^{14}C -labelled compound (Chalmers *et al.*, 2014). Furthermore, pre-clinical PET studies conducted by Reiner *et al.* (2012) using the PARP-1 radiotracer [^{18}F]-BO were successful at imaging PARP-1 *in vivo*, although it is important to bear in mind the structural differences between [^{18}F]-BO and [^{123}I]-4 and [^{18}F]-17. Taking the above under account, the radiolabelled versions of compounds 4 and 17 (i.e. [^{123}I]-4 and [^{18}F]-17) were advanced to pre-clinical *in vivo* studies.

6.2.2 *Ex vivo* biodistribution and specificity of [^{123}I]-4 and [^{18}F]-17.

Ex vivo biodistribution methodology using a gamma-counter was chosen as a preliminary method of assessing the *in vivo* behaviour of the potential SPECT and PET tracers [^{123}I]-4 and [^{18}F]-17 respectively, which could be used to validate future nuclear imaging studies (see chapter 8 for details).

Prior to *in vivo* experiments, the linearity and saturability of the gamma-counter for ^{123}I and ^{18}F had to be established. Therefore, calibration curves were generated by counting the number of gamma-rays emitted per minute by different amounts of radioisotopes (in the form of commercially available [^{123}I]-NaI or $^{18}\text{F}^-/\text{H}_2^{18}\text{O}$) (Figure 6.7). The relationships between the counts per minute and the amounts of radioactivity were highly linear for both ^{123}I and ^{18}F , with R^2 values of 1.00 and 0.99 respectively. Importantly, the calibrations revealed that ^{123}I and ^{18}F radioactivity levels of ≥ 500 KBq resulted in detector saturation.

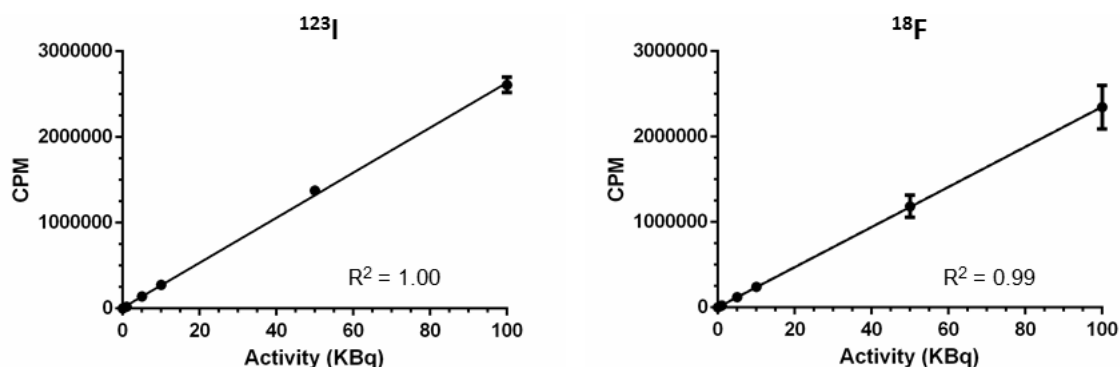


Figure 6.7. Calibration graphs showing the linear relationship between the amount of radioactive ^{123}I or ^{18}F and the counts per minute (CPM) obtained using the Cobra II Auto-Gamma[®] counter. Error bars represent the mean + standard deviation (n = 3). The plot was generated using the GraphPad Prism 6.0 software.

Following calibration of the gamma-counter equipment, focus was shifted to evaluation of [^{123}I]-4 and [^{18}F]-17 *in vivo*. Due to the practical complexities associated with *in vivo* work, a pilot *ex vivo* biodistribution study was conducted using [^{123}I]-4 in healthy female black-6 mice. For the purpose of this study, two timepoints (i.e. 5 and 30 minutes) post radiotracer injection were investigated; the results are summarised in figure 6.8. It is evident from these data that the liver exhibited the highest percentage of the injected radioligand dose per gram of tissue (%ID/g) at both timepoints. This observation is not surprising as olaparib is known to be extensively metabolised by the liver (see section 6.2.1 for details). The statistically significant decrease in the %ID/g of blood, spleen, large bowel, liver, kidney, heart, lung, muscle, and brain tissue between the two timepoints could be explained by rapid *in vivo* elimination of the radiotracer. The apparent increase in %ID/g of small bowel between the 5 and 30 minute timepoints, although not statistically significant, could be a result of residual biological matter containing [^{123}I]-4 and/or its metabolites (eliminated via hepatobiliary means) present in the small bowel tissue. It is noteworthy that only negligible amounts of [^{123}I]-4 were present in brain tissue, which correlated with the observations made by Chalmers *et al.* (2014) using [^{14}C]-olaparib. This can be explained by the fact that 4 (as well as 17) exhibited %PPB and Mw

properties that fall outside of the optimal range for BBB penetration (%PPB = 45–85% (Tavares *et al.*, 2012); $M_w = \leq 450$ (Waterbeemd *et al.*, 1998) (see section 4.2 for details). Another factor that could have contributed to low uptake of [^{123}I]-4 in brain is the fact healthy brains express only low levels of PARP-1 (see section 1.3.2 for details). However, as described in section 4.2, it is envisaged that BBB disruptions associated with GBM brain lesions, as well as PARP-1 overexpression in these tumours, will allow for sufficient brain uptake of the radioligands for nuclear imaging of the pathology.

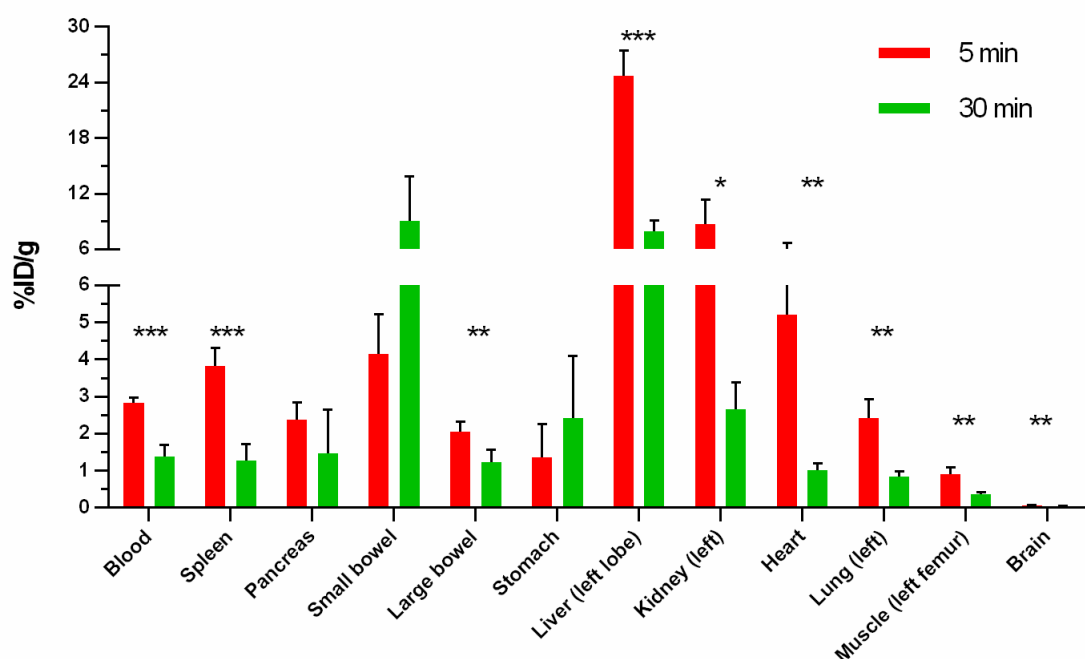


Figure 6.8. A graph showing the biodistribution (expressed as the percentage of injected dose per gram of tissue [%ID/g]) of [^{123}I]-4 in healthy female black-6 mice 5 minutes ($n = 4$) and 30 minutes ($n = 4$) post tracer injection (≤ 1 ng). Error bars represent the mean + standard deviation. Unpaired t test values: * = ≤ 0.05 ; ** = ≤ 0.01 ; *** = ≤ 0.001 . The plot was generated and statistical analyses were performed using the GraphPad Prism 6.0 software.

Importantly, the pilot study allowed for the identification of a number of key limitations in the *ex vivo* biodistribution dataset. Firstly, there were insufficient data to make robust observations regarding potential biliary clearance of [^{123}I]-4. Secondly, it was found that collection of mouse bone marrow tissue of known mass was not possible, and therefore bone marrow uptake of the radioligand could not be quantified. Thirdly, harvest of thyroid tissue proved highly

challenging and could not be achieved successfully. Measurement of radioactivity in thyroid gland after the administration of [^{123}I]-4 could provide useful information concerning [^{123}I]-deiodination, as iodine atoms are actively taken up by the gland (Kaul and Roedler, 1980). Finally, conclusions concerning the renal elimination of the radiotracer could not be made due to the practical challenges associated with urinary collection following animal sacrifice. The former two limitations could be addressed by collecting and gamma-counting stomach, small and large bowel matter, solid faeces, and whole bone (e.g. the femur). However, addressing the latter two limitations would necessitate the use of larger animal species (e.g. rats) and nuclear imaging equipment.

Since a potential key application of PARP-1 SPECT and PET agents would be GBM imaging, efforts were focused on establishing the *ex vivo* biodistribution of [^{123}I]-4 and [^{18}F]-17 in mice bearing a subcutaneous human GBM (U87MG-Luc2) xenograft model. The subcutaneous U87MG-Luc2 model was chosen due to its established use within the research group, predictable and rapid growth, defined lesion shape (Figure 6.9), and most importantly PARP-1 overexpression within the lesion (Figure 6.10). Furthermore, success of subcutaneous engraftment and subsequent tumour growth can be established and monitored using simple visual inspection and calliper measurement techniques. This is in contrast to intracranial xenografts that require the use of bioluminescence imaging, which is associated with greater practical complexity and cost (see sections 7.1.3 and 7.2.3 for details). It is also important to bear in mind, that evaluation of tracer uptake into tumour tissue using gamma-counting techniques requires precise resection of neoplastic tissue, which can be challenging in the case of intracranial tumour lesions.



Figure 6.9. Images of a subcutaneous U87MG-Luc2 GBM tumour xenograft grown in a female CD1 nude mouse for 28 days, pre- and post-excision.

Figure 6.10 shows four different subcutaneous U87MG-Luc2 tumours (A-D) grown in mice, which have been sectioned and characterised by immunohistochemical staining using H&E, and antibodies against Ki67 (a marker of proliferation) and PARP-1. H&E staining of the tumour sections clearly revealed the cellular nuclei (dark blue staining), surrounding cytoplasmic components (pink staining), and tumour vasculature (un-stained regions) (Figure 6.10). Staining of the subcutaneous U87MG-Luc2 tumour sections with an antibody against Ki67 showed that the tissues comprised of large numbers of proliferative cells (brown staining), which was expected for these rapidly growing tumour xenografts. Similarly, by utilising a PARP-1 antibody, high levels of PARP-1 expression were revealed (brown staining) in all of the investigated tumour samples (Figure 6.10), which was in line with previous reports of human GBM (see section 1.3.2 for details). In order to confirm the specificity of the secondary antibody for the primary PARP-1 antibody, the tumour sections were stained with the secondary antibody only; these were PARP-1 negative controls. No brown staining was visible in these negative controls, thereby confirming the high specificity of the secondary stain.

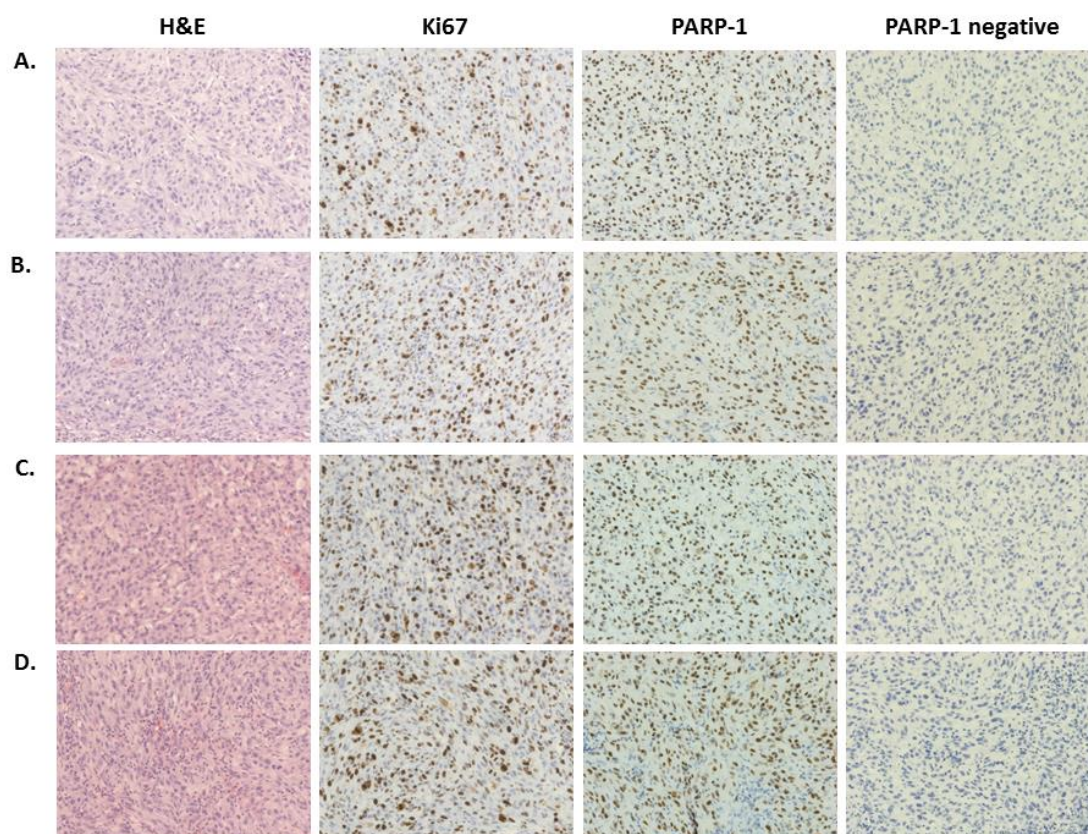


Figure 6.10. Representative immunohistochemistry images of four subcutaneous U87MG-Luc2 GBM tumour xenografts (A to D) grown in female CD1 nude mice, fixed, sectioned and stained with haematoxylin and eosin (H&E), and antibodies against Ki67 (a marker of cellular proliferation) and PARP-1. The PARP-1 negative control was stained with the secondary antibody only. Blue staining shows cellular nuclei and brown staining signifies presence of Ki67 or PARP-1.

Following selection of an appropriate animal model, the *ex vivo* biodistribution of [^{123}I]-4 and [^{18}F]-17 in subcutaneous U87MG-Luc2 tumour bearing mice was evaluated at 30, 60 and 120 minutes post radiotracer administration (Figures 6.11 and 6.12). Choice of the three timepoints was guided by the earlier described pilot data (Figure 6.8), which showed that [^{123}I]-4 exhibited rapid kinetic properties with potentially rapid metabolism and clearance.

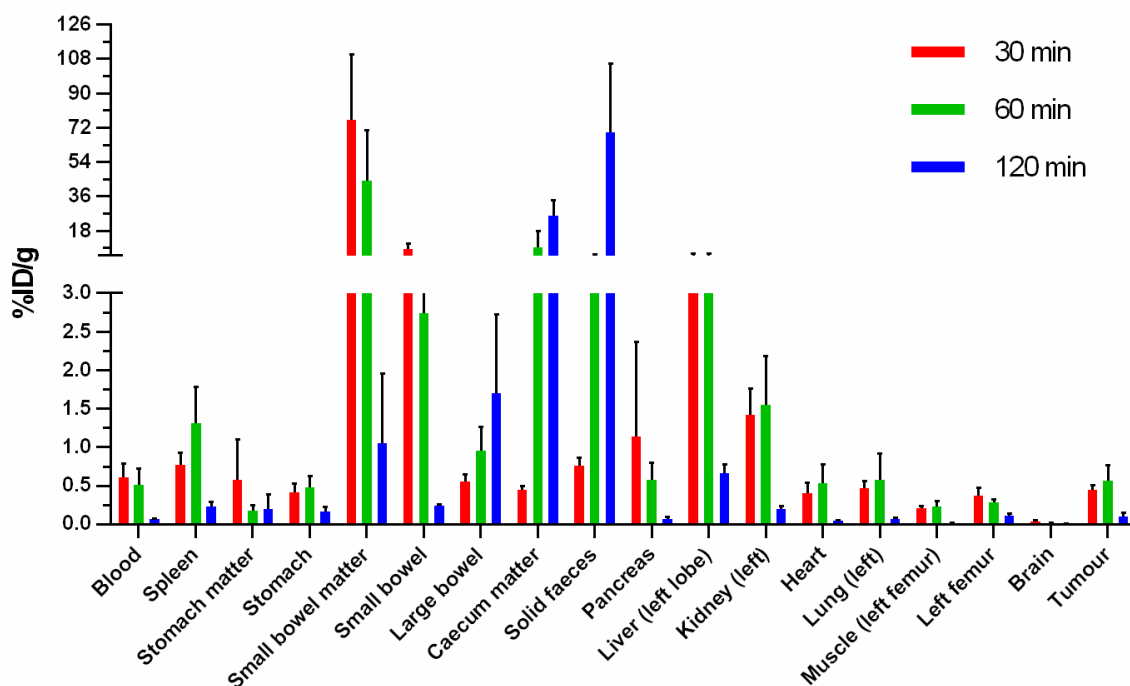


Figure 6.11. A graph showing the biodistribution (expressed as the percentage of injected dose per gram of tissue [%ID/g]) of [^{123}I]-4 in subcutaneous U87Mg-Luc2 GBM bearing female CD1 nude mice 30 minutes ($n = 3$), 60 minutes ($n = 4$), and 120 minutes ($n = 4$) post tracer injection (≤ 1 ng). Error bars represent the mean + standard deviation. The plot was generated using the GraphPad Prism 6.0 software. Modified from Zmuda *et al.* (2015).

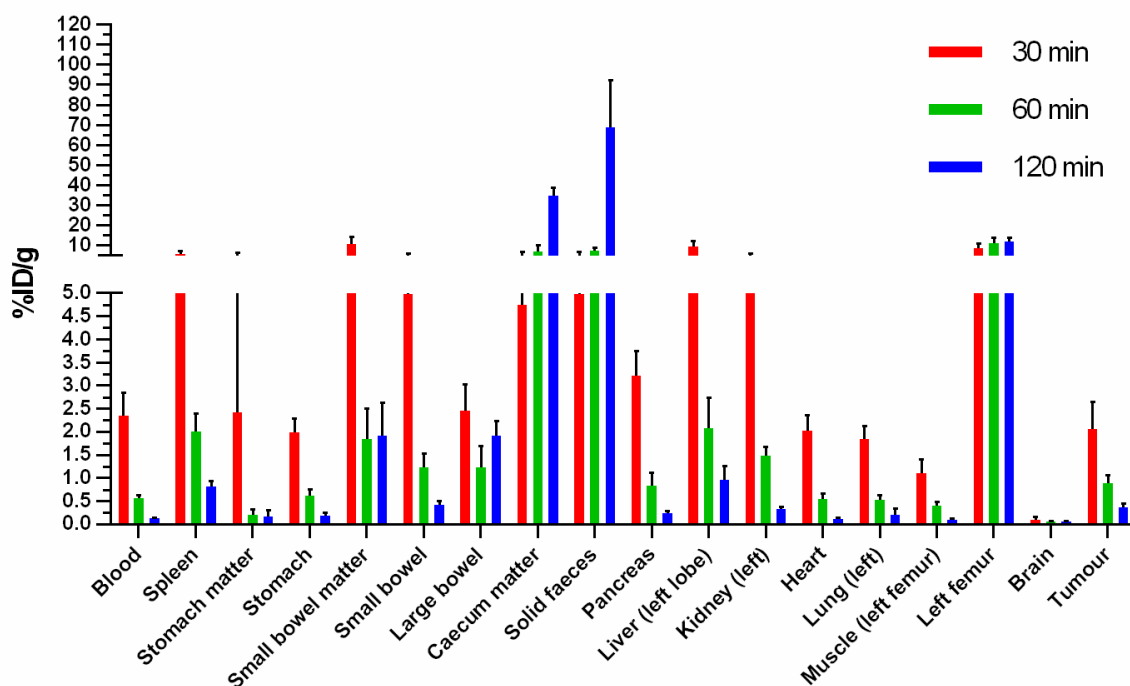


Figure 6.12. A graph showing the biodistribution (expressed as the percentage of injected dose per gram of tissue [%ID/g]) of [^{18}F]-17 in subcutaneous U87Mg-Luc2 GBM bearing female CD1 nude mice 30 minutes ($n = 3$), 60 minutes ($n = 4$), and 120 minutes ($n = 4$) post tracer injection (≤ 8 ng). Error bars represent the mean + standard deviation. The plot was generated using the GraphPad Prism 6.0 software.

It is clear from figures 6.11 and 6.12 that large proportions of radioactivity were detectable in the liver 30 minutes after [^{123}I]-4 and [^{18}F]-17 administration, which is in line with earlier described pilot data for [^{123}I]-4 (Figure 6.8). By expanding the biodistribution dataset to include digestive matter and excrement, it was found that the majority of ^{123}I radioactivity was present in small bowel matter and solid faeces at 30 and 120 minutes post radiotracer injection respectively (Figure 6.11). A similar biodistribution profile was also observed for the [^{18}F]-17 radioligand (Figure 6.12). These results suggested rapid hepatobiliary clearance of [^{123}I]-4 and [^{18}F]-17, which correlated with the earlier stipulated hypothesis (section 6.1.4), *in vitro* intrinsic clearance data (section 6.2.1), [^{14}C]-olaparib pharmacokinetic findings (European Medicines Agency, 2014), [^{131}I]-4 (Salinas *et al.*, 2015), [^{18}F]-11 (Carney *et al.*, 2015), [^{18}F]-BO (Reiner *et al.*, 2012), and [^{18}F]-PARPi-FL (Carlucci *et al.*, 2015). It is noteworthy that the biliary clearance of [^{18}F]-17 appeared

more rapid than for [^{123}I]-4, with mean %ID/g of caecum matter values of $4.8 \pm 2.0\%$ ($n = 4$) and 0.5 ($n = 3$) 30 minutes post tracer injection respectively. Interestingly, *in vitro* %PPB data for compounds 4 and 17 were suggestive of greater vascular retention exhibited by the former compound (see section 4.2 for more details). However, the *ex vivo* biodistribution study revealed greater amounts of radioactivity present in the blood 30 minutes after administration of [^{18}F]-17 when compared to [^{123}I]-4, which appeared to contradict the *in vitro* findings. This could be a consequence of more rapid metabolism of the potential PET tracer that could in turn result in radioactive metabolites circulating in the bloodstream.

The peak uptake of [^{123}I]-4 in tumour tissue occurred at 60 minutes post radioligand injection with a mean %ID/g of tumour of $0.6 \pm 0.2\%$ ($n = 4$). This was in line with the biodistribution data reported by Salinas *et al.* (2015) who utilised the same xenograft tumour model and showed that the mean %ID/g of [^{131}I]-4 at was 0.5 ± 0.1 at 60 minutes. The potential PET tracer [^{18}F]-17 appeared to exhibit greater and more rapid tumour uptake with a peak mean %ID/g of tumour of $2.0 \pm 0.6\%$ ($n = 4$) at 30 minutes. This difference in uptake kinetics could be explained by greater membrane permeability exhibited by 17 when compared to 4 due to a smaller molecular weight, a lower degree of percentage plasma protein binding, and lower lipophilic character (see section 4.2 for details). Interestingly, despite the apparent more rapid biliary clearance of [^{18}F]-17, the mean [^{18}F]-17 %ID/g of tumour at 120 minutes was higher when compared to [^{123}I]-4 ($0.4 \pm 0.1\%$ ($n = 4$) vs. $0.1 \pm 0.1\%$ ($n = 4$)). However, as described later, [^{18}F]-17 actually exhibited weaker tumour retention properties than the radioiodinated SPECT candidate. This suggested that the higher mean [^{18}F]-17 %ID/g of tumour observed at 120 minutes was likely a consequence of faster tissue uptake kinetics.

Using a subcutaneous U251MG GBM xenograft model, Carney *et al.* (2015) reported a mean %ID/g of tumour of $1.8 \pm 0.2\%$ ($n = 6$) 120 minutes post [^{18}F]-11 injection. These data suggested that [^{18}F]-11 exhibited greater tumour retention when compared to [^{18}F]-17, which had a mean %ID/g of tumour of $0.4 \pm 0.1\%$ ($n = 4$) at the same timepoint. This could be explained by the fact that [^{18}F]-17

seemed to undergo a substantial level of *in vivo* metabolic defluorination, as shown by the high mean %ID/g of femur (>8.5%) across all three timepoints, indicative of free [^{18}F]-fluoride accumulation in bone tissue (Pike, 2009) (Figure 6.12). In contrast to this, the reported mean %ID/g of bone for [^{18}F]-11 was <2% (Carney *et al.*, 2015), and the observed peak mean %ID/g of femur for [^{123}I]-4 was $0.4 \pm 0.1\%$ at 30 minutes. It is also important to consider that potential differences in PARP-1 expression between the two GBM xenograft models (i.e. U87MG-Luc2 and U251MG tumours) could have contributed to the pharmacokinetic differences between the two tracers.

Despite rapid hepatobiliary clearance of [^{123}I]-4 and [^{18}F]-17, and metabolic defluorination of [^{18}F]-17, both radioligands exhibited a degree of retention in tumour tissue. The evidence for this comes in the form of an increase in the mean ratio of %ID/g of tumour to muscle from 2.15 ± 0.47 ($n = 3$) to 5.6 ± 2.0 ($n = 4$) for [^{123}I]-4, and 1.9 ± 0.5 ($n = 4$) to 3.6 ± 0.5 ($n = 4$) for [^{18}F]-17 between the 30 and 120 minute timepoints. Since PARP-1 expression in muscle was not detectable (Figure 6.13), the tumour to muscle ratio allowed for normalisation of data such that inter-subject variability of uptake and washout kinetics was rendered negligible. It is also important to note that, based on data reported by Salinas *et al.* (2015), a ratio %ID/g of subcutaneous U87MG tumour to muscle of approximately 5.6 could be calculated for [^{131}I]-4 six hours after injection. This provides further evidence of the retention of compound 4 in subcutaneous GBM tissue.

In the case of [^{123}I]-4, the mean ratio of %ID/g of tumour to femur increased from 1.2 ± 0.2 ($n = 3$) to 2.0 ± 0.9 ($n = 4$) between the 30 and 60 minute timepoints. This suggested that at the time of peak uptake of [^{123}I]-4 in the tumour, the amount of radioligand present in the tumour tissue was approximately two fold greater than in whole bone. Interestingly, the mean ratio of %ID/g of tumour to femur dropped to 0.9 ± 0.2 at 120 minutes, suggesting more rapid radioligand clearance from tumour tissue when compared to whole bone. It was proposed that radioactivity detection in bone following [^{123}I]-4 administration was due to bone marrow uptake of the radioligand. This can be justified by the earlier described clinical observations, which suggested that

olaparib entered bone marrow tissue (see section 1.3.2.3 for details), and reported biodistribution data that showed specific binding of [^{18}F]-11 to PARP-1 in whole bone (Carney *et al.*, 2015), where bone marrow has been shown to express high levels of PARP-1 (The Human Protein Atlas, 2015). This is in contrast to the earlier observations made for [^{18}F]-17 that were, in most part, a likely consequence of free [^{18}F]-fluoride binding to bone tissue.

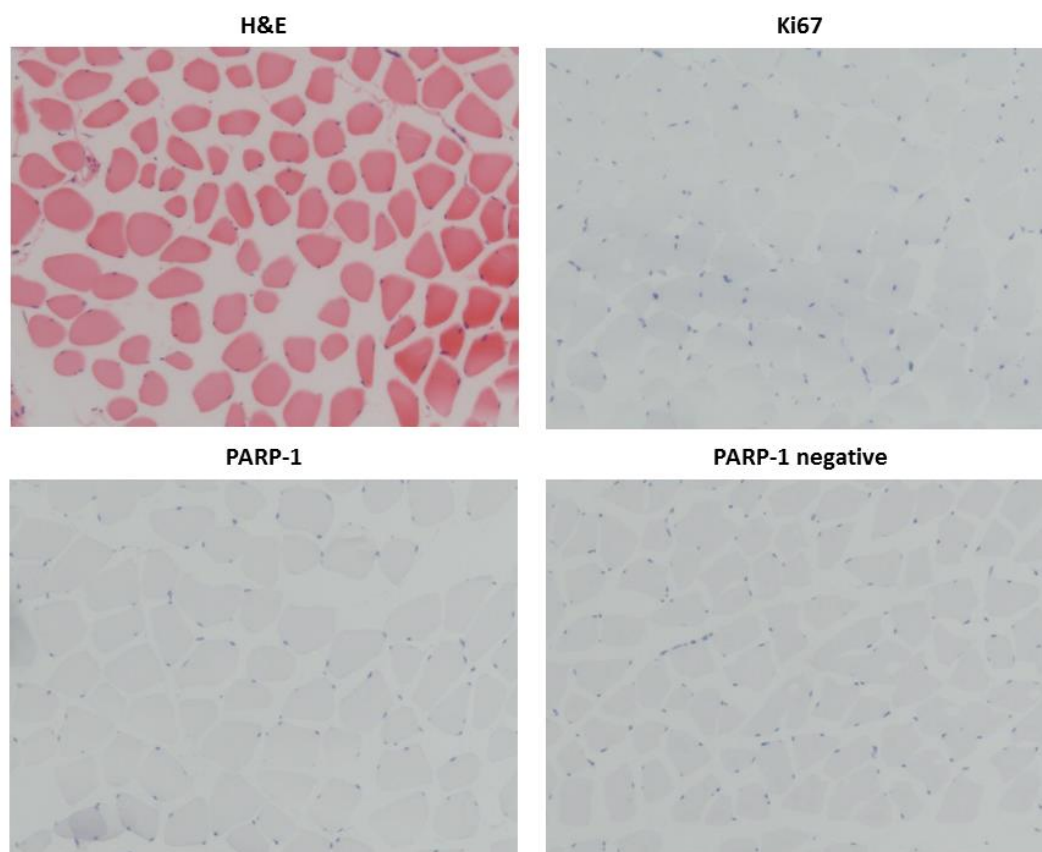


Figure 6.13. Representative immunohistochemistry images of muscle tissue originating from the left femur of a subcutaneous U87MG-Luc2 GBM bearing female CD1 nude mice. The tissue was stained with haematoxylin and eosin (H&E), and antibodies against Ki67 (a marker of cellular proliferation) and PARP-1. The PARP-1 negative control was stained with the secondary antibody only. Blue staining shows cellular nuclei and brown staining signifies presence of Ki67 or PARP-1. Modified from Zmuda *et al.* (2015).

In order to establish whether the uptake of [^{123}I]-4 and [^{18}F]-17 in the various organs was due specific PARP-1 binding, pre-blockade *ex vivo* biodistribution studies were conducted. These involved treatment of subcutaneous U87MG-Luc2 GBM bearing mice with an excess of non-radioactive olaparib, prior to

radiotracer administration, in order to occupy (and block) PARP-1 binding sites. To interpret the uptake data from the ‘blocked’ mice, control cohorts of subcutaneous U87MG-Luc2 GBM bearing mice pre-treated with vehicle were also employed. The results of these studies for [^{123}I]-4 and [^{18}F]-17 are depicted in figures 6.14 and 6.15 respectively.

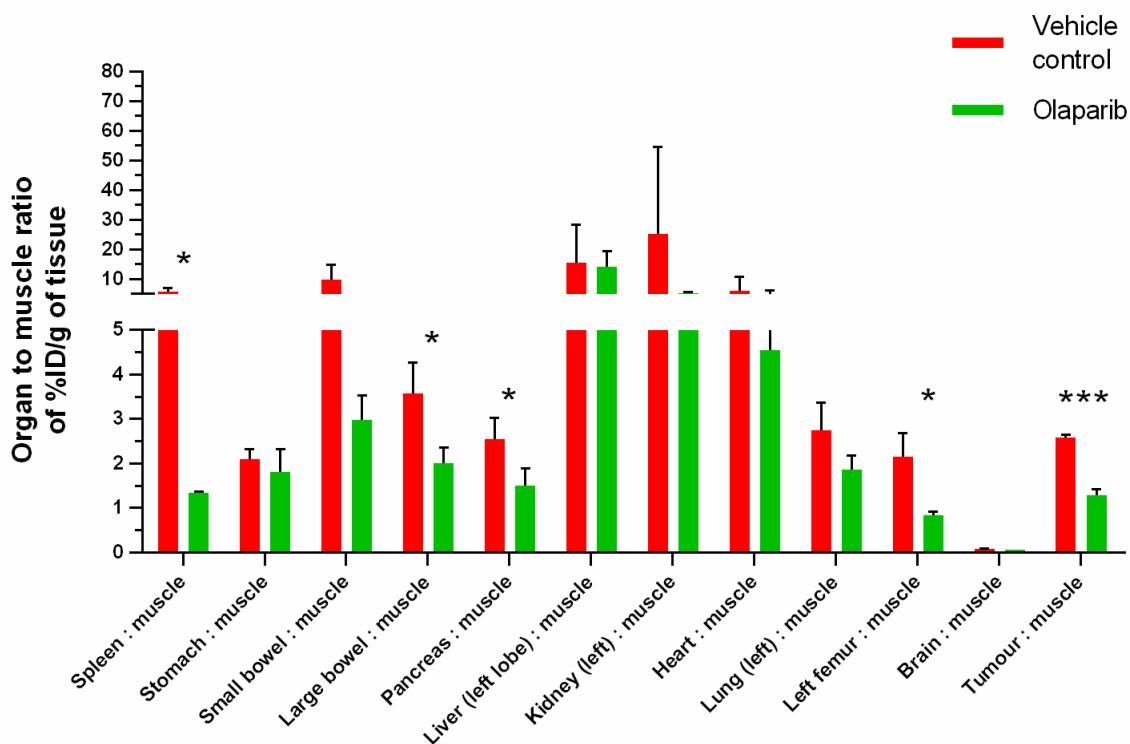


Figure 6.14. A graph showing the organ to muscle ratio of percentage injected dose per gram of tissue (%ID/g) of [^{123}I]-4 (≤ 1 ng) 60 minutes after intravenous injection in subcutaneous U87Mg-Luc2 GBM bearing female CD1 nude mice that were pre-treated with either intraperitoneal vehicle ($n = 3$) or 50 mg/kg olaparib ($n = 3$). Error bars represent the mean + standard deviation. Unpaired t test P values: * = ≤ 0.05 ; ** = ≤ 0.01 ; *** = ≤ 0.001 . The plot was generated and statistical analyses were performed using the GraphPad Prism 6.0 software. Modified from Zmuda *et al.* (2015).

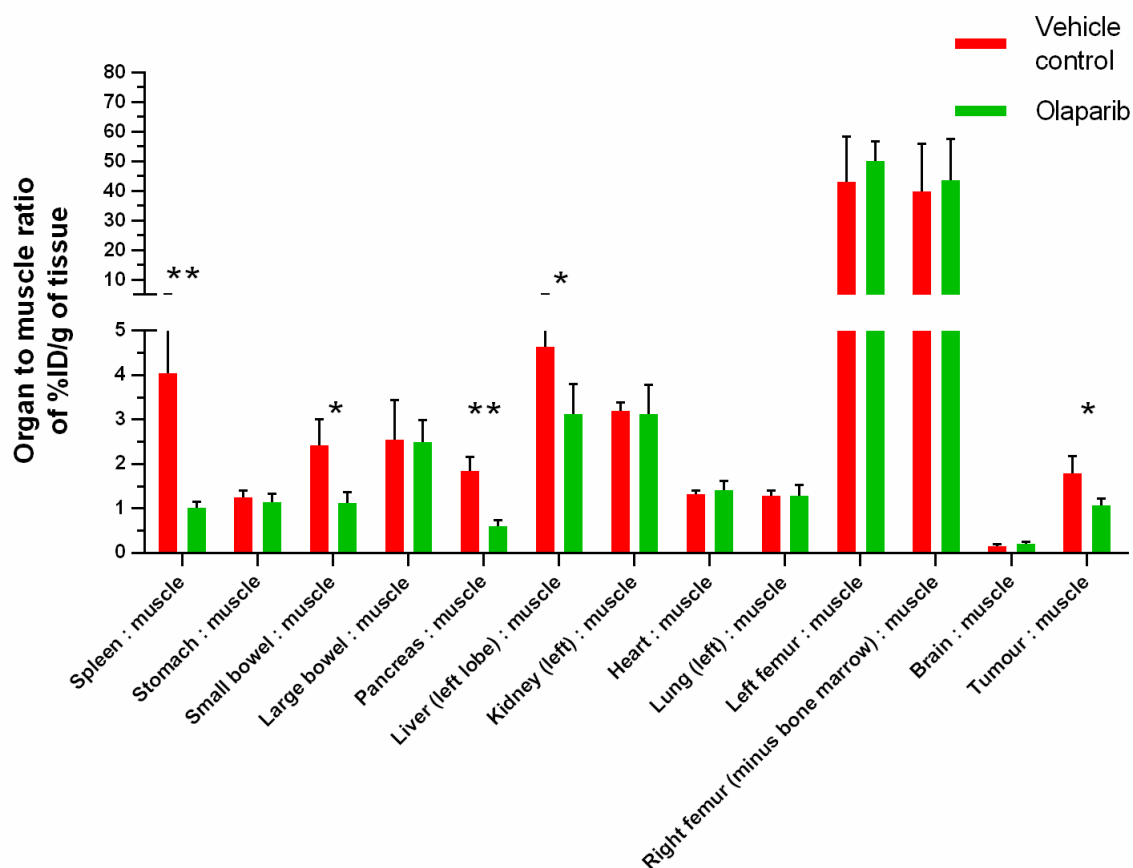


Figure 6.15. A graph showing the organ to muscle ratio of percentage injected dose per gram of tissue (%ID/g) of [^{18}F]-17 (≤ 6 ng) 60 minutes after intravenous injection in subcutaneous U87Mg-Luc2 GBM bearing female CD1 nude mice pre-treated with either intraperitoneal vehicle ($n = 3$) or 50 mg/kg olaparib ($n = 3$). Error bars represent the mean + standard deviation. Unpaired t test P values: * = ≤ 0.05 ; ** = ≤ 0.01 . The plot was generated and statistical analyses were performed using the GraphPad Prism 6.0 software.

It is evident that olaparib pre-treatment resulted in significant reductions in the mean ratios of [^{123}I]-4 and [^{18}F]-17 %ID/g of tumour to muscle when compared to the vehicle pre-treated cohorts. This blockade of radiotracer tumour uptake, in combination with earlier immunohistochemical data showing PARP-1 overexpression in the tumours (Figure 6.10), confirmed the specificity of [^{123}I]-4 and [^{18}F]-17 for PARP-1 *in vivo*. Similar specific binding properties were also exhibited by [^{123}I]-4 in the spleen, pancreas, and large bowel tissues (Figure 6.14), and by [^{18}F]-17 in the spleen, pancreas, small bowel, and liver tissue (Figure 6.15). These data were not surprising as, in humans, all of these tissues are known to express moderate to high levels of PARP-1 (The Human Protein

Atlas, 2015). Furthermore, Carney *et al.* (2015) reported specific binding of [^{18}F]-11 in mouse spleen, liver, and lymph nodes, which have also been shown by the authors to express high levels of PARP-1. Interestingly, despite better physiochemical properties (see section 4.2 for details), of [^{18}F]-17 when compared to [^{123}I]-4, both radiotracers appeared to exhibit a similar degree of blockade in the presence of olaparib, suggesting similar specific binding properties.

The significant level of blockade of [^{123}I]-4 uptake in the whole femur observed in the presence of olaparib provides further evidence that the tracer binds to PARP-1 in the bone marrow (Figure 6.14). In contrast to this, olaparib pre-treatment did not result in a significant reduction of radioactivity uptake in the left femur following [^{18}F]-17 administration (Figure 6.15). In addition to the left femur, the right femur was also gamma-counted with the exception that the bone marrow was flushed out. This was done in order to delineate between bone tissue and bone marrow uptake of the tracer. However, no statistically significant difference was observed between the mean ratio %ID/g of left femur to muscle and the mean ratio of %ID/g of right femur to muscle in either pre-treatment cohort (olaparib pre-treated unpaired t test $P = 0.43$; vehicle pre-treated unpaired t test $P = 0.78$). These data supported that the measured radioactivity in the bone following [^{18}F]-17 administration was due to non-specifically bound [^{18}F]-fluoride, that was likely a consequence of metabolic defluorination. This limits the potential usefulness of [^{18}F]-17 as a GBM PET imaging agent as the free [^{18}F]-fluoride metabolite could lead to signal noise originating from the skull.

6.3 Conclusion.

As hypothesised, compounds 4 and 17 were shown to be stable in mouse plasma following a 20 hour *in vitro* incubation, and exhibited reduced *in vitro* metabolic stability when compared to olaparib, with approximately three fold greater $Cl_{\text{int}, \text{in vitro}}$ values. Evaluation of the *ex vivo* biodistribution of the radiolabelled versions of these compounds (i.e. [^{123}I]-4 and [^{18}F]-17) in subcutaneous GBM bearing mice revealed that both tracers exhibited rapid hepatobiliary clearance, which correlated with *in vitro* intrinsic clearance. Interestingly, [^{18}F]-17 showed

more rapid biliary clearance than the radioiodinated SPECT compound. This was likely a consequence of extensive metabolic defluorination of [^{18}F]-17, with subsequent [^{18}F]-fluoride accumulation in bone tissue. Despite rapid clearance, both tracers exhibited uptake in tumours in levels that have been shown to be sufficient for *in vivo* SPECT (Salinas *et al.*, 2015) and PET (Reiner *et al.*, 2012; Carney *et al.*, 2015) imaging. Out of the two agents, [^{18}F]-17 exhibited more rapid kinetics with a peak %ID/g of tumour occurring at 30 minutes compared to [^{123}I]-4 that peaked at 60 minutes. Importantly, [^{123}I]-4 showed retention in bone marrow tissue, and both [^{123}I]-4 and [^{18}F]-17 were retained in tumour tissue. Retention of the latter in bone marrow was difficult to ascertain due to masking of marrow signal by [^{18}F]-fluoride bone uptake. Furthermore, both the SPECT and PET candidates were shown to bind to PARP-1 *in vivo* with specificity in the tumour tissue, as well as other tissues known to express high levels of PARP-1 (e.g. the spleen).

These results provide grounds for further *in vivo* assessment of the PARP-1 SPECT imaging candidate [^{123}I]-4 using nuclear imaging techniques and in intracranial tumour models. It is envisaged that the substantial levels of defluorination observed with [^{18}F]-17 would limit the usefulness of the tracer as a PET imaging agent due to potential signal noise radiating from the skull due to [^{18}F]-fluoride uptake. However, this would require further investigation using PET imaging techniques (see chapter 8 for details).

6.4 Experimental.

6.4.1 General.

Please see chapter 3 for the experimental information concerning the synthesis of olaparib, 4, 17 and 60, and chapter 5 for details concerning the radiosynthetic, purification and formulation experimental sections of [^{123}I]-4 and [^{18}F]-17. For the purpose of gamma-counter calibration, [^{123}I]-NaI was obtained commercially (PerkinElmer) and [^{18}F]-fluoride was produced by staff employed at the PET Radiopharmaceutical Production Unit at NHS Greater Glasgow Clyde

in a cyclotron (GE PETtrace 6 cyclotron) via the [$^{18}\text{O}(p, n)^{18}\text{F}$] nuclear reaction by irradiation of [^{18}O]-water. All other chemicals, reagents and cell lines were obtained from commercially reputable suppliers and were used as received. Mice used for *in vivo* studies were obtained from Charles River Laboratories, and the animals were housed in individually ventilated cages and had access to sterilised food and water. All animal experiments were carried out in compliance with UK Home Office regulations.

6.4.2 *In vitro* plasma stability of **4** and **17**.

The experiments were conducted as reported by Zmuda *et al.* (2015) using slightly modified methodology from that described by Uchôa *et al.* (2008). Blood (0.5–1.0 mL) was harvested from female black-6 mice and transferred to 1.5 mL Eppendorf vials containing 75 μL of 0.5 M ethylenediaminetetraacetic acid in distilled water. The blood was centrifuged at 5000 g for 5 minutes at room temperature and the plasma supernatant was isolated. The mouse plasma was stored at $-20\text{ }^{\circ}\text{C}$ and was thawed at room temperature immediately prior to use. To 50 μL of mouse plasma supernatant was added 10 μL of 250 μM stock solution of **4** or **17** made in dimethyl sulfoxide and water, such that the final assay concentration of dimethyl sulfoxide was $\leq 1\%$ v/v. Negative controls containing 50 μL of distilled water and 10 μL of 250 μM **4** or **17** minus plasma proteins were also used. The mixtures were incubated at room temperature for either 0 or 20 hours. Following this, 200 μL of ice cold methanol was added to precipitate the plasma proteins, which were then isolated through centrifugation at 2000 g for 5 minutes at room temperature. The supernatant (100 μL) was diluted with 300 μL of a 50:50 mixture of acetonitrile and distilled water, and 10 μL of 250 μM internal standard (**60**) was added. The resulting solution was passed through a 0.22 μm filter and was analysed using LC-MS (Shimadzu LC-2010AHT, LCMS-2010EV). LC was performed on 20 μL sample injections using a Kinetex 5 μm XB-C18 100 \AA (50 \times 4.6 mm) column and the following mobile phase conditions: 0.0–10.0 minutes = 30:70 to 60:40 A:B; 10.0–10.5 minutes = 60:40 to 90:10 A:B; 10.5–12.0 minutes = 90:10 A:B; 12.0–12.5 minutes = 90:10 to 30:70 A:B; 12.5–15.0 minutes 30:70 where A = acetonitrile and B = 0.1% v/v formic acid in

distilled water; flow rate 1.2 mL/min. Compounds were detected using MS under the following conditions: positive ionisation; detector 1.50 kV; SIM m/z 551 (MH^+ internal standard **60**), 571 (MNa^+ internal standard **60**), 597 (MH^+ compound **4**), 503 (MH^+ compound **17**) and 525 (MNa^+ compound **17**). Quantification was performed using the LabSolutions LCMS (Shimadzu Corporation) software by calculating the ratio of the area under the peak of the test article to the internal standard. This ratio was then expressed as the percentage of parent compound remaining relative to the negative control. The experiment was performed in triplicate for each compound under investigation. Corresponding graphs were generated and statistical analyses (unpaired t tests) were performed using the GraphPad Prism 6.0 software.

6.4.3 *In vitro* intrinsic clearance of diclofenac, olaparib, **4 and **17**.**

The experiments were conducted as reported by Zmuda *et al.* (2015) using slightly modified methodology from that described by Walsky and Obach (2004). A 10 mg/mL stock solution of commercially available human liver microsomes pooled from 50 donors (Gibco™ catalogue number: HMMC-PL) was prepared by diluting 100 μ L aliquots of the original 20 mg/mL solution with 100 mM monopotassium phosphate (pH 7.4) buffer. Next, 10 μ L of the microsomal enzyme stock was added to 160 μ L of 100 mM monopotassium phosphate (pH 7.4) buffer, followed by 10 μ L of 60 μ M diclofenac, olaparib, **4** or **17** solution in a mixture of dimethyl sulfoxide and 100 mM monopotassium phosphate (pH 7.4) buffer. The final assay concentration of dimethyl sulfoxide in each case was $\leq 1\%$ v/v. The solutions were warmed to 37 °C using an aluminium block and hotplate for 10 minutes. The incubations were then initiated by adding 20 μ L of 13 mM NADPH stock in 100 mM monopotassium phosphate (pH 7.4) buffer. A negative control was used that contained 10 μ L of the microsomal enzyme stock, 10 μ L of 60 μ M test compound and 180 μ L of 100 mM monopotassium phosphate (pH 7.4) buffer minus NADPH. Incubations were terminated at 0, 5, 15, 30 and 45 minutes by adding 200 μ L of acetonitrile, which precipitated the microsomal enzymes, followed by centrifugation at 1000 g for 5 minutes at room temperature. The

supernatant (350 μL) was removed from each sample and diluted with 200 μL of acetonitrile, followed by the addition of 10 μL of 60 μM internal standard (either papaverine or **60**). The resulting solutions were passed through a 0.22 μm filter and were analysed using LC-MS (Shimadzu LC-2010AHT, LCMS-2010EV). LC was performed on 40 μL sample injections using a Kinetex 5 μm XB-C18 100 \AA (50 \times 4.60 mm) column. The mobile phase conditions were dependant on the compound under investigation and these were: i) diclofenac: 0.0–15.0 minutes = 30:70 to 70:30 A:B; 15.1–17.0 minutes = 70:30 A:B; 17.1–20.0 minutes = 70:30 to 90:10 A:B; 20.1–22.0 minutes = 90:10 to 30:70 A:B; 22.1–25.0 minutes = 30:70 A:B where A = acetonitrile and B = 0.1% v/v formic acid in distilled water; ii) olaparib: 0.0–10.0 minutes = 20:80 to 55:45 A:B; 10.0–12.0 minutes = 55:45 to 20:80 A:B; 12.0–14.0 minutes = 20:80 A:B where A = acetonitrile and B = 0.1% v/v formic acid in distilled water; **4** and **17**: 0.0–10.0 minutes = 30:70 to 60:40 A:B; 10.0–12.0 minutes = 60:40 to 30:70 A:B; 12.0–14.0 minutes 30:70 A:B where A = acetonitrile and B = 0.1% v/v formic acid in distilled water. The mobile phase flow rate in each case was 1.2 mL/min. Parent compounds were detected using MS under the following conditions: positive ionisation; detector 1.50 kV; SIM m/z 551 (MH^+ internal standard **60**), 571 (MNa^+ internal standard **60**), 340 (MH^+ internal standard papaverine), 296 (M^+ diclofenac), 435 (MH^+ olaparib), 597 (MH^+ compound **4**), 503 (MH^+ compound **17**) and 525 (MNa^+ compound **17**). Quantification was performed using the LabSolutions LCMS (Shimadzu Corporation) software by calculating the ratio of the area under the peak of the test article to the internal standard. This ratio was then expressed as the natural logarithm of the percentage of unchanged parent compound remaining relative to the 0 minute incubation timepoint. The natural logarithm of the percentage of parent remaining over time plots were generated using the GraphPad Prism 6 software and the regression models were used to calculate the *in vitro* intrinsic clearance ($Cl_{\text{int},in vitro}$) values using the following equations:

i) $k = -\text{gradient}$

ii) $t_{1/2} \text{ (min)} = \ln(2)/k$

iii) $V_d \text{ (}\mu\text{L/mg)} = \text{volume of incubation (}\mu\text{L)}/\text{protein in incubation (mg)}$

$$\text{iv) } Cl_{\text{int, in vitro}} (\mu\text{L}/\text{min}/\text{mg of protein}) = Vd \times \ln(2)/t_{1/2}$$

where k = elimination rate constant, $t_{1/2}$ = half-life; Vd = volume of distribution, and $Cl_{\text{int, in vitro}}$ = in vitro intrinsic clearance.

Assays were performed in duplicate for each test compound.

6.4.4 Gamma-counter calibration.

[¹²³I]-iodine (in the form of [¹²³I]-NaI) and [¹⁸F]-fluoride (in the form of ¹⁸F⁻/H₂¹⁸O) were serially diluted with 0.05 M sodium hydroxide and distilled water respectively to a final volume of 1 mL, such that the activities (decay corrected for the start of gamma-counting) were 500, 100, 50, 10, 5, 1, 0.5 and 0.1 KBq. In both cases negative controls containing distilled water only were also prepared. Gamma-counting was performed using a Cobra II Auto-Gamma[®] counter and the following counting parameters: i) count time = 1 minute; ii) KeV range = 136–215 for ¹²³I and 311–711 for ¹⁸F; output = counts per minute (CPM). The counts per minute obtained for ¹²³I and ¹⁸F were further decay corrected to account for the counting time between the first and last samples. The decay corrected count per minute values were then plotted against the corresponding amounts of radioactivity (KBq), and linear regression models were applied using the GraphPad Prism 6.0 software.

6.4.5 U87MG-Luc2 cell culture and subcutaneous tumour implantation.

Cell culture and implantation procedures were performed as reported by Zmuda *et al.* (2015). The U87MG-Luc2 GBM cell line was cultured in Minimum Essential Media supplemented with 10% w/v fetal calf serum and 2 mM L-glutamine. Cellular incubations were performed at 37 °C and 5% v/v CO₂. Unconscious female 6–8 week old CD1 nude mice had 5 × 10⁶ U87MG-Luc2 cells injected subcutaneously into the right flank. Subcutaneous xenografts were measured and monitored visually every three days. The work described in this section was

performed Sandeep Chahal from the Chalmer's research group. Tumour bearing animals were used for *in vivo* studies 28–30 days post tumour implantation.

6.4.6 Immunohistochemistry.

Immunohistochemistry was performed as reported by Zmuda *et al.* (2015). Subcutaneous tumour and muscle (from the left femur) tissues were removed and immersion fixed in 4% v/v formaldehyde PBS for 48–168 hours. The fixed tissue was embedded in paraffin blocks and 4 μm sections were cut by the Cancer Research UK Beatson Institute Histology Service. Paraffin was removed by washing the tissue sections in xylene (2 \times 5 minutes), followed by rehydration by washing the sections in 100% v/v ethanol (1 minute and 5 minutes), 70% v/v ethanol (2 \times 5 minutes) and water (5 minutes). Immunohistochemistry was performed using the Dako EnVision™ kit. Briefly, heat induced antigen retrieval using Dako Cytomation Target Retrieval Solution (pH 6.0) was followed by an incubation in 3% v/v hydrogen peroxide in methanol (20 minutes), and then 5% w/v bovine serum albumin and 5% v/v goat serum in PBS (20 minutes) to block peroxidase activity and minimise non-specific binding respectively. Between each step the tissue sections were washed in 0.1% v/v Tween® 20 in TBS (2 \times 5 minutes). The tumour and muscle sections were incubated overnight at 4–8 °C in 1:100 anti-PARP-1 antibody (mouse anti-human and mouse antibody; sc-8007; Santa Cruz). Following this, the tissues were washed with 0.1% v/v Tween® 20 in TBS (2 \times 5 minutes), and a secondary one hour incubation at room temperature was performed using Dako horseradish-peroxidase labelled anti-mouse polymer. The sections were once again washed using 0.1% v/v Tween® 20 in TBS (2 \times 5 minutes) and the presence of antibody was detected using a 3,3'-diaminobenzidine chromagen solution diluted in Dako DAB⁺ substrate buffer. Haematoxylin and eosin, and Ki67 staining was performed by the Cancer Research UK Beatson Institute Histology Service using a Leica ST5020 multistainer. Histology images were acquired using a Zeiss AX10 brightfield microscope at \times 4 magnification and contrast was corrected manually using the ImageJ 1.47v software.

6.4.7 *Ex vivo* biodistribution.

6.4.7.1 [¹²³I]-4 pilot biodistribution study.

Healthy female 6–7 week old black-6 mice were anaesthetised using inhaled isoflurane (in medical oxygen; induction 5.0% v/v; maintenance 2.0–3.0% v/v) and were administered bolus tail vein injections of 1.0–1.1 MBq [¹²³I]-4 in 0.12–0.20 mL 10% v/v ethanol in 0.9% w/v saline by Dr Gaurav Malviya from the Cancer Research UK Beatson Institute Nuclear Imaging department. Body temperature was maintained during anaesthesia using a heating pad. The animals were killed by CO₂ asphyxiation either 5 minutes (n = 3) or 30 minutes (n = 3) following tracer injection. The following tissues were harvested and transferred to preweighed 1.5 mL Eppendorf vials containing 0.5 mL of fixative (4% formaldehyde PBS) immediately after sacrifice: i) blood; ii) spleen; iii) pancreas; iv) small bowel^a; v) large bowel^a; vi) stomach^a; vii) liver (left lobe); viii) kidney (left); ix) heart; x) lung (left lobe); xi) muscle (from left femur); and xii) brain. Each vial was weighed and gamma-counted using a Cobra II Auto-Gamma[®] counter and the counting parameters as described above for ¹²³I (section 6.4.4). A positive control was used containing 0.5 mL of fixative and 10 µL of the [¹²³I]-4 stock solution used to dose the animal. Background counts were defined using a negative control containing 0.5 mL of fixative. The background signal was subtracted from the tissue CPM values, which were then normalised to the weight of each tissue sample. The CPM of each positive control were then used to calculate the theoretical maximum CPM of each injected tracer volume and this was in turn used to calculate the percentage injected dose per gram of tissue (%ID/g). Data analysis was performed using the Microsoft Excel 2010 and software. The corresponding graph was generated and statistical analyses (unpaired t tests) were performed using the GraphPad Prism 6.0 software.

^aBiological material found in these organs was removed prior to transferring the tissues to sample vials.

6.4.7.2 [¹²³I]-4 biodistribution study.

Experiments were performed as reported by Zmuda *et al.* (2015). Subcutaneous U87MG-Luc2 tumour bearing female CD1 nude mice were anaesthetised using inhaled isoflurane (in medical oxygen; induction 5.0% v/v; maintenance 2.0–3.0% v/v) and were administered bolus tail vein injections of 0.9–1.1 MBq [¹²³I]-4 in 0.15–0.20 mL 10% v/v ethanol in 0.9% w/v saline by Dr Gaurav Malviya from the Cancer Research UK Beatson Institute Nuclear Imaging department. The animals were killed by CO₂ asphyxiation either 30 minutes (n = 3), 60 minutes (n = 4) or 120 minutes (n = 4) following tracer injection. The remainder of the experiment was conducted as described above for the [¹²³I]-4 *ex vivo* biodistribution pilot study (section 6.4.7.1), with the exception of the following tissues and biological materials being harvested: i) blood; ii) spleen; iii) stomach matter; iv) stomach tissue^a; v) small bowel matter; vi) small bowel tissue^a; vii) caecum matter; viii) large bowel tissue^a; ix) solid faeces; x) pancreas; xi) liver (left lobe); xii) kidney (left); xiii) heart; xiv) lung (left lobe); xv) muscle (from left femur); xvi) left femur; xvii) brain; and xviii) tumour. The corresponding graph was generated using the GraphPad Prism 6.0 software.

^aBiological material found in these organs was removed prior to transferring the tissues to sample vials.

6.4.7.3 [¹⁸F]-17 biodistribution study.

Subcutaneous U87MG-Luc2 tumour bearing female CD1 nude mice were anaesthetised using inhaled isoflurane (in medical oxygen; induction 5.0% v/v; maintenance 2.0–3.0% v/v) and were administered bolus tail vein of 1.9–2.6 MBq [¹⁸F]-17 in 0.11–0.21 mL 5% v/v dimethyl sulfoxide in 0.9% w/v saline by Dr Gaurav Malviya from the Cancer Research UK Beatson Institute Nuclear Imaging department. The remainder of the experiment was conducted as described above for the [¹²³I]-4 biodistribution study (section 6.4.7.2). Due to the short half-life of ¹⁸F, the counts per minute were decay corrected to account for the

counting time between the first and last samples. The corresponding graph was generated using the GraphPad Prism 6.0 software.

6.4.8 *Ex vivo* biodistribution with pre-blockade.

6.4.8.1 [¹²³I]-4.

Experiments were performed as reported by Zmuda *et al.* (2015). Subcutaneous U87MG-Luc2 tumour bearing female CD1 nude mice received an intraperitoneal injection of either vehicle (13.5% v/v dimethyl sulfoxide and 10% w/v 2-hydroxy- β -cyclodextrin in distilled water) (n = 3) or 50 mg/kg olaparib in vehicle^a (n = 3) 20 minutes prior (Zhou *et al.*, 2014) to bolus tail vein injections of 0.8–1.1 MBq [¹²³I]-4 in 0.15–0.25 mL 10% v/v ethanol in 0.9% w/v saline. All injections were performed on conscious mice by Dr Gaurav Malviya from the Cancer Research UK Beatson Institute Nuclear Imaging department. The animals were killed by CO₂ asphyxiation 60 minutes following tracer injection. The following tissues were harvested and transferred to preweighed 1.5 mL Eppendorf vials containing 0.5 mL of fixative (4% v/v formaldehyde PBS) immediately after sacrifice: i) spleen; ii) stomach^b; iii) small bowel^b; iv) large bowel^b; v) pancreas; vi) liver (left lobe); vii) kidney (left); viii) heart; ix) lung (left lobe); x) muscle (from left femur); xi) left femur; xii) brain; and xiii) tumour. Each vial was gamma-counted and the %ID/g values were calculated as described earlier (section 6.4.7.1). The %ID/g of tissue value obtained for each sample was then divided by the corresponding %ID/g of muscle value from the same animal to obtain the ratio %ID/g of target organ to muscle. Data analysis was performed using the Microsoft Excel 2010 software. The corresponding graph was generated and statistical analyses (unpaired t tests) were performed using the GraphPad Prism 6.0 software.

^aInjections of olaparib were performed using a 4 mg/mL working solution.

^bBiological material found in these organs was removed prior to transferring the tissues to sample vials.

6.4.8.2 [¹⁸F]-17.

The experiment was conducted as described above for the [¹²³I]-4 pre-blockade study (section 6.4.8.1). Mice received bolus tail vein of 1.8–2.0 MBq [¹⁸F]-17 in 0.16–0.20 mL 5% v/v dimethyl sulfoxide in 0.9% w/v saline. In addition to the previously listed organs and biological materials, the right femur was also harvested, from which marrow tissue was flushed out using distilled water prior to gamma-counting.

7 IN VIVO EVALUATION OF THE POTENTIAL TSPO NUCLEAR IMAGING AGENT [¹⁸F]-AB5186.

7.1 Introduction.

7.1.1 Discovery of [¹⁸F]-AB5186.

As highlighted previously (section 1.4.3.2), the first generation isoquinoline carboxamide TSPO nuclear imaging agents [¹¹C]-PK11195 and [¹²³I]-PK11195 suffered from poor brain uptake and high non-specific binding properties, which has limited their application as neuroimaging agents. Furthermore, [¹¹C]-PK11195 is inherently disadvantaged by the rapid decay of ¹¹C, which has practical limitations (see section 1.2.1 for details).

Second and third generation TSPO nuclear imaging agents such as [¹¹C]-PBR28 and [¹⁸F]-DPA-714 exhibited better brain uptake and specific binding properties, but were affected by single nucleotide polymorphism of the human protein (see section 1.4.3.2 for details). In an attempt to address these issues, Dr Adele Blair undertook a PhD project that involved utilising the PK11195 scaffold for the discovery of a novel ¹⁸F-labelled TSPO PET imaging agent (Blair, 2014). This work gave rise to the 3-fluoromethylquinoline-2-carboxamide AB5186 (Figure 7.1), which displayed similar TSPO binding affinity and plasma protein binding properties to PK11195. However, AB5186 exhibited lower membrane permeability (P_m) and membrane partition coefficient (K_m) values (Table 7.1) (Blair, 2014).

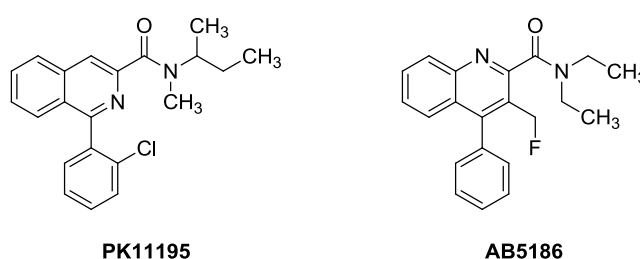


Figure 7.1. Structures of PK11195 and AB5186.

Table 7.1. Inhibition constant (K_i), percentage plasma protein binding (%PPB), membrane permeability (P_m), and the membrane partition coefficient (K_m) parameter values for PK11195 and AB5186.

Parameter	PK11195	AB5186
K_i (nM) ^a	3.1 ± 1.5	2.8 ± 0.8
%PPB ^b	91.5	89.7
P_m ^b	0.7	0.5
K_m ^b	229.4	154.3

^aValues are the mean ± the standard deviation of three independent experiments. ^bAcquired using HPLC methodologies as described by Blair (2014).

The P_m parameter describes the ability of a compound to passively diffuse across biological membranes, and can act as a predictor of passive BBB membrane transport. The parameter has been shown to correlate with radiotracer brain uptake in an inverse manner, where lower P_m values were associated with greater quantities of radiolabelled compound entering brain tissue (Tavares *et al.*, 2012). The K_m is proportional to P_m , and represents the distribution of a solute molecule between the aqueous phase and the biological membrane. The coefficient has been shown to exhibit an inverse relationship with the ratio of specifically bound to non-specifically bound radiotracer, or binding potential (BP_{ND}), in brain tissue (Tavares *et al.*, 2012). In simpler terms, a lower K_m was found to be associated with a lower BP_{ND}, and subsequently a greater degree of specific versus non-specific binding. Therefore, the lower P_m and K_m values observed for AB5186 when compared to PK11195 would suggest that the former compound may exhibit better BBB penetration and brain uptake, as well as specific binding properties. Another advantage of AB5186 is its potential to be radiolabelled with ¹⁸F, which is associated with a longer decay half-life than the ¹¹C radionuclide used to label PK11195 (half-life ¹¹C = 20.3 minutes vs. ¹⁸F = 109.8 minutes). Furthermore, it was proposed that the structural resemblance of AB5186 to PK11195 would minimise the sensitivity of the compound to human TSPO polymorphism. This was rationalised by the fact that Zanotti-Fregonara *et al.* (2014) reported the discovery of ¹¹C-labelled PK11195 azaisosteres **74–76** (Figure 7.2), which exhibited TSPO binding profiles that were not influenced by

single nucleotide polymorphism. *In vivo* evaluation of these radiotracers in healthy non-human primates using PET imaging revealed good brain uptake properties. However, similarly to [^{11}C]-PK11195, **74–76** were disadvantaged by the short-lived nature of the ^{11}C radionuclide.

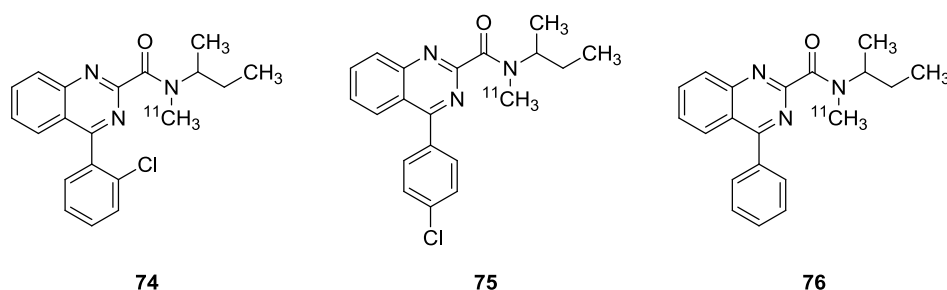


Figure 7.2. ^{11}C -labelled azaisosteres of PK11195 that are not affected by single nucleotide polymorphism of TSPO (Zanotti-Fregonara *et al.*, 2014).

In addition to the discovery, synthesis, and physicochemical characterisation of AB5186, Dr Adele Blair also developed ^{18}F radiolabelling methodology that gave access to [^{18}F]-AB5186 (see section 7.2.1 for details), which she then used in an *in vitro* autoradiography study that aimed to evaluate the binding of the radiotracer to TSPO in a G7 intracranial mouse model of human GBM. This study revealed increased total binding of [^{18}F]-AB5186 in the tumour compared to the contralateral side of the brain, which correlated to the binding of [^3H]-PK11195 and the anatomical location of the tumour as revealed by histological evaluation of the brain tissue. Importantly, the binding of [^{18}F]-AB5186 was displaceable in the presence of excess non-radioactive PK11195, which confirmed the *in vitro* specificity of the novel agent for TSPO (Blair, 2014). Nearing the end of her PhD project, Dr Adele Blair had the opportunity to investigate the *in vivo* behaviour of [^{18}F]-AB5186 by performing a single dynamic PET scan of a healthy baboon post radiotracer administration. Kinetic data extracted from this study showed that [^{18}F]-AB5186 was able enter the primate brain, which supported the ability of the radiotracer to cross the intact BBB (Blair, *et al.*, 2015).

The advantages of [^{18}F]-AB5186 over the ^{11}C and ^{123}I -labelled versions of PK11195, in combination with the potential for negligible sensitivity of [^{18}F]-AB5186 to TSPO polymorphism in humans, justified further pre-clinical development of this radiotracer.

7.1.2 *Ex vivo* autoradiography.

Autoradiography is a qualitative and quantitative technique that can be performed *in vitro* or *ex vivo*, and allows visualisation and measurement of radiolabelled compound bound to solid sections of biological tissue. In the case of *in vitro* autoradiography, tissue sections of interest are incubated in the presence of radioactive ligand, while *ex vivo* autoradiography involves intravenous administration of radioligand to a living animal, followed by removal and sectioning of the desired tissues (Figure 7.3). In both cases, the radioligand will bind to target proteins (i.e. specific binding) or other cellular components (i.e. non-specific binding) present in the tissue. The final step of the autoradiography process involves exposure of the radioactive tissue sections to radiation-sensitive photographic film, which upon development reveals the distribution and density of radioactivity within the tissue section. The main advantage of *ex vivo* autoradiography over the *in vitro* methodology is that the technique provides radiotracer tissue binding information following exposure to *in vivo* conditions. This is important in the context of pre-clinical radiotracer discovery, as the findings can be used to directly inform and validate future nuclear imaging studies (Schmidt and Smith, 2005).

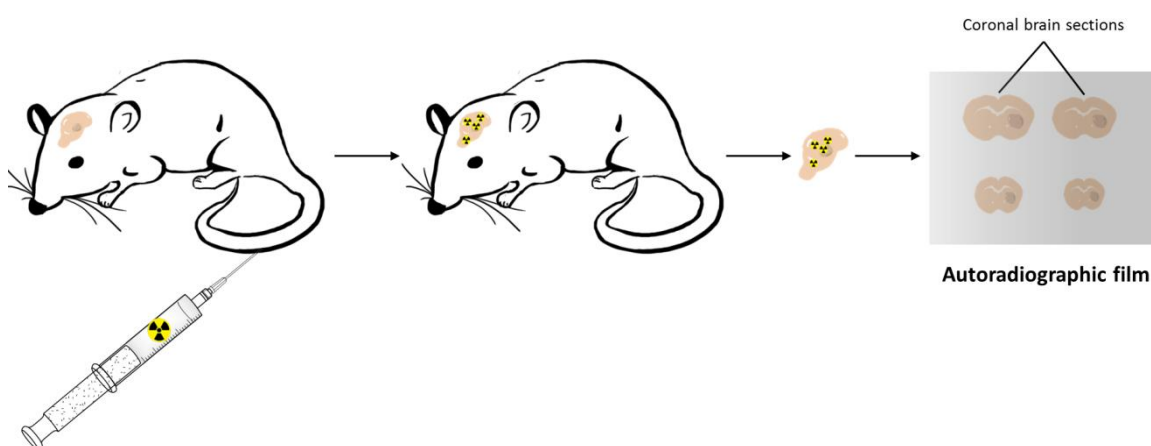


Figure 7.3. Diagrammatic representation of a radiotracer *ex vivo* autoradiography study using an intracranial tumour bearing mouse.

Similarly to the *ex vivo* biodistribution method, *ex vivo* autoradiography is a terminal experimental procedure and may require the use of larger numbers of

animals when compared to nuclear imaging studies (see section 6.1.3 for details). Other limitations of *ex vivo* autoradiography include the possibility of artefacts due to tissue sectioning, the two-dimensional nature of the resulting autoradiograms, and the fact that these data correspond to only a sample of the whole tissue (Schmidt and Smith, 2005). These issues can be overcome by nuclear imaging, which allows for the non-invasive acquisition of three-dimensional (tomographic) information from entire organs within the field of view of the detector. However, it is important to bear in mind that autoradiography is capable of achieving superior spatial resolution, in the order of a few hundred microns, when compared to pre-clinical PET and SPECT imaging (Schmidt and Smith, 2005). Therefore, as with *ex vivo* biodistribution (see section 6.1.3 for details), *ex vivo* autoradiography is often utilised to validate nuclear imaging data (Zhang *et al.*, 2005; Carney *et al.*, 2015; Carlucci *et al.*, 2015; Salinas *et al.*, 2015).

7.1.3 Small animal *in vivo* bioluminescence imaging of glioblastoma.

The luciferase enzyme, present in a number of insects, lower order sea organisms, and bacteria, catalyses the conversion of luciferin to an energetically excited oxyluciferin (i.e. *oxyluciferin) in the presence of ATP and oxygen. The relaxation of *oxyluciferin to its ground state results in the emission of visible light, and the overall process is termed bioluminescence. Transfer of the gene encoding luciferase to cancer cell lines, such that the cells exhibit stable expression of the enzyme, has enabled *in vivo* bioluminescence imaging of neoplastic xenografts in animals. Such imaging involves the subcutaneous or intraperitoneal administration of luciferin to an animal bearing a tumour xenograft capable of expressing luciferase. The subsequent chemical conversion of luciferin to oxyluciferin generates visible light, which is then detected by a charge coupled device camera (Figure 7.4).

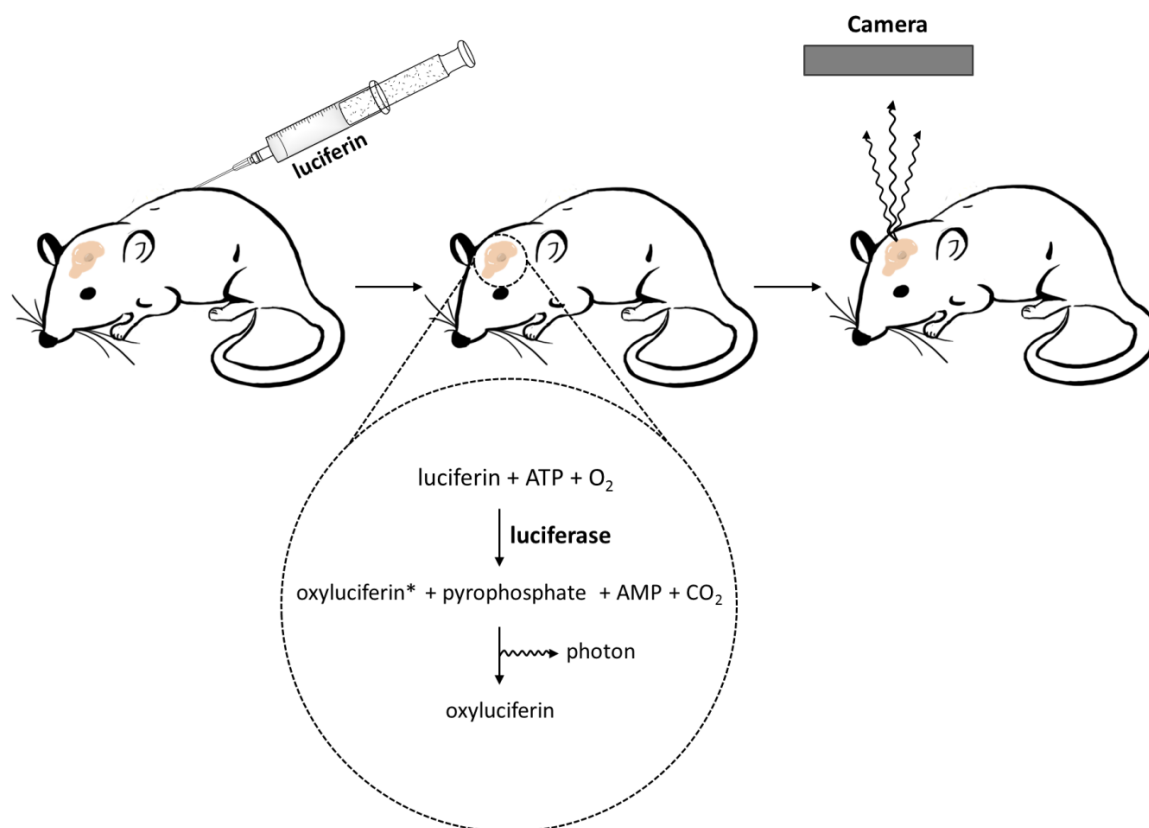


Figure 7.4. Diagrammatic representation of bioluminescence imaging of a mouse bearing an intracranial tumour expressing the luciferase enzyme. ATP = adenosine triphosphate; AMP = adenosine monophosphate.

Bioluminescence imaging is a quantitative technique, as the amount of generated visible light is proportional to the number of luciferase expressing cells. However, it is important to bear in mind that a number of factors can affect the quantification process. Firstly, the emitted light is prone to scatter interactions as it traverses biological tissue, which has a negative effect on spatial resolution. Consequently, *in vivo* bioluminescence imaging is generally limited to smaller animals and superficial tumour xenografts, where scatter interference is minimised. Secondly, emitted light can be absorbed by biological substances such as haemoglobin and melanin, which reduces the amount of light reaching the camera and imaging sensitivity (Edinger *et al.*, 2002). Finally, the technique is prone to experimental error as precise administration of luciferin is required in order to minimise inter-subject variability (Jung and Willard, 2014). Despite these limitations, *in vivo* bioluminescence imaging has been well established in pre-clinical cancer research, as it allows for monitoring of tumour models and their progression in a non-invasive manner that supersedes

previously used techniques such as gross tumour volume measurement using callipers, monitoring of weight changes, or behavioural monitoring (Edinger *et al.*, 2002).

7.1.4 Aims and hypotheses.

The work described in this chapter aimed to utilise intracranial GBM bearing mice in combination with *ex vivo* autoradiography and *in vivo* PET imaging techniques to evaluate the ability of [¹⁸F]-AB5186 to bind to TSPO *in vivo* in a specific manner.

The following hypotheses were set for this work:

i) [¹⁸F]-AB5186 will enter brain tissue and subsequently bind TSPO overexpressed by GBM and associated immune cells. This hypothesis was drawn based on the earlier described observations (see section 7.1.1 for details), which revealed that the *in vitro* predictor of passive BBB transport (P_m) was favourable for AB5186 compared to PK11195, and that [¹⁸F]-AB5186 was able to enter healthy baboon brain *in vivo*. Furthermore, BBB disruptions associated with GBM lesions (see section 4.1.2.2 for details) are likely to facilitate passive brain uptake of [¹⁸F]-AB5186.

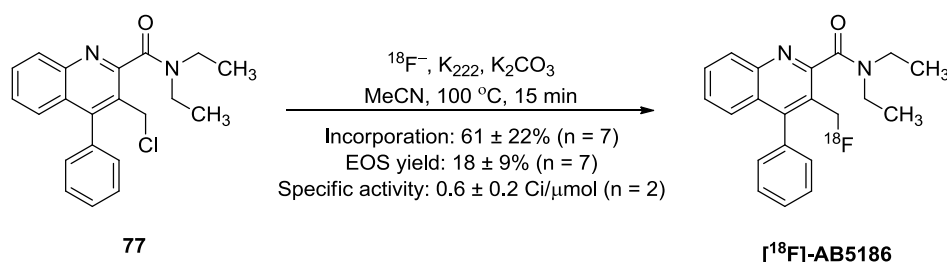
ii) [¹⁸F]-AB5186 will bind to TSPO with specificity *in vivo*. This hypothesis is justified by the earlier described observations that showed specific binding of the radiotracer to TSPO *in vitro* (see section 7.1.1 for details).

iii) Pre-clinical PET imaging of intracranial GBM bearing mice using [¹⁸F]-AB5186 will allow for non-invasive visualisation of TSPO overexpressed in the tumour. The rationale for this hypothesis is based on previous reports of GBM nuclear imaging using radiotracers for TSPO (see section 1.4.3.1 for details).

7.2 Results and discussion.

7.2.1 Radiofluorination, purification, and formulation of [¹⁸F]-AB5186.

The radiosynthetic methodology used to access [¹⁸F]-AB5186 and subsequent purification and formulations steps were developed by Dr Adele Blair as part of her PhD project (Blair, 2014). These methodologies were replicated for the purpose of the work described in this chapter. Manual radiosynthesis involved performing an aliphatic nucleophilic substitution of a benzyl chloride with radiofluoride in the presence of the phase transfer agent K₂₂₂, which allowed for 61 ± 22% (n = 7) incorporation yield (Scheme 7.1). The chlorinated precursor for this reaction was synthesised by Dr Adele Blair, and further information concerning the preparation of this compound can be found in the author's thesis (Blair, 2014). Following the radiosynthetic reaction, [¹⁸F]-AB5186 was purified using a preparatory HPLC system and formulated into a solution of 10% v/v ethanol in 0.9% w/v saline. This enabled access to the radiotracer in an end of synthesis yield of 18 ± 9% (Scheme 7.1) and 99 ± 1% radiochemical purity (n = 7) (Figure 7.5). The specific activity of [¹⁸F]-AB5186 generated using the aforementioned methodology was established by Dr Adele Blair and revealed to be 0.6 ± 0.2 Ci/μmol (n = 2) (Blair, 2014).



Scheme 7.1. Optimised aliphatic nucleophilic substitution radiofluorination methodology for the synthesis of the potential TSPO PET imaging agent [¹⁸F]-AB5186 using the chlorinated precursor **77**. EOS = end of synthesis.

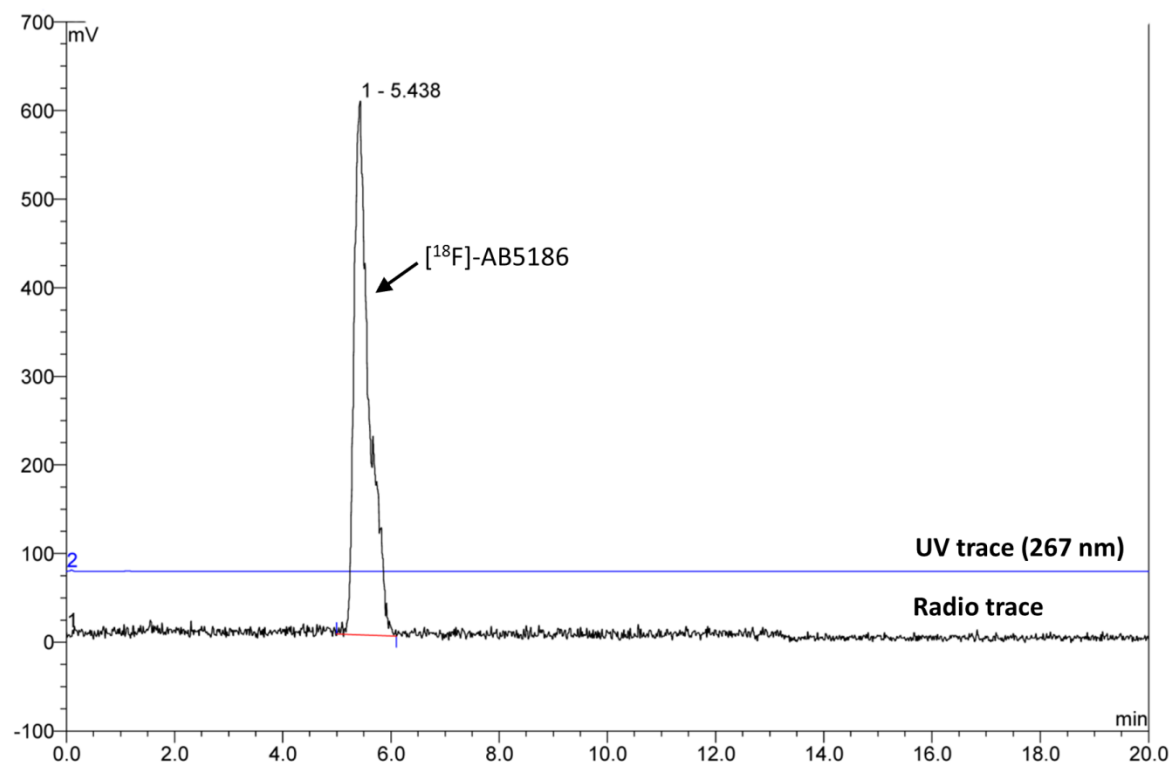


Figure 7.5. An analytical quality control UV (267 nm)/radio-HPLC chromatogram of [^{18}F]-AB5186 showing >99% radiochemical purity of the radiotracer formulated in 10.0% v/v ethanol in 0.9% w/v saline. The identity of [^{18}F]-AB5186 was confirmed by comparing the retention time of the radiolabelled product (i.e. ^{18}F -bearing) against the retention time of unlabelled AB5186 (i.e. ^{19}F -bearing) (Appendix 9.14).

It is important to bear in mind that the above described radiosynthesis of [^{18}F]-AB5186 has potential for further optimisation, which could include the use of TBAHCO_3 as a phase transfer agent in combination with a bulky protic alcohol. This can be rationalised by the improved radiofluoride incorporation yields observed following the addition of *tert*-butyl alcohol when developing radiolabelling methodology for [^{18}F]-17 (see section 5.2.3 for details). The ultimate aim would be to automate the radiosynthetic and purification methodologies to allow for rapid and reproducible access to [^{18}F]-AB5186 (see chapter 8 for details).

7.2.2 Intracranial U87MG-Luc2 glioblastoma xenograft model.

The intracranial U87MG-Luc2 GBM xenograft model was chosen to test the hypotheses outlined earlier (see section 7.1.4), as the wild-type variant of the cell line has been shown generate TSPO overexpressing tumours in rats (Starosta-Rubinstein *et al.*, 1987). Another important driving force for this choice was the ability of the cell line to express luciferase, which in turn allows for non-invasive *in vivo* bioluminescence imaging of viable tumour cells (see section 7.1.3 for details). Furthermore, past experience of the research group with this model revealed that the intracranially implanted U87MG-Luc2 tumours are localised and exhibit a non-invasive phenotype. A low degree of invasiveness can be beneficial for pre-clinical radiotracer evaluation as it permits the use of the contralateral brain region as a reference tissue for quantification purposes.

In order to confirm that the luciferase variant of the U87MG cell line is still capable of generating tumours associated with high levels of TSPO expression, intracranial U87MG-Luc2 tumours grown in mice were characterised by immunohistochemistry. Tumour sections were stained with H&E, and antibodies against Ki67, TSPO, and Iba1 (a marker of microglia) (Figure 7.6). The latter antibody was used in an attempt to delineate between neoplastic and microglial TSPO expression. H&E staining revealed well defined and vascularised GBM lesions located unilaterally, which were found to comprise of a large number of proliferative cells as shown by Ki67 antibody staining. Importantly, high levels of TSPO were present in tumour tissue relative to contralateral brain regions, where expression was low. This observed contrast was in line with previous reports (see section 1.4.2 for details) and provides further evidence to support the use of TSPO as a GBM biomarker.

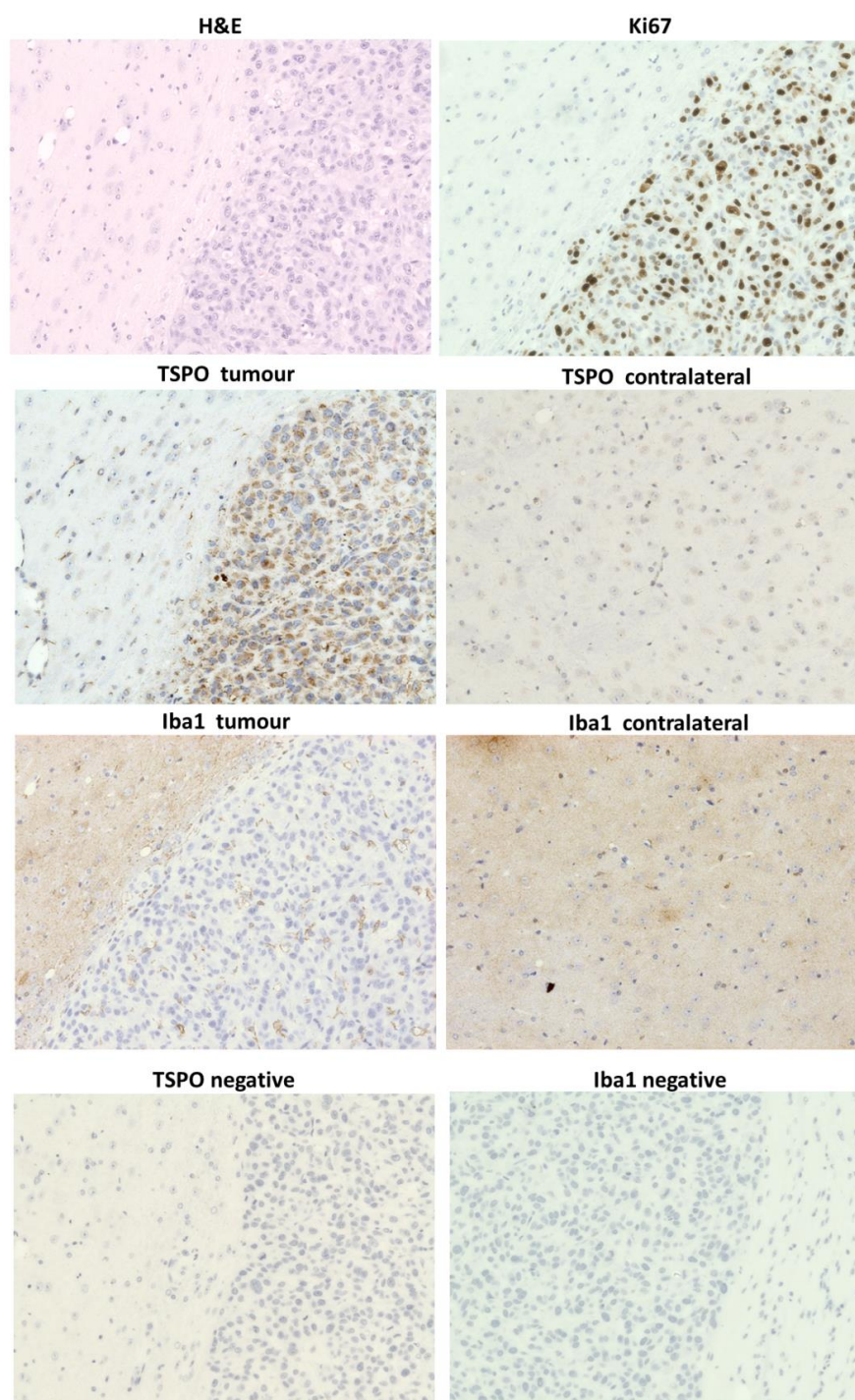


Figure 7.6. Representative immunohistochemistry images ($\times 4$ magnification) of a single intracranial U87MG-Luc2 GBM tumour and contralateral brain regions from a female CD1 nude mouse stained with haematoxylin and eosin (H&E), and antibodies against Ki67 (a marker of cellular proliferation), TSPO, and Iba1 (a microglia marker). TSPO and Iba1 negative control sections were stained with secondary antibody only. Staining was performed on paraffin embedded tissue. Blue staining shows cellular nuclei and brown staining signifies the presence of Ki67, TSPO or Iba1. Modified from Blair *et al.* (2015).

It is important to note that immunohistochemical evaluation of the mouse U87MG-Luc2 tumours using the Iba1 antibody revealed the presence of microglia cells within the main tumour mass. This observation correlated with previous literature reports that showed infiltration of microglial cells into glioma tumours, which can account for up to 30% of the tumour mass (reviewed by Olah *et al.* (2011)). The deramified morphology of these cells was suggestive of an activated microglial phenotype (Raivich *et al.*, 1999; Olah *et al.* 2011). Therefore, it is possible that these activated immune cells contributed to TSPO expression within the U87MG-Luc2 tumours. However, the increased amount of staining observed with the anti-TSPO antibody when compared to the anti-Iba1 antibody suggested that the majority of TSPO expression within the tumour was of neoplastic origin. These findings are in line with those reported by Winkeler *et al.* (2012) who performed immunohistochemical staining of brain tissue sections obtained from rats bearing 9L glioma xenografts. Furthermore, gliomas are known to secrete high levels of factors that can suppress microglia activation and repress expression of co-stimulatory molecules (Olah *et al.*, 2011). Although, it is important to note that Winkeler *et al.* (2012) confirmed the presence of activated microglia within rat 9L glioma lesions. In order to establish the presence of activated microglia in the U87MG-Luc2 GBM tumours, immunohistochemistry staining using a CD68 antibody (a marker of activated microglia) was attempted. However, optimisation of the staining protocol proved challenging due to high non-specific binding and consequently conclusive results could not be obtained (data not shown). The specificity of the secondary antibodies for the primary TSPO and Iba1 antibodies was confirmed by staining the tissues with secondary antibodies only (i.e. TSPO and Iba1 negative controls). No brown staining was observed, thereby confirming the specificity of the secondary stains (Figure 7.6).

7.2.3 *Ex vivo* autoradiography and PET imaging.

Generation of intracranial U87MG-Luc2 tumours requires stereotactic injection of viable tumour cells into the brains of mice that are immunodeficient. CD1 nude mice lack the thymus (i.e. athymic), which is the primary lymphoid organ responsible for producing T-cells. Since T-cells form part of the adaptive immune system and exhibit cytotoxic xenoreactivity, their absence is important in maximising successful tumour xenograft implantation. However, despite an athymic phenotype, nude mice can possess small numbers of T-cells originating from an extrathymic development pathway, which have been shown to negatively affect tumour xenograft transplantability (Zietman *et al.*, 1988). Other factors that can contribute to xenograft implantation failure include procedural error, cancer cell line contamination, and loss of cellular viability during the implantation procedure.

To confirm successful U87MG-Luc2 GBM xenograft implantation, bioluminescence imaging was performed 11 or 15 days after stereotactic cancer cell injection (Figure 7.7). Absence of bioluminescence signal was suggestive of failed tumour engraftment or complete tumour regression, and such animals were excluded from [¹⁸F]-AB5186 *in vivo* studies.

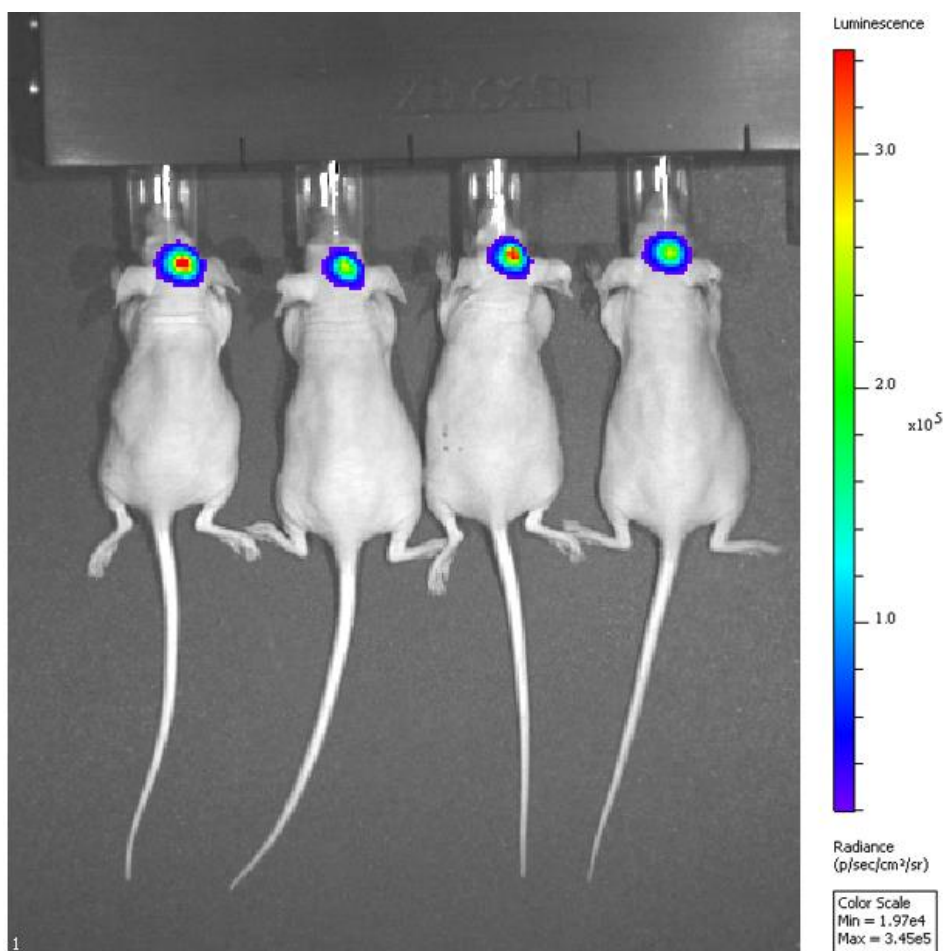


Figure 7.7. Representative bioluminescence image of intracranial U87MG-Luc2 tumours 15 days after implantation acquired using the IVIS[®] Spectrum. The image was processed and generated using the Living Image 4.4 software.

In order to establish whether [¹⁸F]-AB5186 was capable of entering GBM tissue and binding to TSPO with specificity *in vivo*, mice bearing intracranial U87MG-Luc2 tumours were pre-treated with either vehicle or an excess of the non-radioactive TSPO ligand PK11195, followed by intravenous administration of [¹⁸F]-AB5186. Tumour bearing brains of the mice were then removed, frozen, and sectioned. *Ex vivo* autoradiography of brain tissue sections obtained from vehicle pre-treated mice revealed distinct radioactive hotspots in the tumour bearing hemispheres (Figure 7.8 A) with a hotspot to contralateral brain tissue optical density ratio of 2.1 ± 0.1 ($n = 4$). These hotspots correlated with the anatomical location of the tumours, which appeared as blue masses following H&E histochemical staining (Figure 7.8 B), and were shown to express high levels of TSPO (Figure 7.8 C). Importantly, ‘blockade’ of TSPO binding sites with non-radioactive PK11195 resulted in significantly lower *in vivo* uptake of [¹⁸F]-AB5186

into tumour tissue when compared to vehicle pre-treated mice (Figure 7.8 A and Figure 7.9). These observations were in line with the earlier defined hypotheses (section 7.1.4.), as they confirm the ability of [^{18}F]-AB5186 to enter mouse GBM tissue and bind to TSPO with specificity *in vivo*.

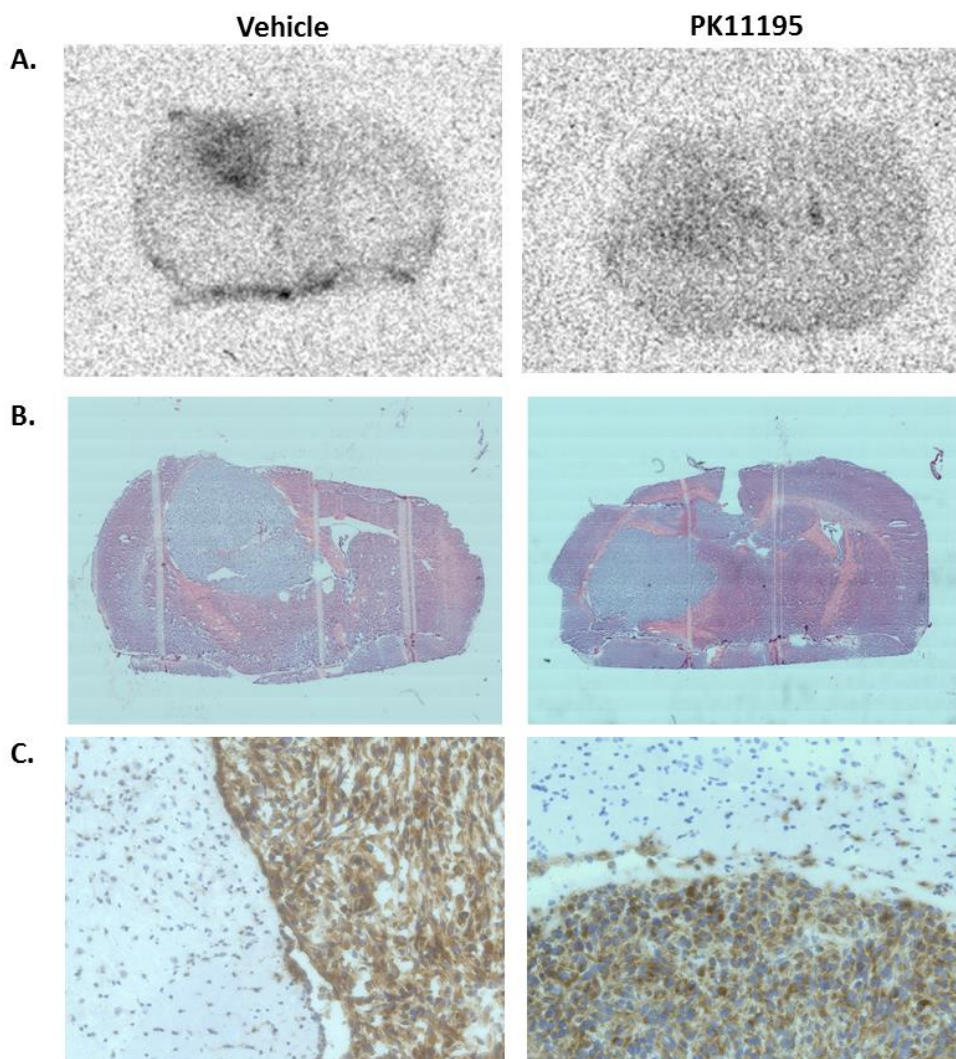


Figure 7.8. Representative coronal brain autoradiograms (A), and immunohistochemistry images showing staining with haematoxylin and eosin (tiled image) (B) and the anti-TSPO antibody (C) ($\times 4$ magnification) obtained from intracranial U87MG-Luc2 GBM bearing female CD1 nude mice that were injected with either vehicle or 1 mg/kg PK11195 followed by [^{18}F]-AB5186 (41 ng) 10 minutes later. Animals were killed and brains were harvested for sectioning 20 minutes after radiotracer administration. Immunohistochemistry staining was performed on frozen tissue. Blue staining shows cellular nuclei and brown staining signifies the presence TSPO. Modified from Blair *et al.* (2015).

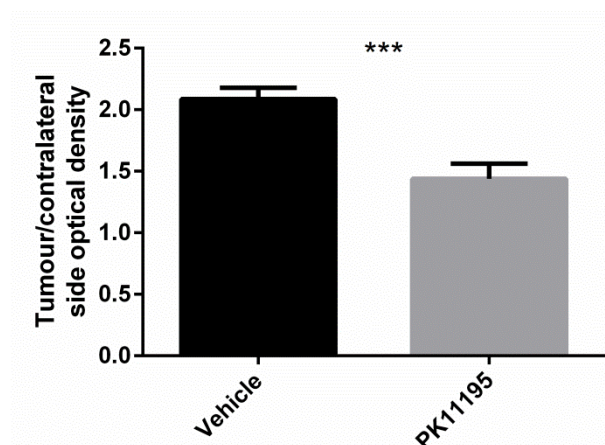


Figure 7.9. A graph showing the ratios of autoradiogram tumour to contralateral side optical densities from vehicle control (n = 4) and PK11195 (n = 4) treated intracranial U87MG-Luc2 GBM bearing mice. Error bars represent the mean + standard deviation. Unpaired t test value: *** = ≤ 0.001 . The plot was generated and statistical analysis was performed using the GraphPad Prism 6.0 software. Modified from Blair *et al.* (2015).

To investigate the potential of [^{18}F]-AB5186 as a TSPO nuclear imaging agent, a 120 minute dynamic PET scan was performed of a single mouse bearing an intracranial U87MG-Luc2 tumour immediately after radiotracer administration. Failure of the nuclear imaging equipment in the department prevented data acquisition from a larger population sample. PET image reconstruction and manual co-registration with a CT image acquired after the dynamic scan revealed a unilateral hotspot, which correlated with the tumour implantation site (Figure 7.10). High uptake of [^{18}F]-AB5186 was also observed in areas outside of the CNS, including the eye and oral cavity regions.

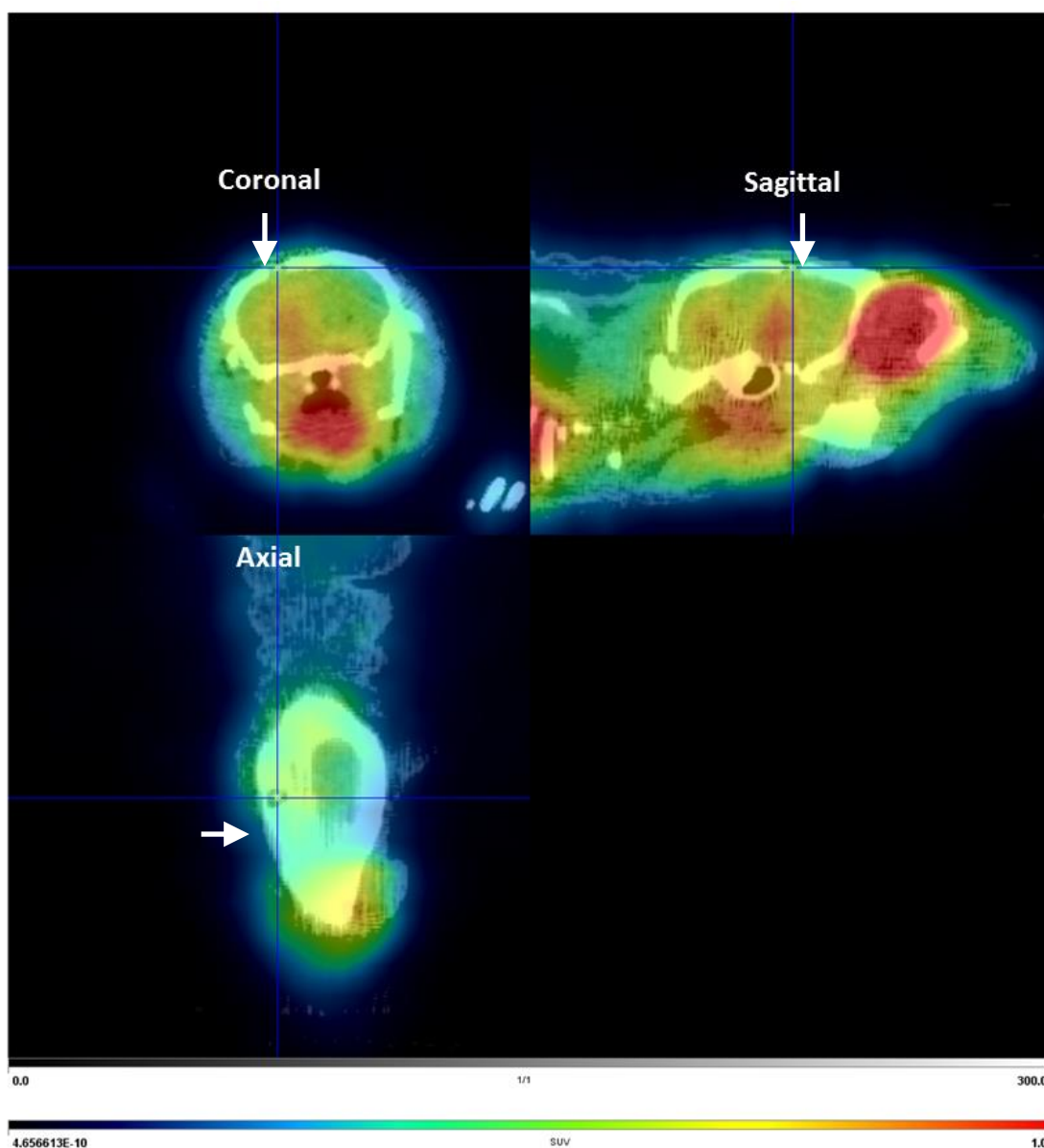


Figure 7.10. Summed dynamic PET data (frames 1–10; 1 acquisition per minute; 120 minute scan) fused with manually co-registered CT of an intracranial U87MG-Luc2 GBM xenograft bearing mouse (29 days post implantation) acquired following [^{18}F]-AB5186 (124 ng) administration. White arrows highlight cranial entrance used for tumour implantation. The image was processed and generated using the PMOD 3.504 software. SUV = standardised uptake value.

In order to minimise interference from extracranial tissue and allow for greater clarity, the PET signal outside of the brain region (as defined by the skull) was masked (Figure 7.11 A to C). Postmortem histological evaluation of the brain collected after PET/CT imaging revealed a large unilateral GBM lesion (Figure 7.11 D) that correlated with the anatomical location of the PET hotspot visible in summed images from the first and mid 40 minute portions of the scan (Figure

7.11 A and B). These observations were suggestive of [^{18}F]-AB5186 uptake in tumour tissue. Summed images from the last 40 minutes of the scan (Figure 7.12 C) revealed negligible difference between [^{18}F]-AB5186 uptake in the tumour bearing and contralateral brain regions, which was indicative of tracer washout from the brain.

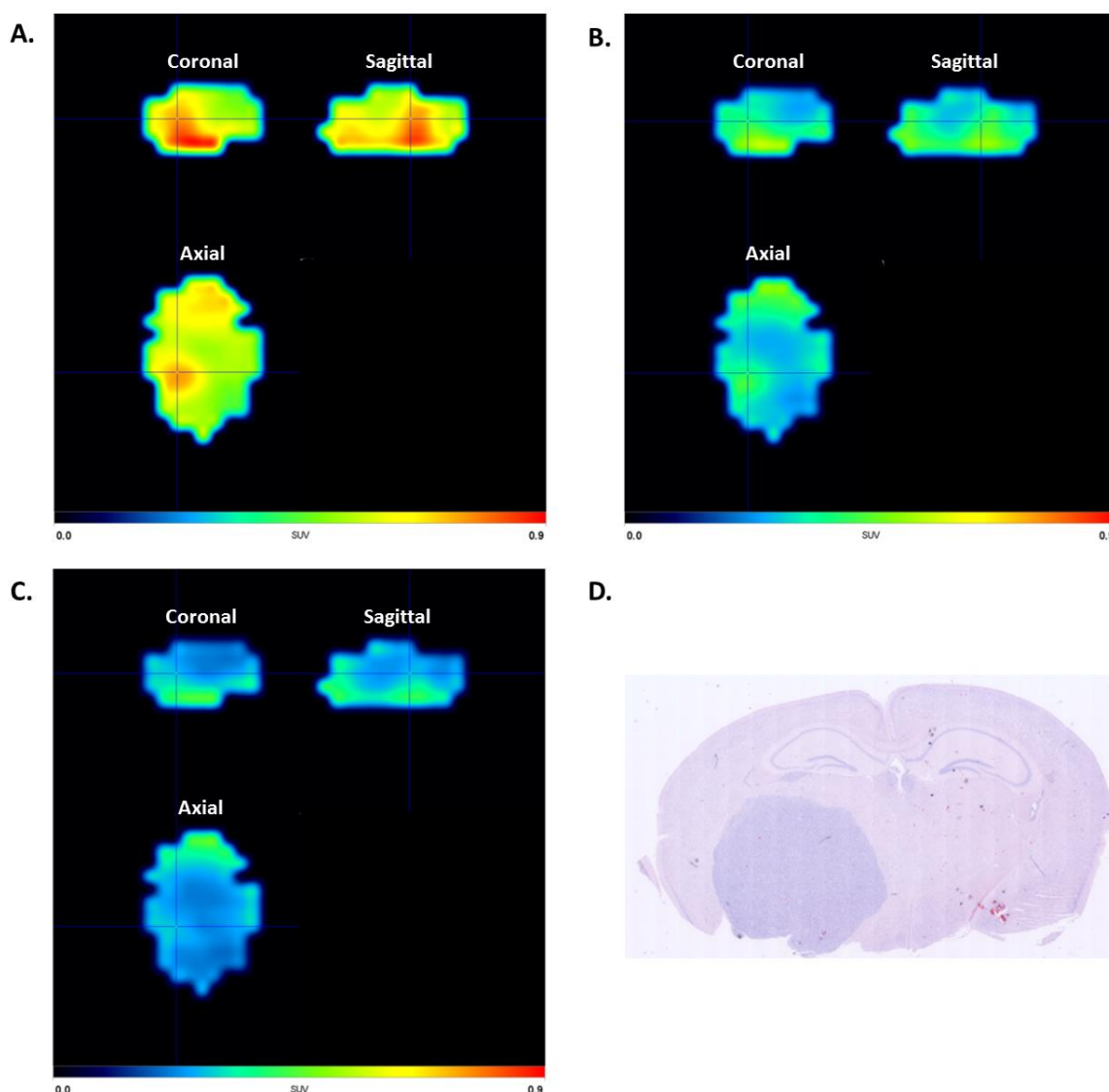


Figure 7.11. Averaged summed dynamic PET images (A = 0–40 minutes; B = 41–80 minutes; C = 81–120 minutes) of a U87MG-Luc2 GBM xenograft bearing mouse brain (29 days post implantation) acquired following [^{18}F]-AB5186 (124 ng) administration, and a coronal histochemistry image (tiled) showing staining of the brain tissue with haematoxylin and eosin (D). Histochemical staining was performed on paraffin embedded tissue. PET images were processed and generated using the PMOD 3.504 software. SUV = standardised uptake value. Modified from Blair *et al.* (2015).

In order to probe the kinetics [^{18}F]-AB5186 further, quantitative analysis of the PET data was performed. This allowed for the generation of [^{18}F]-AB5186 time-activity curves in tumour and contralateral brain regions (Figure 7.12). The amount of radioactivity was represented as a standardised uptake value (SUV), which is the ratio of concentration of tracer in a defined volume of interest to the hypothetical concentration of the tracer in the whole body. The curves revealed rapid uptake of [^{18}F]-AB5186 into the brain and an approximate tumour to contralateral brain tissue SUV ratio of 1.4–1.6 between 20 and 80 minutes post radiotracer administration. It is important to bear in mind that explaining the current data against the published literature is rather challenging, as different study protocols (e.g. different models, animal species, PET imaging equipment, analysis methodologies, etc.) were employed and therefore a direct comparison is strictly impractical. Furthermore, the preliminary PET imaging findings for [^{18}F]-AB5186 were acquired using a single mouse and may not be representative of a larger population. However, the current data can still be discussed within a broader context, bearing the above in mind.

Buck *et al.* (2011) and Winkeler *et al.* (2012) performed PET imaging on intracranial glioma bearing rats using [^{18}F]-PBR06 and [^{18}F]-DPA714 respectively, and reported the corresponding time activity curves for tumour and contralateral brain regions. In both cases, the tumour levels of the radiotracer remained approximately constant throughout the duration of the PET scan, while levels in contralateral tissue steadily decreased. In the case of the current dataset for [^{18}F]-AB5186, radiotracer levels from both tumour and contralateral brain tissue regions decreased with time, albeit at a slower rate from the tumour bearing region. It is possible that non-specific binding of [^{18}F]-AB5186 to cellular components other than TSPO could have contributed to reduced tumour retention. Furthermore, due to spatial resolution limitations of the PET scanner (i.e. 1.55 mm (Sánchez *et al.*, 2013)), precise delineation of the tumour from surrounding grey matter was not attainable, which could have affected the quantification process and therefore the aforementioned observations.

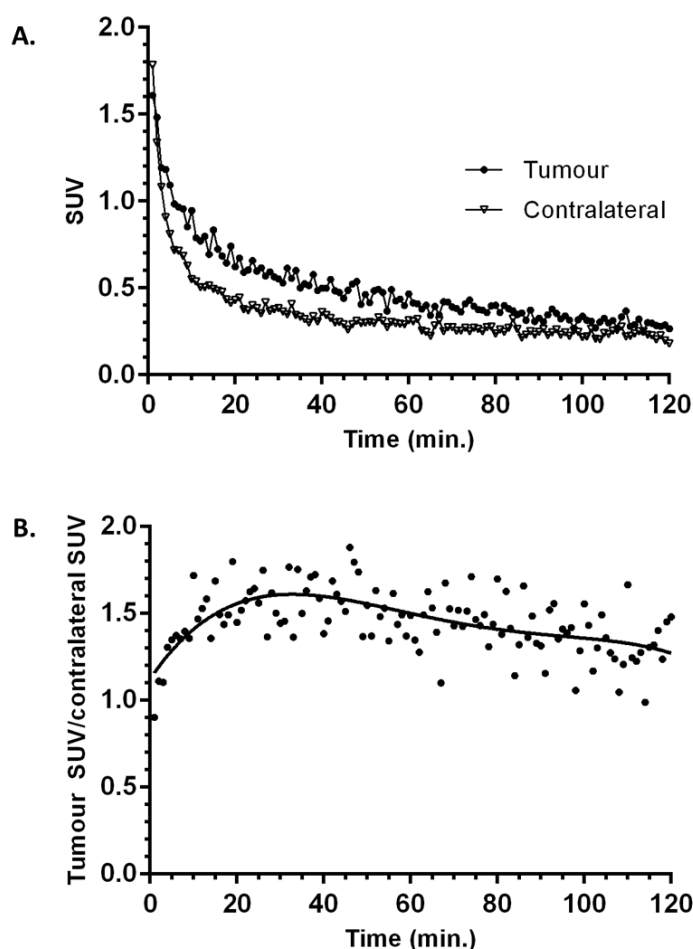


Figure 7.12. Time-activity curves of $[^{18}\text{F}]\text{-AB5186}$ in the U87MG-Luc2 GBM tumour xenograft and contralateral brain regions (A) and tracer kinetics expressed as a ratio of tumour to contralateral brain tissue standardised uptake values (SUV) (B). Modified from Blair *et al.* (2015).

7.3 Conclusion.

Radiolabelling methodology developed by Dr Adele Blair was successfully replicated to access $[^{18}\text{F}]\text{-AB5186}$ in $18 \pm 9\%$ ($n = 7$) end of synthesis yield. *Ex vivo* autoradiography of mouse brains bearing GBM tumour xenografts revealed accumulation of the tracer in tumour lesions in good contrast to surrounding grey matter (tumour to contralateral brain tissue optical density ratio = 2.1 ± 0.1 ($n = 4$)). Furthermore, tumour uptake of $[^{18}\text{F}]\text{-AB5186}$ was revealed to be due to specific binding of the radiotracer to TSPO overexpressed by cells within the lesion. These observations proved the first two hypotheses described earlier in section 7.1.4. The tracer was also used to successfully visualise TSPO in a mouse using non-invasive PET imaging, thereby proving the final hypothesis set for this

chapter of the thesis. However, further research is required in order to obtain more representative imaging data using larger population samples and [^{11}C]-PK11195 as a positive control. The use of the positive control could be used to establish whether the improved *in vitro* P_m and K_m parameters of AB5186 (see section 7.1.1 for details) are translatable to improved BBB permeability and specific binding properties *in vivo* when compared to PK11195 (see chapter 8 for details).

Overall, the preliminary *in vivo* data for [^{18}F]-AB5186 highlight the potential of the agent to act as a TSPO nuclear imaging probe, which has the advantage of being labelled with a longer lived radioisotope compared to the current ‘gold-standard’ PET TSPO imaging agent [^{11}C]-PK11195. [^{18}F]-AB5186 also has the potential to exhibit minimal sensitivity to human single nucleotide TSPO polymorphism, unlike second and third generation TSPO radiotracers (see section 1.4.3.2 for details). At the time of writing, human tissue binding assays aimed at establishing the sensitivity of AB5186 to human TSPO polymorphism were underway. Despite the lack of a complete dataset, preliminary results from these assays showed negligible differences between the binding profiles of genetically ascertained low- (n = 2), mixed- (n = 2), and high-affinity (n = 2) binders.

7.4 Experimental.

7.4.1 General.

Please see section 5.4.1 for details concerning the production of [^{18}F]-fluoride, the preparatory and analytical HPLC systems, and UV/radio-HPLC detection.

7.4.2 Manual radiosynthesis (via aliphatic nucleophilic substitution of chlorinated precursor **77**), purification, and formulation of [¹⁸F]-AB5186.

Synthesis was performed as per the procedure reported by Blair *et al.* (2015). To a 2 mL v-vial containing 532–682 MBq of ¹⁸F⁻/H₂¹⁸O (0.3 mL) was added 0.106 M Kryptofix[®] (K₂₂₂) and 0.0347 M potassium carbonate (0.25 mL). The mixture was vortexed and the [¹⁸F]-fluoride was dried by passing a constant stream of argon over the solution at 100 °C for approximately 20 minutes; aliquots of anhydrous acetonitrile (3 × 0.5 mL) were added to facilitate azeotropic drying. A solution of the chloride precursor **77** (2.4 mg, 0.0068 mmol) in acetonitrile (0.5 mL) was then added to the v-vial and the reaction allowed to proceed for 15 min at 100 °C. Next, the mixture was cooled to room temperature, diluted with distilled water (0.21 mL), and purified using the preparatory HPLC system and the following mobile phase conditions: 0.0–15.0 min 70:30 A:B where A = acetonitrile and B = distilled water. The radiolabelled product was collected at approximately 8 minutes and concentrated *in vacuo* in an evaporator flask. The flask was rinsed with acetonitrile (3 × 0.3 mL) to extract the radiolabelled compound and the solution was transferred to a 2 mL v-vial; the solvent was removed by passing a constant stream of argon over the solution at 100 °C for approximately 15 minutes. The radiotracer was then dissolved in ethanol followed by dilution using 0.9% w/v saline solution such that the final volume was up to 0.8 mL and the final concentration of ethanol was 10% v/v; the mixture was vortexed for up to 0.5 minutes to maximise solubilisation of [¹⁸F]-AB5186. The total radiosynthesis time was 118 ± 14 minutes (n = 7).

A sample of the formulated radiotracer was run on the analytical HPLC system using the following mobile phase conditions: 0.0–15.0 min 70:30 A:B where A = acetonitrile and B = distilled water. To confirm the identity of the radiolabelled product, the retention time of [¹⁸F]-AB5186 was compared to the retention time obtained for non-radioactive AB5186 using the same chromatographic conditions.

7.4.3 U87MG-Luc2 cell culture, intracranial tumour implantation, and bioluminescence imaging.

Procedures were performed as reported by Blair *et al.* (2015). The U87MG-Luc2 GBM cell line was cultured as described in section 6.4.5. Unconscious female 6–8 week old CD1 nude mice had 1×10^5 U87MG-Luc2 cells implanted intracranially into the caudate nucleus using standard stereotactic procedures. Successful implantation of tumours was confirmed by performing bioluminescence imaging either 11 or 15 days after the procedure using an IVIS[®] Spectrum system (PerkinElmer, USA) and the following imaging parameters: i) auto exposure; ii) binning = 8; iii) field of view = 22.8; and iv) f stop = 1. Mice were injected subcutaneously with 150 mg/kg D-luciferin 7 minutes before performing IVIS[®] imaging. Immediately prior to imaging the mice were anaesthetised using inhaled isoflurane (in medical oxygen; induction 5.0% v/v; maintenance 2.0–3.0% w/v). The above practical procedures were performed by Sandeep Chahal and Dr Lesley Gilmour from the Chalmer's research group. Data were quantified using the Living Image 4.4 software. Regions of interest were defined manually around the cranial bioluminescence hotspots and around distal regions to define the background signal. The average background bioluminescence signal was subtracted from the cranial signal, and was expressed as average radiance (photons/sec/cm²/steradian). Tumour bearing animals were used for *in vivo* studies 21-30 days post tumour implantation.

7.4.4 Immunohistochemistry.

7.4.4.1 Paraffin embedded tissue.

Immunohistochemistry was performed as reported by Blair *et al.* (2015). Intracranial U87MG-Luc2 tumour bearing mice were perfusion fixed using 4% v/v formaldehyde PBS. Following this, the brains were harvested and immersion fixed used the same fixative for a further 72 hours. The fixed tissue was embedded in paraffin blocks and 4 μ m sections were cut by the Cancer Research UK Beatson Institute Histology Service. Tissues were prepared and stained using

the same procedures as described previously in section 6.4.6. Primary staining was performed using either 1:250 anti-TSPO antibody (rabbit anti-human, mouse and rat antibody; NBP1-95674; Novus Biologicals), 1:250 anti-Iba1 antibody (mouse anti-human, mouse and rat antibody; ab15690; Abcam), or a range of concentrations of anti-CD68 antibody (rat anti-human antibody; ab53444; Abcam) (i.e. 1:100, 1:250, or 1:500). Staining using the latter antibody was attempted following heat induced antigen retrieval at either pH 6.0 or pH 9.0. Secondary staining was performed using Dako horseradish-peroxidase labelled anti-mouse, anti-rabbit, or anti-rat polymer. Haematoxylin and eosin, and Ki67 staining was performed by the Cancer Research UK Beatson Institute Histology Service using a Leica ST5020 multistainer. Individual or tiled histology images were acquired using a Zeiss AX10 brightfield microscope at $\times 4$ magnification and contrast was corrected manually using the ImageJ 1.47v software.

7.4.4.2 Frozen tissue.

Intracranial U87MG-Luc2 tumour bearing mice were killed using CO₂ asphyxiation, and the brains were removed and frozen using a cryospray (Cellpath). Tissues were stored at -80 °C until ready for use. The frozen brain tissues were warmed to -20 °C and 20 μm sections were cut using a cryomicrotome (Leica CM1950). The frozen sections were transferred to poly-L-lysine coated glass slides (Snowcoat[®]) and were allowed to dry overnight at room temperature. The dried sections were then fixed by washing in pre-cooled (-20 °C) acetone for 10 minutes, followed by two further washes in PBS (pH 7.4) for 5 minutes. Brain sections were incubated in 3% v/v hydrogen peroxide in methanol (20 minutes), and then 5% w/v bovine serum albumin and 5% v/v goat serum in PBS (20 minutes) to block peroxidase activity and minimise non-specific binding respectively. Between each step the tissue sections were washed in 0.1% v/v Tween[®] 20 in TBS (2 \times 5 minutes). The tissues were then stained using 1:250 anti-TSPO antibody (rabbit anti-human, mouse and rat antibody; NBP1-95674; Novus Biologicals) and Dako horseradish-peroxidase anti-mouse or anti-rabbit polymer as described in section 6.4.6. Haematoxylin and eosin staining was performed by the Cancer Research UK Beatson Institute Histology Service using a Leica ST5020 multistainer. Individual or tiled histology images were acquired

using a Zeiss AX10 brightfield microscope at $\times 4$ magnification and contrast was corrected manually using the ImageJ 1.47v software.

7.4.5 Ex vivo autoradiography.

The experiments were performed as reported by Blair *et al.* (2015). Intracranial U87Mg-Luc2 tumour bearing female CD1 nude mice were anaesthetised using inhaled isoflurane (in medical oxygen; induction 5.0% v/v; maintenance 2.0–3.0% v/v) and received bolus tail vein injections of either 0.10 mL of vehicle (20% v/v PEG 400 and 5% v/v ethanol in 0.9% w/v saline) ($n = 4$) or 1 mg/kg of PK11195 in 0.10 mL of vehicle ($n = 4$). After 10 minutes the mice received a slow intravenous injection (0.4 mL/min) of 1.5–2.7 MBq [^{18}F]-AB5186 in 0.20 mL of 10% v/v ethanol in 0.9% w/v saline. Anaesthesia and injections were performed by Dr Gaurav Malviya from the Cancer Research UK Beatson Institute Nuclear Imaging department. After a further 20 minutes the mice were killed by CO_2 asphyxiation, and the brains were removed and frozen using a cryospray (Cellpath). Mice remained under anaesthesia until the time of cull. The frozen brains were cut at 40 μm using a cryomicrotome (Leica CM1950) at $-20\text{ }^\circ\text{C}$, transferred to uncoated glass slides (Snowcoat[®]) and applied to Kodak[®] BioMax[®] film. The film was developed following an overnight incubation at $-20\text{ }^\circ\text{C}$ and scanned using a Bio-Rad GS-800 Calibrated Densitometer with the aid of the Quantity One Basic (version 4.6.3) software. Quantification was performed using the ImageJ 1.47v software. A sliding paraboloid background subtraction algorithm was applied with a rolling ball radius of between 30–50 pixels depending on the size of the tumour hotspot. Optical density values were extracted from regions of interest which were drawn manually around the tumour hotspots and mirrored to define the contralateral side. The mean ratios of the tumour to contralateral optical densities were calculated for both the vehicle control and PK11195 blockade cohorts and an unpaired parametric t-test was performed using the GraphPad Prism 6 software. Error bars represent the mean + standard deviation.

7.4.6 PET/CT imaging.

The imaging study was conducted as reported previously by Blair *et al.* (2015). A single intracranial U87MG-Luc2 tumour bearing female CD1 nude mouse was anaesthetised using inhaled isoflurane (in medical oxygen; induction 5.0% v/v; maintenance 2.0–3.0% v/v) and placed in the multimodal PET/SPECT/CT Albira imaging system (Bruker Corporation, USA). The mouse was placed in the scanner bed and a 120 minute dynamic scan (one acquisition per minute) was performed immediately following a bolus tail vein injection of 8.2 MBq [¹⁸F]-AB5186 in 0.20 mL of 10% v/v ethanol in 0.9% w/v saline. CT was acquired after the dynamic PET scan in best-resolution mode (projections = 600; exposure time = 8 minutes) using high intensity (400 μ A) and low voltage (35 kV) settings. The animal was monitored using a live video feed throughout the imaging session. The dynamic PET data were corrected for random coincidences, dead time, scatter, and decay, and subsequently reconstructed using the maximum likelihood expectation maximisation algorithm with 12 iterations. The above described practical procedures were performed by Dr Gaurav Malviya. The reconstructed PET and CT data were analysed using the PMOD 3.504 software. The PET image was manually co-registered with key anatomical structures of the CT (i.e. the spine, the front limbs, and the eye sockets). The skull of the animal was then used to define the brain and the PET signal outside of the brain region was masked. Frames from the first 10 min of the dynamic PET scan were averaged to allow for tumour hotspot identification. A volume of interest (VOI) was manually drawn around the tumour hotspot region and was used to generate a time-activity curve. Standard uptake values (SUV) were determined as the concentration in the VOI divided by the injected dose divided by the animal weight. A secondary spherical VOI was used to define the contralateral kinetics and the tumour to contralateral SUV ratio was calculated as a function of time. These data were represented graphically using the GraphPad Prism 6 software.

8 CONCLUSIONS AND FUTURE WORK.

The work described in this thesis was successful in identifying and synthesising compounds based on the clinical PARP-1 inhibitor olaparib with potential for PARP-1 SPECT and PET imaging. The lead SPECT and PET candidates, **4** and **17** respectively, were found to be potent inhibitors of PARP-1 in both cell-free and cellular assays, with IC_{50} values in the low nanomolar range. Radiolabelling methodologies were developed that allowed access to [^{123}I]-**4** in one step and an end of synthesis yield of $37 \pm 7\%$ ($n = 6$), and [^{18}F]-**17** in a two-step one-pot reaction and an end of synthesis yield of $9 \pm 2\%$ ($n = 7$). Both radiotracers were isolated using HPLC purification methodology in high specific activity and radiochemical purity. Furthermore, compounds **4** and **17** were found to be stable in mouse plasma but exhibited approximately three fold more rapid *in vitro* metabolic clearance when compared to olaparib. Despite this, *ex vivo* biodistribution studies revealed that [^{123}I]-**4** and [^{18}F]-**17** accumulated in and were retained by subcutaneous human GBM xenografts in mice. Furthermore, uptake of the potential SPECT and PET tracers in the tumours was found to be due to specific binding of the radioligands to PARP-1. These data support the premise that [^{123}I]-**4** and [^{18}F]-**17** could be used to visualise PARP-1 *in vivo* in a non-invasive manner using nuclear imaging techniques. However, it is important to appreciate that [^{18}F]-**17** may have limited utility as a neuroimaging agent. This is rationalised by the marked *in vivo* [^{18}F]-defluorination that was observed in mice, which was associated with characteristic accumulation of the $^{18}F^-$ radioisotope in bone tissue. In the context of nuclear neuroimaging, this is disadvantageous as the PET signal from the radiotracer may be obscured by background signal from radiofluoride in the skull. Moreover, non-specific radiofluoride uptake in bone tissue could obscure the PET signal originating from specific PARP-1 binding of [^{18}F]-**17** in bone marrow. Subsequently, it is unlikely that this radiotracer could be used to assess PARP-1 inhibitor bone marrow occupancy, which is important in the context of addressing the haematological complications that have been reported in patients treated with PARP-1 inhibitors and chemotherapeutic agents (see section 1.3.3.1 for details).

Imaging of PARP-1 in the brain is complicated further by the presence of the BBB, which is usually disrupted in high grade gliomas (such as GBM), but may remain intact in low grade gliomas and in the vicinity of invasive glioma cells (Kracht *et al.*, 2004). It is likely that intracranial tumour uptake of both [^{123}I]-4 and [^{18}F]-17 will be reliant on disruptions of the BBB. This can be justified by the physiochemical properties of 4 and 17 that fall outside of those optimal for passive BBB penetration (see section 4.2 for details), negligible quantities of [^{123}I]-4 and [^{18}F]-17 found in mouse brain following intravenous administration (see section 6.2.2 for details), and the fact that the parent compound (i.e. olaparib) was reported to be unable to cross the BBB in rats (Chalmers *et al.*, 2014).

Bearing in mind the clinical applications of PARP-1 nuclear imaging in GBM (see section 1.3.3.1 for details), it is important to ascertain whether: i) [^{123}I]-4 and [^{18}F]-17 are capable of entering GBM tissue in the brain; ii) a sufficient contrast in the signal can be achieved between the tumorous lesion and surrounding grey matter; and iii) *in vivo* defluorination of [^{18}F]-17 will result in background interference from the skull and bones. This information could be acquired by performing [^{123}I]-4 SPECT and [^{18}F]-17 PET imaging of small animals bearing intracranial human GBM xenografts. Initially, dynamic SPECT and PET imaging may be performed to establish radiotracer kinetics, which could then be used to identify the time of maximum signal contrast between the tumour and surrounding brain tissue. This is particularly important for SPECT imaging where conventional scanners rely on rotatable detectors that can only acquire dynamic data in a single plane, unlike PET scanners that utilise a detector ring capable of acquiring dynamic data in three dimensions (see section 1.2.1 for details). In order to acquire three dimensional tomographic information, static SPECT images at a single timepoint post-radiotracer administration must be performed. Therefore, knowledge of [^{123}I]-4 kinetics could be used to plan static SPECT imaging studies, such that acquisition is performed at a time where a high target to background signal ratio would be expected.

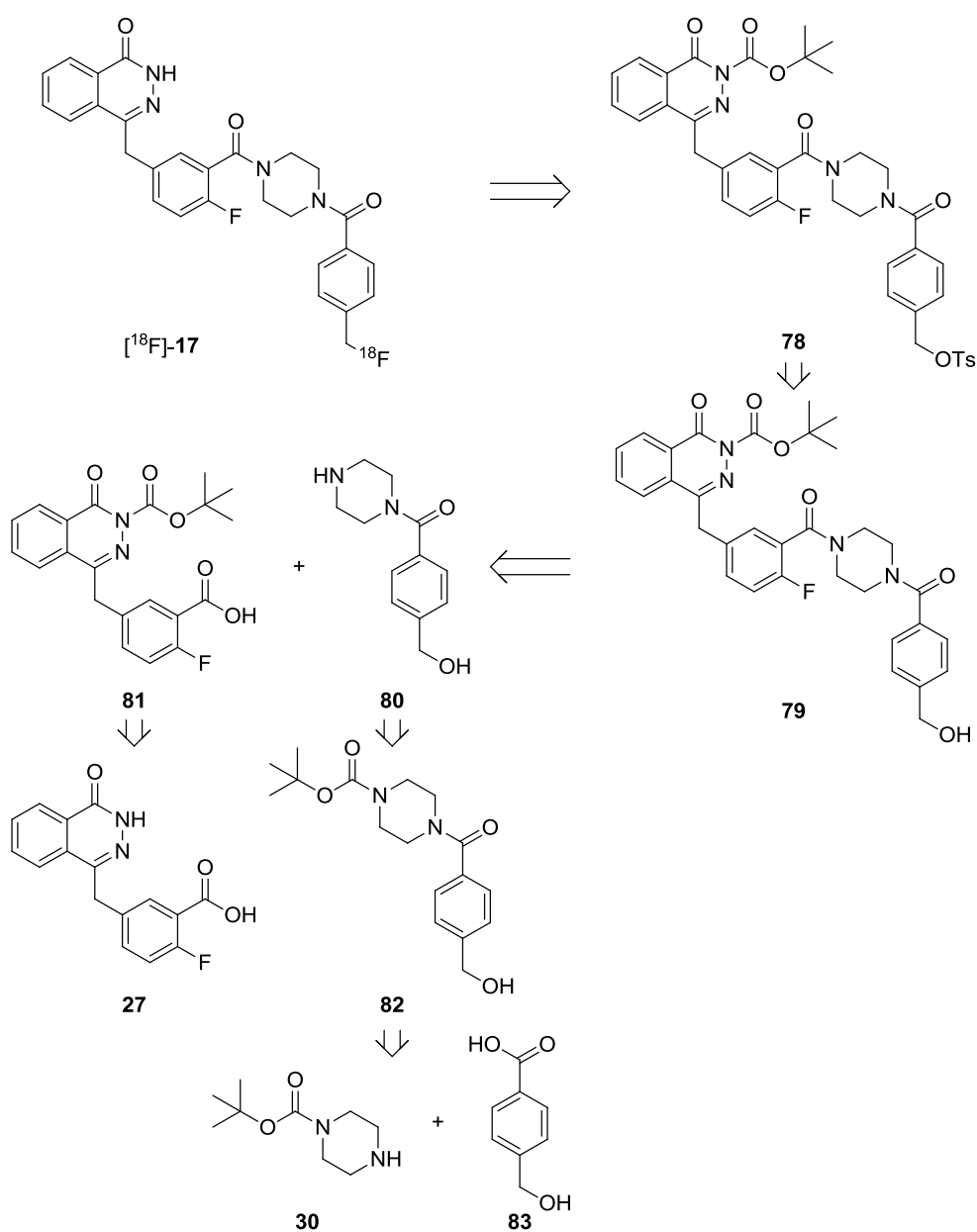
In order to validate the findings from the aforementioned [^{123}I]-4 and [^{18}F]-17 imaging studies, imaging data should be compared with the *ex vivo*

biodistribution data acquired as part of this PhD project (see section 6.2.2 for details) and post-mortem histological analysis of brain tissue sections should be performed using a H&E stain and an anti-PARP antibody. Further validation could also be performed by conducting *ex vivo* autoradiography studies using the same small animal intracranial human GBM xenograft model. The SPECT and PET imaging studies could be further expanded to evaluate the influence of the BBB on intracranial uptake of [^{123}I]-4 and [^{18}F]-17 by using small animal models of low grade astrocytomas, glioblastomas, and meningiomas that exhibit a morphologically intact BBB, a disrupted BBB or an absence of the BBB, respectively (Roelcke *et al.*, 1995).

It is important to bear in mind that progression of novel radiotracers from a pre-clinical to a clinical setting is an expensive and time consuming endeavour, and is dependent on pre-clinical outcomes (see section 1.5 for details). If the above described pre-clinical imaging studies using [^{123}I]-4 or [^{18}F]-17 yield positive results and justify human studies then efforts should be focused on clinical advancement of one or both of these agents. However, prior to human investigations, a number of other key investigations and developments should be performed. Firstly, *in vivo* organ dosimetry following intravenous administration of the radiotracers should be established, which can in turn be used to identify the dose-limiting organ for radiation exposure. This can be achieved by using specialist software that can extract dosimetry information from [^{123}I]-4 SPECT and [^{18}F]-17 PET imaging data (Agdeppa and Spilker, 2009). Secondly, pre-clinical toxicology data for compounds 4 and 17 should be acquired, which is usually achieved by administration of a single dose of the human radiotracer formulation to rodents, followed by toxicity monitoring over a 14 day period (Sharma and Aboagye, 2011). Thirdly, efforts should be focused on the automation of the radiosynthesis and purification methodologies of these tracers. Automation is of value in the context of clinical nuclear imaging as it allows for rapid access to radiotracers in a reproducible manner and with minimal radiation exposure of personnel (Krasikova, 2007). Single step or one-pot radiosyntheses, such as those developed for [^{123}I]-4 and [^{18}F]-17, are generally easier to automate and can be done by modifying apparatus and programming that are already in place for the synthesis of an established

radiotracer such as [^{18}F]-FDG. More complex multi-step radiosyntheses may require bespoke design and construction of automated modules, which can be a time consuming and expensive process (Krasikova, 2007).

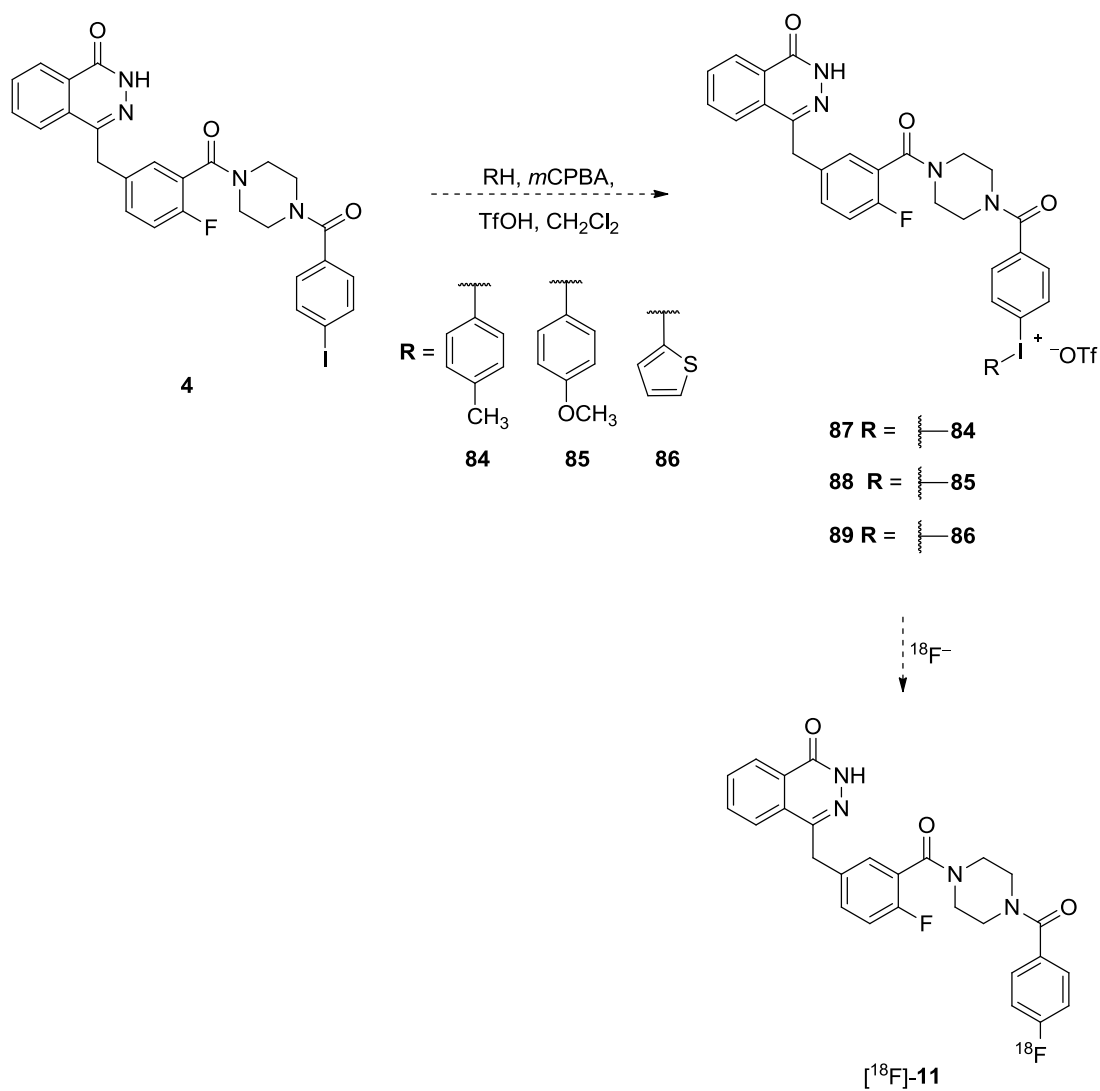
Prior to [^{18}F]-17 radiosynthetic automation, work could be aimed at improving the nucleophilic substitution methodology used to access the radiotracer through the use of an alternative precursor (**78**) bearing a tosylate leaving group with improved leaving ability when compared to the chlorine atom of **72**. A proposed retrosynthetic analysis of such a tosylated precursor can be found in scheme 8.1.



Scheme 8.1. Proposed retrosynthetic analysis of [^{18}F]-17 accessed using the tosylated precursor **78**.

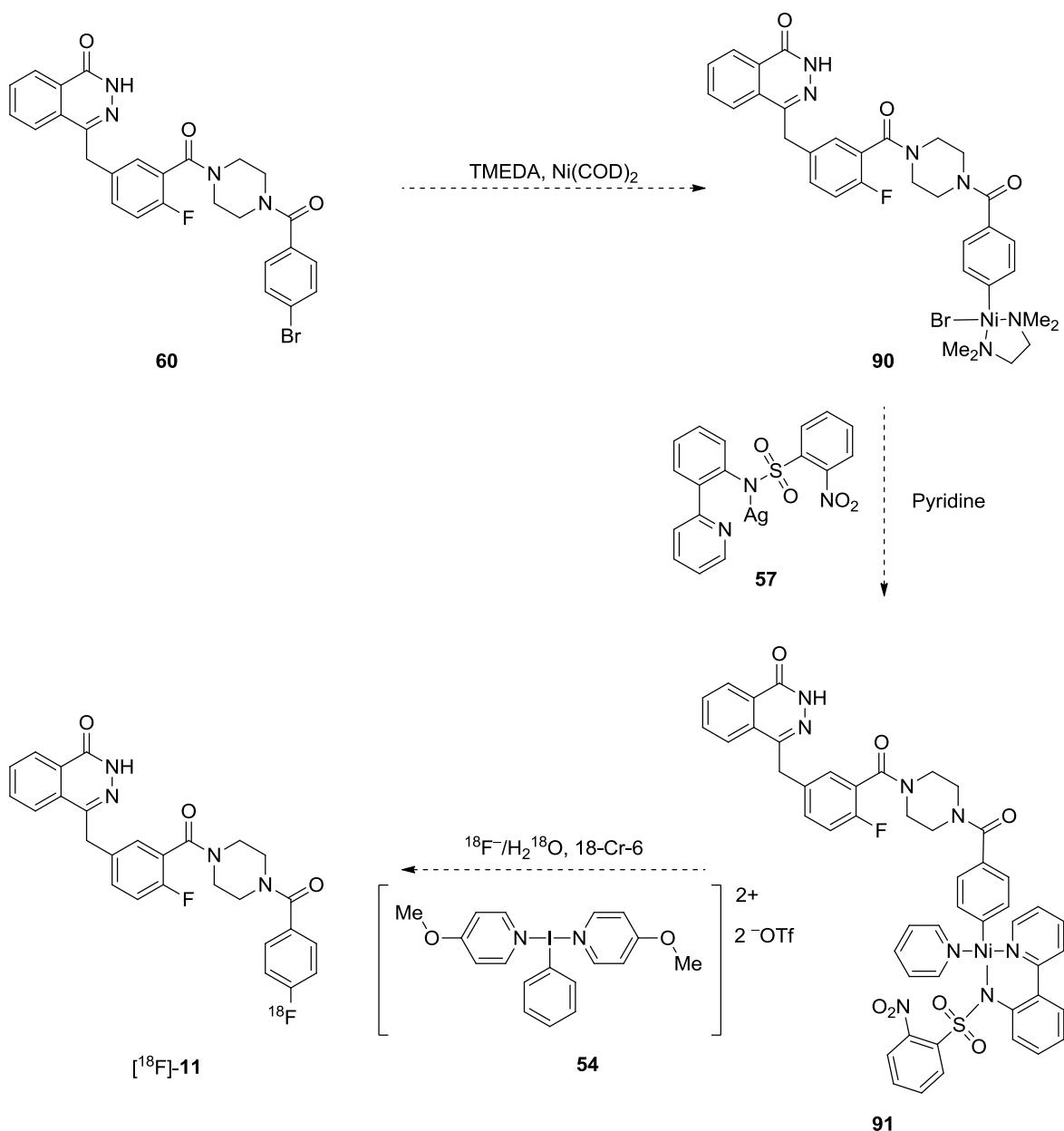
It is envisaged that the use of precursor **78** would allow for improved radiofluoride incorporation yields and better chromatographic separation of the precursor from the radiolabelled product when compared to the chlorinated precursor **72**. The latter could translate into shorter chromatographic runs and the possibility to automate purification using SPE methodology.

The work described in this thesis also identified compound **11** as a potential PARP-1 PET imaging candidate. However, attempts at generating the radiofluorinated version of the compound (i.e. [^{18}F]-**11**) using conventional $\text{S}_{\text{N}}\text{Ar}$ methodologies yielded little success. This was thought to be due to poor activation of the radiolabelling precursors for $\text{S}_{\text{N}}\text{Ar}$ (see section 5.2.2 for details). Since commencing this work, Carney *et al.* (2015) were able to develop radiolabelling methodology for [^{18}F]-**11**, which was reliant on an early stage $\text{S}_{\text{N}}\text{Ar}$ radiofluorination of an ‘activated’ precursor that was then followed by two further reaction steps. The authors also showed that the radiotracer was able to image PARP-1 in mice bearing GBM tumours with good contrast of the tumour lesion to surrounding brain tissue and did not exhibit [^{18}F]-defluorination, unlike [^{18}F]-**17**. However, multi-step radiosynthetic approaches are generally disadvantaged by: i) radiolabelled product losses as a consequence of multiple purification steps; ii) an increase in the overall radiosynthesis time; and iii) possible challenges in automation of the methodology. These shortcomings, coupled with the improved *in vivo* stability of [^{18}F]-**11** over [^{18}F]-**17**, warrant further studies aimed at identifying alternative late stage radiofluorination approaches for accessing [^{18}F]-**11**. It is envisaged that radiofluorination of an unsymmetrical diaryliodonium salt or nickel organometallic precursor could circumvent the issue of a weakly activated system for $\text{S}_{\text{N}}\text{Ar}$ (see section 5.1.2 for details). Scheme 8.2 outlines a proposed route for accessing [^{18}F]-**11** via the unsymmetrical diaryliodonium salts **87–89**, which could be synthesised using methodology developed by Bielawski and Olofsson *et al.* (2007). This method utilises *meta*-chloroperoxybenzoic acid (*m*CPBA) as an oxidant of iodine that is activated by triflic acid (TfOH), which also delivers the triflate anion (^-OTf) to the resulting diaryliodonium salt (Bielawski and Oloffson *et al.*, 2007).



Scheme 8.2. Proposed approach for access to $[^{18}\text{F}]\text{-11}$ using unsymmetrical diaryliodonium salts **87–89**.

Alternatively, a nickel organometallic precursor **91** and the oxidative radiofluorination methodology developed by Lee, Hooker, and Ritter (2012) could be investigated as a means of accessing $[^{18}\text{F}]\text{-11}$ (Scheme 8.3).



Scheme 8.3. Proposed approach for access to $[^{18}\text{F}]\text{-11}$ using the nickel organometallic precursor **91**.

In addition to the discovery of radioligands with potential for PARP-1 SPECT and PET imaging, the work described in this thesis evaluated the utility of $[^{18}\text{F}]\text{-AB5186}$, discovered previously by Dr Adele Blair, as a TSPO PET imaging agent in mice bearing intracranial human GBM (U87MG-Luc2) xenografts. The *in vivo* findings acquired using *ex vivo* autoradiography and PET imaging techniques revealed that the radioligand accumulated in GBM lesions in good contrast to surrounding brain tissue, which was shown to be due to specific binding to TSPO. These observations highlighted the potential of $[^{18}\text{F}]\text{-AB5186}$ to act as a nuclear imaging probe for TSPO in the brain. However, it is important to note that the

PET data consisted of a dynamic scan of a single animal. Therefore, further dynamic imaging studies of animals bearing the same intracranial xenograft tumour model are required in order to obtain a more representative dataset. These studies could be extended to introduce two study arms investigating either [^{18}F]-AB5186 or the existing TSPO radiotracer [^{11}C]-PK11195, each with a cohort of animals pre-treated with either vehicle or an excess of non-radioactive PK11195. Comparison of [^{18}F]-AB5186 and [^{11}C]-PK11195 kinetics in the tumour lesions and the surrounding brain tissue, in the presence or absence of non-radioactive PK11195 blockade, could be used to establish whether [^{18}F]-AB5186 exhibits improved brain uptake and specific binding properties *in vivo* when compared to [^{11}C]-PK11195. It is important to appreciate that implementation of such imaging studies may be challenging due to the complexities associated with ^{11}C production and radiolabelling.

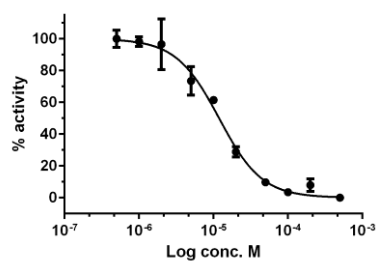
The potential for [^{18}F]-AB5186 to exhibit low sensitivity to human TSPO polymorphism is a key advantage of the radiotracer when compared to existing second and third generation TSPO nuclear imaging agents (see section 7.1.1 for details). As discussed previously (section 7.2.3), studies using genotyped human brain tissue are underway, which were designed to establish whether binding of AB5186 to TSPO will be influenced by polymorphic variability. Preliminary data from these experiments suggested that AB5186 exhibited negligible sensitivity to human TSPO polymorphism, although further replicates are necessary in order to confirm these findings. If conclusive evidence is obtained to support these preliminary observations of low sensitivity to TSPO polymorphism and the above described PET imaging studies yield positive results, then efforts should be focused on acquisition of [^{18}F]-AB5186 organ dosimetry and toxicology data and radiosynthetic automation, as described earlier for [^{123}I]-4 and [^{18}F]-17, with clinical advancement in mind. Human PET imaging studies could then be conducted that are designed to investigate the ability of the radiotracer to: i) delineate invasive glioma tumours when compared to structural imaging or amino acid based radiotracer imaging; ii) detect low grade glioma tumours that are not associated with BBB disruptions; iii) predict GBM tumour progression; and iv) monitor GBM treatment response. In addition to TSPO imaging in brains bearing glioma lesions, [^{18}F]-AB5186 could also be investigated as a tracer for imaging neuroinflammatory pathology.

In summary, this research project was successful in meeting all of the aims and objectives outlined at the start of this thesis (see section 1.6 for details) and the two PARP-1 radiotracer compounds discovered in the course of this work, as well as TSP0 radiotracer [^{18}F]-AB5186, warrant further pre-clinical *in vivo* investigations. The recent acquisition of a nanoScan PET/MRI system (Mediso Medical Imaging Systems; Hungary) at the Cancer Research UK Beatson Institute opens up the possibility of pursuing the earlier proposed PET imaging studies locally. However, the proposed SPECT and [^{11}C]-PK11195 PET imaging studies would require collaboration with other institutes that have access to pre-clinical SPECT scanning equipment and ^{11}C production and radiolabelling facilities.

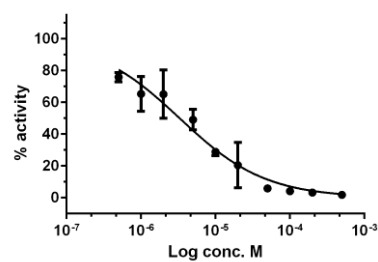
9 APPENDICES

9.1 Cell-free IC₅₀ curves for olaparib and compounds 4-21.

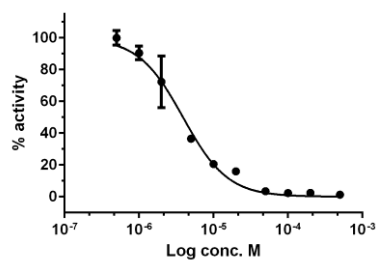
Olaparib



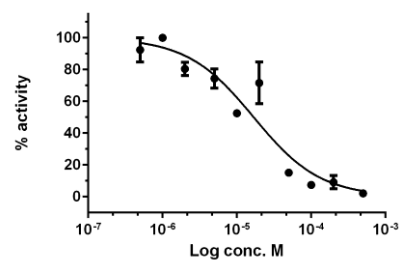
Compound 4



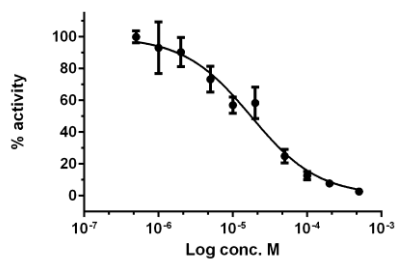
Compound 5



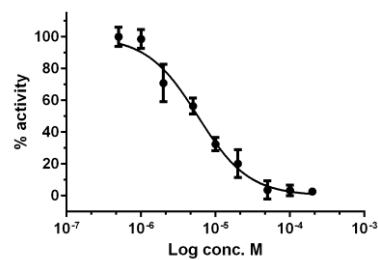
Compound 6



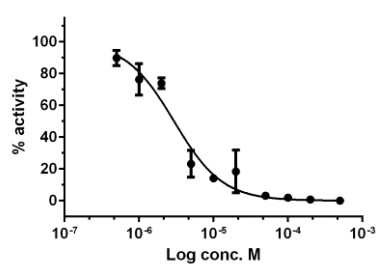
Compound 7



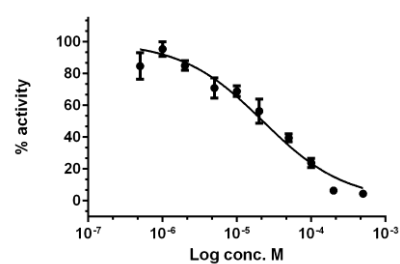
Compound 8

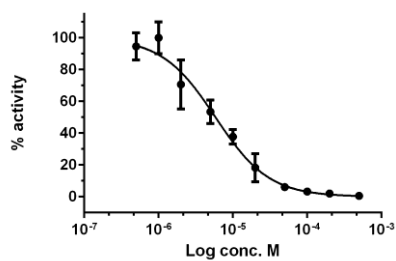
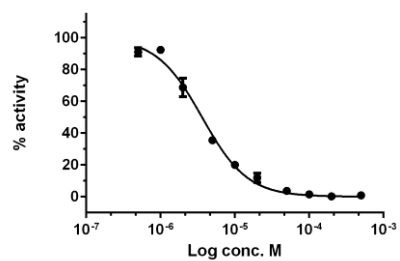
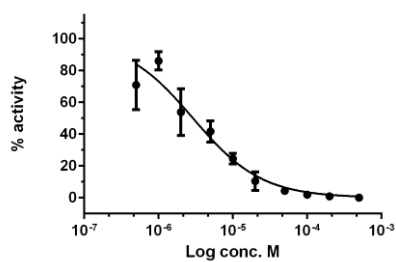
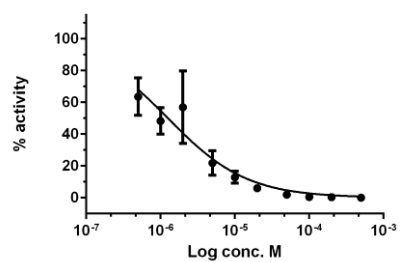
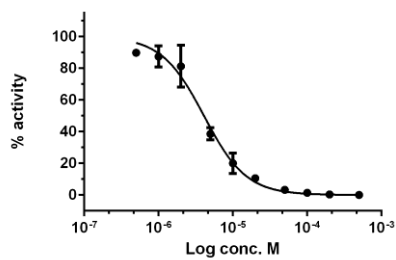
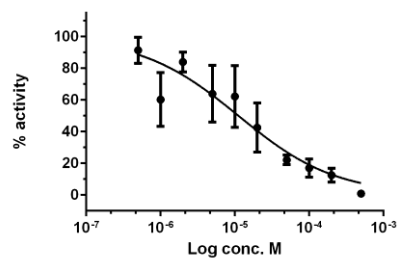
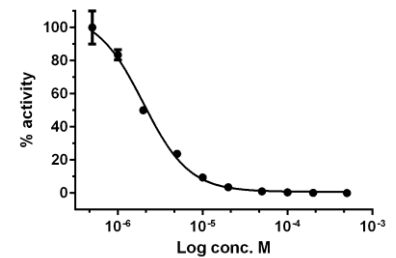
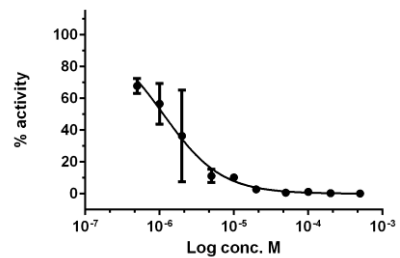


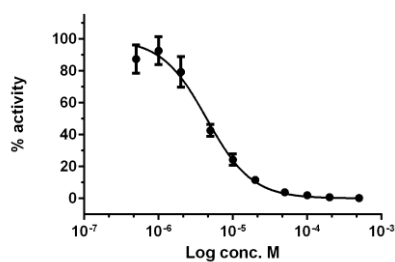
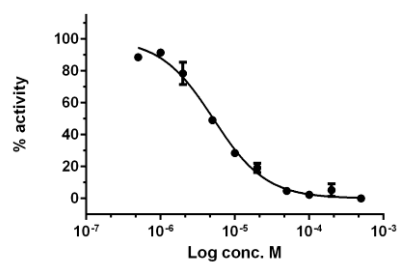
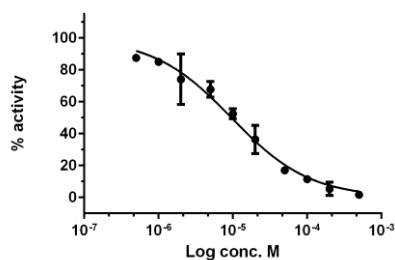
Compound 9



Compound 10

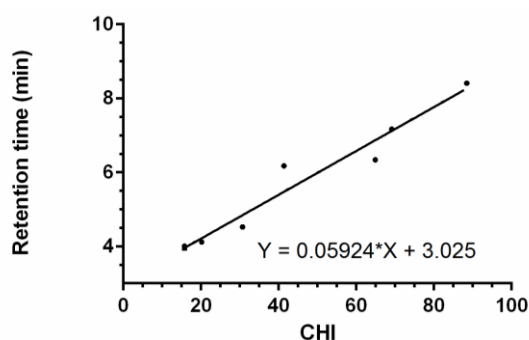


Compound 11**Compound 12****Compound 13****Compound 14****Compound 15****Compound 16****Compound 17****Compound 18**

Compound 19**Compound 20****Compound 21**

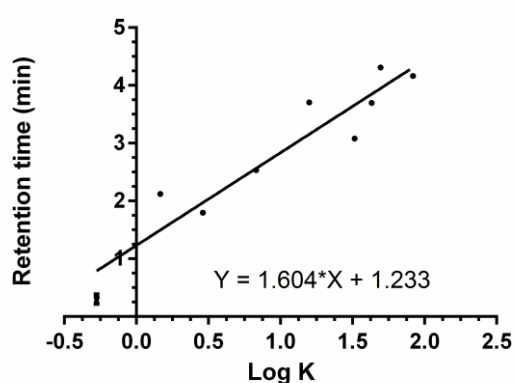
Dose response curves showing the percentage activity of PARP-1 versus the concentration of olaparib and compounds 4–21. Error bars show the mean \pm standard deviation of three experiments. Data were acquired using the TrevigenTM colorimetric assay and curves were fitted as described in section 4.4.2. The plots were generated using the GraphPad Prism 6.0 software.

9.2 Log P_{oct} HPLC calibration curve acquired on C₁₈ column.



A graph of the literature chromatographic hydrophobicity index (CHI) values of theophylline, phenyltetrazole, benzimidazole, colchicine, acetophenone, indole, and butyrophenone versus their HPLC retention times acquired on a C₁₈ column as described in section 4.4.3. Error bars show the mean \pm standard deviation of three measurements. The graph was generated using the GraphPad Prism 6.0 software.

9.3 %PPB HPLC calibration curve acquired using human serum albumin column.

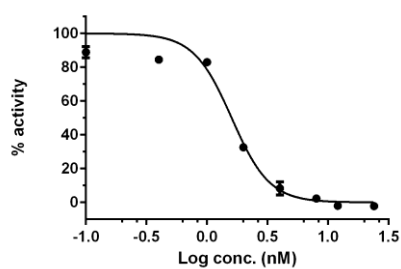


A graph of the literature log apparent affinity constant (log *K*) values of nizatidine, bromazepam, carbamazepine, budesonide, nicardipine, warfarin, ketoprofen, indomethacin, and diclofenac versus their HPLC retention times acquired on a human serum albumin column as described in section 4.4.4. Error bars show the mean \pm standard deviation of three measurements. The graph was generated using the GraphPad Prism 6.0 software.

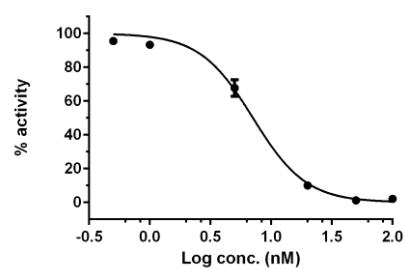
9.4 G7 and T98G cellular IC₅₀ curves for olaparib and compounds 4, 11, 13, 17, and 18.

G7 cell-line

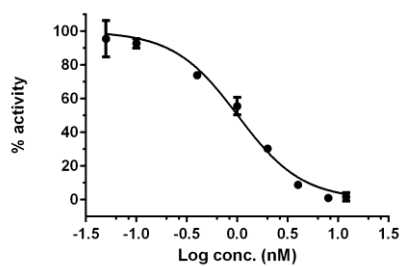
Olaparib



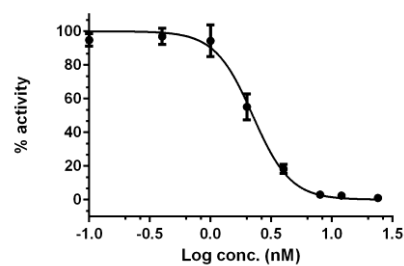
Compound 4



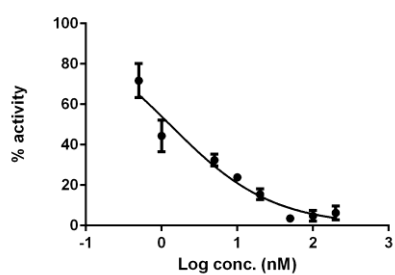
Compound 11



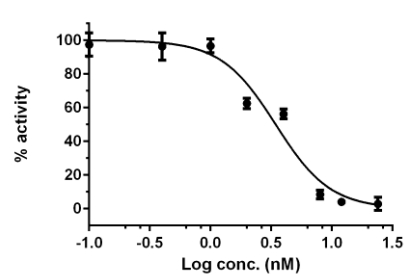
Compound 13

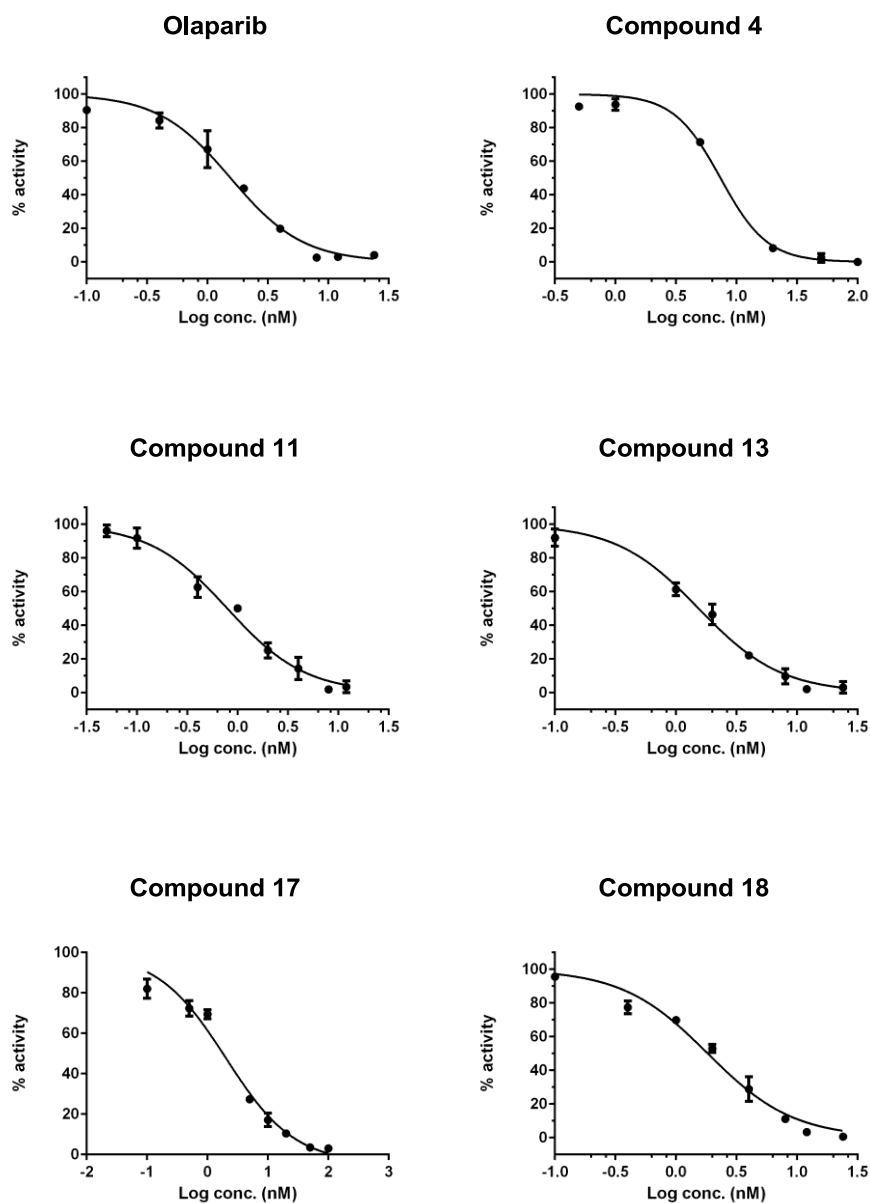


Compound 17



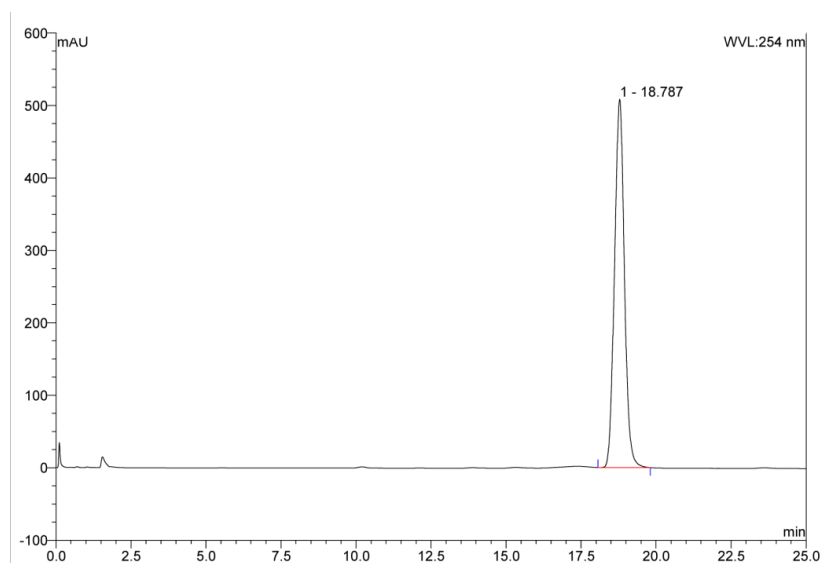
Compound 18



T98G cell-line

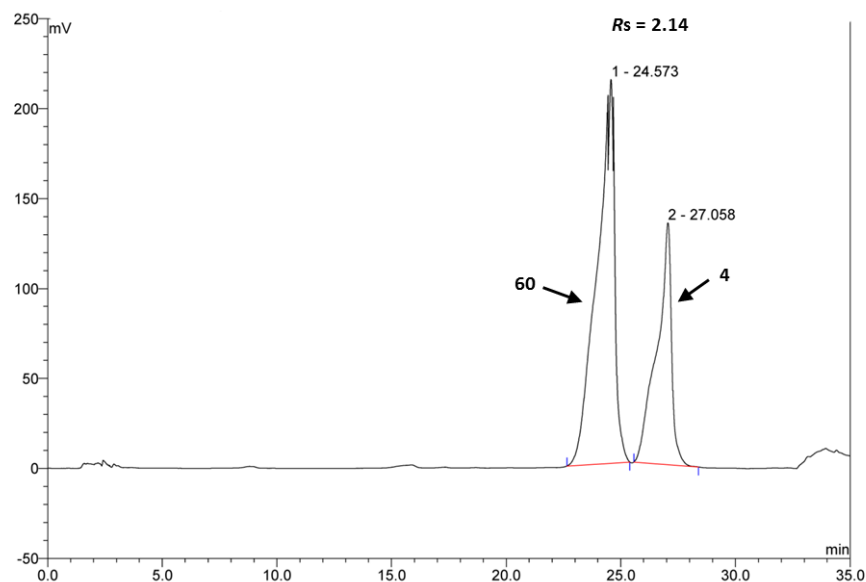
Dose response curves showing the percentage activity of PARP-1 in G7 and T98G cell-lines versus the concentration of olaparib and compounds 4, 11, 13, 17, and 18. Error bars show the mean \pm standard deviation of three experiments. Data were acquired as described in section 4.4.5. The plots were generated using the GraphPad Prism 6.0 software.

9.5 UV-HPLC chromatogram of compound 4.



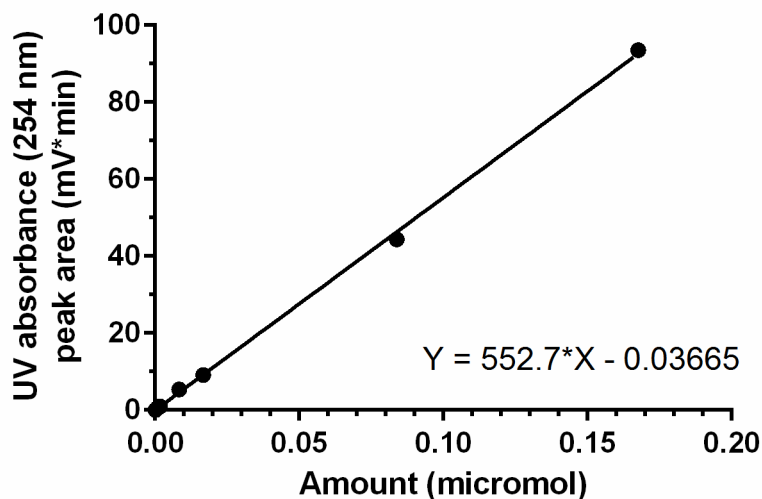
A UV-HPLC chromatogram (254 nm) of compound **4** acquired using an analytical Dionex Ultimate 3000 series HPLC system and a diode array detector (190-800 nm). A Phenomenex Synergi 4 μm Hydro-RP 80 \AA (150 \times 4.60 mm) column was used with the following mobile phase conditions: 0.0–20.0 minutes = 30:70 A:B to 55:45 A:B, 20.0–20.5 minutes = 55:45 A:B to 5:95 A:B, 20.5–25.0 minutes = 5:95 A:B where A = acetonitrile and B = distilled water; flow rate 1.0 mL/min; column temperature = 25 $^{\circ}\text{C}$. The UV chromatogram was recorded and the retention time of **4** was calculated using the Chromoleon 6.8 Chromatography software.

9.6 UV-HPLC chromatogram of a mixture of compounds 4 and 60.



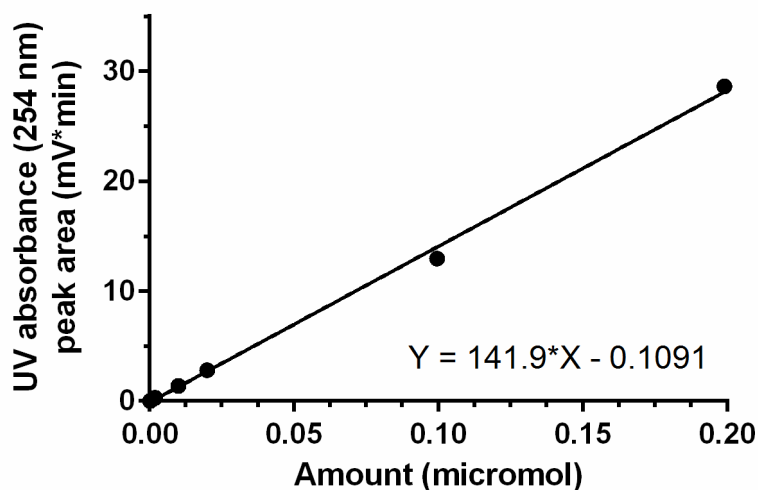
A UV-HPLC chromatogram (254 nm) of a mixture of compounds 4 and 60 acquired using a preparatory Dionex Ultimate 3000 series HPLC system and a Knauer Advanced Scientific Instruments Smartline UV Detector 2500. A Phenomenex Synergi 4 μm Hydro-RP 80Å (150 \times 10.00 mm) column was used with the following mobile phase conditions: 0.0–30.0 minutes = 30:70 A:B to 55:45 A:B where A = acetonitrile and B = distilled water; flow rate 3.0 mL/min; column temperature = 25 °C. The UV chromatogram was recorded, and retention times and resolution were calculated using the Chromleon 6.8 Chromatography software.

9.7 Specific activity UV-HPLC calibration curve for compound 4.



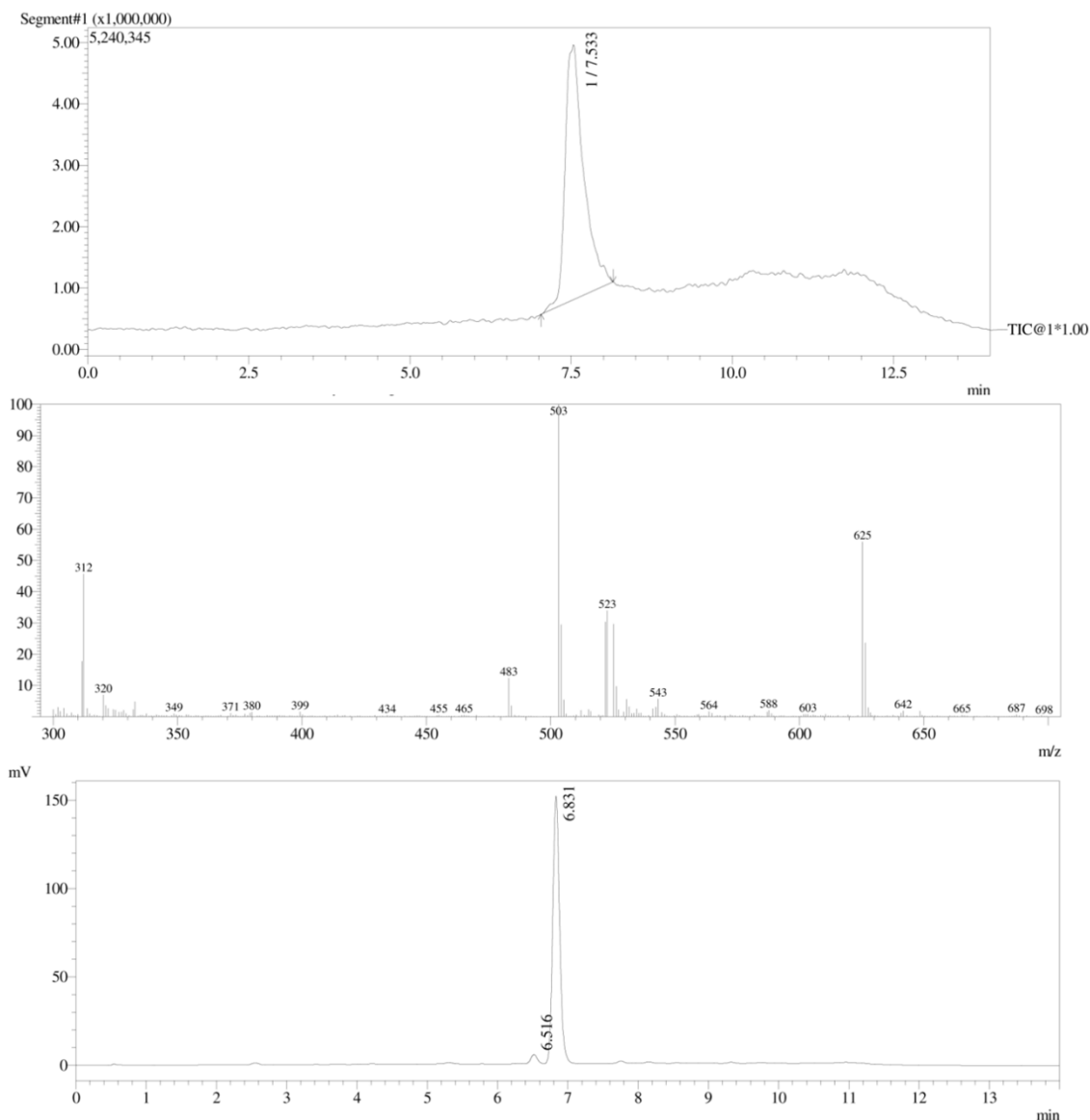
Seven different concentrations of 4 (ranging from 0.001–1.000 mg/mL) were injected onto a Phenomenex Synergi 4 μm Hydro-RP 80Å (150 \times 10.00 mm) column and were exposed to the following mobile phase conditions: 0.0–30.0 minutes = 30:70 A:B to 55:45 A:B where A = acetonitrile and B = distilled water; flow rate 3.0 mL/min; column temperature = 25 °C. UV detection was achieved using a Knauer Advanced Scientific Instruments Smartline UV Detector 2500 (254 nm). The UV chromatograms were recorded and peak area (mV*min) were obtained using the Chromoleon 6.8 Chromatography software. The micromol amounts of compound 4 were plotted against the corresponding UV peak areas and a linear regression model was applied using the GraphPad Prism 6.0 software. $R^2 = 0.993$.

9.8 Specific activity UV-HPLC calibration curve for compound 17.



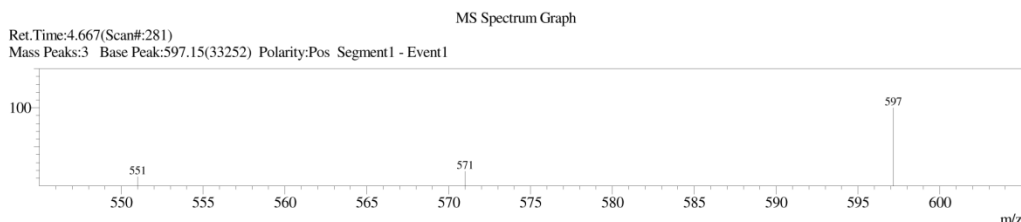
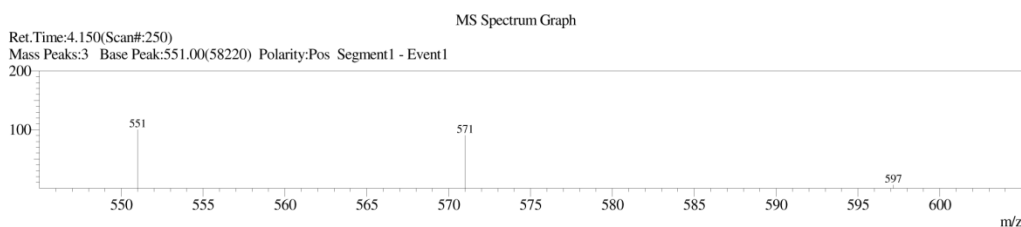
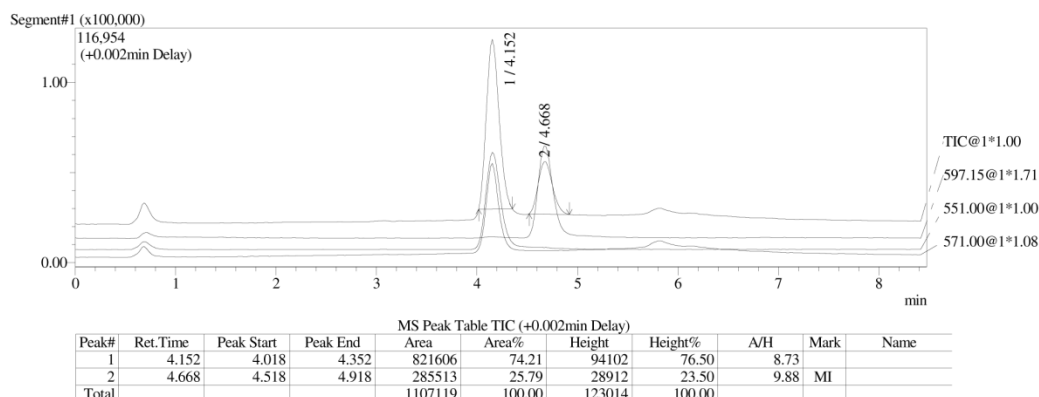
Seven different concentrations of 17 (ranging from 0.001-1.000 mg/mL) were injected onto a Phenomenex Synergi 4 μm Hydro-RP 80 \AA (150 \times 10.00 mm) column and were exposed to the following mobile phase conditions: 0.0–3.0 minutes = 30:70 A:B; 3.0–30.0 minutes 30:70 to 75:25 A:B; 30.0-30.1 minutes = 75:25 to 95:5 A:B; 30.1–35.0 minutes = 95:5 A:B where A = acetonitrile and B = distilled water; flow rate 3.0 mL/min; column temperature = 25 $^{\circ}\text{C}$. UV detection was achieved using a Knauer Advanced Scientific Instruments Smartline UV Detector 2500 (254 nm). The UV chromatograms were recorded and peak area (mV*min) were obtained using the Chromoleon 6.8 Chromatography software. The micromol amounts of compound 17 were plotted against the corresponding UV peak areas and a linear regression model was applied using the GraphPad Prism 6.0 software. $R^2 = 0.998$.

9.9 TIC, MS, and LC-UV (254 nm) chromatograms of compound **73**.



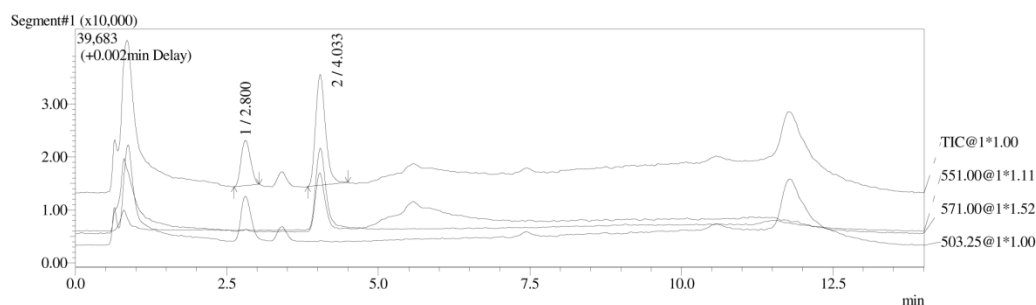
A TIC, MS, and LC-UV (254 nm) chromatograms of compound **73** acquired using a Shimadzu LC-2010AHT and LCMS-2010EV system and a Kinetex 5 μm XB-C18 100 \AA (50 \times 4.60 mm) column. The following mobile phase conditions were used: 0.0–10.0 minutes = 30:70 to 60:40 A:B; 10.0–12.0 minutes = 60:40 to 30:70 A:B; 12.0–14.0 minutes = 30:70 A:B where A = acetonitrile and B = 0.1% v/v formic acid in distilled water; flow rate 1.2 mL/min. MS detection was performed under the following conditions: positive ionisation; detector 1.50 kV; full-scan mode. The chromatograms were recorded and the retention times were measured using the LabSolutions LCMS software.

9.10 MS chromatogram and graphs of compound 4 and internal standard 60.

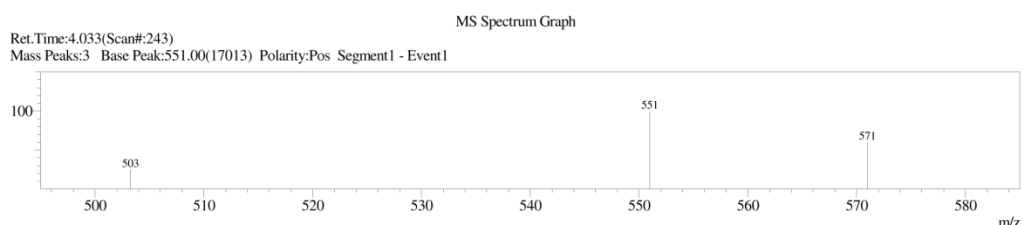
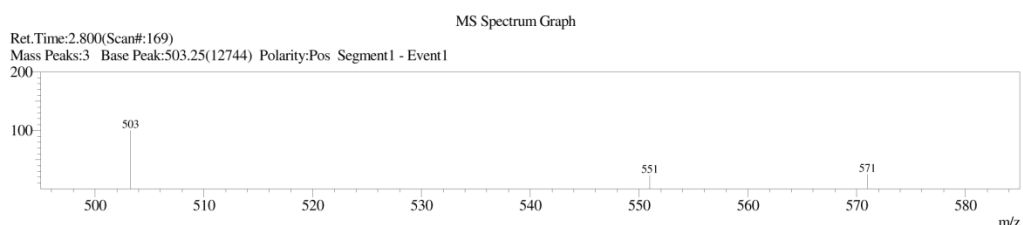


TIC and SIM MS of compound 4 (MH^+ SIM $m/z = 597$) and internal standard 60 (MH^+ SIM $m/z = 551$; MNa^+ SIM $m/z = 571$) following 0 hours incubation in mouse plasma acquired using a Shimadzu LC-2010AHT and LCMS-2010EV system and a Kinetex 5 μm XB-C18 100 \AA (50 \times 4.60 mm) column. The following mobile phase conditions were used: 0.0–10.0 minutes = 30:70 to 60:40 A:B; 10.0–10.5 minutes = 60:40 to 90:10 A:B; 10.5–12.0 minutes 90:10 A:B; 12.0–12.5 minutes 90:10 to 30:70 A:B; 12.5–15.0 minutes 30:70 A:B where A = acetonitrile and B = 0.1% v/v formic acid in distilled water; flow rate 1.2 mL/min. MS detection was performed under the following conditions: positive ionisation; detector 1.50 kV; SIM m/z 551, 571 and 597. The chromatograms were recorded using the LabSolutions LCMS software.

9.11 MS chromatogram and graphs of compound 17 and internal standard 60.

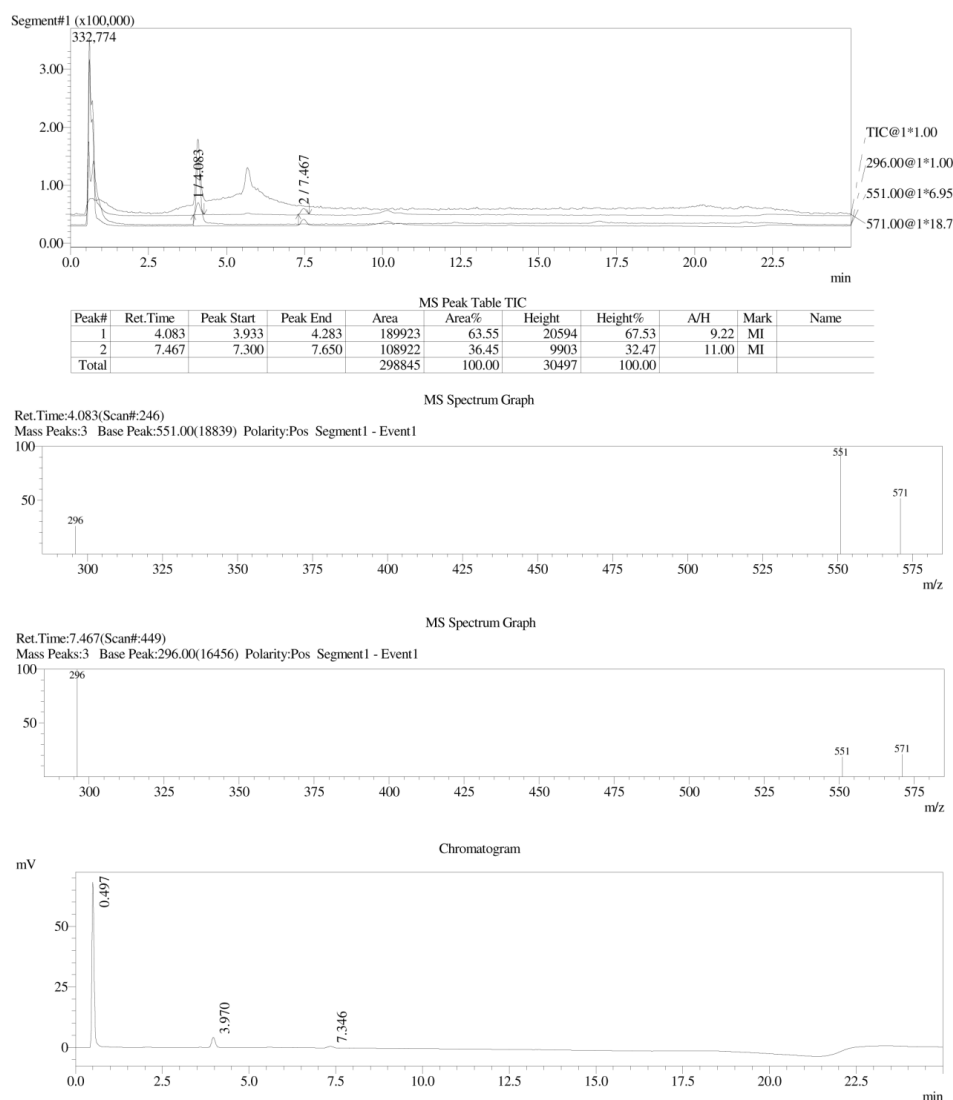


MS Peak Table TIC (+0.002min Delay)										
Peak#	Ret.Time	Peak Start	Peak End	Area	Area%	Height	Height%	A/H	Mark	Name
1	2.800	2.617	3.033	92424	27.87	8567	29.06	10.79	MI	
2	4.033	3.833	4.500	239169	72.13	20911	70.94	11.44	MI	
Total				331593	100.00	29478	100.00			



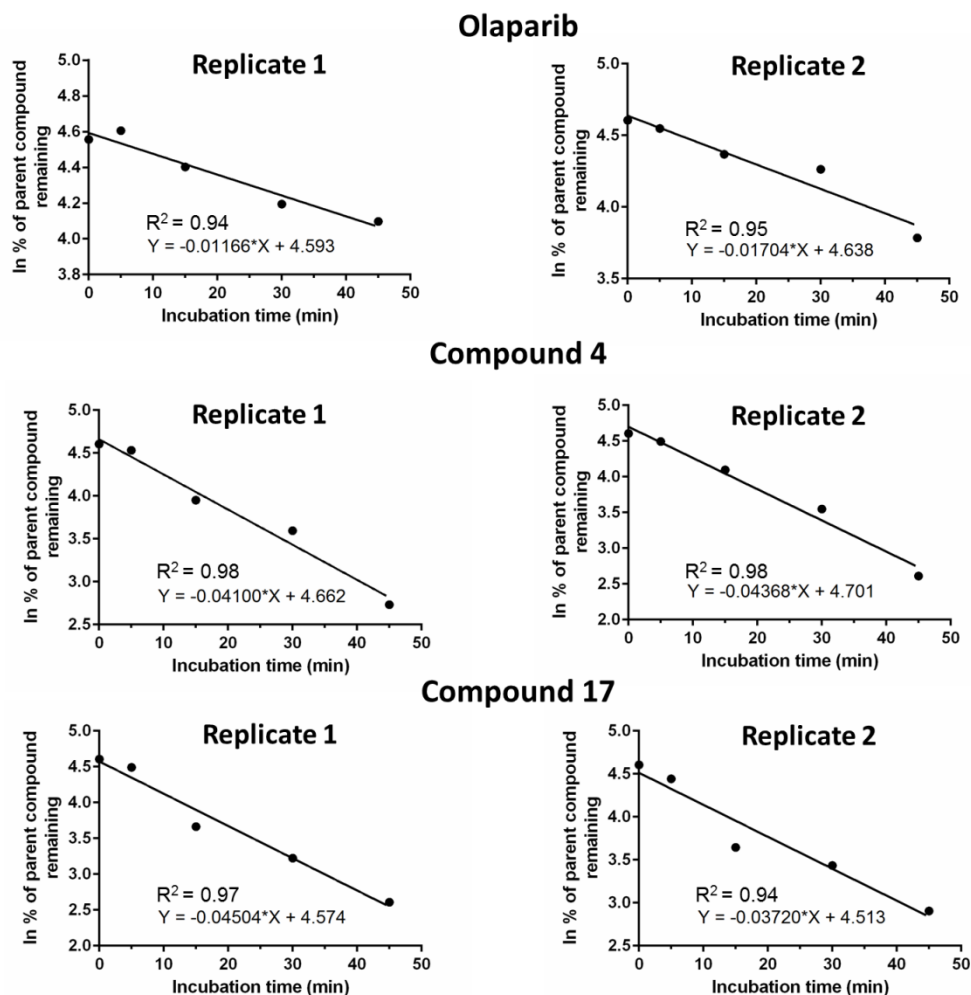
TIC and SIM MS of compound **17** (MH^+ SIM $m/z = 503$) and internal standard **60** (MH^+ SIM $m/z = 551$; MNa^+ SIM $m/z = 571$) following 0 hours incubation in mouse plasma acquired using a Shimadzu LC-2010AHT and LCMS-2010EV system and a Kinetex 5 μm XB-C18 100 \AA (50 \times 4.60 mm) column. The following mobile phase conditions were used: 0.0–10.0 minutes = 30:70 to 60:40 A:B; 10.0–10.5 minutes = 60:40 to 90:10 A:B; 10.5–12.0 minutes 90:10 A:B; 12.0–12.5 minutes 90:10 to 30:70 A:B; 12.5–15.0 minutes 30:70 A:B where A = acetonitrile and B = 0.1% v/v formic acid in distilled water; flow rate 1.2 mL/min. MS detection was performed under the following conditions: positive ionisation; detector 1.50 kV; SIM m/z 503, 571 and 597. The chromatograms were recorded using the LabSolutions LCMS software.

9.12 MS and LC-UV (254 nm) chromatograms of diclofenac and internal standard 60.



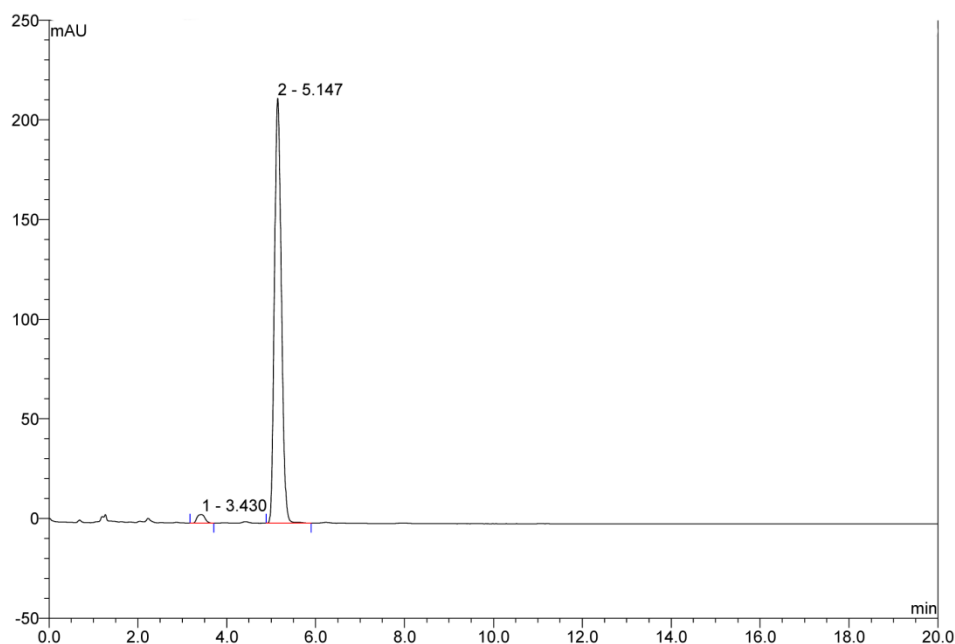
TIC and SIM MS and LC-UV (254 nm) chromatograms of diclofenac (M^+ SIM m/z = 296) and internal standard 60 (MH^+ SIM m/z = 551; MNa^+ SIM m/z = 571) following 0 minutes incubation in human liver microsomes acquired using a Shimadzu LC-2010AHT and LCMS-2010EV system and a Kinetex 5 μ m XB-C18 100 \AA (50 \times 4.60 mm) column. The following mobile phase conditions were used: 0.0–15.0 minutes = 30:70 to 70:30 A:B; 15.1–17.0 minutes = 70:30 A:B; 17.1–20.0 minutes = 70:30 to 90:10 A:B; 20.1–22.0 minutes = 90:10 to 30:70 A:B; 22.1–25.0 minutes = 30:70 A:B where A = acetonitrile and B = 0.1% v/v formic acid in distilled water; flow rate 1.2 mL/min. MS detection was performed under the following conditions: positive ionisation; detector 1.50 kV; SIM m/z 296, 551 and 571. The chromatograms were recorded using the LabSolutions LCMS software.

9.13 *In vitro* human liver microsome metabolism of olaparib, 4 and 17.



Graphs showing the natural logarithm (ln) of the percentage amount of unchanged olaparib, and compounds 4 and 17 remaining after 0, 5, 15, 30 and 45 minute incubations in human liver microsomes. The plots were generated using the GraphPad Prism 6.0 software.

9.14 UV-HPLC chromatogram of AB5186.



A UV-HPLC chromatogram (267 nm) of AB5186 acquired by Dr Adele Blair using an analytical Dionex Ultimate 3000 series HPLC system and a diode array detector (190-800 nm). A Phenomenex Synergi 4 μm Hydro-RP 80 \AA (150 \times 4.60 mm) column was used with the following mobile phase conditions: 0.0–20.0 minutes = 70:30 A:B where A = acetonitrile and B = distilled water; flow rate 1.0 mL/min; column temperature = 25 $^{\circ}\text{C}$. The UV chromatogram was recorded and the retention time of AB5186 was calculated using the Chromoleon 6.8 Chromatography software.

10 BIBLIOGRAPHY

Abbott, N.J., Rönnbäck, L., Hansson, E., 2006. Astrocyte-endothelial interactions at the blood-brain barrier. *Journal of Anatomy*, 200(6), pp.629–638.

Agdeppa, E.D., Spilker, M.E., 2009. A review of imaging agent development. *The AAPS Journal*, 11(2), pp.286–299.

Airas, L., Rissanen, E., Rinne, J.O., 2015. Imaging neuroinflammation in multiple sclerosis using TSPO-PET. *Clinical and Translational Imaging*, 3(6), pp.461–473.

Amé, J., Rolli, V., Schreiber, V., Niedergang, C., Apiou, F., Decker, P., *et al.*, 1999. PARP-2, a novel mammalian DNA damage-dependant poly(ADP-ribose) polymerase. *The Journal of Biological Chemistry*, 274(25), pp.17860–17868.

Amé, J., Spenlenhauer, C., de Murcia, G., 2004. The PARP superfamily. *Bioessays*, 26(8), pp.882–893.

An, H., Wang, T., Mohan, V., Griffery, R.H., Cook, P.D., 1998. Solution phase combinatorial chemistry. Discovery of 13- and 15-membered polyazapyridinocyclophane libraries with antibacterial activity. *Tetrahedron*, 54(16), pp.3999–4012.

Animals (Scientific Procedures) Act 1986. (c.14). London: HMSO.

Antoni, G., 2015. Development of carbon-11 labelled PET tracers - radiochemical and technological challenges in a historic perspective. *Journal of Labelled Compounds and Radiopharmaceuticals*, 58(3), pp.65–72.

Anwar, M., Aslam, H.M., Anwar, S., 2015. PARP inhibitors. *Hereditary Cancer in Clinical Practice*, 13(4), pp.1–4.

Arnott, J.A., Planey, S.L., 2012. The influence of lipophilicity in drug discovery and design. *Expert Opinion on Drug Discovery*, 7(10), pp.863–875.

AstraZeneca, 2014. LynparzaTM approved in the European Union as first-in-class treatment for advanced BRCA-mutated ovarian cancer [online]. Available at: <https://www.astrazeneca.com/media-centre/press-releases/2014/lynparza->

[approved-european-union-brca-mutated-ovarian-cancer-treatment-18122014.html](http://www.nature.com/news/2014/0312/14122014.html) [Accessed 20 March 2016].

Avwioro, G., 2011. Histochemical uses of haematoxylin - a review. *Journal of Pharmacy and Clinical Sciences*, 1, pp.24–34.

Azarashvili, T., Baburina, Y., Grachev, D., Krestinina, O., Papadopoulos, V., Lemasters, J.J., *et al.*, 2014. Carbenoxolone induces permeability transition pore opening in rat mitochondria via the translocator protein TSPO and connexin43. *Archives of Biochemistry and Biophysics*, 558, pp.87–94.

Bahar, F.G., Ohura, K., Ogihara, T., Imai, T., 2012. Species difference of esterase expression and hydrolase activity in plasma. *Journal of Pharmaceutical Sciences*, 101(10), pp.3979–3988.

Bailey, D.L., 2004. Data acquisition and performance characterization in PET. In: D.L. Bailey, D.W. Townsend, P.E. Valk, M.N. Maisey, eds. 2004. *Positron Emission Tomography*. London: Springer-Verlag London Limited. pp.41–63.

Bailey, D.L., Karp, J.S., Surti, S., 2004. Physics and instrumentation in PET. In: D.L. Bailey, D.W. Townsend, P.E. Valk, M.N. Maisey, eds. 2004. *Positron Emission Tomography*. London: Springer-Verlag London Limited. pp.13–40.

Banati, R.B., Middleton, R.J., Chan, R., Hatty, C.R., Kam, W.W., Quin, C., *et al.*, 2014. Positron emission tomography and functional characterization of a complete PBR/TSPO knockout. *Nature Communications*, 5, doi:10.1038/ncomms6452.

Banati, R.B., Newcombe, J., Gunn, R.N., Cagin, A., Turkheimer, F., Heppner, F., *et al.*, 2000. The peripheral benzodiazepine binding site in the brain in multiple sclerosis: Quantitative *in vivo* imaging of microglia as a measure of disease activity. *Brain a Journal of Neurology*, 123(Pt 11), pp.2321–2337.

Banker, M.J., Clark, T.H., 2008. Plasma/serum protein binding determinations. *Current Drug Metabolism*, 9(9), pp.854–859.

Bao, S., Wu, Q., McLendon, R.E., Hao, Y., Shi, Q., Hjelmeland, A.B., *et al.*, 2006. Glioma stem cells promote radioresistance by preferential activation of the DNA damage response. *Nature*, 444(7120), pp.756–760.

Barazzuol, L., Jena, R., Burnett, N.G., Meira, L.B., Jeynes, J.C., Kirkby, K.J., *et al.*, 2013. Evaluation of poly (ADP-ribose) polymerase inhibitor ABT-888 combined with radiotherapy and temozolomide in glioblastoma. *Radiation Oncology*, 8, p.65.

Barbarin, N., Henion, J.D., Wu, Y., 2002. Comparison between liquid chromatography-UV detection and liquid chromatography-mass spectrometry for the characterization of impurities and/or degradants present in trimethoprim tablets. *Journal of Chromatography A*, 970(1-2), pp.141-154.

Baumann, P., Benson, F.E., West, S.C., 1996. Human Rad51 protein promotes ATP-dependant homologous pairing and strand transfer reactions in vitro. *Cell*, 87(4), pp.757-766.

Benavides, J., Fage, D., Carter, C., Scatton, B., 1987. Peripheral type benzodiazepine binding sites are a sensitive indirect index of neuronal damage. *Brain Research*, 421(1-2), pp.167-172.

Beringer, F.M., Brierley, A., Drexler, M., Gindler, M., Lumpkin, C.C., 1952. Diaryliodonium salts. II. The phenylation of organic and inorganic bases. *Journal of the American Chemical Society*, 71(11), pp.2708-2712.

Blair, A., 2014. *The synthesis of biologically active heterocycles: development of novel imaging agents for the translocator protein (18 kDa) and poly(ADP-ribose) polymerase 1*. Ph. D. The University of Glasgow.

Blair, A., Zmuda, F., Malviya, G., Tavares, A.S., Tamagan, G.D., Chalmers, A.J., *et al.*, 2015. A novel ¹⁸F-labelled high affinity agent for PET imaging of the translocator protein. *Chemical Science*, 6(8), pp.4772-4777.

Boulton, S., Pemberton, L.C., Porteous, J.K., Curtin, N.J., Griffin, R.J., Golding, B.T., *et al.*, 1995. Potentiation of temozolomide-induced cytotoxicity: a comparative study of the biological effects of poly(ADP-ribose) polymerase inhibitors. *British Journal of Cancer*, 72(4), pp.849-856.

Braestrup, C., Squires, R.S., 1977. Specific benzodiazepine receptors in rat brain characterized by high-affinity [³H]diazepam binding. *Proceedings of the National Academy of Sciences of the United States of America*, 74(9), pp.3805-3809.

Brat, D.J., Castellano-Sanchez, A.A., Hunter, S.B., Pecot, M., Cohen, C., Hammond, E.H., *et al.*, 2004. Pseudopalisades in glioblastoma are hypoxic, express extracellular matrix proteases, and are formed by an actively migrating cell population. *Cancer Research*, 64(3), pp.920–927.

Brooks, D.J., 2004. Neuroimaging in Parkinson's disease. *NeuroRx*, 1(2), pp.243–254.

Brown, R.C., Degenhardt, B., Kotoula, M., Papadopoulous, V., 2000. Location-dependant role of the human glioma cell peripheral-type benzodiazepine receptor in proliferation and steroid biosynthesis. *Cancer Letters*, 156(2), pp.125–132.

Bryant, H.E., Schultz, N., Thomas, H.D., Parker, K.M., Flower, D., Lopez, E., *et al.*, 2005. Specific killing of BRCA2-deficient tumours with inhibitors of poly(ADP-ribose) polymerase. *Nature*, 434(7035), pp.913–917.

Buck, J.R., McKinley, E.T., Fu, A., Abel, T.W., Thompson, R.C., Chambless, L., *et al.*, 2015. Preclinical TSPO ligand PET to visualize human glioma xenotransplants: a preliminary study. *PLoS One*, 10(10), e0141659.

Buck, J.R., McKinley, E.T., Hight, M.R., Fu, A., Tang, D., Smith, R.A., *et al.*, 2011. Quantitative, preclinical PET imaging of TSPO expression in glioma using [¹⁸F]PBR06. *Journal of Nuclear Medicine*, 52(1), pp.107–114.

Buege, M., Mahajan, P.B., 2015. Clinical trials of poly(ADP-ribose) polymerase inhibitors for cancer therapy: a review. *Reviews on Recent Clinical Trials*, 10(4), pp.326–339.

Buggins, T.R., Dickinson, P.A., Taylor, G., 2007. The effect of pharmaceutical excipients on drug disposition. *Advanced Drug Delivery Reviews*, 59(15), pp.1482–1503.

Bundred, N., Gardovskis, J., Jaskiewicz, J., Eglitis, J., Paramonov, V., McCormack, P., *et al.*, 2013. Evaluation of the pharmacodynamics and pharmacokinetics of the PARP inhibitor olaparib: a phase I multicentre trial in patients schedules for elective breast cancer surgery. *Investigational New Drugs*, 31(4), pp.949–958.

Bürke, A., 2005. Poly(ADP-ribose) the most elaborate metabolite of NAD⁺. *The FEBS Journal*, 272(18), pp.4576–4589.

Cai, L., Lu, S., Pike., V.W., 2008. Chemistry with [¹⁸F]-fluoride ion. *European Journal of Organic Chemistry*, 2008(17), pp.2853–2873.

Calabrese, C.R., Almassy, R., Barton, S., Batey, M.A., Calvert, A.H., Canon-Koch, S., *et al.*, 2004. Anticancer chemosensitisation and radiosensitisation by the novel poly(ADP-ribose) polymerase-1 inhibitor AG14361. *Journal of the National Cancer Insititute*, 96(1), pp.56–67.

Caldecott, K., 2001. Mammalian DNA single-strand break repair: an X-ra(y)ted affair. *Bioessays*, 23(5), pp.447–455.

Caldecott, K.W., 2008. Single-strand break repair and genetic disease. *Nature Reviews Genetics*, 9(8), pp.619–631.

Camsonne, R., Crouzel, C., Comar, D., Mazière, M., Prenant, C., Sastre, J., *et al.*, 1984. Synthesis of N-(¹¹C) methyl, N-(methyl-1 propyl), (chloro-2 phenyl)-1 isoquinoline carboxamide-3 (PK 11195): a new ligand for peripheral benzodiazepine receptors. *Journal of Labelled Compounds and Radiopharmaceuticals*, 21(10), pp.985–991.

Carlucci, G., Carney, B., Brand, C., Kossatz, S., Irwin, C.P., Carlin, S.D., *et al.*, 2015. Dual-modality optical/PET imaging of PARP1 in glioblastoma. *Molecular Imaging and Biology*, 17(6), pp.848–855.

Carney, B., Carlucci, G., Salinas, B., Gialleonardo, V.D., Kossatz, S., Vansteene, A., *et al.*, 2015. Non-invasive PET imaging of PARP1 expression in glioblastoma models. *Molecular Imaging and Biology*, ahead of print, doi:10.1007/s11307-015-0904-y.

Chalmers, A.J., Jackson, A., Swaisland, H., Stewart, W., Halford, S.E., Molife, L.R., *et al.*, 2014. Results of stage 1 of the operatic trial: a phase I study of olaparib in combination with temozolomide in patients with relapsed glioblastoma [abstract]. *Journal of Clinical Oncology*, 32(5s), abstr.2025.

Chalmers, A.J., Johnston, P., Woodcock, M., Joiner, M., Marples, B., 2004. PARP-1, PARP-2, and the cellular response to low doses of ionizing radiation. *International Journal of Radiation Oncology Biology Physics*, 58(2), pp.410–419.

Chalmers, A.J., Lakshman, M., Chan, N., Bristow, R.G., 2010. Poly(ADP-ribose) polymerase inhibition as a model for synthetic lethality in developing radiation oncology targets. *Seminars in Radiation Oncology*, 20(4), pp.274–281.

Chambon, P., Weill, J.D., Mandel, P., 1963. Nicotinamide mononucleotide activation of a new DNA-dependant polyadenylic acid synthesizing nuclear enzyme. *Biochemical and Biophysical Research Communications*, 11(1), pp.39–43.

Chang, L.W., 1990. The neurotoxicity and pathology of organomercury, organolead, and organotin. *The Journal of Toxicological Sciences*, 15(suppl 4), pp.125–151.

Chelli, B., Falleni, A., Salvetti, F., Gremigni, V., Lucacchini, A., Martini, C., 2001. Peripheral-type benzodiazepine receptor ligands: mitochondrial permeability transition induction in rat cardiac tissue. *Biochemical Pharmacology*, 61(6), pp.695–705.

Chen, M., Guilarte, T., 2006. Imaging the peripheral benzodiazepine receptor response in central nervous system demyelination and remyelination. *Toxicological Sciences*, 91(2), pp.532–539.

Chen, M., Guilarte, T., 2008. Translocator protein 18kDa (TSPO): molecular sensor of brain injury & repair. *Pharmacology and Therapeutics*, 118(1), pp.1–17.

Cherry, S.R., 2009. Multimodality imaging: beyond PET/CT and SPECT/CT. *Seminars in Nuclear Medicine*, 39(5), pp.348–353.

Cheung, A., Zhang, J., 2000. A scintillation proximity assay for poly(ADP-ribose) polymerase. *Analytical Biochemistry*, 282(1), pp.24–28.

Chitneni, S.K., Serdons, K., Evens, N., Fonge, H., Celen, S., Deroose, C.M., *et al.*, 2007. Efficient purification and metabolite analysis of radiotracers using high-performance liquid chromatography and on-line solid-phase extraction. *Journal of Chromatography A*, 1189(1–2), pp.323–331.

Clark, J.B., Ferris, G.M., Pinder, S., 1971. Inhibition of nuclear NAD nucleosidase and poly ADP-ribose polymerase activity from rat liver by nicotinamide and 5'-methyl nicotinamide. *Biochimica et Biophysica Acta*, 238(1), pp.82–85.

Cleary, J., Johnson, K.M., Opiari, A.W., Glik, G.D., 2007. Inhibition of the mitochondrial F_1F_0 -ATPase by ligands of the peripheral benzodiazepine receptor. *Bioorganic and Medicinal Chemistry Letters*, 17(6), pp.1667–1670.

ClinicalTrials.gov [online], 2016. Available at: <https://clinicaltrials.gov/> [Accessed 18 April 2016].

Cockcroft, X., Dillon, K.J., Dixon, L., Drzewiecki, J., Kerrigan, F., Loh, V.M., *et al.*, 2006. Phthalazinones 2: optimisation and synthesis of novel potent inhibitors of poly(ADP-ribose)polymerase. *Bioorganic and Medicinal Chemistry Letters*, 16(4), pp.1040–1044.

Coleridge, B.M., Bello, C.S., Leitner, A., 2009. General and user-friendly protocol for the synthesis of functionalized aryl- and heteroaryl-cyclopropanes by Negishi cross-coupling reactions. *Tetrahedron Letters*, 50(31), pp.4475–4477.

Convert, L., Morin-Brassard, G., Cadorette, J., Archambault, M., Bentourkia, M., Lecomte, R., 2007. A new tool for molecular imaging: the microvolumetric β blood counter. *Journal of Nuclear Medicine*, 48(7), pp.1197–1206.

Cook, G.J., Maisey, M.N., Fogelman, I., 1999. Normal variants, artefacts and interpretative pitfalls in PET imaging with 18-fluoro-2-deoxyglucose and carbon-11 methionine. *European Journal of Nuclear Medicine*, 26(10), pp.1363–1378.

Cornford, E.M., Braun, L.D., Oldendorf, W.H., Hill, M.A., 1982. Comparison of lipid-mediated blood-brain-barrier penetrability in neonates and adults. *The American Journal of Physiology*, 243(3), C161–168.

Cornu, P., Benavides, J., Scatton, B., Hauw, J.J., Philippon, J., 1992. Increase in ω_3 (peripheral-type benzodiazepine) binding site densities in different types of human brain tumours. *Acta Neurochirurgica*, 119(1–4), pp.146–152.

Council Directive 2010/63/EU of 22 September 2010 on the protection of animals used for scientific purposes.

Curtin, N.J., Wang, L., Yiakouvaki, A., Suzanne, K., Arris, C.A., Canan-Koch, S., *et al.*, 2004. Novel poly(ADP-ribose) polymerase-1 inhibitor, AG14361, restores sensitivity to temozolomide in mismatch mismatch repair-deficient cells. *Clinical Cancer Research*, 10(3), pp.881–889.

Davalos, D., Grutzendler, J., Yang, G., Kim, J.V., Zuo, Y., Jung, S., *et al.*, 2005. ATP mediates rapid microglial response to local brain injury in vivo. *Nature Neuroscience*, 8(6), pp.752–758.

Davis, A.J., Chen, D.J., 2013. DNA double strand break repair via non-homologous end-joining. *Translational Cancer Research*, 2(3), pp.130–143.

Davies, A.A., Masson, J., McIlwraith, M.J., Stasiak, A.Z., Stasiak, A., Venkitaraman, A.R., 2001. Role of BRCA2 in control of the RAD51 recombination and DNA repair protein. *Molecular Cell*, 7(2), pp.273–282.

de Goeij, J.J., Bonardi, M.L., 2005. How do we define the concepts of specific activity, radioactive concentration, carrier, carrier-free and no-carrier-added? *Journal of Radioanalytical and Nuclear Chemistry*, 263(1), pp.13–18.

Dean, M., Fojo, T., Bates, S., 2005. Tumour stem cells and drug resistance. *Nature Reviews Cancer*, 5(4), pp.275–284.

Deeks, E.D., 2015. Olaparib: first global approval. *Drugs*, 75(2), pp.231–240.

Deimling, A., Louis, D.N., Wiestler, O.D., 1995. Molecular pathways in the formation of gliomas. *Glia*, 15(3), pp.328–338.

del Valle, E.M., 2004. Cyclodextrins and their uses: a review. *Process Biochemistry*, 39(9), pp.1033–1046.

Dent, R.A., Lindeman, G.J., Clemons, M., Wildiers, H., Chan, A., McCarthy, N.J., *et al.*, 2013. Phase I trial of the oral PARP inhibitor olaparib in combination with paclitaxel for first- or second-line treatment of patients with metastatic triple-negative breast cancer. *Breast Cancer Research*, 15(5), R88.

Di, L., Kerns, E.H., Hong, Y., Chen, H., 2005. Development and application of high throughput plasma stability assay for drug discovery. *International Journal of Pharmaceutics*, 297(1–2), pp.110–119.

Diaz, G.J., Squires, E.J., 2003. Phase II *in vitro* metabolism of 3-methylindole metabolites in porcine liver. *Xenobiotica: the fate of foreign compounds in biological systems*, 33(5), pp.485–498.

Dischino, D.D., Welch, M.J., Kilbourn, M.R., Raichle, M.E., 1983. Relationship between lipophilicity and brain extraction of C-11-labeled radiopharmaceuticals. *Journal of Nuclear Medicine*, 24(11), pp.1030–1038.

Doble, A., Malgouris, C., Daniel, M., Daniel, N., Imbault, F., Basbaum, A., *et al.*, 1987. Labelling of peripheral-type benzodiazepine binding sites in human brain with [³H]PK 11195: anatomical and subcellular distribution. *Brain Research Bulletin*, 18(1), pp.49–61.

Donawho, C.K., Luo, Y., Luo, Y., Penning, T.D., Bauch, J.L., Bouska, J.J., *et al.*, 2007. ABT-888, an orally active poly(ADP-ribose) polymerase inhibitor that potentiates DNA-damaging agents in preclinical tumor models. *Clinical Cancer Research*, 13(9), pp.2728–2737.

Eadsforth, C.V., Moser, P., 1983. Assessment of reverse-phase chromatographic methods for determining partition coefficients. *Chemosphere*, 12(11–12), pp.1459–1475.

Edinger, M., Cao, Y., Hornig, Y.S., Jenkins, D.E., Verneris, M.R., Bachmann, M.H., *et al.*, 2002. Advancing animal models of neoplasia through *in vivo* bioluminescence imaging. *European Journal of Cancer*, 38(16), pp.2128–2136.

Edmonds, C.E., Makvandi, M., Lieberman, B.P., Xu, K., Zeng, C., Li, S., *et al.*, 2016. [¹⁸F]FluorThanatrace uptake as a marker of PARP1 expression and activity in breast cancer. *American Journal of Nuclear Medicine and Molecular Imaging*, 6(1), pp.94–101.

Efimova, E.V., Mauceri, H.J., Golden, D.W., Labay, E., Bindokas, V.P., Darga, T.E., *et al.*, 2010. Poly(ADP-ribose) polymerase inhibitor induces accelerated senescence in irradiated breast cancer cells and tumors. *Cancer Research*, 70(15), pp.6277–6282.

Ehrenkauf, R.E., Potocki, J.F., Jewett, D.M., 1984. Simple synthesis of F-18-labeled 2-fluoro-2-deoxy-D-glucose: concise communication. *Journal of Nuclear Medicine*, 25(3), pp.333–337.

Esposito, E., Matteo, V.D., Benigno, A., Pierucci, M., Crescimanno, G., Giovanni, G.D., 2007. Non-steroidal anti-inflammatory drugs in Parkinson's disease. *Experimental Neurology*, 205(2), pp.295–312.

European Medicines Agency, 2014. CHMP assessment report: Lynparza [pdf]. London: European Medicines Agency. Available at: http://www.ema.europa.eu/docs/en_GB/document_library/EPAR_-_Public_assessment_report/human/003726/WC500180154.pdf [Accessed 20 March 2016].

Farmer, H., McCabe, N., Lord, C.J., Tutt, A.N., Johnson, D.A., Richardson, T.B., 2005. Targeting the DNA repair defect in BRCA mutant cells as a therapeutic strategy. *Nature*, 434(7035), pp917–921.

Feng, L., Svarer, C., Thomsen, G., de Nijs, R., Larsen, V.A., Jensen, P., *et al.*, 2014. In vivo quantification of cerebral translocator protein binding in humans using 6-chloro-2-(4'-¹²³I-iodophenyl)-3-(*N,N*-diethyl)-imidazo[1,2-*a*]pyridine-3-acetamide SPECT. *Journal of Nuclear Medicine*, 55(12), pp.1966–1972.

Ferraris, D.V., 2010. Evolution of poly(ADP-ribose) polymerase-1 (PARP-1) inhibitors. From concept to clinic. *Journal of Medicinal Chemistry*, 53(12), pp.4561–4584.

Filimonov, V.D., Trusova, M., Postnikov, P., Krasnokustskaya, E.A., Lee, Y.M., Hwang, H.Y., 2008. Unusually stable, versatile, and pure arenediazonium tosylates: their preparation, structures, and synthetic applicability. *Organic Letters*, 10(18), pp.3961–3964.

Floeth, F.W., Pauleit, D., Sabel, M., Reifenberger, G., Stoffels, G., Stummer, W., *et al.*, 2006. ¹⁸F-FET PET differentiation of ring-enhancing brain lesions. *The Journal of Nuclear Medicine*, 47(5), pp.776–782.

Fong, P.C., Boss, D.S., Yap, T.A., Tutt, A., Wu, P., Mergui-Roelvink, M., *et al.*, 2009. Inhibition of poly(ADP-ribose) polymerase in tumors from BRCA mutation carriers. *The New England Journal of Medicine*, 361(2), pp.123–134.

Food and Drug Administration, 2014. *FDA approves Lynparza to treat advanced ovarian cancer* [online]. Available at: <http://www.fda.gov/newsevents/newsroom/pressannouncements/ucm427554.htm> [Accessed 20 March 2016].

Gagnon, A., Ahmad, M.H., Bonneau, P.R., Coulombe, R., DeRoy, P.L., Doyon, L., *et al.*, 2007. Thiotetrazole alkynylacetanilides as potent and bioavailable non-nucleoside inhibitors of the HIV-1 wild type and K103N/Y181C double mutant

reverse transcriptases. *Bioorganic and Medicinal Chemistry Letters*, 17(16), pp.4437–4441.

Gail, R., Hocke, C., Coenen, H.H., 1997. Direct n.c.a. ^{18}F -fluorination of halo- and alkylarenes via corresponding diphenyliodonium salts [abstract]. *Journal of Labelled Compounds and Radiopharmaceuticals*, 40(1), pp.50–52.

Galia, A., Calogero, A.E., Condorelli, R.A., Fraggetta, F., Corte, C., Ridolfo, F., *et al.*, 2012. PARP-1 protein expression in glioblastoma multiforme. *European Journal of Histochemistry*, 56(1), pp.45–48.

Galli, R., Binda, E., Orfanelli, U., Cipelletti, B., Gritti, A., Vittis, S., *et al.*, 2004. Isolation and characterization of tumorigenic, stem-like neural precursors from human glioblastoma. *Cancer Research*, 64(19), pp.7011–7021.

Gildersleeve, D.L., Lin, T., Wieland, D.M., Ciliax, B.J., Olson, J.M., Young, A.B., 1989. Synthesis of high specific activity ^{125}I -labeled analog of PK 11195, potential agent for SPECT imaging of the peripheral benzodiazepine binding site. *International Journal of Radiation Applications and Instrumentation. Part B, Nuclear Medicine and Biology*. 16(4), pp.423–429.

Gildersleeve, D.L., van Dort, M.E., Johnson, J.W., Sherman, P.S., Wieland, D.M., 1996. Synthesis and evaluation of [^{123}I]-iodo-PK11195 for mapping peripheral-type benzodiazepine receptors (ω_3) in heart. *Nuclear Medicine and Biology*, 23(1), pp.23–28.

Giorgio, V., von Stockum, S., Antoniel, M., Fabbro, A., Fogolari, F., Forte, M., *et al.*, 2013. Dimers of mitochondrial ATP synthase from the permeability transition pore. *Proceedings of the National Academy of Sciences of the United States of America*, 110(15), pp.5887–5892.

Gottipati, P., Vischioni, B., Schultz, N., Solomons, J, Bryant, H.E., Djureinovic, T., *et al.*, 2010. Poly(ADP-ribose) polymerase is hyperactivated in homologous recombination-defective cells. *Cancer Research*, 70(13), pp.5389–5398.

Götz, I., Spehl, T.S., Weber, W.A., Grosu, A.L., 2012. PET and SPECT for radiation treatment planning. *The Quaternary Journal of Nuclear and Molecular Imaging*, 56(2), pp.163–172.

Greemup, R., Buchanan, A., Lorizio, W., Rhoads, K., Chan, S., Leedom, T., *et al.*, 2013. Prevalence of BRCA mutations among women with triple-negative breast cancer (TNBC) in a genetic counselling cohort. *Annals of Surgical Oncology*, 20(10), pp.3254–3258.

Griffon, R.J., Srinivasan, S., Bowman, K., Calbert, A.H., Curtin, N.J., Newell, D.R., 1998. Resistance-modifying agents. 5. Synthesis and biological properties of quinazolinone inhibitors of the DNA repair enzyme poly(ADP-ribose) polymerase (PARP). *Journal of Medicinal Chemistry*, 41(26), pp.5247–5256.

Guarente, L., 1993. Synthetic enhancement in gene interaction: a genetic tool come of age. *Trends in Genetics*, 9(10), pp.362–366.

Guengerich, F.P., 2006. Cytochrome P450s and other enzymes in drug metabolism and toxicity. *The AAPS Journal*, 8(1), E101– 111.

Hani, T., 1999. *HPLC a practical guide*. Cambridge: The Royal Society of Chemistry.

Hansch, C., Steward, A.R., Anderson, S.M., Bentley, D., 1967. The parabolic dependence of drug action upon lipophilic character as revealed by a study of hypnotics. *Journal of Medicinal Chemistry*, 11(1), pp.1–11.

Hartman, D.A., 2003. Determination of the stability of drugs in plasma. *Current Protocols in Pharmacology*, Chapter 7, Unit 7.6, doi: 10.1002/0471141755.ph0706s19.

Hashizume, K., Tamakawa, H., Hashimoto, N., Miyake, Y., 1997. Single-step synthesis of [¹⁸F]haloperidol from the chloro-precursor and its applications in PET imaging of a cat's brain. *Applied Radiation and Isotopes*, 48(9), pp.1179–1185.

Helleday, T., 2011. The underlying mechanism for the PARP and BRCA synthetic lethality: clearing up the misunderstandings. *Molecular Oncology*, 5(4), pp.387–393.

Helmkamp, R.W., Contreras, M.A., Bale, W.F., 1967. I¹³¹-labeling of proteins by the iodine monochloride method. *International Journal of Applied Radiation and Isotopes*, 18(11), pp.737–746.

Helmer, F., Kiehs, K., Hansch, C., 1968. The linear free-energy relationship between partition coefficients and the binding and conformational perturbation of macromolecules by small organic compounds. *Biochemistry*, 7(8), pp.2858–2863.

Heneka, M.T., Carson, M.J., Khoury, J., Landreth, G.E., Brosseron, F., Feinstein, D., *et al.*, 2015. Neuroinflammation in Alzheimer's disease. *The Lancet Neurology*, 14(4), pp.388–405.

Hirai, T., Shirai, H., Fujimori, H., Okayasu, R., Sasai, K., Masutani, M., 2012. Radiosensitization effect of poly(ADP-ribose) polymerase inhibition in cells exposed to low and high linear energy transfer radiation. *Cancer Science*, 103(6), pp.1045–1050.

Hirsch, E.C., Vyas, S., Hunot, S., 2012. Neuroinflammation in Parkinson's disease. *Parkinsonism and Related Disorders*, 18(suppl 1), S210–212.

Hoeijmakers, J.H., 2001. Genome maintenance mechanisms for preventing cancer. *Nature*, 411(6835), pp.366–374.

Hoeijmakers, J.H., 2009. DNA damage, aging, and cancer. *The New England Journal of Medicine*, 361(15), pp.1475–1485.

Hoffman, J.M., Gambhir, S.S., Kelloff, G.J., 2007. Regulatory and reimbursement challenges for molecular imaging. *Radiology*, 245(3), pp.645–60.

Horner, L., Hoffmann, H., Wippel, H.G., 1958. Phosphororganische verbindungen, XII. Phosphinoxyde als olefinierungsreagenzien. *European Journal of Inorganic Chemistry*, 91(1), pp.61–63.

Hottiger, M.O., Hassa, P.O., Lüscher, B., Schüler, H., Koch-Nolte, F., 2010. Toward a unified nomenclature for mammalian ADP-ribosyltransferases. *Trends in Biochemical Sciences*, 35(4), pp.208–219.

Hygino da Cruz, L.C., Rodriguez, I., Domingues, R.C., Gasparetto, E.L., Sorensen, A.G., 2009. Pseudoprogression and pseudoresponse: imaging challenges in the assessment of posttreatment glioma. *American Journal of Neuroradiology*, 32(11), pp.1978–1985.

International Atomic Energy Agency, 2008. *Cyclotron produced radionuclides: principles and practice* [pdf]. Austria: International Atomic Energy Agency. Available at: <http://www-pub.iaea.org/books/IAEABooks/7849/Cyclotron-Produced-Radionuclides-Principles-and-Practice> [Accessed 20 March 2016].

Isakoff, S.J., Overmoyer, B., Tung, N.M., Gelman, R.S., Giranda, V.L., Bernhard, K.M., *et al.*, 2010. A phase II trial of the PARP inhibitor veliparib (ABT888) and temozolomide in metastatic breast cancer [abstract]. *Journal of Clinical Oncology*, 28(15s), abstr.1019.

Iyer, K.R., Sinz, M.W., 1999. Characterization of phase I and phase II hepatic drug metabolism activities in a panel of human liver preparations. *Chemico-Biological Interactions*, 118(2), pp.151–169.

Jacobson, O., Chen, X., 2013. Interrogating tumor metabolism and tumor microenvironments using molecular positron emission tomography imaging. Theranostic approaches to improve therapeutics. *Pharmacological Reviews*, 65(4), pp.1214–1256.

Janssens, G.O., Rademakers, S.E., Terhaard, C.H., Doornaert, P.A., Bijl, H.P., van der Ende, P., *et al.*, 2012. Accelerated radiotherapy with carbogen and nicotinamide for laryngeal cancer: results of a phase III randomized trial. *Journal of Clinical Oncology*, 30(15), pp.1777–1783.

Jensen, P., Feng, L., Law, I., Svarer, C., Knudsen, G.M., Mikkelsen, J.D., *et al.*, 2015. TSPO imaging in glioblastoma multiforme: a direct comparison between ¹²³I-CLINDE SPECT, ¹⁸F-FET PET, and gadolinium-enhanced MR imaging. *Journal of Nuclear Medicine*, 56(9), pp.1386–1390.

Johnson, K.A., Fox, N.C., Sperling, R.A., Klunk, W.E., 2012. Brain imaging in Alzheimer Disease. *Cold Spring Harbor Perspectives in Medicine*, 2(4), a006213.

Josephy, P.D., Guengerich, F.P., Miners, J.O., 2005. “Phase I and phase II” drug metabolism: terminology that we should phase out? *Drug Metabolism Reviews*, 37(4), pp.575–580.

Juarez-Salinas, H., Sims, J.L., Jacobson, M.K., 1979. Poly(ADP-ribose) levels in carcinogen-treated cells. *Nature*, 282(5740), pp.740–741.

Juhász, C., Dwivedi, S., Kamson, D.O., Michelhaugh, S.K., Mittal, S., 2014. Comparison of amino acid positron emission tomographic radiotracers for molecular imaging of primary and metastatic brain tumors. *Molecular Imaging*, 13, 10.2310/7290.2014.00015.

Junck, L., Olson, J.M., Ciliax, B.J., Koeppe, R.A., Warkins, G.L., Jewett, D.M., *et al.*, 1989. PET imaging of human gliomas with ligands for the peripheral benzodiazepine binding site. *Annals of Neurology*, 26(6), pp.752–758.

Jung, S., Willard, S.T., 2014. Quantitative bioluminescence imaging of transgene expression in intact porcine antral follicles *in vitro*. *Reproductive Biology and Endocrinology*, 12(11), doi:10.1186/1477-7827-12-11.

Kaelin, W., 2005. The concept of synthetic lethality in the context of anticancer therapy. *Nature Reviews Cancer*, 5(9), pp.689–698.

Kaanders, J.H., Bussink, J., van der Kogel, A.J., 2002. ARCON: a novel biology-based approach in radiotherapy. *The Lancet Oncology*, 3(12), pp.728–737.

Karlberg, T., Hammarström, M., Schütz, P., Svensson, L., Schüler, H., 2010. Crystal structure of the catalytic domain of human PARP2 in complex with PARP inhibitor ABT-888. *Biochemistry*, 49(6), pp.1056–1058.

Kaul, A., Roedler, H.D., 1980. Radioiodine: biokinetics, mean dose and dose distribution. *Radiation and Environmental Biophysics*, 18(3), pp.185–195.

Kawamitsu, H., Hoshino, H., Okada, H., Miwa, M., Momoi, H., Sugimura, T., 1984. Monoclonal antibodies to poly(adenosine diphosphate ribose) recognize different structures. *Biochemistry*, 23(16), pp.3771–3777.

Keith, L.B., Ikezaki, K., Santori, E., Becker, D.P., Vinters, H.V., 1990. Specific high-affinity binding of peripheral benzodiazepine receptor ligands to brain tumors in rat and man. *Cancer*, 65(1), pp.93–97.

Kelly, P.N., Dakic, A., Adams, J.M., Nutt, L.M., Strasser, A., 2007. Tumour growth need not be driven by rare cancer stem cells. *Science*, 317(5836), p.337.

Kern, S.E., Shiabata, D., 2007. The fuzzy math of solid tumour stem cells: a perspective. *Cancer Research*, 67(19), pp.8985–8988.

Keunen, O., Taxt, T., Grüner, R., Lund-Johansen, M., Tonn, J., Pavlin, T., *et al.*, 2014. Multimodal imaging of gliomas in the context of evolving cellular and molecular therapies. *Advanced Drug Delivery Reviews*, 76, pp.98–115.

Khalil, M.M., Tremoleda, J.L., Bayomy, T.B., Gsell, W., 2011. Molecular SPECT imaging: an overview. *International Journal of Molecular Imaging*, 2011, 796025.

Khan, O.A., Gore, M., Lorigan, P., Stone, J., Greystoke, A., Burke, W., *et al.*, 2011. A phase I study of the safety and tolerability of olaparib (AZD2281, KU0059436) and dacarbazine in patients with advanced solid tumours. *British Journal of Cancer*, 104(5), pp.750–755.

Kharasch, E.D., Tummel, K.E., 1993. Identification of cytochrome P450 2E1 as the predominant enzyme catalysing human liver microsomal defluorination of sevoflurane, isoflurane, and methoxyflurane. *Anesthesiology*, 79(4), pp.795–807.

Kim, D.W., Jeong, H., Lim, S.T., Sohn, M., Katzenellenbogen, J.A., Chi, D.Y., 2008. Facile nucleophilic fluorination reactions using *tert*-Alcohols as a reaction medium: significantly enhanced reactivity of alkali metal fluorides and improved selectivity. *The Journal of Organic Chemistry*, 73(3), pp.957–962.

Kim, J.E., Kim, Y.J., Kang, T.C., 2014. PARP1 activation/expression modulates regionalspecific neuronal and glial responses to seizure in a hemodynamic-independent manner. *Cell Death and Disease*, 5(8), e1362.

Kim, C., Kim, I.H., Kim, S., Kim, Y.S., Kang, S.H, Moon, S.H., 2011. Comparison of the intraperitoneal, retroorbital and per oral routes for F-18 FDG administration as effective alternatives to intravenous administration in mouse tumor models using small animal PET/CT studies. *Nuclear Medicine and Molecular Imaging*, 45(3), pp.169–176.

Kleihues, P., Ohgaki, H., 1999. Primary and secondary glioblastomas: from concept to clinical diagnosis. *Neuro-Oncology*, 1(1), pp.44–51.

Kovács, L., Szegezdi, J., 2003. New way of mono-Boc protection of diamines [pdf]. Unpublished poster presentation at: *Advancing Library Design and Organic Synthesis*, February 24–27 2003, La Jolla, California. Available at: https://www.chemaxon.com/conf/New_Way_of_Mono-BOC_Protection_of_Diamines.pdf [Accessed 20 March 2016].

Kracht, L.W., Miletic, H., Busch, S., Jacobs, A.H., Voges, J., Hoevels, M., *et al.*, 2004. Delineation of brain tumour extent with [¹¹C]L-methionine positron emission tomography: local comparison with stereotactic histopathology. *Clinical Cancer Research*, 10(21), pp.7163–7170.

Krasikova, R., 2007. Synthesis modules and automation in F-18 labelling. In: P.A. Schubiger, L. Lehmann, M. Friebe, eds. 2007. *PET chemistry: the driving force in molecular imaging*. New York: Springer. pp. 290–312.

Krebs, H.A., 1950. Chemical composition of blood plasma and serum. *Annual Review of Biochemistry*, 19, pp.409–430.

Kreisl, W.C., Jenko, K.J., Hines, C.S., Lyoo, C.H., Corona, W., Morse, C.L., *et al.*, 2013. A genetic polymorphism for translocator protein 18 kDa affects both *in vitro* and *in vivo* radioligand binding in human brain to this putative biomarker of neuroinflammation. *Journal of Cerebral Blood Flow and Metabolism*, 33(1), pp.53–58.

Kremer, P., Fardanesh, M., Ding, R., Pritsch, M., Zoubaa, S., Frei, E., 2009. Intraoperative fluorescence staining of malignant brain tumors using 5-aminofluorescein-labeled albumin. *Neurosurgery*, 64(suppl 3), pp.53–60.

Kristian, A., Alstrup, O., Smith, D.F., 2013. Anaesthesia for positron emission tomography scanning of animal brains. *Laboratory Animals*, 47(1), pp.12–18.

Kummar, S., Kinders, R., Gutierrez, M.E., Rubinstein, L., Parchment, R.E., Phillips, L.R., *et al.*, 2009. Phase 0 clinical trial of the poly(ADP-ribose) polymerase inhibitor ABT-888 in patients with advanced malignancies. *Journal of Clinical Oncology*, 27(16), pp.2705–2711.

Landy, H.J., Lee, T.T., Potter, P., Feun, L., Markoe, A., 2000. Early MRI findings in high grade glioma. *Journal of Neuro-Oncology*, 47(1), pp.65–72.

Ledermann, J., Harter, P., Gourley, C., Friedlander, M., Vergote, I., Rustin, G., *et al.*, 2012. Olaparib maintenance therapy in platinum-sensitive relapsed ovarian cancer. *The New England Journal of Medicine*, 366(15), pp.1382–1392.

Ledermann, J., Harter, P., Gourley, C., Friedlander, M., Vergote, I., Rustin, G., *et al.*, 2014. Olaparib maintenance therapy in patients with platinum-sensitive relapsed serous ovarian cancer: a preplanned retrospective analysis of outcomes

by BRCA status in a randomised phase 2 trial. *The Lancet Oncology*, 15(8), pp.852–861.

Lee, E., Hooker, J.M., Ritter, T., 2012. Nickel-mediated oxidative fluorination for PET with aqueous [^{18}F]fluoride. *Journal of the American Chemical Society*, 134(42), pp.17456–17458.

Lee, S.J., Oh, S.J., Chi, D.Y., Lee, B.S., Ryu, J.S., *et al.*, 2007. Comparison of synthesis yields of 3'-deoxy-3'-[^{18}F]fluorothymidine by nucleophilic fluorination in various alcohol solvents. *Journal of Labelled Compounds and Radiopharmaceuticals*, 51(1), pp.80–82.

Leopold, W.R., Sebolt-Leopold, J.S., 1992. Chemical approaches to improved radiotherapy. In: F.A. Valeriote, T.H. Corbett, L.H. Baker, eds. 1992. *Cytotoxic anticancer drugs: models and concepts for drug discovery and development*. Dordrecht: Kluwer Academic Publishers. pp.179–196.

Leppälä, J., Kallio, M., Nikula, T., Nikkinen, P., Liewendahl, K., Jääskeläinen, J., *et al.*, 1995. Accumulation of $^{99\text{m}}\text{Tc}$ -low-density lipoprotein in human malignant glioma. *British Journal of Cancer*, 71(2), pp.383–387.

Lerman, O., Tor, Y., Rozen, S., 1981. Acetyl hypofluorite as a taming carrier of elemental fluorine for novel electrophilic fluorination of activated aromatic rings. *The Journal of Organic Chemistry*, 46(22), pp.4639–4631.

Lieber, M.R., Gu, J., Lu, H., Shimazaki, N., Tsai, A.G., 2010. Nonhomologous DNA end joining (NHEJ) and chromosomal translocations in humans. In: H.P. Nasheuer, ed. 2010. *Genome stability and human disease*. New York: Springer. pp.279–296.

Liu, Z., Hundal-Jabal, N., Wong, M., Yapp, D., Lin, K., Bénard, F., *et al.*, 2014. A new ^{18}F -heteroaryltrifluoroborate radioprosthesis with greatly enhanced stability that is labelled by ^{18}F – ^{19}F -isotope exchange in good yield at high specific activity. *Medicinal Chemistry Communication*, 5(2), pp.171–179.

Loh, V.M., Cockroft, X., Dillon, K.J., Dixon, L., Drzewiecki, J., Eversley, P.J., *et al.*, 2005. Phthalazinones. Part 1: the design and synthesis of novel series of potent inhibitors of poly(ADP-ribose)polymerase. *Bioorganic and Medicinal Chemistry Letters*, 15(9), pp.2235–2238.

Louis, D.N., Gusella, J.F., 1995. A tiger behind many doors: multiple genetic pathways to malignant glioma. *Trends in Genetics*, 11(10), pp.412–415.

Louis, D.N., Ohgaki, H., Wiestler, O.D., Cavenee, W.K., Burger, P.C., Jouvett, A., *et al.*, 2007. The 2007 WHO classification of tumours of the central nervous system. *Acta Neuropathologica*, 114(2), pp.97–109.

Luus, C., Hanani, R., Reynolds, A., Kassiou, M., 2010. The development of PET radioligands for imaging the translocator protein (18 kDa): what have we learned? *Journal of Labelled Compounds and Radiopharmaceutical*, 53(7), pp.501–510.

Ma, J., Vija, A.H., 2014. Noise and resolution characteristics for xSPECT reconstruction method [abstract]. *Journal of Nuclear Medicine*, 55(suppl 1), abstr.2129.

Malmgren, J., Santoro, S., Jalalian, N., Himo, F., Olofsson, B., 2013. Arylation with unsymmetrical diaryliodonium salts: a chemoselective study. *Chemistry (Weinheim an Der Bergstrasse, Germany)*, 19(31), pp.10334–10342.

Mangner, T.J., Wu, J., Wieland, D.M., 1982. Solid-phase exchange radioiodination of aryl iodides. Facilitation by ammonium sulfate. *The Journal of Organic Chemistry*, 47(8), pp.1484–1488.

Marchetti, C., Imperiale, L., Gasparri, M.L., Palaia, I., Pignata, S., Boni, T., *et al.*, 2012. Olaparib, PARP-1 inhibitor in ovarian cancer. *Expert Opinion on Investigational Drugs*, 21(10), pp.1575–1584.

Maryanoff, B.E., Reitz, A.B., 1989. The Wittig olefination reaction and modifications involving phosphoryl-stabilized carbanions. Stereochemistry, mechanism, and selected synthetic aspects. *Chemical Reviews*, 89(4), pp.863–927.

Mason, N.S., Mathis, C.A., 2004. Radiohalogens for PET imaging. In: D.L. Bailey, D.W. Townsend, P.E. Valk, M.N. Maisey, eds. 2004. *Positron Emission Tomography*. London: Springer-Verlag London Limited. pp.203–222.

Mason, K.A., Valdecanas, D., Hunter, N.R., Milas, L., 2008. INO-1001, a novel inhibitor of poly(ADP-ribose) polymerase, enhances tumor response to doxorubicin. *Investigational New Drugs*, 26(1), pp.1–5.

Mattner, F., Mardon, K., Katsifis, A., 2008. Pharmacological evaluation of [¹²³I]-CLINDE: a radioiodinated imidazopyridine-3-acetamide for the study of peripheral benzodiazepine binding sites (PBBS). *European Journal of Nuclear Medicine and Molecular Imaging*, 35(4), pp.779–789.

Mayer, M., Reimand, J., Lan, X., Head, R., Zhu, X., Kushida, M., *et al.*, 2015. Single cell-derived clonal analysis of human glioblastoma links functional and genomic heterogeneity. *Proceedings of the National Academy of Sciences of the United States of America*, 112(3), pp.851–856.

McEnergy, M.W., Snowman, A.M., Trifletti, R.R., Snyder, S.H., 1992. Isolation of the mitochondrial benzodiazepine receptor: association with the voltage-dependent anion channel and the adenine nucleotide carrier. *Proceedings of the National Academy of Sciences of the United States of America*, 89(8), pp.3170–3174.

Menear, K.A., Adcock, C., Boulter, R., Cockroft, X., Copsey, L., Cranston, A., *et al.*, 2008. 4-[3-(4-Cyclopropanecarbonylpiperazine-1-carbonyl)-4-fluorobenzyl]-2H-phthalazin-1-one: A Novel Bioavailable Inhibitor of Poly(ADP-ribose) Polymerase-1. *Journal of Medicinal Chemistry*, 51(20), pp.6581–6591.

Merritt, E.A., Olofsson, B., 2009. Diaryliodonium salts: a journey from obscurity to fame. *Angewandte Chemie International Edition*, 48(48), pp.9052–9070.

Meunier, B., de Visser, S.P., Shaik, S., 2004. Mechanism of oxidation reactions catalyzed by cytochrome P450 enzymes. *Chemical Reviews*, 104(9), pp.3947–3980.

Miettinen, H., Kononen, J., Haapasalo, H., Helén, P., Sallinen, P., Harjuntausta, T., *et al.*, 1995. Expression of peripheral-type benzodiazepine receptor and diazepam bindings inhibitor in human astrocytomas: relationship to cell proliferation. *Cancer Research*, 55(12), pp.2691–2695.

Miknyoczki, S., Chang, H., Grobelny, J., Prichard, S., Worrell, C., McGann, N., *et al.*, 2007. The selective poly(ADP-ribose) polymerase-1(2) inhibitor, CEP-8983, increases the sensitivity of chemoresistant tumor cells to temozolomide and irinotecan but does not potentiate myelotoxicity. *Molecular Cancer Therapeutics*, 6(8), pp.2290–2302.

Miknyoczki, S., Jones-Bolin, S., Prichard, S., Hunter, K., Zhao, H., Wan, W., *et al.*, 2003. Chemopotential of temozolomide, irinotecan, and cisplatin activity

by CEP-6800, a poly(ADP-ribose) polymerase inhibitor. *Molecular Cancer Therapeutics*, 2(4), pp.371–382.

MILabs, 2015. *Breakthrough scanning technology: G-SPECT* [online]. Available at <http://www.milabs.com/breakthrough-scanning-technology-g-spect/> [Accessed 20 March 2016].

Miller, P.W., Long, N.J., Vilar, R., Gee, A.D., 2008. Synthesis of ^{11}C , ^{18}F , ^{15}O , and ^{13}N radiolabels for positron emission tomography. *Angewandte Chemie International Edition*, 47(47), pp.8998–9033.

Mizrahi, R., Rusjan, P.M., Kennedy, J., Pollock, B., Mulsant, B., Suridjan, I., *et al.*, 2012. Translocator protein (18 kDa) polymorphism (rs6971) explains *in-vivo* brain binding affinity of the PET radioligand [^{18}F]-FEPPA. *Journal of Cerebral Blood Flow and Metabolism*, 32(6), pp.968–972.

Moon, B.S., Kil, H.S., Park, J.H., Kim, J.S., Park, J., Chi, D.Y., *et al.*, 2011. Facile aromatic radiofluorination of [^{18}F]flumazenil from diaryliodonium salts with evaluation of their stability and selectivity. *Organic and Biomolecular Chemistry*, 9(24), pp.8346–8355.

Moravan, M.J., Olschowka, J.A., Williams, J.P., O'Banion, M.K., 2011. Cranial irradiation leads to acute and persistent neuroinflammation with delayed increases in T-cell infiltration and CD11c expression in C57BL/6 mouse brain. *Radiation Research*, 176(4), pp.459–473.

Morohaku, K., Pelton, S.H., Daugherty, D.J., Butler, W.R., Deng, W., Selvaraj, V., 2014. Translocator protein/peripheral benzodiazepine receptor is not required for steroid hormone biosynthesis. *Endocrinology*, 155(1), pp.89–97.

Moussa, I.A., Banister, S.D., Beinat, C., Giboureau, N., Reynolds, A.J., Kassiou, M., *et al.*, 2010. Design, synthesis, and structure - affinity relationships of regioisomeric *N*-benzyl alkyl ether piperazine derivative as σ -1 receptor ligands. *Journal of Medicinal Chemistry*, 53(16), pp.6228–6239.

Mukhin, A.G., Papadopoulos, V., Costa, E., Krueger, K.E., 1989. Mitochondrial benzodiazepine receptors regulate steroid biosynthesis. *Proceedings of the National Academy of Sciences of the United States of America*, 86(24), pp.9813–9816.

National Institute for Health and Clinical Excellence, 2007. Carmustine implants and temozolomide for the treatment of newly diagnosed high-grade glioma [pdf]. London: National Institute for Health and Clinical Excellence. Available at: <https://www.nice.org.uk/guidance/ta121> [Accessed 20 March 2016].

Nelson, D.R., Zeldin, D.C., Hoffman, S.M., Maltais, L.J., Wain, H.M., Nebert, D.W., 2004. Comparison of cytochrome P450 (CYP) genes from the mouse and human genomes, including nomenclature recommendations for genes, pseudogenes and alternative-splice variants. *Pharmacogenetics*, 14(1), pp.1–8.

Nimmerjahn, A., Kirchhoff, F., Helmchen, F., 2005. Resting microglial cells are highly dynamic surveillants of brain parenchyma in vivo. *Science*, 308(5726), pp.1314–1318.

Nomeir, A.A., McComish, M.F., Ferrala, N.F., Silveira, D., Covey, J.M., Chadwick, M., 1998. Liquid chromatographic analysis in mouse, dog and human plasma; stability, absorption, metabolism and pharmacokinetics of the anti-HIV agent 2-chloro-5-(2-methyl-5,6-dihydro-1,4-oxathiin-3-yl carboxamido) isopropylbenzoate (NSC 615985, UC84). *Journal of Pharmaceutical and Biomedical Analysis*, 17(1), pp.27–38.

Obach, S.R., 1999. Prediction of human clearance of twenty-nine drugs from hepatic microsomal intrinsic clearance data: an examination of in vitro half-life approach and nonspecific binding to microsomes. *Drug METabolism and Disposition*, 27(11), pp.1350–1359.

Okada, Y., Hurwitz, E.E., Esposito, J.M., Brower, M.A., Nutt, C.L., Louis, D.N., 2003. Selection pressures of TP53 mutation and microenvironmental location influence epidermal growth factor receptor gene amplification in human glioblastomas. *Cancer Research*, 63(2), pp.413–416.

Olah, M., Biber, K., Vinet, J., Boddeke, H.W., 2011. Microglia phenotype diversity. *CNS & Neurological Disorders - Drug Targets*, 10(1), pp.108–118.

Oliver, A.W., Amé, J., Roe, S.M., Good, V., de Murcia, G., Pearl, L.H., 2004. Crystal structure of the catalytic fragment of murine poly(ADP-ribose) polymerase-2. *Nucleic Acids Research*, 32(2), pp.456–464.

Olsson, I.A., Franco, N.H., Weary, D.M., Sandøe, P., 2012. The 3Rs principle - mind the ethical gap! [pdf] 8th World Congress on Alternatives and Animal Use in the Life Sciences. August 21-25 2011, Montreal, Canada. Available at:

http://www.altex.ch/resources/WC8proceedings_full_issue1.pdf [Accessed 21 March 2016].

Omuro, A., DeAngelis, L.M., 2013. Glioblastoma and other malignant gliomas a clinical review. *The Journal of the American Medical Association*, 310(17), pp.1842–1850.

Ossovskaya, V., Koo, I.C., Kaldjian, E.P., Alvares, C., Sherman, B.M., 2010. Upregulation of poly (ADP-ribose) polymerase-1 (PARP1) in triple-negative breast cancer and other primary human tumor types. *Genes and Cancer*, 1(8), pp.812–821.

Ostrom, Q.T., Bauchet, L., Davis, F.G., Deltour, I., Fisher, J. L., Langer, C. E., *et al.*, 2014. The epidemiology of glioma in adults: a “state of the science” review. *Neuro-Oncology*, 16(7), pp.896–913.

Owen, D.R., Gunn, R.N., Rabiner, E.A., Bennacef, I., Fujita, M., Kreisl, W.C., *et al.*, 2011. Mixed-affinity binding in humans with 18-kDa translocator protein ligands. *Journal of Nuclear Medicine*, 52(1), pp.24–32.

Owen, D.R., Yeo, A.J., Gunn, R.N., Song, K., Wadsworth, G., Lewis, A., *et al.*, 2012. An 18-kDa translocator protein (TSPO) polymorphism explains differences in binding affinity of the PET radioligand PBR28. *Journal of Cerebral Blood Flow and Metabolism*, 32(1), pp.1–5.

Papadopoulos, V., Amri, H., Li, H., Boujrad, N., Vidic, B., Garnier, M., 1997. Targeted disruption of the peripheral-type benzodiazepine receptor gene inhibits steroidogenesis in the R2C Leydig tumor cell line. *The Journal of Biological Chemistry*, 272(51), pp.32129–32135.

Papadopoulos, V., Baraldi, M., Guilarte, T.R., Knudsen, T.B., Lacapère, J., Lindemann, P., *et al.*, 2006. Translocator protein (18kDa): new nomenclature for the peripheral-type benzodiazepine receptor based on its structure and molecular function. *Trends in Pharmacological Sciences*, 27(8), pp.402–409.

Patel, A.G., Sarkaria, J.N., Kaufmann, S.H., 2011. Nonhomologous end joining drives poly(ADP-ribose) polymerase (PARP) inhibitor lethality in homologous recombination-deficient cells. *Proceedings of the National Academy of Sciences of the United States of America*, 108(8), pp.3406–3411.

Patel, A.P., Tirosh, I., Trombetta, J.J., Shalek, A.K., Gillespie, S.M., Wakimoto, H., *et al.*, 2014. Single-cell RNA-seq highlights intratumoral heterogeneity in primary glioblastoma. *Science*, 344(6190), pp.1396–1401.

Pauliet, D., Floeth, F., Hamacher, K., Riemenschneider, M.J., Reifenberger, G., Müller, H., *et al.*, 2005. O-(2-[¹⁸F]fluoroethyl)-L-tyrosine PET combined with MRI improves the diagnostic assessment of cerebral gliomas. *Brain*, 128(3), pp.678–687.

Penning, T.D., Zhu, G., Gandhi, V.B., Gong, J., Thomas, S., Lubisch, W., *et al.*, 2008. Discovery and SAR of 2-(1-propylpiperidin-4-yl)-1H-benzimidazole-4-carboxamide: a potent inhibitor of poly(ADP-ribose) polymerase (PARP) for the treatment of cancer. *Bioorganic and Medicinal Chemistry*, 16(14), pp.6965–6975.

Penning, T.D., Zhu, G., Gandhi, V.B., Gong, J., Liu, X., Shi, Y., *et al.*, 2009. Discovery of the poly(ADP-ribose) polymerase (PARP) inhibitor 2-[(R)-2-methylpyrrolidin-2-yl]-1H-benzimidazole-4-carboxamide (ABT-888) for the treatment of cancer. *Journal of Medicinal Chemistry*, 52(2), pp.514–523.

Petit-Taboué, M., Baron, J., Barré, L., Travère, J., Speckel, D., Camsonne, R., *et al.*, 1991. Brain kinetics and specific binding of [¹¹C]PK 11195 to ω_3 sites in baboons: positron emission tomography study. *European Journal of Pharmacology*, 200(2–3), pp.347–351.

Pettitt, S.J., Rehman, F.L., Bajrami, I., Brough, R., Wallber, F., Kozarewa, I., *et al.*, 2013. A genetic screen using the piggyback transposon in haploid cells identified PARP1 as a mediator of olaparib toxicity. *PLoS ONE*, 8(4), e61520.

Pike, V.W., 2009. PET radiotracers: crossing the blood-brain barrier and surviving metabolism. *Trends in Pharmacological Sciences*, 30(8), pp.431–440.

Pike, V.W., Aigbirhio, F.I., 1995. Reactions of cyclotron-produced [¹⁸F]fluoride with diaryliodonium salts - a novel single-step route to no-carrier added [¹⁸F]fluoroarenes. *Journal of the Chemical Society, Chemical Communications*, 1995(21), pp.2215–2216.

Pilkington, G.J. Tumour cell migration in the central nervous system., 1994. *Brain Pathology*, 4(2), pp.157–166.

Pimlott, S.L., Stevenson, L., Wyper, D.J., Sutherland, A., 2008. Rapid and efficient radiosynthesis of [^{123}I]I-PK11195, a single photon emission computed tomography tracer for peripheral benzodiazepine receptors. *Nuclear Medicine and Biology*, 35(5), pp.537–542.

Pimlott, S.L., Sutherland, A., 2011. Molecular tracers for the PET and SPECT imaging of disease. *Chemical Society Reviews*, 40(1), pp.149–162.

Pirotte, B., Goldman, S., Dewitte, O., Massager, N., Wikler, D., Lefranc, F., *et al.*, 2006. Integrated positron emission tomography and magnetic resonance imaging-guided resection of brain tumors: a report of 103 consecutive procedures [abstract]. *Journal of Neurosurgery*, 104(2), pp.238–253.

Pirotte, B., Levivier, M., Goldman, S., Wikler, D., Dewitte, O., Bruneau, M., *et al.*, 2009. Positron emission tomography-guided volumetric resection of supratentorial high-grade gliomas: a survival analysis in 66 consecutive patients. *Neurosurgery*, 64(3), pp.471–481.

Pirotte, B., Goldman, S., Bogaert, P., David, P., Wikler, D., Rorive, S., 2005. Integration of [^{11}C]methionine-positron emission tomographic and magnetic resonance imaging for image-guided surgical resection of infiltrative low-grade brain tumors in children. *Operative Neurosurgery*, 57(suppl 1), pp.128–139.

Pirzkall, A., McKnight, T.R., Graves, E.E., Carol, M.P., Sneed, P.K., Wara, W.W., *et al.*, 2001. MR-spectroscopy guided target delineation for high-grade gliomas. *International Journal of Radiation Oncology*, 50(4), pp.915–928.

Plummer, R., Jones, C., Middleton, M., Wilson, R., Evans, J., Olsen, A., *et al.*, 2008. Phase I study of the poly(ADP-ribose) polymerase inhibitor, AG014699, in combination with temozolomide in patients with advanced solid tumors. *Clinical Cancer Research*, 14(23), pp.7917–7923.

Plummer, R., Stephens, P., Aissat-Daudigny, L., Cambois, A., Moachon, G., Brown, P.D., *et al.*, 2014. Phase 1 dose-escalation study of the PARP inhibitor CEP-9722 as monotherapy or in combination with temozolomide in patients with solid tumors. *Cancer Chemotherapy and Pharmacology*, 74(2), pp.257–265.

Pöpperl, G., Goldbrunner, R., Gildehaus, F.J., Kreth, F.W., Tanner, P., Holtmannspötter, M., *et al.*, 2005. O-(2-[^{18}F]-fluoroethyl)-L-tyrosine PET for monitoring the effects of convection-enhanced delivery of paclitaxel in patients

with recurrent glioblastoma. *European Journal of Nuclear Medicine and Molecular Imaging*, 32(9), pp.1018–1025.

Pöpperl, G., Götz, C., Rachinger, W., Schnell, O., Gildehaus, F.J., Tonn, J.C., *et al.*, 2006. Serial O-(2-[¹⁸F]-fluoroethyl)-L-tyrosine PET for monitoring the effects of intracavitary radioimmunotherapy in patients w malignant glioma. *European Journal of Nuclear Medicine and Molecular Imaging*, 33(7), pp.792–800.

Prescott, J.W., 2013. Quantitative imaging biomarkers: the application of advanced image processing and analysis to clinical and preclinical decision making. *Journal of Digital Imaging*, 26(1), pp.97–108.

Purnell, M.R., Whish, W.J., 1980. Novel inhibitors of poly(ADP-ribose) synthetase. *Biochemical Journal*, 185(3), pp.775–777.

Rahmim, A., Zaidi, H., 2008. PET versus SPECT: strengths, limitations and challenges. *Nuclear Medicine Communications*, 29(3), pp.193–207.

Raivich, G., Bohatschek, M., Kloss, C.U., Werner, A., Jones, L.L., Kreutzberg, G.W., 1999. Neuroglial activation repertoire in the injured brain: graded response, molecular mechanisms and cues to physiological function. *Brain Research Reviews*, 30(1), pp.77–105.

Rajan, A., Carter, C.A., Kelly, R.J., Gutierrez, M., Kummear, S., Szabo, E., *et al.*, 2012. A phase I combination study of olaparib with cisplatin and gemcitabine in adults with solid tumors. *Clinical Cancer Research*, 18(8), pp.2344–2351.

Rang, H.P., Dale, M.M., Ritter, J.M., Flower, R.J., 2007. *Rang and Dale's Pharmacology*. 6th ed. London: Churchill Livingstone Elsevier.

Reiner, T., Lacy, J., Keliher, E.J., Yang, K.S., Ullal, A., Kohler, R.H., *et al.*, 2012. Imaging therapeutic PARP inhibition *in vivo* through bioorthogonally developed companion imaging agents. *Neoplasia*, 14(3), pp.169–177.

Ren, H., Wey, H., Strebl, M., Neelamegam, R., Ritter, T., Hooker, J.M., 2014. Synthesis and imaging validation of [¹⁸F]MDL100907 enabled by Ni-mediated fluorination. *ACS Chemical Neuroscience*, 5(7), pp.611–615.

Riss, P.J., Soskic, V., Schratzenholz, A., Roesch, F., 2009. Synthesis and radiosynthesis of N⁵-[¹⁸F]fluoroethyl-pirenzepine and its metabolite N⁵-

[¹⁸F]fluprpyethyl-LS 75. *Labelled Compounds and Radiopharmaceuticals*, 52(14), pp.576–579.

Ritt, P., Sanders, J., Kuwert, T., 2014. SPECT/CT technology. *Clinical and Translational Imaging*, 2(6), pp.445–457.

Rodrigues, A.D., 1994. Use of *in vitro* human metabolism studies in drug development. *Biochemical Pharmacology*, 48(12), pp.2147–2156.

Roelcke, U., Radü, E.W., Ammon, K., Hausmann, O., Maguire, R.P., Leenders, K.L., 1995. Alteration of blood-brain barrier in human brain tumors: comparison of [¹⁸F]fluorodeoxyglucose, [¹¹C]methionine and rubidium-82 using PET. *Journal of the Neurological Sciences*, 132(1), pp.20–27.

Rojas, A., Hirst, V.K., Calvert, A.S., Johns, H., 1996. Carbogen and nicotinamide as radiosensitizers in a murine mammary carcinoma using conventional and accelerated radiotherapy. *International Journal of Radiation Oncology Biology Physics*, 34(2), pp.357–365.

Ross, T.L., Ermert, J., Hocke, C., Coenen, H.H., 2007. Nucleophilic ¹⁸F-fluorination of heteroaromatic iodonium salts with no-carrier-added [¹⁸F]fluoride. *Journal of American Chemical Society*, 129(25), pp.8018–8025.

Roth, J., Peer, C.J., Mannargudi, B., Swaisland, H., Lee, J., Kohn, E.C., *et al.*, 2014. A sensitive and robust ultra HPLC assay with tandem mass spectrometric detection for the quantification of the PARP inhibitor olaparib (AZD2281) in human plasma for pharmacokinetic application. *Chromatography*, 1(2), pp.82–95.

Rottenberg, S., Jaspers, J.E., Karsbergen, A., Burg, E., Nygren, A.O., Zander, S.A., *et al.*, 2008. High sensitivity of BRCA1-deficient mammary tumors to the PARP inhibitor AZD2281 alone and in combination with platinum drugs. *Proceedings of the National Academy of Science of the United States of America*, 105(44), pp.17079–17084.

Rudebusch, G.E., Zakharov, L.N., Liu, S., 2013. Rhodium-catalysed boron arylation of 1,2-azaborines. *Angewandte Chemie International Edition*, 52(35), pp.9316–9319.

Ruf, A., de Murcia, J.E., de Murcia, G.M., Schulz, G.E., 1996. Structure of the catalytic fragment of poly(ADP-ribose) polymerase from chicken. *Proceedings of the National Academy of Sciences of the United States of America*, 93(15), pp.7481–7485.

Ruf, A., de Murcia, G., Schulz, G.E., 1998. Inhibitor and NAD⁺ binding of poly(ADP-ribose) polymerase as derived from crystal structures and homology modelling. *Biochemistry*, 37(11), pp.3893–3900.

Russell, W.M., Burch, R.L., 1959. *The principles of humane experimental technique* [e-book]. London: Methuen. Available at: AltWeb http://altweb.jhsph.edu/pubs/books/humane_exp/het-toc [Accessed 20 March 2016].

Sage, M.R., Wilson, A.J., 1994. The blood-brain barrier: an important concept in neuroimaging. *American Journal of Neuroradiology*, 15(4), pp.601–622.

Salber, D., Stoffels, G., Pauliet, D., Oros-Peusquens, A., Shah, N.J., Klauth, P., *et al.*, 2007. Differential uptake of O-(2-¹⁸F-fluoroethyl)-L-tyrosine, L-³H-methionine, and ³H-deoxyglucose in brain abscesses. *Journal of Nuclear Medicine*, 48(12), pp.2056–2062.

Salinas, B., Irwin, C.P., Kossatz, S., Bolaender, A., Chiosis, G., Pillarsetty, N., *et al.*, 2015. Radioiodinated PARP1 tracers for glioblastoma imaging. *EJNMMI Research*, 5(46), doi:10.1186/s13550-015-0123-1.

Salvadori, P.A., 2008. Radiopharmaceuticals, drug development and pharmaceutical regulation in Europe. *Current Radiopharmaceuticals*, 1(1), pp.7–11.

Salvi, A., Carrupt, P., Mayer, J.M., Testa, B., 1997. Esterase-like activity of human serum albumin toward prodrug esters of nicotinic acid. *Drug Metabolism and Disposition*, 25(4), pp.395–398.

Samol, J., Ranson, M., Scott, E., Macpherson, E., Carmichael, J., Thomas, A., *et al.*, 2012. Safety and tolerability of the poly(ADP-ribose) polymerase (PARP) inhibitor, olaparib (AZD2281) in combination with topotecan for the treatment of patients with advanced solid tumors: a phase I study. *Investigational New Drugs*, 30(4), pp.1493–1500.

Sandhu, S.K., Schelman, W.R., Wilding, G., Moreno, V., Barid, R.D., Miranda, S., *et al.*, 2013. The poly(ADP-ribose) polymerase inhibitor niraparib (MK4827) in BRCA mutation carriers and patients with sporadic cancer: a phase 1 dose-escalation trial. *The Lancet Oncology*, 14(9), pp.882–892.

Sánchez, F., Orero, A., Soriano, A., Correncher, C., Conde, P., González, A., *et al.*, 2013. ALBIRA: a small animal PET/SPECT/CT imaging system [abstract]. *Medical Physics*, 40(5), 051906.

Schifter, T., Hoffman, J.M., Hanson, M.W., Boyko, O.B., Beam, C., Paine, S., *et al.*, 1993. Serial FDG-PET studies in the prediction of survival in patients with primary brain tumors. *Journal of Computer Assisted Tomography*, 17(4), pp.509–516.

Schmidt, K.C., Smith, C.B., 2005. Resolution, sensitivity and precision with autoradiography and small animal positron emission tomography: implications for functional brain imaging in animal research. *Nuclear Medicine and Biology*, 32(7), pp.719–725.

Schnell, U., Dijk, F., Sjollem, K.A., Giepmans, B.N., 2012. Immunolabeling artifacts and the need for live-cell imaging. *Nature methods*, 9(2), pp.152–158.

Schoemaker, H., Morelli, M., Deshmukh, P., Yamamura, H.I., 1982. [³H]Ro5-4864 benzodiazepine binding in the kainite lesioned striatum and Huntington's diseased basal ganglia. *Brain Research*, 248(2), pp.396–401.

Schreiber, V., Amé, J., Dollé, P., Schultz, I., Rinaldi, B., Fraulob, V., *et al.*, 2002. Poly(ADP-ribose) polymerase-2 (PARP-2) is required for efficient base excision DNA repair in association with PARP-1 and XRCC1. *The Journal of Biological Chemistry*, 277(25), pp.23028–23036.

Schwartzbaum, J.A., Fisher, J.L., Aldape, K.D., Wrensch, M., 2006. Epidemiology and molecular pathology of glioma. *Nature Clinical Practice Neurology*, 2(9), pp.494–503.

Scott, M.T., Sinsheimer, J.E., 1983. *In vitro* dehalogenation of *para*-substituted aromatic halides in rat liver preparations. *Journal of Pharmaceutical Sciences*, 73(8), pp.1101–1104.

Seevers, R.H., Counsell, R.E., 1982. Radioiodination techniques for small organic molecules. *Chemical Reviews*, 82(6), pp.575–590.

Selvaraj, V., Stocco, D.G., 2015. The changing landscape in translocator protein (TSPO) function. *Trends in Endocrinology and Metabolism*, 26(7), pp.341–348.

Senra, J.M., Telfer, B.A., Cherry, K.E., McCrudden, C.M., Hirst, D.G., O'Connor, M.J., *et al.*, 2011. Inhibition of PARP-1 by olaparib (AZD2281) increases the radiosensitivity of a lung tumor xenograft. *Molecular Cancer Therapeutics*, 10(10), pp.1949–1958.

Shah, F., Hume, S.P., Pike, V.W., Ashworth, S., McDermott, J., 1994. Synthesis of the enantiomers of [*N*-methyl-¹¹C]PK 11195 and comparison of their behaviours as radioligands for PK binding sites in rats. *Nuclear Medicine and Biology*, 21(4), pp.573–581.

Shall, S., 1975. Experimental manipulation of the specific activity of poly(ADP-ribose) polymerase. *Journal of Biochemistry*, 77(1), p.2.

Sharma, R., Aboagye, E., 2011. Development of radiotracers for oncology - the interface with pharmacology. *British Journal of Pharmacology*, 163(8), pp.1565–1585.

Shieh, W.M., Amé, J., Wilson, M.V., Wang, Z., Koh, D.W., Jacobson, M.K., *et al.*, 1998. Poly(ADP-ribose) polymerase null mouse cells synthesize ADP-ribose polymers. *The Journal of Biological Chemistry*, 273(46), pp.30069–30072.

Shitara, Y., Horie, T., Sugiyama, Y., 2005. Transporters as a determinant of drug clearance and tissue distribution. *European Journal of Pharmaceutical Sciences*, 27(5), pp.425–446.

Siddiqui, M.R., AlOthman, Z.A., Rahman, N., 2013. Analytical techniques in pharmaceutical analysis: a review. *Arabian Journal of Chemistry*, ahead of print, doi:10.1016/j.arabjc.2013.04.016.

Šileikyte, J., Blachy-Dyson, E., Sewell, R., Carpi, A., Menabò, R., Lisa, F.D., 2014. Regulation of the mitochondrial permeability transition pore by the outer membrane does not involve the peripheral benzodiazepine receptor (translocator protein of 18 kDa (TSPO)). *The Journal of Biological Chemistry*, 289(20), pp.13769–13781.

Singh, S.K., Hawkins, C., Clarke, I.D., Squire, J.A., Bayani, J., Hide, T., *et al.*, 2004. Identification of human brain tumour initiating cells. *Nature*, 432(7015), pp.396–401.

Skalitzky, D.J., Marakovits, J.T., Maegley, K.A., Ekker, A., Yu, X., Hostomsky, Z., *et al.*, 2003. Tricyclic benzimidazoles as potent poly(ADP-ribose) polymerase-1 inhibitors. *Journal of Medicinal Chemistry*, 46(2), pp.210–213.

Sluiter, W., Oomens, L.W., Brand, A., Furth, R.V., 1984. Determination of blood volume in the mouse with ⁵¹chromium-labelled erythrocytes. *Journal of Immunological Methods*, 73(1), pp.221–225.

Smith, D.A., Di, L., Kerns, E.H., 2010. The effect of plasma protein binding on *in vivo* efficacy: misconceptions in drug discovery. *Nature Reviews Drug Discovery*, 9(12), pp.929–939.

Soars, M.G., Gelboin, H.V., Krausz, K.W., Riley, R.J., 2003. A comparison of relative abundance, activity factor and inhibitory monoclonal antibody approaches in the characterization of human CYP enzymology. *British Journal of Clinical Pharmacology*, 55(2), pp.175–181.

Spaeth, N., Wyss, M.T., Weber, B., Scheidegger, S., Lutz, A., Verwey, J., *et al.*, 2004. Uptake of ¹⁸F-fluorocholine, ¹⁸F-fluoroethyl-L-tyrosine, and ¹⁸F-FDG in acute cerebral radiation injury in the rat: implications for separation of radiation necrosis from tumor recurrence. *Journal of Nuclear Medicine*, 45(11), pp.1931–1938.

Sparidans, R.W., Martens, I., Valkenburg-van Iersel, L.B., den Hartigh, J., Schellens, J.H., Beijnen, J.H., 2011. Liquid chromatography-tandem mass spectrometric assay for the PARP-1 inhibitor olaparib in combination with the nitrogen mustard melphalan in human plasma. *Journal of Chromatography B*, 879(21), pp.1851–1856.

Starosta-Rubinstein, S., Ciliax, B.J., Penney, J.B., McKeever, P., Young, A.B., 1987. Imaging of a glioma using peripheral benzodiazepine receptor ligands. *Proceedings of the National Academy of Sciences of the United States of America*, 84(3), pp.891–895.

Ström, C.E., Johansson, F., Uhlén, M., Szigartyo, C.A., Erixon, K., Helleday, T., 2011. Poly (ADP-ribose) polymerase (PARP) is not involved in base excision repair

but PARP inhibition traps a single-strand intermediate. *Nucleic Acids Research*, 39(8), pp.3166–3175.

Stupp, R., Hegi, M.E., Mason, W.P., Bent, M.J., Taphoorn, M.J., Janzer, R.C., *et al.*, 2009. Effects of radiotherapy with concomitant and adjuvant temozolomide versus radiotherapy alone on survival in glioblastoma in a randomised phase III study: 5-year analysis of the EORTC-NCIC trial. *The Lancet Oncology*, 10(5), pp.459–466.

Su, Z., Roncaroli, F., Durrenberger, P.F., Coope, D.J., Karabatsou, K., Hinz, R., *et al.*, 2015. The 18-kDa mitochondrial translocator protein in human gliomas: an ¹¹C-(R)PK11195 PET imaging and neuropathology study. *Journal of Nuclear Medicine*, 56(4), pp.512–517.

Takata, M., Sasaki, M.S., Sonoda, E., Morrison, C., Hashimoto, M., Utsumi, H., *et al.*, 1998. Homologous recombination and non-homologous end-joining pathways of DNA double-strand break repair have overlapping roles in the maintenance of chromosomal integrity in vertebrate cells. *The EMBO Journal*, 17(18), pp.5497–5508.

Tang, W., Lu, A.Y., 2010. Metabolic bioactivation and drug-related adverse effects: current status and future directions from a pharmaceutical research perspective. *Drug Metabolism Reviews*, 42(2), pp.225–249.

Tavares, A.A., Jobson, N.A., Dewar, D., Sutherland, A., Pimlott, S., 2011. ¹²³I-NKJ64: a novel single photon emission computed tomography radiotracer for imaging the noradrenaline transported in brain. *Synapse*, 65(7), pp.658–667.

Tavares, A.A., Lewsey, J., Dewar, D., Pimlott, S., 2012. Radiotracer properties by high performance liquid chromatography: a potential tool for brain radiotracer discovery. *Nuclear Medicine and Biology*, 39(1), pp.127–135.

Taylor, L.P., 2010. Diagnosis, treatment, and prognosis of glioma. *Neurology*, 75(18), S28–S32.

Tentori, L., Leonetti, C., Scarsella, M., D'Amati, G., Portarena, I., Zupi, G., *et al.*, 2002. Combined treatment with temozolomide and poly(ADP-ribose) polymerase inhibitor enhances survival of mice bearing hematologic malignancy at the central nervous system site. *Blood*, 99(6), pp.2241–2244.

Tentori, L., Leonetti, C., Scarsella, M., D'Amati, G., Vergati, M., Portarena, I., *et al.*, 2003. Systemic administration of GPI 15427, a novel poly(ADP-ribose) polymerase-1 inhibitor, increases the antitumor activity of temozolomide against intracranial melanoma, glioma, lymphoma. *Clinical Cancer Research*, 9(14), pp.5370–5379.

Tentori, L., Portarena, I., Torino, F., Scerrati, M., Navarra, P., Graziani, G., *et al.*, 2002. Poly(ADP-ribose) polymerase inhibitor increases growth inhibition and reduces G₂/M cell accumulation induced by temozolomide in malignant glioma cells. *Glia*, 40(1), pp.45–54.

Tentori, L., Ricci-Vitiani, L., Muzi, A., Ciccarone, F., Pelacchi, F., Calabrese, R., 2014. Pharmacological inhibition of poly(ADP-ribose) polymerase-1 modulates resistance of human glioblastoma stem cells to temozolomide. *BMC Cancer*, 14, p.151.

Testa, B., Crivori, P., Reist, M., Carrupt, P., 2000. The influence of lipophilicity on the pharmacokinetic behaviour of drugs: concepts and examples. *Perspectives in Drug Discovery and Design*, 19(1), pp.179–211.

Thackaberry, E.A., Wang, X., Schweiger, M., Messick, K., Valle, N., Dean, B., *et al.*, 2014. Solvent-based formulations for intravenous mouse pharmacokinetic studies: tolerability and recommended solvent dose limits. *Xenobiotica: the fate of foreign compounds in biological systems*, 44(3), pp.235–241.

The Human Protein Atlas [online], 2015. Available at: <http://www.proteinatlas.org/> [Accessed 20 March 2016].

Thomas, H.D., Calabrese, C.R., Batey, M.A., Canan, S., Hostomsky, Z., Kyle, S., *et al.*, 2007. Preclinical selection of a novel poly(ADP-ribose) polymerase inhibitor for clinical trial. *Molecular Cancer Therapeutics*, 6(3), pp.945–956.

Tipre, D.N., Zoghbi, S.S., Liow, J., Green, M.V., Seidel, J., Ichise, M., 2006. PET imaging of brain 5-HT_{1A} receptors in rat in vivo with ¹⁸F-FCWAY and improvement by successful inhibition of radioligand defluorination with miconazole. *The Journal of Nuclear Medicine*, 47(2), pp.345–353.

Tu, Z., Chu, W., Zhang, J., Dence, C.S., Welch, M.J., Mach, R.H., 2005. Synthesis and in vivo evaluation of [¹¹C]PJ34, a potent radiotracer for imaging the role of PARP-1 in necrosis. *Nuclear Medicine and Biology*, 32(5), pp.437–443.

Tu, L.N., Morohaku, K., Manna, P.R., Pelton, S.H., Butler, W.R., Stocco, D.M., *et al.*, 2014. Peripheral benzodiazepine receptor/translocator protein global knock-out mice are viable with no effects on steroid hormone biosynthesis. *The Journal of Biological Chemistry*, 289(40), pp.27444–27454.

Tu, L.N., Zhao, A.H., Stocco, D.M., Selvaraj, V., 2015. PK11195 effects on steroidogenesis is not mediated through the translocator protein (TSPO). *Endocrinology*, 156(3), pp.1033–1039.

Uchôa, F.D., Cattani, V.B., Lima, M.C., Galdino, S.L., Pitta, I.R., Costa, T.D., 2008. Development and application of LC-UV method for the quantification of the anti-inflammatory thiazolidinone PG15 in rat plasma. *Journal of the Brazilian Chemical Society*, 19(8), pp.1553–1559.

Vajkoczy, P., Menger, M.D., 2000. Vascular microenvironment in gliomas. *Journal of Neuro-Oncology*, 50(1–2), pp.99–108.

Valeur, E., Bradley, M., 2009. Amide bond formation: beyond the myth of coupling reagents. *Chemical Society Reviews*, 38(2), pp.606–631.

Valkó, K., 2004. Application of high-performance liquid chromatography based measurements of lipophilicity to model biological distribution. *Journal of Chromatography A*, 1037(1–2), pp.299–310.

Valkó, K., Bevan, C., Reynolds, D., 1997. Chromatographic hydrophobicity index by fast-gradient RP-HPLC: a high-throughput alternative to log P/log D. *Analytical Chemistry*, 69(11), pp.2022–2029.

Valkó, K., Nunhuck, S., Bevan, C., Abraham, M.H., Reynolds, D.P., 2003. Fast gradient HPLC method to determine compounds binding to human serum albumin. Relationships with octanol/water and immobilized artificial membrane lipophilicity. *Journal of Pharmaceutical Sciences*, 91(11), pp.2236–2248.

VanBrocklin, H.F., 2010. The radiotracer approval bottleneck: improving the flow through the pipeline. *The Clinical Trials Network Newsletter*, 1(3).

van de Waterbeemd, H., Camenisch, G., Folkers, G., Chretien, J.R., Raevsky, O.A., 1998. Estimation of blood-brain barrier crossing of drugs using molecular size and shape, and H-bonding descriptors. *Journal of Drug Targeting*, 6(2), pp.151–165.

van de Waterbeemd, H., Smith, D.A., Beaumont, K., Walker, D.K., 2001. Property-based design: optimization of drug absorption and pharmacokinetics. *Journal of Medicinal Chemistry*, 44(9), pp.1313–1333.

Vemula, V.R., Lagishetty, V., Lingala, S., 2010. Solubility enhancement techniques. *International Journal of Pharmaceutical Sciences Review and Research*, 5(1), pp.41–51.

Verhaak, R.G., Hoadley, K.A., Purdom, E., Wang, V., Qi, Y., Wilkerson, M.D., *et al.*, 2010. An integrated genomic analysis identifies clinically relevant subtypes of glioblastoma characterized by abnormalities in PDGFRA, IDH1, EGFR and NF1. *Cancer Cell*, 17(1), pp.98–110.

Visvader, J.E., Lindeman, G.J., 2008. Cancer stem cells in solid tumours: accumulating evidence and unresolved questions. *Nature Reviews Cancer*, 8(10), pp.755–768.

Vivash, L., O'Brien, T.J., 2015. Imaging microglial activation with TSPO PET: lighting up neurological diseases? *Journal of Nuclear Medicine*, 57(2), pp.165–168.

Wadsworth, W.S., Emmons, W.D., 1961. The utility of phosphate carbanions in olefin synthesis. *Journal of the American Chemistry Society*, 83(7), pp.1733–1738.

Waerzeggers, Y., Ullrich, R.T., Monfared, P., Viel, T., Weckesser, M., Stummer, W., *et al.*, 2011. Specific biomarkers of receptors, pathways of inhibition and targeted therapies: clinical applications. *The British Journal of Radiology*, 84(Spec Iss 2), S179–195.

Wager, K.M., Jones, G.B., 2010. Radio-iodination methods for the production of SPECT imaging agents. *Current Radiopharmaceuticals*, 3(1), pp.37–45.

Walsky, R.L., Obach, R.S., 2004. Validated assay for human cytochrome P450 activities. *Drug Metabolism and Disposition*, 32(6), pp.647–660.

Wang, X., D'Andrea, A.D., 2004. The interplay of Fanconi anemia proteins in the DNA damage response. *DNA Repair*, 3(8–9), pp.1063–1069.

Wang, J., Liang, Y., Qu, J., 2009. Boiling water-catalyzed neutral and selective *N*-Boc deprotection. *Chemical Communications*, 2009(34), pp.5144–5146.

Wang, Z., Wang, F., Tang, T., Guo, C., 2012. The role of PARP-1 in the DNA damage response and its application in tumor therapy. *Frontiers of Medicine*, 6(2), pp.156–164.

Watabe, H., Ikoma, Y., Kimura, Y., Naganawa, M., Shidahara, M., 2006. PET kinetic analysis - compartmental model. *Annals of Nuclear Medicine*, 20(9), pp.583–588.

Wedge, S.R., Porteous, J.K., Newlands, E.S., 1996. 3-Aminobenzamide and/or *O*⁶-benzylguanine evaluated as an adjuvant to temozolomide or BCNU treatment in cell lines of variable mismatch repair status and *O*⁶-alkylguanine-DNA alkyltransferase activity. *British Journal of Cancer*, 74(7), pp.1030–1036.

Wehrstedt, K.D., Wandrey, P.A., Heitkamp, D., 2005. Explosive properties of 1-hydroxybenzotriazoles. *Journal of Hazardous Materials*, 126(1–3), pp.1–7.

Weissman, B.A., Raveh, L., 2003. Peripheral benzodiazepine receptors: on mice and human brain imaging. *Journal of Neurochemistry*, 84(3), pp.432–437.

Wharton, S.B., McNelis, U., Bell, H.S., Whittle, I.R., 2000. Expression of poly(ADP-ribose) polymerase and distribution of poly(ADP-ribosylation) in glioblastoma and in glioma multicellular tumour spheroid model. *Neuropathology and Applied Neurobiology*, 26(6), pp.528–535.

White, A.X., Almassy, R., Calvert, H., Curtin, N.J., Griffin, R.J., Hostomsky, Z., *et al.*, 2000. Resistance-modifying agents. 9. Synthesis and biological properties of benzimidazole inhibitors of the DNA repair enzyme poly(ADP-ribose) polymerase. *Journal of Medicinal Chemistry*, 43(22), pp.4084–4097.

Winkeler, A., Boisgard, R., Awde, A.R., Dubois, A., Thézé, B., Zheng, J., *et al.*, 2012. The translocator protein ligand [¹⁸F]DPA-714 images glioma and activated microglia in vivo. *European Journal of Nuclear Medicine and Molecular Imaging*, 39(5), pp.811–823.

Wolburg, H., Noell, S., Fallier-Becker, P., Mack, A.F., Wolburg-Buchholz, K., 2012. The disrupted blood-brain barrier in human glioblastoma. *Molecular Aspects of Medicine*, 33(5–6), pp.579–589.

Wu, C., Li, F., Niu, G., Chen, X., 2013. PET imaging of inflammation biomarkers. *Theranostics*, 3(7), pp.448–466.

Xu, C., Li, C.Y., Kong, A.T., 2005. Induction of phase I, II and III drug metabolism/transport by xenobiotics. *Archives of Pharmacal Research*, 28(3), pp.249–268.

Xu, R., Zanolri-Fregonara, P., Zoghbi, S.S., Gladding, R.L., Woock, A.E., Innis, R.B., 2013. Synthesis and evaluation in monkey of [¹⁸F]4-fluoro-*N*-methyl-*N*-(4-(6-(methylamino)pyrimidin-4-yl)thiazol-2-yl)benzamide ([¹⁸F]FIMX): a promising radioligand for PET imaging of brain metabotropic glutamate receptor 1 (mGluR1). *Journal of Medicinal Chemistry*, 56(22), pp.9146–9155.

Yamamoto, N., Nokihara, H., Yamada, Y., Goto, Y., Tanioka, M., Shibata, T., *et al.*, 2012. A phase I, dose-finding and pharmacokinetic study of olaparib (AZD2281) in Japanese patients with advanced solid tumors. *Cancer Science*, 103(3), pp.504–509.

Yamasaki, T., Fujinaga, M., Yoshida, Y., Kumata, K., Yui, J., Kawamura, K., *et al.*, 2011. Radiosynthesis and preliminary evaluation of 4-[¹⁸F]fluoro-*N*-[4-[6-(isopropylamino)pyrimidin-4-yl]-1,3-thiazol-2-yl]-*N*-methylbenzamide as a new positron emission tomography ligand for metabotropic glutamate receptor subtype 1. *Bioorganic and Medicinal Chemistry Letters*, 21(10), pp.2998–3001.

Ye, N., Chen, C., Chen, T., Song, Z., He, J., Huan, X., *et al.*, 2013. Design, synthesis, and biological evaluation of a series of benzo[*de*][1,7]naphthyridin-7(8*H*)-ones bearing functionalized longer chain appendage as novel PARP1 inhibitors. *Journal of Medicinal Chemistry*, 56(7), pp.2885–2903.

Young, R.C., Mitchell, R.C., Brown, T.H., Ganellin, R., Griffiths, R., Jones, M., 1988. Development of a new physicochemical model for brain penetration and its application to the design of centrally acting H₂ receptor histamine antagonists. *Journal of Medicinal Chemistry*, 31(3), pp.656–671.

Yuan, X., Curtin, J., Xiong, Y., Liu, G., Waschsmann-Hogiu, S., Farkas, D.L., *et al.*, 2004. Isolation of cancer stem cells from adult glioblastoma multiforme. *Oncogene*, 23(58), pp.9392–9400.

Yuan, S.F., Lee, S., Chen, G., Song, M., Tomlinson, G.E., Lee, E.Y., 1999. BRCA2 is required for ionizing radiation-induced assembly of Rad51 complex *in vivo*. *Cancer Research*, 59(15), pp.3547–3551.

Zaidi, H., Hasegawa, B.H., 2006. Attenuation correction strategies in emission tomography. In: H. Zaidi, ed. 2006. *Quantitative analysis in nuclear medicine imaging*. New York: Springer. pp.167–204.

Zanotti-Fregonara, P., Zhang, Y., Jenko, K.J., Gladding, R.L., Zoghbi, S.S., Fujita, M., *et al.*, 2014. Synthesis and evaluation of translocator 18 kDa protein (TSPO) positron emission tomography (PET) radioligands with low binding sensitivity to human single nucleotide polymorphism rs6971. *ACS Chemical Neuroscience*, 5(10), pp.963–971.

Zhang, M., Maeda, J., Ito, T., Okauchi, T., Ogawa, M., Noguchi, J., *et al.*, 2005. Synthesis and evaluation of *N*-(5-fluoro-2-phenoxyphenyl)-*N*-(2-[¹⁸F]fluoromethoxy-*d*₂-5-methoxybenzyl)acetamide: a deuterium-substituted radioligand for peripheral benzodiazepine receptor. *Bioorganic and Medicinal Chemistry*, 13(5), pp.1811–1818.

Zheng, Q., Mock, B.H., 2005. Purification of carbon-11 PET radiotracers from unlabelled precursors by preparative HPLC and SPE. *Biomedical Chromatography*, 19(9), pp.671–676.

Zhou, D., Chu, W., Xu, J., Jones, L.A., Peng, X., Li, S., *et al.*, 2014. Synthesis, [¹⁸F] radiolabelling, and evaluation of poly (ADP-ribose) polymerase-1 (PARP-1) inhibitors for *in vivo* imaging of PARP-1 using positron emission tomography. *Bioorganic and Medicinal Chemistry*, 22(5), pp.1700–1707.

Zhu, G., Gandhi, V.B., Gong, J., Thomas, S., Luo, Y., Liu, X., *et al.*, 2008. Synthesis and SAR of novel, potent and orally bioavailable benzimidazole inhibitors of poly(ADP-ribose) polymerase (PARP) with a quaternary methylene-amino substituent. *Bioorganic and Medicinal Chemistry Letters*, 18(14), pp.3955–3958.

Zietman, A.L., Suit, H.D., Ramsay, J.R., Silobrcic, V., Sedlacek, R.S., 1988. Quantitative studies on the transplantability of murine and human tumors into the brain and subcutaneous tissues of NCr/Sed nude mice. *Cancer Research*, 48(22), pp.6510–6516.

Zmuda, F., Malviya, G., Blair, A., Boyd, M., Chalmers, A.J., Sutherland, A., 2015. Synthesis and evaluation of a radioiodinated tracer with specificity for poly(ADP-ribose) polymerase-1 (PARP-1) *in vivo*. *Journal of Medicinal Chemistry*, 58(21), pp.8683–8693.

Żwir-Ferenc, A., Biziuk, M., 2006. Solid phase extraction technique - trends, opportunities and applications. *Polish Journal of Environmental Studies*, 15(5), pp.677–690.